

Production and operation in the HOR Experimental Activation Loop

An applied numerical study on several aspects of the production of radioisotopes within the HOR Experimental Activation Loop

M. Boéré

Delft University of Technology
Faculty of Applied Sciences
Department of Radiation Science Technology
Transport Phenomena in Nuclear Applications



Production and operation in the HOR Experimental Activation Loop

An applied numerical study on several aspects of the
production of radioisotopes within the HOR
Experimental Activation Loop

by

M. Boeré

to obtain the degree of Master of Science
at the Delft University of Technology,
to be defended publicly on Wednesday July 13, 2022 at 13:00.

Student number: 5169747
Project duration: September 6, 2021 – July 3, 2022
Thesis committee: Dr. ir. M. Rohde, TU Delft, supervisor
Dr. T.E. Burdyny, TU Delft
Dr.ir. R.M. de Kruijff, TU Delft

An electronic version of this thesis is available at <http://repository.tudelft.nl/>.

Acknowledgements

In the last year I've had the pleasure to work on advancing knowledge on many different aspects of the HOR Experimental Activation Loop. This work wouldn't have been possible without the help of the people around me and therefore I would like to show my gratitude to some people.

I would like to thank my supervisor dr. ir. Martin Rohde for allowing me to work on this extensive and challenging project. The final weeks of the project have been difficult for me and allowing the space and time to finish my thesis helped me a lot for which I'm very thankful for.

Secondly, I would like to thank Wout Schenk for helping me understand important chemical aspects and for the few discussions we've had on the HOR Experimental Activation Loop which helped me understand the system further.

My thanks also goes to the members of the Transport Phenomena in Nuclear Applications group for sharing their interesting projects and insights in the weekly meetings.

Last but definitely not least, I would like to thank my family in helping me mentally push the project forward and finishing this project.

*M. Boéré
Delft, June 2022*

Abstract

The HOR Experimental Activation Loop, also known as its abbreviation HEAL, is a vessel for the production of radioisotopes that is to be placed next to the nuclear Hoger Onderwijs Reactor in Delft. The proposed vessel utilizes neutrons coming from the reactor for neutron activation reactions with a target isotope to produce radioisotopes for the use in medical applications. The target isotope in this case would be dissolved in water forming a target solution.

The geometry of the HEAL vessel consists of a circular pipe forming loop and would be vertically placed within a nearby beam tube. Utilizing the vertical placement and heat- and cooling the target solution in different sections of the loop a buoyancy driven flow is generated. The energy required for the heating of the target solution is generated within the wall material of the HEAL from energy deposition from gamma radiation originating from the nearby reactor. The required cooling capacity is provided by water that is present in the beam tube where the HEAL is placed in and by utilizing different wall thicknesses or wall materials in specific heating/cooling sections of the loop.

The first item of this thesis provides an expansion on a previous model that numerically approaching the velocity of the target solution and the temperatures of both the solution and wall materials to include axial and radial heat conduction. With this improved model an extensive analysis was made of the influence of different variables of the HEAL to aid in the further design. These variables included the wall thickness, inner radius, pipe angle, system length and various wall materials and combinations with aluminium, zirconium and lead. The results show that there is a large range of variables that can provide a design for the HEAL within safe temperature limits that provide a velocity within the system. The results also contain an extensive database of the effects which can be used to estimate the effect of certain design changes.

The second item of this thesis focusses on the gamma and neutron shielding capabilities of the HEAL that is provided by the wall materials and wall thicknesses of the geometry. Both the radial energy deposition within the wall as well as the dose rate received to the target solution were analyzed using the monte-carlo particle transport software Serpent. For this the geometry of the HEAL with different wall thicknesses and wall materials of aluminium, zirconium and lead were generated. The results of this analysis show that the energy deposition is very much dependent the wall material that is used. Generally lead systems provide the largest gamma energy deposition rates. As a result of the large gamma cross section of lead a very significant, almost exponential, drop in the deposition rate over the radius was found. A similar profile was shown with zirconium walls while systems with aluminium walls only showed a linear drop in the energy deposition over the radius, similar to that over the target solution within the loop. The dose rates from gamma radiation received by the target solution showed the largest drop in systems made from lead, dropping further as the wall thickness increased. A smaller drop was seen with zirconium following its lower gamma cross section. Aluminium systems did not show any drop in dose rate at any wall thickness showing the inability of aluminium to shield the target solution from gamma radiation. Shielding to neutrons by the different materials were shown to be relatively similar in terms of the drop in the neutron flux reaching the target solution over the wall thickness of the loop.

Thirdly this thesis focusses on the control of the target solution flow and the residence time distribution present within different sections of the loop in different geometries. This was performed by utilizing the CFD software OpenFOAM with its buoyantBoussinesqPimpleFOAM solver to approach the velocity field and the scalarTransportFoam the transport of target solution from a pulse input present inside certain loop geometries at different in- and outlet flow rates. The residence time distribution curves received from the CFD simulations showed large difference in shape and forms at different flow rate and geometries suggesting significantly different velocity fields present. The overall dimensionless variance was higher in systems with larger inner radii showing a larger dispersion in these systems. The residence time distributions were also modelled using a combination of the Tanks-In-Series and compartment model which showed a general good overlap of the data. These models of different sections were attached to form a complete loop inside a dynamic HEAL model which numerically simulates each tank in series from which a system flush was performed showing

insignificant differences between large and small variance systems in terms of flushing performance.

The final part of the thesis is on the production of the radioisotope Lu-177 by neutron capture reaction of naturally enriched Lu-176 and utilization of the Szilard-Chalmers effect to increase the specific activity of the product was explored within the HEAL. For this an interaction rate model including the chemical, neutron, gamma and decay rates was set up. The model includes the present components where the DOTA molecule was used as a chelator in combination with naturally enriched lutetium. The model was coupled to the dynamic HEAL model in which the production of Lu-177 with different radiolysis cross sections of the complexed DOTA molecules were analysed for both a batch and continuous operation of the HEAL. The analysis showed the very large effect on the specific activity of the product from the different cross sections, and therefore importance of shielding of the loop. It also showed that with continuous operation the maximum specific activity that is reached will be lower than with batch operation of the HEAL.

Acronyms

ACRR Annular Core Research Reactor
BDF Backwards Differentiation Formula
CAD Computer aided design
CFD Computational Fluid Dynamics
CSTR Continuously Stirred Reactor
DOTA Dodecane Tetraacetic Acid
HEAL HOR Experimental Activation Loop
HFR Hoge Flux Reactor
HOR Hoger Onderwijs Reactor
MCNP Monte Carlo N-Particle Transport Code
PFR Plug Flow Reactor
RTD Residence Time Distribution

Glossary

- Chelator** Water soluble ligand which can form a stable bond to metal ions via chelation
- DLDR** Beam tube next to the Hoger Onderwijs Reactor
- enrichment** The process of purifying specific isotopes of an element
- Fusion360** 3D CAD modeling software developed by AutoDesk
- lanthanides** A group of elements between atomic number 57 and 71 (lanthanum and lutetium)
- natural abundance** The isotopic composition of an element generally seen within the crust of the earth
- ODEPACK** ODEPACK is a collection of solvers for initial value problems for systems of ordinary differential equations
- OpenFOAM** Open source computational fluid dynamic software developed primarily by OpenCFD
- Serpent** Monte Carlo based particle transport code developed at the VTT Technical Research Centre of Finland
- Szilard-Chalmers effect** Effect that breaks the chemical bond of an isotope within a molecule from the recoil of gamma rays after a neutron activation interaction
- Target** Isotopic material that is irradiated to produce a specific radioisotope
- Target solution** The solution flowing through the HEAL in which the target is dissolved

Symbols

A	Contact area	[m ²]
a	Mean age of components at a point in space	[s]
$A(t)$	Activity	[Bq or GBq]
$A_{i,ax}$	Axial cross sectional contact area in radial section i of a cylinder	[m ²]
$A_{i,lm}$	Logarithmic mean radial contact area in radial section i of a cylinder	[m ²]
$A_{i,rad}$	Outer radial contact area in radial section i of a cylinder	[m ²]
α	Thermal diffusivity	[m ² s ⁻¹]
α	Mean age of component at a point in space	[s]
$\bar{\alpha}$	Average age of components in flow	[s]
B	Buoyancy force	[N]
β	Thermal expansion coefficient	[K ⁻¹]
C	Concentration	[molL ⁻¹]
c	Speed of light	[m s ⁻¹]
C_ρ	Heat capacity	[Jkg ⁻¹ K ⁻¹]
$C_{\rho n,m}$	Heat capacity of node (n, m)	[Jkg ⁻¹ K ⁻¹]
D	Dose	[Gy]
ΔT	Temperature difference	[K]
\bar{t}_Θ	Dimensionless mean residence time	[-]
σ_Θ^2	Dimensionless variance RTD curve	[-]
$dr_{n,m}$	Wall thickness in node (n, m)	[m]
dr_{sec}	Wall thickness in section(s) sec	[-]
E_γ	Energy of gamma ray	[eV]
E_{recoil}	Recoil energy	[eV]
η	Dynamic viscosity	[m ⁻¹ s ⁻¹]
$\bar{\epsilon}$	Imparted energy	[J]
F	Mass feed rate	[kg s ⁻¹]
F_D	Darcy friction	[-]
F_{D_n}	Darcy friction in node n	[-]
$Frac$	Section 2 length fraction	[-]
g	Gravitational constant	[Nm ² /kg ²]
Gr	Grashof number	[-]
h	Heat transfer coefficient	[W m ⁻² K ⁻¹]
h_i	Heat transfer coefficient of radial section i of a cylinder	[W m ⁻² K ⁻¹]
I	Intensity	[-]
K_w	Friction coefficient for bends	[-]
κ	Thermal conductivity	[W m ⁻¹ K ⁻¹]
L	Length of the HEAL	[m]
l	Length of a section of the HEAL	[m]
$l_{n,m}$	Length of a section of the node (n, m)	[m]
λ	Decay constant	[s ⁻¹]
M	Number of radial nodes	[-]
m_{prod}	Product mass	[kg or mg]
μ	Attenuation coefficient	[cm ⁻¹]
N	Number of axial nodes	[-]
n	Number density	[m ³ or cm ³]
ν	Kinematic viscosity	[m s ⁻²]
P	Heat generation	[-]
ϕ	Heat transfer rate	[W]
$\phi_{n,m}$	Heat transfer rate to node (n, m)	[W]

Pr	Prandtl number	[-]
R_{DLDR}	Radius of DLDR tube	[m]
R_i	Inner pipe radius of the HEAL	[m]
r_i	Chemical interaction rate	[mols ⁻¹]
R_i	Outer radius of radial section i of a cylinder	[m]
$r_{start_{n,m}}$	Inner radius of node (n, m)	[m]
$r_{stop_{n,m}}$	Outer radius of node (n, m)	[m]
Ra	Rayleigh number	[-]
Re	Reynolds number	[-]
ρ	Density	[kgm ⁻³]
$\rho_{n,m}$	Density of node (n, m)	[kgm ⁻³]
$S.A.$	Specific Activity	[GBqmg ⁻¹]
σ	Cross section	[barn or cm ²]
\bar{t}	Mean residence time	[s]
$T_{n,m}$	Temperature in node (n, m)	[K]
T_{ref}	Density reference temperature	[kgm ⁻³]
Θ	Horizontal angle of the pipe in section 1 and 3 of the HEAL	[° or rad]
Θ_n	Horizontal angle of the pipe in node n	[° or rad]
U	Overall heat transfer coefficient	[Wm ⁻² K ⁻¹]
u	Gamma heating deposition per mass of material	[Wkg ⁻¹]
$u_{n,m}$	Gamma heating deposition per mass of material in node (n, m)	[Wkg ⁻¹]
V	Volume	[m ³]
v	Velocity of the target solution	[ms ⁻¹]
$V_{n,m}$	Volume of node (n, m)	[m ³]
σ_t^2	Variance RTD curve	[s ²]
σ_α^2	Component age variance	[s ²]
σ_a^2	Component mean age variance	[s ²]

Contents

Acronyms	vii
Glossary	ix
Symbols	xi
1 Introduction	1
1.1 Research Questions	3
2 HEAL Background Theory	5
2.1 HOR Experimental Activation Loop	5
2.1.1 DLDR tube and HEAL location.	5
2.1.2 General HEAL Geometry.	6
2.2 Discretized model.	7
3 Background Theory	9
3.1 Axial and radial heat conduction through a cylinder	9
3.2 Production of Lu-177 in the HEAL.	11
3.2.1 Neutron Capture Interaction.	11
3.2.2 Specific activity	12
3.2.3 The Szilard-Chalmers effect	12
3.2.4 Kinetics of the production of Lu-177 with DOTA	13
3.3 Shielding	14
3.3.1 Gamma interactions	15
3.3.2 Gamma dose rate	16
3.3.3 Heat deposition	16
3.3.4 Neutron shielding	16
3.4 Dispersion and HEAL operation	17
3.4.1 Buoyancy and mixed convection induced flow.	17
3.4.2 Computational Fluid Dynamics - OpenFOAM	18
3.4.3 Dispersion modeling.	18
3.4.4 Operation of the HEAL.	20

4	Methods	25
4.1	Discretized HEAL Model	25
4.1.1	Model coordinates	25
4.1.2	Python Model Geometry	26
4.1.3	Improved energy balance	27
4.1.4	Numerical methods and implementation	30
4.1.5	Material Properties and Model Parameters.	32
4.2	Shielding	33
4.2.1	Serpent Model	33
4.2.2	Photon/Gamma source generation	33
4.2.3	Neutron source	33
4.2.4	HEAL Geometries & Materials	34
4.3	Lu-177 Production Model	37
4.3.1	Kinetics	37
4.3.2	Components	39
4.3.3	Production Model Parameters	39
4.4	Dispersion modelling	41
4.4.1	OpenFOAM CAD model	41
4.4.2	Tanks-In-Series compartment model	42
4.4.3	Dynamic HEAL model	44
5	Results and Discussion	47
5.1	Discretized HEAL model results.	47
5.1.1	Wall thickness	47
5.1.2	Inner radius	51
5.1.3	Pipe angle & Length	52
5.1.4	Dynamic Results	54
5.2	Gamma and Neutron Shielding	57
5.2.1	System Walls	57
5.2.2	Target solution	59
5.3	Residence Time Distribution	62
5.3.1	CFD Flowrate and Recycle Results	62
5.3.2	RTD curves and Tanks-In-Series compartment models	64
5.4	Production Lu-177	68
5.4.1	Batch operation	68
5.4.2	Continuous operation	69

6	Conclusion	71
7	Recommendations	75
7.1	Research/Model improvements	75
7.1.1	Discretized model	75
7.1.2	Serpent	75
7.1.3	Dispersion and Control	75
7.1.4	Production & Kinetics	76
7.2	Design	76
A	Appendix - Overview of the functions used inside the discretized model	81
A.1	Previous model	81
A.1.1	Previous Model - Energy and momentum balance	81
A.1.2	Previous Model - Heat transfer	82
A.2	Energy balance	82
A.2.1	Heat transfer	83
A.2.2	Heat generation	84
A.3	Momentum balance	84
A.3.1	Boussinesq approximation.	84
A.3.2	Darcy Friction	85
A.3.3	Friction from bends	85
A.4	Model Heat Conduction Verification	85
A.4.1	Steady state radial conduction	85
A.4.2	Time dependent axial conduction	87
A.4.3	Code	87
B	Appendix - Extended Discretized Model Results	89
B.1	Wall Materials & Wall thicknesses	90
B.1.1	Single layer wall materials	90
B.1.2	Multi layer materials wall	110
B.2	Inner Radius R_i , Wall material & Wall thickness	129
B.2.1	Al/Al - Inner Radius (R_i) & Wall thickness	131
B.2.2	Pb/Pb - Inner Radius (R_i) & Wall thickness.	138
B.2.3	Zr/Zr - Inner Radius (R_i) & Wall thickness	146
B.2.4	Pb/Al - Inner Radius (R_i) & Wall thickness	154
B.3	Pipe angle, System length & Inner radius	163
B.3.1	Al/Al - Pipe angle, System length & Inner radius	164
B.3.2	Pb/Pb - Pipe angle, System length & Inner radius	177
B.3.3	Zr/Zr - Pipe angle, System length & Inner radius	190

B.4	Section 2 length fraction & Wall thickness	203
B.4.1	Al/Al - Section 2 length fraction & Wall thickness	204
B.4.2	Pb/Pb - Section 2 length fraction & Wall thickness	212
B.4.3	Zr/Zr - Section 2 length fraction & Wall thickness	220
C	Appendix - Gamma and neutron source normalization	229
C.0.1	Gamma source profile and normalisation	229
C.0.2	Neutron Source Normalization.	229
C.0.3	Code Example	230
D	Appendix - LuDOTA Kinetics	233
D.1	Chemical reaction fitting	233
D.2	Gamma damage cross section.	233
E	Appendix - OpenFOAM code and settings	235
F	Appendix - Extra CFD and Tanks-In-Series results.	237
F1	Extended flowrate results	237
F2	Tank-In-Series Compartment Model	240
F2.1	Vessel segment RTD curves	243
F2.2	Recycle segment RTD curves.	251

1

Introduction

Radioisotopes have essential applications in several industries with the largest consumer being the medical industry. In the medical field there are two different uses for radioisotopes: imaging for diagnosis and radio-therapeutic treatment. For these applications not only the choice of radionuclide is important, but also the available quality of the radionuclide in terms of the specific activity [50]. One of the ways to produce radioisotopes is via neutron capture reactions (n,γ) with a target material. This reaction is mainly performed using neutrons coming from a nuclear reactor such as the High Flux Reactor (HFR) in Petten, The Netherlands which provides a large fraction of the world supply of radioisotopes [9, 46].

To aid in the production of radioisotopes and be able to conduct further research on this topic, a production vessel, called the HOR Experimental Activation Loop (HEAL), is proposed to be placed in the DLDR tube next to the Hoger Onderwijs Reactor (HOR) at the Technical University of Delft. Current iterations of this proposed vessel consist of a circular pipe in the shape of a parallelogram, forming a loop. By dissolving the target material for the neutron interaction in water allows the target to flow through the HEAL and can therefore easily be introduced and extracted without removal of the vessel itself. The HEAL would make it possible to provide a continuous or batch production of radioisotopes such as Mo-99 and/or produce a product with increased specific activity by utilizing the Szilard-Chalmers effect in combination with neutron capture (n,γ) reactions [60]. A previous thesis by Naaktgeboren looked at the production of radioisotopes Lu-177 and Ho-166 within the HEAL utilizing the Szilard-Chalmers effect. A model including the important chemical processes and radiolysis of the compounds showed that an increase in the specific activity in the product could be achieved using the HEAL. This model also showed that for reaching higher specific activities within the HEAL shielding the target solution from gamma radiation is important [42].

Several theses have also been written on the HEAL that have focused more on the functionality in terms of generating a flow and controlling the temperatures throughout the loop. The flow of the target solution within the HEAL would be induced without a pump by making use of a buoyancy induced flow. Dresen and Haffmans have looked at both the functionality and safety of this concept in combination with the production of Mo-99 by fission of U-235 [21, 30]. Heating of the solution was provided by energy deposition from gamma radiation within the wall material of the loop, cooling of the solution was provided by a cooling mantle at the top of the loop acting as a heat exchanger. The heating and cooling of the solution introduces a density difference between the sections, inducing a buoyancy driven flow within the loop.

A requirement for the HEAL is passive safety, and therefore being dependent on a heat exchanger for the provided cooling was a concern. Therefore Roovers expanded this concept by exploring if the loop would be feasible without the inclusion of a cooling mantle [51]. This by utilizing a previous cooling concept by Pendse that utilized the water present within the DLDR tube as coolant [49]. To provide the buoyancy induced flow different wall thicknesses at different sections of the loop would be used. This introduces a larger heat deposition in one section, heating the solution, and cooling in another section providing the density difference required for a buoyancy induced flow. To approach the velocity of the flow and the temperatures in different configurations of the HEAL, Roovers constructed a model of the loop by discretizing the system,

splitting the HEAL in several sections and solving the energy and momentum balance(s) numerically [51]. This model however approaches the heat conduction in the system in one dimension and assumes a singular temperature of each wall section and therefore does not include a radial temperature profile. Expansion on this model that includes these effects and a broader expansion on the influence of different design decisions for the HEAL would therefore give a better basis for the design.

For both continuous or batch production of different radioisotopes inside the HEAL it would be beneficial to be able to represent the system in terms of dispersion and residence time distribution throughout the vessel as well as seeing if this can be controlled in some way with the geometry or by the in- and outlet flowrates. Vessels with a large amount of mixing inside, and therefore a large dispersion, would offer worse flushing conditions for removing or adding components to the system efficiently for batch production. Within continuous operation the dispersion and residence time distribution could also play a role for shorter irradiation cycles.

In this thesis the loop will be further analysed on three different aspects:

- Expanding the discretized model.
An expansion will be made on the previous model by Roovers [51] by including a radial and axial heat conduction through the walls and solution of the loop. This model will then be used to explore the effects that different system variables/parameters have on the functionality in terms of velocity and temperatures seen inside the HEAL. Examples are the wall materials and wall thicknesses.
- Gamma and neutron radiation shielding capabilities.
Effectively utilizing the Szilard-Chalmers effect is very dependent on radiolysis from gamma radiation [42], and a possible heating profile within the wall could exist from this shielding. In this thesis the gamma shielding capabilities and radial gamma heating profiles that the wall of the HEAL can provide with different wall configurations will be looked at. This by using the neutron and photon transport software Serpent. Additionally, the reduction of the neutron flux and neutron capture cross section of Lu-176 in the different wall configurations are explored.
- Production & operation.
Two operational schemes for the production of the radioisotope Lu-177 are explored for the HEAL: batch and continuous. For the production of Lu-177, a model will be created that includes the Szilard-Chalmers effect utilizing data from other studies [42, 60].

To get a better understanding about the dispersion of the target solution present in the loop. CFD simulations will be explored for finding the residence time distributions of different segments which will then be modelled in Tanks-In-Series compartment models for approaching the dispersion inside the complete loop. These CFD simulations will also be used to explore how the flowrate in the recycle stream of the loop can be controlled.

Overall, this thesis is meant to give a better understanding about the important parameters for the design of the loop and give insights into how the production would be influenced by said parameters, this to further guide the design of the HOR Experimental Activation Loop.

1.1. Research Questions

Several research questions have been formed to answer in this thesis:

1. In what way does the addition of heat conduction in the wall of the loop have an influence on the functionality of the system?

- What is the influence of the design parameters, as listed below, on the HOR Experimental Activation Loop on both the velocity and temperatures in the system?
 - Wall thickness
 - Wall materials
 - Inner radius
 - Length
 - Angle of pipe
- How does the velocity and temperatures in the HEAL react to changes from outside variables over time in systems with different wall materials?

2. What is the effect of different wall configurations to the shielding from gamma radiation and functionality of the HEAL?

- What amount of shielding to gamma radiation is provided by different wall configurations such as the wall material, wall thickness and multiple wall material layers?
- Does the shielding to gamma radiation provide a heating profile throughout the wall of the HEAL?
- To what extent do different wall configurations shield the system from neutrons and what is the effect on the production rate of Lu-177 from these wall configurations?

3. How does the operation of the HEAL influence the production of Lu-177, utilizing the Szilard-Chalmers effect?

- What factors controlled by the HEAL have an effect on the production of Lu-177 in continuous and batch operation?
- How does the radius of the HEAL as well as the radius and position of the inlet and outlet affect the dispersion inside the loop?
- How does the recycle rate/fraction influence the residence time distribution of the different segments inside the loop and how can this recycle rate be controlled?

2

HEAL Background Theory

This chapter will discuss some background information on the HOR Experimental Activation loop. Firstly a general introduction of the HOR Experimental Activation Loop (HEAL) will be given together with its position in relation to the the HOR. This is then followed by an introduction of the previously discretized model of the HEAL by Roovers [51].

2.1. HOR Experimental Activation Loop

2.1.1. DLDR tube and HEAL location

The HOR Experimental Activation Loop, also known as its abbreviation HEAL, is a vessel that is to be placed within the DLDR beam tube of the Hoger Onderwijs Reactor (HOR). The DLDR beam tube is a cylindrical tube made from the aluminium magnesium alloy AlMg3 and has an inner diameter of 14cm [34]. Inside the tube water is slowly circulated which is kept at an average temperature of 40°C . The DLDR tube is positioned very close to the reactor core at a distance of 4.15cm , which can be seen as indicated in red in figure 2.1. As it is closely positioned next to the reactor core it is exposed to a large number of both neutrons and gamma ray's coming from the reactor. More precisely, the flux of both the neutrons and gamma ray's were previously simulated within MCNP to a thermal neutron flux of $3.7 \times 10^{12} \text{ cm}^{-2} \text{ s}^{-1}$ and a gamma flux of $1.35 \times 10^{13} \text{ cm}^{-2} \text{ s}^{-1}$ through the center of the DLDR tube [34].

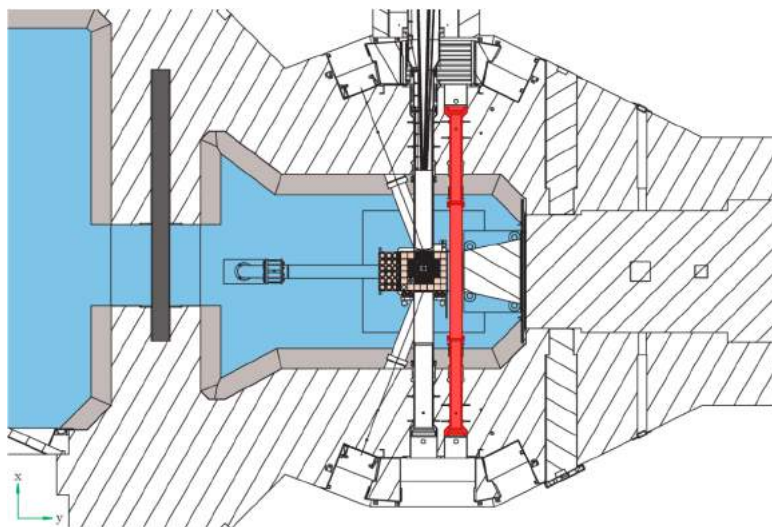


Figure 2.1: Schematic top view of the HOR which includes the DLDR tube as indicated in red positioned close to the reactor core [34]

Neutrons reaching the DLDR tube can be used inside of the HEAL to produce radioisotopes via neutron capture reactions of a target isotope, e.g. Lu-177 with Lu-176 as the target isotope. Within the HEAL the target isotope would be placed inside a solution, referred to as the "target solution", which would constantly flow through the HEAL during operation/production.

2.1.2. General HEAL Geometry

Current geometrical iterations of the vessel consist of a circular pipe, shaped as a parallelogram forming a loop. Within this loop a target solution would be placed that flows through this geometry. An example for this design and some of the most important variables of the geometry can be seen in figure 2.2. This system is split up in two sectors: A heating sector, consisting of section 1 and 2, and a cooling sector, consisting of section 3 and 4 in the figure.

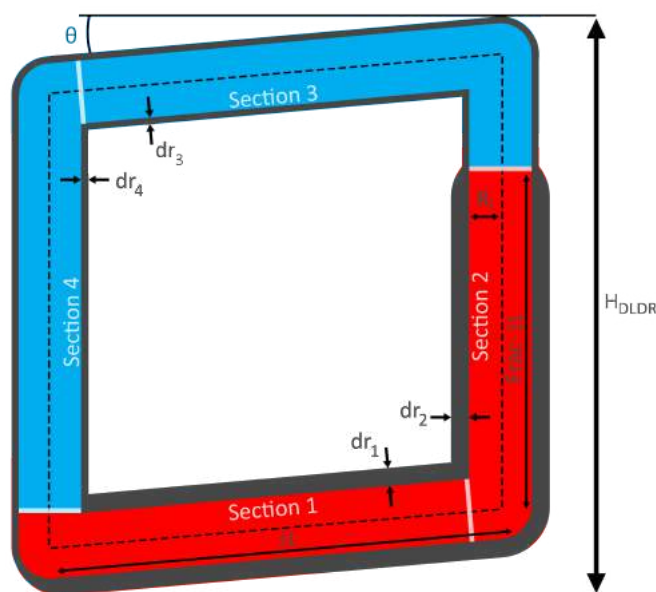


Figure 2.2: A cross section of a general design of the HEAL. The heating sector is indicated in red and the cooling sector is indicated by blue. Important variables of this design are included.

During irradiation from neutron and gamma ray's from the reactor, energy will be deposited inside the material of the pipe walls of the HEAL which is converted to thermal energy. Utilizing different wall thicknesses and/or materials, influencing the energy deposition as well as the heat transfer properties, the target solution can be heated and cooled in different sections. By heating the solution in the heating sector and cooling it in the cooling sector a density difference in the sections can be generated which can induce a buoyancy driven flow of the target solution throughout the loop [51].

In the geometric setup of the HEAL, as seen in figure 2.2, there are many variables which can be changed. Examples are the inner pipe radius (R_i), the wall thicknesses in the different sections (dr_{sec}), the materials of the wall and/or utilizing a multi layered wall with different materials, and the angle of the top and bottom pipes of the parallelogram (θ). All of these variables can have an effect on the velocity and temperatures that are seen in the overall system [51].

2.2. Discretized model

To describe the effect of these variables on the functionality of the HEAL, a model was previously discretized by Roovers [51]. This model divides the HEAL system in N sections over the length, defined as nodes. An example of a system divided in nodes is shown in figure 2.3. Within each node an energy balance is solved for the temperatures of the wall and the target solution and an overall momentum balance is solved for the velocity inside the system. For the buoyancy calculation, the density of the target solution is approached using the Boussinesq approximation (see equation 3.19) [51].

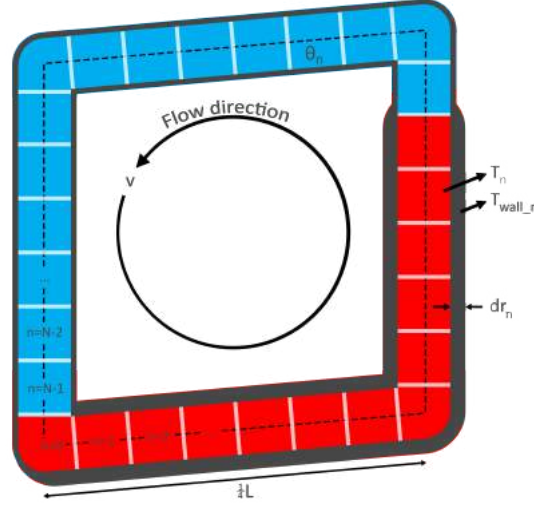


Figure 2.3: Example of a HEAL system divided into nodes over the length of the system with a coordinate system over N nodes indicated by n . Indicated in this figure is the flow direction and important parameters used within the discretized model. The first node, $n=0$, exists in section 1 in which consecutive n coordinates are given continuing in the flow direction.

Energy balance

The energy balance that is solved inside the model for both the target solution and the walls of the HEAL are given in the equations 2.1. In these equations the water temperature in the DLDR tube is assumed have a constant temperature of 40°C . Extended information about the model and how the different material and heat transfer parameters in 2.1 get calculated can be found in appendix A.1.1 and are extensively explained in the thesis by Roovers [51].

$$\frac{\partial T_n}{\partial t} = -\frac{2h_{inner_fluid_wall_n}}{R_i\rho_0C_p}(T_n - T_{wall_n}) - \frac{N}{L}(T_n - T_{n-1})v \quad (2.1a)$$

$$\frac{\partial T_{wall_n}}{\partial t} = \frac{u}{C_{p_wall}} + \frac{2h_{inner_fluid_wall_n}}{C_{p_wall}\rho_{wall}}\frac{R_i}{2R_idr_n + dr_n^2}(T_n - T_{wall_n}) - \frac{2h_{wall_nouter_fluid}}{C_{p_wall}\rho_{wall}}\frac{(R_i + dr_n)}{2R_idr_n + dr_n^2}(T_{wall_n} - T_{outer_fluid}) \quad (2.1b)$$

In these equations v is the velocity of the solution inside the system in $[\frac{m}{s}]$, N is the number of nodes in the model, u the gamma heating deposition rate in $[W/kg]$, T_n and T_{wall_n} the respective temperature of the solution and the wall in node n in $[K]$, T_{outer_fluid} is the temperature of the water in the DLDR tube, outside of the system. $h_{inner_fluid_wall_n}$ is the combined heat transfer coefficient between the solution and the wall in node n in $[\frac{W}{m^2K}]$, $h_{wall_nouter_fluid}$ is the combined heat transfer coefficient between the wall and the water in the DLDR tube in node n in $[\frac{W}{m^2K}]$, R_i is the radius of the pipe in $[m]$, dr_n is the wall thickness of node n in $[m]$, ρ_0 is the density of the solution at the reference temperature in $[\frac{kg}{m^3}]$, ρ_{wall} is the density of the wall in $[\frac{kg}{m^3}]$, C_p the heat capacity of the fluid and C_{p_wall} is the heat capacity of the wall in $[\frac{J}{kgK}]$.

Momentum balance

The overall momentum balance over the nodes in the model is given in equation 2.2 [51]. This momentum balance consists of a summation of the pressure loss by friction inside the nodes, pressure loss from the bends inside the HEAL, and the pressure generated by buoyancy in the system. This is calculated by utilizing the Boussinesq approximation (3.19) to find the density of the solution in each node. An overview of the calculation of the different parameters (e.g. the friction coefficient f_{D_n}) of the momentum balance can be found in appendix A.3.

$$\frac{\partial v}{\partial t} = -\frac{1}{N} \sum_{n=1}^N f_{D_n} \frac{1}{4R_i} v^2 - \frac{v^2}{L} (K_{w1} + K_{w2}) + \frac{g}{N} \sum_{n=1}^N (1 - \beta(T_n - T_{ref})) \sin(\Theta_n) \quad (2.2)$$

Where N is the number of nodes in the model, f_{D_n} is the Darcy friction in node n , R_i the inner radius of the HEAL in $[m]$, v the velocity in the system in $[\frac{m}{s}]$, L the length of the system in $[m]$, K_{w1} and K_{w2} the friction coefficient from the bends, g the gravitational constant in $[\frac{m}{s^2}]$, β the thermal expansion coefficient in $[K^{-1}]$, T_n the temperature of the fluid inside the HEAL in node n in $[K]$ and Θ_n the angle of node n in $[^\circ]$ or $[rad]$

3

Background Theory

In this chapter the background theory will be given on the conduction of heat through cylindrical walls. This is followed by the background of the production of Lu-177 in combination with the Szilard-Chalmers effect. After this, a closer look is given on gamma shielding together with the neutron and photon transport software Serpent. Finally, the theory behind dispersion and residence time distribution of the target solution inside the loop will be discussed in combination with continuous and batch operation of the HEAL.

3.1. Axial and radial heat conduction through a cylinder

From Newton's law of cooling the heat transfer rate over a plate can be expressed as shown in equation 3.1. Expanding this heat transfer through multiple wall layers of different materials this equation can be expressed with the overall heat transfer coefficient U which consists of a sum of the influence of the heat transfer coefficients h . Within these equations the $(UA)^{-1}$ can be viewed as the total thermal resistance in the system [14].

$$\phi = hA\Delta T = \frac{\Delta T}{\frac{1}{hA}}, \quad \phi_{overall} = UA\Delta T = \frac{\Delta T}{\frac{1}{UA}} \quad (3.1)$$

Where ϕ is the heat transfer rate in [W], ΔT the steady state temperature difference between the inner and outer layer of the material in [K], A the surface area of heat transfer in [m^2], and h the heat transfer coefficient in [$\frac{W}{m^2K}$].

While in axial conduction through a pipe the heat transfer area A remains constant over the length, in radial heat conduction the surface area of heat transfer increases with the radius. To account for this, the area in the thermal resistance term $((UA)^{-1})$ for conduction can be expressed as the logarithmic mean area logarithmic mean area A_{lm} , as shown in 3.2c. An example for the equations used for the total thermal resistance for the system in figure 3.1 can be found in the equations 3.3. In these equations the conduction through the wall A_i is expressed using the logarithmic mean area A_{lm} and for the convective transport A_i is expressed as the contact area.

$$A_{i,ax} = \pi(R_i - R_{i-1})^2 l \quad (3.2a)$$

$$A_{i,rad} = 2\pi R_i l \quad (3.2b)$$

$$A_{i,lm} = \frac{A_{i,rad} - A_{(i-1),rad}}{\ln(\frac{A_{i,rad}}{A_{(i-1),rad}})} = \frac{2\pi l(R_i - R_{i-1})}{\ln(\frac{R_i}{R_{i-1}})} \quad (3.2c)$$

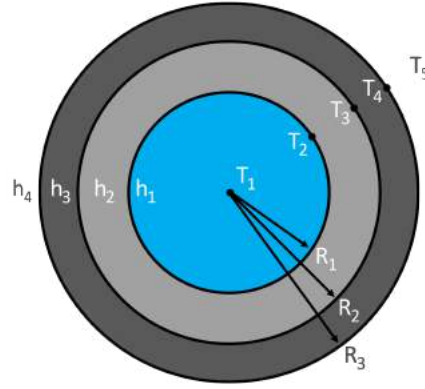


Figure 3.1: Simple cylindrical pipe wall with two wall material layers

$$\phi_{overall} = \frac{\Delta T}{\frac{1}{UA}} = \frac{T_5 - T_1}{\sum_i \frac{1}{h_i A_i}} \quad (3.3a)$$

$$\sum_i \frac{1}{h_i A_i} = \frac{1}{h_1 A_{1,rad}} + \frac{1}{h_2 A_{1,lm}} + \frac{1}{h_3 A_{2,lm}} + \frac{1}{h_4 A_{3,rad}} \quad (3.3b)$$

Where ϕ is the heat transfer rate, ΔT the steady state temperature difference between the T_1 and T_4 in the figure in $[K]$, A_i the surface area at i in $[m^2]$, $A_{i,lm}$ the logarithmic mean area of heat transfer at i in $[m^2]$, U the overall heat transfer coefficient in $[\frac{W}{m^2K}]$.

The axial and radial heat transfer coefficients h_2 and h_3 for the conduction through a pipe wall as seen in figure 3.1 can be expressed by functions as seen in 3.4 [29, 11].

$$h_{i,ax} = \frac{\kappa}{l} \quad (3.4a)$$

$$h_{i,rad} = \frac{2\kappa}{R_i \ln(\frac{R_i}{R_{i-1}})} \quad (3.4b)$$

Where $h_{i,ax}$ is the axial and $h_{i,rad}$ the radial heat transfer coefficient for conduction through a cylindrical material in $[\frac{W}{m^2K}]$, κ the thermal conductivity coefficient of the material in $[\frac{W}{mK}]$, R_i the radius of the cylinder i in $[m]$, and l the axial length in $[m]$.

3.2. Production of Lu-177 in the HEAL

The main purpose of the HEAL is the production of radioisotopes. One of the proposed radioisotopes to be produced is Lu-177. Lu-177 is a β^- and γ emitter with a half-life of 6.716 days which decays into Hf-177 [25]. A by-product of the production of Lu-177 is the meta-stable isomer Lu-177m, which can decay via isomeric transition towards Lu-177 or decay directly into Hf-177 with a total half life of 160.4 days. A simplified decay scheme of both Lu-177 and Lu-177m can be seen in figure 3.2 [25, 57]. The radioisotope Lu-177 can be used in radiotherapy, for instance for improving the time of survival in hard to treat forms of prostate cancer [52].

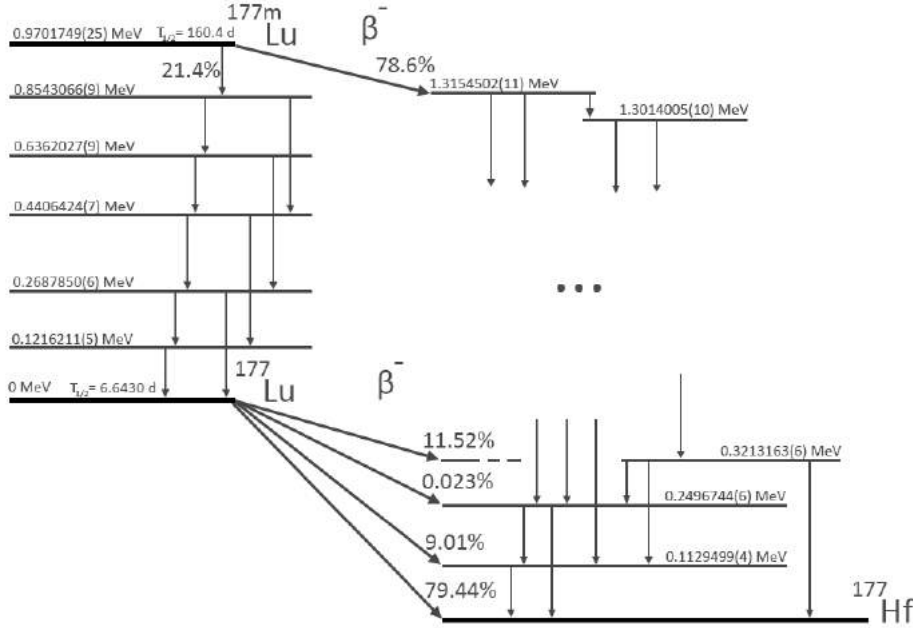
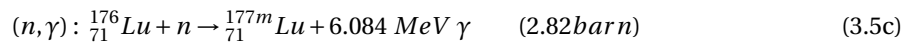
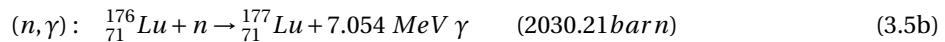
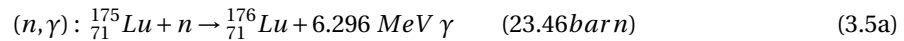


Figure 3.2: Simplified decay scheme of Lu-177 and Lu-177m [25, 57]

3.2.1. Neutron Capture Interaction

Lu-177 and Lu-177m can be produced by neutron capture reactions with the target isotope Lu-176 (equation 3.5b & 3.5c).

The natural abundance of lutetium consists of $2.60 \pm 0.01\%$ Lu-176 and $97.40 \pm 0.01\%$ Lu-175 [17]. Therefore without Enrichment, a large fraction of the target material will consist of the Lu-175 isotope which does not contribute directly to the production of Lu-177. Neutron capture reaction of Lu-175 can take place to produce Lu-176, but with a significantly lower neutron capture cross section of 23.46barn in comparison to that of Lu-176 at 2030.21b [2, 35]. The spectrum of the total neutron capture cross section of Lu-176 can be seen in figure 3.3.



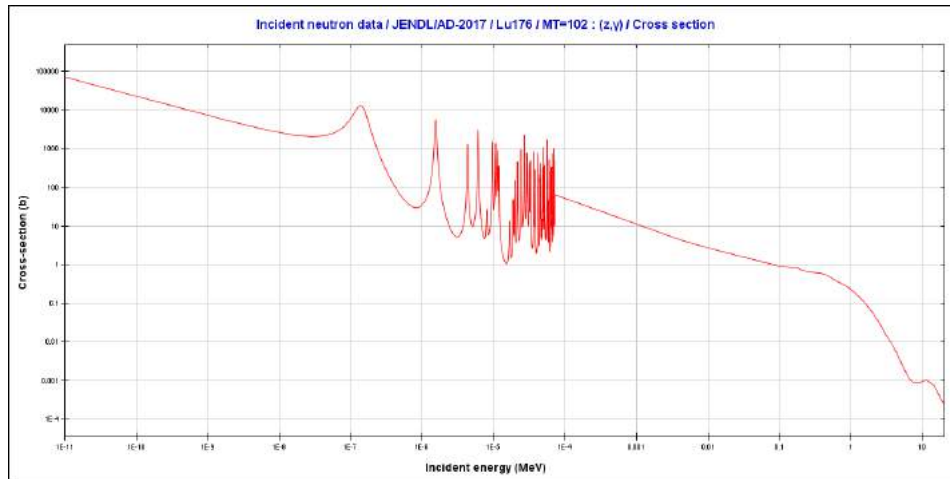


Figure 3.3: Total neutron capture cross section of Lu-176 [2]

3.2.2. Specific activity

One of the measures for the quality of the produced radioisotope is its specific activity. The specific activity is the number of disintegration's due to decay per time per mass of the product, as seen in equation 3.6b, often measured in $[Ci/mg]$ or $[GBq/mg]$.

$$A(t) = \frac{dn}{dt} = \lambda n(t) \quad (3.6a)$$

$$S.A. = \frac{A(t)}{m_{prod}} \quad (3.6b)$$

With n being the number of decaying atoms, t the time in $[s]$, λ as the decay constant in either $[Bq]$, $[GBq]$ or $[Ci]$, $S.A.$ being the specific activity in $[Bq/mg]$ or $[GBq/mg]$ or $[Ci/mg]$, $A(t)$ the activity in $[Bq]$, $[GBq]$ or $[Ci]$ and m_{prod} the mass of the product, most often in $[mg]$

While the activity in equation 3.6b is defined in equation 3.6a, the mass in this equation is not always equal to the mass of only the produced radioisotope. For instance, the product can include impurities from other isotopes, lowering the specific activity of the product. To increase the specific activity, impurities could be separated from the produced radioisotope. Impurities of a different element compared to the produced radioisotope are relatively easy to separate as these elements are chemically different from each other allowing chemical separation. Impurities from isotopes of the same element, such as the isotopes Lu-175 and Lu-176, chemical separation is not possible as they are chemically the same. Separation of these elements requires the use of separation methods based on the difference in mass of the isotopes, e.g. gaseous diffusion or centrifuges as used in the Enrichment of uranium [54].

3.2.3. The Szilard-Chalmers effect

Chemical separation can however still play a role to increase the specific activity of a product with impurities of the same element. This by utilizing the Szilard-Chalmers effect during the production of the radioisotope.

The Szilard-Chalmers effect, discovered by L. Szilard and T.A. Chalmers in 1934 [56], is an effect that occurs when prompt gamma ray(s) are emitted during a neutron capture reaction. This emission provides recoil energy to the nucleus where the gamma ray(s) originated from, the recoil energy follows equation 3.7. This recoil energy provided to the nucleus can be larger than the energy of chemical bonds the nucleus is bound to (e.g. $\sim 151eV$ of recoil energy from a single prompt γ ray emission of $7.054MeV$ from production of Lu-177 from Lu-176 via neutron capture interaction [18]), and can therefore break these chemical bonds, dissociating

the reacted nuclear from a compound. This allows for chemical separation during production between a chemically bound target isotopes and the dissociated produced radioisotope.

$$E_{recoil} = \frac{E_{\gamma}^2}{2Mc^2} \quad (3.7)$$

Where E_{recoil} is the recoil energy, E_{γ} the energy of the emitted gamma ray, M the mass of the isotope and c the speed of light.

For increasing the specific activity of the Lu-177 product, the Szilard-Chalmers effect can be utilized. This by binding natural abundant lutetium atoms to a chelator named DOTA, which is an organic compound that can form a very stable complex with lanthanides such as lutetium [58]. The LuDOTA complex can be dissolved inside the target solution in the HEAL. During irradiation in the HEAL, the Szilard-Chalmers effect can take place after a neutron capture interaction, releasing Lu-177 (3+) ions the from DOTA molecule. Chemically separating the released lutetium ions from the still bound lutetium in the DOTA complex therefore allows for an increase in the specific activity of the final product [60].

3.2.4. Kinetics of the production of Lu-177 with DOTA

This section gives background information on the production and consumption rates of the different components present in the production of Lu-177 with naturally enriched lutetium.

Neutron interaction rate

The production rates of Lu-177 and Lu-177m in the target solution are dependent on the neutron flux, the neutron energy spectrum, and the cross sections of the neutron interactions as seen in 3.5. The general neutron interaction rate can be found in equation 3.8a. Production and consumption rates by neutron interactions for the present isotopes of lutetium can be found in the other equations of 3.8.

$$\frac{dC_{prod}}{dt} = -\frac{dC_{target}}{dt} = C_{target} \int_0^{\infty} \varphi(E) \sigma_i(E) dE = C_{target} \varphi \sigma_i \quad (3.8a)$$

$$\frac{dC_{prod}}{dt} = -\frac{dC_{target}}{dt} = C_{target} \varphi \sigma_{(n,\gamma)} \quad (3.8b)$$

$$-\frac{dC_{Lu-175}}{dt} = -C_{Lu-175} \varphi \sigma_{176} \quad (3.8c)$$

$$\frac{dC_{Lu-176}}{dt} = C_{Lu-175} \varphi \sigma_{176} - C_{Lu-176} \varphi \sigma_{177} - C_{Lu-176} \varphi \sigma_{177m} \quad (3.8d)$$

$$\frac{dC_{Lu-177}}{dt} = C_{Lu-176} \varphi \sigma_{177} \quad (3.8e)$$

$$\frac{dC_{Lu-177m}}{dt} = C_{Lu-176} \varphi \sigma_{177m} \quad (3.8f)$$

Where C is the concentration the target or product, $\varphi(E)$ and φ are neutron flux and integrated neutron flux over the energy spectrum in [$cm^{-2}s^{-1}$], $\sigma_i(E)$ and σ_i are the cross section and integrated cross section over the energy spectrum of interaction "i" such as the neutron capture interaction (n, γ) in [cm^2].

Retention of lutetium in LuDOTA

After a neutron capture reaction of lutetium within the LuDOTA complex there is a possibility that the Szilard-Chalmers effect won't break the chemical bond and therefore the produced radioisotope remains inside the LuDOTA complex. This retention in the complex can be described by the retention fraction R , which is defined as the fraction of formed radioisotopes after a neutron capture reaction that remain in the complex. Retention fractions for holmium DOTA complexes have been studied and found to be between 10.3 to 25.4%. For a short irradiation period, in which the least amount of holmium is released from radiolysis, was found at 13.2% [60].

Decay of Lu-177 and Lu-177m

The rate of decay from Lu-177 and Lu-177m and production of Hf-177 follow the decay scheme in figure 3.2 and can be expressed by the activity using equations 3.9.

$$\frac{dC_{decay_prod}}{dt} = -\frac{dC_{decay_react}}{dt} = \lambda_{decay_react} C_{decay_react} \quad (3.9a)$$

$$\frac{dC_{Lu-177}}{dt} = -\lambda_{Lu-177} C_{Lu-177} + 0.214 \lambda_{Lu-177m} C_{Lu-177m} \quad (3.9b)$$

$$\frac{dC_{Lu-177m}}{dt} = -\lambda_{Lu-177m} C_{Lu-177m} \quad (3.9c)$$

$$\frac{dC_{Hf-177}}{dt} = \lambda_{Lu-177} C_{Lu-177} + 0.786 \lambda_{Lu-177m} C_{Lu-177m} \quad (3.9d)$$

Chemical kinetics LuDOTA

Besides the nuclear interactions taking place, chemical reactions will also play a large role in the production. For instance, lutetium ions bind and release from the DOTA complex following the equilibrium reaction 3.10a [58]. Experimental research has been performed for finding the reaction rate for the binding of the lutetium ions to DOTA [42] as well as finding the stability constant for the equilibrium reaction as seen in 3.10b [58].

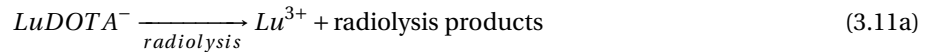


$$K = \frac{k_1}{k_2} = \frac{[LuDOTA^-]}{[Lu^{3+}][DOTA^{4-}]} = e^{23.5 \pm 0.1} \quad (@37^\circ C) \quad (3.10b)$$

With K being the stability constant in $[\frac{L}{mol}]$ with it's value of $e^{23.5 \pm 0.1}$ as found by Tóth and Brücher [58], $[LuDOTA^-]$ the $LuDOTA^-$ concentration, $[Lu^{3+}]$ the concentration of Lu^{3+} , and $[DOTA^{4-}]$ the $DOTA^{4-}$ concentration inside the solution.

Radiolysis of DOTA

Finally, lutetium ions can release from the LuDOTA complex via radiolysis. Radiolysis of the DOTA molecule is a very complex process, which from alpha radiation alone has over 24 different identified degradation products [26].



$$\frac{dC_{radiolysis\ products}}{dt} = -\frac{dC_{DOTA}}{dt} = C_{DOTA} \int_0^\infty \varphi(E) \sigma_i(E) dE = C_{DOTA} \varphi \sigma_\gamma \quad (3.11b)$$

$$(3.11c)$$

Experimentally found neutron decomposition cross sections for the decomposition of a holmium DOTA complex during irradiation from a nuclear reactor were found at $7.5 \times 10^5 \pm 1.5 \times 10^5$ barn [60]. This neutron cross section includes the interactions with gamma radiation, which seem to be much more important compared to that of neutron interactions as the cross section that was found is significantly higher than the sum of all the neutron interactions from the individual atoms in the complex [60].

3.3. Shielding

As mentioned in the production of Lu-177, it is important to limit the amount of gamma radiation that reaches the target solution inside the HEAL. This to obtain an as high as possible specific activity of the product. To achieve this, the target solution could be shielded by utilising materials with a high gamma ray cross section. Either by placing these materials as a wall in front of the HEAL or by implementing the material in the cylindrical walls of the HEAL.

3.3.1. Gamma interactions

The main purpose of shielding the HEAL is to lower the amount of ionising particles such as gamma rays that reach the target solution to lower the rate at which radiolysis takes place. Shielding the HEAL by placing a material in front of the target solution can reduce the amount and/or lower the energy of the photons. This by interacting with the photons before they can reach the target solution. A measure for how well a particular material is able to interact with a photon is the photon linear attenuation coefficient.

The photon linear attenuation coefficient μ is a measure for the probability per unit distance that a gamma photon undergoes an interaction within a specific medium. These photon interactions include: Photoelectric absorption (σ_{ph}), pair production (σ_{pp}), coherent scattering (σ_c) and incoherent scattering (σ_{ic}) [54]. The attenuation coefficient is often expressed in the mass attenuation coefficient $\frac{\mu}{\rho}$ for which is defined in equation 3.12.

$$\frac{\mu(E)}{\rho} = \frac{N_a}{M} [\sigma_{ph}(E) + \sigma_{pp}(E) + \sigma_c(E) + \sigma_{ic}(E)] \quad (3.12)$$

Where μ is the attenuation coefficient in [cm^{-1}], ρ the mass density in [$\frac{g}{cm^3}$], N_a is Avogadro's constant in [mol^{-1}], M the atomic weight of the medium in [$\frac{g}{mol}$], σ_{ph} , σ_{pp} , σ_c and σ_{ic} the cross sections for the interactions in b or cm^2 .

The attenuation coefficients can be used to determine the intensity of a uniform parallel beam of photons with an intensity I that move through a slab in direction x by the Lambert-Beer law as shown in equation 3.13 [54]. This equations shows that larger attenuation coefficients result in a faster decrease in the intensity of a beam of particles at a specific energy.

$$I(E, x) = I(E, 0)e^{-\mu x} \quad (3.13)$$

In figure 3.4 the total mass attenuation coefficients for aluminium, lead and zirconium are shown from data from the XCOM database [8]. This figure shows the large photon attenuation coefficient from lead, as well as zirconium over the whole photon energy spectrum.

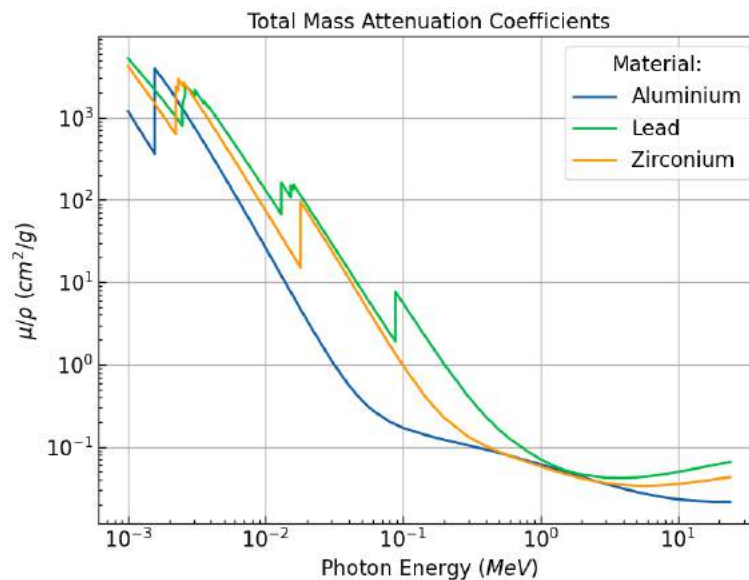


Figure 3.4: The total photon mass attenuation coefficients of aluminium, lead and zirconium between photon energies of 10^{-3} and $10^{1.1}$ MeV [8]

While the attenuation coefficients of different materials show the general shielding capabilities of different materials, and the Lambert-Beer law can only be used to make simple calculations for the intensity drop for an isotropic source. For determining the shielding capabilities in more complex geometries, photon sources

and scattering interactions the attenuation coefficients alone are not enough.

A step up from the simple attenuation coefficients and the Lambert-Beer law is the inclusion of a buildup factor. The buildup factor is defined as the ratio of uncollided particles to collided particles at the same penetration depth [3]. This factor allows for better approximations and/or simulations of the capabilities of shielding materials in terms of the energy deposition of photons [40].

For complex geometries such as the HEAL, including a non isotropic photon source and a complete set of scattering effects, Monte Carlo based particle transport software such as MCNP or Serpent are required. These software packages use the Monte Carlo method to solve problems of particle transport through an environment [10]. This by simulating a large number of particles and their interactions in the environment, such as scattering or photoelectric absorption, with their respective probabilities/cross sections.

3.3.2. Gamma dose rate

The absorbed dose D is quotient of the mean imparted energy ϵ to the mass m as shown in equation 3.14 [54]. In this equation the imparted energy ϵ is defined as the sum of energy that is imparted by ionization or excitation of atoms within a specific volume by ionizing particles [55].

$$D = \lim_{m \rightarrow 0} \frac{\bar{\epsilon}}{m} \quad (3.14)$$

The absorbed dose D is generally expressed in the unit gray (Gy), which is equal to an energy deposition of $1J/kg$. Within a radiation field such as the target solution in the HEAL, the rate at which the absorbed dose is imparted is defined by the dose rate (3.15). As a reference value for the dose rate in the BP3 irradiation facility of the HOR, a γ radiation dose rate was measured at $265 Gy/hr$ [59, 42].

$$\text{dose rate} = \frac{dD}{dt} \quad (3.15)$$

3.3.3. Heat deposition

The energy deposited from the absorbed dose D almost entirely gets converted into thermal energy [54] which as previously mentioned in the HEAL background theory (Chapter 2) is utilized inside of the walls of the HEAL to heat the target solution and produce a buoyancy driven flow inside the system.

Inside the wall temperature energy balance of the discretized model (equation 2.1b) an important variable u is present, which is defined as the thermal gamma energy deposition inside the wall in $[W/kg]$. This variable was previously measured within the DLDR tube at $300W/kg$ [19]. By changing the wall material of the HEAL this variable could be influenced from the different gamma dose rates following the attenuation coefficients of different materials, as shown in figure 3.4 [2, 8].

Following the Lambert-Beer law (equation 3.13) the intensity/flux of photons will drop over the wall thickness. This also means that by following the general nuclear reaction rates from equation 3.8a, the interaction rate of photons will drop. This would lower the energy deposition over the radius of the wall. Looking at the walls of the HEAL, if this energy deposition profile exists it could have a significant influence on the u variable used inside the discretized model.

3.3.4. Neutron shielding

Neutron shielding can be described similarly to shielding of gamma radiation in terms of attenuation, however neutron shielding can be significantly more complex by the different nuclear interactions that can take place such as the generating secondary neutron particles by fission and/or the production of gamma photons after capture interaction [54]. For simple analysis of the interactions over a slab instead of using the attenuation coefficient $\mu(E)$, the total macroscopic cross section Σ_t is generally referred to as the probability per unit distance that a neutron undergoes an interaction through a specific medium.

The total macroscopic cross section (Σ_t) for neutrons is the sum of the cross sections of the different interactions of the neutron with the interacting medium as shown in equation 3.16. These interactions can be split into four categories: the elastic scattering cross section σ_{ei} , inelastic scattering cross section σ_i , capture cross section σ_{cc} , and fission cross section σ_f . For the intensity of a neutron beam through a slab the Lambert-Beer law holds true as shown in 3.17.

$$\sigma_t(E) = \sigma_{ei}(E) + \sigma_i(E) + \sigma_{cc}(E) + \sigma_f(E) \quad (3.16a)$$

$$\Sigma_t(E) = N\sigma_t(E) = \frac{\rho N_a}{M} \sigma_t(E) \quad (3.16b)$$

$$I(x) = I_0 e^{-\Sigma_t x} \quad (3.17)$$

As the interactions for neutrons with a medium are more complex compared to photons the more advanced methods for shielding analysis such as the inclusion of a buildup factor is significantly more difficult [54]. For accurate shielding analysis within a geometry that accounts for the interactions of neutrons the use of Monte Carlo based particle transport software is therefore preferred [41].

3.4. Dispersion and HEAL operation

In this section background theory on buoyancy driven flow is given and the use of computational fluid dynamics with OpenFOAM will be introduced. This will be followed by background theory on dispersion modeling of a vessel utilizing different models from Levenspiel [38]. Finally, continuous and batch operation of the HEAL is discussed together with the importance of the dispersion.

3.4.1. Buoyancy and mixed convection induced flow

The buoyancy force in the momentum equation for a fluid is given in equation 3.18.

$$B = -g(\rho - \rho_r) \quad (3.18)$$

Where g is the gravitational force, ρ the density of the fluid and ρ_r is a reference density.

The density of the fluid in this equation can be estimated via the Boussinesq equation 3.19 [27] as is also performed in the momentum balance of the discretized model by Roovers [51].

$$\rho = \rho_0(1 - \beta(T - T_0)) \quad (3.19)$$

Where ρ is the density at temperature T , β the expansion coefficient and ρ_0 is the reference density at temperature T_0 .

A dimensionless number that is often used to describe the ratio of buoyancy to viscous forces is the Grashof number which is defined in equation 3.20

$$\text{Gr} = \frac{g\beta d^3(T - T_0)}{\nu^2} \quad (3.20)$$

With d the characteristic length, g the gravitational force, β the expansion coefficient, T and T_0 the temperature and reference temperature and ν the kinematic viscosity.

During operation of the HEAL a flow of the target solution is present inside the system. This flow can be induced by buoyancy alone, such as in steady state situations. If the velocity inlet into the HEAL is sufficient enough, the flow can also be induced by mixed convection, which is a combination of forced and natural convection effects [27]. Generally mixed convection situations are characterized by the magnitude of $\frac{\text{Gr}}{\text{Re}^n}$ which is a measure of the natural convection versus the forced convection effects [27].

Flows induced by mixed convection inside cylindrical pipes are extensively investigated for both vertical and horizontal geometries from which velocity and temperature profiles can be estimated utilizing different models [27]. However when introducing bends within these cylindrical pipes, like present in the geometry of the HEAL, laminar velocity profiles can get significantly disturbed [6, 47]. Therefore in these more complex geometries these profiles can't be estimated and can realistically only be approached numerically via CFD simulations.

3.4.2. Computational Fluid Dynamics - OpenFOAM

OpenFOAM is an open source computational fluid dynamics software developed by OpenCFD. OpenFOAM consists of many different CFD libraries of solvers which can be freely edited to meet the requirements for particular systems or analysis that are analyzed.

One of the solvers that is included into OpenFOAM is the buoyantBoussinesqPimpleFoam solver for the use in transient or steady state heat transfer and buoyancy induced flow problems. This solver is based on the pressure velocity coupling algorithm PIMPLE, which is a combination of the PISO and SIMPLE algorithms for solving the navier stokes equations for incompressible fluids as found in equation 3.21. The solver uses the boussinesq approximation as shown in equation 3.19 for the approximation of the density of the fluid that is simulated [28].

$$\nabla \cdot U = 0 \quad (3.21a)$$

$$\rho_0 \left[\frac{\delta U}{\delta t} + (U \cdot \nabla) V \right] = -\nabla p + \rho_0 g + \mu \nabla^2 U + f_p \quad (3.21b)$$

$$f_p = -\rho g \beta (T - T_0) \quad (3.21c)$$

Where V is the velocity vector, ρ the density, p the pressure, T the temperature, T_0 the density reference temperature, μ the dynamic viscosity, f_p the body force volume, and β the expansion coefficient.

For problems that include convection-diffusion problems a separate solver is included in OpenFOAM, the scalarTransportFoam solver. This solver uses the convection-diffusion equation as shown in 3.22 within a velocity field [44].

$$\frac{\delta T}{\delta t} + \nabla U T - \nabla^2 (D_T T) = 0 \quad (3.22)$$

Where T is the transport scalar, U the velocity vector, and D_T the diffusion coefficient divided by the fluid density [44].

3.4.3. Dispersion modeling

Generally dispersion models of a vessel are modelled from the Residence Time Distribution curves from either a pulse or step input experiment inside a vessel. This Residence Time Distribution or RTD describes the distribution of time a particle or component resides inside a vessel after introduction [38]. For a vessel in which reactions take place this RTD therefore also describes the distribution of time a component has to react with neutrons or other components. This RTD is often described using an exit age distribution curve, also known as the E-curve.

In a pulse input experiment, a tracer component is introduced for a split second into the inlet of a vessel. After introduction the concentration of this tracer in the outlet is measured over time. From this response both the mean residence time, variance and and Residence Time Distribution of the tracer in the vessel can be calculated/retrieved. Where the mean residence time \bar{t} and variance σ_t^2 is calculated from equations in 3.23. Dimensionless variables of the residence time and variance can also be used for comparing RTD's with

$$\bar{t} = \int_0^\infty t E(t) dt = \frac{\int_0^\infty t c(t) dt}{\int_0^\infty c(t) dt} - (\bar{t})^2 \quad (\text{Pulse Input}) \quad (3.23a)$$

$$\sigma_t^2 = \int_0^\infty (t - \bar{t})^2 E(t) dt = \frac{\int_0^\infty t^2 c(t) dt}{\int_0^\infty c(t) dt} - (\bar{t})^2 \quad (\text{Pulse Input}) \quad (3.23b)$$

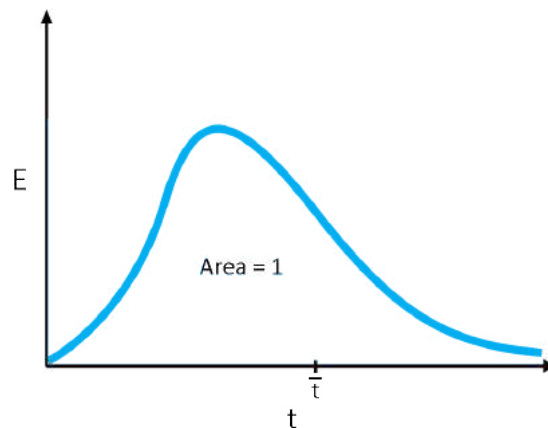


Figure 3.5: Example of an RTD or E-curve showing the exit age distribution of a material within a vessel. Indicated is the mean residence time \bar{t} . Figure inspired by Levenspiel [38]

Describing the dispersion inside the HEAL during operation can be of importance in terms of the kinetics of the produced radioisotope, especially in combination with isotopes with short half life's. For approaching the dispersion inside vessels like the HEAL, Levenspiel [38] defines four different models: The Compartment Model, Dispersion Model, Tanks-In-Series model and The Convection Model.

The Convection Model would not be a sufficient model for describing the HEAL as the HEAL will not contain a stable laminar velocity profile required for this model. While the Dispersion and Tanks-In-Series Model can generally be used equivalently [38], kinetics inside the Dispersion Model are more difficult to implement numerically. This leaves the Compartment and Tanks-In-Series Model.

- **The Compartment Model** In this model the vessel is approached by describing the system in (multiple) different compartments of ideal vessels such as a CSTR or PFR as well as a dead volume compartment where no flow is present, referring to a stagnant region within a vessel. By setting the compartments and flows in different configurations, e.g. positioning compartments in series or in parallel, adding a flow that bypasses a compartment or implementing a recycle stream inside the model, the RTD curves of a particular vessel can often be very reasonably approached [38].
- **The Tanks-In-Series Model** In this model a vessel is approached by describing the system in a series of equal CSTR tanks. Compared to the dispersion model this also has the advantage that it is simpler and any kinetics can be implemented [38]. Describing this model numerically including kinetics is also relatively simple as each individual CSTR tank can be described with the mass balance 3.24.

$$\frac{dC_{i,tank}}{dt} = \frac{vC_{i,prev,tank}}{V_{tank}} - \frac{vC_{i,tank}}{V_{tank}} - r_i V_{tank} \quad (3.24)$$

This model does however only model an axial dispersion inside a vessel and does not allow for more complex systems with internal recycle streams as seen in the HEAL.

The Compartment and Tanks-In-Series Model can be used in combination with each other. For instance, a PFR compartment can be approached by a large number of tanks in series. Bypass or recycle flows can therefore also be implemented between these compartments. A use for this type of model is for instance the prediction of the axial dispersion over the length of a vessel with non-ideal laminar flow regimes [24].

3.4.4. Operation of the HEAL

The HEAL can be operated in two ways: Continuous or as a batch reactor. In both of these operations an in- and outlet flow have to be present at a certain time introducing or removing target solution inside the HEAL. With these in- and outlet flows the HEAL can be compartmentalized in two sections which are shown in figure 3.6. Indicated as the vessel and the recycle segment. In the vessel segment the flowrate consists of the flow through the recycle segment and the inlet flowrate, as followed by the mass balance in equations 3.25.

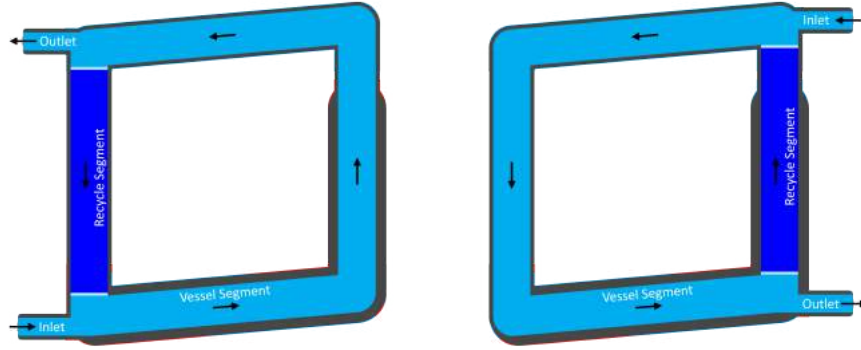


Figure 3.6: A cross section of a general design of the HEAL including the flow direction with an in- and outlet. This system is split into two segments, the vessel segment and the recycle segment. The recycle segment is placed in between the in- and outlet against the flow direction and acts as a "recycle" of the target solution in the vessel. For the in- and outlet on the left the inlet is on the bottom and the outlet on the top (left figure). This is reversed when placed on the right side of the HEAL (right figure)

$$F_{vessel} = F_{inlet} + F_{recycle} \quad (3.25a)$$

$$F_{recycle} = F_{vessel} - F_{outlet} \quad (3.25b)$$

With F_{vessel} being the feed rate through the vessel segment, $F_{recycle}$ through the recycle, F_{inlet} through the inlet, and F_{outlet} the outlet.

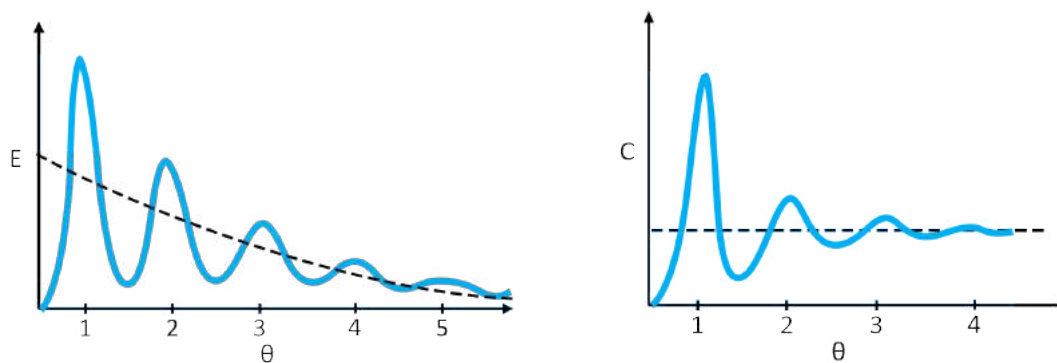
The mass balance can be further expressed using the recycle fraction (RF) and/or recycle ratio (RR) within the system as defined in equations 3.26.

$$RF = \frac{F_{recycle}}{F_{vessel}} \quad (3.26a)$$

$$RR = \frac{F_{recycle}}{F_{outlet}} \quad (3.26b)$$

With RF the recycle fraction defined as the fraction of the feed rate of the vessel segment that flows through the recycle segment, and RR the recycle ratio as defined by the ratio of returned fluid compared to leaving the system.

As previously mentioned in 3.4.1, by introducing an in- and outlet flow a the flow inside the HEAL will be induced by mixed convection. This could have an influence on the overall velocities seen in the recycle segment, and possibly have an influence on the dispersion that is seen inside the loop.



(a) RTD curve of a circulation system in with a throughflow present following a CSTR behaviour as shown by the dotted line.

(b) Concentration curve of a system with no or a small throughflow

Figure 3.7: RTD curve and concentration profile over the mean residence times within a circulation system with a throughflow. Figures inspired by Levenspiel [38]

Continuous operation

Continuous operation of the HEAL consists of a constant in- and outlet flow to and from the vessel. The mean residence time in this operation can be calculated from equation 3.27 [38].

$$\bar{t} = \frac{V}{v} \quad (3.27)$$

Where V is the volume of the HEAL, v the volumetric flowrate through the in- and outlet, and \bar{t} the mean residence time.

The RTD of a system with a large recirculation flow compared to the in- and outlet flow in the will follow a concentration drop of a CSTR over time [38]. This results in a very spread out RTD for the reactants with peaks for the initial cycles through the HEAL.

Batch operation

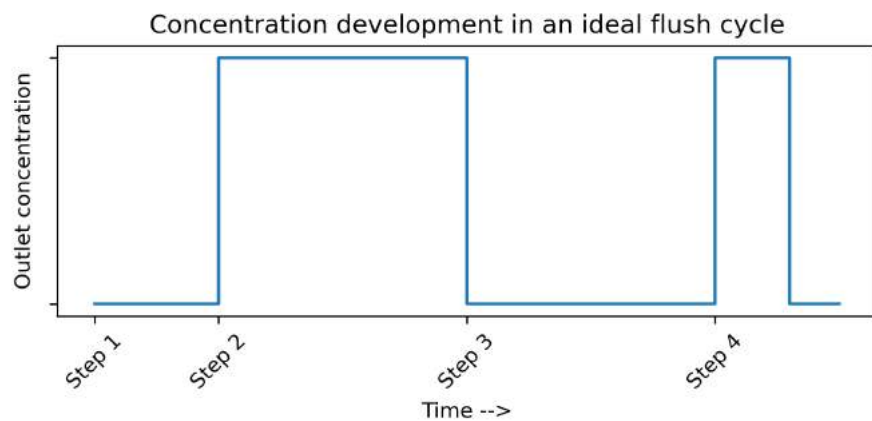
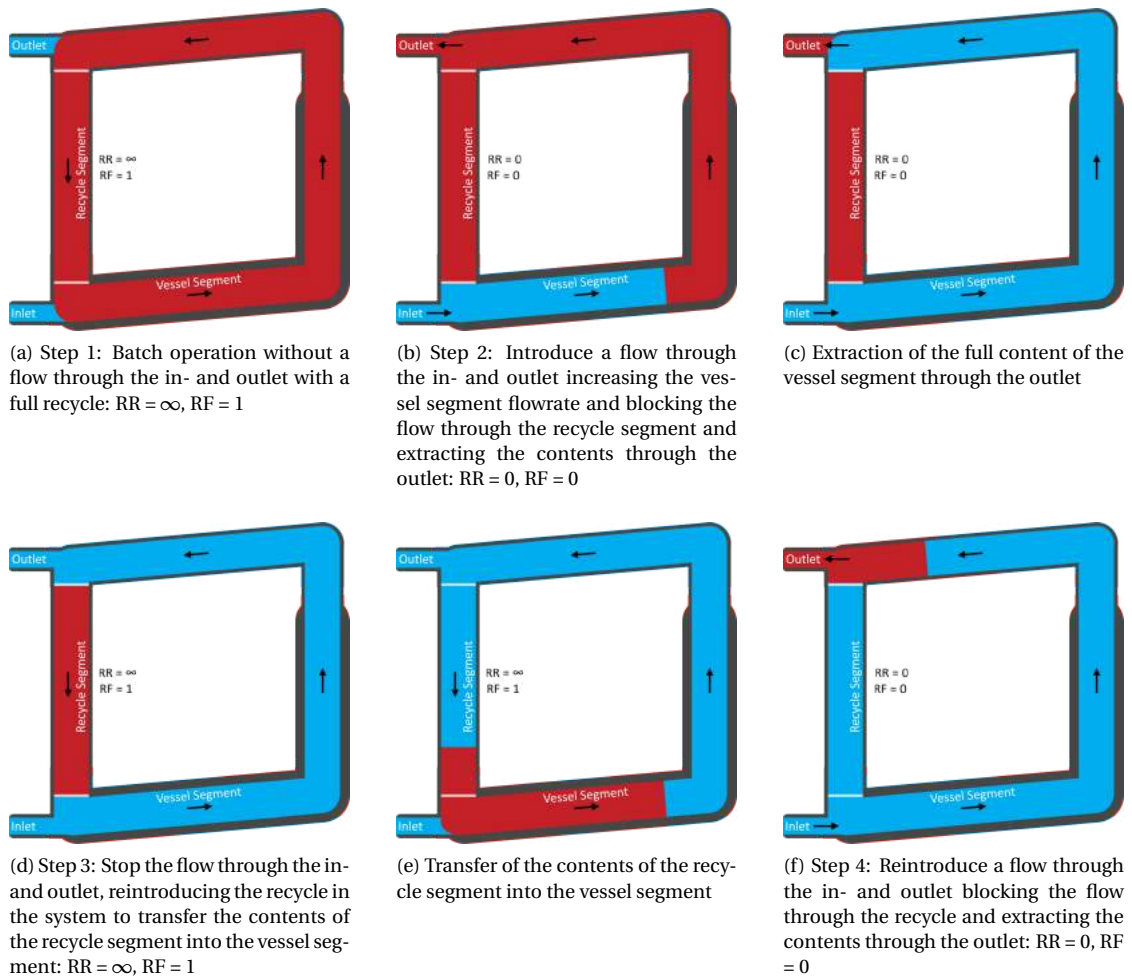
For a batch operation within the HEAL the target solution has to be introduced into the vessel. Once introduced, the in- and outlet flowrate are stopped or significantly reduced from which the reactants stay inside the vessel. Once a required concentration or specific activity of the product has been reached, the vessel has to be emptied/flushed.

An ideal flushing cycle for the HEAL is explained in the figures of 3.8. For this cycle, a flowrate through the inlet has to be reintroduced that lets the product in the vessel flow out through the outlet. This introduction of mass of will dilute the product inside the vessel. This dilution can be described using the degree of mixing J which was defined by Zwietering as shown in equation 3.28 [61].

$$J = \frac{\sigma_a^2}{\sigma_{\bar{a}}^2} = \frac{\overline{(a - \bar{a})^2}}{(\alpha - \bar{\alpha})^2} \quad (3.28a)$$

Where σ_a^2 is the variance of the ages of all the components in the system, $\sigma_{\bar{a}}^2$ is the variance of the mean age, α the mean age at a point in space, $\bar{\alpha}$ the average age of all components in a flow, and a the mean age of components at a point in space.

Zwietering showed that σ_a^2 can be calculated with the residence time distribution (RTD) of the system. Calculation of the variance of the mean age $\sigma_{\bar{a}}^2$ however requires the spatial distribution of the mean age of the components inside the system for which only few advanced methods have been developed that require the use of CFD simulations [39]. For an ideal systems such as a CSTR the degree of mixing J is 0, and within an ideal PFR J is 1.



(g) Ideal output concentration for flushing over the steps of the cycle.

Figure 3.8: Example steps of an ideal flushing cycle ($J = 1$) at the end or start of a batch operation as well as the concentration development in the outlet over time in this ideal flushing cycle. In these figures the color red indicates the contents that are inside the system that have to be removed, an example would be the radioisotopic products after irradiation. The blue color in the figures indicate new content inside the system that is introduced through the inlet. This is an ideal flushing cycle as intermixing between initial content (red) and new content (blue) is omitted and the recycle ratio/fraction for the flow through the recycle segment are under full control within the system.

The RTD individually can also be used as an initial indication for the mixing and flow patterns that are present inside the system, this by the variance of the distribution and shape of the RTD curve [38, 1].

Dilution of the product in the HEAL during a flushing operation is not only dependent on mixing/dispersion present inside each segment but also on the amount of control that is given in terms of flowrates in each of the segments. The ideal flushing cycle as shown in 3.8 requires the flowrate in the recycle segment to be completely stopped to prevent intermixing of the product in the two segments. As mentioned in the continuous operation before, if a large recirculation is still present compared to the inlet flowrate, the RTD of the total system will follow a CSTR profile which is not productive in keeping the exit concentration of the product as high as possible.

4

Methods

Within this chapter different models that were made are explained in detail together with geometry and material property definitions that were made for each model.

The models explained include the addition of axial and radial conduction within the discretized HEAL model, the geometries defined within Serpent for approaching the HEAL within the DLDR tube, a kinetic model for the production of Lu-177 utilizing the Szilard-Chalmers effect, a tanks in series model for approaching the dispersion in the different sections of the HEAL and a model that combines the tanks in series model with the kinetics.

4.1. Discretized HEAL Model

4.1.1. Model coordinates

To implement radial and axial conduction in the existing model, the system is discretized further into both axial and radial coordinates. For this discretization the system is split up over axially over the length in N axial nodes and over the radius in M radial wall nodes.

By splitting up the system in $N \times M$ nodes, a coordinate system is put in place referring to each node by coordinate values n and m . In this coordinate system n refers to the n^{th} axial node and m refers to the m^{th} radial node. An example of this coordinate system is shown in figure 4.1. This figure shows a partial cross section over the length of one of the pipes of the HEAL, where $N = 28$ and $M = 8$. In this figure the start and end of the N sections of the system within the model can be seen, where $n = 0$ refers to the first axial node and $n = 39$ refers to the final axial node in the model. Within the model, $m = 0$ always refers to the nodes that consist of the target solution inside the HEAL. m coordinates between 0 and $M - 1$ refer to a radial node and the final coordinate refers to the water of the DLDR tube.

Each individual node receives material properties that correspond to their respective materials such as their thermal conductivity constant, density, heat capacity, etc. These values are used in the calculations of the energy and momentum balances (4.5 and 4.10). The density and viscosity of the target solution are linked to the temperature within each node following the boussinesq and viscosity equations as specifically shown in the appendix (equation A.11 and A.14).

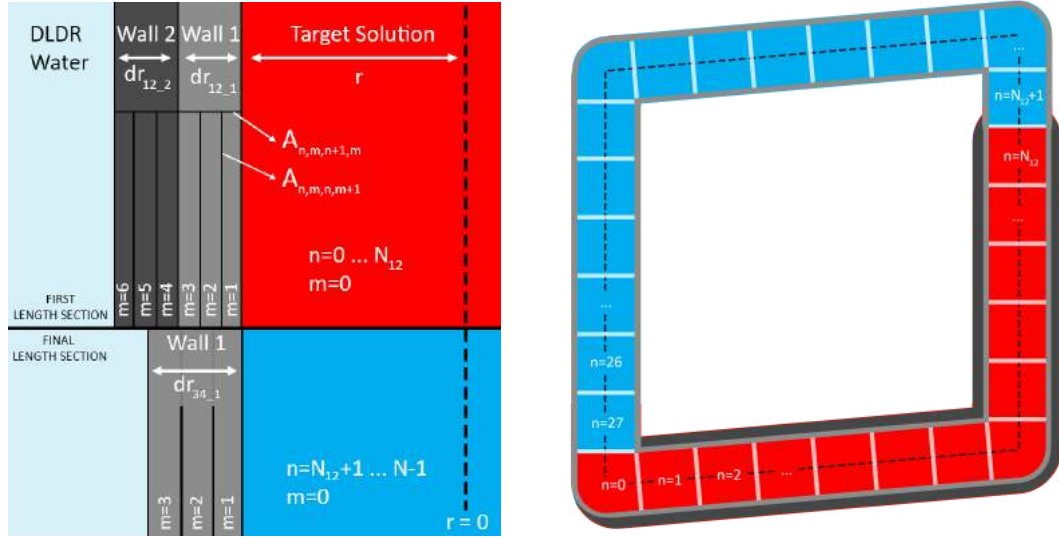


Figure 4.1: An example of the coordinate system used within the discretized HEAL model for both the sections in the n coordinate and in the m coordinate in a system with $N=28$ and $M=8$ over a partial cross section over the length of one of the pipes (left) and a cross section of the full HEAL system (right). Included into this figure is the implementation of multiple walls with different materials ("Wall 1" and "Wall 2") which can be defined inside of the model. N_{12} is defined as the last axial node contained within the heating sections 1 and 2.

4.1.2. Python Model Geometry

Next to material properties each individual node (n, m) also receives information about their own geometry. For instance each node receives their material volume $V_{n,m}$, radial thickness $dr_{n,m}$, length $dl_{n,m}$, angle $\theta_{n,m}$, and their starting and stop radius $r_{start_{n,m}}$, $r_{stop_{n,m}}$. These geometry variables for each node (n, m) are controlled via main system variables, such as the ones seen in figure 2.2. Dependent on where the node resides in respect to the HEAL (2.2) the geometry variables are set or calculated.

One of the variables that is calculated is the wall thickness. This thickness is defined by the overall wall thickness variable dr and the number of radial sections M . For a single layer wall material, the wall thickness for m is defined as 4.1a. If two wall layers are implemented inside of a section of the model, for instance indicated by "Wall 1" and "Wall 2" in figure 4.1, the wall thickness of each m coordinate is calculated differently as shown by the equations in 4.1.

$$\text{Single wall layer: } dr_{n,m} = \frac{dr_1}{M-2} \quad (4.1a)$$

$$\text{Multiple wall layers: } \begin{cases} dr_{1_n,m} = \frac{dr_1}{(M-2)/2}, & \text{Inner wall layer node thicknesses} \\ dr_{2_n,m} = \frac{dr_2}{(M-2)/2}, & \text{Outer wall layer node thicknesses} \end{cases} \quad (4.1b)$$

The main system length (L) variable of the geometry can either be set to a static value or can be calculated with regards to the maximum within the DLDR tube of 0.14m as given by the equations in 4.2. For this calculation it is assumed that each straight section of the HEAL has an equal length as shown in figure 2.2.

The length of the individual sectors of the HEAL are calculated via the equations in 4.3.

$$L = \begin{cases} \frac{2R_{DLDR} - (dr_{1_1} + dr_{1_2}) - (dr_{3_1} + dr_{3_2}) - 2R_i}{4(1 + \sin\theta)}, & \text{(Linked to DLDR radius)} \\ L, & \text{(Static Length)} \end{cases} \quad (4.2)$$

The individual lengths of the sections as given by L_{sec} are calculated via the equations as shown in 4.3 in which the $Frac$ variable is used to increase or decrease the length of both sections 2 and 3.

$$L_1 = \frac{1}{4} L, \quad L_2 = \frac{1}{4} L Frac, \quad L_3 = \frac{1}{4} L (1 - Frac), \quad L_4 = \frac{1}{4} L \quad (4.3)$$

The length variable for the individual nodes within the discretized system $dl_{n,m}$ can then be calculated using the system length L by equation 4.4.

$$dl_{n,m} = \frac{L}{N} \quad (4.4)$$

An overview of all of the main system variables that are defined for the geometry inside the system modelled in python can be found in table 4.1. These main system variables can either be set as a variable used in the overall system or individually be defined in certain sectors/sections as indicated by the figure in 2.2.

4.1.3. Improved energy balance

In the model each node receives their own energy balance. These balances consist of the conduction of heat from neighbouring nodes, generation of heat from gamma heating and the transfer of heat from the flowing target solution. The overall energy balance for both the nodes containing the target solution ($\frac{\delta T_{n,0}}{dt}$) and the nodes containing the wall materials ($[\frac{\delta T_{n,m}}{dt}]_{M>m>0}$) can be found in the equations of 4.5.

$$\frac{\delta T_{n,0}}{\delta t} = -\frac{1}{\rho_{n,0} C_{\rho_{n,0}} V_{n,0}} (\phi_{n,m,n,m_conn} + \phi_{n,m,n_conn,m}) - \frac{N}{L} (T_{n,0} - T_{n-1,0}) v \quad (4.5a)$$

$$[\frac{\delta T_{n,m}}{\delta t}]_{M>m>0} = \frac{u_{n,m}}{C_{\rho}} - \frac{1}{\rho_{n,m} C_{\rho_{n,m}} V_{n,m}} \left(\sum_{m_conn=0}^M \sum_{n_conn=0}^N \phi_{n,m,n_conn,m_conn} \right) \quad (4.5b)$$

In these equations N is the number of axial node coordinates in the model, M the number of radial node coordinates in the model, v is the velocity of the fluid inside the system in $[\frac{m}{s}]$, $u_{n,m}$ as the gamma heating deposition at coordinate n, m in $[\frac{W}{kg}]$, $T_{n,m}$ is the temperature of the node at coordinate n, m given in $[K]$, $\rho_{n,m}$ the density of the node at n, m in $[\frac{kg}{m^3}]$, $C_{\rho_{n,m}}$ the heat capacity of the node at n, m in $[\frac{J}{kgK}]$, and ϕ_{n,m,n_conn,m_conn} is given as the heat transfer rate between the nodes with coordinates n, m and n_conn, m_conn in $[W]$.

In the energy balance equations of 4.5 the heat transfer rates between nodes (ϕ_{n,m,n_conn,m_conn}) are calculated differently dependent on the material type and coordinate system to which node (n, m) and node (n_conn, m_conn) are connected as will be explained in the next sections on axial and radial heat transfer.

Axial heat transfer

Nodes that are axially in contact with each other can transfer heat via axial conduction. Following Newtons law of cooling (3.3a) the heat flow between axially connected nodes (n, m) & (n_conn, m) is defined by equation 4.6a. For nodes that are not axially in contact with each other the heat transfer rate (ϕ_{n,m,n_conn,m_conn}) is set to 0.

$$\phi_{n,m,n_conn,m} = \begin{cases} -A_{n,m,n_conn,m} \kappa_{n,m} \frac{T_{n,m} - T_{n_conn,m}}{(l_n + l_{n_conn})/2}, & \text{same material between nodes} \\ -A_{n,m,n_conn,m} U_{n,m,n_conn,m} (T_{n,m} - T_{n_conn,m}), & \text{different material between nodes} \end{cases} \quad (4.6a)$$

$$\text{where } U_{n,m,n_conn,m} = \left(\frac{1}{h_{n,m,ax}} + \frac{1}{h_{n_conn,m,ax}} + \frac{1}{h_c} \right)^{-1} \quad (4.6b)$$

Where $\phi_{n,m,n_conn,m}$ is the heat flow between nodes on coordinates (n, m) and (n_conn, m) in $[W]$, $A_{n,m,n_conn,m}$ the contact area between nodes in $[m^2]$, $U_{n,m,n_conn,m}$ as the overall heat transfer coefficient between the node materials in $[\frac{W}{m^2K}]$, $T_{n,m}$ the temperature of node (n, m) and $T_{n_conn,m}$ the temperature of node (n_conn, m) in $[K]$, $\kappa_{n,m}$ the heat conductivity in $[\frac{W}{mK}]$, l_n and l_{n_conn} are the respective lengths of the nodes in $[m]$, $h_{n,m,ax}$ and $h_{n_conn,m,ax}$ the respective axial heat transfer coefficient of the materials in $[\frac{W}{m^2K}]$, and finally h_c as the heat transfer coefficient for the the contact resistance between different materials in $[\frac{W}{m^2K}]$.

Table 4.1: An overview of the variables and parameters defined inside the python model of the HEAL system for definition of the geometry

Main Variable (Symbol)	Sector Variable (Symbol)	Section Variable (Symbol)	Layer Variable (Symbol)	Unit
Wall thickness (dr)	Heating Sector (dr_{12})	Section 1 (dr_1)	Layer 1 (dr_{1_1})	m
		Section 2 (dr_2)	Layer 2 (dr_{1_2})	
		Section 3 (dr_3)	Layer 1 (dr_{2_1})	
		Section 4 (dr_4)	Layer 2 (dr_{2_2})	
	Cooling Sector (dr_{34})	Section 1 (dr_1)	Layer 1 (dr_{3_1})	
		Section 2 (dr_2)	Layer 2 (dr_{3_2})	
		Section 3 (dr_3)	Layer 1 (dr_{4_1})	
		Section 4 (dr_4)	Layer 2 (dr_{4_2})	
Wall Material (mat)	Heating Sector (mat_{heat})	Section 1 (mat_1)	Layer 1 Material (mat_{1_1})	-
		Section 2 (mat_2)	Layer 2 Material (mat_{1_2})	
		Section 3 (mat_3)	Layer 1 Material (mat_{2_1})	
		Section 4 (mat_4)	Layer 2 Material (mat_{2_2})	
	Cooling Sector (mat_{cool})	Section 1 (mat_1)	Layer 1 Material (mat_{3_1})	
		Section 2 (mat_2)	Layer 2 Material (mat_{3_2})	
		Section 3 (mat_3)	Layer 1 Material (mat_{4_1})	
		Section 4 (mat_4)	Layer 2 Material (mat_{4_2})	
System Length (L)	Heating Sector (L_{heat})	Section 1 (L_1)	m	
		Section 2 (L_2)		
		Section 3 (L_3)		
		Section 4 (L_4)		
Section 2 Length Fraction (Frac)	Cooling Sector (L_{cool})	Section 1 (L_1)	-	
		Section 2 (L_2)		
		Section 3 (L_3)		
		Section 4 (L_4)		
DDDR tube radius (R_{DDR})	Inner radius (R_i)	Section 1 (θ_1) = θ	m	
		Section 2 (θ_2) = 1		
		Section 3 (θ_3) = θ		
		Section 4 (θ_4) = -1		
Pipe Angle (θ)	Pipe Angle (θ)	Section 1 (θ_1) = θ	Degrees or radians	
		Section 2 (θ_2) = 1		
		Section 3 (θ_3) = θ		
		Section 4 (θ_4) = -1		
Number of axial nodes (N)				#
Number of radial nodes (M)				#

Radial heat transfer

The radial heat transfer rates from conduction between two nodes in the model are calculated as shown in the equations of 4.7.

$$\phi_{n,m,n,m_conn} = \begin{cases} -A_{n,m,n,m_conn} \kappa_{n,m} \frac{T_{n,m} - T_{n_conn,m}}{r_{n,m} \log\left(\frac{r_{n,m_conn}}{r_{n,m}}\right)}, & \text{same material between nodes} \\ -A_{n,m,n,m_conn} U_{n,m,n,m_conn} (T_{n,m} - T_{n_conn,m}), & \text{different material between nodes} \end{cases} \quad (4.7)$$

Where $A_{n,m,n,m_conn} U_{n,m,n,m_conn}$ is defined within the equations of 4.8.

$$A_{n,m,n,m_conn} U_{n,m,n,m_conn} = \begin{cases} \left(\frac{1}{h_{n,m} A_{n,m,n,m_conn}} + \frac{1}{h_{n,m_conn} A_{lm(n,m_conn)}} \right)^{-1}, & \text{inner fluid and wall} \\ \left(\frac{1}{h_{n,m,rad} A_{lm(n,m)}} + \frac{1}{h_{n,m_conn,rad} A_{lm(n,m_conn)}} + \frac{1}{h_c A_{n,m,n,m_conn}} \right)^{-1}, & \text{different wall materials} \\ \left(\frac{1}{h_{n,m,rad} A_{lm(n,m)}} + \frac{1}{h_{n,m_conn,rad} A_{n,m_conn,n,m}} \right)^{-1}, & \text{wall and outer fluid} \end{cases} \quad (4.8)$$

Where A_{n,m,n,m_conn} and $A_{lm(n,m)}$ are defined the equations in 4.9.

$$A_{n,m,n,m_conn} = 2\pi l_{n,m} r_{n,m,n,m_conn} \quad (4.9a)$$

$$A_{lm(n,m)} = \frac{2\pi l_{n,m} (r_{stop_{n,m}} - r_{start_{n,m}})}{\ln\left(\frac{r_{stop_{n,m}}}{r_{start_{n,m}}}\right)} \quad (4.9b)$$

In these equations r_{n,m,n,m_conn} is the radius at which the nodes (n, m) and (n, m_conn) contact each other in $[m]$, $r_{start(n,m)}$ is the inner radius of the node in $[m]$, $r_{stop_{n,m}}$ is the outer radius of the node in $[m]$, A_{n,m,n,m_conn} is the contact area between the nodes in $[m^2]$, $A_{lm(n,m)}$ is the logarithmic mean area of the node (n, m) in $[m^2]$, $h_{n,m,rad}$ and $h_{n,m_conn,rad}$ the respective radial heat transfer coefficient of the materials in $[\frac{W}{m^2K}]$.

Momentum balance

The momentum balance in respect of the nodes of the target solution only receives a small change by the implementation of the the coordinate system as seen in equation 4.10.

$$\frac{\partial v}{\partial t} = -\frac{1}{N} \sum_{n=1}^N f_{D_{n,0}} \frac{1}{4r_{stop_{n,m}}} v^2 - \frac{v^2}{L} (\kappa_1 + \kappa_2) + \frac{g}{N} \sum_{n=1}^N (1 - \beta (T_{n,0} - T_{ref})) \sin(\phi_{n,0}) \quad (4.10)$$

Where N is the number of nodes in the model, $f_{D_{n,0}}$ is the Darcy friction in node $(n, 0)$, $r_{stop_{n,m}}$ the inner radius of the HEAL within node (n, m) in $[m]$, v the velocity in the system in $[\frac{m}{s}]$, L the system length of the system in $[m]$, κ_1 and κ_2 the friction coefficient from the bends, g the gravitational constant in $[\frac{m}{s^2}]$, β the thermal expansion coefficient in $[K^{-1}]$, T_{ref} the reference temperature for the thermal expansion coefficient from the boussinesq equation in $[K]$, $T_{n,0}$ the temperature of the target solution inside the HEAL in node n in $[K]$ and $\phi_{n,0}$ the angle of node $(n, 0)$ in $[\circ]$ or $[rad]$.

4.1.4. Numerical methods and implementation

The energy and momentum balances as shown in equations 4.5 and 4.10 result in a large system of ordinary differential equations to be solved for both the temperature within the individual nodes and the velocity within the discretized system. The general form of this matrix is shown in 4.11. For solving this system of equations in time dependent and steady state problems, two numerical methods were utilized. In time dependent problems the LSODA method was used and for steady state problems a combination of both the LSODA and the Jacobian-free Newton-Krylov method were utilized [36, 43, 32].

$$F(t) = A(t)Y(t) + b(t) \quad (4.11)$$

Where $Y(t)$ is a $(N \times M+1, 1)$ matrix of variables including the temperature of each node and the internal velocity, $F(t)$ is the vector matrix of the derivatives of variables $Y(t)$, $A(t)$ the known functions within the balances such, e.g. the energy transfer rate between specific nodes $\phi_{n,m,n_{conn},m_{conn}}$, and $b(t)$ a matrix including additional functions excluding the variables from $Y(t)$. An example is the energy deposition within a node from equation 4.5.

The LSODA method is included in ODEPACK that combines the implicit Adams-Moulton method, used for solving for nonstiff problems, and the Backwards Differentiation Formula (BDF) for solving stiff problems and switches between these methods dynamically [16, 32]. The step size and order used by the methods used are based on asymptotic local error analysis by maximising the step size without exceeding a set error tolerance [32].

$$y_{i+1} = y_i + h \sum_{k=0}^{n-1} \beta_k f(t_{i+1-k}, y_{i+1-k}), \quad \text{Adams-Moulton} \quad (4.12a)$$

$$y_i = \sum_{k=0}^n \alpha_k y_{i-k} + h \beta_0 f(t_n, y_n), \quad \text{Backwards Differentiation Formula} \quad (4.12b)$$

Where y is the variable, t the time, $f(t, y)$ as the derivative of variable y at time t , n the order of accuracy, α and β method specific coefficients, and h the step size.

The Jacobian-free Newton-Krylov method is a method which combines the Newton method for solving systems of linearly convergent solutions with a Krylov subspace method which is used to bypass the Jacobian calculation that normally results from the calculation within a Newton method based solver in systems with multiple variables [36]. The implementation of this method results in a lower computational cost compared to evaluating the full Jacobian within the Newton method alone [20].

$$Y_{n+1} = Y_n - J(y_n)^{-1} F(y_n), \quad \text{Newton Method for systems of equations} \quad (4.13)$$

With Y_n as the variable vector, $J(y_n)^{-1}$ the inverse of the Jacobian at y_n , and $F(y_n)$ the function matrix for a system of equations.

Both of these methods were imported in Python from the Scipy library and used in conjunction with Python code managing the systems of equations for the different HEAL configurations that were analyzed in time dependent and steady state situations.

Solving the system of equations for a time dependent problem requires an initial state of the system, for startup situations the velocity inside the system of equations was set at 0.0 m/s and all temperatures were set at 40°C , the same as the water temperature inside the DLDR tube.

For solving the system of equations at steady state, the root of the set of equations ($\frac{dy}{dt} = 0$) is found by utilizing the Newton-Krylov method. Using the same input parameters as the time dependent problems generally resulted in non-physical results. Therefore, for steady state problems an initial time dependent problem is solved using the LSODA method, the temperature and velocity results from these calculations were then used as input parameters for the Newton-Krylov method.

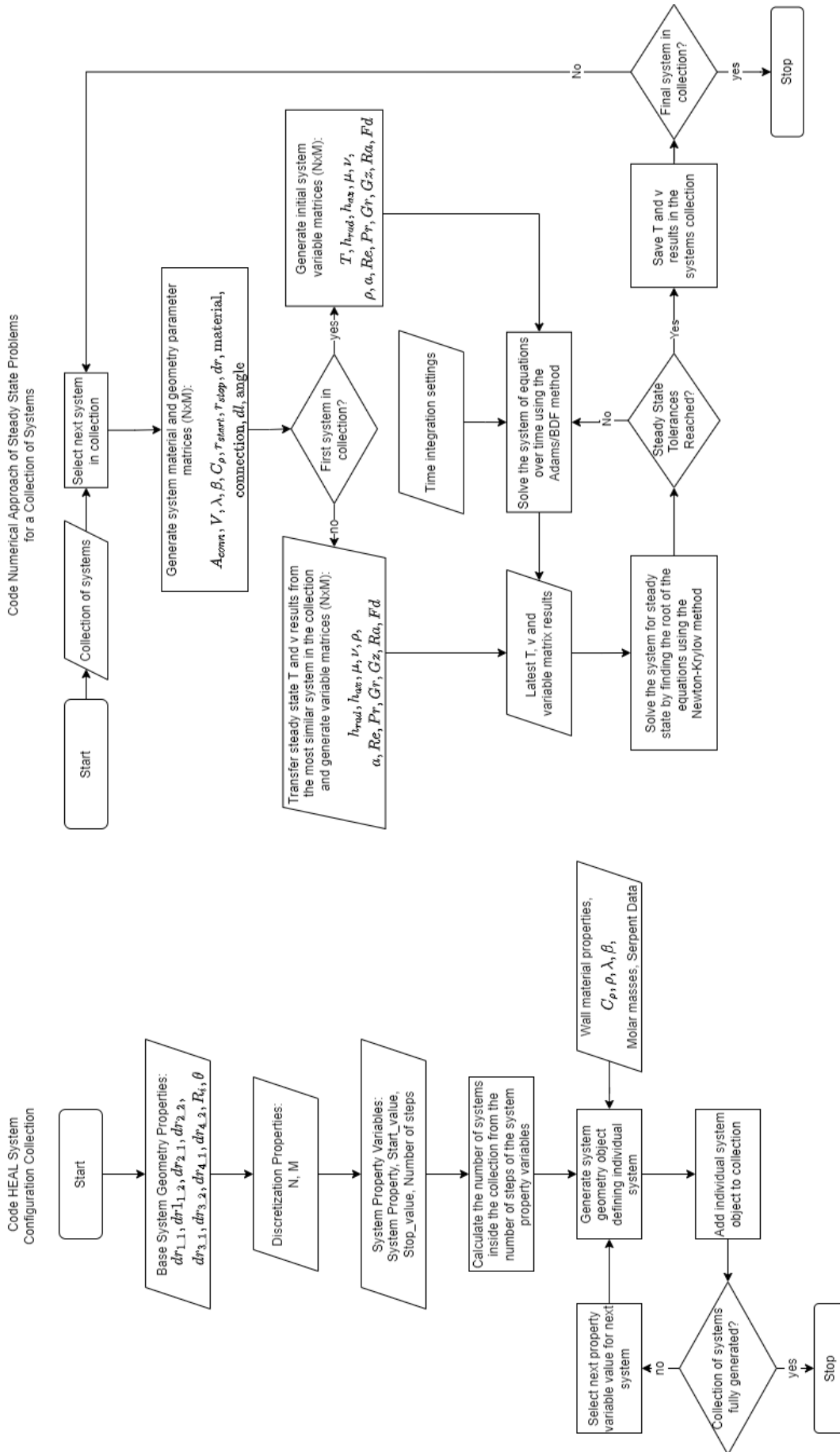


Figure 4.2: Flow chart of the written Python code for defining a collection of HEAL configuration systems (left) and using the collection of systems to solve steady state problems (right)

As the LSODA method proved to be computationally intensive, code was developed to use steady state temperature and velocity results from previously computed systems at steady state as an input. This still required the systems from which the results were taken to contain similar parameters, as otherwise unsteady results would still be present. To achieve this, systems with either one or two parameter variables were assembled inside a collection of systems. From this collection, an initial system would be solved using both the LSODA and Newton-Krylov methods. The next system with a slightly different configuration would then use the results from the first system as input parameters directly to the Newton-Krylov method. If tolerances are not met, the time dependent LSODA method is still used. A flow chart for the program for the definition of the collection of systems and the solving of steady state problems can be found in figure 4.2. Solving of dynamic situations utilizes the time integration using the LSODA method after which the code is stopped.

Tolerances defined in the Scipy functions that differ from the default values of the numerical methods can be found in table 4.2.

Table 4.2: Tolerance and settings that differ from the default values of the Scipy functions of the numerical methods

Method	Tolerance/Settings
Jacobian-free Newton-Krylov	$rdiff = 5 \times 10^{-9}$, $f_tol = 1 \times 10^{-8}$, $maxiter=100$, $line_search=wolfe$
LSODA	$r_tol = 1 \times 10^{-2}$, $first_step=1 \times 10^{-6}$, $max_step=0.5$

4.1.5. Material Properties and Model Parameters

In table 4.3 the defined material properties for aluminium, zircaloy and lead that were used in the model for the results are shown. Most model geometry parameters as shown in table 4.1 are varied throughout the results except the number of axial and radial nodes N and M . For steady state results these are set to $N = 40$ and $M = 7$. For the dynamic results they are set to $N = 160$ and $M = 7$.

All performed simulations with this discretized HEAL model assumed the measured energy deposition rate u of $300W/kg$ [19] within each wall material.

Table 4.3: The material properties of different materials used in the discretized model

Property (Symbol)	Material	Value	Unit	Reference
Specific heat capacity (C_p)	Aluminium (Al)	890.0	$\frac{J}{kgK}$	[31]
	Zircaloy (Zr)	285.0		[30]
	Lead (Pb)	129.0		[37]
	Target solution	4187.5		[34]
Density (ρ)	Aluminium (Al)	2.70×10^3	$\frac{kg}{m^3}$	[35]
	Zircaloy (Zr)	6.55×10^3		[30]
	Lead (Pb)	11.34×10^3		[35]
Thermal conductivity coefficient (κ)	Aluminium (Al)	239	$\frac{W}{mK}$	[13]
	Zircaloy (Zr)	21.5		[30]
	Lead (Pb)	35		[37]
	Target solution	0.65		[35]
Expansion coefficient @50 °C (β)	Target solution	4.57×10^{-4}	K^{-1}	[35]
Reference expansion temperature (T_{ref})	Target solution	293.15	K^{-1}	[51]
Reference expansion density (ρ_{ref_p})	Target solution	998.23	$\frac{kg}{m^3}$	[35]
Reference dynamic viscosity (η_{ref})	Target solution	1.002×10^{-3}	$Pa\cdot s$	[35]
Reference dynamic viscosity temperature (T_{ref_eta})	Target solution	293.15	K^{-1}	[35]
Reference thermal conductivity temperature (T_{ref_a})	Target solution	353.15	K^{-1}	

4.2. Shielding

4.2.1. Serpent Model

To approach the energy deposition and target doserates in the geometries of the HEAL, the Monte Carlo based neutron and photon transport software Serpent was utilized. Within Serpent the DLDR tube geometry was coded following the geometry of the tube from Huisman [34] with the wall material being AlMg3.

4.2.2. Photon/Gamma source generation

For the generation of photons that move through the DLDR tube, a plane source within Serpent was defined. This plane source consists of a $30 \times 30\text{cm}$ plane, placed in front of the middle of the DLDR tube as indicated in figure 4.3. Photons that are generated from this source move in an isotropic direction from the normal of the plane towards the DLDR geometry. For the photon energy spectrum of this source, a calculated spectrum from MCNP was used from the free field of the ACRR (Annular Core Research Reactor)[48]. Verification of the spectrum of the plane source and normalization within Serpent can be found in appendix C.0.1.

The ACRR is a pool-type light water research reactor from Sandia National Laboratories with an operating power of $2\text{-}4\text{MW}_{th}$ [48], similar to the operating power of 2MW_{th} of the HOR [12].

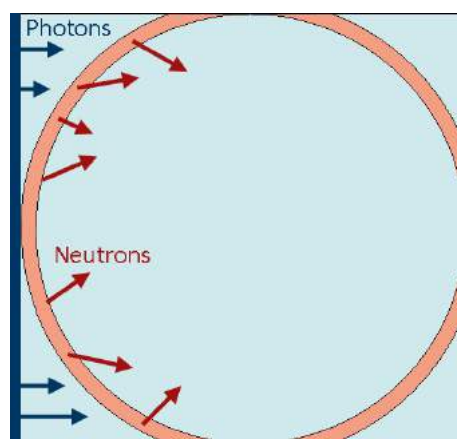


Figure 4.3: Axial cross section through the middle of the DLDR tube. The cylinder wall of the DLDR tube is indicated by orange with the water present in- and outside of the tube indicated by light blue in the figure. The HOR is located to the left side of the DLDR tube in this figure, from which the planar photon source the within in Serpent was defined as indicated by marine blue. The source of neutrons within the simulations originate from the wall of the DLDR tube themselves as indicated by the arrows in red.

Photon source normalization

Normalization of the gamma source rate was performed by iterating over the heat deposition within the wall of the HEAL to be equal to $300\text{W}/\text{kg}$ [19]. This normalization was specifically performed in a generated HEAL geometry made from Zr with a wall thickness of 3mm where the average heat deposition from the macroscopic total heating cross section (detector response $MT = -26$ in Serpent) over the wall was calculated.

4.2.3. Neutron source

For describing the reaction rate and the deposition rate of neutrons within the target in the HEAL the neutrons originating from the HOR that go through the DLDR tube have to be obtained.

To obtain these neutrons within Serpent, a model for the HOR core and the DLDR tube is required. Serpent code of a detailed model of the HOR within Serpent was previously made by [23] which was edited by van Egmond [22] to include a more detailed geometry within the DLDR tube.

Performing these calculations for every experiment on the HEAL within Serpent is very computationally expensive as the whole core would be simulated in each experiment. This is where the use of a so called "source file" comes in. The source file is a file that contains coordinates, direction and energy information about neutrons passing through a specific volume/geometry. This information can then be used to describe arbitrary

distributions for a source geometry within Serpent [53]. By using a source coupled to a source file the neutron generating core doesn't have to be simulated any more and a much more selective system geometry can be simulated while reducing the computational time significantly.

To generate such a source file the complete simulated system only has to be simulated once by "capturing" any particle that moves through a selected geometry such as the wall of the DLDR tube.

Neutron source generation and normalization

The HOR Serpent code from van Egmond [22] was edited to only include the HOR core and DLDR tube. Using this model a source file for neutrons passing through the wall of the DLDR tube was generated by simulating the neutron output of the HOR at a power of $2MW_{th}$ within Serpent. The simulation was performed with a population of 1.5×10^6 in a total of 1500 bins. This resulted in a source file with 744191 individual neutron coordinate, direction and energy data points in a $40cm$ long section of the wall of the DLDR tube.

Normalization of the neutron sourcerate was calculated using the same simulation and can be found in appendix C.0.2. This normalization of the neutron flux was then used in further neutron transport simulations within Serpent for the gathering of results for different HEAL geometries within the DLDR tube.

4.2.4. HEAL Geometries & Materials

Geometries

Code for the geometry of the HEAL in the DLDR tube in Serpent is generated using code written in Python. In this code the defined system parameters from the system objects in 4.1 are used as an input. This code generates both the geometry of the HEAL and the Serpent detectors required for analysis of photon and neutron interactions. The code generates geometry of the HEAL that represents the defined system as closely as possible according to both the length in equation 4.3 and places this in the middle of the DLDR tube as previously defined. One assumption that is made for the geometry is that the radius of the bends is equal to the total radius of the cylinder.

Another thing that is not implemented into the code is the implementation of the angle of the horizontal pipes. This is due to the significantly increased complexity that it would bring within defining the geometry in Serpent. To compensate for the angle a gap is created between the horizontal pipes and the DLDR tube that correspond to the space inhibited by the pipe with an angle. An example of a HEAL geometry generated by this code can be seen in figure 4.4.

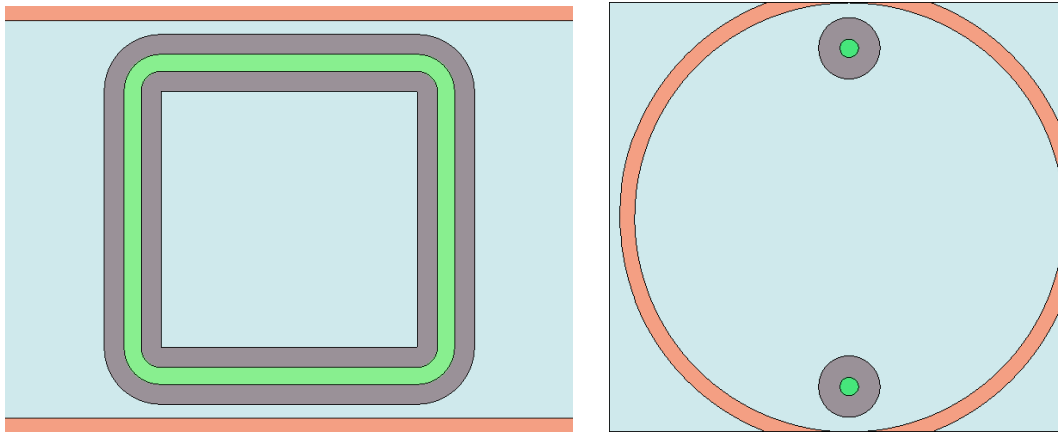


Figure 4.4: Radial (left) and axial (right) cross section of a HEAL geometry in the DLDR tube within Serpent. The radial cross section shows the DLDR tube from the viewpoint of the Hoger Onderwijs Reactor. The axial cross section is through the middle of the DLDR tube. The HEAL geometry consists of an inner radius of $3mm$ and a single wall layer thickness of $7mm$. The target solution in the HEAL is indicated by green in the figures. The grey material is the wall material of the HEAL, the orange material is the material of the DLDR tube and the water present in- and outside of the DLDR tube is indicated by blue.

For the simulations on photon and neutron interactions to the materials in the HEAL, Serpent geometries of the HEAL were generated for systems with two different types of walls:

1. Single wall layer consisting of one material at different wall thicknesses
2. Two layer wall with two different materials at different wall thicknesses.

An overview of the properties and wall thicknesses that were used for both these different types can be seen in table 4.4.

Table 4.4: Wall thicknesses of single and multi wall material HEAL systems for Serpent

Single layer wall systems	Multiple layer wall systems	
Wall thickness (mm)	Inner material wall thickness (mm)	Outer material wall thickness (mm)
3	1	1, 3, 5, 7, 9, 11, 13, 15
4.5	3	1, 3, 5, 7, 9, 11, 13
6	5	1, 3, 5, 7, 9, 11
7.5	7	1, 3, 5, 7, 9
9	9	1, 3, 5, 7
10.5	11	1, 3, 5
12	13	1, 3
13.5		
15		

Materials and photonuclear database

Three different materials were implemented for the wall of the HEAL systems: Aluminium, lead and zirconium. These materials were chosen for their respective thermal transfer, gamma interaction and neutron interaction rates as well as their previous use in research on the HEAL in which Zircaloy was used, an alloy which mainly consists of zirconium [51, 34, 30].

The properties of these materials and their isotropic definition within the Serpent code can be found in table 4.6. For an extended definition of each material and how the HEAL geometry is defined, the materials properties code as found in appendix C.0.3 and the geometry code can be referenced.

Table 4.5: Photonuclear interaction databases used inside the Serpent simulations of the HEAL

Interaction libraries	Library/Database	Reference
Neutron interactions	ENDF/B-VII.1	[15]
Decay data library	ENDF/B-VII.1	[15]
Neutron-induced fission yield library	ENDF/B-VII.1	[15]
Branching ratio library	JEFF 3.1a	[45]
Photon interactions	NIST Standard Reference Database 126	[33]

Table 4.6: Isotropic materials definition within Serpent

Material	Density ($\frac{g}{cm^3}$)	Isotopes	Molar fraction	ENDF/B-VII.1 & JEFF 3.1a reference
Aluminium	2.7	^{27}Al	1.000	13027.80c
Zirconium	6.55	^{90}Zr	0.5145	40090.80c
		^{91}Zr	0.1122	40091.80c
		^{92}Zr	0.1715	40092.80c
		^{94}Zr	0.1738	40094.80c
		^{96}Zr	0.028	40096.80c
Lead	11.34	^{204}Pb	0.014	82204.80c
		^{206}Pb	0.241	82206.80c
		^{207}Pb	0.221	82207.80c
		^{208}Pb	0.524	82208.80c
AlMg3	2.66	^{27}Al	0.9500	13027.80c
		^{24}Mg	0.0395	12024.80c
		^{25}Mg	0.0050	12025.80c
		^{26}Mg	0.0055	12026.80c
H2O	0.99823	^1H	0.66667	1001.80c
		^{16}O	0.33333	8016.80c
^{176}Lu Target	-	^{176}Lu	1.000	71176.80c

4.3. Lu-177 Production Model

4.3.1. Kinetics

For the kinetic model, four different types of rate functions have been defined: Chemical reaction rate, neutron interaction rate, gamma interaction rate, and decay rates respectively based on the rate equations as previously defined in 3.10b, 3.8b, 3.11b, and 3.9a. With these individual functions the overall rate function of a component can be described as the equation in 4.14.

$$\frac{dC}{dt} = \left(\frac{dC}{dt}\right)_{chem} + \left(\frac{dC}{dt}\right)_n + \left(\frac{dC}{dt}\right)_\gamma + \left(\frac{dC}{dt}\right)_\lambda \quad (4.14)$$

Next to the four different rate functions, four component types are defined:

- Isotopic metal ions in solution (${}^A_Z\text{Me}^{(+3)}$)
- Bound metals to DOTA (${}^A_Z\text{MeDOTA}$)
- DOTA in solution (DOTA)
- Damaged DOTA products (DOTA_{dam})

Each of these component types have their own individual set of rate equations for every rate function type.

Chemical reaction rates, $\left(\frac{dC}{dt}\right)_{chem}$

Based on the equilibrium reaction of 3.10b, the chemical reaction rates between the unlabeled and labeled components are defined in the model as a first and second order elementary reactions as seen in 4.15. In these equations the equilibrium constant K was defined in the reaction rate constants k_1 and k_2 .

$$K = \frac{k_1}{k_2} = \frac{[\text{LuDOTA}^-]}{[\text{Lu}^{3+}][\text{DOTA}^{4-}]} \quad (4.15a)$$

$$\frac{dC_{\text{Lu}^{3+}}}{dt} = \frac{dC_{\text{DOTA}^{4-}}}{dt} = -\frac{dC_{\text{LuDOTA}^-}}{dt} = k_1[\text{Lu}^{3+}][\text{DOTA}^{4-}] - k_2[\text{LuDOTA}^-] \quad (4.15b)$$

Where k_1 and k_2 are the reaction rate constants for the reactions of binding/labeling and releasing the metal ions in $[\frac{L^2}{mol^2}]$ and $[\frac{L}{mol}]$ respectively.

Generalising these rate equations for metals (${}^A_Z\text{Me}$) and assuming that the reaction rate constants for the labeling between these metals is equal, results in the chemical reaction rate equations as shown in 4.16.

$$\left(\frac{dC_{{}^A_Z\text{Me}^{(+3)}}}{dt}\right)_{chem} = k_1 C_{{}^A_Z\text{Me}^{(+3)}} C_{\text{DOTA}} - k_2 C_{{}^A_Z\text{MeDOTA}} \quad (4.16a)$$

$$\left(\frac{dC_{{}^A_Z\text{MeDOTA}}}{dt}\right)_{chem} = k_2 C_{{}^A_Z\text{MeDOTA}} - k_1 C_{{}^A_Z\text{Me}^{(+3)}} C_{\text{DOTA}} \quad (4.16b)$$

$$\left(\frac{dC_{\text{DOTA}}}{dt}\right)_{chem} = \sum_{{}^A_Z\text{Me}}^{Isotopes} k_1 C_{{}^A_Z\text{Me}^{(+3)}} C_{\text{DOTA}} - \sum_{{}^A_Z\text{Me}}^{Isotopes} k_2 C_{{}^A_Z\text{MeDOTA}} \quad (4.16c)$$

With C_i as the concentration of component i in $[\frac{mol}{L}]$, k_1 and k_2 the reaction rate constants for the bind and release reactions in $[\frac{L^2}{mol^2}]$ and $[\frac{L}{mol}]$ respectively.

Neutron interaction rates, $(\frac{dC}{dt})_n$

The rate functions for the neutron interaction rates in the model are based the general neutron rate equation from 3.8a, both in terms of production as radiolysis. The rate equations for each of the component types are given in 4.17. In these functions three neutron cross sections are defined: $\sigma_{A(n,\gamma)A+1}$ as the neutron capture cross sections, σ_{n_dam1} as the total cross section for releasing metal ions from the ${}^A_Z\text{MeDOTA}$, and σ_{n_dam2} as the cross section for the release of metals from the DOTA complex without damaging the DOTA molecule.

$$\left(\frac{dC_{{}^A_Z\text{Me}^{(+3)}}}{dt}\right)_n = C_{A-1}{}^A_Z\text{Me}^{(+3)}\varphi_n\sigma_{A-1(n,\gamma)A} + (1-R)C_{A+1}{}^A_Z\text{MeDOTA}\varphi_n\sigma_{A(n,\gamma)A+1} + C_{{}^A_Z\text{MeDOTA}}\varphi_n\sigma_{n_dam1} \quad (4.17a)$$

$$\left(\frac{dC_{{}^A_Z\text{MeDOTA}}}{dt}\right)_n = RC_{A-1}{}^A_Z\text{MeDOTA}\varphi_n\sigma_{A-1(n,\gamma)A} - C_{{}^A_Z\text{MeDOTA}}\varphi_n(\sigma_{A(n,\gamma)A+1} + \sigma_{n_dam1}) \quad (4.17b)$$

$$\left(\frac{dC_{\text{DOTA}}}{dt}\right)_n = (1-R)C_{A+1}{}^A_Z\text{MeDOTA}\varphi_n\sigma_{A(n,\gamma)A+1} - \sum_{\substack{\text{Isotopes} \\ {}^A_Z\text{Me}}} C_{{}^A_Z\text{MeDOTA}}\varphi_n\sigma_{n_dam1} - C_{\text{DOTA}}\varphi_n(\sigma_{n_dam1} - \sigma_{n_dam2}) \quad (4.17c)$$

$$\left(\frac{dC_{\text{DOTA}_{dam}}}{dt}\right)_n = \left(\sum_{\substack{\text{Isotopes} \\ {}^A_Z\text{Me}}} C_{{}^A_Z\text{MeDOTA}} + C_{\text{DOTA}}\right)\varphi_n(\sigma_{n_dam1} - \sigma_{n_dam2}) \quad (4.17d)$$

With $\sigma_{A(n,\gamma)A+1}$ as the neutron capture cross section for ${}^A_Z\text{Me}$ to ${}^{A+1}_Z\text{Me}$ in [cm^2] or [b], σ_{n_dam1} as the total cross section for the release of metal ions in [cm^2] or [b], σ_{n_dam2} as the cross section for the release of metals without damaging the DOTA molecule in [cm^2] or [b], φ_n as the neutron flux in [$cm^{-2}s^{-1}$], and R the metal atom retention fraction.

Gamma interaction rates, $(\frac{dC}{dt})_\gamma$

The rate functions for the gamma interactions are only based on radiolysis via the general gamma rate equation from 3.8a and can be found in the equations of 4.18. These functions contain similar cross sections as the neutron rate functions where σ_{γ_dam1} is the total cross section for releasing metal ions from the ${}^A_Z\text{MeDOTA}$ complex and σ_{γ_dam2} is the cross section for the release of metal ions from the DOTA complex without damaging the DOTA molecule.

$$\left(\frac{dC_{{}^A_Z\text{Me}^{(+3)}}}{dt}\right)_\gamma = C_{{}^A_Z\text{MeDOTA}}\varphi_\gamma\sigma_{\gamma_dam1} \quad (4.18a)$$

$$\left(\frac{dC_{{}^A_Z\text{MeDOTA}}}{dt}\right)_\gamma = -C_{{}^A_Z\text{MeDOTA}}\varphi_\gamma(\sigma_{\gamma_dam1}) \quad (4.18b)$$

$$\left(\frac{dC_{\text{DOTA}}}{dt}\right)_\gamma = -\sum_{\substack{\text{Isotopes} \\ {}^A_Z\text{Me}}} C_{{}^A_Z\text{MeDOTA}}\varphi_\gamma\sigma_{\gamma_dam1} - C_{\text{DOTA}}\varphi_\gamma(\sigma_{\gamma_dam1} - \sigma_{\gamma_dam2}) \quad (4.18c)$$

$$\left(\frac{dC_{\text{DOTA}_{dam}}}{dt}\right)_\gamma = \left(\sum_{\substack{\text{Isotopes} \\ {}^A_Z\text{Me}}} C_{{}^A_Z\text{MeDOTA}} + C_{\text{DOTA}}\right)\varphi_\gamma(\sigma_{\gamma_dam1} - \sigma_{\gamma_dam2}) \quad (4.18d)$$

With σ_{γ_dam1} as the total cross section for the release of metal ions in [cm^2] or [b], σ_{γ_dam2} as the cross section for the release of metal ions without damaging the DOTA molecule in [cm^2] or [b], φ_γ as the gamma radiation flux in [$cm^{-2}s^{-1}$].

Decay rates, $(\frac{dC}{dt})_\lambda$

The decay rate functions defined in the model are purely based on β^- decay and isomeric transitions. The rate functions can be found in 4.19.

$$\left(\frac{dC_{Z^{A\text{Me}}^{(+3)}}}{dt}\right)_\lambda = \lambda_{\beta^-} C_{Z-1^{A\text{Me}}^{(+3)}} + \lambda_{iso} C_{Z^{A\text{Me}}^{(+3)}} - \lambda_{\beta^-} C_{Z^{A\text{Me}}^{(+3)}} \quad (4.19a)$$

$$\left(\frac{dC_{Z^{\text{MeDOTA}}}}{dt}\right)_\lambda = \lambda_{\beta^-} C_{Z-1^{A\text{MeDOTA}}} + \lambda_{iso} C_{Z^{\text{MeDOTA}}} - \lambda_{\beta^-} C_{Z^{\text{MeDOTA}}} \quad (4.19b)$$

4.3.2. Components

The components defined inside the model with their respective decay and cross section properties for the production of Lu-177 can be found in table 4.7. This table contains the lutetium and hafnium ions, lutetium and hafnium DOTA complexes, DOTA and damaged DOTA as a species.

Table 4.7: The chemical components defined in the model containing lutetium and hafnium isotopes in both ionic and bound states with the chelator DOTA. For each component their individual material properties are shown which are used inside the model.

Model Components	Property	Value	Unit	Reference
$^{175}\text{Lu}^{(+3)}$	Molar mass	0.17497	kg/mol	[2]
	$\sigma_{175(n,\gamma)176}$	23.46	barn	
$^{176}\text{Lu}^{(+3)}$	Molar mass	0.17594	kg/mol	Serpent Results
	$\sigma_{176(n,\gamma)177}$	4561.45	barn	
	$\sigma_{176(n,\gamma)177m}$	4.56	barn	Serpent Results
$^{177}\text{Lu}^{(+3)}$	Molar mass	0.17694	kg/mol	[25]
	λ_{β^-}	1.1945×10^{-6}	s^{-1}	
$^{177m}\text{Lu}^{(+3)}$	Molar mass	0.17694	kg/mol	[25]
	λ_{β^-}	1.0853×10^{-8}	s^{-1}	
	λ_{iso}	3.9162×10^{-9}	s^{-1}	[25]
$^{177}\text{Hf}^{(+3)}$	Molar mass	0.17694	kg/mol	
$^{175}\text{LuDOTA}$	Molar mass	0.5794	kg/mol	[2]
	$\sigma_{175(n,\gamma)176}$	23.46	barn	
$^{176}\text{LuDOTA}$	Molar mass	0.5804	kg/mol	Serpent Results
	$\sigma_{176(n,\gamma)177}$	4561.45	barn	
	$\sigma_{176(n,\gamma)177m}$	4.56	barn	Serpent Results
$^{177}\text{LuDOTA}$	Molar mass	0.5814	kg/mol	[25]
	λ_{β^-}	1.1945×10^{-6}	s^{-1}	
$^{177m}\text{LuDOTA}$	Molar mass	0.5814	kg/mol	[25]
	λ_{β^-}	1.0853×10^{-8}	s^{-1}	
	λ_{iso}	3.9162×10^{-9}	s^{-1}	[25]
$^{177}\text{HfDOTA}$	Molar mass	0.5814	kg/mol	
DOTA	Molar mass	0.4044	kg/mol	
DOTA_{dam}	Molar mass	-	kg/mol	

4.3.3. Production Model Parameters

For the kinetic model the reaction rate constant k_1 was determined by fitting measurements from LuDOTA labeling over time from Naaktgeboren [42] to the second order reaction from 4.15b. These measurements were taken using a 1:1 ratio of lutetium ions and DOTA molecules at 40°C in a 1M acetic acid buffer with a pH of 4.3. The best fit to the second order reaction rate resulted in a k_1 of $-9.00826 \frac{L^2}{mol^2}$ of which the fit can be found in appendix D.1. Utilizing the fitted k_1 and the equilibrium constant K of $e^{23.5 \pm 0.1}$ as found by Tóth and Brücher in 4.15b, the reaction rate constant k_2 was found as $-2.85 \times 10^{-23} \frac{L}{mol}$.

The radiolysis cross section of the gamma interactions for the MeDOTA complex ($\sigma_{\gamma,dam1}$) was calculated to a value of 1280.976barn from the total photon attenuation coefficients of LuDOTA by photons at 0.1MeV.

These attenuation coefficients were retrieved from the XCOM v1.5 photon interaction database[8]. The secondary radiolysis cross section σ_{γ_dam2} was calculated as the photon cross section of lutetium at 109.27barn. This cross section was also calculated from the total attenuation coefficient retrieved from the XCOM database.

For the main radiolysis cross section of the neutron interactions (σ_{n_dam1}) the experimentally found decomposition cross section for the neutron flux of $7.5 \times 10^5 \pm 1.5 \times 10^5$ barn from Zhernosekov, Filosofov, and Rösch [60] was implemented as well as 7.5×10^4 and 7.5×10^3 barn to simulate lower interaction rates if significant shielding was implemented in front of the HEAL. As a significant part of this cross section is based around background components such as the photon interactions, it was assumed that the secondary cross section σ_{n_dam2} is directly related to the photon cross section as calculated from the total attenuation coefficients from the XCOM database [8]. Therefore, the secondary radiolysis cross section was calculated using the fraction of the photon interaction cross sections of $\frac{\sigma_{\gamma_dam2}}{\sigma_{\gamma_dam1}}$, and was therefore set to 6.4×10^4 barn.

As the neutron radiolysis cross sections are based around both interactions from neutron and photons [60] the model only allows for one set of cross sections to be active. If the neutron cross sections are enabled, the gamma cross sections are set to $0b$. On the other hand if the gamma cross sections are enabled the neutron cross sections are not and therefore are set to $0b$.

Parameter	Description	Values	Unit	Reference
Retention fraction (R)	The retention fraction of radioisotopes in the DOTA complex after neutron capture reaction	0.132	[-]	[60]
k_1	Reaction rate constant 1 in 4.15b	-9.00826	$[\frac{L^2}{mol^2}]$	Calculated from data [42, 58]
k_2	Reaction rate constant 2 in 4.15b	$-2.85E - 23$	$[\frac{L}{mol}]$	Calculated from data [42, 58]
σ_{n_dam1}	Neutron damage cross section 1	0 or 750000	[barn]	[58]
σ_{n_dam2}	Neutron damage cross section 2	0 or 63975	[barn]	Approximated from gamma cross section XCOM Database @ 0.1 MeV [8]
σ_{γ_dam1}	Gamma damage cross section 1	0 or 1280.976	[barn]	XCOM Database @ 0.1 MeV [8]
σ_{γ_dam2}	Gamma damage cross section 2	0 or 109.27	[barn]	XCOM Database @ 0.1 MeV [8]
φ_n	Neutron flux	6.44×10^{12}	$[cm^{-2}s^{-1}]$	[34]
φ_γ	Gamma flux	1.35×10^{13}	$[cm^{-2}s^{-1}]$	[34]

Table 4.8: Used kinetic model parameters

4.4. Dispersion modelling

4.4.1. OpenFOAM CAD model

OpenFOAM was used to numerically simulate the RTD of both the vessel and recycle segments as indicated in 3.6 within different HEAL geometries, inlet/outlet positions and inlet/outlet radii.

For the OpenFOAM simulations 3D CAD models of the inner radius of the HEAL were created in the CAD software Fusion360. These CAD models try to follow the geometries as defined in the discretized model 4.1.2 as closely as possible, e.g. using the lengths as defined in 4.2 & 4.3 linked to the DLDR radius. In these models the geometries for an inlet and outlet were also included by adding cylinders extending out of the geometry. These cylinders follow the axis of the top and bottom pipe and extend out of the geometry by $R_i + 2mm$. The radius of this in- and outlet cylinders was set at $2mm$ or to the same inner radius of the system R_i . The radius of the corners in these geometries was assumed to be the same as the inner radius R_i . Examples of two different 3D CAD models of the HEAL can be seen in figure 4.5. An overview of the created models and their parameters can be seen in table 4.9



Figure 4.5: Two examples of CAD models automatically made in OpenFOAM with different system parameters. The system on the left shows a system with the inlet and outlet on the right side of the HEAL and has an inner radius R_i of $15mm$. The model on the right is based on a system with an inner radius of $4mm$. Both systems have a heating (dr_{12}) and cooling (dr_{34}) wall thickness of 15 and $5mm$ respectively with a pipe angle θ of 5° . The inlet and outlet radius is set at $2mm$.

From the 3D CAD models STL files were generated and the walls from the straight sections of the pipe in the model were divided in either 40 or 42 sections dependent on the STL file. Each of these sections consisted of an equal wall area. From these edited STL files, low and high resolution meshes for OpenFOAM were generated utilizing SnappyHexMesh with a blockmesh resolution of $0.0017 \times 0.0017m$ and $0.00085 \times 0.00085m$ respectively. The blockmesh resolution for the high resolution mesh was chosen from a convergence study that was performed.

For each system, two other high resolution meshes were generated. One consisting of the recycle segment and the other consisting of the vessel segment including the inlet and outlet as indicated by the figures 3.6.

OpenFOAM boundary conditions and transport properties

Using the parameters in table 4.9, the improved discretized model of the HEAL including the radial and axial heat conduction was used to calculate the heat flux between the wall and the target solution in each node as well as the average temperature of the target solution.

Using these results, the initial internal field temperature was set at the average target solution temperature. Utilizing the Neumann fixedGradient boundary condition in OpenFOAM the heat flux values from the python model were transferred for each of the 40 or 42 defined wall sections. Flowrates in the inlet were set using velocities in the uniformFixedValue boundary condition. The different velocity values used for the inlet

Table 4.9: The different systems that were used in the generation of the 3D CAD models of the HEAL for the OpenFOAM simulations and their respective parameters.

System Geometry	Inner radius, R_i (mm)	inlet/outlet		Other parameters
		position	radius (mm)	
1	3	bottom/top	2	Zr/Zr Systems Heating Wall Thickness (mm) = 15 Cooling Wall Thickness (mm) = 5 Pipe angle (mm) = 5° Section 2 Pipe Fraction = 1
2		left	3	
3		top/bottom	2	
4		right	3	
5	5	bottom/top	2	
6		left	5	
7	7	bottom/top	2	
8		left	7	
9		top/bottom	2	
10		right	7	
11	11	bottom/top	2	
12		left	11	
13	13	bottom/top	2	
14		left	11	
15		top/bottom	2	
16		right	13	
17	15	bottom/top	2	
18		left	15	

conditions within each system geometry can be found in the appendix E.1. To simulate water a Newtonian transport model was used.

These properties together with the velocity, temperature and pressure boundary conditions that were used can be found in the code linked in appendix F.

OpenFOAM velocity field generation

Utilizing the PIMPLE based solver buoyantBoussinesqPimpleFoam and the low resolution mesh the system was simulated. After steady state was reached the temperature and velocity field were transferred to the high resolution mesh and simulated further until steady state was reached.

OpenFOAM residence time distribution

For each system, the generated velocity field from the high resolution mesh was then transferred to both the vessel and recycle segment meshes of their respective systems. These meshes were then used to simulate a pulse input using the scalarTransportFoam solver in OpenFOAM. This pulse was introduced at the start of the simulation in which for 0.05 seconds the concentration at the inlet was set to a value of 20 after which the concentration was set back to 0. The concentration at the outlet was recorded over time from which residence time distribution curves for both meshes were determined.

4.4.2. Tanks-In-Series compartment model

Compartment definition

Following the general RTD curves of the OpenFOAM pulse injection simulations on both the recycle and vessel segments certain configurations for a compartment model were theorized. These RTD curves generally start with a lag in response before an initial peak forms followed by a tail or other peaks. From the compartment model [38] this indicates an initial PFR creating a lag in the response. Generating the tail and/or other peaks from these RTD curves within a compartment model inspiration was taken from Fazli-Abukheyli and Darvishi to put Tanks-In-Series in several parallel streams including potential recycle streams [24].

After testing of several models with different parallel configurations a general model was set up which an overview can be found in figure 4.6. This model consists of an initial Tanks-In-Series section that provides the lag in the response, followed by either 1 or a maximum of 4 parallel Tanks-In-Series sections with each their own number of tanks and volumes. In the figure F_{in} and F_{out} are the in- and outgoing flowrates, V_n represents

the total volume of the Tanks-In-Series n , N_n represents the number of tanks that are placed in series for the Tanks-In-Series n and the $frac_n$ is the fraction of the flowrate coming from the initial Tanks-In-Series that will flow through the the Tanks-In-Series n .

$$V_{tot} = \sum V_n \tag{4.20a}$$

$$\sum frac_n = 1.0 \tag{4.20b}$$

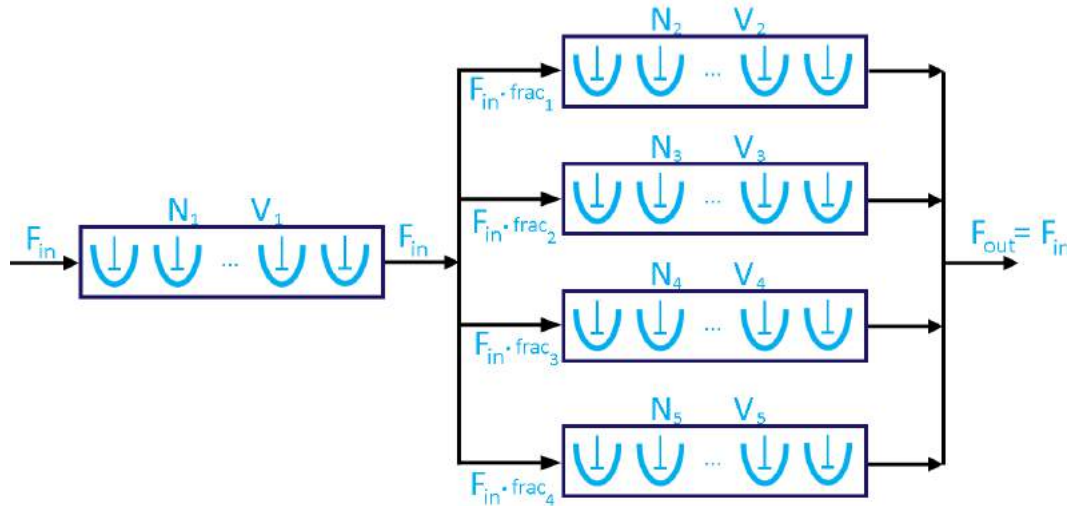


Figure 4.6: Overview of the Tanks-In-Series Compartment model to which the RTD curves of both the vessel and recycle segment of the HEAL CFD simulations were modelled on.

Modelling to RTD curves

For fitting the models of 4.6 to the residence time distribution curves from both the recycle and vessel segments python code was written. This code requires a manual initial guess for the V , N and $frac$ variables inside the model for which the RTD curve is simulated. By individual iteration through each variable it tries to find the closest match using the coefficient of determination R^2 and the residual sum of squares as a measurement of the fitment of the model to the CFD results. A block scheme for this code can be found in 4.7. Using this code all RTD curves from the recycle and vessel segments received from OpenFOAM were modelled.

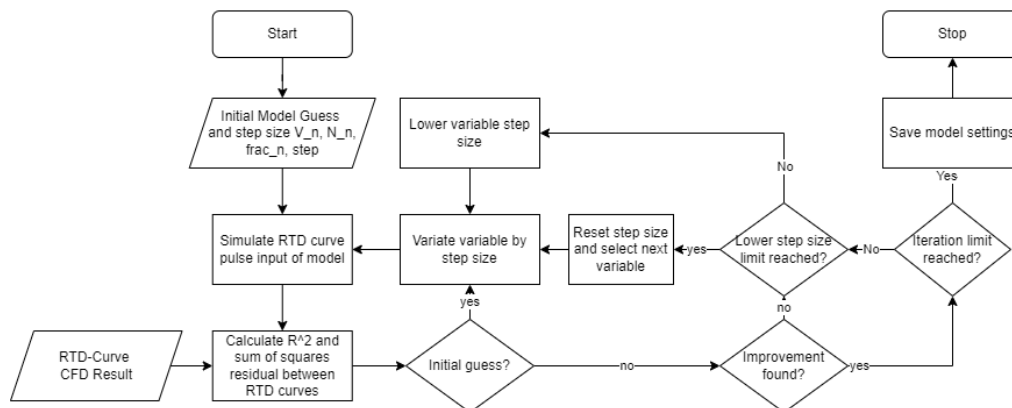


Figure 4.7: Block scheme of the code for approaching the RTD curve with the Tanks-In-Series compartment model via iteration of the different variables N , V & $frac$.

4.4.3. Dynamic HEAL model

The Dynamic HEAL model is a separate model that attaches the Tanks-In-Series compartment models of both the recycle and vessel segments to form a complete loop of the HEAL. Each tank represented in this model is approached with their own mass balance for different components as seen in 3.24. In these mass balances each tank receives kinetics involving chemical, neutron, gamma, and decay interactions of different components via their interaction rates (e.g. the Lu-177 production model 4.3).

To the first and last tank of the vessel segment Tanks-In-Series compartment model an in- and output are defined with which are used to define the recycle fraction and recycle ratio together with a set feed rate through the vessel segment as shown in 3.25.

The result of the model is a large system of ordinary differential equations solving both mass and kinetic balances as shown in 3.24 and 4.14. This system can then be solved over time using the explicit Midpoint method. This method is derived from the Euler's method and uses the results from the Euler's method as a prediction to estimate the slope of the differential equations [16].

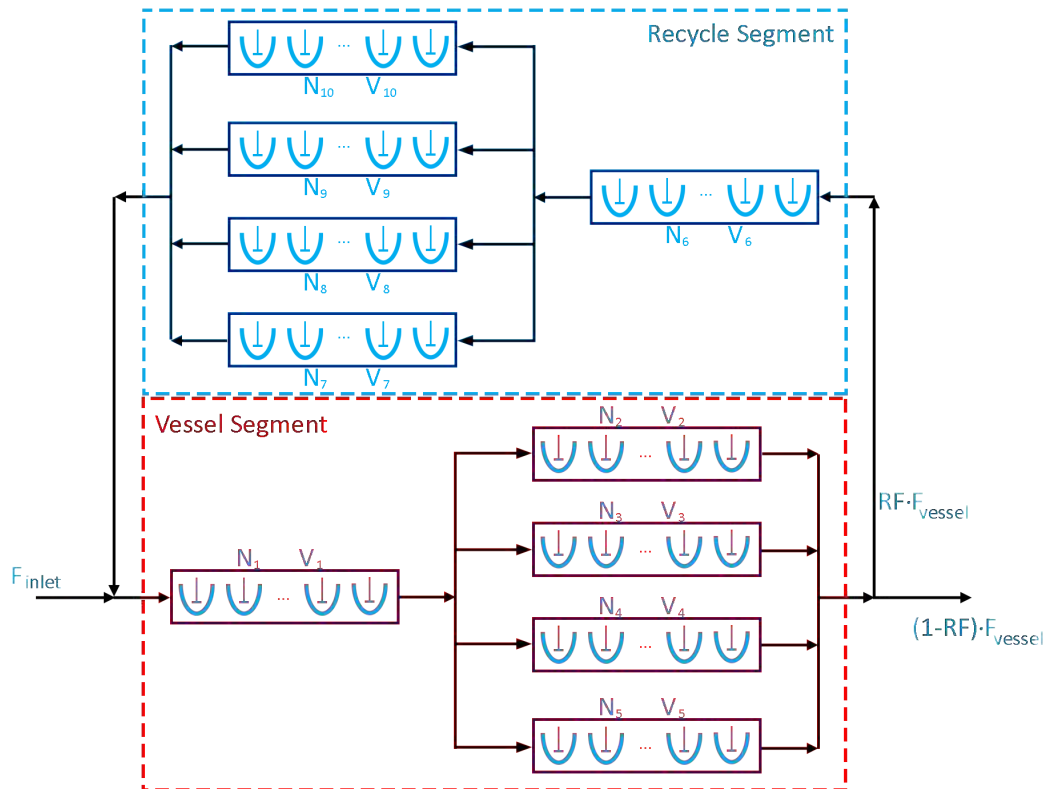


Figure 4.8: Example of two Tanks-In-Series compartment models of the vessel and recycle segment attached to each other including an in- and outflow attached to the vessel segment in- and outputs.

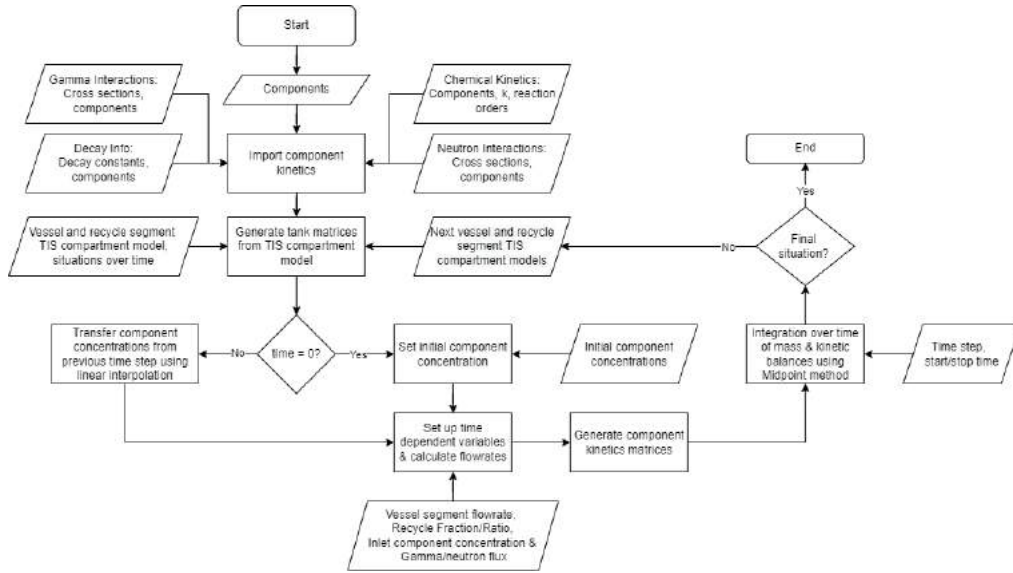


Figure 4.9: Block scheme of the python code for the Dynamic HEAL model.

To allow transfer between different flow/feed rate situations within the HEAL over time the transfer of components between different Tanks-In-Series compartment models of the vessel and recycle segment is implemented. This via linear interpolation of the concentration within the initial tanks by utilizing their position inside the segment. Initially the concentration of a segment (vessel or recycle) is transferred to a single Tanks-In-Series model with 500 equally sized tanks which afterwards is transferred to the new Tanks-In-Series compartment model. The interpolation follows equation 4.21. A general overview of the block scheme of the complete python code for the Dynamic HEAL model can be found in figure 4.9.

$$C_m = \frac{1}{V_m} \sum_{n=0}^{N_{segment}} \begin{cases} V_n C_n, & l_{start,n} \leq l_{start,m} \& l_{stop,n} \geq l_{stop,m} \\ V_n C_n \frac{l_{stop,m} - l_{start,n}}{l_{stop,m} - l_{start,m}}, & l_{start,n} \geq l_{start,m} \& l_{stop,n} > l_{stop,m} \& l_{start,n} < l_{stop,m} \\ V_n C_n \frac{l_{stop,n} - l_{start,m}}{l_{stop,m} - l_{start,m}}, & l_{start,n} < l_{start,m} \& l_{stop,n} \leq l_{stop,m} \& l_{stop,n} \geq l_{start,m} \\ V_n C_n \frac{l_{stop,n} - l_{start,n}}{l_{stop,m} - l_{start,m}}, & l_{start,n} \geq l_{start,m} \& l_{stop,n} \leq l_{stop,m} \end{cases} \quad (4.21)$$

Where n and m are the respective tank coordinates from the transferred model and interpolated model, $N_{segment}$ the number of tanks in the transferred segment model, $C_{n/m}$ the concentration in tank n or m , $l_{start,n/m}$ & $l_{stop,n/m}$ the start and stop location over the length of the segment of tank n or m , and $V_{n/m}$ the volume of the segment tank n or m .

5

Results and Discussion

5.1. Discretized HEAL model results

Table 5.1 gives an overview of the variables of the HEAL systems that were looked at within the discretized model. For each variable, the table gives a reference to the section in which the main effects of the variable on the systems is shown. Extended plots of the results from systems over these variables are given in the appendix B.4.3.

Table 5.1: The list of system variables that were explored in the improved discretized model of the HEAL together with a reference to both the results and appendix with extended discussion and plots over these variables.

Main Variable(s)	Sub Variable(s)	Result Section	Extended Results
Wall Materials & Wall thickness	Single layer wall materials	5.1.1 (page 47)	B.1.1 (page 90)
	Multi layer wall materials	5.1.1 (page 50)	B.1.2 (page 110)
Inner Radius (R_i)	Wall Materials & Wall thickness	5.1.2 (page 51)	B.2 (page 129)
Pipe angle (Θ)	System length (L) & Inner Radius (R_i)	5.1.3 (page 52)	B.3 (page 163)
System length (L)	Pipe angle (Θ) & Inner Radius (R_i)	5.1.3 (page 52)	B.3 (page 163)
Section 2 length fraction ($Frac$)	Wall thickness		B.4 (page 203)

5.1.1. Wall thickness dr_{sec}

Single layer wall materials

Velocity and temperature results from 5 different systems with different heating wall materials and thicknesses are shown in figure 5.1. The systems that are shown consist of either one or two wall materials in either the heating and cooling sectors as indicated by (HEAT/COOL). These systems are: Al/Al, Pb/Pb, Zr/Zr, Pb/Al, Al/Pb. The plotted systems have a system length L of $0.4m$, an inner radius R_i of $0.007m$ and a pipe angle Θ of 5° . In these figures the velocity and maximum target solution temperature over the cooling wall thickness, together with the temperature profile of the target solution over the length of systems with a heating wall thickness (dr_{12}) of $0.0133m$. The length of the system starts at section 1 inside the heating sector as indicated by figure 2.2 and travels consecutively through section 1 to 4.

The velocity plots in figure 5.1 show that the largest velocities can be found when the cooling wall thickness is the smallest. It is also shown that in systems with that consist of one material, once the cooling wall thickness is larger than the heating wall thickness, the flow in the systems reverses. This negative velocity is then limited in all systems and does not significantly increase or decrease from that point onwards. The plot of the maximum solution temperatures over the cooling wall thicknesses show that with the increase in the overall wall thickness, the maximum temperatures increase as well. The largest increase in target solution temperatures

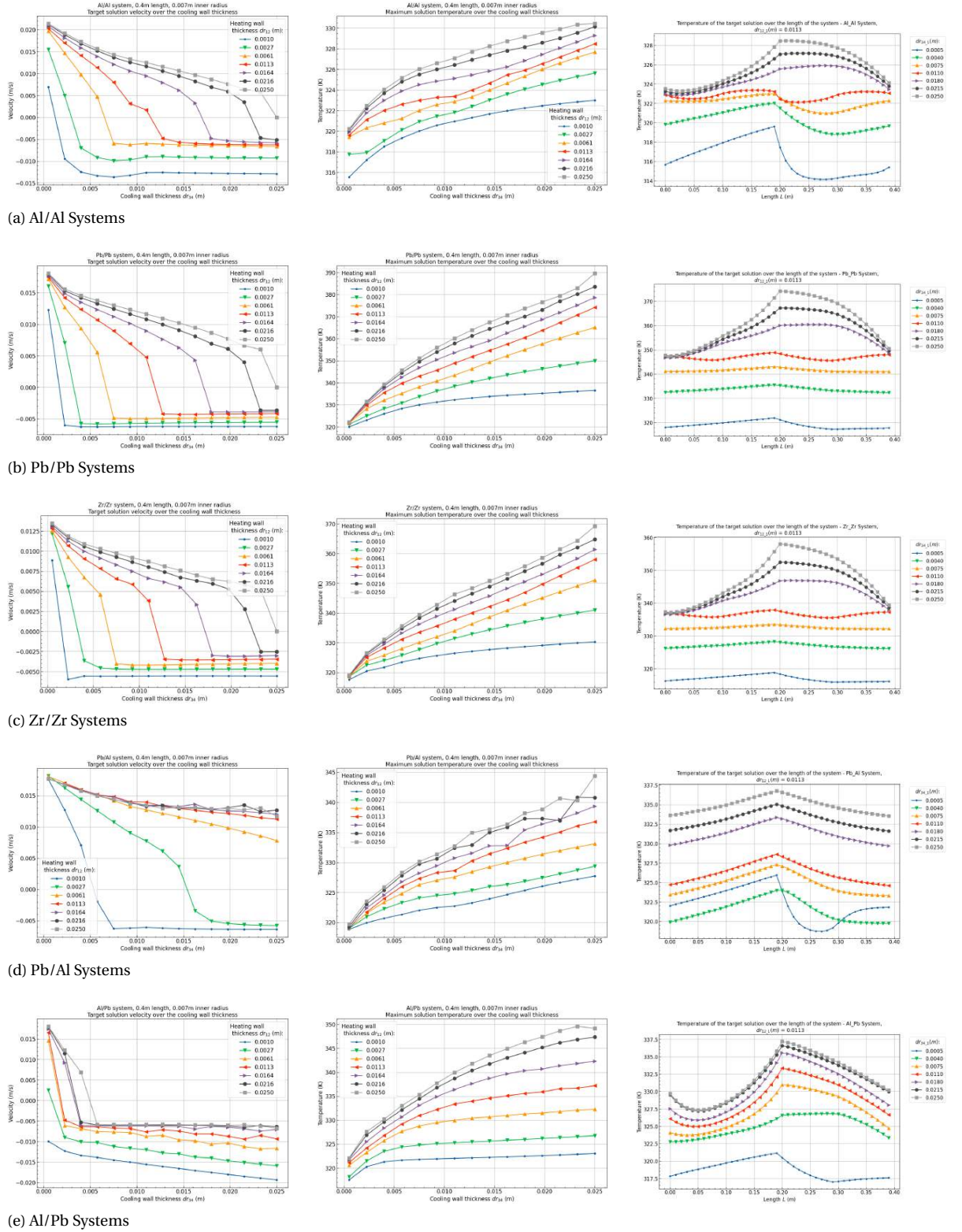


Figure 5.1: Plots of the velocity, maximum target solution temperature and temperature profile over the length in systems with different heating wall thicknesses and material combinations over the cooling wall thickness. The system parameters consist of a length of $0.4m$, an inner radius of $0.007m$ and a pipe angle of 5° . The plots show a decrease in velocity as the cooling wall thickness increases. Once the cooling wall thickness is larger than the heating wall thickness the velocity becomes negative in the system. The temperature profile over the length shows this transition.

over the cooling wall thickness are seen in the Pb/Pb systems as lead has the largest gamma energy deposition rate of all the materials plotted. Interestingly, in systems with a large heating wall and small cooling wall thickness the maximum target solution temperature is not much higher than seen in systems with small heating and cooling wall thicknesses. This stems from higher velocities at the smaller cooling wall thicknesses as in these systems the heating wall gets less time to increase the temperature of the solution as well as that the dissipation of heat provided by the small cooling wall thickness is larger. This results in a small target solution temperature difference through the HEAL, as can be seen in the Pb/Pb system target solution temperature profile with a cooling wall thickness (dr_{34_1}) of $0.0005m$.

The flow reverses in all systems as the cooling wall thickness is increased. With this reversal the original heating and cooling walls swap in function. The heating of the target solution in these systems is provided in the cooling sector (section 3 and 4) and the cooling is provided inside the heating sector (section 1 and 2). This can also be seen in the temperature profiles over the length of the systems where a system with a positive velocity (e.g. Al/Al system with $dr_{34_1} = 0.0005m$) the target solution is heated in section 1 and 2. In systems with a negative velocity (e.g. Al/Al system with $dr_{34_1} = 0.0180m$) the target solution is cooled these sectors. Following the momentum balance in 4.10, the density difference between the target solution in the vertical sections 2 and 4 are the main driving force for the buoyancy driven flow. For a reversed flow situation, this density difference is limited as most heating and cooling takes place in these sections instead of sections 1 and 3. This causes the temperatures, and therefore the densities found in these sections to overlap. This limits the overall density difference and gives an explanation why higher negative velocities are not seen in systems with a reversed flow.

What can also be seen inside the velocity figures is that in the systems with the same wall materials the reversed flow stabilizes around a particular velocity at larger cooling wall thicknesses. This originates from a feedback loop that is present in these systems. Following the energy balance over the nodes, as seen in equation 4.5, energy between the target solution nodes is partially transferred by the flow between the nodes, which is dependent on the velocity inside the system. As the velocity increases, the increased flowrate and allows the temperature of the target solution to travel further at similar thermal transfer rates because the target solution, per volume, receives a smaller amount of heating/cooling capacity. This limits the range of the target solution temperatures over the length of the system and therefore the difference in density. This limit, combined with the fact that in reversed flow systems the largest amount of heating and cooling is provided in the vertical sections buoyancy driven flow results in a stable velocity over the cooling wall thickness.

The velocities that are seen in the Zr/Zr systems in the figures 5.1 are lower than the Al/Al and Pb/Pb counterparts. This could be the result of the lower thermal conductivity of zirconium compared to aluminium and lead which results in a smaller density difference in sections 1 and 3 at the same wall thicknesses. Systems consisting of different wall materials in the heating and cooling sector, such as Pb/Al and Al/Pb, show very different velocities over the cooling wall thicknesses compared to systems with one single material. For instance in the Pb/Al systems, the velocity drops over the cooling wall thickness but only two systems with the smallest heating wall thickness reverse in flow direction within the range shown. In the Al/Pb systems the velocity almost immediately drops to negative values as the cooling wall thickness is increased. This contrast between the Pb/Al and Al/Pb systems stem from the difference in gamma energy deposition rates between the materials and their position in the geometry. Maximum target solution temperatures in the Pb/Al and Al/Pb systems increase with the wall thickness. Compared to the Pb/Pb systems the temperatures that are seen are significantly lower, especially in systems with larger heating wall thicknesses. Comparing the temperature profiles between the Pb/Al and Al/Pb systems show the large difference between the systems with a positive and negative velocity. In systems with a negative velocity the temperature range is much broader to sustain similar velocities.

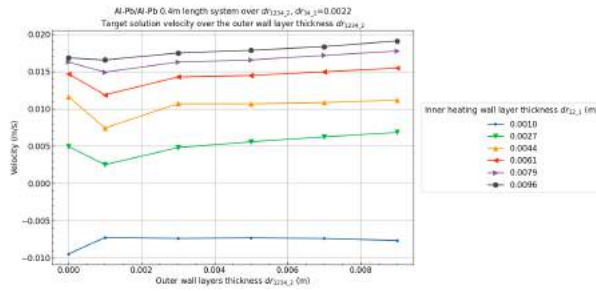
Velocity and extended temperature plots of more single layered wall systems over the wall thicknesses with different materials can be found in the appendix B.1.1 on page 90.

Multiple layered wall materials

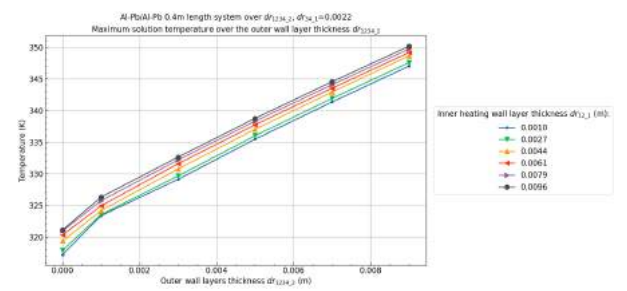
The materials inside multiple layered wall systems are expressed in the following scheme: Inner heat-outer heat/inner cool-outer cool, an example is Al-Zr/Zr-Al in which the inner layer of the heating sector consists of aluminium and the outer layer of zirconium. The inner layer of the cooling sector consists of zirconium and the outer layer of aluminium.

Systems with multiple layers can be separated into a parallel and staggered wall layer design. An example of a parallel design is the system with wall materials: Al-Pb/Al-Pb, where the inner wall layers of both the heating and cooling sector consists of the same material as well as the outer wall layer. An example for a staggered design with the same materials can be made in the form: Al-Pb/Pb-Al, where the inner and outer layer of the heating and cooling sector consist of different materials.

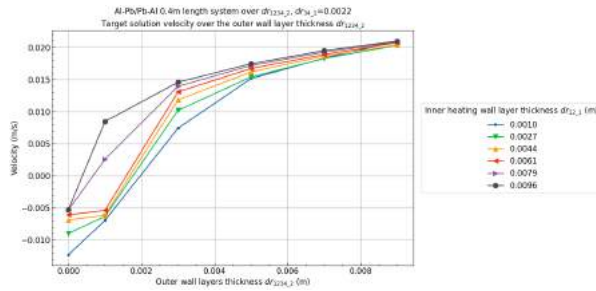
The figures in 5.2 are plots of the velocity and maximum target solution temperature over the outer wall layer thickness dr_{1234_2} of the systems: Al-Pb/Al-Pb, Al-Pb/Pb-Al, and Pb-Al/Al-Pb.



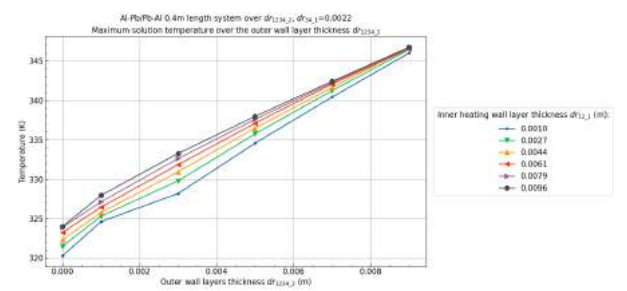
(a) Velocity over the outer wall layer thickness dr_{1234_2} of the Al-Pb/Al-Pb systems showing a slight overall increase over the outer wall layer thickness.



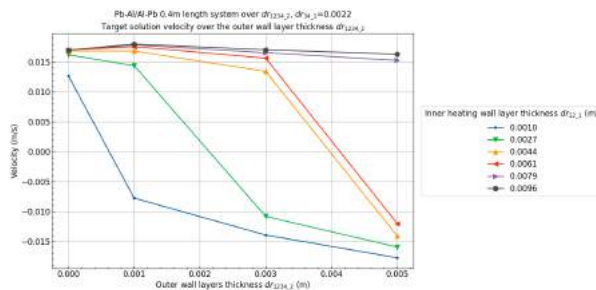
(b) Maximum target solution temperature over the outer wall layer thickness dr_{1234_2} of the Al-Pb/Al-Pb systems showing a large temperature increase with the outer wall layer thickness.



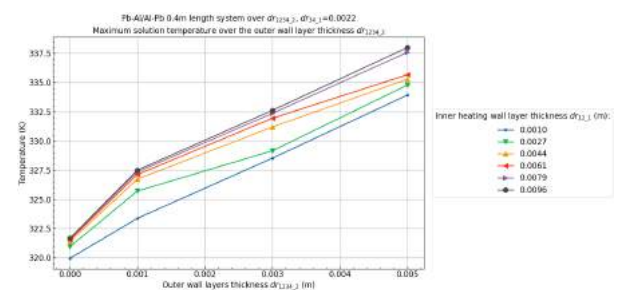
(c) Velocity over the outer wall layer thickness dr_{1234_2} of the Al-Pb/Pb-Al systems showing a significant increase as the outer wall layer thickness increases.



(d) Maximum target solution temperature over the outer wall layer thickness dr_{1234_2} of the Al-Pb/Pb-Al systems showing the temperature increase with the outer wall layer thickness.



(e) Velocity over the outer wall layer thickness dr_{1234_2} of the Pb-Al/Al-Pb systems showing a slight initial increase at large inner heating wall thicknesses and an immediate decrease in other systems.



(f) Maximum target solution temperature over the outer wall layer thickness dr_{1234_2} of the Pb-Al/Al-Pb systems showing a relatively small temperature increase with the outer wall layer thickness.

Figure 5.2: Velocity and maximum solution temperature results of systems with multiple layered walls over the outer wall layer thickness dr_{1234_2} . These systems have a system length L of $0.4m$, an inner radius R_i of $0.007m$, pipe angle Θ of 5° and an inner cooling wall thickness dr_{12_1} of $0.0022m$

Parallel system

In the parallel system of Al-Pb/Al-Pb, an initial slight decrease in the the absolute velocity can be observed at an outer wall layer thickness of $0.001m$, thereafter the velocity increases with the outer wall layer thickness. The maximum target solution temperature increases significantly over the outer wall layer thickness which falls in line with the temperature increase as seen in the single walled Pb/Pb system as shown in figure 5.1b.

By these results the implementation of a lead outer wall to the system, care has to be taken with the resulting increase in the target solution temperature which is significant.

Staggered systems

The staggered systems in the figure 5.2, Al-Pb/Pb-Al and Pb-Al/Al-Pb, show different profiles of the velocity over the outer wall layer thickness dr_{1234_2} . The Al-Pb/Pb-Al systems increase in velocity over the outer wall layer thickness as the thickness of lead in the outer layer of the heating sector increases. This increases the energy deposition inside the heating sector to a larger energy deposition than the cooling sector which generates the density difference for the velocity to increase.

Compared to single wall layer systems in figure 5.1 the velocity that is seen is significantly higher at similar total wall thicknesses in both the heating and cooling sector. The maximum target solution temperature increase is also lower than that of the other parallel systems of Al-Pb/Al-Pb which makes it more suitable for the HEAL design.

The Pb-Al/Al-Pb systems shows a similar increase in the maximum target solution temperature over the outer wall thickness. The maximum velocities reached are lower than the Al-Pb/Pb-Al counterpart and show that as the outer wall layer thickness increases, the positive velocity eventually reverses. Compared to single layer systems like the Al/Al system as seen in 5.1 the velocities are similar at comparable wall thicknesses.

Both these staggered systems contain a lining of lead which aids in the gamma shielding abilities while keeping the maximum target solution temperature increase limited. While the Al-Pb/Pb-Al system seems to be more promising in terms of the velocity that can be reached at larger wall thicknesses, both these staggered systems could be very interesting choices for the design of the HEAL.

Velocity and extended temperature plots of more multi layered wall systems can be found in the appendix B.1.2 on page 110.

5.1.2. Inner radius R_i

In the figure 5.3 velocity, maximum target solution temperatures and profiles over the system length are plotted of single wall layer systems Pb/Pb and Zr/Zr. These plots are shown over the inner radius R_i and different cooling wall thicknesses dr_{34_1} . The plotted systems have a system length L of $0.4m$, a pipe angle Θ of 5° , a section 2 length fraction $Frac$ of 1.0, and a heating wall thickness dr_{12_1} of $0.0110m$.

From the figures in 5.3 it can be seen that as the inner radius increases the absolute velocity in all the systems increase until a maximum velocity is reached. After this maximum the absolute velocity starts to drop. This drop is significantly larger for systems with negative velocities where the heat- and cooling sectors have reversed in their roles in heating and cooling the target solution. This is a result of the temperature differences within the vertical sectors that is required for higher velocities can't be obtained due to the larger amount of target solution that has to be heated and cooled within these sectors.

The inner radius R_i at which the maximum velocity for each geometry is reached lowers as the total wall thickness increases. An example can be seen in the velocities seen in the Zr/Zr system in figure 5.3. At each increase of the cooling wall thickness position the maximum velocity drops to a slightly smaller inner radius R_i .

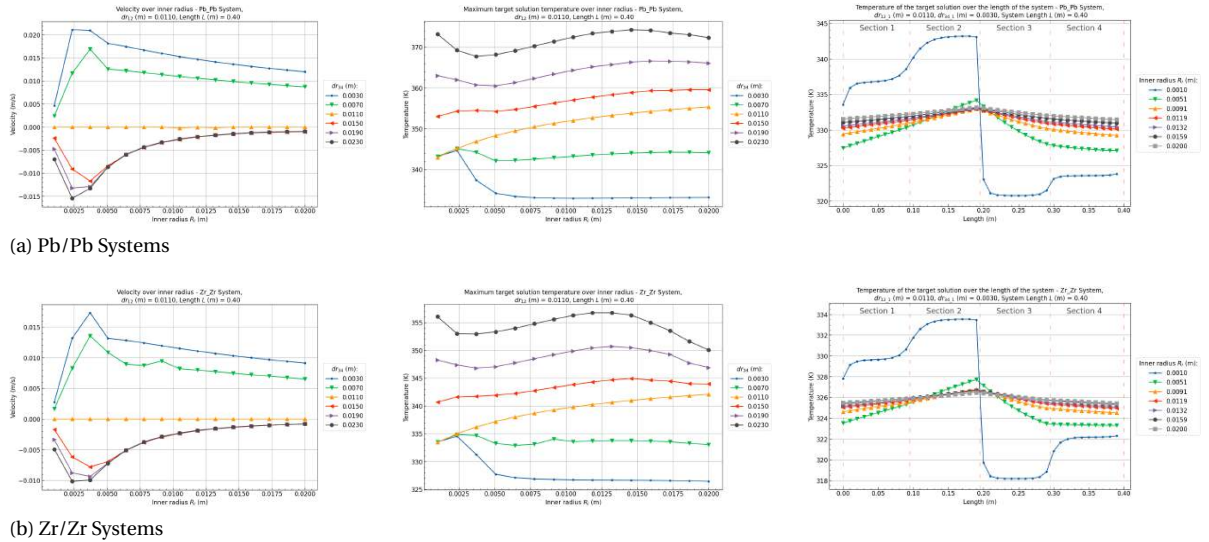


Figure 5.3: Plots of the velocity, maximum target solution temperature and temperature profile over the inner radius R_i in Pb/Pb and Zr/Zr systems with a system length L of $0.4m$, a section 2 length fraction $Frac$ of 1.0 , a pipe angle Θ of 5° , heating wall thickness dr_{12_1} of $0.0110m$ and a variable cooling wall thickness dr_{34_1} .

Velocity and extended temperature plots of more over systems with different materials and wall thicknesses over the inner radius R_i can be found in the appendix B.2 on page 129.

5.1.3. Pipe angle Θ & Length L

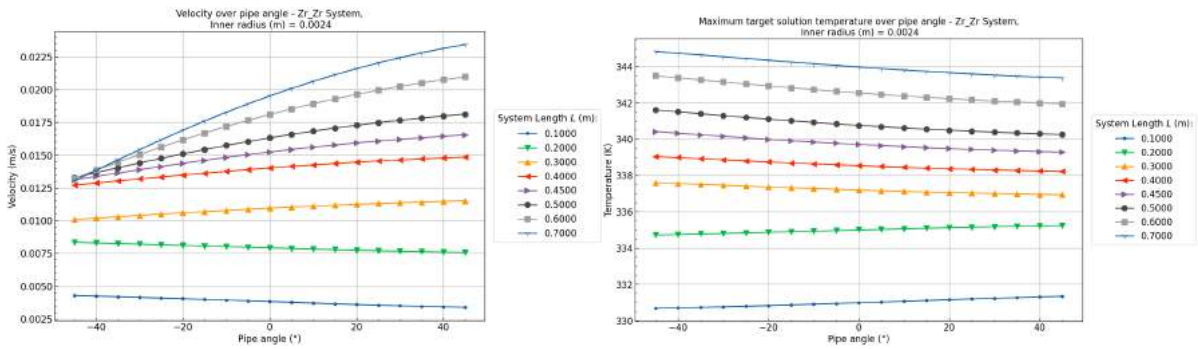
In figure 5.4 velocity and maximum target solution temperature results are plotted of systems with different system lengths L and inner radius values R_i and plotted over the pipe angle. The systems that are plotted are Zr/Zr single layer wall systems with a section 2 length fraction $Frac$ of 1.0 , a heating wall thickness dr_{12_1} of $0.015m$, and a cooling wall thickness dr_{34_1} of $0.005m$.

The effect of the pipe angle on the systems with a small inner radius R_i of $0.0024m$ shows that the velocity significantly increases with the pipe angle in systems with larger system lengths. In systems with shorter lengths, e.g. $L = 0.100m$, the velocity decreases with the pipe angle. With this change in velocity for the longer systems the maximum target solution temperature drops very slightly. In shorter systems the opposite is true.

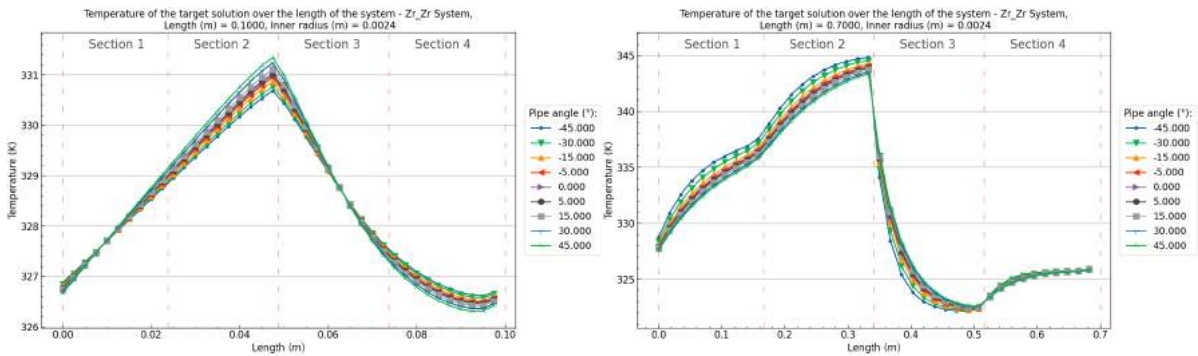
The difference in velocities over the pipe angle can be explained by looking at the sections of the HEAL in the target solution temperature profiles in 5.4. Increasing or decreasing the pipe angle in sections 1 and 3 influences the impact of these sections on the buoyancy from the momentum balance (4.10). For longer systems (e.g. $L = 0.700m$) there is a sharp decrease in the target solution temperature in section 3. Therefore a large temperature difference between the cooling and heating sector exists which is advantageous for the velocity at these pipe angles. In the smaller systems (e.g. $L = 0.100m$) the temperatures between the heating and cooling sectors are very similar which results in smaller velocities. Another factor that aids in the velocity for the longer systems is the larger temperature range which relates to larger density differences in the target solution.

At the inner radius of $R_i = 0.0051m$, the velocity drops in all systems over the pipe angle. At pipe angles Θ below -20° , steady state systems can exist with many different velocities in all simulated system lengths. Above a pipe angle of -20° the velocity drops slightly in all systems, similar to the drop in velocity of the smaller systems at an inner radius of $R_i = 0.0024m$. The maximum target solution temperature increases slightly with the pipe angle.

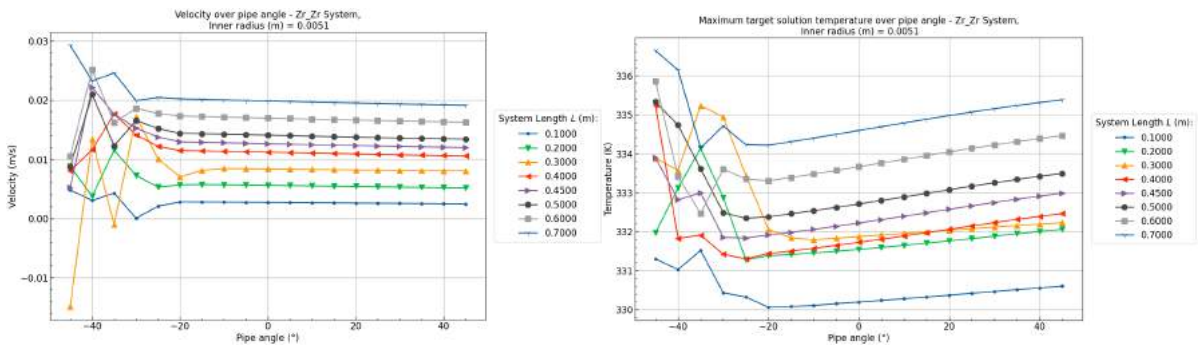
Velocity and extended temperature plots of more over systems with different materials, system lengths and more detailed pipe angles between -10 and 10° can be found in the appendix B.3 on page 163.



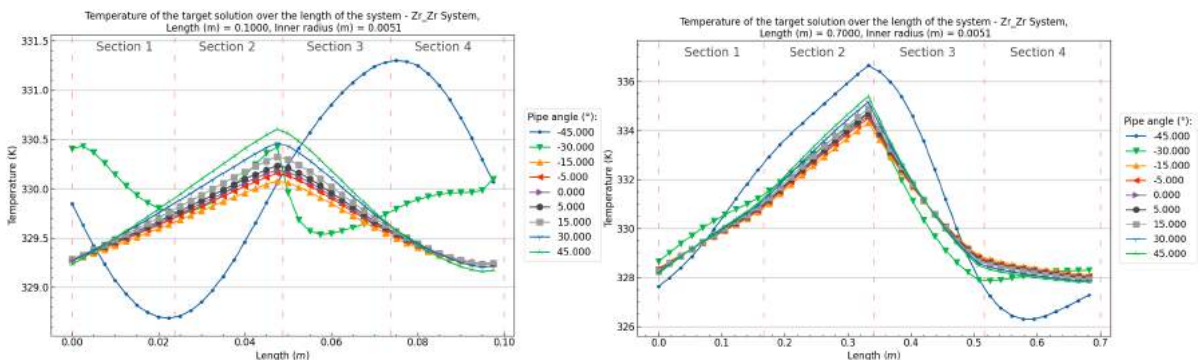
(a) $Zr/Zr - R_i = 0.0024m$ - Velocity (left) and maximum target solution temperature (right) of sys



(b) $Zr/Zr - R_i = 0.0024m$ - Temperature profiles of system length $L = 0.1000m$ (left), and $L = 0.7000m$ (right) showing the large temperature and profile differences in both system lengths.



(c) $Zr/Zr - R_i = 0.0051m$ - Velocity and maximum target solution temperature



(d) $Zr/Zr - R_i = 0.0051m$ - Temperature profiles of system length $L = 0.1000m$ (left), and $L = 0.7000m$ (right) showing the large temperature and profile differences in both system lengths

Figure 5.4: Plots of the velocity, maximum target solution temperature and temperature profiles over the pipe angle Θ in Zr/Zr systems with an inner radius R_i of $0.0024m$ and $0.0051m$, a variable system length, a section 2 length fraction $Frac$ of 1.0, a heating wall thickness d_{r12_1} of $0.015m$, and a cooling wall thickness d_{r34_1} of $0.005m$.

5.1.4. Dynamic Results

Three situations were set up for the discretized model: a startup, sudden peak of the energy deposition, and shutdown situation. These situations are further explained within their respective section below. The defined situations that are presented try to show the response of HEAL systems with different wall materials but might not be fully representative to what would happen next to the HOR. As an example within the startup situation the energy deposition rate u within the walls is set from 0 to $300 \frac{W}{kg}$ instantaneously. During a realistic startup of the HOR however this would most likely be a lower (almost) instantaneous increase from prompt gamma rays after which u would increase over time from delayed gamma rays from decay products that are produced within the core as seen in other reactor designs [5].

Startup

The dynamic startup situation consists of the walls and target solution inside the HEAL having a $40^\circ C$ temperature with a target solution velocity of $0 \frac{m}{s}$. At $t = 0s$ the energy deposition rate within the walls u is increased from 0 to $300 \frac{W}{kg}$. In figure 5.5 the velocity and temperatures over time of systems made from aluminium, lead and zirconium are plotted over time for the startup situation.

The initial reaction in all systems is a spike of negative velocity within the HEAL which is the largest within the lead system followed by zirconium and aluminium. This reaction stems from the initial negative temperature difference between the heating and cooling sectors present at the start. This temperature difference is a result from the initial higher heat transfer rate in the cooling sector from the wall to the target solution which, as approached by the model, is initially higher in the section with the smallest wall thickness due to the smaller node wall thicknesses present.

The aluminium system reaches steady state velocity and temperatures the quickest with the lead and zirconium systems following at a slower pace. The reason for the aluminium system to react the quickest out of the materials is likely the result of the high thermal conductivity coefficient κ compared to the other materials. Overall, all systems reach steady state velocity and temperatures within 5 minutes.

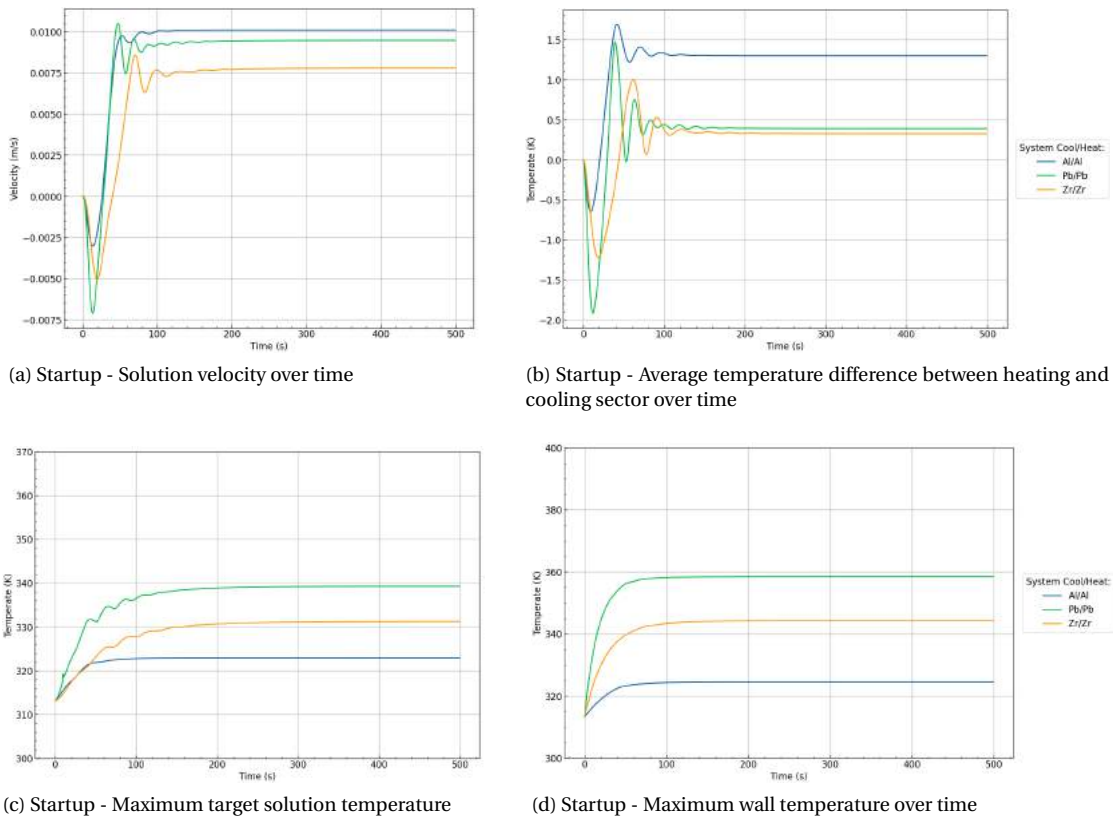
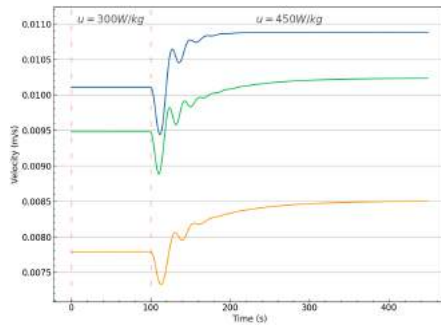


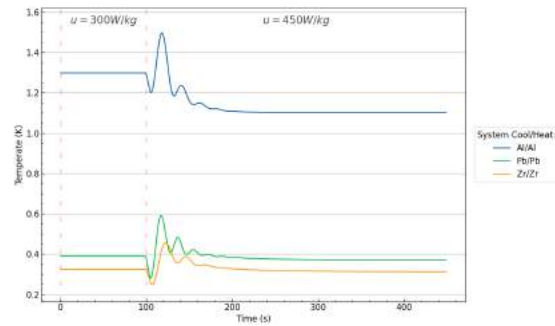
Figure 5.5: Velocity and temperature results during a startup situation over time in different material systems with $N = 160$, $M = 5$, inner radius R_i of $0.005m$, pipe angle Θ of 5° , heating wall thickness dr_{12} of $0.015m$ and a cooling wall thickness dr_{34} of $0.005m$.

Energy deposition peak

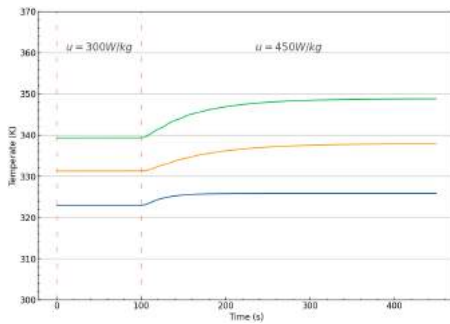
Similar trends of the reaction speeds as seen in the startup situation are found in a situation where the energy deposition is suddenly increased. The situation was set up consisting of an initial HEAL system running at steady state with an energy deposition rate u of $300 \frac{W}{kg}$, at $t = 100s$ this energy deposition is increased to $450 \frac{W}{kg}$. In figure 5.6 the velocity and temperatures over time of systems made from aluminium, lead and zirconium are plotted for this situation. The figure shows the aluminium system reacting the quickest to steady state velocity and temperature values.



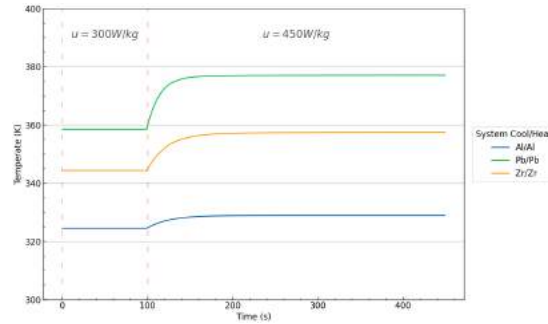
(a) Deposition Peak - Solution velocity over time



(b) Deposition Peak - Average temperature difference between heating and cooling sector over time



(c) Maximum target solution temperature over time



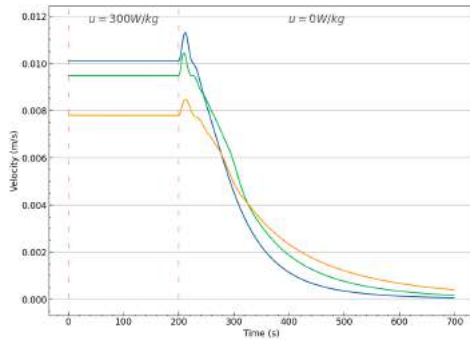
(d) Deposition Peak - Maximum wall temperature over time

Figure 5.6: Deposition Peak - Velocity and temperature results during a energy deposition peak situation over time for which at $t = 100s$ the energy deposition rate u is set from 300 to $450 \frac{W}{kg}$. This within systems with different materials with model settings: $N = 160$, $M = 5$, inner radius R_i of $0.005m$, pipe angle Θ of 5° , heating wall thickness dr_{12} of $0.015m$ and a cooling wall thickness dr_{34} of $0.005m$.

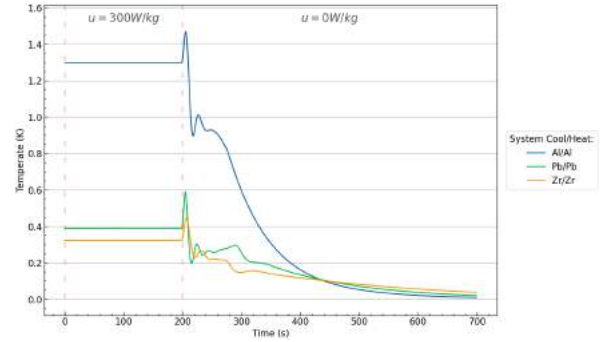
Shutdown

The shutdown situation consists of an initial HEAL system running at steady state with an energy deposition rate u of $300 \frac{W}{kg}$, at $t = 200s$ this energy deposition is dropped to $0 \frac{W}{kg}$. In figure 5.7 the velocity and temperatures over time of systems made from aluminium, lead and zirconium are plotted over time for this situation. While showing similar trends as seen in the other situations between the aluminium and lead systems, the zirconium system clearly shows a slower transient compared to the other materials.

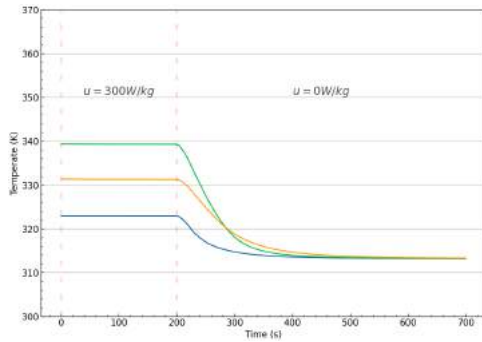
This slower transient most likely is the result of the lower heat transfer coefficient of zirconium and its higher relative thermal mass in comparison to lead. The zirconium system is therefore slower to remove its thermal energy to the environment.



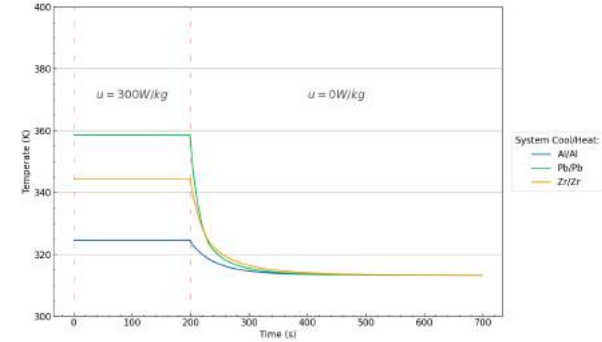
(a) Shutdown - Solution velocity over time



(b) Shutdown - Average temperature difference between heating and cooling sector over time



(c) Shutdown - Maximum target solution temperature over time



(d) Shutdown - Maximum wall temperature over time

Figure 5.7: Velocity and temperature results during a shutdown situation over time for which at $t = 100s$ the energy deposition rate u is set from 300 to $0 \frac{W}{kg}$. This within systems with different materials with model settings: $N = 160$, $M = 5$, inner radius R_i of $0.005m$, pipe angle Θ of 5° , heating wall thickness dr_{12} of $0.015m$ and a cooling wall thickness dr_{34} of $0.005m$.

5.2. Gamma and Neutron Shielding

5.2.1. System Walls

Average energy deposition different wall thicknesses

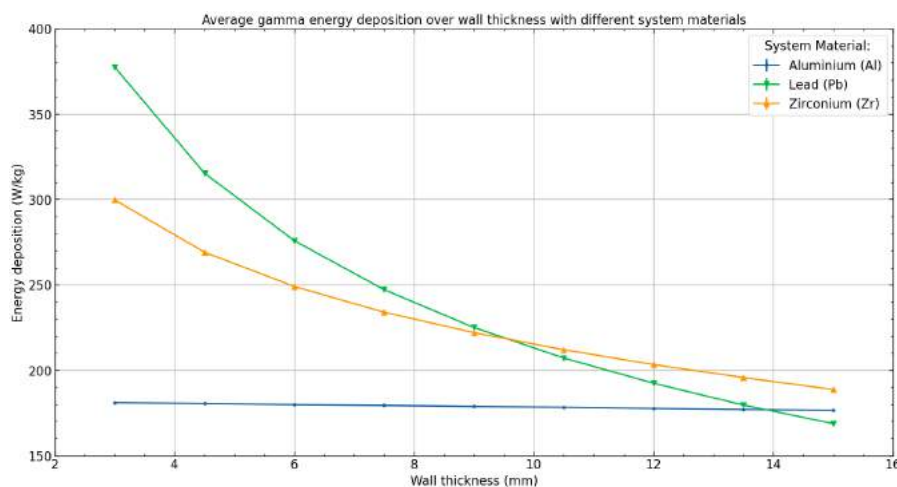


Figure 5.8: Average energy deposition rate from gamma radiation in HEAL systems with different wall thicknesses and materials. Showing the drop of the average energy deposition rate from gamma radiation over the wall thickness in both Zr and Pb systems.

In figure 5.8 the average gamma energy deposition rate within the wall of the HEAL with different wall thicknesses and materials are plotted. This figure shows that the average energy deposition for a wall made of aluminium doesn't significantly change over the wall thickness with an overall energy deposition of around $180 \frac{W}{kg}$ at all wall thicknesses plotted. The average energy deposition in the other materials, zirconium and lead, do have a significant drop in the average energy deposition as the wall thickness increases.

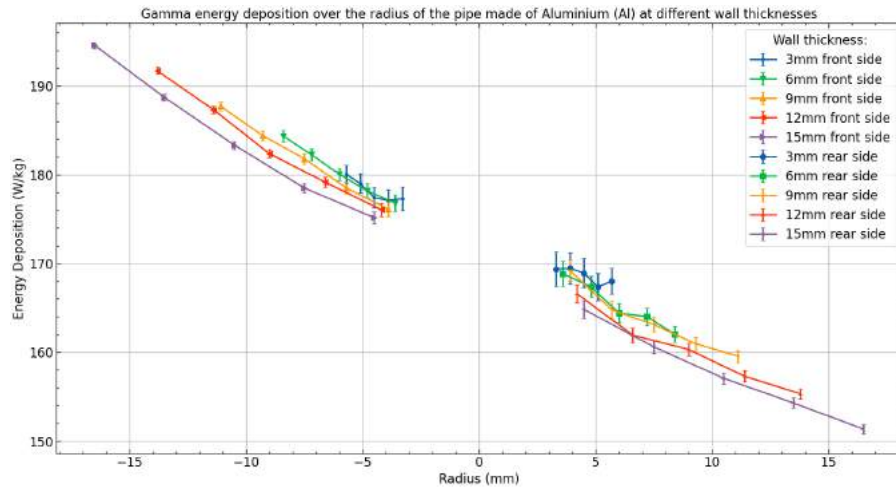
The large energy deposition from both the lead and zirconium wall show that the interaction rate with gamma radiation is significantly higher than that of aluminium and are therefore in line with the attenuation coefficients from each material as shown in 3.4.

These results show that the assumption of a $300 \frac{W}{kg}$ energy deposition rate for the materials inside the discretized model should actually scale with the material and wall thickness of the HEAL geometry for more accurate simulation of the systems. For aluminium this could be set to $180 \frac{W}{kg}$ however for the other tested materials this should scale with the thickness.

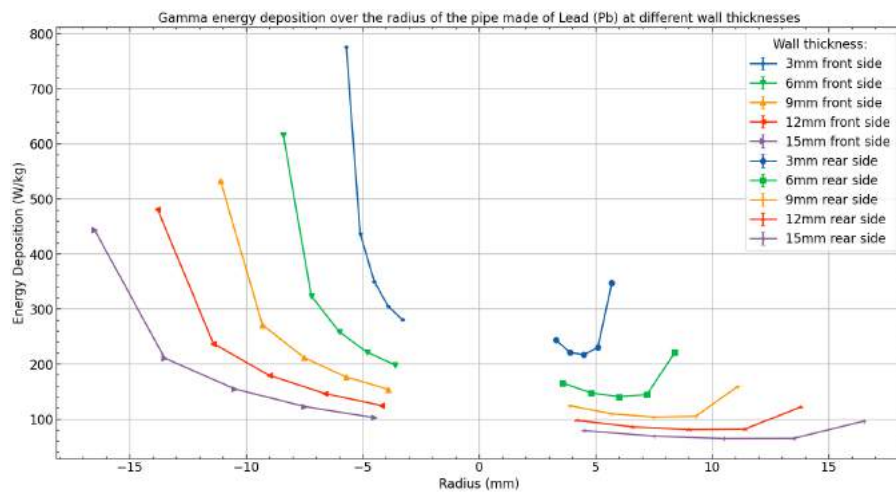
Radial energy deposition profile

The profiles seen in the figures from 5.9 show the energy deposition from gamma radiation in different HEAL wall configurations over the radius of the walls. This energy deposition is split in both the front side of the pipe, facing the gamma source, and the rear side of the pipe, facing away from the gamma source. The energy deposition rates in the front side of the pipe are indicated by the negative radius, the positive radii indicate deposition rate for rear side of the pipe. The gap between the front and rear side energy deposition values indicates the radius in which the target solution is present inside the HEAL system with an inner radius of $3mm$.

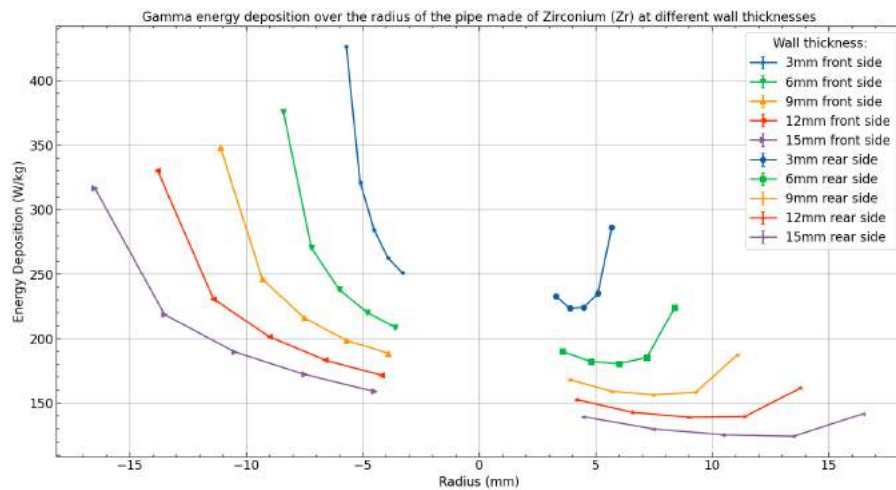
Before discussing the results it has to be noted that the individual points of each system represent an average gamma energy deposition within a radial region. For instance, within the figures of 5.9 all the energy deposition points of a $3mm$ system represent the same radial thickness as the first point of the $15mm$ system results. This becomes important when the energy deposition difference over the radius between different systems is significant.



(a) Energy deposition drop over the radius in the walls of Aluminium (Al) systems



(b) Energy deposition drop over the radius in the walls of Lead (Pb) systems



(c) Energy deposition drop over the radius in the walls of Zirconium (Zr) systems

Figure 5.9: The average energy deposition rates from gamma radiation in different radial sections of the detector within Serpent representing the walls of the system with different wall thicknesses (3–15 mm), materials and inner radius for the target solution of 3 mm. In these figures the energy deposition over the radius in both the "front" side (facing the gamma source) and "rear" side (facing away from the gamma source) are plotted, indicated by the data with the negative radius for the "front" side of the system and positive radius values for the "rear" side of the system. The error as indicated by the error bars is given by the $1.96 \times$ standard error (SE) from Serpent.

Aluminium

The radial energy deposition in an aluminium system as seen in 5.9a contains an almost linear decrease in the energy deposition over the radius of the wall in all system configurations. Comparing the front and rear side of the pipe, the energy deposition is significantly larger in the front which is positioned closest to the gamma source.

What can also be observed is that the energy deposition on the outer radius of the walls drops slightly over a decrease in the wall thickness. For instance, an energy deposition rate at the outer radius of the 15 and 3mm were found at 194.57 and 180.04 $\frac{W}{kg}$ respectively. This could be an indication that the energies of gamma rays that are likely to interact with aluminium are partially removed by interaction with water present inside the DLDR tube. As gamma rays have to travel slightly further through water to reach the outer radius of the walls in the 3mm system, this would explain the lower energy deposition rate at the outer radius.

Lead and Zirconium

Radial energy deposition of both the lead and zirconium walled systems can be seen in 5.9b and 5.9c. The profiles between the lead and zirconium systems are very similar, however the lead systems show a much wider energy deposition range compared to that of zirconium.

The profiles on the front side of the pipe show a significant exponential drop of the energy deposition over the radius. This shows the large interaction cross section of the gamma rays with both of the materials, especially for lead which for a 3mm system shows a 63.9% drop in the energy deposition in the front side of the pipe alone. For zirconium this drop is significantly lower and only accounts for a 41.2% drop in energy deposition within the same section. The profile continues on the rear side of the pipe until the energy deposition increases near the outer radius.

The basis for this increase in the energy deposition on the outer radius at the rear side of the pipe most likely comes from scattered gamma rays within the DLDR tube. These could reach the rear without going through the front side material that is used for shielding, increasing the energy deposition on the outer radius of the rear side.

As the wall thickness in the systems increases, the overall energy deposition rates over the profiles drop similar to as shown in figure 5.8. Within these profiles this drop now contains more context showing that the outer radius interacts with more photons, hence the larger energy deposition rate, decreasing the number of photons interacting at lower radii of the material.

In all profiles a slight drop of the energy deposition over the target solution can be observed. However as noted before, the radial thicknesses of the points between the different systems are different. Therefore no direct comparison between the different systems on this drop in energy deposition can be made.

The presence of an energy deposition profile over the pipe radius as well as the drop in the overall energy deposition rate over the wall thickness will result in different temperature profiles than previously assumed within the discretized model at a constant energy deposition rate of 300 $\frac{W}{kg}$ throughout the wall. Therefore these deposition profiles could have an effect on the expected thermal transfer rates within the HEAL. For lead and zirconium systems this would increase the thermal transfer rates between the wall and the water inside the DLDR tube significantly as a larger fraction of the energy is deposited on the outside of the pipe. For aluminium systems this would most likely be less of a concern as the profile between the front and rear of the pipe linearly drops significantly less.

5.2.2. Target solution

Gamma Dose rate

In figure 5.10 the fractional gamma dose rate within the target solution over the wall thickness of HEAL systems with different wall materials is plotted.

The system made from aluminium shows no significant decrease in the fractional dose rate over the wall thickness. This indicates that even at large wall thicknesses of the HEAL, an aluminium wall doesn't shield the target solution from the gamma radiation.

The lead system shows the largest drop in the fractional dose rate over the wall thickness with zirconium showing a smaller drop, this seems to follow the expected behaviour from the attenuation coefficients of

both materials as shown in 3.4. Both materials greatly reduce the gamma dose rate that the target solution is exposed to in an almost linear fashion over the wall thickness.

To shield the target solution in the HEAL from using the wall of the system as shielding material a lead wall is therefore preferred. Even at a small wall thickness of 3mm the implementation of a lead wall would provide a large difference on the photon dose rate to the target solution.

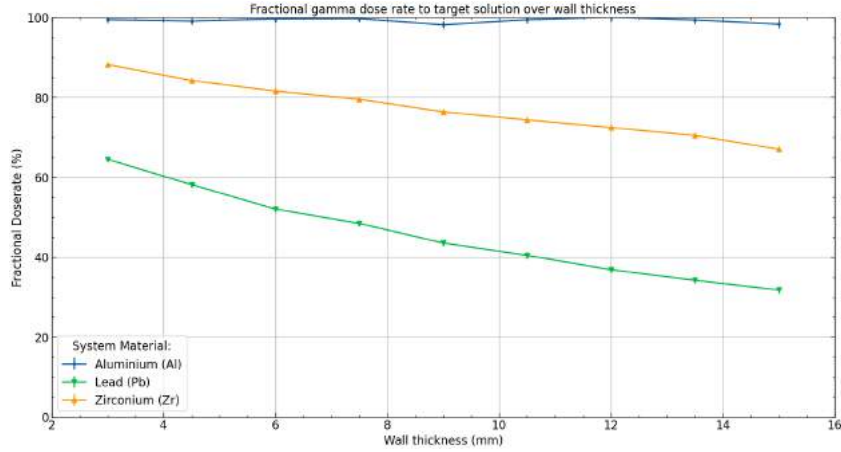


Figure 5.10: The fractional gamma dose rate deposited to the target solution over systems with different wall thicknesses and materials compared to a system without a wall. The fractional gamma dose rate that is shown is normalized to the gamma dose rate received in the target solution in a system without a wall. The error as indicated by the error bars is given by the $1.96 \times$ standard error (SE) from Serpent.

Neutron flux

Figure 5.11 shows the neutron flux inside the target solution over the wall thickness of HEAL systems with different wall materials. The drop in the neutron flux inside the target solution over the wall thickness of the different wall materials are very similar.

In contrast to the gamma dose rate results, a system with aluminium walls does have an effect on the neutron flux present inside the target solution which drops over the wall thickness as seen in figure 5.11. The drop in the neutron flux is larger than in systems made from lead or zirconium following their different interactions with neutrons compared to aluminium.

In figure 5.12 the neutron flux in systems with a 15mm wall thickness are shown that include combinations of different inner and outer wall materials. In this figure a similar trend is seen as in figure 5.11 where systems including aluminium show a larger drop in the neutron flux as the wall thickness of aluminium increases.

As the neutron flux is directly related to the reaction rate for neutron capture reactions as shown in equation 3.8, increasing the wall thickness will affect the production rate of the product in a negative way. For products utilizing the Szilard-Chalmers effect this lower neutron flux could be less important than the shielding provided to gamma radiation by the thicker walls, even at lower production rates.

Both the larger drop in neutron flux and the lack in gamma shielding capabilities of aluminium as a wall material within the HEAL significantly influence the use case for aluminium within the system which should only be considered when low energy deposition rates are required or its thermal properties are more preferred compared to other materials.

Lu-177 production

The microscopic neutron capture cross section of the $Lu - 176(n, \gamma) Lu - 177$ (3.5b) interaction over the wall thickness of different materials in HEAL systems can be found in figure 5.13. The microscopic cross sections shown in this figure are on average about $4545b$, significantly higher than cross sections found from thermal neutrons from literature of $2030.21b$ [2]. The higher neutron cross section is present as the average energy of neutrons reaching the target solution is different within the Serpent simulations than the thermal neutron spectrum at $0.025eV$ resulting in an increase of the neutron capture cross section as seen in the spectrum of 3.3.

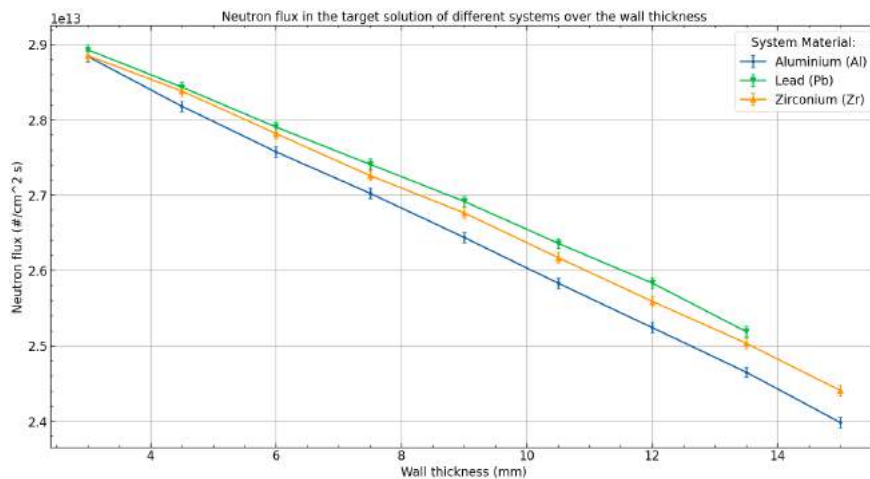


Figure 5.11: The neutron flux within the target solution over systems with different wall thicknesses and materials. The error as indicated by the error bars is given by the $1.96 \times$ standard error (SE) from Serpent.

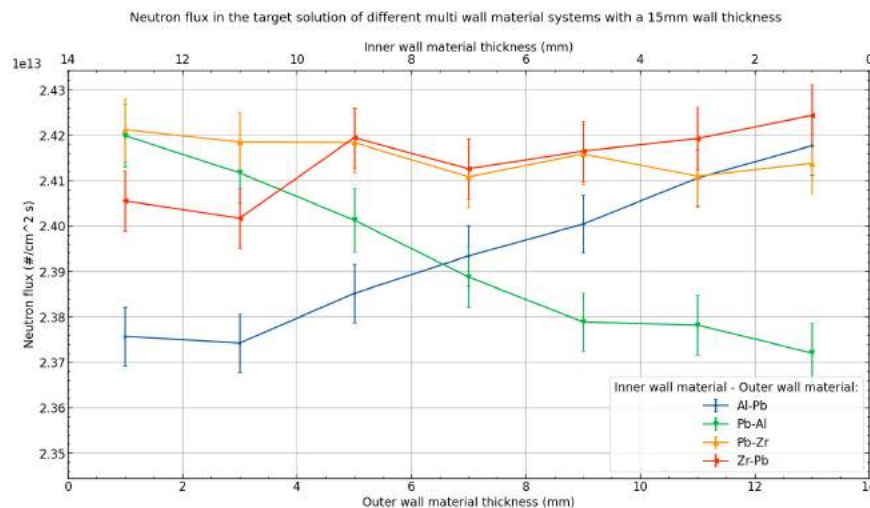


Figure 5.12: The neutron flux within the target solution over the inner and outer wall material thickness within systems with multiple wall material layers. The total wall thickness of these systems is 15mm with an inner radius of 3mm.

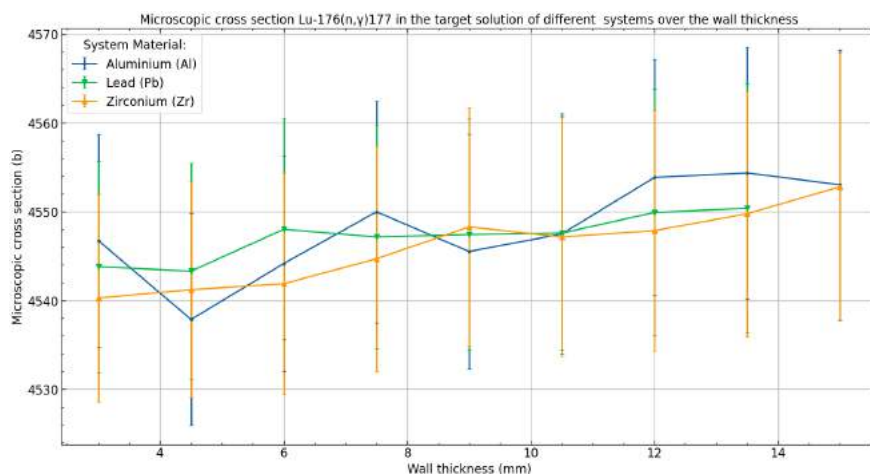


Figure 5.13: The microscopic cross section in the target solution for the neutron capture interaction $Lu - 176(n, \gamma)177$ over the wall thickness of different systems with different wall materials. The error as indicated by the error bars is given by the $1.96 \times$ standard error (SE) from Serpent.

5.3. Residence Time Distribution

5.3.1. CFD Flowrate and Recycle Results

The figures in 5.14, plots of the flowrates in the vessel and recycle segment can be found over the inlet flowrate together with the recycle fraction with these flowrates, as calculated by the equations in 3.26. In these plots HEAL systems with an 3, 7 and 13mm inner radius are shown with both different inlet/outlet radii as well as different inlet/outlet positions.

The vessel segment flowrates in all HEAL systems show that an increase in the inlet flowrate increases the flowrate the vessel segment in all systems. This agrees with the mass balance of 3.25 the system. The vessel flowrate does not increase 1:1 with the inlet flowrate as the recycle flowrate changes as well.

In the smallest inner radius systems of 3mm (5.14a) the recycle segment flowrate decreases with the inlet flowrate in all systems. This suggests that the outlet in both the 2 and 3mm inlet/outlet radius cases provides the path of with less resistance compared to the recycle segment.

In the 7mm inner radius systems (5.14b) a difference in the recycle segment flowrate with different inlet/outlet radii can be observed. Initially, the recycle segment flowrate decreases over the inlet flowrate similar to the 3mm systems. However at an inlet flowrate of around $2.5 \times 10^{-7} \text{ m}^3/\text{s}$, the recycle flowrates between systems with a small and large inlet/outlet radius diverge from each other. Systems with the 2mm inlet/outlet radius increase flowrate in the recycle as the inlet flowrate increases. This is presumably mainly the cause of the increase in resistance through the outlet from the sudden contraction of the large 7mm inner radius to the small 2mm outlet radius.

The systems with the 7mm inlet/outlet radius decrease the recycle flowrate over the increase in inlet flowrate. This drop in the recycle flowrate is lower compared to the 3mm inner radius systems at the same change in the inlet flowrate.

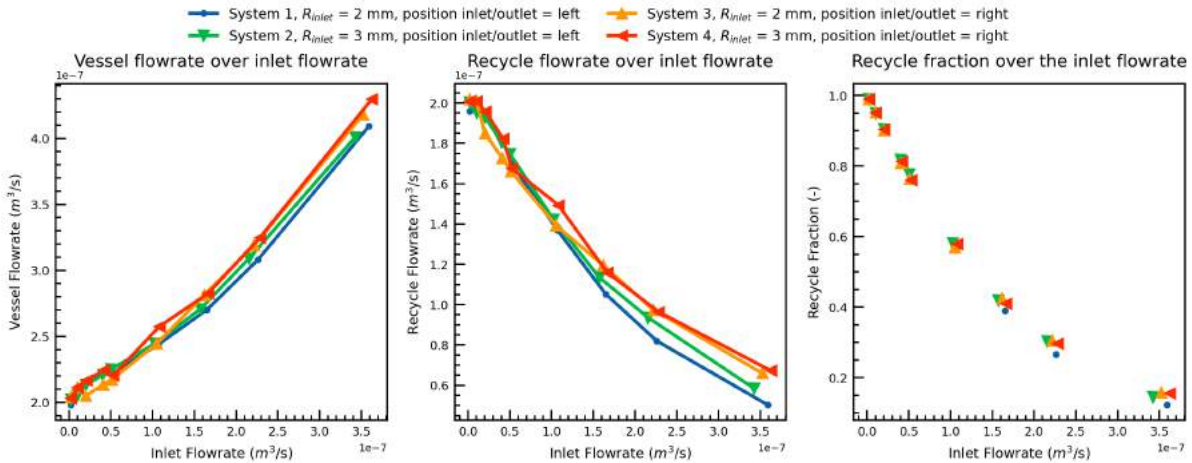
The 13mm inner radius systems (5.14c) show the same divergence of the recycle segment flowrate between the 2 and 13mm inlet/outlet radius. The increase in the recycle segment flowrate over the inlet flowrate in the 2mm system is steeper compared to the 7mm inner radius systems as seen in 5.14b. Another difference that can be observed is that the recycle flowrate in the 13mm inlet/outlet radius remains relatively stable over the inlet flowrate.

In systems where the recycle segment flowrate increases with the inlet flowrate, the recycle ratio has a much narrower range of operation compared to the systems where the recycle flowrate drops. For more control of the recycle ratio, systems with a smaller resistance through the outlet compared to the recycle segment are therefore preferred.

Similar vessel and recycle segment flowrate trends are observed in the other systems from the table 4.9. The CFD results for these systems can be found in the appendix F.1.

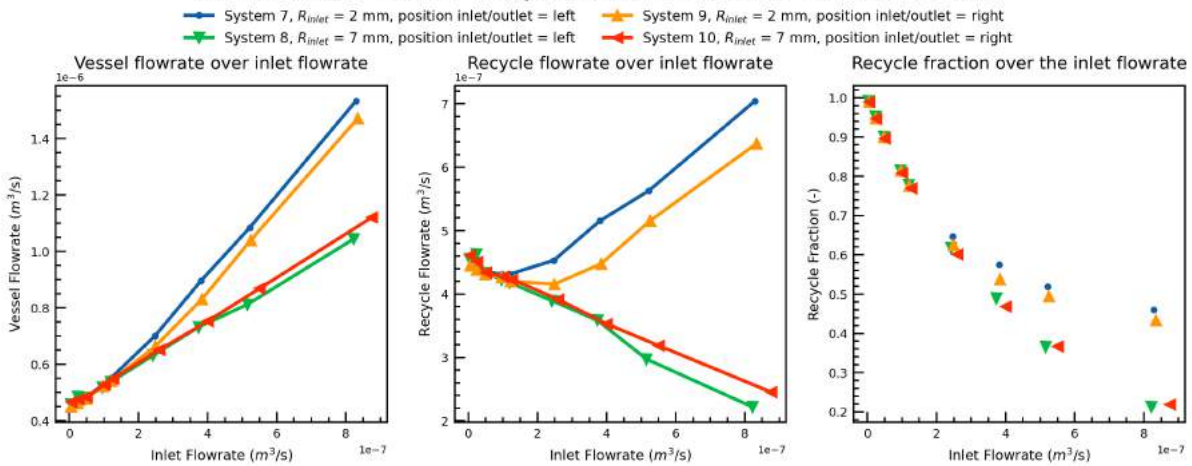
Overall, these results show that the geometry of the inlet and outlet radius in the HEAL have a large influence in the flowrates that are seen inside the system during mixed convection situations. For controlling the flowrate in the recycle segment, smaller radius systems are preferred within this set of geometries. For controlling this flowrate in larger radius systems the in- and outlet radius are of large importance.

CFD flowrate results on systems with an inner radius of 3 mm



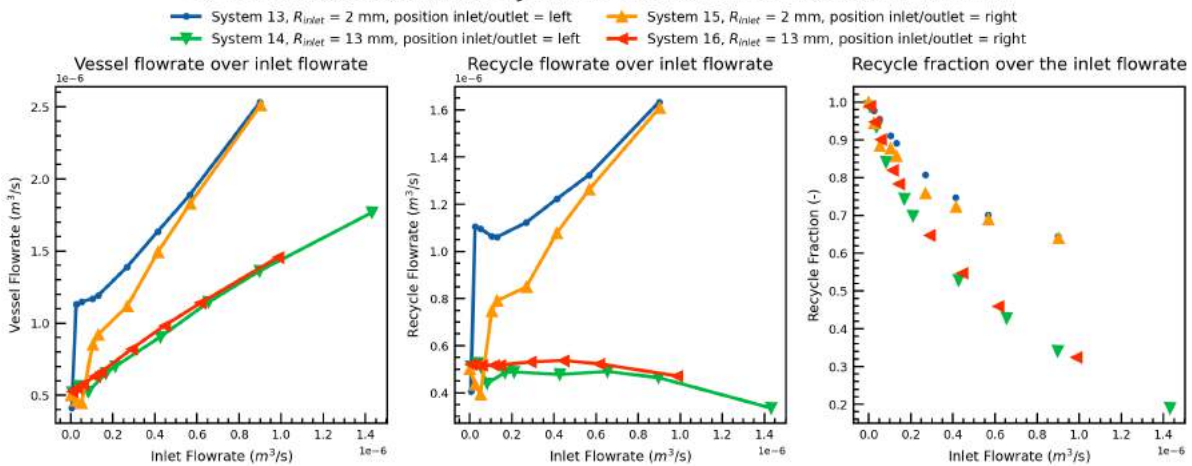
(a) Systems with an 3 mm inner radius

CFD flowrate results on systems with an inner radius of 7 mm



(b) Systems with an 7 mm inner radius

CFD flowrate results on systems with an inner radius of 13 mm



(c) Systems with an 13 mm inner radius

Figure 5.14: CFD results on HEAL systems with an inner radius of 3, 7 and 13 mm (a, b, and c respectively) from the vessel and recycle segments with different inlet/outlet radii and positions. Showing the increase in flowrate in the vessel segment at higher inlet flowrates and differing flowrates in the recycle segment.

5.3.2. RTD curves and Tanks-In-Series compartment models

In the figures in 5.15 some RTD curves of vessels segments from different systems in 4.9 have been plotted. In each plot two curves are shown, indicated by "CFD data" and "TIS model". The "CFD data" refers to the RTD curves as found by the CFD simulation of the pulse input, the "TIS model" refers to the RTD curves retrieved from modeling of the "CFD data" to the Tanks-In-Series compartment model as shown in 4.4.2. Similar plots from the RTD curves of the recycle vessels can be found in the figures in 5.16.

Extended plots including all the individual system RTD curves of the other systems and flowrates can be found in the appendix in figures F.2-F.17 for the vessel segment and figures F.18-F.33 for the recycle segment.

Vessel Segment

RTD curves of the vessel segments in systems with an inner radius between 3 and 7mm are generally very similar, consisting of a singular peak in front of the mean residence time to which a trailing tail is attached. This trailing tail slightly widens over the mean residence time as the flowrate increases resulting in larger variances. An example of the widening of the trailing tail can be seen in the RTD curves of system 1 in 5.15a and 5.15b.

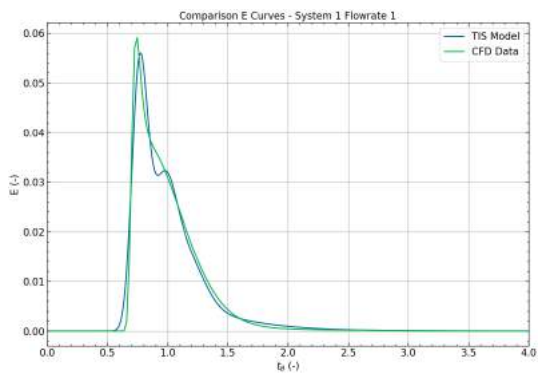
In systems with larger inner radii, the RTD peak of the vessel segment widens considerably at lower flowrates. Increasing the flowrate narrows this peak back to a profile as seen in the smaller radius systems. An example of this can be seen in the RTD curves of system 11 in 5.15d and 5.15e. Profiles in these larger radius systems can also contain multiple peaks suggesting the existence of parallel paths inside the vessel segment.

Recycle Segment

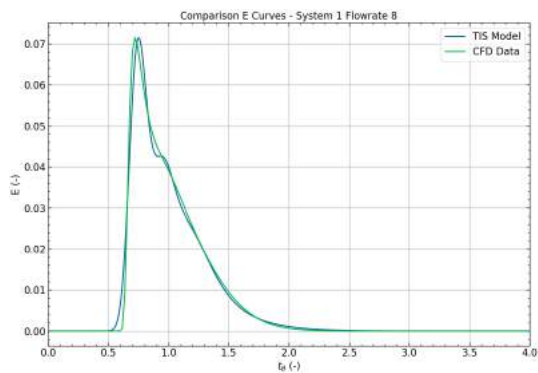
In the systems with a 3mm inner radius, e.g. system 1, the RTD curves of the recycle segment contain a peak before the mean residence time to which a trailing tail is attached. As the flowrate in the segment decreases, the tail becomes less pronounced and eventually vanishes into the initial peak as the velocity difference in the velocity profile narrows.

Within the RTD curves of systems 5 to 10 with a larger inner radius from 5 to 7mm, multiple peaks exist as can be seen in system 8 in 5.16c. This can indicate parallel paths that exist within the larger volume compared to the 3mm inner radius systems.

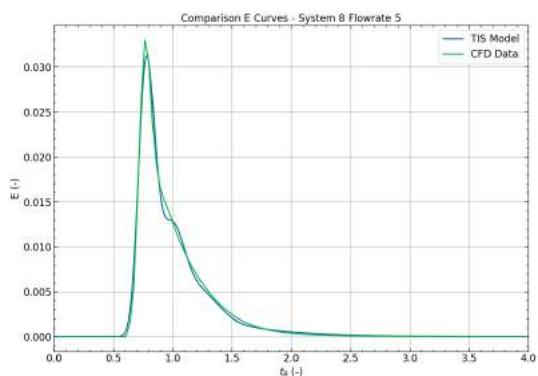
As the inner radius increases from 11mm and up (system 11 and above), the RTD curves of the recycle segment show a different profile, generally containing a wider range of variances across the different inlet velocities. The RTD curves consist of (multiple) initial smaller peaks with a more pronounced peak following. Only at high flowrates in these systems the curves significantly change into a singular peak as seen in the smaller radius systems, an example of the of system 17 in 5.16d and 5.16e.



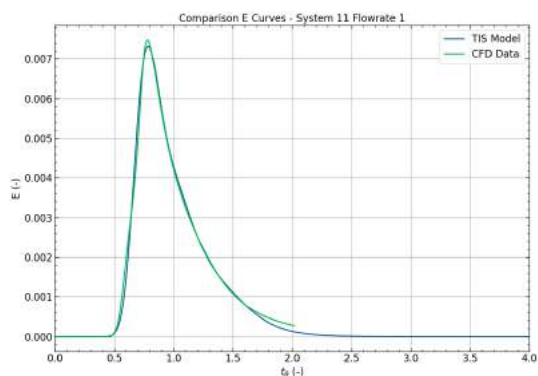
(a) System 1, velocity setting 1, mean velocity $7.00E-3$ m/s, with flowrate = 0.198 cm³/s



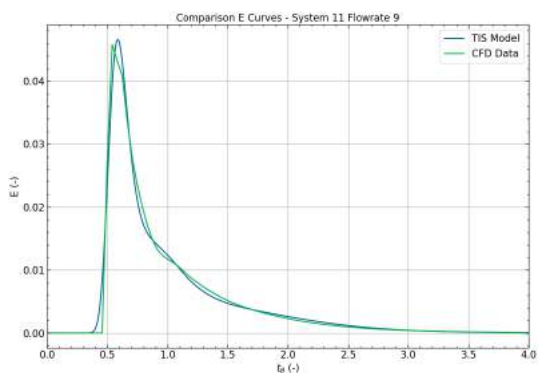
(b) System 1, velocity setting 8, mean velocity $1.09E-2$ m/s, with flowrate = 0.308 cm³/s



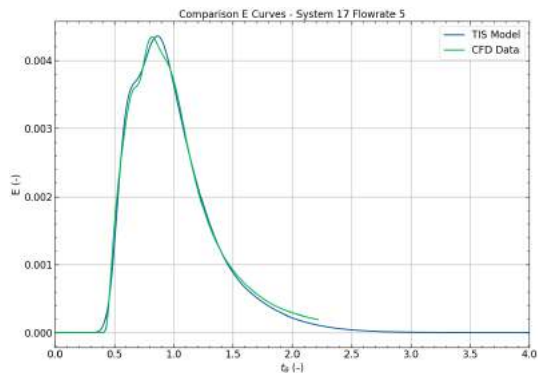
(c) System 8, velocity setting 5, mean velocity $3.49E-3$ m/s, with flowrate = 0.537 cm³/s



(d) System 11, velocity setting 1, mean velocity $1.07E-3$ m/s, with flowrate = 0.406 cm³/s

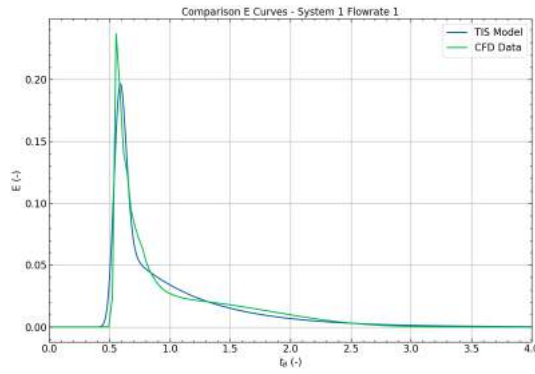


(e) System 11, velocity setting 9, mean velocity $5.89E-3$ m/s, with flowrate = 2.237 cm³/s

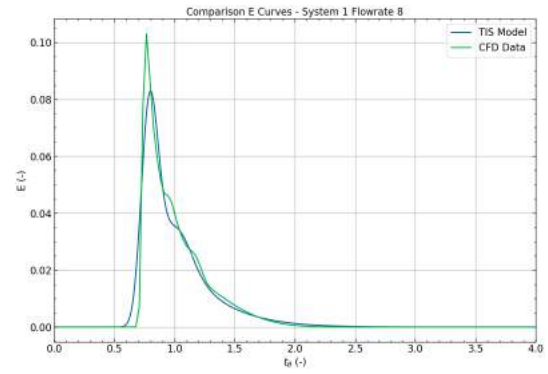


(f) System 17, velocity setting 5, mean velocity $7.77E-4$ m/s, flowrate = 0.549 cm³/s

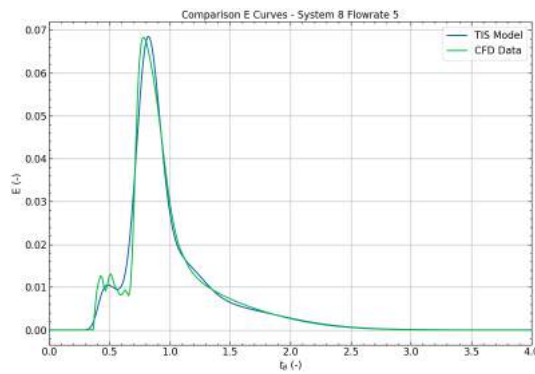
Figure 5.15: Vessel segment RTD Curves of both the CFD data and the developed Tanks-In-Series compartment model in systems 1, 8, 11 and 17 at at different vessel flowrates.



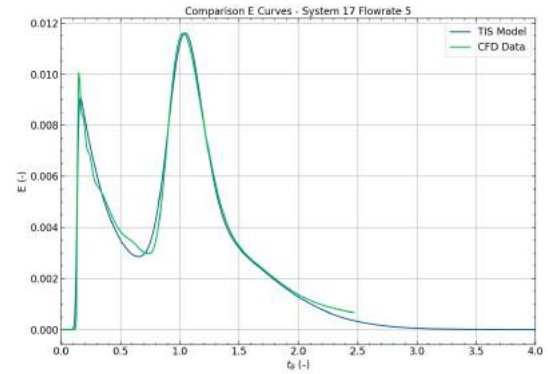
(a) System 1, velocity setting 1, mean velocity $6.93\text{E-}3$ m/s, flowrate = 0.196 cm^3/s



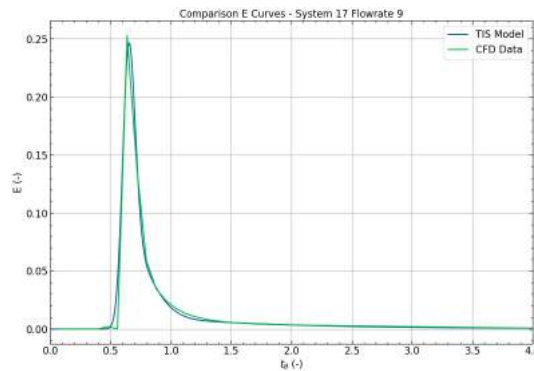
(b) System 1, velocity setting 8, mean velocity $2.90\text{E-}3$ m/s, flowrate = 0.082 cm^3/s



(c) System 8, velocity setting 5, mean velocity $2.71\text{E-}3$ m/s, flowrate = 0.418 cm^3/s



(d) System 17, velocity setting 5, mean velocity $5.77\text{E-}4$ m/s, flowrate = 0.408 cm^3/s



(e) System 17, velocity setting 9, mean velocity $3.34\text{E-}3$ m/s, flowrate = 2.358 cm^3/s

Figure 5.16: Recycle segment RTD Curves of both the CFD data and the developed Tanks-In-Series compartment model in three different systems, system 1, 8 and 17 at different vessel flowrates.

RTD curve variances

In figure 5.17 plots are shown of the dimensionless variance σ_{θ}^2 of the RTD curves of different systems over the mean velocity of both the vessel and recycle sectors.

This figure shows that the dimensionless variance of the RTD curves of systems with a 3mm inner radius linearly increase with the velocity, especially within the recycle segments.

Systems with larger inner radii have distinct profiles over the velocity. For instance within both segments of system 7 the dimensionless variance initially drops as the velocity is increased after which the variance significantly increases as the velocity is further increased. Similar profiles can be found in system 11, 17 and 8 within the figures. The initial drop of the dimensionless variance could possibly be explained by a shift between a buoyancy and convection driven flow. In this case the convection driven flow results in a smaller variance within the segments.

A different trend that can be observed is that systems with larger radii overall have larger variances at similar velocities compared to that of systems with smaller inner radii. Overall, smaller systems are therefore preferred for more control of the residence time within for shorter irradiations or possibly for batch operation in flushing the system. Continuous operation for longer irradiation periods should not be affected by these results as the system would act as a CSTR following figure 3.7.

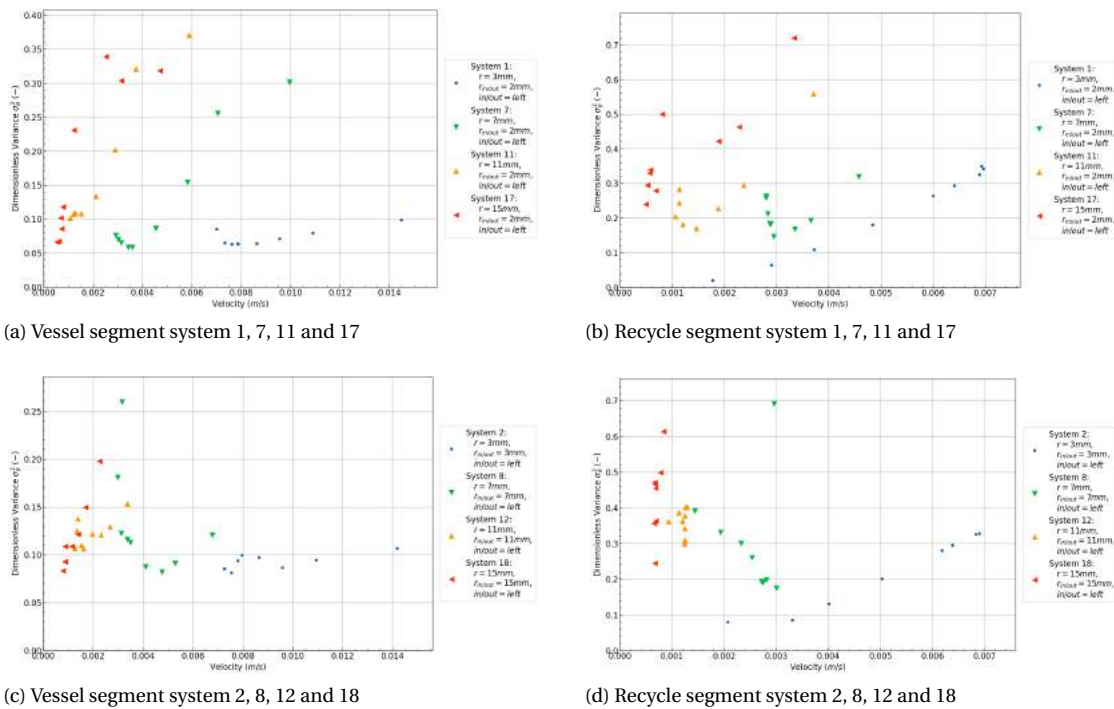


Figure 5.17: Dimensionless variance over the velocity in both the vessel and recycle segments in systems with 2mm inlet/outlet radius (a and b) and variable inlet/outlet radius (c and d). Showing the different profiles of each system and general increase in variance as the system radius increases.

Flushing

Using the found Tanks-In-Series compartment models of the vessel and recycle segment at the lowest and highest inlet velocity a flushing cycle was set up within the dynamic HEAL model consisting of the steps as shown in figure 3.8. The defined flushing cycle, the time each step is taken and flowrates used can be seen in table 5.2. In figure 5.18 the concentrations within the segments and the outlet are shown over time for system 2 and 12.

The flushing plots show that while system 2 keeps a higher concentration for a larger fraction of step 2 and contains a smaller concentration of product left in the vessel segment. Within step 3 slightly more product is also transferred to the vessel segment within the lower variance system 2. However the difference between the systems is very limited in terms of their flushing capabilities within this flushing cycle.

These results show that within the different variances seen in the systems, for the direct flushing cycle at the highest flowrates of both the recycle and vessel segments the difference is not significant.

Table 5.2: Defined flushing cycle for each step within the dynamic HEAL model

Step	Step Time (s)	Tanks-In-Compartment Model Inlet velocity	Flowrate Vessel Segment	Flowrate Recycle	RF
1	20	Lowest	CFD	CFD	1
2	$2 \times \bar{t}_{vessel}$	Highest	CFD	0	0
3	$2 \times \bar{t}_{recycle}$	Lowest	CFD	CFD	1
4	$4 \times \bar{t}_{vessel}$	Highest	CFD	0	0

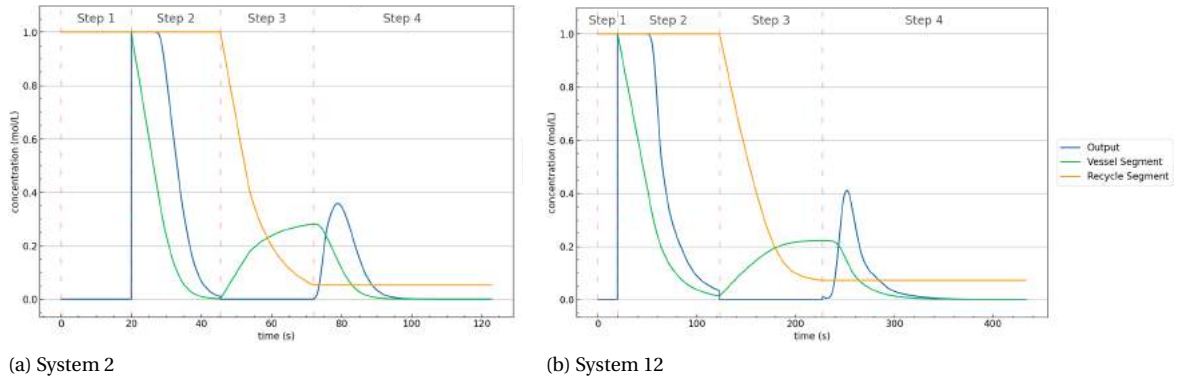


Figure 5.18: Concentration profiles over time of a simulated flushing cycle of system 2 (left) and 12 (right) within the dynamic HEAL model showing the concentration at the output, vessel segment and recycle segment.

5.4. Production Lu-177

5.4.1. Batch operation

By attaching the Lu-177 production model from 4.3 to the Dynamic HEAL model as shown in 4.4.3 figure 5.19 was made showing the theoretical specific activity of a Lu-177 product and the the Lu-177 concentration over time with different radiolysis cross sections within the HEAL during a batch operation. The specific activity as shown in these figures was calculated as given in equation 3.6b where the m_{prod} consists of the metal ion mass of both the present lutetium and hafnium isotopes. Information on the maximum specific activity reached by the model, the time at which this is reached and the metal ion concentration is shown in table 5.3.

The theoretical specific activity over time shows a sharp increase in the specific activity seen at the start of irradiation with all radiolysis cross sections. For the lower radiolysis cross sections ($\sigma_{\gamma_dam1} = 1281$ and $\sigma_{n_dam1} = 7500$) the theoretical specific activity reaches a maximum after which the specific activity drops as the Lu-177 concentration relative to the other metal ion concentration drops from radiolysis and chemical

interactions. The larger radiolysis cross sections ($\sigma_{n_dam1} = 75000$ and $\sigma_{n_dam1} = 750000$) quickly change into a slow gain in S.A. after irradiation as to what could be seen during irradiation without utilization of the Szilard-Chalmers effect. These plots reach their maximum S.A. significantly later than their lower cross section counterparts.

The Lu-177 concentration profile shows a similar initial increase between the plots which drops as DOTA is released from the MeDOTA complexes, increasing the rate of chemical labelling. This drop in the concentration gradient takes place earlier in systems with larger radiolysis cross sections as the release rate of DOTA is significantly higher. In longer time frames more Lu-177 is released from the systems with larger radiolysis cross section as the DOTA molecules are damaged and can't form complexes with the metal ions any more.

These results show that decreasing the cross section of radiolysis, and therefore lowering the effect of gamma radiation on radiolysis, significantly increases the theoretical specific activity that is able to be retrieved from the product. This therefore stresses the importance for shielding of gamma radiation within the HEAL for the production of Lu-177.

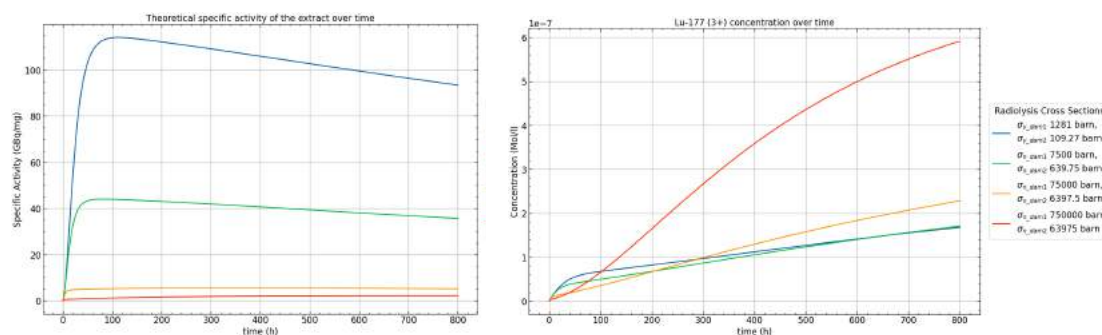


Figure 5.19: Theoretical specific activity of the Lu-177 product (left) and the Lu-177 ion concentration (right) from an initial 96% labelled 0.0014 Mol/L LuDOTA solution with naturally enriched lutetium atoms inside the HEAL during production over time without in- or outflow. In this plot the product is the extracted metal ions of both lutetium and hafnium. Plotted are profiles of different radiolysis cross sections based on either the gamma (σ_γ) or neutron (σ_n) flux of 1.36×10^{13} and $3.71 \times 10^{12} \text{ cm}^{-2} \text{ s}^{-1}$ respectively [30]. For these results experimental values for the extraction factor $f_{\text{extraction}}$ of 0.84 was used [42] and the σ_γ cross section of 750000 barn is included [60] in one of the plots.

Table 5.3: The maximum specific activity reached from batch operation of the HEAL with an initial 96% labelled 0.0014 Mol/L LuDOTA solution containing naturally enriched lutetium atoms. This together with the time at which this S.A. is reached, the concentration of the Lu-177 ions, and metal ion concentration at the maximum specific activity.

Cross Section Type	Cross Section (barn)	Max. S.A. (GBq/mg)	Time (h)	Lu-177 (3+) Concentration (Mol/L)	Metal ion concentration (Mol/L)
σ_γ_dam1	1281	114.087	112.43	$6.954E-8$	$2.104E-6$
σ_n_dam1	7500	44.026	80.89	$4.653E-8$	$3.650E-6$
σ_n_dam1	75000	5.575	339.97	$1.115E-7$	$6.910E-5$
σ_n_dam1	750000	2.141	760.61	$5.764E-7$	$9.297E-4$

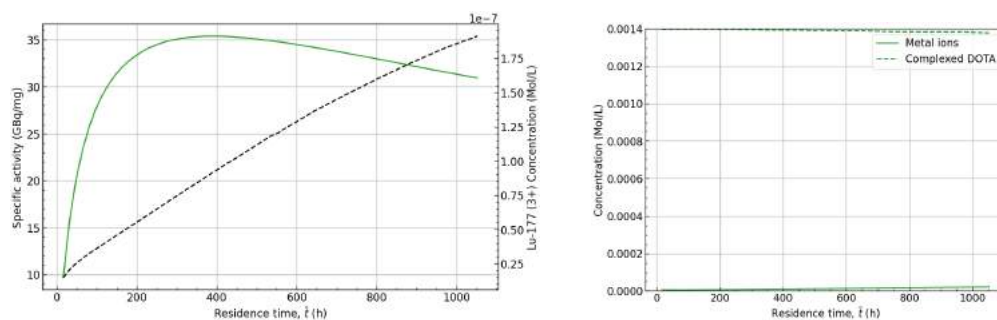
5.4.2. Continuous operation

The specific activities as shown in table 5.3 could be reached with batch operation of the HEAL. Compared to batch operation, continuous operation contains a constant in- and outflow of reactant and products present inside the system. With the complex kinetics this will have an effect on the concentrations and therefore interaction rates of the different components within the HEAL. Using the Dynamic HEAL model HEAL systems with different residence times, and therefore in- and outlet flowrates have been tested. The inlet concentration within these simulations was set at an 96% labelled 0.0014 Mol/L LuDOTA solution containing naturally enriched lutetium atoms.

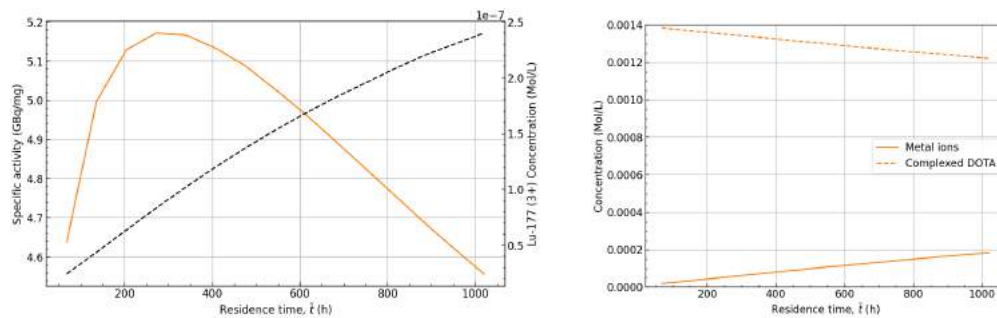
The figures in 5.20 show the steady state specific activities and the Lu-177 concentration over the residence time within the HEAL at different radiolysis cross sections. These figures show that at the same radiolysis cross sections during continuous operation the maximum steady state specific activity is lower than during batch operation as show in table 5.3.

This difference can be attributed to both dilution of the product and changes in the kinetic rates by the incoming reactants. It also has to be noted that the residence times where the specific activity of the product is the highest are at very large time frames in the hundreds of hours. These residence times would result in a very low flowrate of reactant through the inlet. As an example a 100ml HEAL vessel with a residence time of 300 hours would have an input flowrate of 0.33ml/h, which is possibly too low to allow for extraction gaseous radiolysis by products that could form during operation.

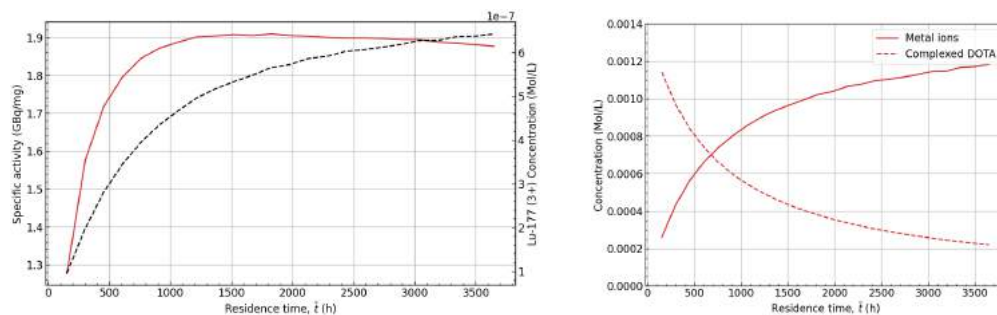
A possible way to improve the in- and outlet flowrate would be to recycle the product flowing through the outlet back into the inlet of the HEAL with extraction of by products in between outside of the HEAL. This will however lower the amount of time the reactants will be exposed to neutrons within a complete system, which in turn will lower the specific activity further within this particular system for the production of Lu-177.



(a) $\sigma_{n_dam1} = 7500b, \sigma_{n_dam2} = 639.75b$



(b) $\sigma_{n_dam1} = 75000b, \sigma_{n_dam2} = 6397.5b$



(c) $\sigma_{n_dam1} = 750000b, \sigma_{n_dam2} = 63975b$

Figure 5.20: Steady state specific activities, concentration of Lu-177, metal ions, and complexed DOTA in the product stream over the residence time within the HEAL at different radiolysis cross sections. The specific activity is indicated in the left figures by the solid line and the Lu-177 concentration by the dashed line. The metal ion and complexed DOTA concentration are shown in the figures on the right.

6

Conclusion

Within this chapter a conclusion will be given answering the research questions of this thesis. These questions will be individually answered.

1. In what way does the addition of heat conduction in the wall of the loop have an influence on the functionality of the system?

- *What is the influence of the design parameters, as listed below, on the HOR Experimental Activation Loop on both the velocity and temperatures in the system?*

– Wall thickness

Generally increasing the wall thickness of either the heating or cooling wall increases the average and maximum temperatures seen within both the target solution and walls of the system. For systems consisting of a single wall material this increase in temperature is very much dependent on the wall material and its total energy deposition. Lead walls increases these temperature significantly more than that of zirconium and aluminium walls of which aluminium has the smallest effect on the temperature.

Overall, lowering the energy deposition difference between the heating and cooling sector by increasing or decreasing the individual heat- or cooling wall thicknesses decrease the velocities that are seen within the HEAL.

– Wall materials

Systems made from a single material in both the heat- and cooling wall reverse in velocity at the point at which the cooling wall thickness is larger than the heating wall thickness. This effectively comes from the reversal of roles in heating and cooling the target solution of the defined heat- and cooling sectors. This negative velocity is relatively stable over any cooling wall thickness changes which is a result from a feedback loop that is present when most of the heating and cooling takes place in the vertical sections of the loop.

Combining two different heat- and cooling wall materials inside a system affects the temperatures seen within the system to be in between systems made purely from the individual materials. Velocities in these systems generally show a similar profile over the wall thicknesses as their single material system counterparts except for when the energy deposition within the cooling wall is much higher than the heating wall such as in the Al/Pb systems which increases the negative velocities seen in the system as the cooling wall thickness increases.

Staggered multi-layered wall designs have shown interesting results in terms of velocity and temperatures, especially the Pb-Al/Al-Pb and Al-Pb/Pb-Al systems. These systems show that at larger inner wall thicknesses the velocity can remain very stable over increases in the outer wall layer thickness as well as that the increase in temperature of the target solution is comparable to the same increase in wall thicknesses of Al/Al systems while being able to provide gamma shielding properties from the lead walls.

– **Inner radius**

The inner radius R_i has a large effect on the velocities seen within the systems. Maximum velocities are generally found at inner radius R_i values between 0.0025 and 0.0050m. After this maximum velocity is reached the velocity starts to drop as the inner radius increases. In systems with negative velocities, where the roles of the heat- and cooling sectors in heating and cooling the target solution are reversed, an increase in the inner radius drops the velocity significantly more than in systems with a positive velocity.

– **Length**

Increasing the length L of the system significantly increases the velocities and temperatures seen within most systems by allowing more time within each section for heat transfer between the walls and target solution. This in turn increases the temperature and density difference between the vertical heat- and cooling sections, increasing the velocity according to the momentum balance.

– **Angle of pipe**

The pipe angle does have a slight effect on the velocities that are seen in the systems, especially in longer systems with smaller inner radii R_i . E.g. at an inner radius of 0.0024m increasing the pipe angle increases the velocity and decreases the temperatures. At slightly larger inner radii from 0.0051m and above this impact is significantly less compared to the other variables such as the length, inner radius and wall thicknesses. In these systems at low pipe angles of less than -20° multiple steady states can occur with both positive and negative velocities.

- *How does the velocity and temperatures in the HEAL react to changes from outside variables over time in systems with different wall materials?*

During the startup situation all systems show an initial negative velocity as the energy deposition rate is increased. This negative velocity quickly changes into a positive velocity as the temperature difference between the target solution and the walls increase. Within the shutdown situation the opposite trend is shown where an initial spike in velocity is seen after which it drops to zero.

In all situations tested the system made from aluminium showed the fastest reaction towards a steady state situation in terms of the velocity and the temperatures within 120 seconds for the startup situation. Both the zirconium and lead systems with their lower thermal conductivity coefficient were slower. The shutdown situation showed that zirconium was the slowest reaching steady state velocity and temperatures.

2. What is the effect of different wall configurations to the shielding from gamma radiation and functionality of the HEAL?

- *What amount of shielding to gamma radiation is provided by different wall configurations such as the wall material, wall thickness and multiple wall material layers?*

The dose rate of gamma radiation delivered to the target solution can be significantly reduced by implementing a zirconium or lead system wall. At a 3mm wall thickness these materials respectively provide a fractional dose rate reduction to 88.2 and 64.5% compared to a system without any shielding. Increasing the wall thickness further decreases the delivered dose rate almost linearly. At the largest explored wall thickness of 15mm the respective zirconium and lead fractional dose rate reductions were found at values of 67.0 and 31.8%.

While implementing aluminium in the wall did show a small influence the energy deposition within the wall over the radius. A significant effect of the aluminium wall thickness on the delivered dose rate to the target solution was not found within the explored wall thicknesses between 3 and 15mm.

- *Does the shielding to gamma radiation provide a heating profile throughout the wall of the HEAL?*

Shielding of gamma radiation does provide a radial heating profile through the wall of the HEAL in which the front at the outside radius of the HEAL receives the largest amount of energy deposition in all materials.

The gamma energy deposition over the radius in systems with lead and zirconium walls show a different profile compared to systems with aluminium walls. Within these systems the energy deposition is the largest on the outer radius of the pipe on the side which faces the reactor. As the radius decreases the energy deposition decreases almost exponentially. On the rear side of the pipe, facing away from the reactor this energy deposition drop continues until the outer radius at which the deposition increases slightly. For the aluminium walled systems the largest energy deposition is the same on the front side of the pipe facing the reactor, however the drop over the radius is linear and continues to drop on the rear side of the pipe without increasing on the outer radius.

- *To what extent do different wall configurations shield the system from neutrons and what is the effect on the production rate of Lu-177 from these wall configurations?*

Neutrons do get partially shielded from the target solution, especially from systems containing aluminium. The neutron flux drop over the wall thickness is relatively low compared to the drop in gamma dose rate that is delivered to the target solution. For production of radioisotopes shielding by these materials will affect the reaction rate negatively, however shielding provided by gamma radiation for the production in combination with the Szilard-Chalmers effect with Lu-177 can still benefit in terms of the specific activity of the product dependent on the kinetics.

The different wall thicknesses and materials have not shown to have a significant effect within the standard errors on the cross section of the neutron capture reaction $^{176}\text{Lu}(n, \gamma)^{177}\text{Lu}$ for the production of Lu-177.

3. How does the operation of the HEAL influence the production of Lu-177, utilizing the Szilard-Chalmers effect?

- *What factors controlled by the HEAL have an effect on the production of Lu-177 in continuous and batch operation?*

A model for the production of Lu-177 with the Szilard-Chalmers effect was made and coupled to a dynamic HEAL systems coupled to a Tanks-In-Series compartment model. The highest specific activities were reached at the lowest radiolysis cross section in both continuous and batch operation of the HEAL. Batch operation within the HEAL showed higher specific activities than at the steady state values in continuous operation showing the advantage of batch operation without dilution from an inlet flow.

Within continuous operation the residence time plays a large role in defining the output concentration and specific activity. The optimal steady state specific activities within the HEAL were also very dependent on the radiolysis cross sections. As the cross sections used in the model were related on the gamma flux present, this specific activity is therefore dependent on the amount of shielding that the HEAL can provide where a high amount of shielding can provide significant gains in the maximum specific activity that can be reached.

- *How does the radius of the HEAL as well as the radius and position of the inlet and outlet affect the dispersion inside the loop?*

The variance of the dispersion of the RTD curves through the loop generally increase with the inner radius of the systems. Larger radius systems often contain multiple peaks within the RTD curve suggesting parallel streams inside the velocity field which increase their variance and therefore dispersion. No significant difference in terms of dispersion between the small and large in- and outlet radii were found.

Modelling the RTD curves of the defined segments of the HEAL with a Tanks-In-Series compartment model and coupling the segments to form a complete HEAL in the dynamic HEAL model showed a slight advantage in flushing the system for systems with smaller variances. However the differences in dispersion between the systems at higher flowrates were not significant enough for flushing to warrant the preferred use of either small or large inner radius system.

- *How does the recycle rate/fraction influence the residence time distribution of the different segments inside the loop and how can this recycle rate be controlled?*

Increasing the in- and outlet flowrate lowers the recycle ratio/fraction within the HEAL. The rate and range at which this recycle ratio can be lowered is very much dependent on the geometrical in- and outlet configuration of the HEAL. For instance, the largest range of achievable recycle ratios were found in systems where the in- and outlet radius were set to the same radius as the inner radius of the systems. This by providing a path of smaller resistance through the outlet that a higher in- and outlet flowrate provides, lowering the flowrate within the recycle segment and therefore decreasing the recycle ratio further than the smaller in- and outlet radius counterparts.

In systems with 3mm in- and outlet radii increasing the inlet flowrate decreased the recycle ratio/fraction and increased the flowrates in both the recycle and vessel segments. Initially increasing the inlet flowrate within these systems resulted in a decrease the dimensionless variance after which at a sufficient flowrate change within the segments an increase in the variance was seen.

In the systems with the in- and outlet radius similar to that of the inner radius an increase in the inlet flowrate increased the flowrate within the vessel segment and dropped the flowrate within the recycle segment giving more control on the recycle ratio/fraction. Within these systems the increase in the dimensionless variance was not always seen at lower recycle ratios/fractions, especially within the recycle segment where only in the smaller inner radius system a significant increase over the velocity was found.

7

Recommendations

7.1. Research/Model improvements

7.1.1. Discretized model

From the Serpent simulation results it was shown that the gamma radiation can induce very significant radial energy deposition profiles through the cylinder walls of the proposed HEAL. This energy deposition profile is currently not implemented in the discretized model, and the results for this discretized model have assumed a constant energy deposition of 300W/kg. It would therefore be recommended to develop a model that accounts for these profiles from Serpent simulations including the difference of energy deposition in the front and rear side of the HEAL based on Serpent simulations. This will require the implementation of another dimension for the front and rear side of the pipe and implement this within the radial slices of the HEAL walls.

With the implementation of this extra dimension a Serpent simulation will be required to obtain the energy deposition rates in each node within the model before a proper simulation of the HEAL within the discretized model can be properly analyzed.

7.1.2. Serpent

The photons simulated within the Serpent model originate isotropically from a plane source moving in the same direction towards the DLDR tube. For a more accurate simulations of the photons that reach the DLDR tube including axial and radial flux profiles over the length and height of the tube it is recommended to perform Serpent or MCNP photon transport simulations including the full HOR geometry and decay products. These simulations would serve the creation of a source file for the gamma rays within the DLDR tube wall for a more accurate representation of the photons reaching the HEAL, similar to what was performed for the neutron source.

7.1.3. Dispersion and Control

Limited amount of geometries and energy deposition rates were explored within the CFD models. Controlling the internal recycle rate/fraction in the HEAL itself was limited by the in- and outlet flowrates tested and the simulation time. Geometries allowing a smaller path of resistance through the in- and outlet compared to the recycle segment showed that the recycle rate can be controlled by the in- and outlet flowrates. However, these geometries can only go so far in reducing this resistance. It is therefore recommended to look at different geometries of the recycle section within the HEAL to increase its resistance compared to the in- and outlet streams. Examples could be decreasing the inner radius of the recycle section compared to the vessel section or implementing several bends within these sectors to increase the resistance within this section. Important is that during irradiation without an in- and outflow the passive flow through this system is still present and maximum target solution temperatures are not exceeded for safety reasons.

From the results it was shown that the recycle segment overall has a larger dimensionless variance when look-

ing at the RTD curve. Within the flushing cycle this resulted in some loss in the concentration that remained within this segment. What can therefore be looked at is placing the in- and outlet in a position of the loop that limits the size of the defined recycle segment. An example could be by placing the in- and outlet closer together.

7.1.4. Production & Kinetics

There is a lot uncertainty in the radiolysis cross section(s) of either gamma or neutron radiation within the kinetic model for the production of Lu-177. The radiolysis cross section used is based on a different reactor and not specifically for the HOR and is based around the flux of neutrons within this reactor. Another parameter that is uncertain is the fraction of DOTA molecules that get released from a radiolysis interaction which remains in tact for relabeling. Within the kinetic model it was assumed that this fraction comes from the cross section of lutetium atoms v.s. the DOTA molecule of gamma radiation. To approach the kinetics more accurately it is therefore recommended to perform a study on the gamma and neutron cross sections causing the unlabeled and/or damaging of the DOTA molecule specifically within the HOR for the neutron and gamma flux.

The maximum achievable specific activities in batch operation that followed from the model are at irradiation times of 80 hours. In literature all found irradiations of lanthanides with DOTA as Chelator are only approached over a few hours. From the model within these few hours the chemical relabelling aspect shouldn't play a large role. At longer irradiations however the concentration of the metal ions and free DOTA complexes increase significantly which would induce the chemical relabelling following the model. It is therefore recommended to perform longer irradiation experiments for verifying and/or fitting the model parameters.

7.2. Design

From the discretized model results it was shown that the pipe angle within the systems has a limited effect on the velocities as found in the systems, even at extreme values. This combined with the fact that the pipe angle limits the length of the system within the limited space within the DLDR tube. It is therefore recommended to leave the pipe angle at 0° to increase the total volume of target solution that is present in the middle of the DLDR tube.

The results of the discretized model of the parallel and staggered wall designs: Al-Pb/Al-Pb, Pb-Al/Al-Pb, and Al-Pb/Pb-Al all have shown that a system shielded with lead walls can still result in velocities close or even higher to as found in the single walled Al/Al systems with thicker walls. This without increasing the maximum solution temperature compared to Pb/Pb systems with similar wall thicknesses. It could therefore be very interesting to look further into these systems for the design as the inclusion of lead walls in both the heating and cooling sector have shown to create a significant drop in the dose rate within the target solution.

As shown in the shielding results, utilizing aluminium within the walls of the HEAL does not aid with any shielding ability and reduces the neutron flux reaching the target solution more than lead or zirconium. For this reason it is recommended to only look at the implementation of aluminium as a wall material in combination with either lead or zirconium inner/outer layer. This to still be able to provide some form of shielding to the HEAL from the walls with a possible advantage of using the favourable thermal conductivity properties from aluminium.

From the CFD simulations and dispersion and RTD modelling an overall smaller variance of the dispersion was found in systems with smaller inner radii. For batch operation or continuous operation with a very short irradiation time within the HEAL it would therefore be preferred to limit the inner radius to smaller values below 11 mm. This would allow a more predictable residence time distribution within these short irradiations.

Bibliography

- [1] John T. Adeosun and Adeniyi Lawal. “Mass transfer enhancement in microchannel reactors by reorientation of fluid interfaces and stretching”. In: *Sensors and Actuators B: Chemical* 110.1 (2005), pp. 101–111. ISSN: 0925-4005. DOI: <https://doi.org/10.1016/j.snb.2005.01.016>. URL: <https://www.sciencedirect.com/science/article/pii/S0925400505001073>.
- [2] Japan Atomic Energy Agency. *JENDL Activation Cross Section File for Nuclear Decommissioning 2017*. 2017. URL: [https://www.ndc.jaea.go.jp/ftpnd/jendl/jendl-ad-2017.html#:~:text=JENDL%20FAD%202017&text=%20FAD%202017\)-,JENDL%20Activation%20Cross%20Section%20File%20for%20Nuclear%20Decommissioning%202017%20\(JENDL,on%20decommissioning%20of%20nuclear%20facilities..](https://www.ndc.jaea.go.jp/ftpnd/jendl/jendl-ad-2017.html#:~:text=JENDL%20FAD%202017&text=%20FAD%202017)-,JENDL%20Activation%20Cross%20Section%20File%20for%20Nuclear%20Decommissioning%202017%20(JENDL,on%20decommissioning%20of%20nuclear%20facilities..)
- [3] Hakan Akyildirim, Faez Waheed, and K. Günoğlu. “Investigation of Buildup Factor in Gamma-Ray Measurement”. In: *Acta Physica Polonica A* 132 (Sept. 2017), pp. 1203–1206. DOI: 10.12693/APhysPolA.132.1203.
- [4] A. A. Aleksandrov, E. V. Dzhuraeva, and V. F. Utenkov. “Viscosity of aqueous solutions of sodium chloride”. In: *High Temperature* 50 (May 2012), pp. 354–358. DOI: 10.1134/s0018151x12030029. (Visited on 05/03/2020).
- [5] K. Ambrožič and L. Snoj. “JSIR2S code for delayed radiation simulations: Validation against measurements at the JSI TRIGA reactor”. In: *Progress in Nuclear Energy* 129 (2020), p. 103498. ISSN: 0149-1970. DOI: <https://doi.org/10.1016/j.pnucene.2020.103498>. URL: <https://www.sciencedirect.com/science/article/pii/S0149197020302432>.
- [6] Konstantinos D. Arvanitis, Demetri Bouris, and Elias Papanicolaou. “Laminar flow and heat transfer in U-bends: The effect of secondary flows in ducts with partial and full curvature”. In: *International Journal of Thermal Sciences* 130 (2018), pp. 70–93. ISSN: 1290-0729. DOI: <https://doi.org/10.1016/j.ijthermalsci.2018.03.027>. URL: <https://www.sciencedirect.com/science/article/pii/S1290072917307986>.
- [7] Vasilis Bellos, Ioannis Nalbantis, and George Tsakiris. “Erratum for Friction Modeling of Flood Flow Simulations”; by Vasilis Bellos, Ioannis Nalbantis, and George Tsakiris”. In: *Journal of Hydraulic Engineering* 146.10 (2020), p. 08220005. DOI: 10.1061/(ASCE)HY.1943-7900.0001802. eprint: <https://ascelibrary.org/doi/pdf/10.1061/%28ASCE%29HY.1943-7900.0001802>. URL: <https://ascelibrary.org/doi/abs/10.1061/%28ASCE%29HY.1943-7900.0001802>.
- [8] Martin Berger et al. *XCOM: Photon Cross Section Database (version 1.2)*. en. Jan. 1999.
- [9] D. Bergmans. “Radioisotope production at the high flux reactor at Petten”. In: *Utilization Related Design Features of Research Reactors*. Vienna: International Atomic Energy Agency, 2007. Chap. 3.2, pp. 87–100.
- [10] Alex Bielajew. “Fundamentals of the Monte Carlo method for neutral and charged particle transport”. In: (Oct. 2001).
- [11] R.B. Bird, W.E. Stewart, and E.N. Lightfoot. *Transport Phenomena*. J. Wiley, 2002. ISBN: 9780471364740.
- [12] M de Bruin. “Further development around the Hoger Onderwijs reactor of IRI in Delft”. In: *Transactions of the American Nuclear Society; (United States)* 65 (Jan. 1992). ISSN: 0003-018X. URL: <https://www.osti.gov/biblio/6965302>.
- [13] J. Carvill. “3 - Thermodynamics and heat transfer”. In: *Mechanical Engineer's Data Handbook*. Ed. by J. Carvill. Oxford: Butterworth-Heinemann, 1993, pp. 102–145. ISBN: 978-0-08-051135-1. DOI: <https://doi.org/10.1016/B978-0-08-051135-1.50008-X>. URL: <https://www.sciencedirect.com/science/article/pii/B978008051135150008X>.
- [14] Y.A. Çengel and Ghajar A.J. *Steady Heat Conduction*. New York, NY: McGraw-Hill Education, 2015. Chap. 3, pp. 142–238.
- [15] M.B. Chadwick et al. “ENDF/B-VII.1 Nuclear Data for Science and Technology: Cross Sections, Covariances, Fission Product Yields and Decay Data”. In: *Nuclear Data Sheets* 112.12 (2011). Special Issue on ENDF/B-VII.1 Library, pp. 2887–2996. ISSN: 0090-3752. DOI: <https://doi.org/10.1016/>

- j.nds.2011.11.002. URL: <https://www.sciencedirect.com/science/article/pii/S009037521100113X>.
- [16] Steven C. Chapra and Raymond P. Canale. *Numerical methods for engineers*. Seventh Edition. McGraw-Hill Higher Education, 2015. ISBN: 9780071267595.
- [17] Commission on Isotopic Abundances and Atomic Weights. *Atomic Weight of Lutetium*. Ciaaw.org, 2015. URL: <https://www.ciaaw.org/lutetium.htm> (visited on 03/13/2022).
- [18] *Database of Prompt Gamma Rays from Slow Neutron Capture for Elemental Analysis*. Non-serial Publications. Vienna: INTERNATIONAL ATOMIC ENERGY AGENCY, 2007. ISBN: 92-0-101306-X. URL: <https://www.iaea.org/publications/7030/database-of-prompt-gamma-rays-from-slow-neutron-capture-for-elemental-analysis>.
- [19] T. Delorme. *Meetrappport gamma-opwarming HOR-O*. 1997.
- [20] Christophe Demazière. “6 - Neutronic/thermal-hydraulic coupling”. In: *Modelling of Nuclear Reactor Multi-physics*. Ed. by Christophe Demazière. Academic Press, 2020, pp. 311–336. ISBN: 978-0-12-815069-6. DOI: <https://doi.org/10.1016/B978-0-12-815069-6.00006-4>. URL: <https://www.sciencedirect.com/science/article/pii/B9780128150696000064>.
- [21] Luuk R. Dresen. “The MPML: 99Molybdenum Producing Mini Loop driven by natural circulation”. Bachelor’s Thesis. Delft University of Technology, July 2019.
- [22] C. van Egmond. “Calculating the interdependency of the temperature and power production inside the Mo-99 research loop”. Bachelor’s Thesis. Delft University of Technology, July 2016.
- [23] K. Elgin. “A study of the feasibility of 99Mo production inside the TU Delft Hoger Onderwijs Reactor”. Delft University of Technology, 2014.
- [24] Ruhollah Fazli-Abukheyli and Parviz Darvishi. “Combination of axial dispersion and velocity profile in parallel tanks-in-series compartment model for prediction of residence time distribution in a wide range of non-ideal laminar flow regimes”. In: *Chemical Engineering Science* 195 (Feb. 2019), pp. 531–540. ISSN: 00092509. DOI: 10.1016/J.CES.2018.09.052. URL: <https://doi.org/10.1016/j.ces.2018.09.052>.
- [25] K M Ferreira, S M Collins, and A J Fenwick. “Half-life measurement of the medical radioisotope 177 Lu produced from the 176 Yb(n,y) reaction”. In: *EPJ Web of Conferences* 146 (2017), p. 8002. DOI: 10.1051/epjconf/201714608002.
- [26] Vincent Fiegel et al. “Alpha radiolysis of DOTA ligand in aqueous solutions with helium ion beams”. In: *Radiation Physics and Chemistry* 165 (2019), p. 108409. ISSN: 0969-806X. DOI: <https://doi.org/10.1016/j.radphyschem.2019.108409>. URL: <https://www.sciencedirect.com/science/article/pii/S0969806X19304724>.
- [27] Benjamin Gebhart et al. *Buoyancy-induced flows and Transport textbook edition*. Hemisphere, 1988.
- [28] Esi group. *OpenFOAM: API Guide: applications/solvers/heatTransfer/buoyantBoussinesqPimpleFoam/buoyantBoussinesqPimpleFoam*. File Reference. Openfoam.com, 2022. URL: https://www.openfoam.com/documentation/guides/latest/api/buoyantBoussinesqPimpleFoam_8C.html#details (visited on 01/18/2022).
- [29] R.F. Mudde H.E.A. van den Akker. *Fysische Transportverschijnselen 1*. Delft: Delft University Press, 1998, pp. 97–124. ISBN: 90-407-1204-2.
- [30] Laurens T.B. Haffmans. “A feasibility and safety evaluation of the 99Molybdenum Producing Mini Loop”. Bachelor’s Thesis. Delft University of Technology, Apr. 2021.
- [31] *Heat Capacities for Some Select Substances*. Utxas.edu, 2022. URL: <https://gchem.cm.utexas.edu/data/section2.php?target=heat-capacities.php> (visited on 11/14/2021).
- [32] A Hindmarsh. “ODEPACK. A Collection of ODE System Solvers”. In: (Jan. 1992). URL: <https://www.osti.gov/biblio/145724>.
- [33] J.H. Hubbell and S.M. Seltzer. *Tables of X-Ray Mass Attenuation Coefficients and Mass Energy-Absorption Coefficients (version 1.4)*. Gaithersburg, MD: National Institute of Standards and Technology, 2004. URL: <http://physics.nist.gov/xaamdi>.
- [34] Jurriaan A.R. Huisman. “Heat Transfer of the Mo-99 Research Loop - Optimising Heat Transfer of the Closed Reactor Loop Aimed at the Efficient Production of Molybdenum-99”. Bachelor’s Thesis. Delft University of Technology, May 2016.
- [35] L.P.B.M. Janssen and M.M.C.G. Warmoeskerken. *Transport Phenomena Data Companion*. VSSD, 2006. ISBN: 90-71301-59-1.
- [36] D.A. Knoll and D.E. Keyes. “Jacobian-free Newton–Krylov methods: a survey of approaches and applications”. In: *Journal of Computational Physics* 193.2 (2004), pp. 357–397. ISSN: 0021-9991. DOI: <https://doi.org/10.1016/j.jcp.2003.08.013>.

- //doi.org/10.1016/j.jcp.2003.08.010. URL: <https://www.sciencedirect.com/science/article/pii/S0021999103004340>.
- [37] Lead (Pb) - Chemical properties, Health and Environmental effects. Lenntech.com, 2022. URL: <https://www.lenntech.com/periodic/elements/pb.htm> (visited on 11/14/2021).
- [38] Octave Levenspiel. *Chemical Reaction Engineering - Third Edition*. Ed. by Ken Santor. John Wiley & Sons, Inc., 1999. ISBN: 978-0-471-25424-9.
- [39] Minye Liu. "A method for computing the degree of mixing in steady continuous flow systems". In: *Chemical Engineering Science* 66.13 (2011), pp. 3045–3048. ISSN: 0009-2509. DOI: <https://doi.org/10.1016/j.ces.2011.03.049>. URL: <https://www.sciencedirect.com/science/article/pii/S0009250911002211>.
- [40] Kulwinder Mann et al. "Investigations of mass attenuation coefficients and exposure buildup factors of some low-Z building materials". In: *Annals of Nuclear Energy* 43 (May 2012), pp. 157–166. DOI: 10.1016/j.anucene.2012.01.004.
- [41] Daniel R. McAlister. "Neutron Shielding Materials". In: (Feb. 2016).
- [42] M. M. Naaktgeboren. "The Hot Atom Production Loop - The investigation of a new radionuclide production loop based on the Szilard-Chalmers effect". MA thesis. Delft University of Technology, May 2021.
- [43] *Newton—Krylov Methods*, pp. 57–83. DOI: 10.1137/1.9780898718898.ch3. eprint: <https://epubs.siam.org/doi/pdf/10.1137/1.9780898718898.ch3>. URL: <https://epubs.siam.org/doi/abs/10.1137/1.9780898718898.ch3>.
- [44] OpenFOAMWiki. *ScalarTransportFoam - OpenFOAMWiki*. Openfoamwiki.net, 2022. URL: <https://openfoamwiki.net/index.php/ScalarTransportFoam>.
- [45] Organisation for Economic Co-operation and Development. *JEFF Report 21: The JEFF-3.1 Nuclear Data Library*. Ed. by Arjan Koning et al. 2006. URL: https://www.oecd-nea.org/dbdata/nds_jefreports/jefreport-21/jeff21.pdf.
- [46] Organisation for Economic Co-operation and Development and Nuclear Energy Agency. *The supply of Medical Radioisotopes - 2017 Medical Isotope Supply Review: 99Mo/99mTc Market Demand and Production Capacity Projection 2017-2022*. Tech. rep. 2. The Organisation for Economic Co-operation and Development & Nuclear Energy Agency, Apr. 2017.
- [47] Asterios Pantokratoras. "Steady laminar flow in a 90 bend". In: *Advances in Mechanical Engineering* 8 (Aug. 2016). DOI: 10.1177/1687814016669472.
- [48] Edward J. Parma. "Neutron and Gamma-Ray Radiation Environments for the Annular Core Research Reactor Central Cavity and the FRECI Cavity." In: (Apr. 2017). URL: <https://www.osti.gov/biblio/1456577>.
- [49] S. Pendse. "COOLING SYSTEM DESIGN FOR 99MO RESEARCH LOOP". MA thesis. Delft University of Technology, Mar. 2018.
- [50] Syed M. Qaim. "Nuclear data for production and medical application of radionuclides: Present status and future needs". In: *Nuclear Medicine and Biology* 44 (Jan. 2017), pp. 31–49. ISSN: 0969-8051. DOI: 10.1016/J.NUCMEDBIO.2016.08.016.
- [51] R. Roovers. "A study of the feasibility of molybdenum99 production by neutron capture of molybdenum98 in a mini loop using natural convection". Bachelor's Thesis. Delft University of Technology, June 2021.
- [52] Oliver Sartor et al. "Lutetium-177-PSMA-617 for Metastatic Castration-Resistant Prostate Cancer". In: *New England Journal of Medicine* 385 (12 Sept. 2021), pp. 1091–1103. ISSN: 0028-4793. DOI: 10.1056/NEJMOA2107322/SUPPL_FILE/NEJMOA2107322_DATA-SHARING.PDF. URL: <https://www.nejm.org/doi/10.1056/NEJMOa2107322>.
- [53] *Serpent Wiki - Input syntax manual*. URL: https://serpent.vtt.fi/mediawiki/index.php/Input_syntax_manual.
- [54] J. Kenneth Shultis and Richard E. Faw. *Fundamentals of Nuclear Science and Engineering*. Third Edition. CRC Press, 2017. ISBN: 978-1-4987-6929-7.
- [55] J. Kenneth Shultis and Richard E. Faw. "Radiation Shielding and Radiological Protection". In: *Handbook of Nuclear Engineering: Vol. 1: Nuclear Engineering Fundamentals; Vol. 2: Reactor Design; Vol. 3: Reactor Analysis; Vol. 4: Reactors of Generations III and IV; Vol. 5: Fuel Cycles, Decommissioning, Waste Disposal and Safeguards*. Handbook of Nuclear Engineering. Springer, 2010, pp. 1314–1448. ISBN: 9780387981307.

- [56] LEO SZILARD and T. A. CHALMERS. "Chemical Separation of the Radioactive Element from its Bombarded Isotope in the Fermi Effect". In: *Nature* 134 (Sept. 1934), pp. 462–462. DOI: 10.1038/134462b0. URL: <https://www.nature.com/articles/134462b0> (visited on 04/21/2022).
- [57] *Table of Isotopes decay data*. URL: <http://nucldata.nuclear.lu.se/toi/nuclide.asp?iZA=710177>.
- [58] È. Tóth and E. Brücher. "Stability constants of the lanthanide(III)-1,4,7,10-tetraazacyclododecane-N,N',N",N"-tetraacetate complexes". In: *Inorganica Chimica Acta* 221.1 (1994), pp. 165–167. ISSN: 0020-1693. DOI: [https://doi.org/10.1016/0020-1693\(94\)03964-X](https://doi.org/10.1016/0020-1693(94)03964-X). URL: <https://www.sciencedirect.com/science/article/pii/002016939403964X>.
- [59] Jan Willem J. van Dorp et al. "Towards the production of carrier-free ⁹⁹Mo by neutron activation of ⁹⁸Mo in molybdenum hexacarbonyl Szilard-Chalmers enrichment". In: *Applied Radiation and Isotopes* 140 (2018), pp. 138–145. ISSN: 0969-8043. DOI: <https://doi.org/10.1016/j.apradiso.2018.06.002>. URL: <https://www.sciencedirect.com/science/article/pii/S096980431730828X>.
- [60] K.P. Zhernosekov, D.V. Filosofov, and F. Rösch. "The Szilard–Chalmers effect in macrocyclic ligands to increase the specific activity of reactor-produced radiolanthanides: Experiments and explanations". In: *Radiochimica Acta* 100.8-9 (2012), pp. 669–674. DOI: doi : 10.1524/ract.2012.1960. URL: <https://doi.org/10.1524/ract.2012.1960>.
- [61] Th.N. Zwietering. "The degree of mixing in continuous flow systems". In: *Chemical Engineering Science* 11.1 (1959), pp. 1–15. ISSN: 0009-2509. DOI: [https://doi.org/10.1016/0009-2509\(59\)80068-3](https://doi.org/10.1016/0009-2509(59)80068-3). URL: <https://www.sciencedirect.com/science/article/pii/0009250959800683>.

A

Appendix - Overview of the functions used inside the discretized model

A.1. Previous model

A.1.1. Previous Model - Energy and momentum balance

The energy balance for both the fluid inside the HEAL and the energy balance of the walls of the HEAL from the previous model by Roovers [51] are given in the equations A.1. In equation A.1a the energy balance is given for the temperature of the fluid flowing inside the system, equation A.1b shows the energy balance of the wall of the HEAL. For the temperature of the water outside of the HEAL system in the DLDR tube a constant temperature is assumed of 40°C.

$$\frac{\partial T_n}{\partial t} = -\frac{2h_{inner_fluid_wall_n}}{R_i \rho_0 C_p} (T_n - T_{wall_n}) - \frac{N}{L} (T_n - T_{n-1}) v \quad (A.1a)$$

$$\begin{aligned} \frac{\partial T_{wall_n}}{\partial t} = & \frac{u}{C_{p_{wall}}} + \frac{2h_{inner_fluid_wall_n}}{C_{p_{wall}} \rho_{wall}} \frac{R_i}{2R_i dr_n + dr_n^2} (T_n - T_{wall_n}) \\ & - \frac{2h_{wall_n_outer_fluid}}{C_{p_{wall}} \rho_{wall}} \frac{(R_i + dr_n)}{2R_i dr_n + dr_n^2} (T_{wall_n} - T_{outer_fluid}) \end{aligned} \quad (A.1b)$$

In these equations v is the velocity of the fluid inside the system in [$\frac{m}{s}$], u as the gamma heating deposition in [$\frac{W}{kg}$], N is the number of nodes in the model, T_n is the temperature of the fluid in node n in [K], T_{wall_n} is the temperature of the wall in node n in [K], T_{outer_fluid} is the temperature of the fluid on the outside of the system, $h_{inner_fluid_wall_n}$ is the combined heat transfer coefficient between the fluid and the wall in node n in [$\frac{W}{m^2K}$], $h_{wall_n_outer_fluid}$ is the combined heat transfer coefficient between the wall and the fluid on the outside of the system in node n in [$\frac{W}{m^2K}$], R_i is the radius of the pipe in [m], dr_n is the wall thickness of node n in [m], ρ_0 is the density of the fluid at the reference temperature in [$\frac{kg}{m^3}$], ρ_{wall} is the density of the wall in [$\frac{kg}{m^3}$], C_p the heat capacity of the fluid and $C_{p_{wall}}$ is the heat capacity of the wall in [$\frac{J}{kgK}$].

The momentum balance of the previous model is given in A.2

$$\frac{\partial v}{\partial t} = -\frac{1}{N} \sum_{n=1}^N f_{D_n} \frac{1}{4R_i} v^2 - \frac{v^2}{L} (\kappa_1 + \kappa_2) + \frac{g}{N} \sum_{n=1}^N (1 - \beta(T_n - T_0)) \sin(\Theta_n) \quad (A.2)$$

Where N is the number of nodes in the model, $f_{D_{n,m}}$ is the Darcy friction in node (n, m) , R_i the inner radius of the HEAL in [m], v the velocity in the system in [$\frac{m}{s}$], L the length of the system in [m], κ_1 and κ_2 the friction

coefficient from the bends, g the gravitational constant in $[\frac{m}{s^2}]$, β the thermal expansion coefficient in $[K^{-1}]$, T_{ref} the reference temperature for the thermal expansion coefficient from the boussinesq equation in K , $T_{n,0}$ the temperature of the target solution inside the HEAL in node n in $[K]$ and Θ_n the angle of node n in $[^\circ]$ or $[rad]$

A.1.2. Previous Model - Heat transfer

Utilizing Newton's law of cooling the flux of heat flowing from material 1 to material 2 is calculated via equation A.3a for which the heat transfer coefficient is calculated via equation A.3b.

$$\phi_{q_{1,2}} = h_{1,2} A_{1,2} (T_2 - T_1) \quad (A.3a)$$

$$h_{1,2} = (h_1^{-1} + h_2^{-1})^{-1} \quad (A.3b)$$

Where $\phi_{q_{1,2}}$ is the heat flux from/to material 1/2 in $[W]$, $h_{1,2}$ the heat transfer coefficient in $[\frac{W}{m^2K}]$, $A_{1,2}$ the contact area between materials 1 and 2 in $[m^2]$, and T the temperature of a material in $[K]$.

The heat transfer coefficient for a particular material is calculated via either of the equations in A.4 dependent on the material, if it is one of the liquids (solution inside the HEAL or the DLDR water) A.4a is used. For the wall A.4b is used.

$$h_{liq} = \frac{Nu\kappa}{d} \quad (A.4a)$$

$$h_{wall} = \frac{\kappa}{dr} \quad (A.4b)$$

Where h_{liq} is the heat transfer coefficient of a fluid/liquid and h_{wall} the heat transfer coefficient of the wall in $[\frac{W}{m^2K}]$, Nu is the Nusselt number, d the characteristic length in $[m]$, κ the thermal conductivity of the material in $[\frac{W}{mK}]$ and dr the thickness of the wall in $[m]$.

A.2. Energy balance

In the new model the heat transfer is remodelled to include axial and radial conduction through the walls of the system. In the previous model the system was split up in N nodes over the axial length of the system. With the inclusion of radial conduction extra nodes are added in the radial coordinates which are referred to as nodes M . With these nodes we receive a coordinate system of nodes n and m where $m = 0$ refers to the target solution, $M > m > 0$ refers to the wall materials and $m = M$ refers to the water in the DLDR tube.

The overall heat balance of the target solution in each node ($\frac{\delta T_{n,0}}{dt}$) and the walls ($[\frac{\delta T_{n,m}}{dt}]_{M>m>0}$) can be found in equation A.5. The target solution heat balance consist of convective heat transfer from the target solution to the wall is indicated by $\phi_{n,m,n,m+1}$, axial heat transfer from the $\phi_{n,m,n+1,m}$ term, and transfer of heat between the target solution nodes is given by the $\frac{N}{L}(T_{n,0} - T_{n-1,0})v$ terms. For the energy balance of the walls, as indicated by $[\frac{\delta T_{n,m}}{dt}]_{m>0}$, energy deposition is given by *the* $\frac{u_{n,m}}{C_\rho}$ term, heat transfer between nodes are in contact with each other are indicated by the heat transfer rate ϕ_{n,m,n_conn,m_conn} term which are summed for all the nodes.

$$\frac{\delta T_{n,0}}{dt} = -\frac{1}{\rho_{n,0} C_{\rho_{n,0}} V_{n,0}} (\phi_{n,m,n,m+1} + \phi_{n,m,n+1,m}) - \frac{N}{L} (T_{n,0} - T_{n-1,0}) v \quad (A.5a)$$

$$[\frac{\delta T_{n,m}}{dt}]_{M>m>0} = \frac{u_{n,m}}{C_\rho} - \frac{1}{\rho_{n,m} C_{\rho_{n,m}} V_{n,m}} \left(\sum_{m_conn=0}^M \sum_{n_conn=0}^N \phi_{n,m,n_conn,m_conn} \right) \quad (A.5b)$$

In these equations N is the number of axial node coordinates in the model, M the number of radial node coordinates in the model, v is the velocity of the fluid inside the system in [$\frac{m}{s}$], $u_{n,m}$ as the gamma heating deposition at coordinate n, m in [$\frac{W}{kg}$], $T_{n,m}$ is the temperature of the node at coordinate n, m given in [K], $\rho_{n,m}$ the density of the node at n, m in [$\frac{kg}{m^3}$], $C\rho_{n,m}$ the heat capacity of the node at n, m in [$\frac{J}{kgK}$], and ϕ_{n,m,n_conn,m_conn} is given as the heat transfer rate between the nodes with coordinates n, m and n_conn, m_conn in [W].

A.2.1. Heat transfer

In the overall energy balance (A.5) the heat transfer rates are indicated by the ϕ terms. Dependent on the connection and the materials of the nodes, the radial and axial heat transfer rates, ϕ_{n,m,n,m_conn} and $\phi_{n,m,n_conn,m}$ are calculated as shown in equation A.6a and A.6b respectively.

$$\phi_{n,m,n_conn} = \begin{cases} -A_{n,m,n,m_conn} \kappa_{n,m} \frac{T_{n,m} - T_{n_conn,m}}{r_{n,m} \log(\frac{r_{n,m_conn}}{r_{n,m}})}, & \text{same material between nodes} \\ -A_{n,m,n,m_conn} U_{n,m,n,m_conn} (T_{n,m} - T_{n_conn,m}), & \text{different material between nodes} \end{cases} \quad (\text{A.6a})$$

$$\phi_{n,m,n_conn,m} = \begin{cases} -A_{n,m,n_conn,m} \kappa_{n,m} \frac{T_{n,m} - T_{n_conn,m}}{(l_n + l_{n_conn})/2}, & \text{same material between nodes} \\ -A_{n,m,n_conn,m} U_{n,m,n_conn,m} (T_{n,m} - T_{n_conn,m}), & \text{different material between nodes} \end{cases} \quad (\text{A.6b})$$

Where:

$$U_{n,m,n_conn,m} = \left(\frac{1}{h_{n,m,ax}} + \frac{1}{h_{n_conn,m,ax}} + \frac{1}{h_c} \right)^{-1} \quad (\text{A.7a})$$

$$A_{n,m,n,m_conn} U_{n,m,n,m_conn} = \begin{cases} \left(\frac{1}{h_{n,m} A_{n,m,n,m_conn}} + \frac{1}{h_{n,m_conn} A_{l_{m(n,m_conn)}}} \right)^{-1}, & \text{inner fluid and wall} \\ \left(\frac{1}{h_{n,m,rad} A_{l_{m(n,m)}}} + \frac{1}{h_{n,m_conn,rad} A_{l_{m(n,m_conn)}}} + \frac{1}{h_c A_{n,m,n,m_conn}} \right)^{-1}, & \text{different wall materials} \\ \left(\frac{1}{h_{n,m,rad} A_{l_{m(n,m)}}} + \frac{1}{h_{n,m_conn,rad} A_{n,m_conn,n,m}} \right)^{-1}, & \text{wall and outer fluid} \end{cases} \quad (\text{A.7b})$$

Where $\phi_{n,m,n_conn,m}$ is the heat flow between nodes on coordinates (n, m) and (n_conn, m) in [W], A the contact area between nodes in [m^2], U as the overall heat transfer coefficient between the node materials in [$\frac{W}{m^2K}$], $T_{n,m}$ the temperature of node (n, m) and $T_{n_conn,m}$ the temperature of node (n_conn, m) in [K], $\kappa_{n,m}$ the heat conductivity in [$\frac{W}{mK}$], l_n and l_{n_conn} are the respective lengths of the nodes in [m], $h_{n,m,ax}$ and $h_{n_conn,m,ax}$ the respective axial heat transfer coefficient of the materials in [$\frac{W}{m^2K}$], and finally h_c as the heat transfer coefficient for the the contact resistance between different materials in [$\frac{W}{m^2K}$].

The Nusselt number for calculating the heat transfer coefficient of the liquids in the system can be seen in equations A.8. The Nusselt number for the heat transfer coefficient for the fluid inside the HEAL is calculated via equation A.8a []. The Nusselt number for the water outside of the HEAL is split into two sections, vertical and horizontal sections. Convection of the water outside of the HEAL will behave differently in these sections [51]. For the horizontal and vertical sections of the HEAL, equations A.8b and A.8c are used respectively [51]. All of the equations have a respective range in which they can be used as indicated behind every equation.

$$\text{Nu} = \begin{cases} 0.027\text{Re}^{0.8}\text{Pr}^{0.33}, & \text{Re} > 10^4 \& \text{Pr} \geq 0.7 \\ 1.62\text{Gz}^{-1/3}, & \text{Gz} < 0.05 \& \text{Re} < 2000 \\ 3.66, & \text{Gz} > 0.1 \& \text{Re} < 2000 \end{cases} \quad (\text{A.8a})$$

$$\text{Nu} = \left(0.6 + \frac{0.387\text{Ra}^{\frac{1}{6}}}{\left(1 + \frac{0.559}{\text{Pr}}\right)^{\frac{8}{27}}} \right)^2, \quad 10^{-5} < \text{Ra} < 10^{12} \quad (\text{A.8b})$$

$$\text{Nu} = \begin{cases} \frac{4}{3}\text{Ra}^{0.25} \left(\frac{7\text{Pr}}{100+105\text{Pr}}\right)^{0.25} + \frac{4}{35} \frac{272+315\text{Pr}}{64+63\text{Pr}} \frac{\frac{1}{4}L}{2(R_i+dr)}, & 10^8 < \text{Gr} < 4 \cdot 10^9 \\ 0.48\text{Ra}^{0.25}, & 10^4 < \text{Ra} < 10^9 \end{cases} \quad (\text{A.8c})$$

Where Nu is the Nusselt number, Re the Reynolds number, Gz the Graetz number, Ra the Rayleigh number, Pr the Prandtl number, L the length of the system in $[m]$, R_i the inner radius of the HEAL and dr the wall thickness of the system, both in $[m]$.

A.2.2. Heat generation

Heat is generated inside the wall of the model from gamma heating following equation A.9.

$$P = u\rho_{wall}V_{wall_n} \quad (\text{A.9})$$

Where P is the heat generated in $[W]$, u is the heat deposition per kg of wall material in $[\frac{W}{kg}]$, ρ is the material density in $[\frac{kg}{m^3}]$ and V_{wall_n} is the volume of the wall in node n in $[m^3]$.

A.3. Momentum balance

The overall momentum balance over all the axial nodes in the model is given in equation A.10. This momentum balance consists of a summation of the friction over the nodes by Darcy friction and friction for the bends inside the HEAL. Added to this is the hydrostatic pressure generated by buoyancy in the system, this by utilizing the boussinesq approximation (A.11) to find the density of the fluid in every individual node.

$$\frac{\partial v}{\partial t} = -\frac{1}{N} \sum_{n=1}^N f_{D_{n,0}} \frac{1}{4r_{stop_{n,m}}} v^2 - \frac{v^2}{L} (K_{w1} + K_{w2}) + \frac{g}{N} \sum_{n=1}^N (1 - \beta(T_{n,0} - T_{ref})) \sin(\phi_{n,0}) \quad (\text{A.10})$$

Where N is the number of nodes in the model, $f_{D_{n,0}}$ is the Darcy friction in node $(n, 0)$, $r_{stop_{n,0}}$ the inner radius of the HEAL within node (n, m) in $[m]$, v the velocity in the system in $[\frac{m}{s}]$, L the system length of the system in $[m]$, K_{w1} and K_{w2} the friction coefficient from the bends, g the gravitational constant in $[\frac{m}{s^2}]$, β the thermal expansion coefficient in $[K^{-1}]$, T_{ref} the reference temperature for the thermal expansion coefficient from the boussinesq equation in K , $T_{n,0}$ the temperature of the target solution inside the HEAL in node n in $[K]$ and $\phi_{n,0}$ the angle of node $(n, 0)$ in $[rad]$

A.3.1. Boussinesq approximation

The boussinesq equation with which the density of the target solution is calculated is given in equation A.11.

$$\rho = \rho_{ref}(1 - \beta(T - T_{ref})) \quad (\text{A.11})$$

Where ρ is the density at temperature T in $[\frac{kg}{m^3}]$, β the expansion coefficient and ρ_{ref} is the reference density at temperature T_{ref} .

A.3.2. Darcy Friction

The Darcy friction factor f_D in the overall momentum equation is described by the expression given in A.12 [7].

$$f_D = \left(\frac{64}{\text{Re}}\right)^2 \left(0.75 \ln\left(\frac{\text{Re}}{5.37}\right)\right)^{2(a-1)b} \left(0.88 \ln\left(3.41 \frac{2R_i}{\epsilon}\right)\right)^{2(a-1)(1-b)} \quad (\text{A.12})$$

with

$$a = \frac{1}{1 + \left(\frac{\text{Re}}{2712}\right)^{8.4}} \quad \text{and} \quad b = \frac{1}{1 + \left(\frac{\text{Re}}{150 \frac{2R_i}{\epsilon}}\right)^{1.8}} \quad (\text{A.13})$$

Where R_i is the radius of the pipe in $[m]$ and ϵ the effective roughness in $[m]$.

The dynamic viscosity for the Reynolds equation η_{sol} is calculated using equation A.14 which was previously used by Roovers from Aleksandrov, Dzhuraeva, and Utenkov [4].

$$\eta_{wat} = \eta_{ref} e^{\frac{(1.1709(293.15-T) - 0.001827(T-20)^2)}{T+89.93}} \quad (\text{A.14a})$$

$$\eta_{rel} = \frac{\eta_{sol}}{\eta_{wat}} = 1 + (0.008 - \frac{0.005}{60}(T - 293.15))C_{target}^{0.5} + 0.06 + \frac{0.06}{60}(T - 293.15)C_{target} \quad (\text{A.14b})$$

$$\eta_{sol} = \eta_{water} * \eta_{rel} \quad (\text{A.14c})$$

Where T is the temperature of the target solution in $[K]$, C_{target} the molar concentration of the solution in $[\frac{mol}{kg}]$, η_{wat} the dynamic viscosity of water at temperature T in $[Pas]$, η_{rel} the fractional viscosity between water and the solution at temperature T . η_{sol} the dynamic viscosity of the solution in $[Pas]$.

A.3.3. Friction from bends

Friction from the bends in the HEAL is implemented by the inclusion of the friction coefficient for a sharp bend of 90° of $\kappa_1 = \kappa_2 = 1.30$ [35]

A.4. Model Heat Conduction Verification

A.4.1. Steady state radial conduction

In figure A.1 the radial temperature profiles of two systems calculated via the discretized model are shown together with the analytical solution at steady state without energy deposition. The analytical steady state solution is given in equation A.15 [14].

$$T(r) = T_1 - (T_1 - T_2) \frac{\ln \frac{r}{R_1}}{\ln \frac{R_2}{R_1}} \quad (\text{A.15})$$

With R_1 and R_2 the inner and outer radius in $[m]$, T_1 and T_2 the inner and outer wall temperature in $[K]$.

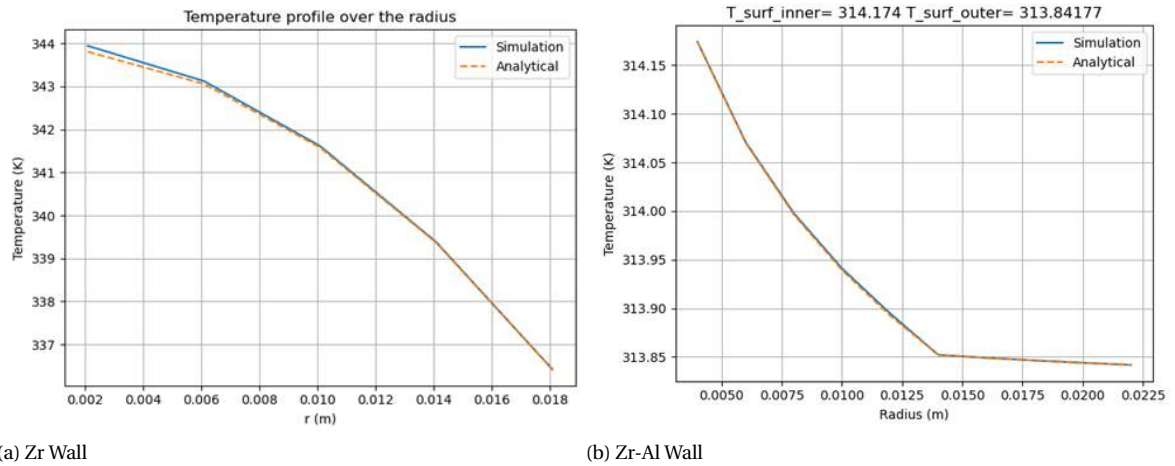


Figure A.1: Plots of two systems with a single 8mm thick zirconium wall (left) and a multi wall system made from two 8mm walls made from zirconium and aluminium together with their analytical solutions. The temperature profiles were generated within the discretized model without deposition of energy inside the walls and using $M=5$ within the model.

In figure A.1 the radial temperature profiles over the radius of the wall of a system calculated via the discretized model is shown including energy deposition q . The analytical steady state solution is given in equation A.16 [14].

$$T(r) = T_2 + \frac{q}{4\kappa}(R_2^2 - r^2) \quad (\text{A.16})$$

With q the energy deposition in $[W]$, κ the thermal conductivity in $[\frac{W}{mK}]$, R_2 the outer radius in $[m]$, and T_2 the outer wall temperature in $[K]$.

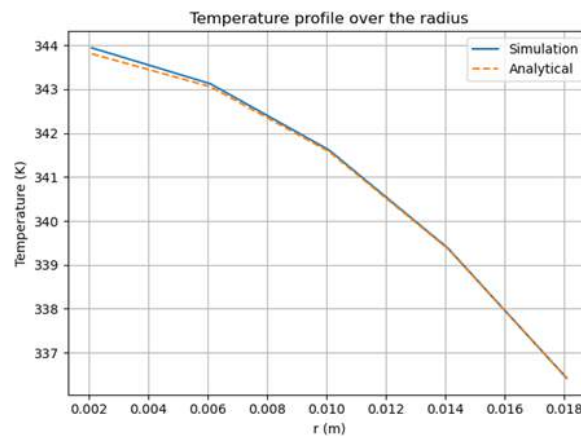


Figure A.2: Temperature profile over the radius of a system with an 8mm zirconium wall including energy deposition v.s. the analytical solution, with $M=5$

A.4.2. Time dependent axial conduction

In figures A.3 plots of the average axial temperature over the length and time of two systems are shown. Within these systems the wall consists of zirconium and the length was set at $0.32m$. In these systems the temperature at $n=0$ was set to a static temperature of $370K$ after which the temperature was plotted over time over the length of half of the the systems. The analytical solution that is plotted is given in equation A.17 [14].

$$T(l) = T_0 + (T_1 - T_0)(1 - erf(\frac{l}{2\sqrt{\alpha t}})) \tag{A.17}$$

Where T_0 and T_1 is the temperature at $l = 0$ and $l = 0.16$ in $[m]$, t is the time in $[s]$, and α as the thermal diffusivity in $\frac{m^2}{s}$.

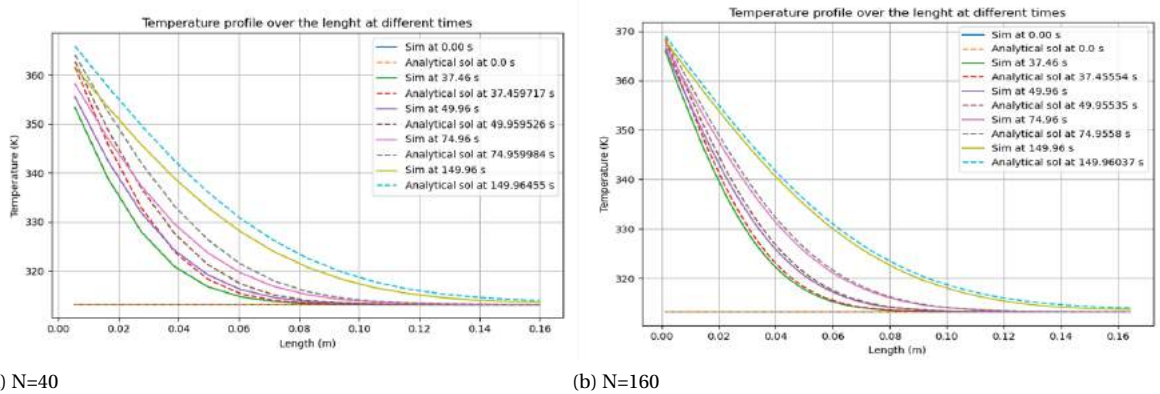


Figure A.3: Axial time dependent heat conduction plots of the temperature over the length of the system over time. Both for $0.32m$ long zirconium systems with $N=40$ (left) and $N = 160$ (right) where $T(0)$ is set to $370K$.

A.4.3. Code

The python code for the discretized HEAL model can be found in a GitLab repository via the QR code in figure A.4.



Figure A.4: QR code to the GitLab repository of the discretized HEAL model

B

Appendix - Extended Discretized Model Results

This appendix consists of a large collection of results of different HEAL configurations within the extended discretized model. In table B.1 a list of the main sections of this appendix referring to specific HEAL configuration variables can be found. At the start of each section general points are given on the trends that are seen by changing the variables as well as a table that shows the system configurations and variable values that have are used in the results with a reference to the figures representing those systems.

Table B.1: Overview of the different system variable results in the appendix for the extended discretized model

Variable Section	Subsection	Link/Reference
Wall Materials & Wall thicknesses	Single layer wall materials	B.1.1 (page 90)
	Multi layer wall materials	B.1.2 (page 110)
Inner Radius (R_i), Wall material & Wall thickness		B.2 (page 129)
Pipe angle (θ), System length (L) & Inner radius (R_i)		B.3 (page 163)
Section 2 length fraction ($Frac$) & Wall thickness		B.4 (page 203)

B.1. Wall Materials & Wall thicknesses

B.1.1. Single layer wall materials

The general trends for the single layer wall materials and wall thicknesses in these systems are:

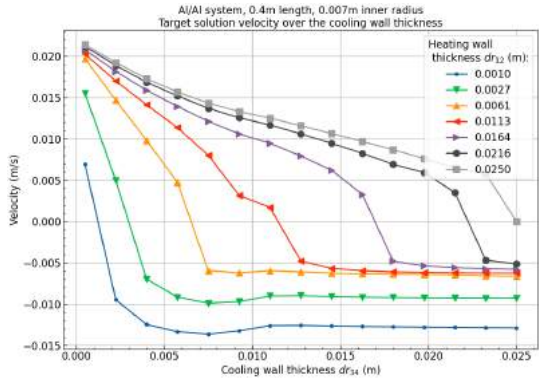
- In systems with the same cooling and heating wall material the velocity is always positive if the energy deposition in the heating sector is higher and negative if the energy deposition in the cooling sector is higher.
- In systems with different cooling and heating wall materials the velocity is not always dependent on the energy deposition between the heating or cooling wall. If the material of the heating wall has a larger energy deposition rate compared to the cooling wall a smaller total energy deposition in the heating wall compared to the cooling wall can still result in a positive velocity through the system. The opposite is true when the materials are reversed.
- In all systems at small cooling wall thicknesses, the average and maximum target solution temperatures are very similar over all heating wall thicknesses. Significant differences only start to show when the cooling wall thickness is increased.
- For positive velocity values the velocity decreases as the cooling wall thickness increases. Once the cooling wall thickness crosses a certain threshold, the velocity reverses after which an increase in cooling wall thickness results in only a limited change in velocity. This is the result of reversing the roles of the defined heating and cooling walls when the velocity becomes negative.
- Increasing the wall thicknesses increase the average and maximum target solution temperatures. The increase over the wall thickness is the largest at smaller wall thicknesses and slows down at larger wall thicknesses.
- Using aluminium as one of the walls significantly decreases the average and maximum temperatures that are seen in the target solution compared to systems that do not include an aluminium wall.
- The maximum contact temperature between the wall and the target solution is almost entirely dependent on the material with the largest energy deposition rate.

Table B.2: System specifications for the single layer wall material results

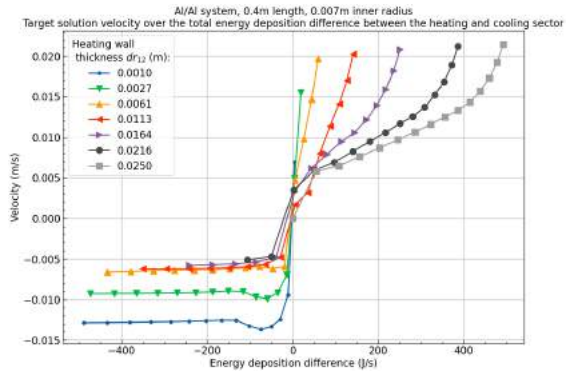
System Variable	Values	Reference
Single layer wall materials	Al/Al	B.1 - B.2 (Page 91 - 92)
	Al/Pb	B.3 - B.4 (Page 93 - 94)
	Al/Zr	B.5 - B.6 (Page 95 - 96)
	Pb/Al	B.7 - B.8 (Page 97 - 98)
	Pb/Pb	B.9 - B.10 (Page 99 - 100)
	Pb/Zr	B.11 - B.12 (Page 102 - 103)
	Zr/Al	B.13 - B.14 (Page 104 - 105)
	Zr/Pb	B.15 - B.16 (Page 106 - 107)
	Zr/Zr	B.17 - B.18 (Page 108 - 109)
Heating wall thickness (dr_{12})	0.001 – 0.0250m	
Cooling wall thickness (dr_{34})	0.0005 – 0.0250m	
Inner radius (R_i)	0.007m	
Length (L)	0.4m	
Pipe angle (θ)	5°	
Section 2 length fraction ($Frac$)	1.0	

Al/Al - Wall thicknesses

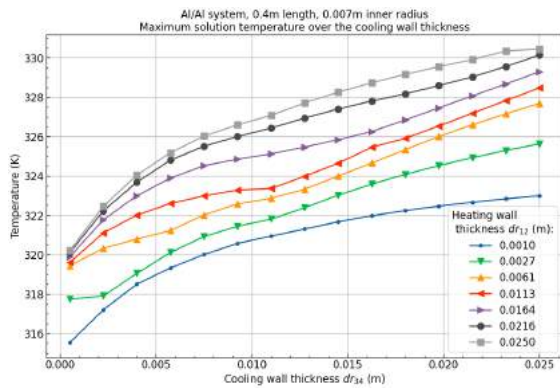
Back to overview - B.1.1



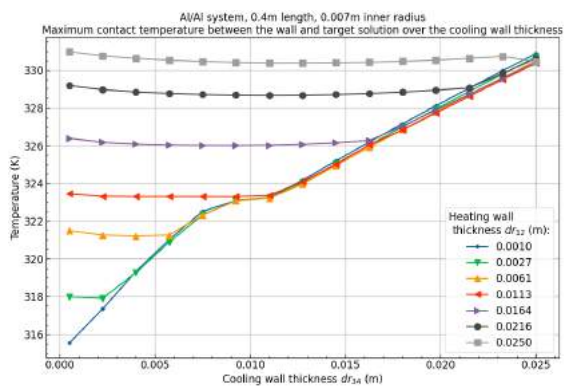
(a) Velocity over the cooling wall thickness showing the drop in velocity as the cooling wall thickness increases and flat velocity curve once the cooling wall thickness is larger than the heating wall thickness.



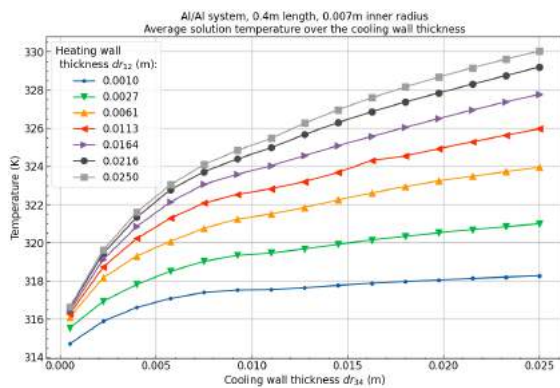
(b) Velocity over the energy deposition difference showing the requirements for a positive energy deposition in the heating section for a positive velocity in the system.



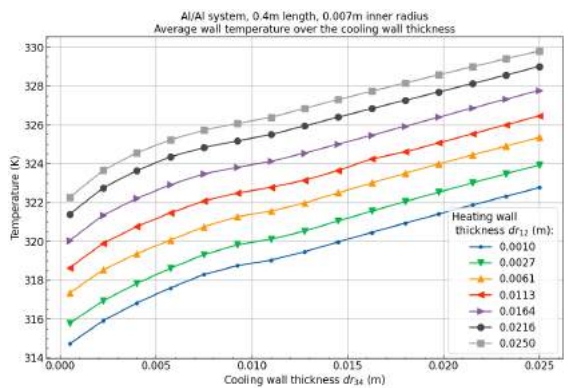
(c) Maximum target solution temperature over the cooling wall thickness showing the increase in maximum solution temperature as the wall thickness increases. The increase in temperature slows down at larger cooling wall thicknesses from the larger temperature delta between the solution and water in the DLD tube.



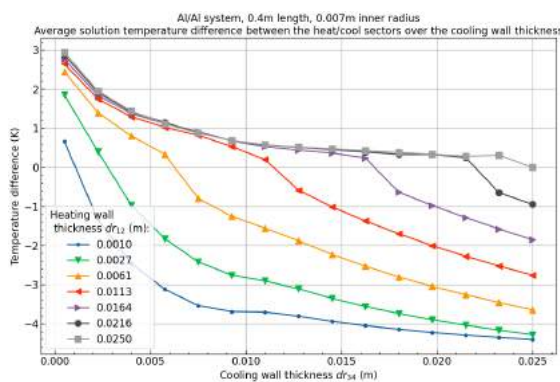
(d) Maximum contact temperature between the wall and the target solution showing that the maximum contact temperature is very much related to the cooling wall thickness of either the cooling or heating wall.



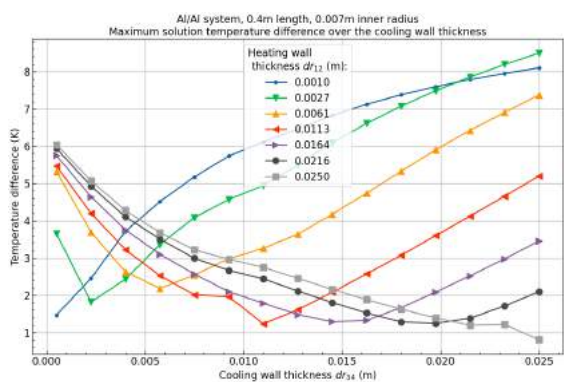
(e) Average target solution temperature over the cooling wall thickness showing the same trend as the maximum solution temperature.



(f) Average wall temperature over the cooling wall thickness showing the increase in the average wall temperature over the cooling wall thickness.

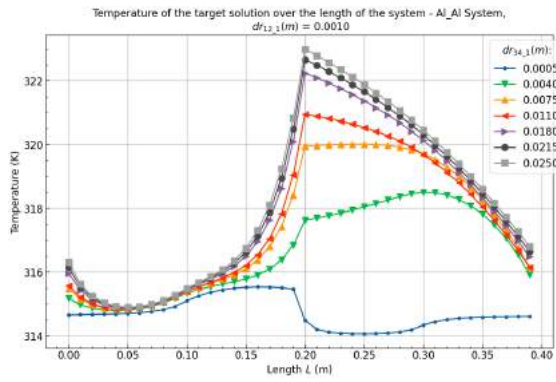


(g) Average target solution temperature difference between heating and cooling sectors showing an almost exponential decay for systems with a positive velocity and larger negative values once the velocity is negative.

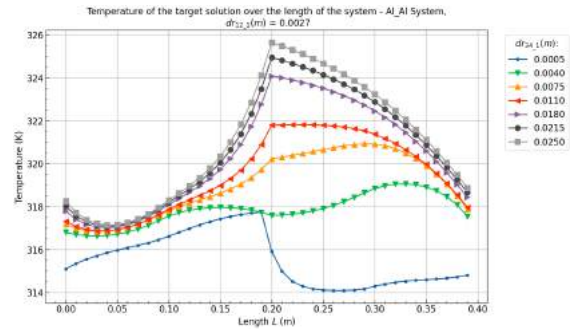


(h) Maximum target solution temperature difference between heating and cooling sectors showing a similar trend as the average solution temperature difference.

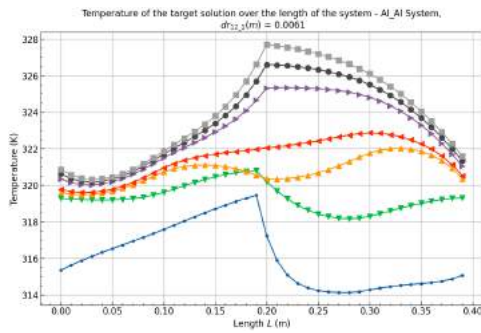
Figure B.1: Al/Al (Heat/Cool) System results over the heating and cooling wall thickness (dr_{12} and dr_{34} respectively) with a system length (L) of $0.4m$, an inner radius (Ri) of $0.007m$ and a pipe angle (θ) of 5° .



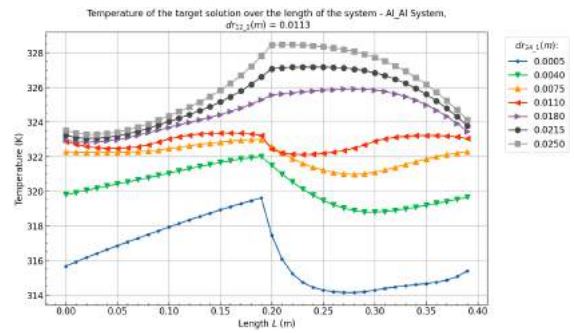
(a) Target solution temperature profiles over the length in systems with $dr_{12_1} = 0.0010m$. The figure shows the large difference between the system with a positive ($dr_{34_1} = 0.0050m$) and negative velocity values in section 3 and 4. At this cooling wall thickness the temperature in section 1 and 2 is very similar over the different systems.



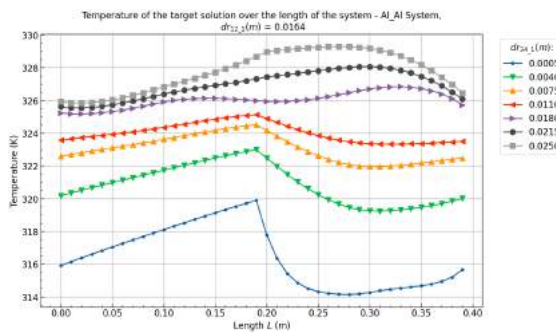
(b) Target solution temperature profiles over the length in systems with $dr_{12_1} = 0.0027m$. Showing a clear transition from positive velocity ($dr_{34_1} = 0.0040m$) towards the negative velocity systems with a heating wall thickness $0.0075m$ and above.



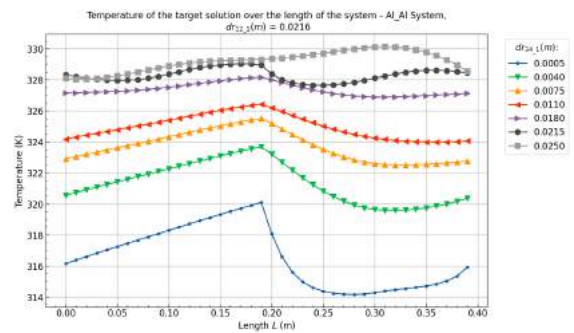
(c) Target solution temperature profiles over the length in systems with $dr_{12_1} = 0.0061m$. Showing similar transitionally trends and also a larger difference between the temperatures in all sectors between the systems.



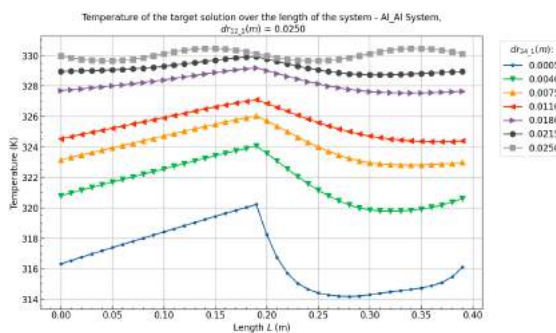
(d) Target solution temperature profiles over the length in systems with $dr_{12_1} = 0.0113m$. Showing a significantly larger deviation in temperatures in the sectors of systems with a positive velocity.



(e) Target solution temperature profiles over the length in systems with $dr_{12_1} = 0.0164m$.



(f) Target solution temperature profiles over the length in systems with $dr_{12_1} = 0.0216m$. Almost all plotted systems have a positive velocity (B.1a) which again shows the significantly larger difference in temperatures seen in systems with positive velocities.

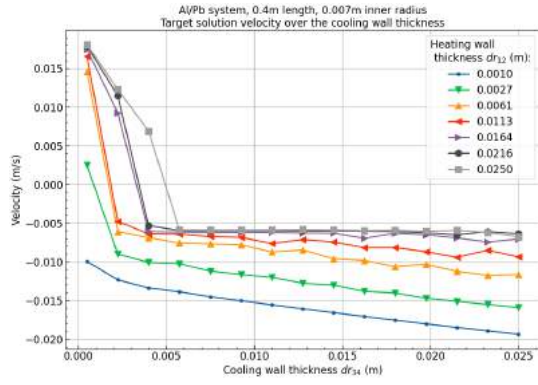


(g) Target solution temperature profiles over the length in systems with $dr_{12_1} = 0.0250m$. Showing similar trends as the systems with $dr_{12_1} = 0.0216m$.

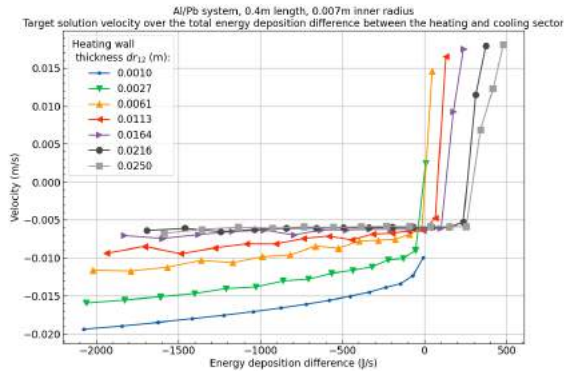
Figure B.2: Al/Al (Heat/Cool) System target solution temperature profiles over the heating and cooling wall thickness (dr_{12} and dr_{34} respectively) with a system length (L) of $0.4m$, an inner radius (R_i) of $0.007m$ and a pipe angle (θ) of 5° .

Al/Pb - Wall thicknesses

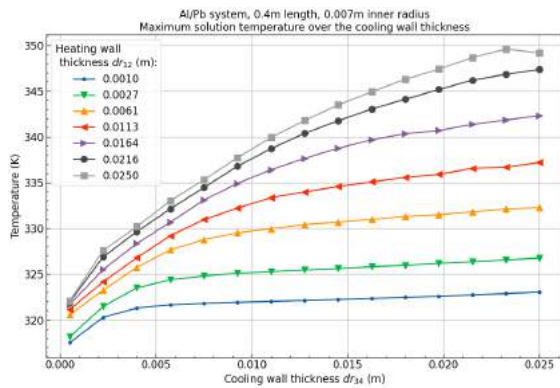
Back to overview - B.1.1



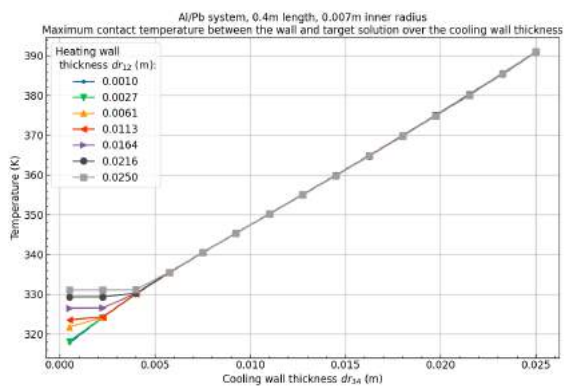
(a) Velocity over the cooling wall thickness showing the significant drop in the velocity over the cooling wall thickness as significantly more energy is deposited in the lead "cooling" wall.



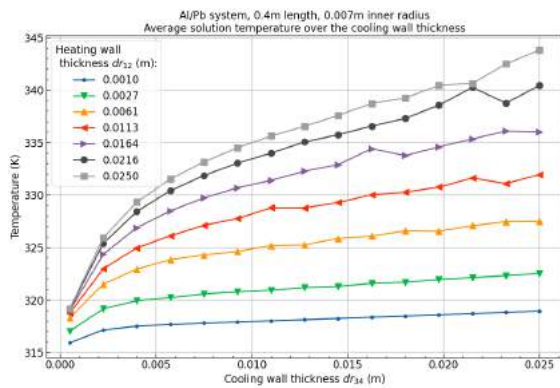
(b) Velocity over the energy deposition difference showing that with these materials the energy deposition difference can be positive and still result in a negative velocity in systems with a large heating wall thickness.



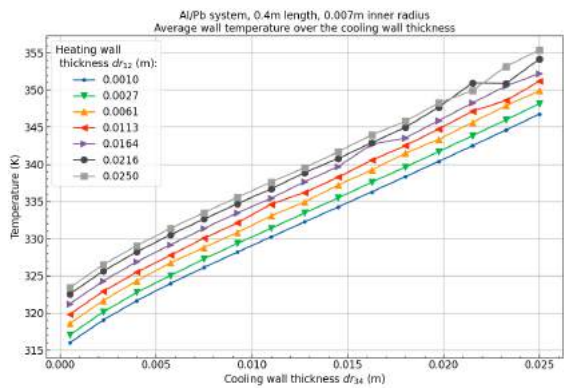
(c) Maximum target solution temperature over the cooling wall thickness showing the increase as the wall thicknesses get larger. As the cooling wall thickness increases the increase in temperature decreases.



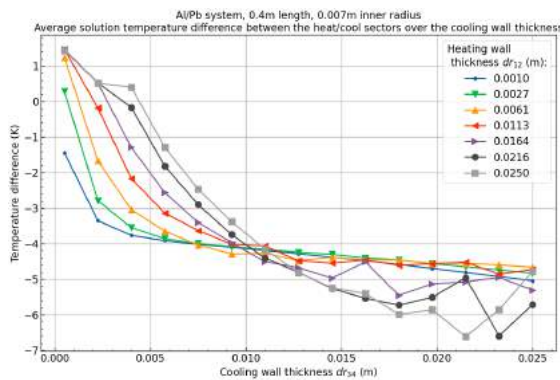
(d) Maximum contact temperature between the wall and the target solution showing that the maximum contact temperature is mostly defined by the lead cooling walls.



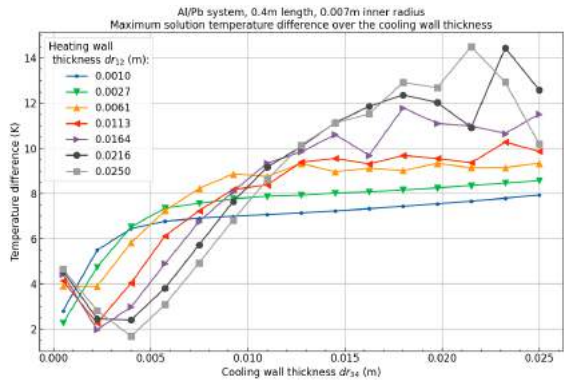
(e) Average target solution temperature over the cooling wall thickness showing a similar trend as the maximum target solution temperature.



(f) Average wall temperature over the cooling wall thickness showing a linear increase as the wall thicknesses increase.

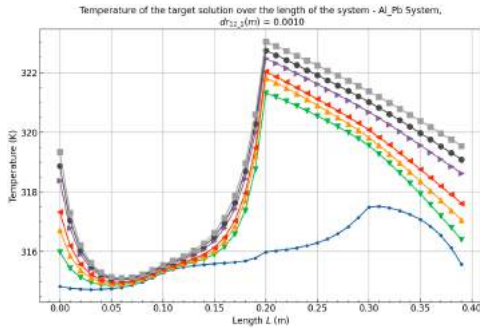


(g) Average target solution temperature difference between heating and cooling sectors showing a large negative difference in all systems that increase with the cooling wall thickness. The temperature difference at smaller cooling wall thicknesses seem in general to be more stable.

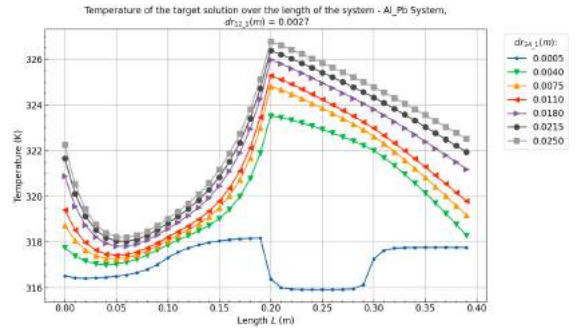


(h) Maximum target solution temperature difference between heating and cooling sectors showing a smaller maximum solution temperature difference in systems with smaller heating wall thicknesses, most likely from the higher velocity seen in these systems limiting the rate of cooling and heating.

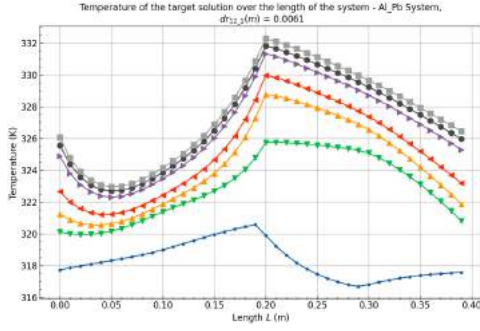
Figure B.3: Al/Pb (Heat/Cool) System results over the heating and cooling wall thickness (dr_{12} and dr_{34} respectively) with a system length (L) of $0.4m$, an inner radius (Ri) of $0.007m$ and a pipe angle (θ) of 5° .



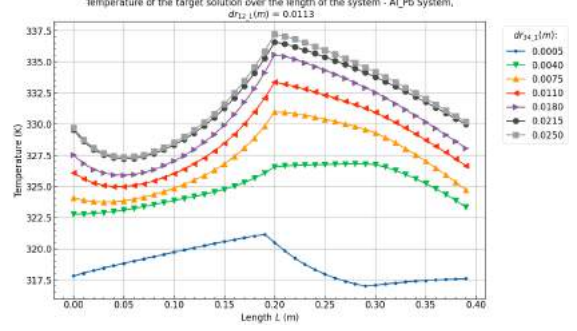
(a) Target solution temperature profiles over the length in systems with $dr_{12_1} = 0.0010m$. Showing small differences in section 3 and 4 between systems with a negative velocity and a transitory profile for the system with the positive velocity



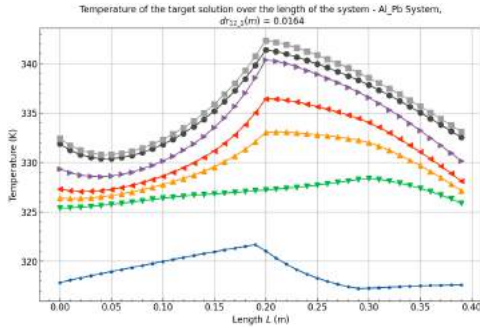
(b) Target solution temperature profiles over the length in systems with $dr_{12_1} = 0.0027m$. The temperature differences over the profile start to increase between the plotted systems. The small cooling wall thickness with a positive velocity has a completely different profile with much smaller temperature differences between the sectors.



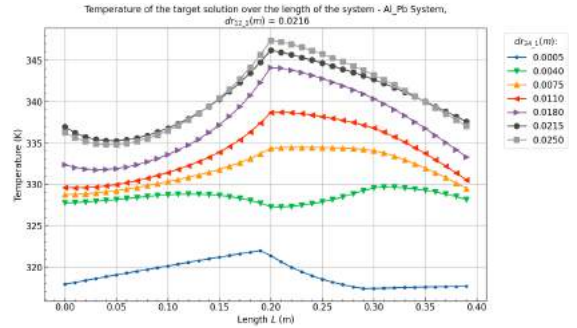
(c) Target solution temperature profiles over the length in systems with $dr_{12_1} = 0.0061m$. Showing that the systems with a positive velocity move further away from the systems that still contain a negative velocity. The range of the profiles of systems with a negative velocity also seem to flatten compared to the negative velocity systems.



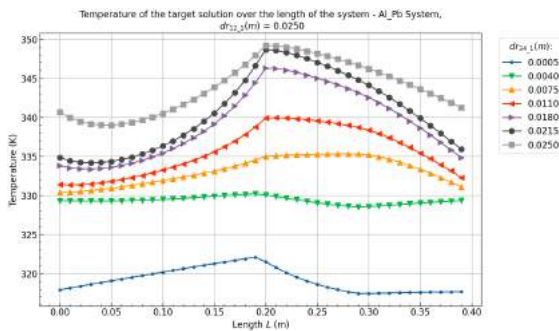
(d) Target solution temperature profiles over the length in systems with $dr_{12_1} = 0.0113m$.



(e) Target solution temperature profiles over the length in systems with $dr_{12_1} = 0.0164m$.



(f) Target solution temperature profiles over the length in systems with $dr_{12_1} = 0.0216m$. Showing a clear transition of the temperature profile between positive (dr_{34_1} between $0.0005m$ and $0.0075m$) and negative velocities in the systems.

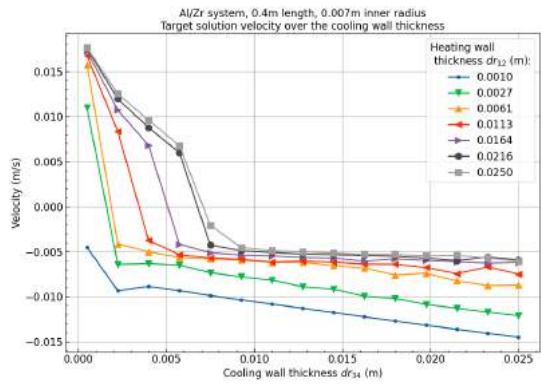


(g) Target solution temperature profiles over the length in systems with $dr_{12_1} = 0.0250m$. Showing the largest differences between temperature profiles in both temperature and profiles.

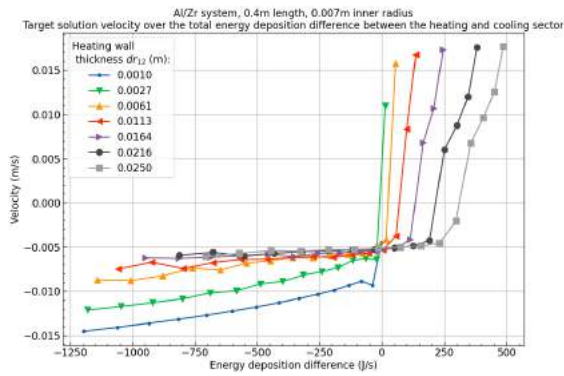
Figure B.4: Al/Pb (Heat/Cool) System target solution temperature profiles over the heating and cooling wall thickness (dr_{12} and dr_{34} respectively) with a system length (L) of $0.4m$, an inner radius (R_i) of $0.007m$ and a pipe angle (θ) of 5° .

Al/Zr - Wall thicknesses

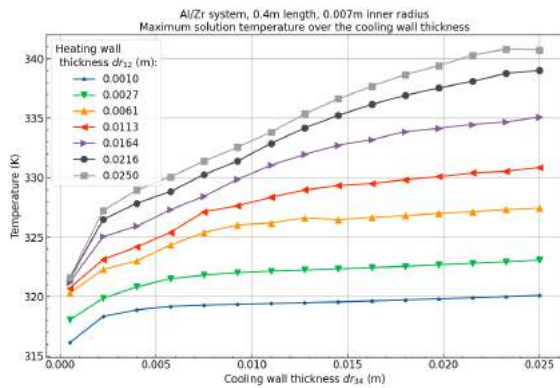
Back to overview - B.1.1



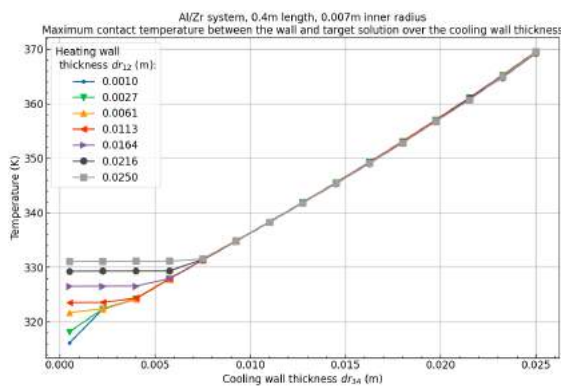
(a) Velocity over the cooling wall thickness showing a similar trend as the Al/Pb systems but with lower overall velocities and from the lower energy deposition of zirconium compared to lead.



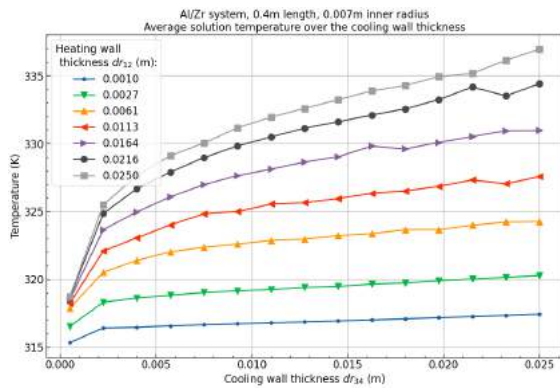
(b) Velocity over the energy deposition difference showing the same trend as Al/Pb system where a negative velocity can also be obtained in systems with a positive energy deposition difference.



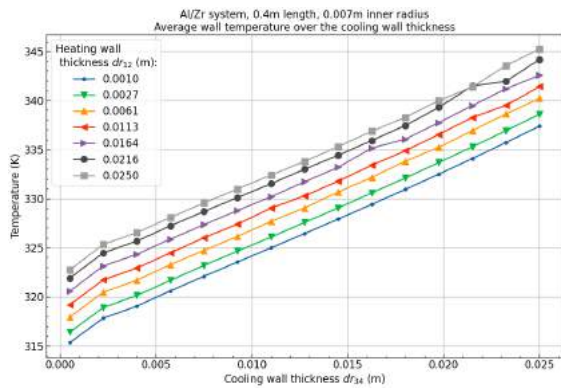
(c) Maximum target solution temperature over the cooling wall thickness showing the increase in maximum solution temperature as the wall thicknesses increase. This increase slows down as the temperatures increase, especially in the system with the smallest cooling wall thickness. Most likely from the increase in temperature difference between the walls and the water in the DLDR tube increasing the heat transfer rate.



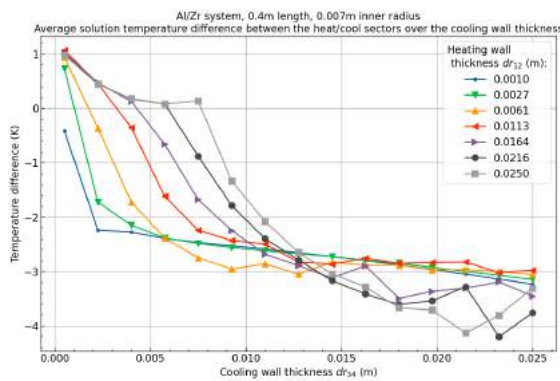
(d) Maximum contact temperature between the wall and the target solution which is mostly dependent on the wall thickness of the zirconium "cooling" wall.



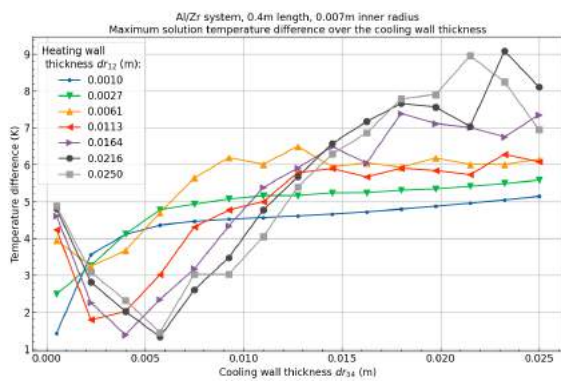
(e) Average target solution temperature over the cooling wall thickness showing a similar trend as the maximum heating temperatures.



(f) Average wall temperature over the cooling wall thickness showing an almost linear trend upwards as the wall thicknesses increase.

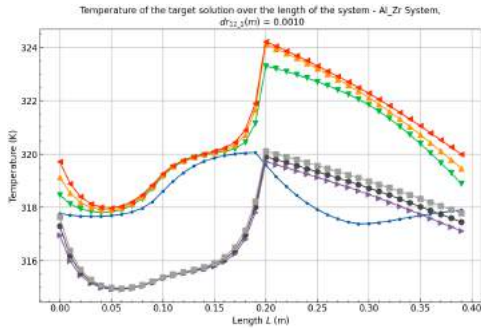


(g) Average target solution temperature difference between heating and cooling sectors showing a smaller temperature difference compared to the Al/Pb systems but a similar trend.

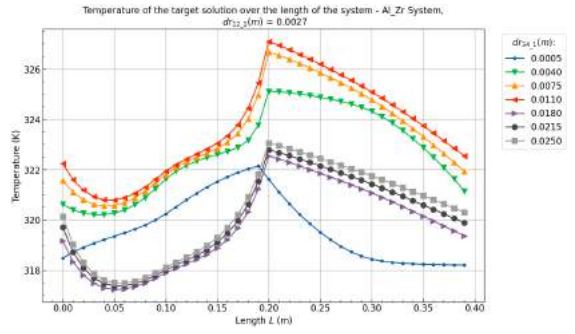


(h) Maximum target solution temperature difference between heating and cooling sectors.

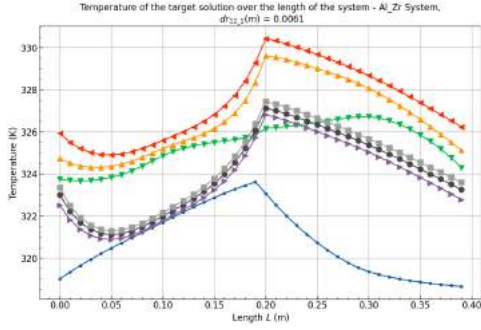
Figure B.5: Al/Zr (Heat/Cool) System results over the heating and cooling wall thickness (dr_{12} and dr_{34} respectively) with a system length (L) of $0.4m$, an inner radius (Ri) of $0.007m$ and a pipe angle (θ) of 5° .



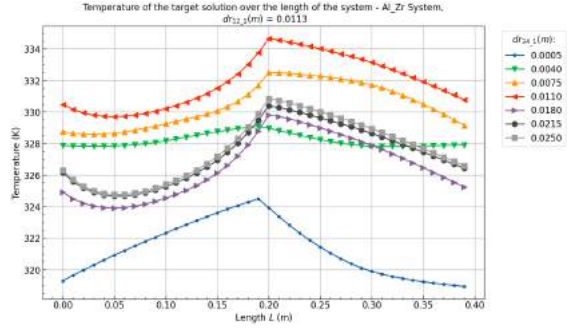
(a) Target solution temperature profiles over the length in systems with $dr_{12_1} = 0.0010m$. The data seems to be corrupt as the average temperature in systems with a larger thicknesses have a lower overall temperature than systems with smaller energy depositions. This data also doesn't reflect the average solution temperatures as seen in B.5g



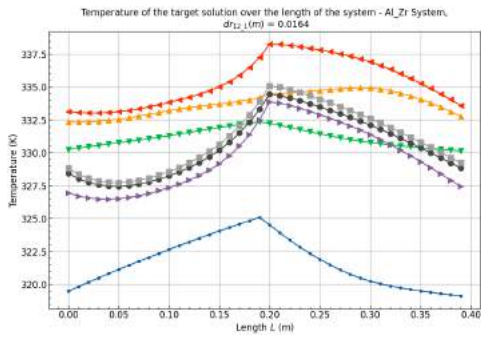
(b) Target solution temperature profiles over the length in systems with $dr_{12_1} = 0.0027m$.



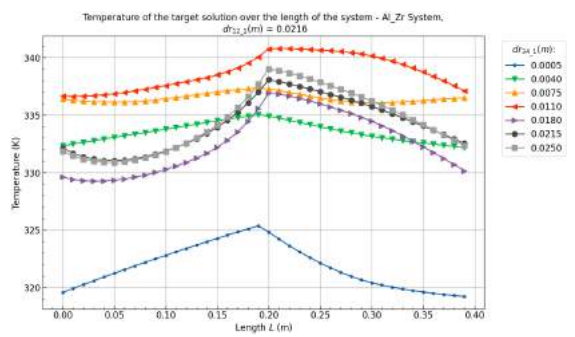
(c) Target solution temperature profiles over the length in systems with $dr_{12_1} = 0.0061m$.



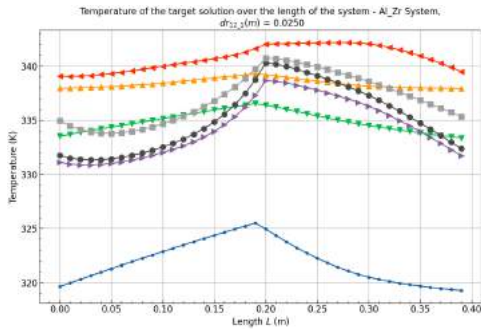
(d) Target solution temperature profiles over the length in systems with $dr_{12_1} = 0.0113m$.



(e) Target solution temperature profiles over the length in systems with $dr_{12_1} = 0.0164m$.



(f) Target solution temperature profiles over the length in systems with $dr_{12_1} = 0.0216m$.

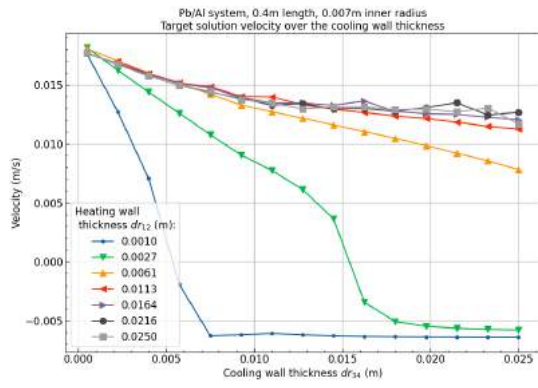


(g) Target solution temperature profiles over the length in systems with $dr_{12_1} = 0.0250m$.

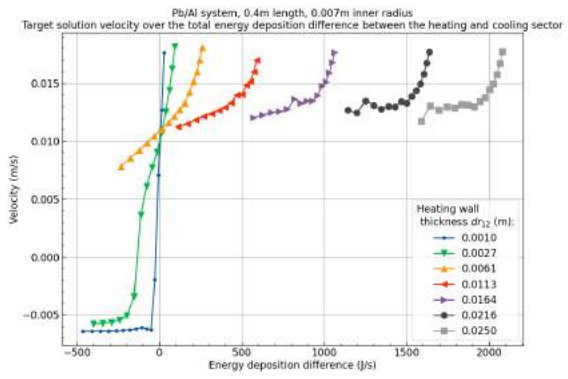
Figure B.6: Al/Zr (Heat/Cool) System target solution temperature profiles over the heating and cooling wall thickness (dr_{12} and dr_{34} respectively) with a system length (L) of $0.4m$, an inner radius (R_i) of $0.007m$ and a pipe angle (θ) of 5° .

Pb/Al - Wall thicknesses

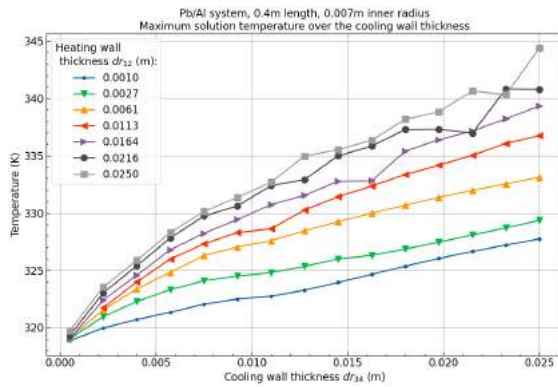
Back to overview - B.1.1



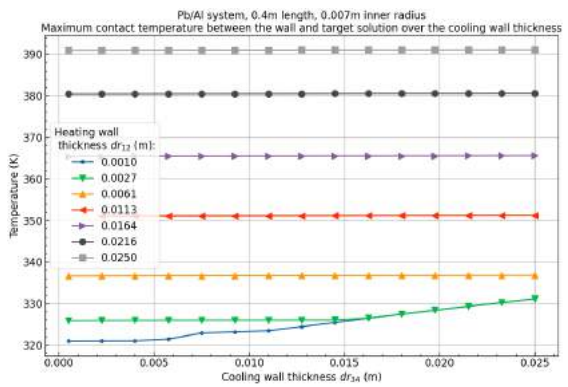
(a) Velocity over the cooling wall thickness showing an almost linear drop in velocity as the cooling wall thickness increases. Systems with larger heating wall thicknesses descend slower in velocity.



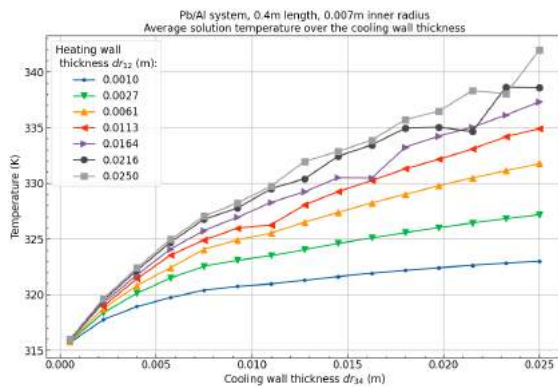
(b) Velocity over the energy deposition difference showing a large range of energy deposition differences between the heating and cooling sector in which the velocity remains positive. Even at a negative energy deposition difference, where the aluminium cooling wall receives a larger deposition than the heating wall, the velocity can remain positive.



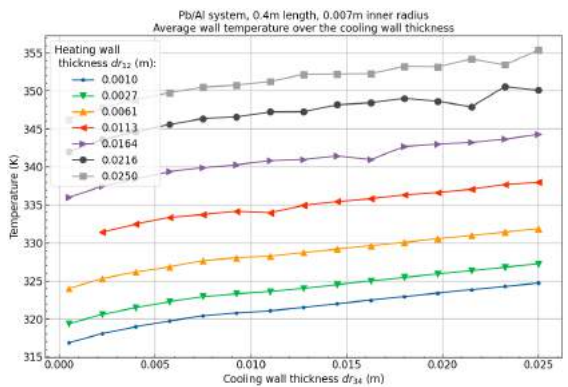
(c) Maximum target solution temperature over the cooling wall thickness showing the trend of the increase in temperature as the wall thicknesses increase, interestingly compared to systems with a heating wall made out of aluminium the temperature increases linearly at higher cooling wall thicknesses. Most likely this has to do with the overall higher energy deposition that is present in the lead wall.



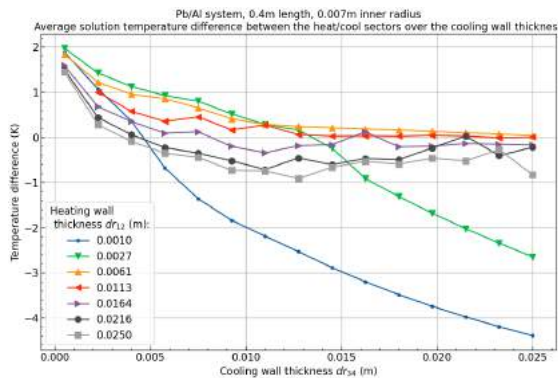
(d) Maximum contact temperature between the wall and the target solution showing that the lead heating wall thickness is the most important factor.



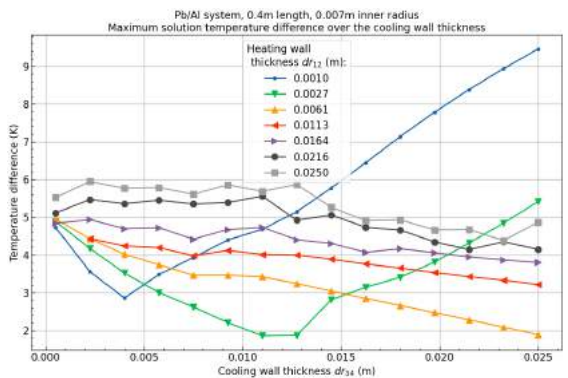
(e) Average target solution temperature over the cooling wall thickness showing a similar trend as the maximum target solution temperature.



(f) Average wall temperature over the cooling wall thickness showing a slight trend upwards as the aluminium cooling wall thickness increases.

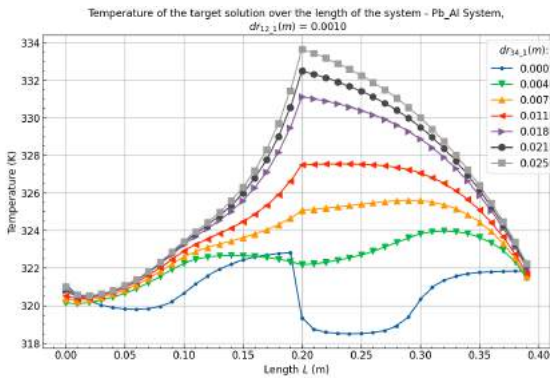


(g) Average target solution temperature difference between heating and cooling sectors

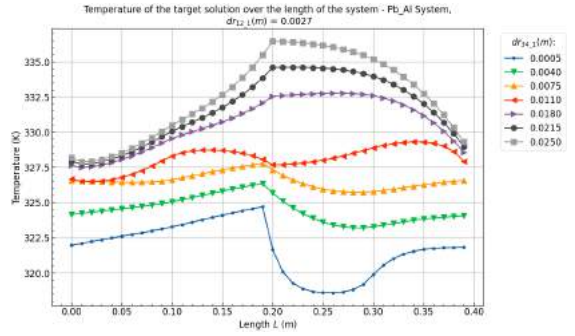


(h) Maximum target solution temperature difference between heating and cooling sectors

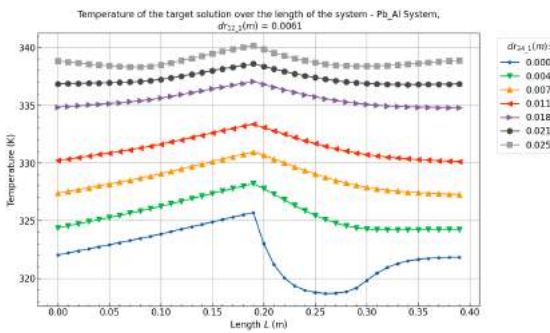
Figure B.7: Pb/Al (Heat/Cool) System results over the heating and cooling wall thickness (dr_{12} and dr_{34} respectively) with a system length (L) of $0.4m$, an inner radius (Ri) of $0.007m$ and a pipe angle (θ) of 5° .



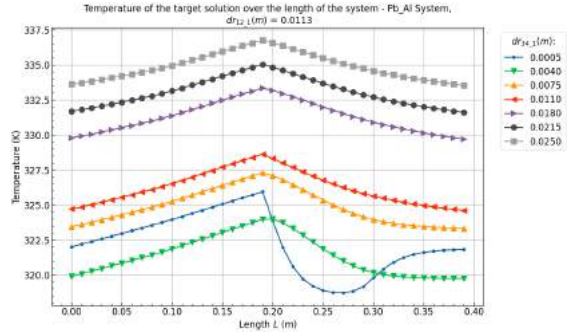
(a) Target solution temperature profiles over the length in systems with $dr_{12_1} = 0.0010m$. Showing the transition between positive and negative velocities.



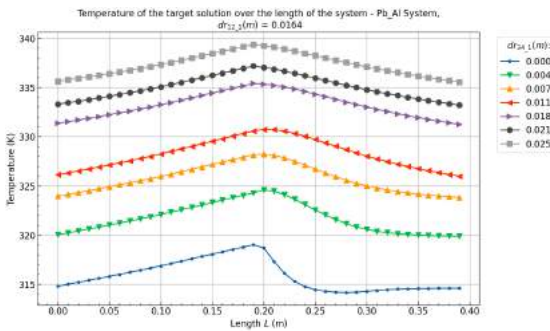
(b) Target solution temperature profiles over the length in systems with $dr_{12_1} = 0.0027m$. The transition now spreads out over more systems with positive velocities (dr_{34_1} between $0.0005m$ and $0.0110m$) which clearly shows the effect of a larger cooling wall thickness the in section 3 and 4. Once the velocity is negative the temperatures in section 1 and 2 are very similar.



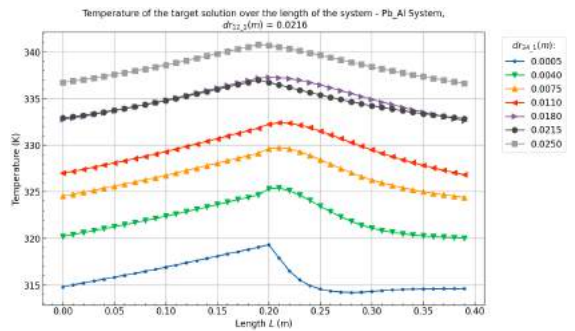
(c) Target solution temperature profiles over the length in systems with $dr_{12_1} = 0.0061m$. All systems in this plot have a positive velocity. With the increase of the cooling wall thickness the profile becomes more flat. The overall temperature increases significantly with the cooling wall thickness.



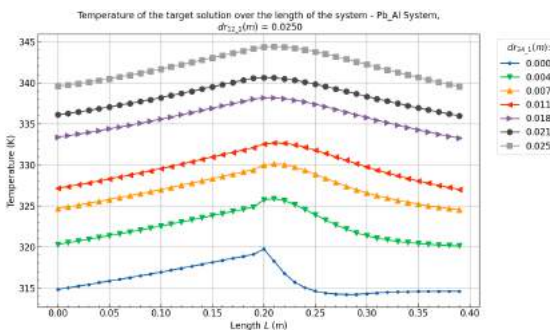
(d) Target solution temperature profiles over the length in systems with $dr_{12_1} = 0.0113m$. Interestingly the system with a cooling wall thickness $dr_{34_1} = 0.0040m$ shows a lower temperature in section 1, 2 and 4 compared to the system with $dr_{34_1} = 0.0005m$.



(e) Target solution temperature profiles over the length in systems with $dr_{12_1} = 0.0164m$.



(f) Target solution temperature profiles over the length in systems with $dr_{12_1} = 0.0216m$.

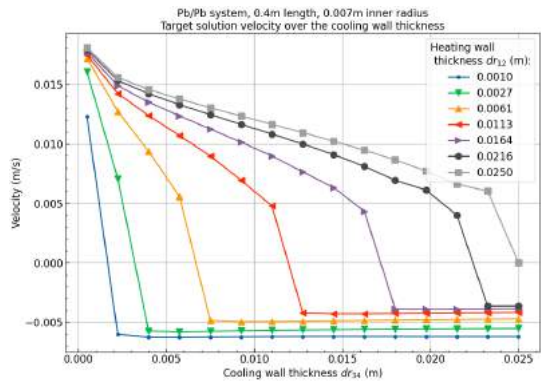


(g) Target solution temperature profiles over the length in systems with $dr_{12_1} = 0.0250m$.

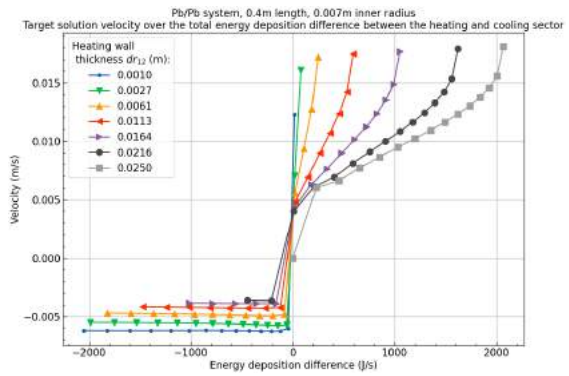
Figure B.8: Pb/Al (Heat/Cool) System target solution temperature profiles over the heating and cooling wall thickness (dr_{12} and dr_{34} respectively) with a system length (L) of $0.4m$, an inner radius (Ri) of $0.007m$ and a pipe angle (θ) of 5° .

Pb/Pb - Wall thicknesses

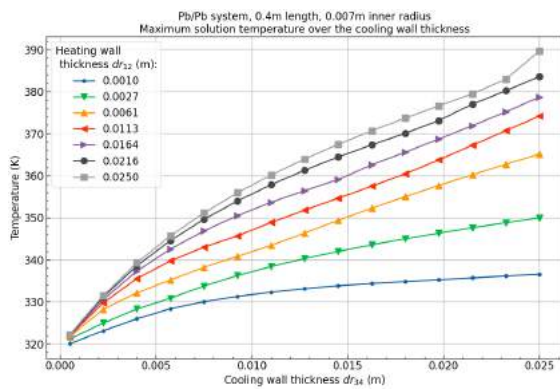
[Back to overview - B.1.1](#)



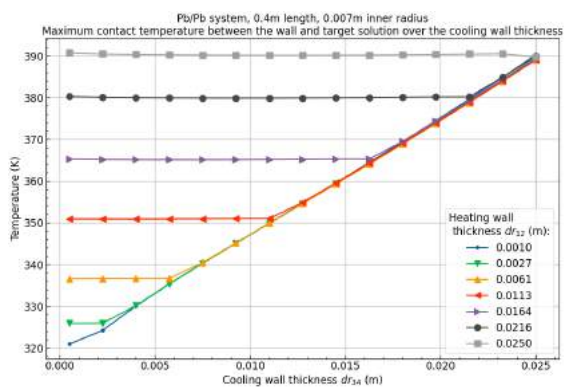
(a) Velocity over the cooling wall thickness showing that at smaller cooling wall thicknesses compared to the heating wall thickness a positive velocity is found. The velocity drops over the cooling wall thickness at positive velocities and remains almost constant at negative velocities.



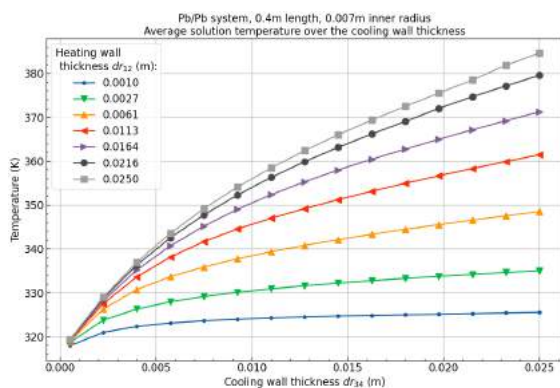
(b) Velocity over the energy deposition difference showing that a positive velocity is present if there is more energy deposition in the heating sector compared to the cooling sector. Negative velocities are present when this is reversed.



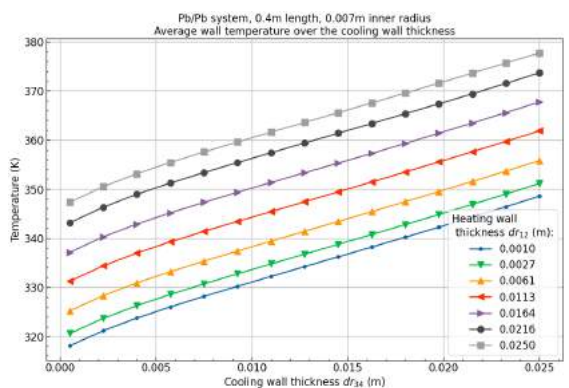
(c) Maximum target solution temperature over the cooling wall thickness showing a much faster increase in the maximum solution temperatures compared to systems containing aluminium.



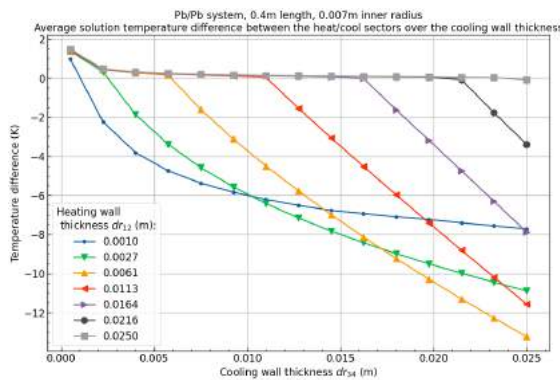
(d) Maximum contact temperature between the wall and the target solution showing that the maximum contact temperature is fully dependent on the wall with the largest thickness.



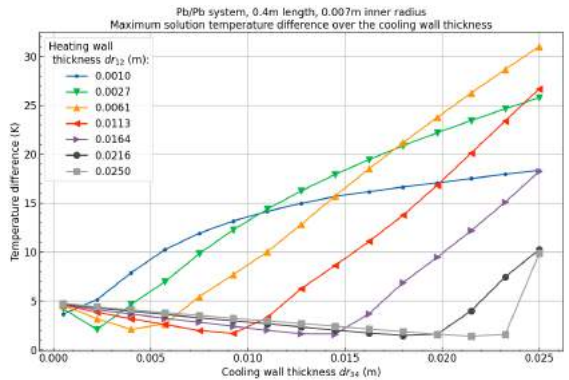
(e) Average target solution temperature over the cooling wall thickness showing a similar trend as the maximum solution temperature, the temperatures are however significantly lower.



(f) Average wall temperature over the cooling wall thickness.

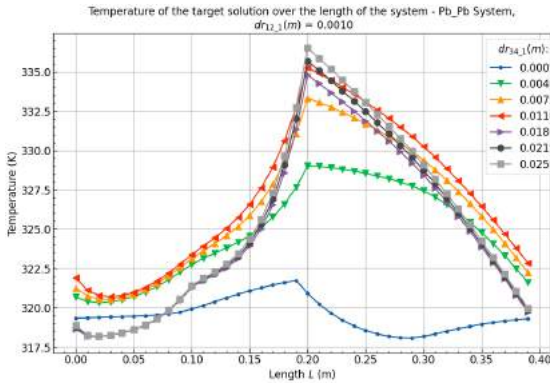


(g) Average target solution temperature difference between heating and cooling sectors showing that in systems with a small heating wall thickness the temperature differences at negative velocities reach a smaller negative value compared to systems with larger heating wall thicknesses. This most likely comes from the fact that the average temperatures seen in these systems are significantly lower.

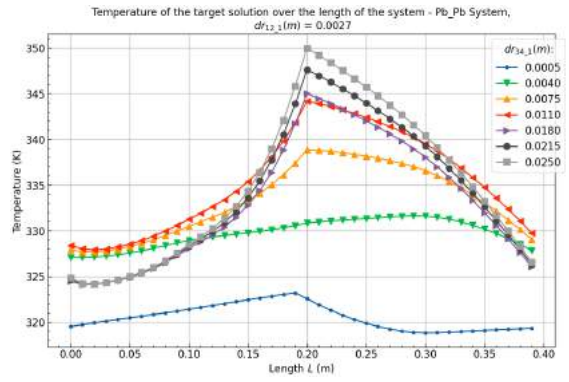


(h) Maximum target solution temperature difference between heating and cooling sectors. A similar trend is seen as the average target solution temperature difference.

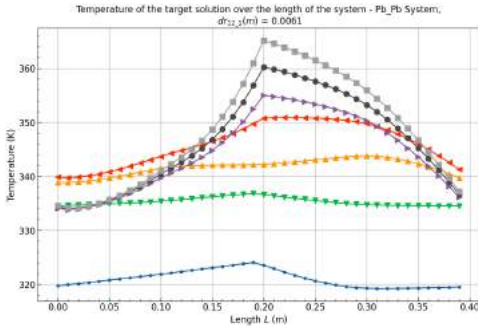
Figure B.9: Pb/Pb (Heat/Cool) System results over the heating and cooling wall thickness (dr_{12} and dr_{34} respectively) with a system length (L) of $0.4m$, an inner radius (Ri) of $0.007m$ and a pipe angle (θ) of 5° .



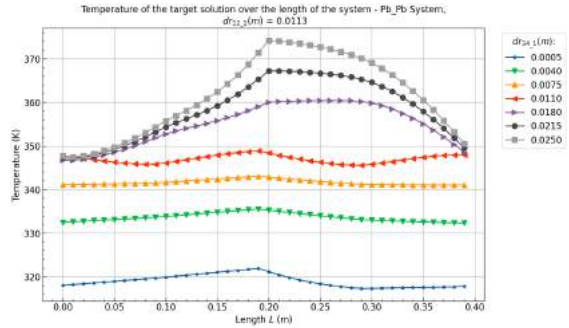
(a) Target solution temperature profiles over the length in systems with $dr_{12_1} = 0.0010m$. This shows the single positive velocity system at this heating wall thickness with the rest of the profiles from system with a negative velocity. The temperatures seen in the negative velocity profiles are generally close to each other. Interestingly the temperatures seen in section 1 and 2 are lower in the systems with the largest cooling wall thickness $dr_{34_1} > 0.0180m$ compared to the other systems.



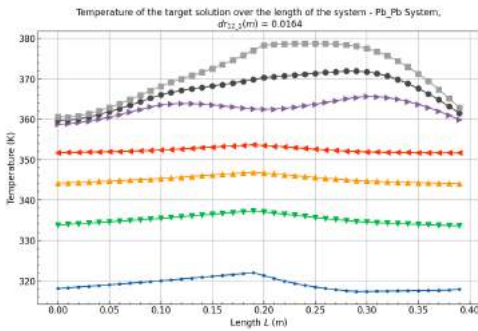
(b) Target solution temperature profiles over the length in systems with $dr_{12_1} = 0.0027m$.



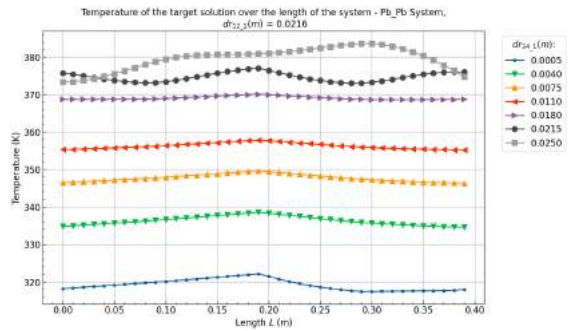
(c) Target solution temperature profiles over the length in systems with $dr_{12_1} = 0.0061m$ Showing that the temperature differences between the systems become larger in systems with positive velocities (dr_{34_1} between $0.0005m$ and $0.0110m$) while systems with negative velocities are relatively close to each other in section 1, 2 and 4.



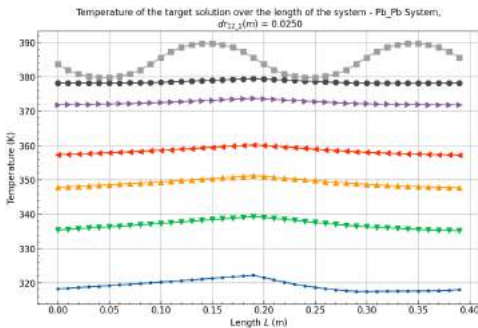
(d) Target solution temperature profiles over the length in systems with $dr_{12_1} = 0.0113m$.



(e) Target solution temperature profiles over the length in systems with $dr_{12_1} = 0.0164m$.



(f) Target solution temperature profiles over the length in systems with $dr_{12_1} = 0.0216m$.

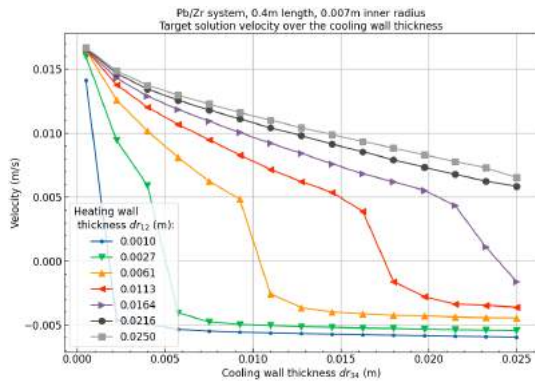


(g) Target solution temperature profiles over the length in systems with $dr_{12_1} = 0.0250m$. Clearly showing the temperature difference in systems with large wall thicknesses as the cooling provided by smaller wall thicknesses is much larger. The profile of a system with equal wall thicknesses is also seen at $dr_{12_1} = dr_{34_1} = 0.0250m$.

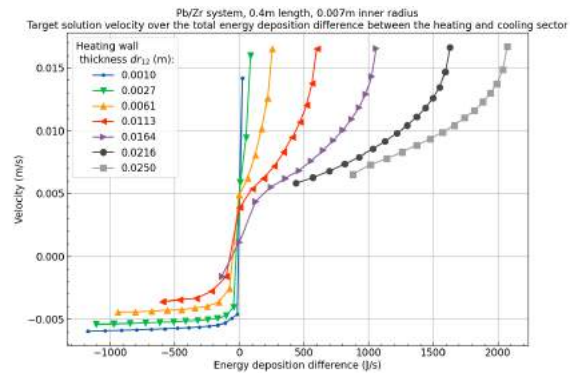
Figure B.10: Pb/Pb (Heat/Cool) System target solution temperature profiles over the heating and cooling wall thickness (dr_{12} and dr_{34} respectively) with a system length (L) of $0.4m$, an inner radius (Ri) of $0.007m$ and a pipe angle (θ) of 5° .

Pb/Zr - Wall thicknesses

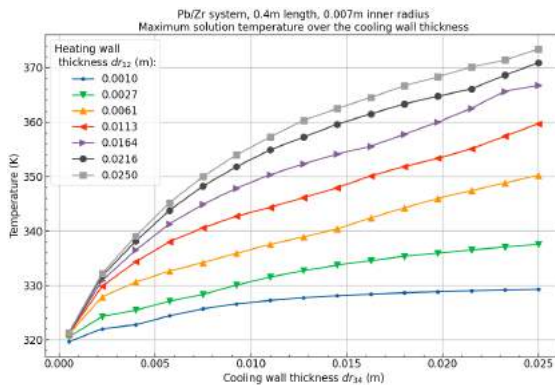
Back to overview - B.1.1



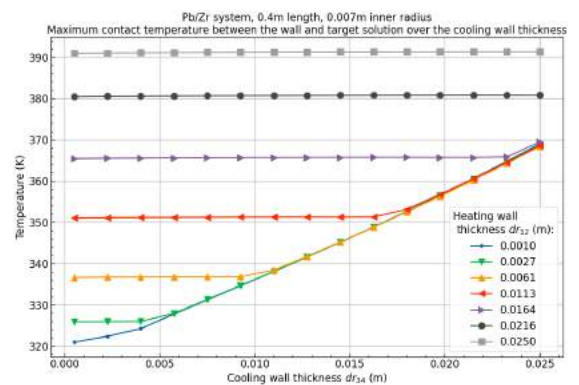
(a) Velocity over the cooling wall thickness showing similar results as the Pb/Pb systems but with more positive velocities.



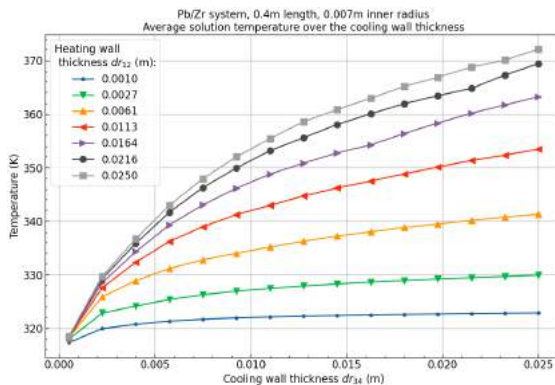
(b) Velocity over the energy deposition difference showing a large range of energy deposition difference between the heating and cooling sector that give a positive velocity. As the energy deposition rates between zirconium and lead are more similar than between aluminium and lead the systems shown here still require a positive energy deposition difference for a positive velocity and vice versa for negative velocities.



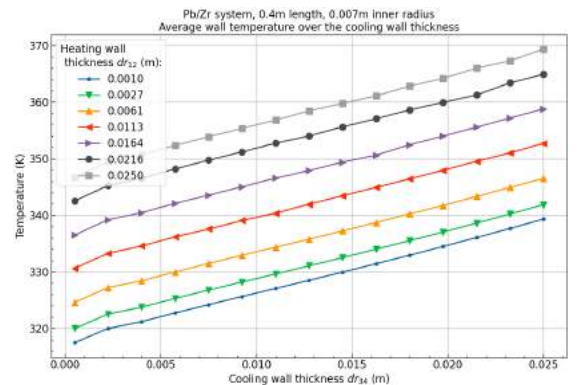
(c) Maximum target solution temperature over the cooling wall thickness showing a lower maximum target solution temperature compared to the Pb/Pb systems at the same wall thicknesses.



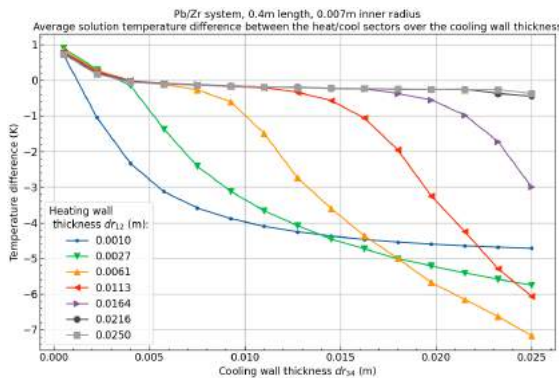
(d) Maximum contact temperature between the wall and the target solution showing that the lead heating wall overall is more important for the contact temperature from the larger energy deposition in lead.



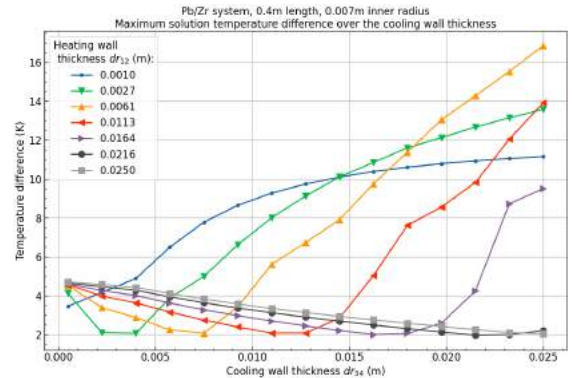
(e) Average target solution temperature over the cooling wall thickness showing the same trend as other systems increasing with the cooling wall thickness. This increase is however lower than that of the Pb/Pb systems.



(f) Average wall temperature over the cooling wall thickness.

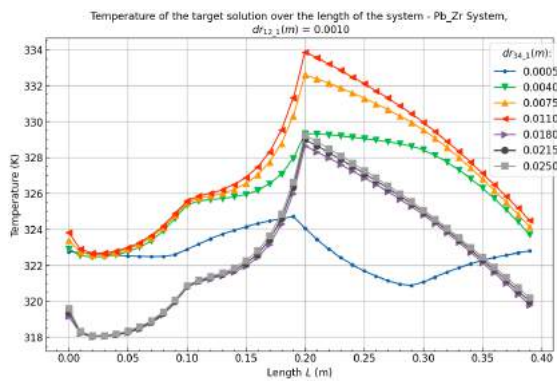


(g) Average target solution temperature difference between heating and cooling sectors

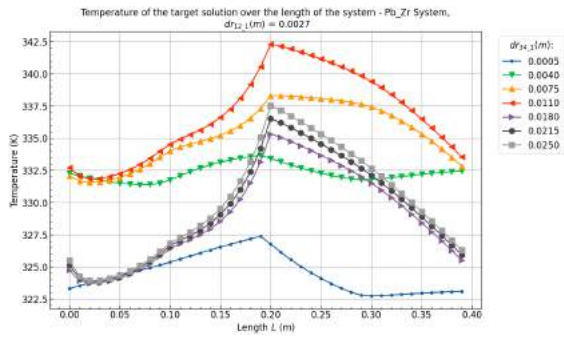


(h) Maximum target solution temperature difference between heating and cooling sectors

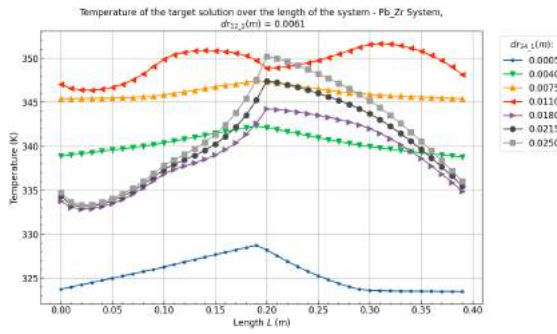
Figure B.11: Pb/Zr (Heat/Cool) System results over the heating and cooling wall thickness (dr_{12} and dr_{34} respectively) with a system length (L) of $0.4m$, an inner radius (Ri) of $0.007m$ and a pipe angle (θ) of 5° .



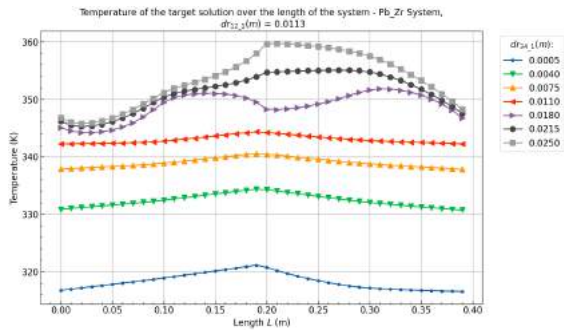
(a) Target solution temperature profiles over the length in systems with $dr_{12_1} = 0.0010m$. These values seem to be corrupt like the values for Al/Zr system.



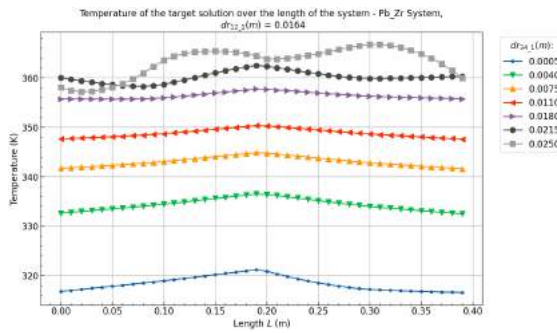
(b) Target solution temperature profiles over the length in systems with $dr_{12_1} = 0.0027m$.



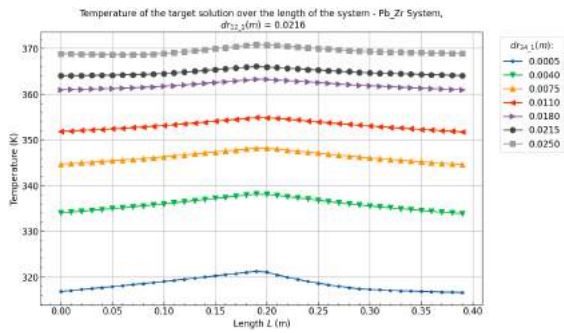
(c) Target solution temperature profiles over the length in systems with $dr_{12_1} = 0.0061m$.



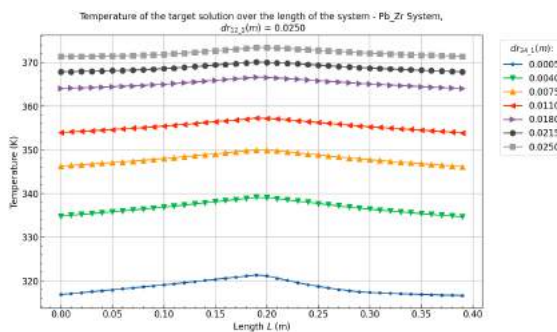
(d) Target solution temperature profiles over the length in systems with $dr_{12_1} = 0.0113m$.



(e) Target solution temperature profiles over the length in systems with $dr_{12_1} = 0.0164m$.



(f) Target solution temperature profiles over the length in systems with $dr_{12_1} = 0.0216m$.

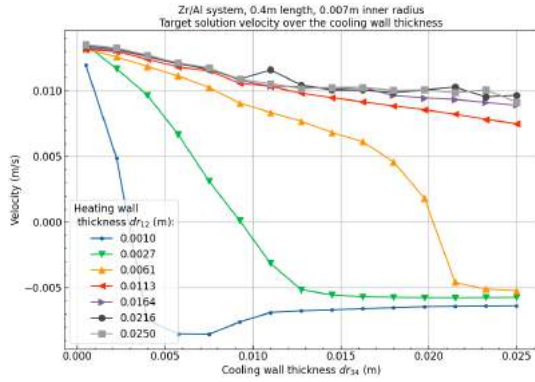


(g) Target solution temperature profiles over the length in systems with $dr_{12_1} = 0.0250m$.

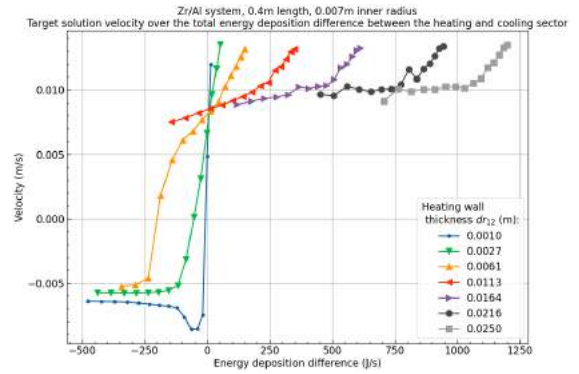
Figure B.12: Pb/Zr (Heat/Cool) System target solution temperature profiles over the heating and cooling wall thickness (dr_{12} and dr_{34} respectively) with a system length (L) of $0.4m$, an inner radius (Ri) of $0.007m$ and a pipe angle (θ) of 5° .

Zr/Al - Wall thicknesses

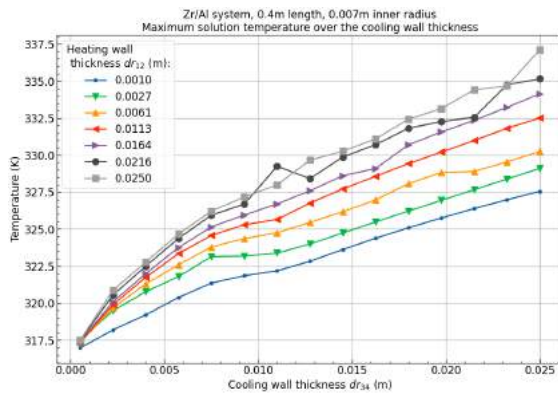
Back to overview - B.1.1



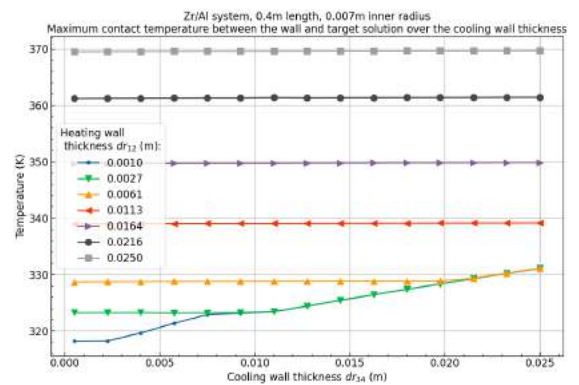
(a) Velocity over the cooling wall thickness showing a drop over the cooling wall thickness which slows down as the heating wall thickness increases. Negative values are also seen in systems with a small heating wall thickness.



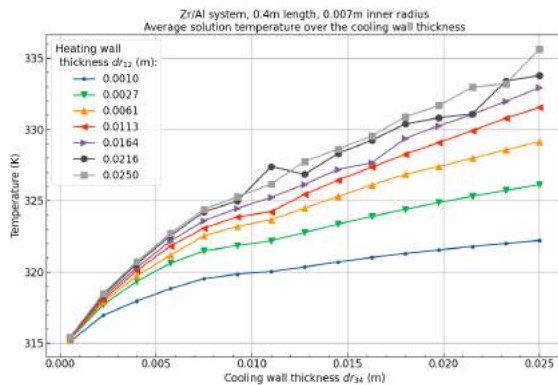
(b) Velocity over the energy deposition difference showing that positive velocities can even be achieved at negative energy deposition difference between the heating and cooling sector, like the Pb/Al system.



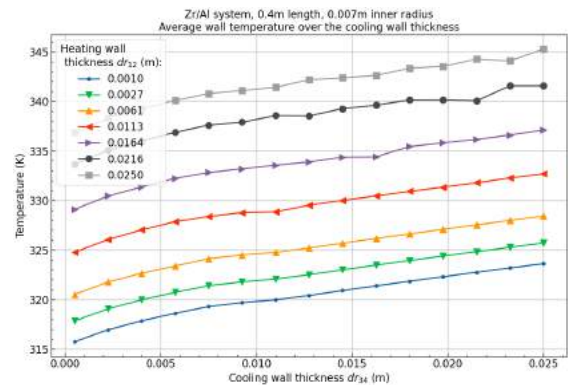
(c) Maximum target solution temperature over the cooling wall thickness showing an increase over the cooling wall thickness. The total increase is lower than the Al/Zr system which could possibly be explained by the velocity difference.



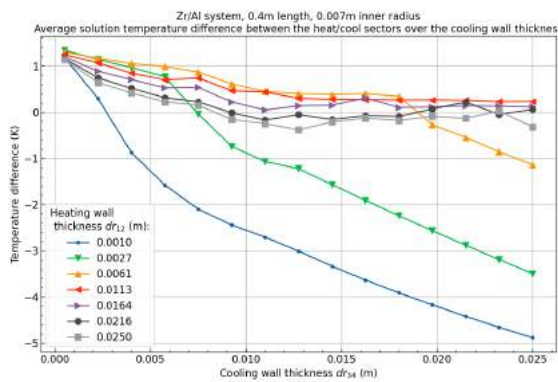
(d) Maximum contact temperature between the wall and the target solution showing that the maximum contact temperature is mainly dependent on the thickness of the zirconium heating wall as zirconium has the most energy deposited.



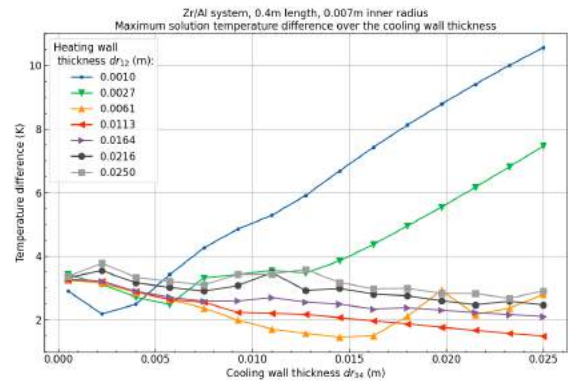
(e) Average target solution temperature over the cooling wall thickness showing a similar trend as the maximum temperatures.



(f) Average wall temperature over the cooling wall thickness showing an almost linear increase as the wall thickness increases.

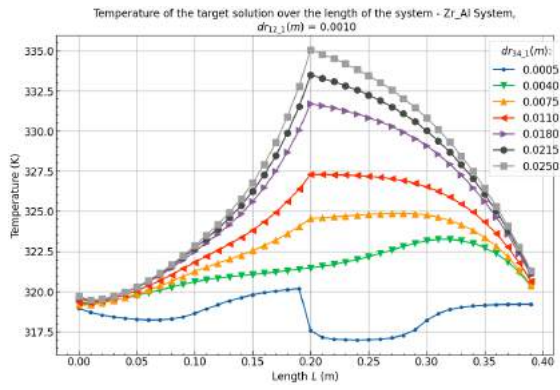


(g) Average target solution temperature difference between heating and cooling sectors

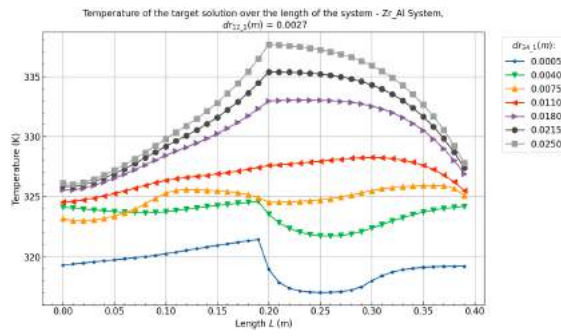


(h) Maximum target solution temperature difference between heating and cooling sectors

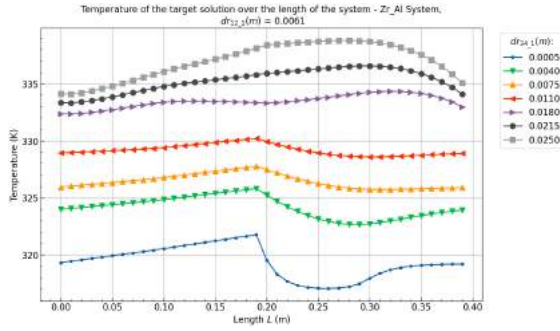
Figure B.13: Zr/Al (Heat/Cool) System results over the heating and cooling wall thickness (dr_{12} and dr_{34} respectively) with a system length (L) of $0.4m$, an inner radius (Ri) of $0.007m$ and a pipe angle (θ) of 5° .



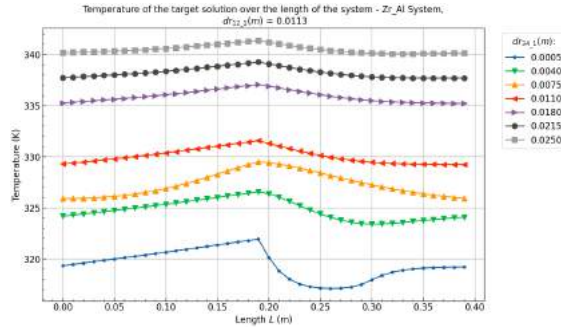
(a) Target solution temperature profiles over the length in systems with $dr_{12_1} = 0.0010m$. Showing a large spread between the temperatures seen between the systems. The system with a positive velocity as shown in $dr_{34_1} = 0.0005m$ has a completely different profile compared to the other results.



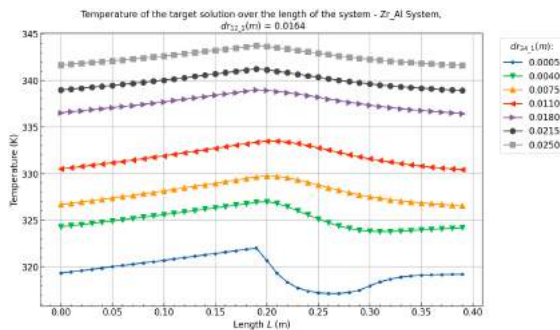
(b) Target solution temperature profiles over the length in systems with $dr_{12_1} = 0.0027m$. Showing more transitional profiles for systems with a positive velocity towards the negative velocity profiles.



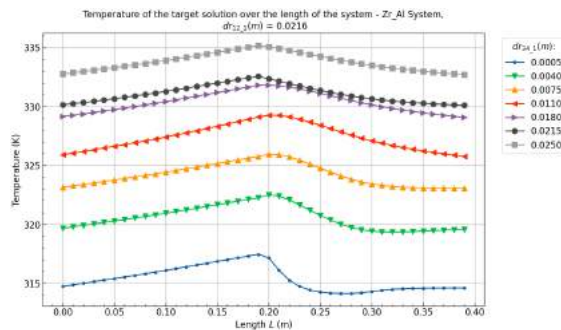
(c) Target solution temperature profiles over the length in systems with $dr_{12_1} = 0.0061m$.



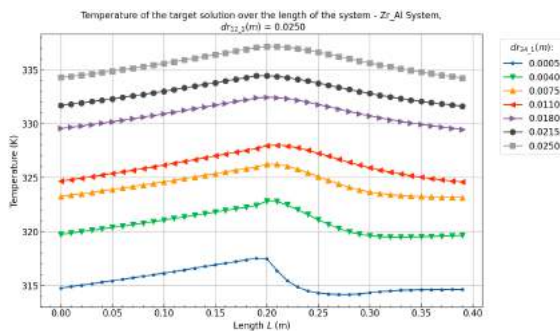
(d) Target solution temperature profiles over the length in systems with $dr_{12_1} = 0.0113m$.



(e) Target solution temperature profiles over the length in systems with $dr_{12_1} = 0.0164m$. All of these profiles belong to systems with a positive velocity, the system with $dr_{34_1} = 0.0005m$ shows the largest range of temperatures. This is most likely from the small cooling wall thickness that helps significantly more with cooling within section 3.



(f) Target solution temperature profiles over the length in systems with $dr_{12_1} = 0.0216m$. At these higher heating wall thicknesses the profiles have become increasingly more flat as well as that difference in the average temperature between the systems over the cooling wall thickness increases.

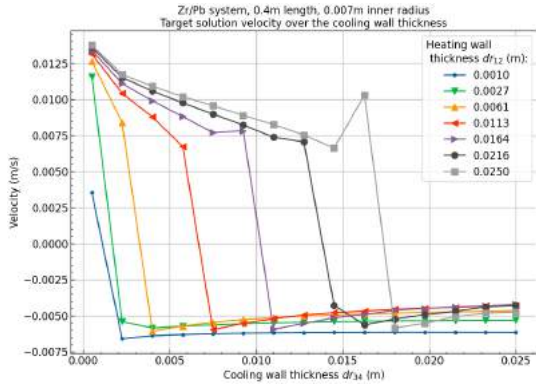


(g) Target solution temperature profiles over the length in systems with $dr_{12_1} = 0.0250m$.

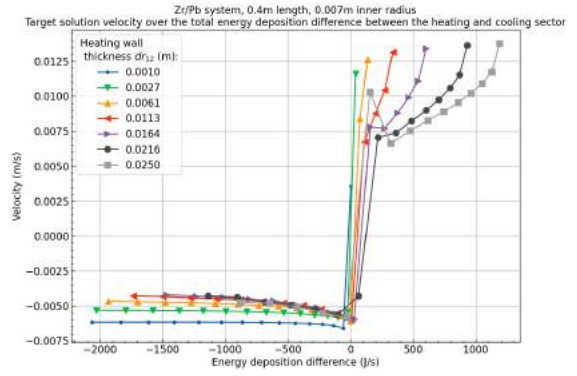
Figure B.14: Zr/Al (Heat/Cool) System target solution temperature profiles over the heating and cooling wall thickness (dr_{12} and dr_{34} respectively) with a system length (L) of $0.4m$, an inner radius (Ri) of $0.007m$ and a pipe angle (θ) of 5° .

Zr/Pb - Wall thicknesses

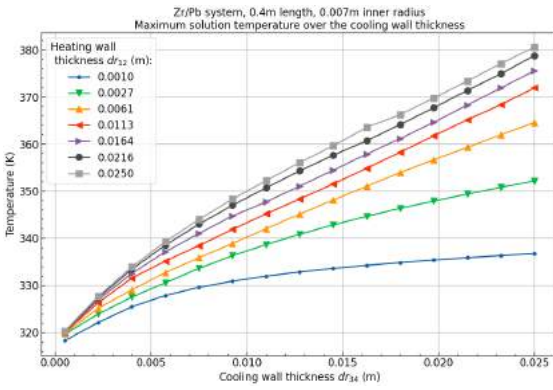
Back to overview - B.1.1



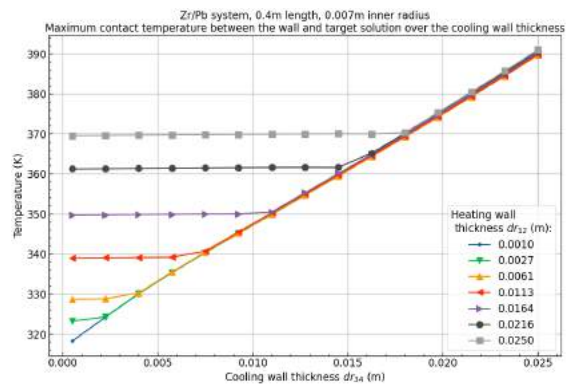
(a) Velocity over the cooling wall thickness showing the decrease of velocity over the cooling wall thickness. Interestingly in almost all systems (except $dr_{12,1} = 0.0010m$) once the velocity has reached a negative value, the velocity starts to increase slightly over the cooling wall thickness. This was not seen in systems with other materials



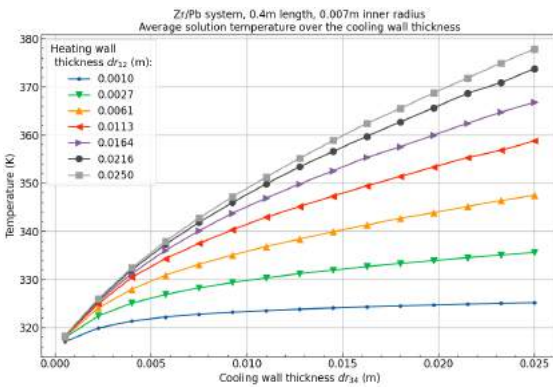
(b) Velocity over the energy deposition difference showing that in general more energy deposition in the heating sector corresponds to a positive velocity.



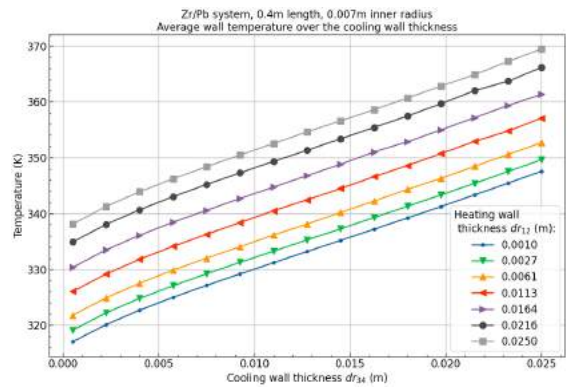
(c) Maximum target solution temperature over the cooling wall thickness showing an increase with the cooling wall thickness. In this system the smallest heating wall thickness of $dr_{12,1} = 0.0010m$ seems to deviate from the trend set by the other systems more than previously seen.



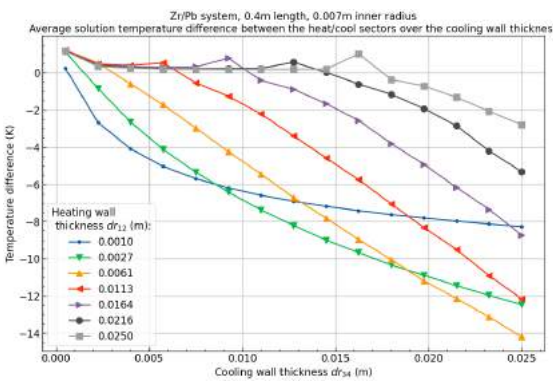
(d) Maximum contact temperature between the wall and the target solution is mainly based around which material has the largest wall thickness.



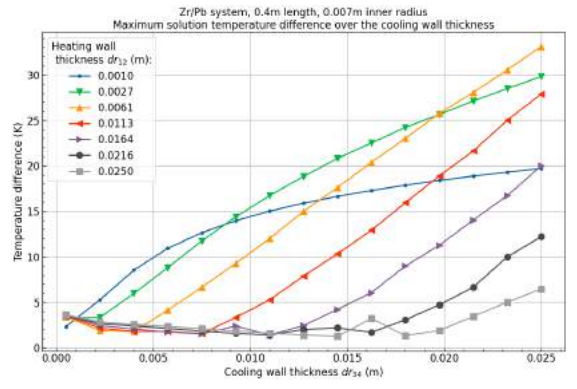
(e) Average target solution temperature over the cooling wall thickness showing a similar trend as the maximum temperature but with a smaller difference between the plots.



(f) Average wall temperature over the cooling wall thickness

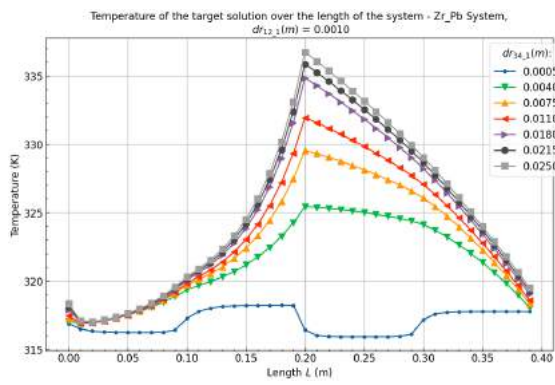


(g) Average target solution temperature difference between heating and cooling sectors showing that systems with a positive velocity show a small temperature difference between the heating and cooling sectors, but once the velocity becomes negative, and therefore the temperature profile changes, this difference increases limited by the average temperature of the solution.

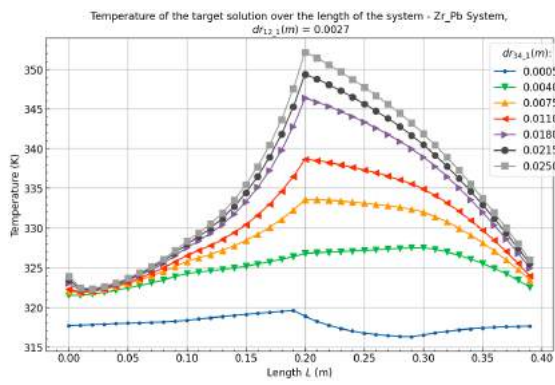


(h) Maximum target solution temperature difference between heating and cooling sectors

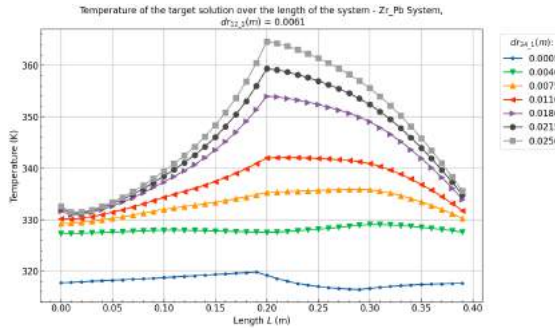
Figure B.15: Zr/Pb (Heat/Cool) System results over the heating and cooling wall thickness (dr_{12} and dr_{34} respectively) with a system length (L) of $0.4m$, an inner radius (Ri) of $0.007m$ and a pipe angle (θ) of 5° .



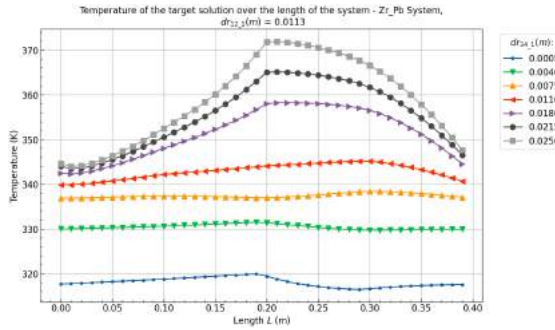
(a) Target solution temperature profiles over the length in systems with $dr_{12_1} = 0.0010m$. Showing very similar trends as the other systems that have been analyzed with a completely different profile for the smallest cooling wall thickness as this is the only system with a positive velocity.



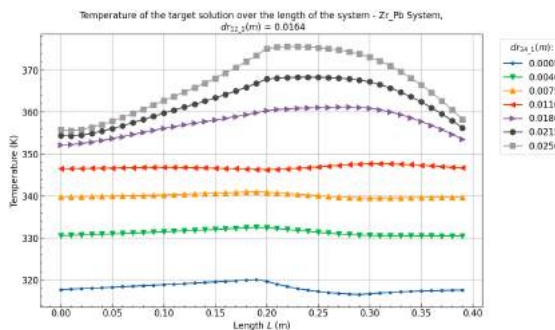
(b) Target solution temperature profiles over the length in systems with $dr_{12_1} = 0.0027m$. Showing more transitional profiles for systems with a positive velocity towards the negative velocity profiles.



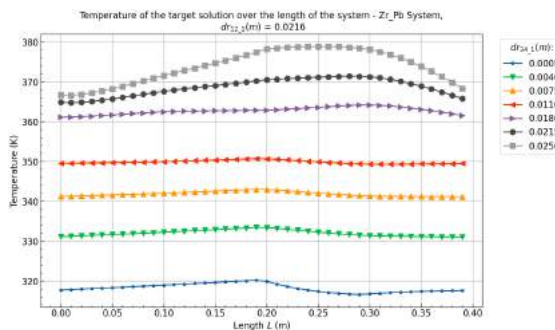
(c) Target solution temperature profiles over the length in systems with $dr_{12_1} = 0.0061m$.



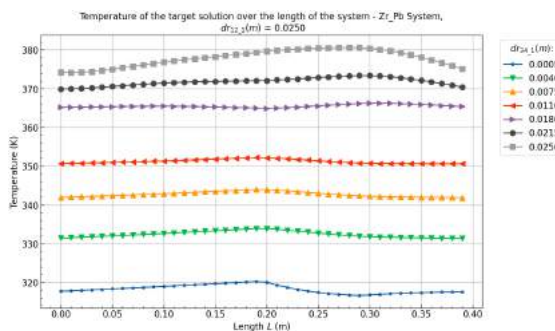
(d) Target solution temperature profiles over the length in systems with $dr_{12_1} = 0.0113m$. Showing the transitions between positive and negative velocities with an increased range of temperatures compared to systems with a smaller cooling wall thickness.



(e) Target solution temperature profiles over the length in systems with $dr_{12_1} = 0.0164m$.



(f) Target solution temperature profiles over the length in systems with $dr_{12_1} = 0.0216m$. At this thickness almost all systems have a positive velocity.

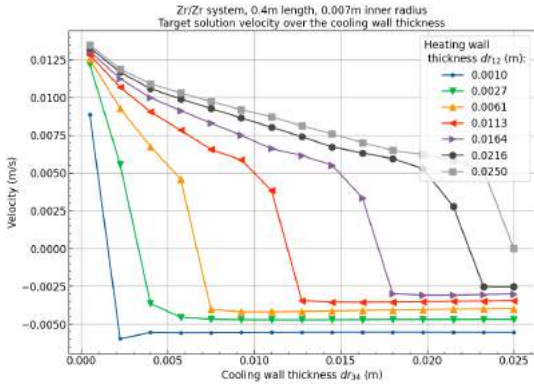


(g) Target solution temperature profiles over the length in systems with $dr_{12_1} = 0.0250m$.

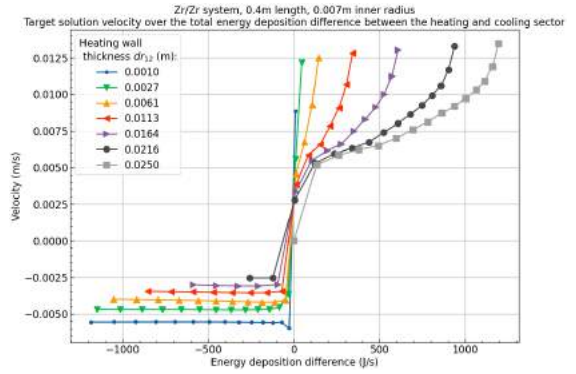
Figure B.16: Zr/Pb (Heat/Cool) System target solution temperature profiles over the heating and cooling wall thickness (dr_{12} and dr_{34} respectively) with a system length (L) of $0.4m$, an inner radius (Ri) of $0.007m$ and a pipe angle (θ) of 5° .

Zr/Zr - Wall thicknesses

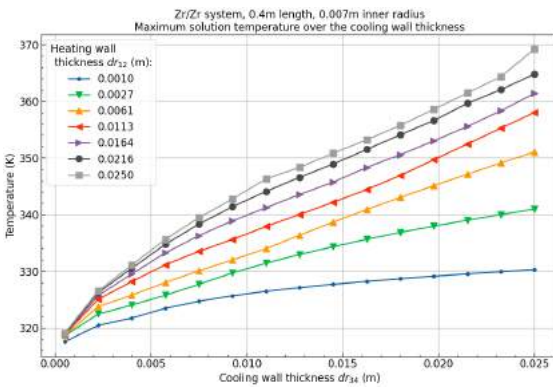
Back to overview - B.1.1



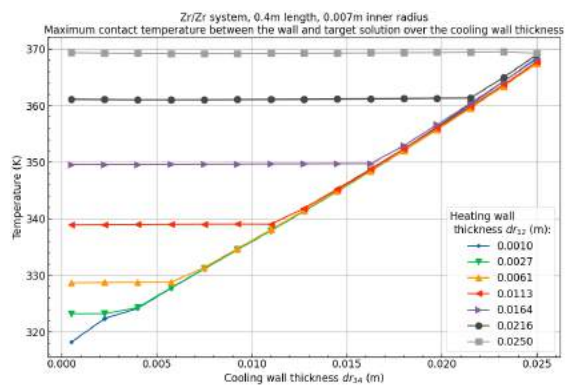
(a) Velocity over the cooling wall thickness decreasing at a similar rate as Pb/Pb systems but overall contain lower velocities. Most likely from the lower energy deposition differences that can be obtained by zirconium.



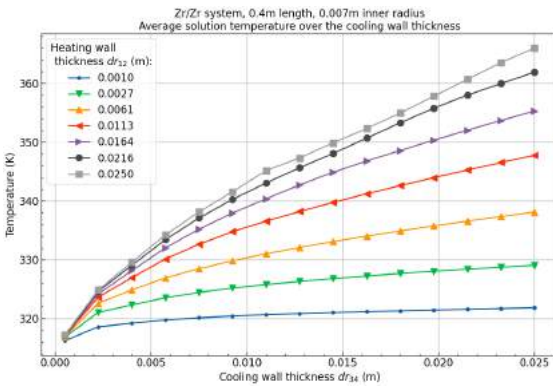
(b) Velocity over the energy deposition difference showing that for a positive velocity a positive energy deposition difference between the heating and cooling wall is required. For a negative velocity this energy deposition difference has to be negative.



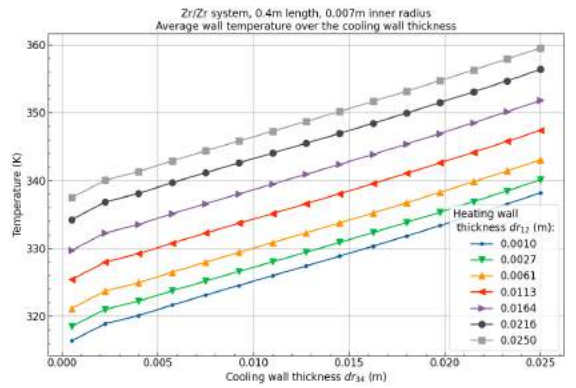
(c) Maximum target solution temperature over the cooling wall thickness increasing over the cooling wall thickness.



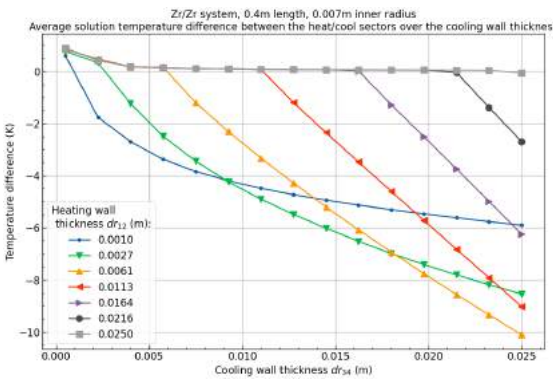
(d) Maximum contact temperature between the wall and the target solution showing a linear increase of either wall thickness.



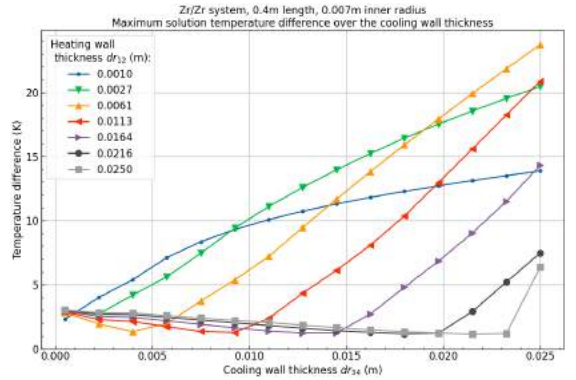
(e) Average target solution temperature over the cooling wall thickness showing an increase as the cooling wall thickness increases.



(f) Average wall temperature over the cooling wall thickness

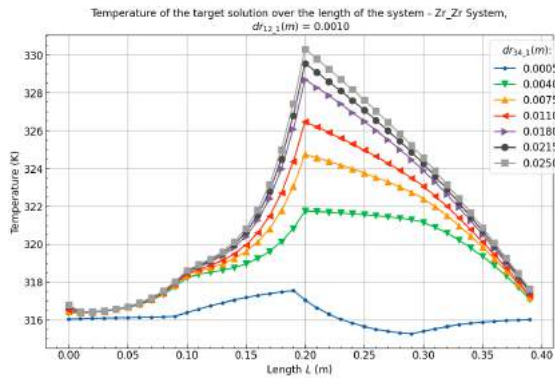


(g) Average target solution temperature difference between heating and cooling sectors

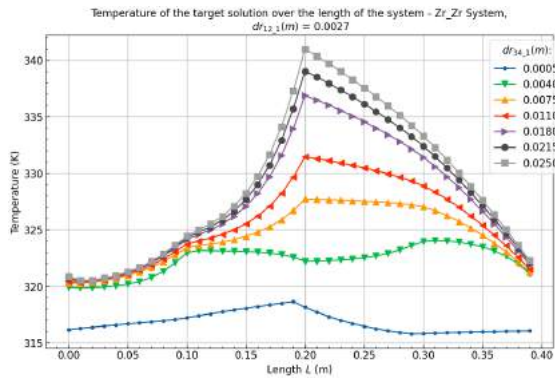


(h) Maximum target solution temperature difference between heating and cooling sectors

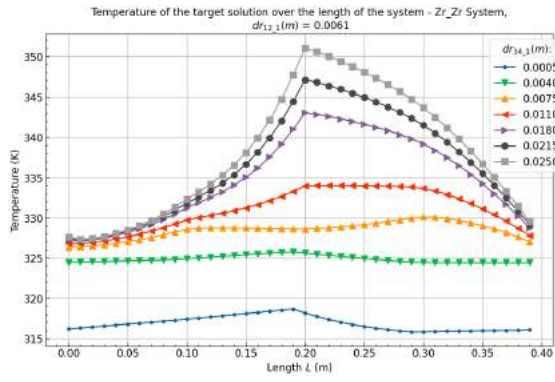
Figure B.17: Zr/Zr (Heat/Cool) System results over the heating and cooling wall thickness (dr_{12} and dr_{34} respectively) with a system length (L) of 0.4m, an inner radius (Ri) of 0.007m and a pipe angle (θ) of 5°.



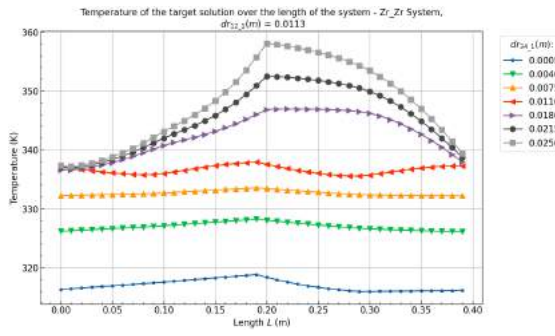
(a) Target solution temperature profiles over the length in systems with $dr_{12_1} = 0.0010m$.



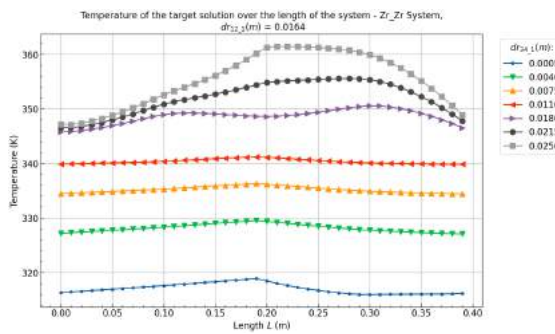
(b) Target solution temperature profiles over the length in systems with $dr_{12_1} = 0.0027m$.



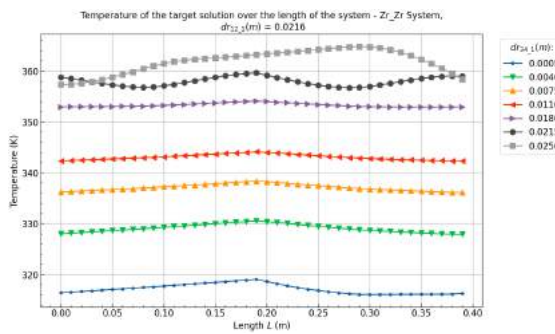
(c) Target solution temperature profiles over the length in systems with $dr_{12_1} = 0.0061m$.



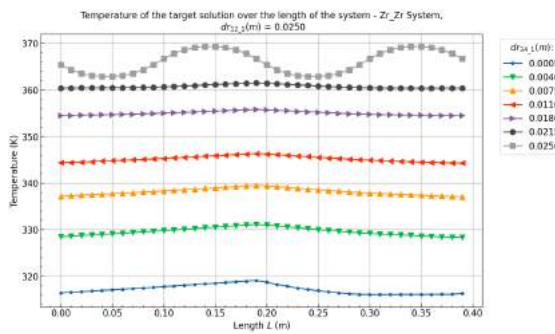
(d) Target solution temperature profiles over the length in systems with $dr_{12_1} = 0.0113m$.



(e) Target solution temperature profiles over the length in systems with $dr_{12_1} = 0.0164m$.



(f) Target solution temperature profiles over the length in systems with $dr_{12_1} = 0.0216m$.



(g) Target solution temperature profiles over the length in systems with $dr_{12_1} = 0.0250m$.

Figure B.18: Zr/Zr (Heat/Cool) System target solution temperature profiles over the heating and cooling wall thickness (dr_{12} and dr_{34} respectively) with a system length (L) of $0.4m$, an inner radius (Ri) of $0.007m$ and a pipe angle (θ) of 5° .

B.1.2. Multi layer materials wall

The general trends for the multi layer wall materials and wall thicknesses in these systems are:

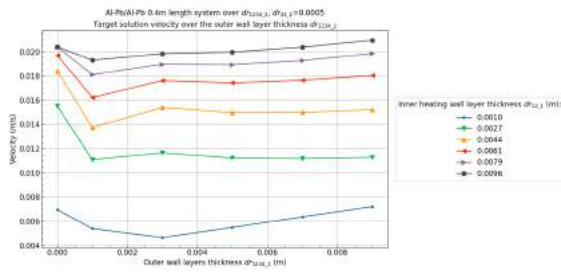
- Small outer layer thicknesses increase the temperatures in parallel walled system significantly (e.g. Al-Pb/Al-Pb), both in terms of the target solution and the wall temperatures.
- The staggered design Al-Pb/Pb-Al systems show significantly larger velocities than found in single layered wall systems at the same wall thicknesses.
- The staggered design Pb-Al/Al-Pb systems show relatively large negative velocities as the outer wall layer thickness is increased. The temperature increase over the outer wall layer thickness is significantly less than other systems.
- Adding a layer of lead on the outside of either a Zr/Zr or Al/Al (Heat/Cool) system increases the average and maximum target solution temperature significantly more than the same increase of wall thickness in a single layer Pb/Pb system.
- A small initial layer thickness of lead on the outside of an Al/Al system decreases the velocity in the system, increasing the outer layer thickness improves this.
- A small layer of lead on the outside of an Zr/Zr system can increase the absolute velocities, especially if the zirconium cooling wall thickness is smaller than the heating wall thickness.
- The staggered of Al-Pb/Pb-Al and Zr-Pb/Pb-Zr show an increase in the velocity as the outer wall layer thickness increases. The energy deposition in the heating sector increases more than the cooling sector.
- The staggered Pb-Zr/Zr-Pb does show an initial absolute increase in velocity with an outer wall layer thickness of $0.001m$. However, the velocity drops after the outer layer thickness increases further.
- In the staggered Pb-Al/Al-Pb system the velocity drops with an increase of the outer wall layer thickness.

Table B.3: System specifications for the multi layer wall material results

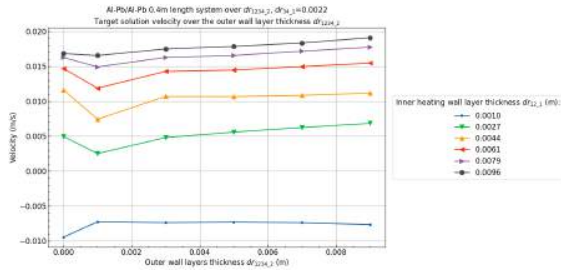
System Variable	Values	Reference
Multi layer wall materials	Al-Pb/Al-Pb	B.19 - B.21 (Page 111 - 113)
	Al-Pb/Pb-Al	B.22 - B.24 (Page 114 - 116)
	Pb-Al/Al-Pb	B.25 - B.27 (Page 117 - 119)
	Pb-Zr/Zr-Pb	B.28 - B.30 (Page 120 - 122)
	Zr-Pb/Pb-Zr	B.31 - B.33 (Page 123 - 125)
	Zr-Pb/Zr-Pb	B.34 - B.36 (Page 126 - 128)
Inner layer heating wall thickness (dr_{12_1})	0.001 – 0.0096m	
Inner layer cooling wall thickness (dr_{34_1})	0.0005 – 0.0092m	
Outer wall layer thickness (dr_{1234_2})	0.001 – 0.0096m	
Inner radius (R_i)	0.007m	
Length (L)	0.4m	
Pipe angle (θ)	5°	
Section 2 length fraction ($Frac$)	1.0	

Al-Pb/Al-Pb - Wall thicknesses

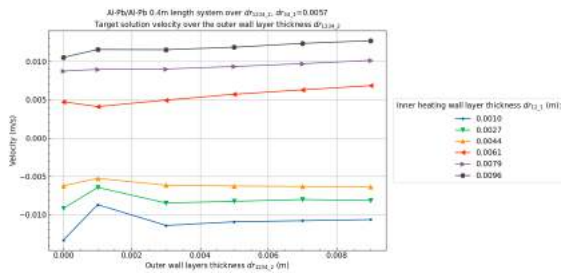
Back to overview - B.1.2



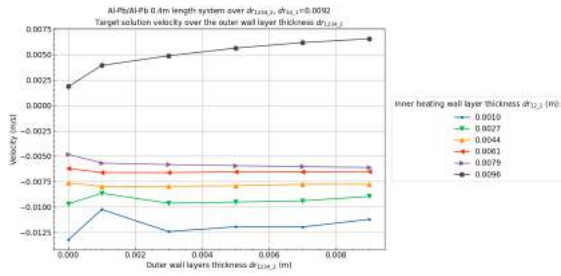
(a) Velocity over the outer wall layer thickness $dr_{1234,2}$ and inner heating wall thickness $dr_{12,1}$ at a cooling wall thickness $dr_{34,1} = 0.0005m$



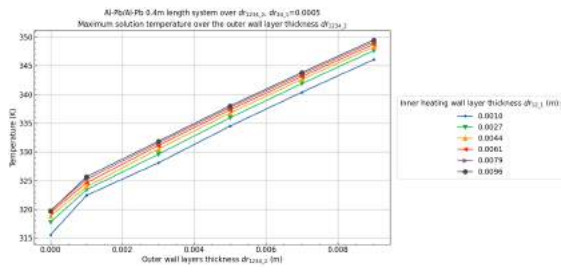
(b) Velocity over the outer wall layer thickness $dr_{1234,2}$ and inner heating wall thickness $dr_{12,1}$ at a cooling wall thickness $dr_{34,1} = 0.0022m$



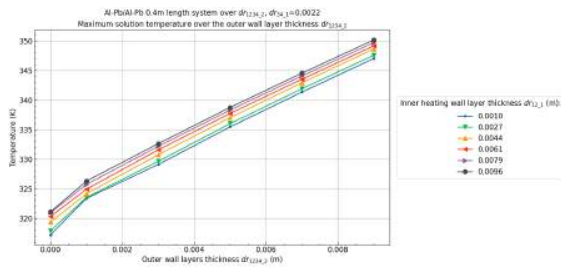
(c) Velocity over the outer wall layer thickness $dr_{1234,2}$ and inner heating wall thickness $dr_{12,1}$ at a cooling wall thickness $dr_{34,1} = 0.0057m$



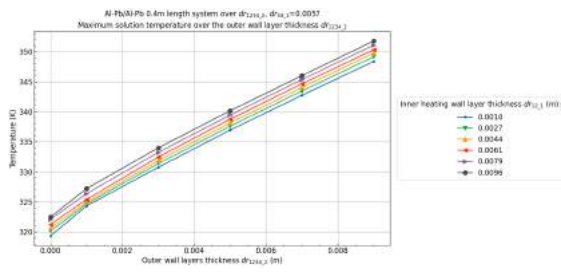
(d) Velocity over the outer wall layer thickness $dr_{1234,2}$ and inner heating wall thickness $dr_{12,1}$ at a cooling wall thickness $dr_{34,1} = 0.0092m$



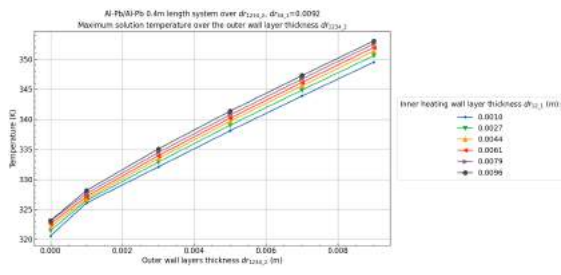
(e) Maximum target solution temperature over the outer wall layer thickness $dr_{1234,2}$ and inner heating wall thickness $dr_{12,1}$ at a cooling wall thickness $dr_{34,1} = 0.0005m$



(f) Maximum target solution temperature over the outer wall layer thickness $dr_{1234,2}$ and inner heating wall thickness $dr_{12,1}$ at a cooling wall thickness $dr_{34,1} = 0.0022m$

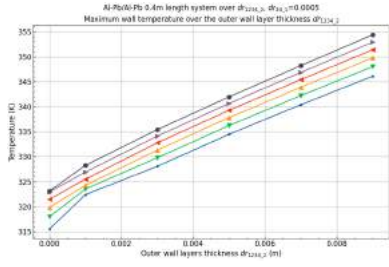


(g) Maximum target solution temperature over the outer wall layer thickness $dr_{1234,2}$ and inner heating wall thickness $dr_{12,1}$ at a cooling wall thickness $dr_{34,1} = 0.0057m$

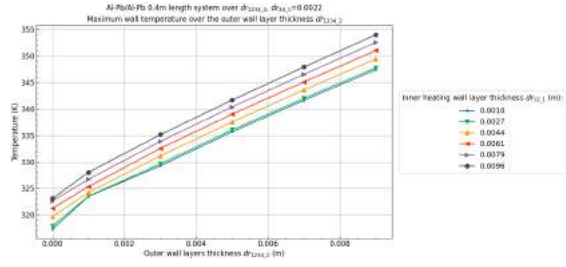


(h) Maximum target solution temperature over the outer wall layer thickness $dr_{1234,2}$ and inner heating wall thickness $dr_{12,1}$ at a cooling wall thickness $dr_{34,1} = 0.0092m$

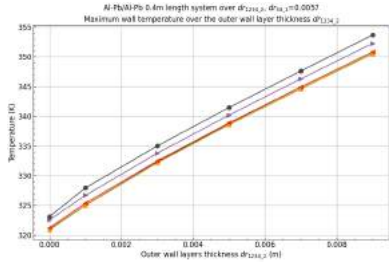
Figure B.19: Al-Pb/Al-Pb (Inner Heat_Outer Heat/Inner Cool_Outer Cool) system results over the wall thicknesses of the inner heating, inner cooling and outer wall ($dr_{12,1}$, $dr_{34,1}$, and $dr_{1234,2}$ respectively) with a system length (L) of $0.4m$, an inner radius (Ri) of $0.007m$ and a pipe angle (θ) of 5° .



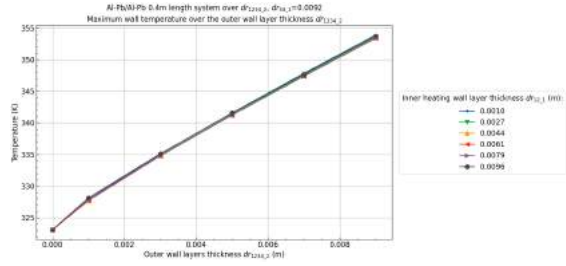
(a) Maximum wall temperature over the outer wall layer thickness $dr_{1234,2}$ and inner heating wall thickness $dr_{12,1}$ at a cooling wall thickness $dr_{34,1} = 0.0005m$



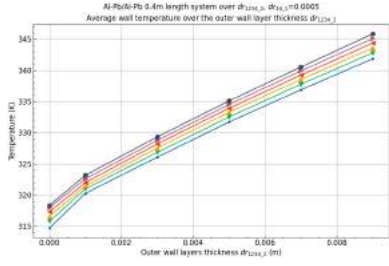
(b) Maximum wall temperature over the outer wall layer thickness $dr_{1234,2}$ and inner heating wall thickness $dr_{12,1}$ at a cooling wall thickness $dr_{34,1} = 0.0022m$



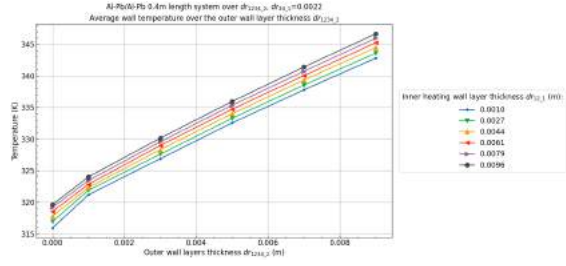
(c) Maximum wall temperature over the outer wall layer thickness $dr_{1234,2}$ and inner heating wall thickness $dr_{12,1}$ at a cooling wall thickness $dr_{34,1} = 0.0057m$



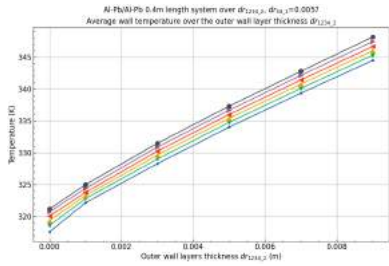
(d) Maximum wall temperature over the outer wall layer thickness $dr_{1234,2}$ and inner heating wall thickness $dr_{12,1}$ at a cooling wall thickness $dr_{34,1} = 0.0092m$



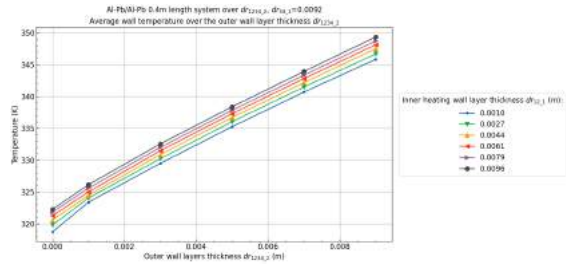
(e) Average wall temperature over the outer wall layer thickness $dr_{1234,2}$ and inner heating wall thickness $dr_{12,1}$ at a cooling wall thickness $dr_{34,1} = 0.0005m$



(f) Average wall temperature over the outer wall layer thickness $dr_{1234,2}$ and inner heating wall thickness $dr_{12,1}$ at a cooling wall thickness $dr_{34,1} = 0.0022m$

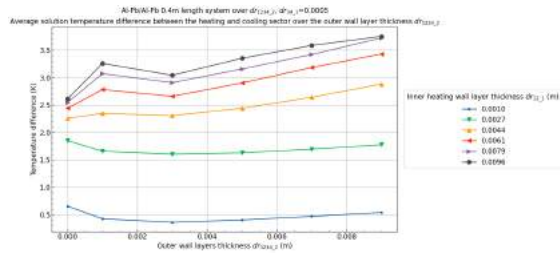


(g) Average wall temperature over the outer wall layer thickness $dr_{1234,2}$ and inner heating wall thickness $dr_{12,1}$ at a cooling wall thickness $dr_{34,1} = 0.0057m$

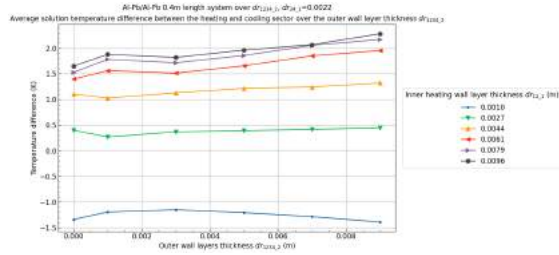


(h) Average wall temperature over the outer wall layer thickness $dr_{1234,2}$ and inner heating wall thickness $dr_{12,1}$ at a cooling wall thickness $dr_{34,1} = 0.0092m$

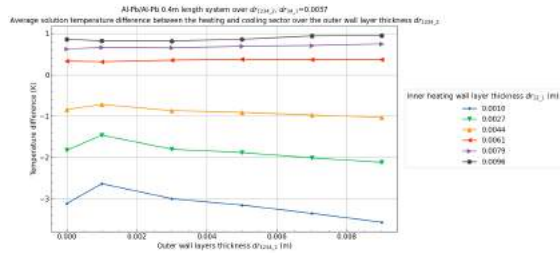
Figure B.20: Al-Pb/Al-Pb (Inner Heat_Outer Heat/Inner Cool_Outer Cool) continued system results over the wall thicknesses of the inner heating, inner cooling and outer wall ($dr_{12,1}$, $dr_{34,1}$, and $dr_{1234,2}$ respectively) with a system length (L) of $0.4m$, an inner radius (R_i) of $0.007m$ and a pipe angle (θ) of 5° .



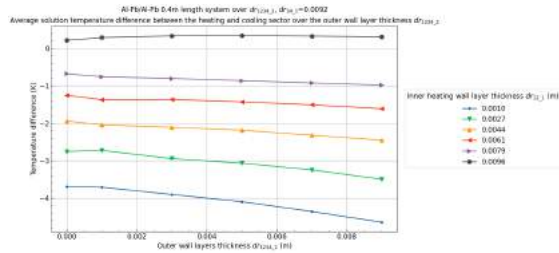
(a) Average target solution temperature difference between the heating and cooling sectors over the outer wall layer thickness dr_{1234_2} and inner heating wall thickness dr_{12_1} at a cooling wall thickness $dr_{34_1} = 0.005m$



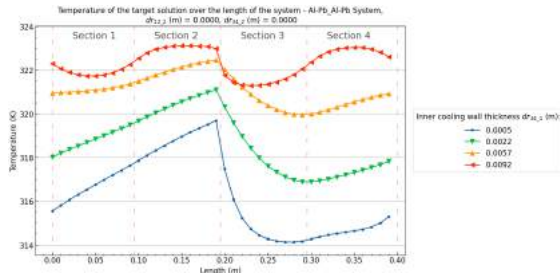
(b) Average target solution temperature difference between the heating and cooling sectors over the outer wall layer thickness dr_{1234_2} and inner heating wall thickness dr_{12_1} at a cooling wall thickness $dr_{34_1} = 0.022m$



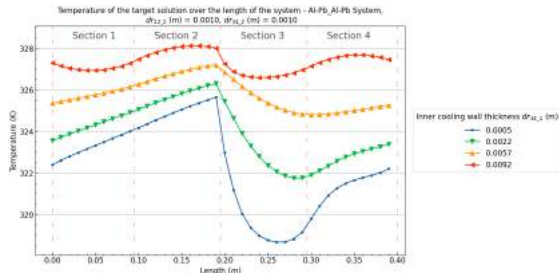
(c) Average target solution temperature difference between the heating and cooling sectors over the outer wall layer thickness dr_{1234_2} and inner heating wall thickness dr_{12_1} at a cooling wall thickness $dr_{34_1} = 0.057m$



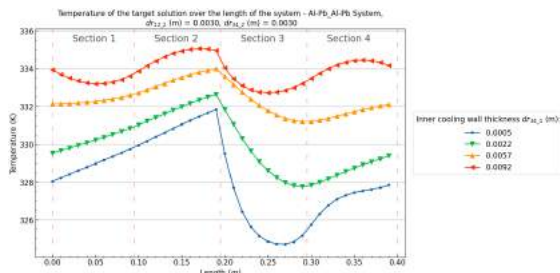
(d) Average target solution temperature difference between the heating and cooling sectors over the outer wall layer thickness dr_{1234_2} and inner heating wall thickness dr_{12_1} at a cooling wall thickness $dr_{34_1} = 0.092m$



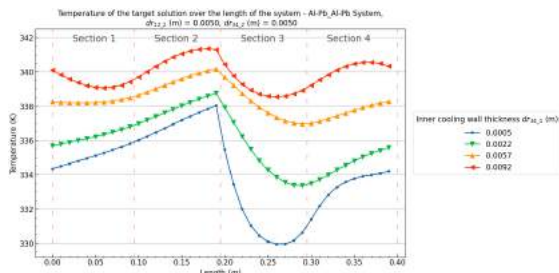
(e) Target solution temperature profile over the length of the Al-Pb/Al-Pb system with an inner heating wall thickness of $dr_{12_1} = 0.0096$ and an outer wall thickness of $dr_{1234_2} = 0.000m$



(f) Target solution temperature profile over the length of the Al-Pb/Al-Pb system with an inner heating wall thickness of $dr_{12_1} = 0.0096$ and an outer wall thickness of $dr_{1234_2} = 0.010m$



(g) Target solution temperature profile over the length of the Al-Pb/Al-Pb system with an inner heating wall thickness of $dr_{12_1} = 0.0096$ and an outer wall thickness of $dr_{1234_2} = 0.030m$

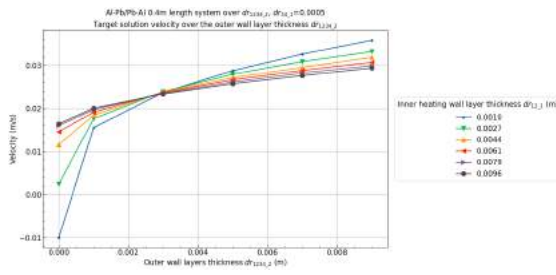


(h) Target solution temperature profile over the length of the Al-Pb/Al-Pb system with an inner heating wall thickness of $dr_{12_1} = 0.0096$ and an outer wall thickness of $dr_{1234_2} = 0.050m$

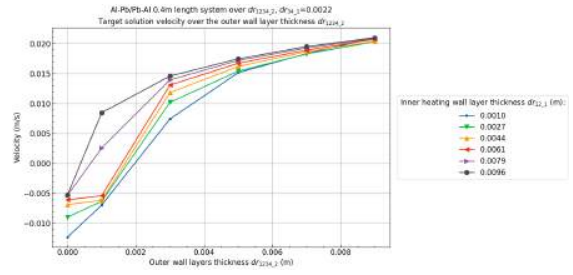
Figure B.21: Al-Pb/Al-Pb (Inner Heat_Outer Heat/Inner Cool_Outer Cool) continued system results over the wall thicknesses of the inner heating, inner cooling and outer wall (dr_{12_1} , dr_{34_1} , and dr_{1234_2} respectively) with a system length (L) of $0.4m$, an inner radius (Ri) of $0.007m$ and a pipe angle (θ) of 5° .

Al-Pb/Pb-Al - Wall thicknesses

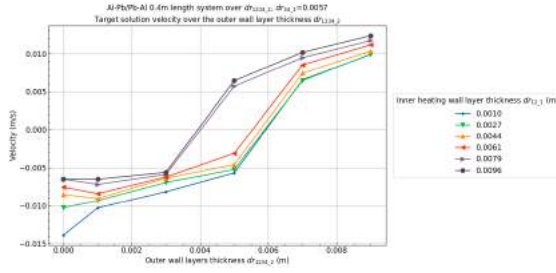
Back to overview - B.1.2



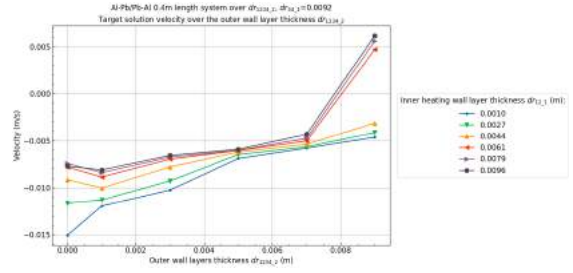
(a) Velocity over the outer wall layer thickness dr_{1234_2} and inner heating wall thickness dr_{12_1} at a cooling wall thickness $dr_{34_1} = 0.0005m$



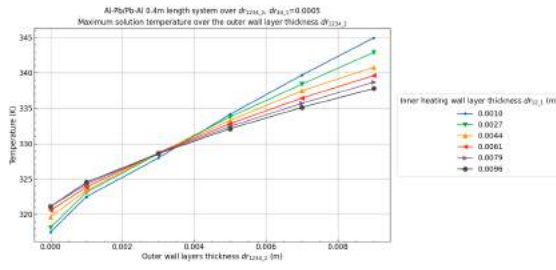
(b) Velocity over the outer wall layer thickness dr_{1234_2} and inner heating wall thickness dr_{12_1} at a cooling wall thickness $dr_{34_1} = 0.0022m$



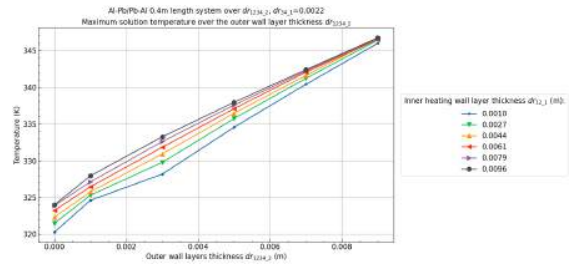
(c) Velocity over the outer wall layer thickness dr_{1234_2} and inner heating wall thickness dr_{12_1} at a cooling wall thickness $dr_{34_1} = 0.0057m$



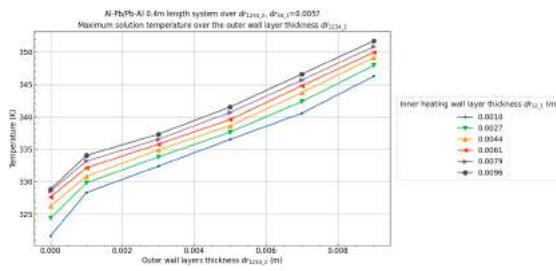
(d) Velocity over the outer wall layer thickness dr_{1234_2} and inner heating wall thickness dr_{12_1} at a cooling wall thickness $dr_{34_1} = 0.0092m$



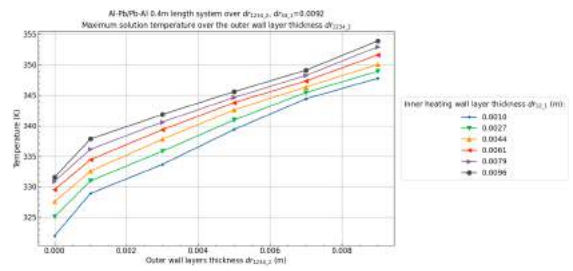
(e) Maximum target solution temperature over the outer wall layer thickness dr_{1234_2} and inner heating wall thickness dr_{12_1} at a cooling wall thickness $dr_{34_1} = 0.0005m$



(f) Maximum target solution temperature over the outer wall layer thickness dr_{1234_2} and inner heating wall thickness dr_{12_1} at a cooling wall thickness $dr_{34_1} = 0.0022m$

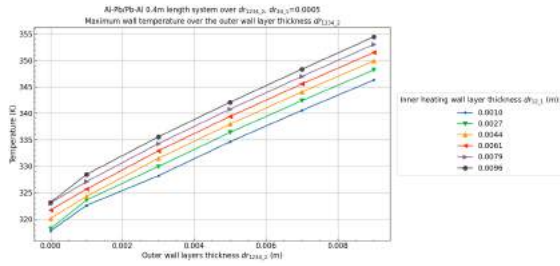


(g) Maximum target solution temperature over the outer wall layer thickness dr_{1234_2} and inner heating wall thickness dr_{12_1} at a cooling wall thickness $dr_{34_1} = 0.0057m$

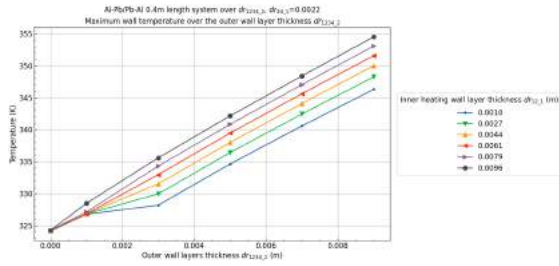


(h) Maximum target solution temperature over the outer wall layer thickness dr_{1234_2} and inner heating wall thickness dr_{12_1} at a cooling wall thickness $dr_{34_1} = 0.0092m$

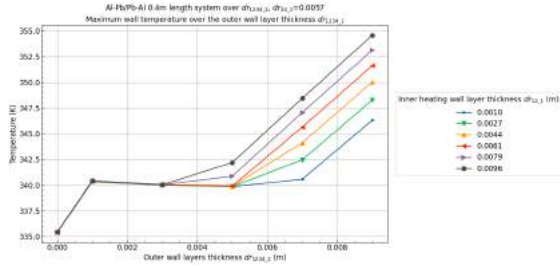
Figure B.22: Al-Pb/Pb-Al (Inner Heat_Outer Heat/Inner Cool_Outer Cool) system results over the wall thicknesses of the inner heating, inner cooling and outer wall (dr_{12_1} , dr_{34_1} , and dr_{1234_2} respectively) with a system length (L) of $0.4m$, an inner radius (Ri) of $0.007m$ and a pipe angle (θ) of 5° .



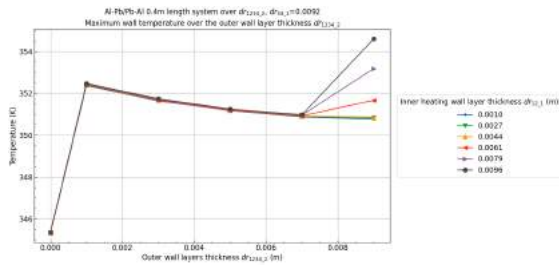
(a) Maximum wall temperature over the outer wall layer thickness dr_{1234_2} and inner heating wall thickness dr_{12_1} at a cooling wall thickness $dr_{34_1} = 0.0005m$



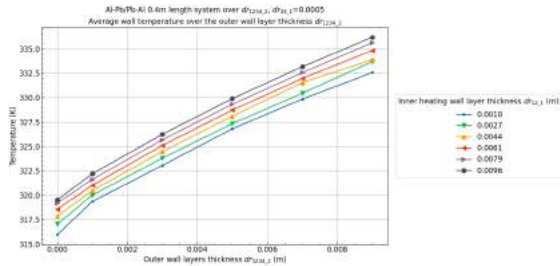
(b) Maximum wall temperature over the outer wall layer thickness dr_{1234_2} and inner heating wall thickness dr_{12_1} at a cooling wall thickness $dr_{34_1} = 0.0022m$



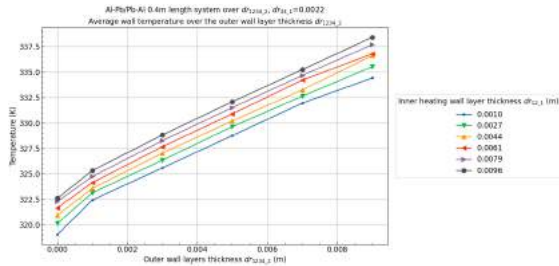
(c) Maximum wall temperature over the outer wall layer thickness dr_{1234_2} and inner heating wall thickness dr_{12_1} at a cooling wall thickness $dr_{34_1} = 0.0057m$



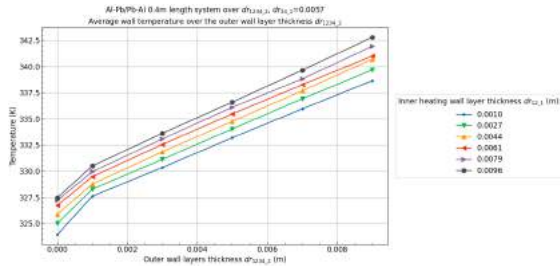
(d) Maximum wall temperature over the outer wall layer thickness dr_{1234_2} and inner heating wall thickness dr_{12_1} at a cooling wall thickness $dr_{34_1} = 0.0092m$



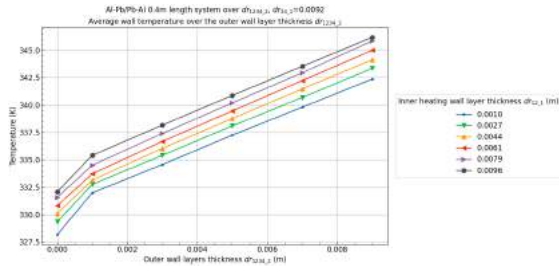
(e) Average wall temperature over the outer wall layer thickness dr_{1234_2} and inner heating wall thickness dr_{12_1} at a cooling wall thickness $dr_{34_1} = 0.0005m$



(f) Average wall temperature over the outer wall layer thickness dr_{1234_2} and inner heating wall thickness dr_{12_1} at a cooling wall thickness $dr_{34_1} = 0.0022m$

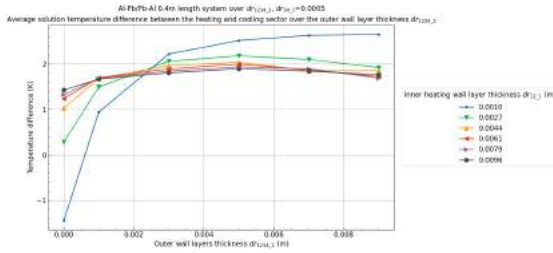


(g) Average wall temperature over the outer wall layer thickness dr_{1234_2} and inner heating wall thickness dr_{12_1} at a cooling wall thickness $dr_{34_1} = 0.0057m$

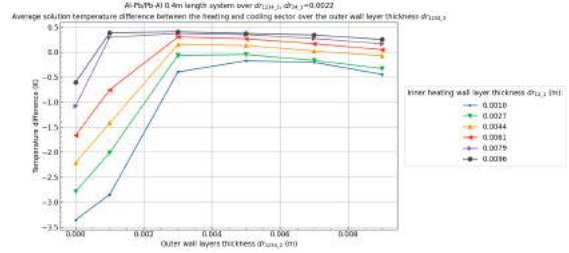


(h) Average wall temperature over the outer wall layer thickness dr_{1234_2} and inner heating wall thickness dr_{12_1} at a cooling wall thickness $dr_{34_1} = 0.0092m$

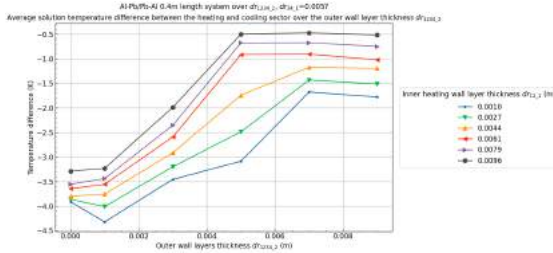
Figure B.23: Al-Pb/Pb-Al (Inner Heat_Outer Heat/Inner Cool_Outer Cool) continued system results over the wall thicknesses of the inner heating, inner cooling and outer wall (dr_{12_1} , dr_{34_1} , and dr_{1234_2} respectively) with a system length (L) of $0.4m$, an inner radius (Ri) of $0.007m$ and a pipe angle (θ) of 5° .



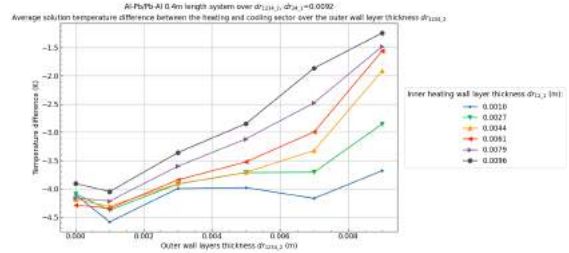
(a) Average target solution temperature difference between the heating and cooling sectors over the outer wall layer thickness dr_{1234_2} and inner heating wall thickness dr_{12_1} at a cooling wall thickness $dr_{34_1} = 0.005m$



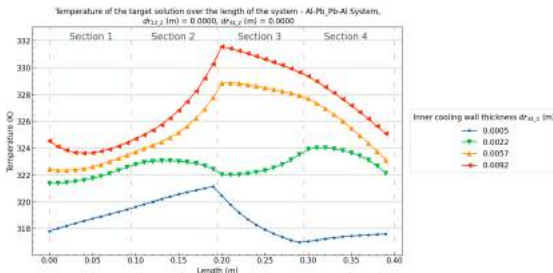
(b) Average target solution temperature difference between the heating and cooling sectors over the outer wall layer thickness dr_{1234_2} and inner heating wall thickness dr_{12_1} at a cooling wall thickness $dr_{34_1} = 0.022m$



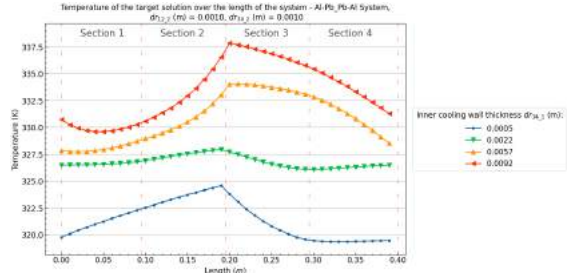
(c) Average target solution temperature difference between the heating and cooling sectors over the outer wall layer thickness dr_{1234_2} and inner heating wall thickness dr_{12_1} at a cooling wall thickness $dr_{34_1} = 0.057m$



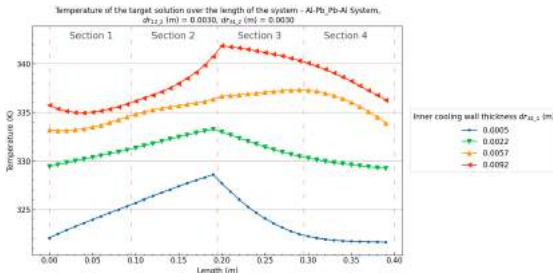
(d) Average target solution temperature difference between the heating and cooling sectors over the outer wall layer thickness dr_{1234_2} and inner heating wall thickness dr_{12_1} at a cooling wall thickness $dr_{34_1} = 0.092m$



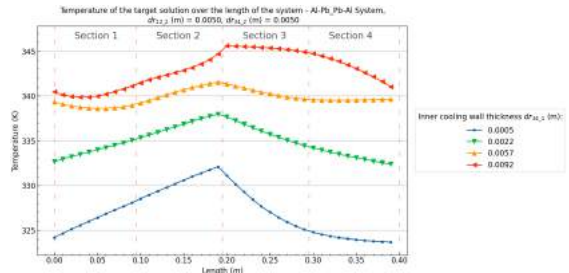
(e) Target solution temperature profile over the length of the Al-Pb/Pb-Al system with an inner heating wall thickness of $dr_{12_1} = 0.0096$ and an outer wall thickness of $dr_{1234_2} = 0.000m$



(f) Target solution temperature profile over the length of the Al-Pb/Pb-Al system with an inner heating wall thickness of $dr_{12_1} = 0.0096$ and an outer wall thickness of $dr_{1234_2} = 0.010m$



(g) Target solution temperature profile over the length of the Al-Pb/Pb-Al system with an inner heating wall thickness of $dr_{12_1} = 0.0096$ and an outer wall thickness of $dr_{1234_2} = 0.030m$

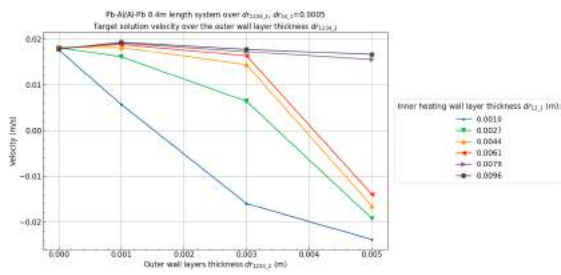


(h) Target solution temperature profile over the length of the Al-Pb/Pb-Al system with an inner heating wall thickness of $dr_{12_1} = 0.0096$ and an outer wall thickness of $dr_{1234_2} = 0.050m$

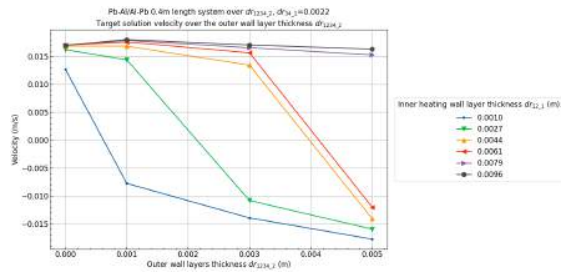
Figure B.24: Al-Pb/Pb-Al (Inner Heat_Outer Heat/Inner Cool_Outer Cool) continued system results over the wall thicknesses of the inner heating, inner cooling and outer wall (dr_{12_1} , dr_{34_1} , and dr_{1234_2} respectively) with a system length (L) of $0.4m$, an inner radius (Ri) of $0.007m$ and a pipe angle (θ) of 5° .

Pb-Al/Al-Pb - Wall thicknesses

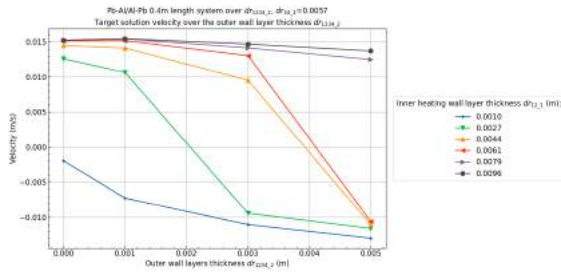
Back to overview - B.1.2



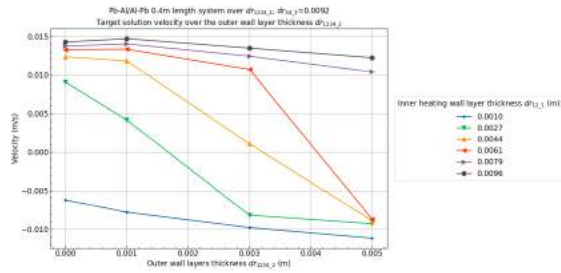
(a) Velocity over the outer wall layer thickness dr_{1234_2} and inner heating wall thickness dr_{12_1} at a cooling wall thickness $dr_{34_1} = 0.0005m$



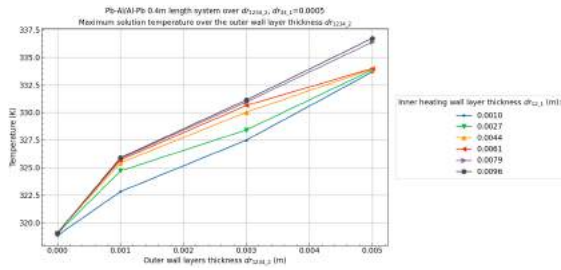
(b) Velocity over the outer wall layer thickness dr_{1234_2} and inner heating wall thickness dr_{12_1} at a cooling wall thickness $dr_{34_1} = 0.0022m$



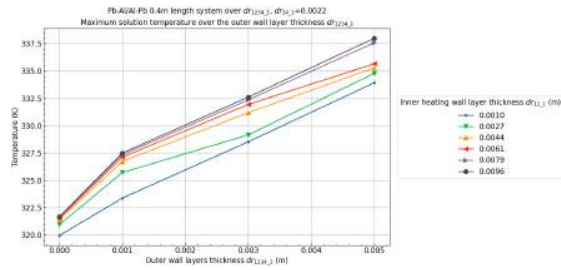
(c) Velocity over the outer wall layer thickness dr_{1234_2} and inner heating wall thickness dr_{12_1} at a cooling wall thickness $dr_{34_1} = 0.0057m$



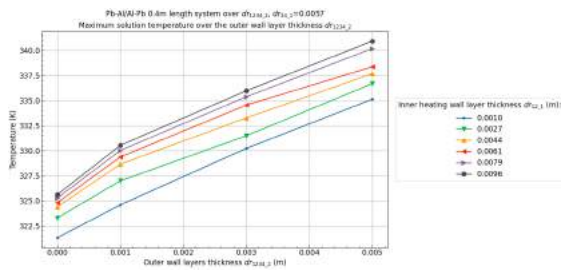
(d) Velocity over the outer wall layer thickness dr_{1234_2} and inner heating wall thickness dr_{12_1} at a cooling wall thickness $dr_{34_1} = 0.0092m$



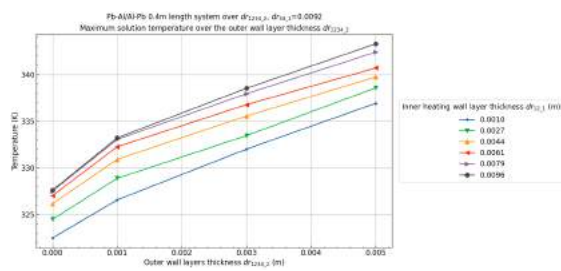
(e) Maximum target solution temperature over the outer wall layer thickness dr_{1234_2} and inner heating wall thickness dr_{12_1} at a cooling wall thickness $dr_{34_1} = 0.0005m$



(f) Maximum target solution temperature over the outer wall layer thickness dr_{1234_2} and inner heating wall thickness dr_{12_1} at a cooling wall thickness $dr_{34_1} = 0.0022m$

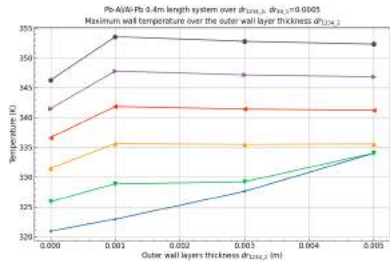


(g) Maximum target solution temperature over the outer wall layer thickness dr_{1234_2} and inner heating wall thickness dr_{12_1} at a cooling wall thickness $dr_{34_1} = 0.0057m$

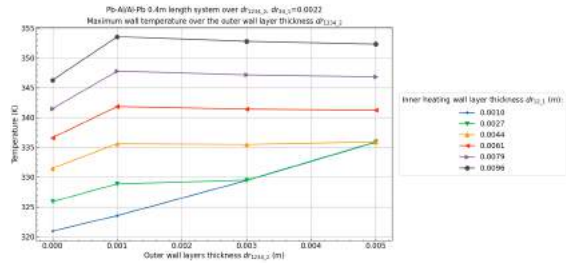


(h) Maximum target solution temperature over the outer wall layer thickness dr_{1234_2} and inner heating wall thickness dr_{12_1} at a cooling wall thickness $dr_{34_1} = 0.0092m$

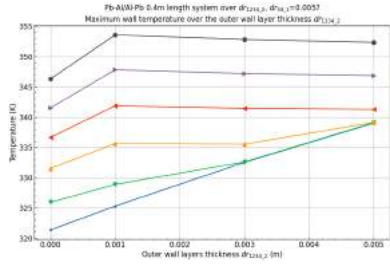
Figure B.25: Pb-Al/Al-Pb (Inner Heat_Outer Heat/Inner Cool_Outer Cool) system results over the wall thicknesses of the inner heating, inner cooling and outer wall (dr_{12_1} , dr_{34_1} , and dr_{1234_2} respectively) with a system length (L) of $0.4m$, an inner radius (Ri) of $0.007m$ and a pipe angle (θ) of 5° .



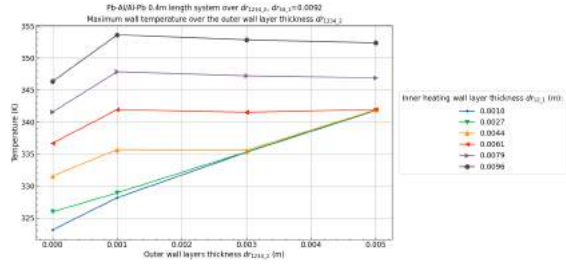
(a) Maximum wall temperature over the outer wall layer thickness dr_{1234_2} and inner heating wall thickness dr_{12_1} at a cooling wall thickness $dr_{34_1} = 0.0005m$



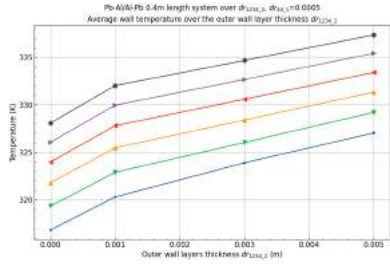
(b) Maximum wall temperature over the outer wall layer thickness dr_{1234_2} and inner heating wall thickness dr_{12_1} at a cooling wall thickness $dr_{34_1} = 0.0022m$



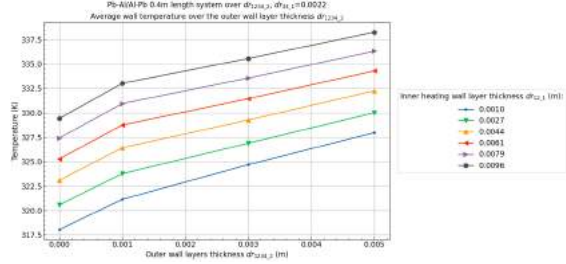
(c) Maximum wall temperature over the outer wall layer thickness dr_{1234_2} and inner heating wall thickness dr_{12_1} at a cooling wall thickness $dr_{34_1} = 0.0057m$



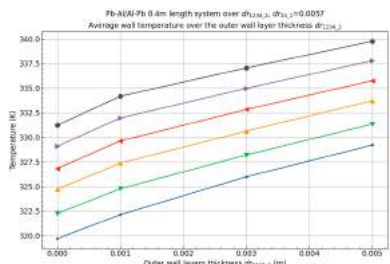
(d) Maximum wall temperature over the outer wall layer thickness dr_{1234_2} and inner heating wall thickness dr_{12_1} at a cooling wall thickness $dr_{34_1} = 0.0092m$



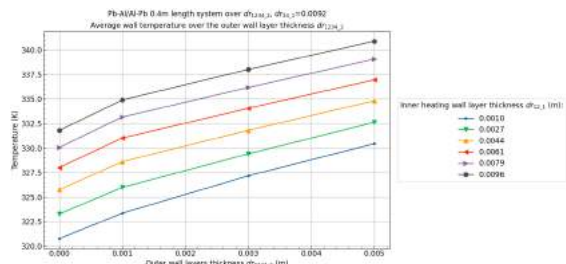
(e) Average wall temperature over the outer wall layer thickness dr_{1234_2} and inner heating wall thickness dr_{12_1} at a cooling wall thickness $dr_{34_1} = 0.0005m$



(f) Average wall temperature over the outer wall layer thickness dr_{1234_2} and inner heating wall thickness dr_{12_1} at a cooling wall thickness $dr_{34_1} = 0.0022m$

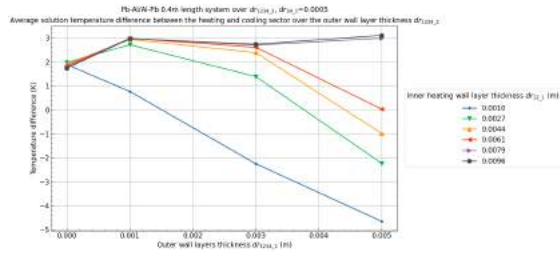


(g) Average wall temperature over the outer wall layer thickness dr_{1234_2} and inner heating wall thickness dr_{12_1} at a cooling wall thickness $dr_{34_1} = 0.0057m$

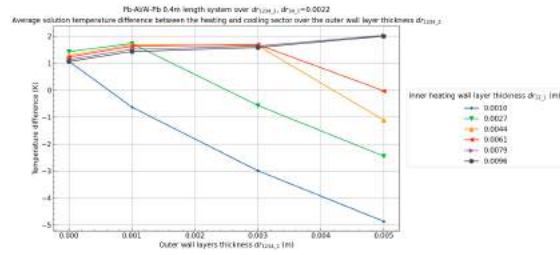


(h) Average wall temperature over the outer wall layer thickness dr_{1234_2} and inner heating wall thickness dr_{12_1} at a cooling wall thickness $dr_{34_1} = 0.0092m$

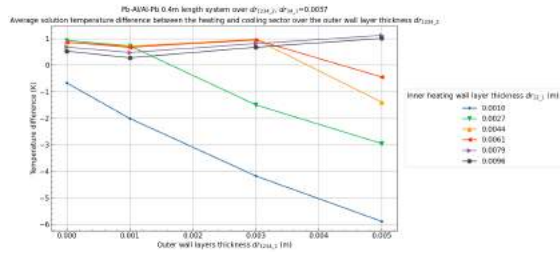
Figure B.26: Pb-Al/Al-Pb (Inner Heat_Outer Heat/Inner Cool_Outer Cool) continued system results over the wall thicknesses of the inner heating, inner cooling and outer wall (dr_{12_1} , dr_{34_1} , and dr_{1234_2} respectively) with a system length (L) of $0.4m$, an inner radius (Ri) of $0.007m$ and a pipe angle (θ) of 5° .



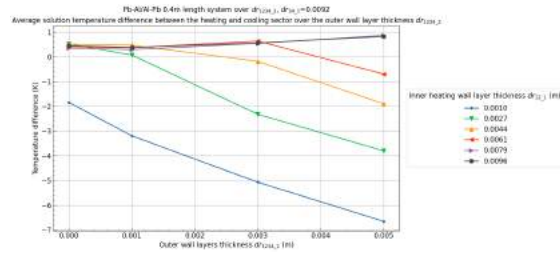
(a) Average target solution temperature difference between the heating and cooling sectors over the outer wall layer thickness dr_{1234_2} and inner heating wall thickness dr_{12_1} at a cooling wall thickness $dr_{34_1} = 0.005m$



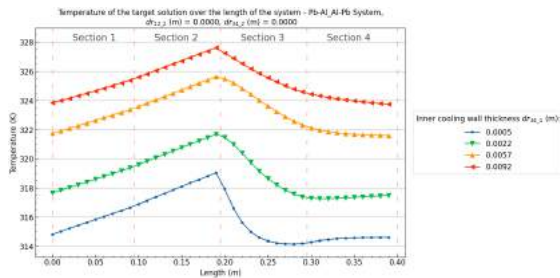
(b) Average target solution temperature difference between the heating and cooling sectors over the outer wall layer thickness dr_{1234_2} and inner heating wall thickness dr_{12_1} at a cooling wall thickness $dr_{34_1} = 0.022m$



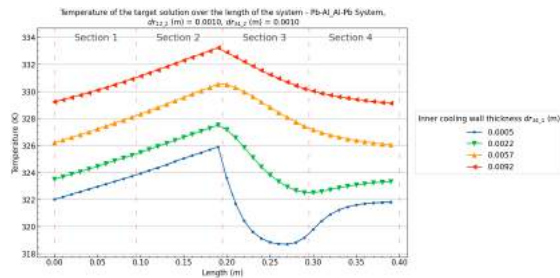
(c) Average target solution temperature difference between the heating and cooling sectors over the outer wall layer thickness dr_{1234_2} and inner heating wall thickness dr_{12_1} at a cooling wall thickness $dr_{34_1} = 0.057m$



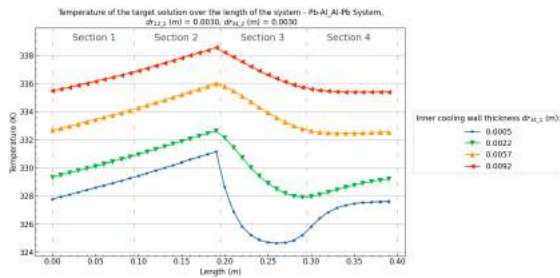
(d) Average target solution temperature difference between the heating and cooling sectors over the outer wall layer thickness dr_{1234_2} and inner heating wall thickness dr_{12_1} at a cooling wall thickness $dr_{34_1} = 0.092m$



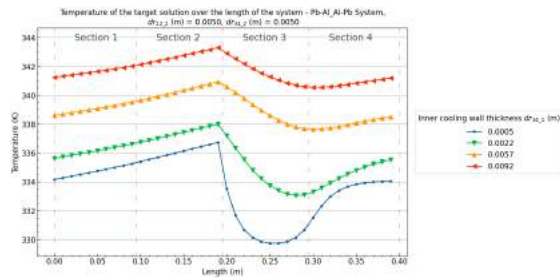
(e) Target solution temperature profile over the length of the Pb-Al/Al-Pb system with an inner heating wall thickness of $dr_{12_1} = 0.0096$ and an outer wall thickness of $dr_{1234_2} = 0.000m$



(f) Target solution temperature profile over the length of the Pb-Al/Al-Pb system with an inner heating wall thickness of $dr_{12_1} = 0.0096$ and an outer wall thickness of $dr_{1234_2} = 0.010m$



(g) Target solution temperature profile over the length of the Pb-Al/Al-Pb system with an inner heating wall thickness of $dr_{12_1} = 0.0096$ and an outer wall thickness of $dr_{1234_2} = 0.030m$

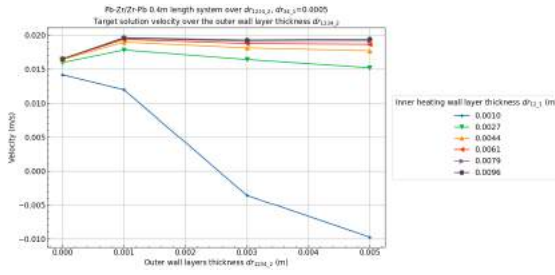


(h) Target solution temperature profile over the length of the Pb-Al/Al-Pb system with an inner heating wall thickness of $dr_{12_1} = 0.0096$ and an outer wall thickness of $dr_{1234_2} = 0.050m$

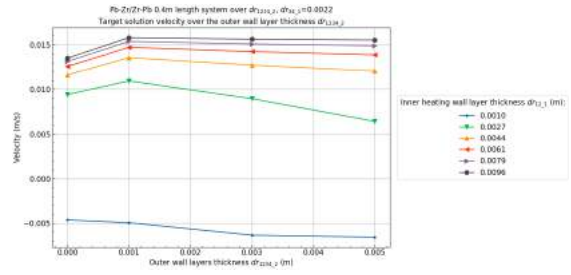
Figure B.27: Pb-Al/Al-Pb (Inner Heat_Outer Heat/Inner Cool_Outer Cool) continued system results over the wall thicknesses of the inner heating, inner cooling and outer wall (dr_{12_1} , dr_{34_1} , and dr_{1234_2} respectively) with a system length (L) of $0.4m$, an inner radius (Ri) of $0.007m$ and a pipe angle (θ) of 5° .

Pb-Zr/Zr-Pb - Wall thicknesses

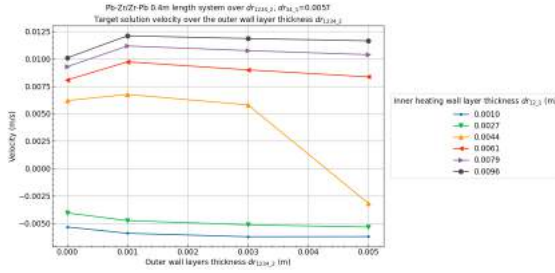
Back to overview - B.1.2



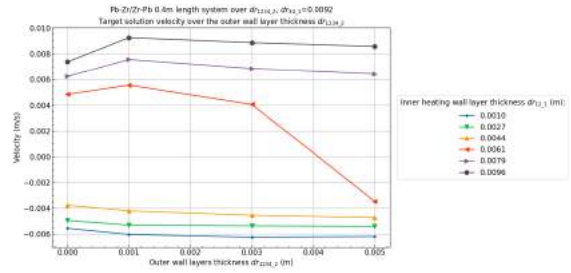
(a) Velocity over the outer wall layer thickness $dr_{1234,2}$ and inner heating wall thickness $dr_{12,1}$ at a cooling wall thickness $dr_{34,1} = 0.0005m$



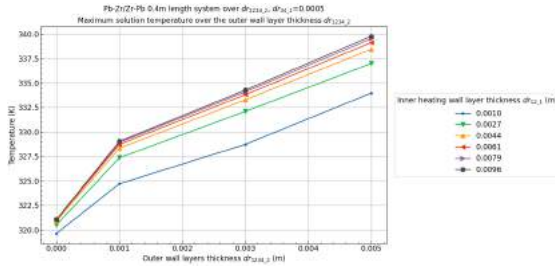
(b) Velocity over the outer wall layer thickness $dr_{1234,2}$ and inner heating wall thickness $dr_{12,1}$ at a cooling wall thickness $dr_{34,1} = 0.0022m$



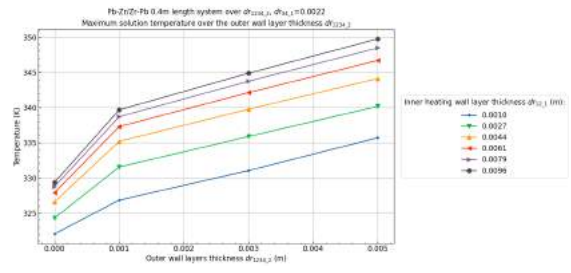
(c) Velocity over the outer wall layer thickness $dr_{1234,2}$ and inner heating wall thickness $dr_{12,1}$ at a cooling wall thickness $dr_{34,1} = 0.0057m$



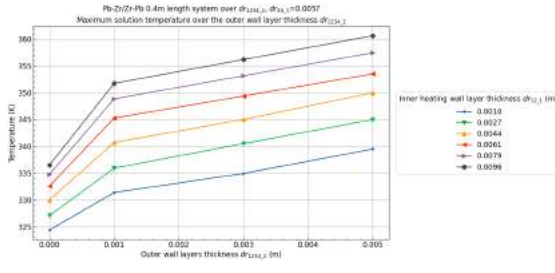
(d) Velocity over the outer wall layer thickness $dr_{1234,2}$ and inner heating wall thickness $dr_{12,1}$ at a cooling wall thickness $dr_{34,1} = 0.0092m$



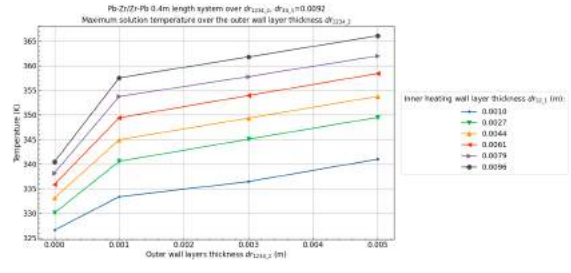
(e) Maximum target solution temperature over the outer wall layer thickness $dr_{1234,2}$ and inner heating wall thickness $dr_{12,1}$ at a cooling wall thickness $dr_{34,1} = 0.0005m$



(f) Maximum target solution temperature over the outer wall layer thickness $dr_{1234,2}$ and inner heating wall thickness $dr_{12,1}$ at a cooling wall thickness $dr_{34,1} = 0.0022m$

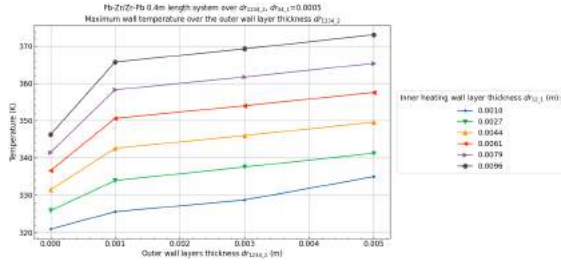


(g) Maximum target solution temperature over the outer wall layer thickness $dr_{1234,2}$ and inner heating wall thickness $dr_{12,1}$ at a cooling wall thickness $dr_{34,1} = 0.0057m$

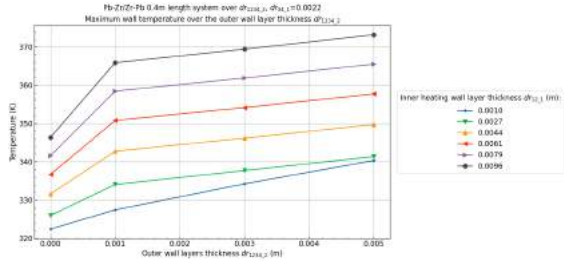


(h) Maximum target solution temperature over the outer wall layer thickness $dr_{1234,2}$ and inner heating wall thickness $dr_{12,1}$ at a cooling wall thickness $dr_{34,1} = 0.0092m$

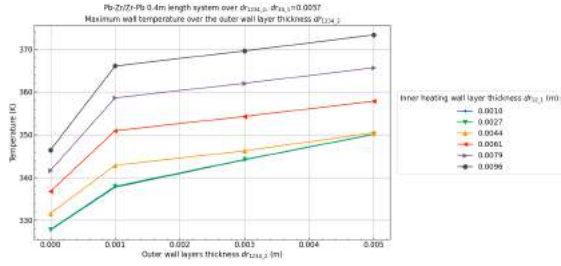
Figure B.28: Pb-Zr/Zr-Pb (Inner Heat_Outer Heat/Inner Cool_Outer Cool) system results over the wall thicknesses of the inner heating, inner cooling and outer wall ($dr_{12,1}$, $dr_{34,1}$, and $dr_{1234,2}$ respectively) with a system length (L) of $0.4m$, an inner radius (R_i) of $0.007m$ and a pipe angle (θ) of 5° .



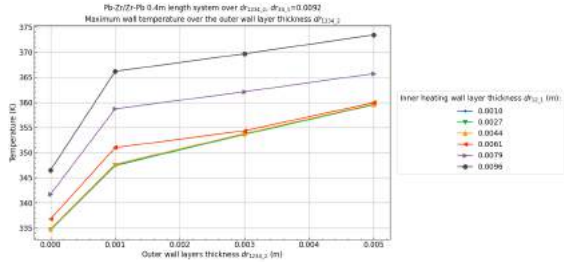
(a) Maximum wall temperature over the outer wall layer thickness dr_{1234_2} and inner heating wall thickness dr_{12_1} at a cooling wall thickness $dr_{34_1} = 0.0005m$



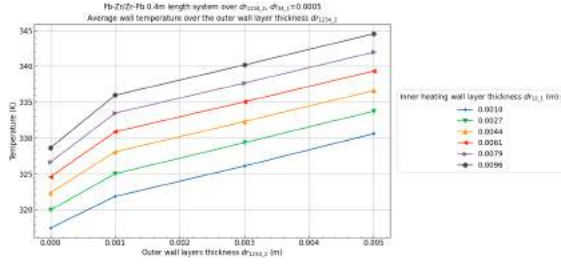
(b) Maximum wall temperature over the outer wall layer thickness dr_{1234_2} and inner heating wall thickness dr_{12_1} at a cooling wall thickness $dr_{34_1} = 0.0022m$



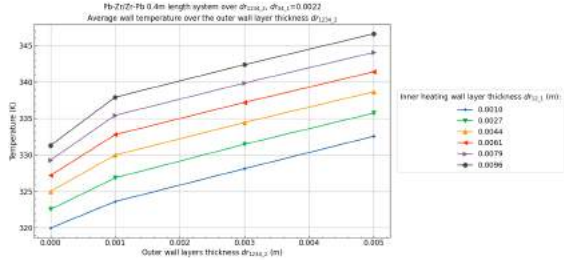
(c) Maximum wall temperature over the outer wall layer thickness dr_{1234_2} and inner heating wall thickness dr_{12_1} at a cooling wall thickness $dr_{34_1} = 0.0057m$



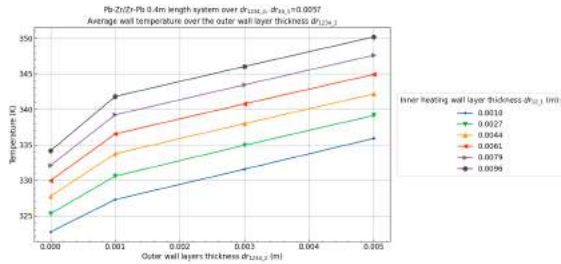
(d) Maximum wall temperature over the outer wall layer thickness dr_{1234_2} and inner heating wall thickness dr_{12_1} at a cooling wall thickness $dr_{34_1} = 0.0092m$



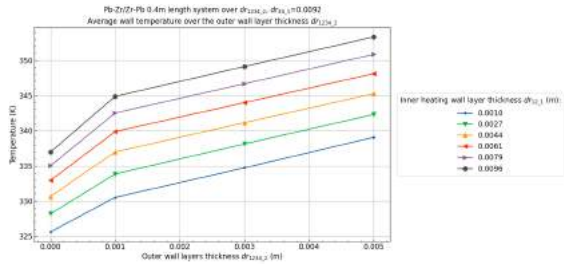
(e) Average wall temperature over the outer wall layer thickness dr_{1234_2} and inner heating wall thickness dr_{12_1} at a cooling wall thickness $dr_{34_1} = 0.0005m$



(f) Average wall temperature over the outer wall layer thickness dr_{1234_2} and inner heating wall thickness dr_{12_1} at a cooling wall thickness $dr_{34_1} = 0.0022m$

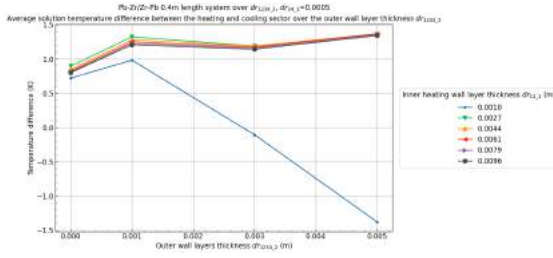


(g) Average wall temperature over the outer wall layer thickness dr_{1234_2} and inner heating wall thickness dr_{12_1} at a cooling wall thickness $dr_{34_1} = 0.0057m$

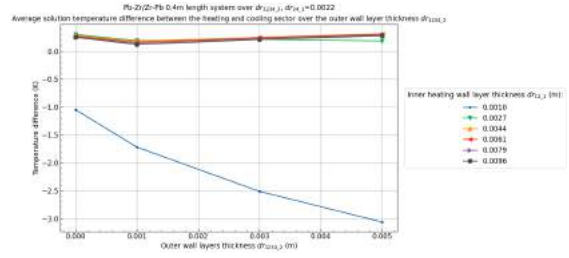


(h) Average wall temperature over the outer wall layer thickness dr_{1234_2} and inner heating wall thickness dr_{12_1} at a cooling wall thickness $dr_{34_1} = 0.0092m$

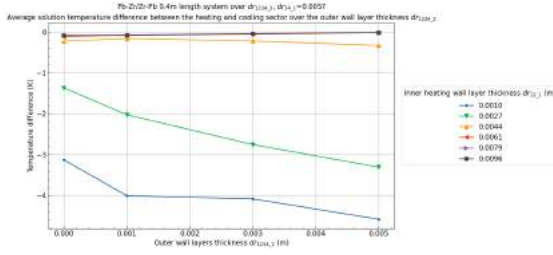
Figure B.29: Pb-Zr/Zr-Pb (Inner Heat_Outer Heat/Inner Cool_Outer Cool) continued system results over the wall thicknesses of the inner heating, inner cooling and outer wall (dr_{12_1} , dr_{34_1} , and dr_{1234_2} respectively) with a system length (L) of $0.4m$, an inner radius (Ri) of $0.007m$ and a pipe angle (θ) of 5° .



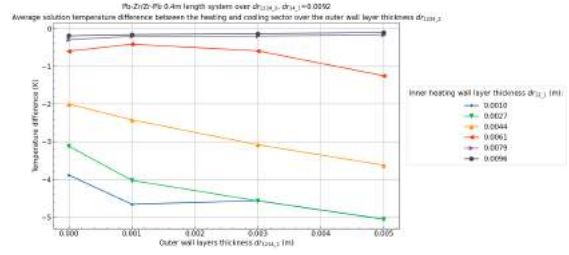
(a) Average target solution temperature difference between the heating and cooling sectors over the outer wall layer thickness dr_{1234_2} and inner heating wall thickness dr_{12_1} at a cooling wall thickness $dr_{34_1} = 0.005m$



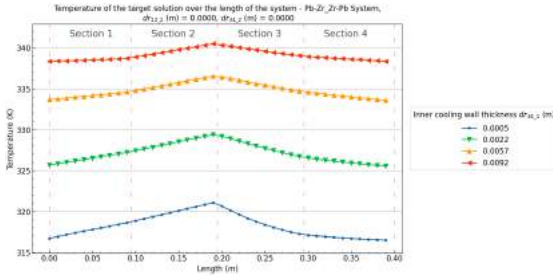
(b) Average target solution temperature difference between the heating and cooling sectors over the outer wall layer thickness dr_{1234_2} and inner heating wall thickness dr_{12_1} at a cooling wall thickness $dr_{34_1} = 0.022m$



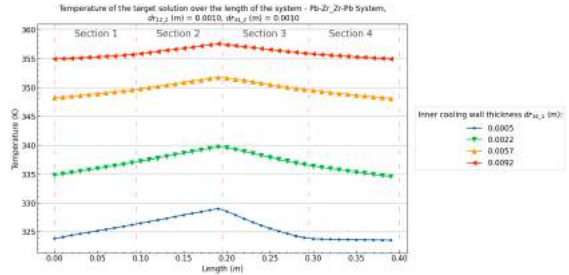
(c) Average target solution temperature difference between the heating and cooling sectors over the outer wall layer thickness dr_{1234_2} and inner heating wall thickness dr_{12_1} at a cooling wall thickness $dr_{34_1} = 0.057m$



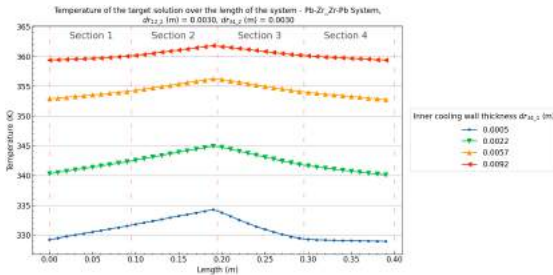
(d) Average target solution temperature difference between the heating and cooling sectors over the outer wall layer thickness dr_{1234_2} and inner heating wall thickness dr_{12_1} at a cooling wall thickness $dr_{34_1} = 0.092m$



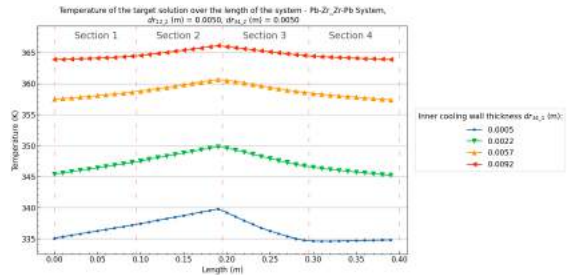
(e) Target solution temperature profile over the length of the Pb-Zr/Zr-Pb system with an inner heating wall thickness of $dr_{12_1} = 0.0096$ and an outer wall thickness of $dr_{1234_2} = 0.000m$



(f) Target solution temperature profile over the length of the Pb-Zr/Zr-Pb system with an inner heating wall thickness of $dr_{12_1} = 0.0096$ and an outer wall thickness of $dr_{1234_2} = 0.010m$



(g) Target solution temperature profile over the length of the Pb-Zr/Zr-Pb system with an inner heating wall thickness of $dr_{12_1} = 0.0096$ and an outer wall thickness of $dr_{1234_2} = 0.030m$

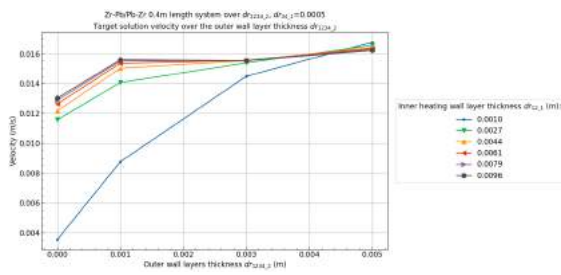


(h) Target solution temperature profile over the length of the Pb-Zr/Zr-Pb system with an inner heating wall thickness of $dr_{12_1} = 0.0096$ and an outer wall thickness of $dr_{1234_2} = 0.050m$

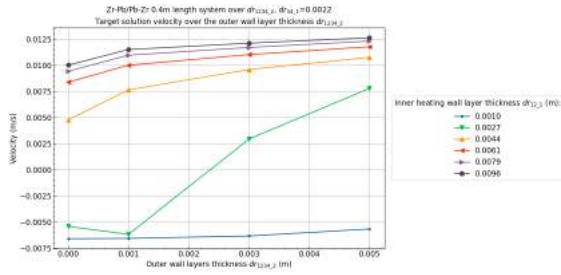
Figure B.30: Pb-Zr/Zr-Pb (Inner Heat_Outer Heat/Inner Cool_Outer Cool) continued system results over the wall thicknesses of the inner heating, inner cooling and outer wall (dr_{12_1} , dr_{34_1} , and dr_{1234_2} respectively) with a system length (L) of $0.4m$, an inner radius (Ri) of $0.007m$ and a pipe angle (θ) of 5° .

Zr-Pb/Pb-Zr - Wall thicknesses

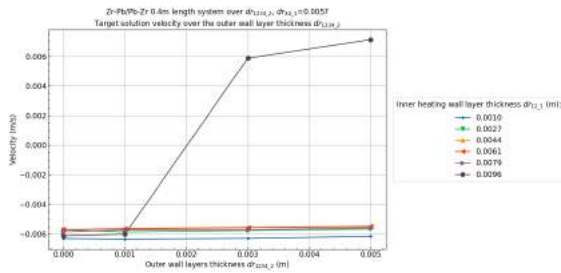
Back to overview - B.1.2



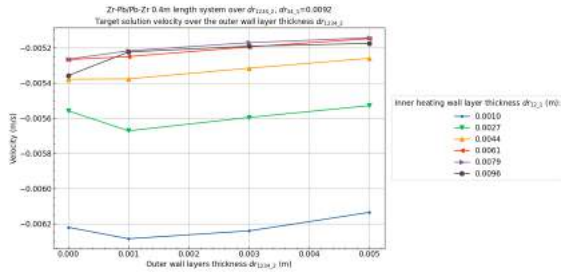
(a) Velocity over the outer wall layer thickness $dr_{1234,2}$ and inner heating wall thickness $dr_{12,1}$ at a cooling wall thickness $dr_{34,1} = 0.0005m$



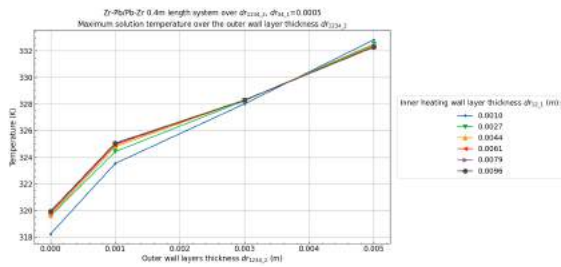
(b) Velocity over the outer wall layer thickness $dr_{1234,2}$ and inner heating wall thickness $dr_{12,1}$ at a cooling wall thickness $dr_{34,1} = 0.0022m$



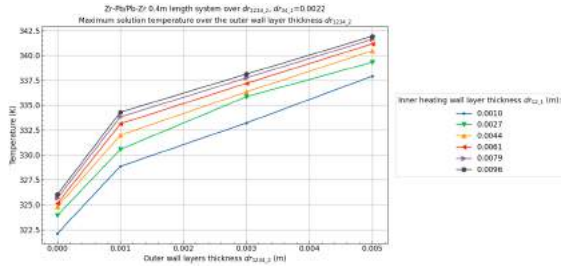
(c) Velocity over the outer wall layer thickness $dr_{1234,2}$ and inner heating wall thickness $dr_{12,1}$ at a cooling wall thickness $dr_{34,1} = 0.0057m$



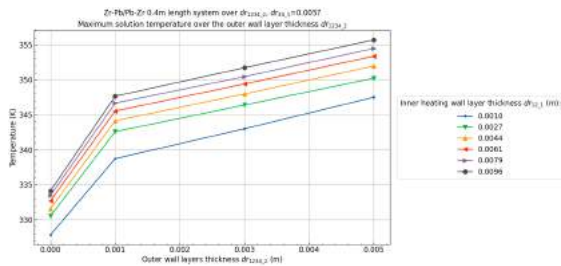
(d) Velocity over the outer wall layer thickness $dr_{1234,2}$ and inner heating wall thickness $dr_{12,1}$ at a cooling wall thickness $dr_{34,1} = 0.0092m$



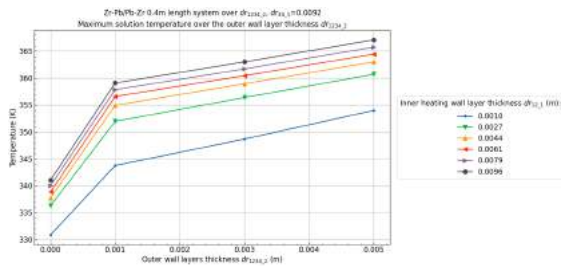
(e) Maximum target solution temperature over the outer wall layer thickness $dr_{1234,2}$ and inner heating wall thickness $dr_{12,1}$ at a cooling wall thickness $dr_{34,1} = 0.0005m$



(f) Maximum target solution temperature over the outer wall layer thickness $dr_{1234,2}$ and inner heating wall thickness $dr_{12,1}$ at a cooling wall thickness $dr_{34,1} = 0.0022m$

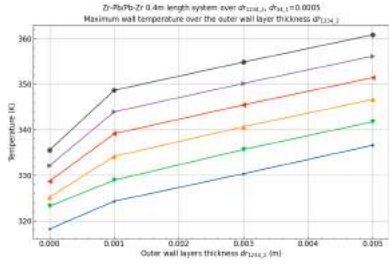


(g) Maximum target solution temperature over the outer wall layer thickness $dr_{1234,2}$ and inner heating wall thickness $dr_{12,1}$ at a cooling wall thickness $dr_{34,1} = 0.0057m$

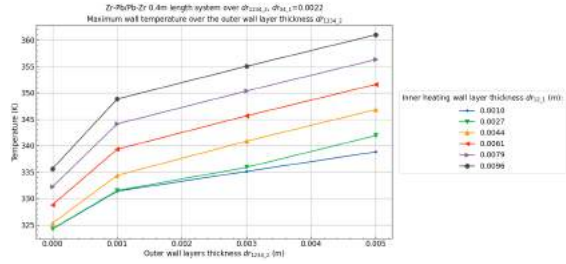


(h) Maximum target solution temperature over the outer wall layer thickness $dr_{1234,2}$ and inner heating wall thickness $dr_{12,1}$ at a cooling wall thickness $dr_{34,1} = 0.0092m$

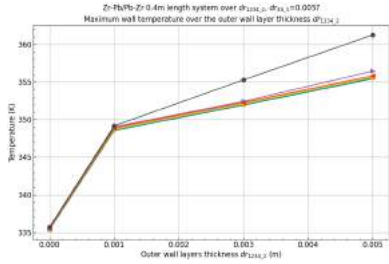
Figure B.31: Zr-Pb/Pb-Zr (Inner Heat_Outer Heat/Inner Cool_Outer Cool) system results over the wall thicknesses of the inner heating, inner cooling and outer wall ($dr_{12,1}$, $dr_{34,1}$, and $dr_{1234,2}$ respectively) with a system length (L) of $0.4m$, an inner radius (R_i) of $0.007m$ and a pipe angle (θ) of 5° .



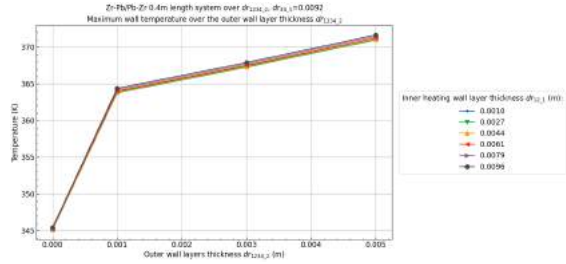
(a) Maximum wall temperature over the outer wall layer thickness $dr_{1234,2}$ and inner heating wall thickness $dr_{12,1}$ at a cooling wall thickness $dr_{34,1} = 0.0005m$



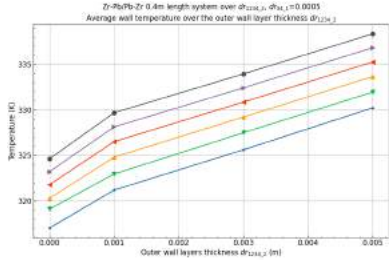
(b) Maximum wall temperature over the outer wall layer thickness $dr_{1234,2}$ and inner heating wall thickness $dr_{12,1}$ at a cooling wall thickness $dr_{34,1} = 0.0022m$



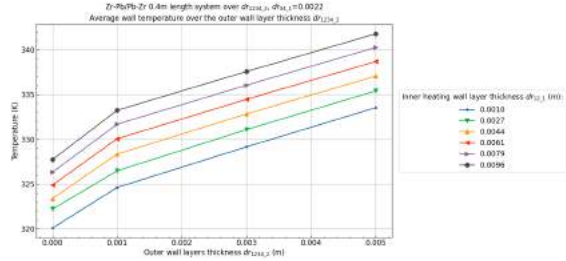
(c) Maximum wall temperature over the outer wall layer thickness $dr_{1234,2}$ and inner heating wall thickness $dr_{12,1}$ at a cooling wall thickness $dr_{34,1} = 0.0057m$



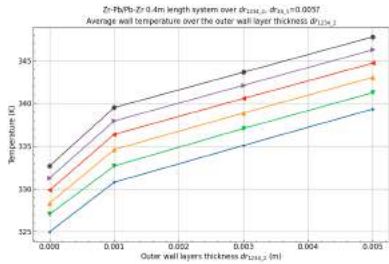
(d) Maximum wall temperature over the outer wall layer thickness $dr_{1234,2}$ and inner heating wall thickness $dr_{12,1}$ at a cooling wall thickness $dr_{34,1} = 0.0092m$



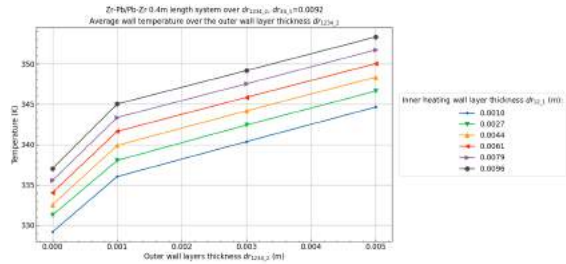
(e) Average wall temperature over the outer wall layer thickness $dr_{1234,2}$ and inner heating wall thickness $dr_{12,1}$ at a cooling wall thickness $dr_{34,1} = 0.0005m$



(f) Average wall temperature over the outer wall layer thickness $dr_{1234,2}$ and inner heating wall thickness $dr_{12,1}$ at a cooling wall thickness $dr_{34,1} = 0.0022m$

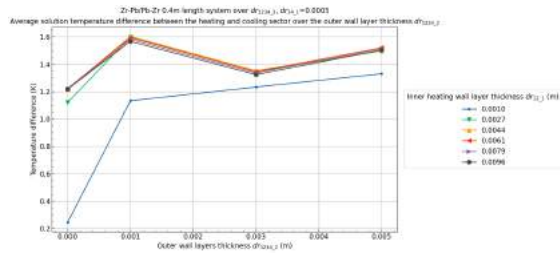


(g) Average wall temperature over the outer wall layer thickness $dr_{1234,2}$ and inner heating wall thickness $dr_{12,1}$ at a cooling wall thickness $dr_{34,1} = 0.0057m$

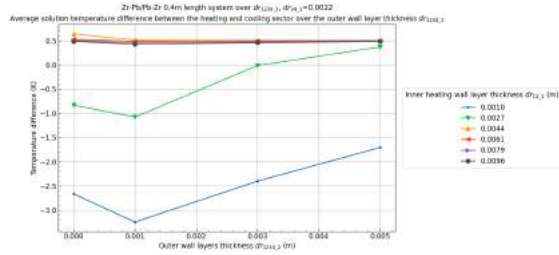


(h) Average wall temperature over the outer wall layer thickness $dr_{1234,2}$ and inner heating wall thickness $dr_{12,1}$ at a cooling wall thickness $dr_{34,1} = 0.0092m$

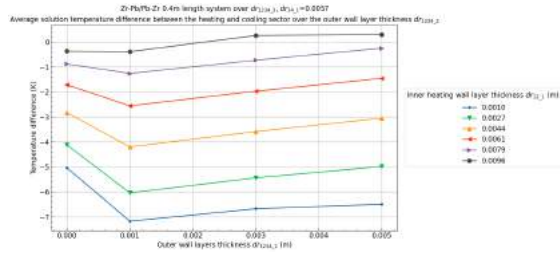
Figure B.32: Zr-Pb/Pb-Zr (Inner Heat_Outer Heat/Inner Cool_Outer Cool) continued system results over the wall thicknesses of the inner heating, inner cooling and outer wall ($dr_{12,1}$, $dr_{34,1}$, and $dr_{1234,2}$ respectively) with a system length (L) of $0.4m$, an inner radius (R_i) of $0.007m$ and a pipe angle (θ) of 5° .



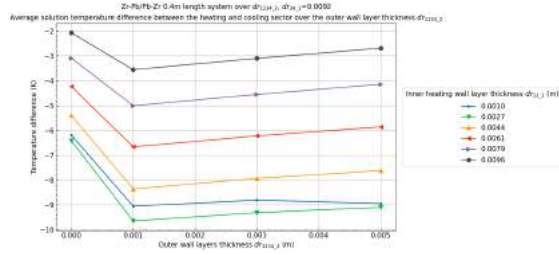
(a) Average target solution temperature difference between the heating and cooling sectors over the outer wall layer thickness dr_{1234_2} and inner heating wall thickness dr_{12_1} at a cooling wall thickness $dr_{34_1} = 0.005m$



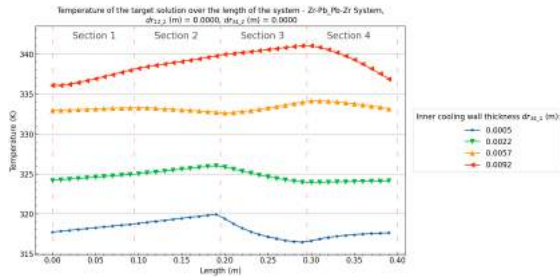
(b) Average target solution temperature difference between the heating and cooling sectors over the outer wall layer thickness dr_{1234_2} and inner heating wall thickness dr_{12_1} at a cooling wall thickness $dr_{34_1} = 0.022m$



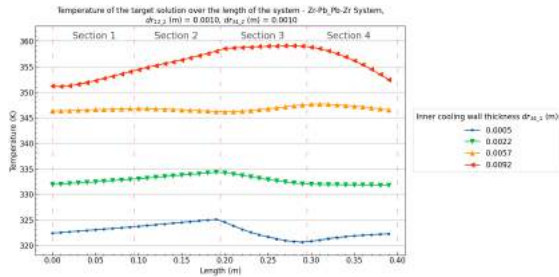
(c) Average target solution temperature difference between the heating and cooling sectors over the outer wall layer thickness dr_{1234_2} and inner heating wall thickness dr_{12_1} at a cooling wall thickness $dr_{34_1} = 0.057m$



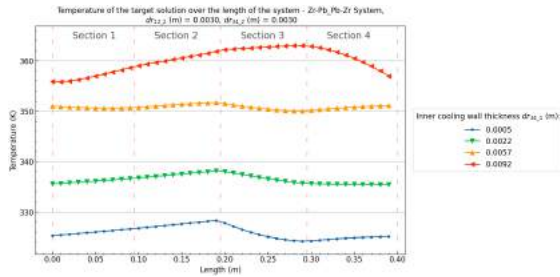
(d) Average target solution temperature difference between the heating and cooling sectors over the outer wall layer thickness dr_{1234_2} and inner heating wall thickness dr_{12_1} at a cooling wall thickness $dr_{34_1} = 0.092m$



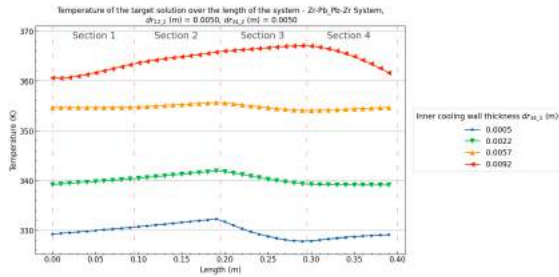
(e) Target solution temperature profile over the length of the Zr-Pb/Pb-Zr system with an inner heating wall thickness of $dr_{12_1} = 0.0096$ and an outer wall thickness of $dr_{1234_2} = 0.000m$



(f) Target solution temperature profile over the length of the Zr-Pb/Pb-Zr system with an inner heating wall thickness of $dr_{12_1} = 0.0096$ and an outer wall thickness of $dr_{1234_2} = 0.010m$



(g) Target solution temperature profile over the length of the Zr-Pb/Pb-Zr system with an inner heating wall thickness of $dr_{12_1} = 0.0096$ and an outer wall thickness of $dr_{1234_2} = 0.030m$

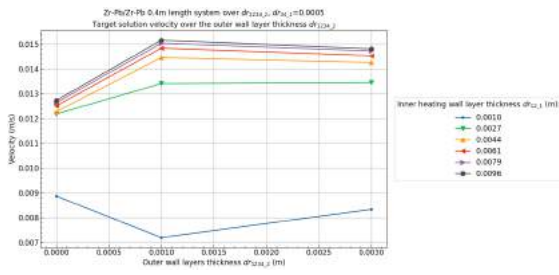


(h) Target solution temperature profile over the length of the Zr-Pb/Pb-Zr system with an inner heating wall thickness of $dr_{12_1} = 0.0096$ and an outer wall thickness of $dr_{1234_2} = 0.050m$

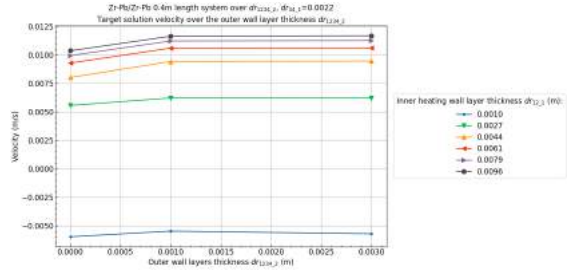
Figure B.33: Zr-Pb/Pb-Zr (Inner Heat_Outer Heat/Inner Cool_Outer Cool) continued system results over the wall thicknesses of the inner heating, inner cooling and outer wall (dr_{12_1} , dr_{34_1} , and dr_{1234_2} respectively) with a system length (L) of $0.4m$, an inner radius (Ri) of $0.007m$ and a pipe angle (θ) of 5° .

Zr-Pb/Zr-Pb - Wall thicknesses

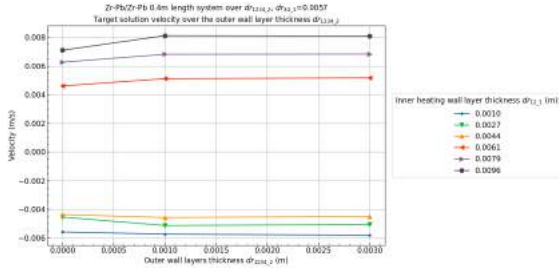
Back to overview - B.1.2



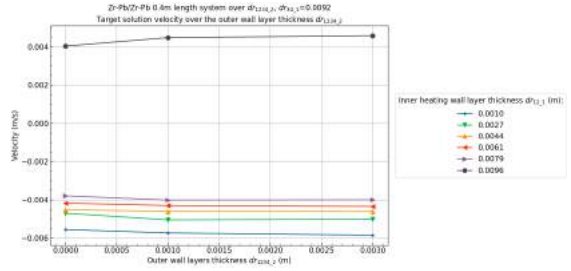
(a) Velocity over the outer wall layer thickness $dr_{1234,2}$ and inner heating wall thickness $dr_{12,1}$ at a cooling wall thickness $dr_{34,1} = 0.0005m$



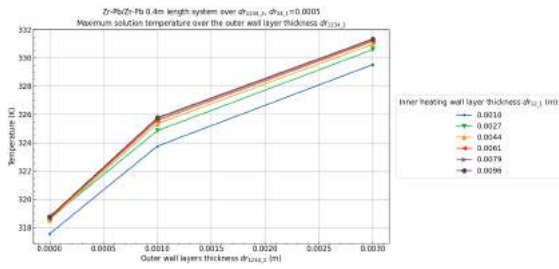
(b) Velocity over the outer wall layer thickness $dr_{1234,2}$ and inner heating wall thickness $dr_{12,1}$ at a cooling wall thickness $dr_{34,1} = 0.0022m$



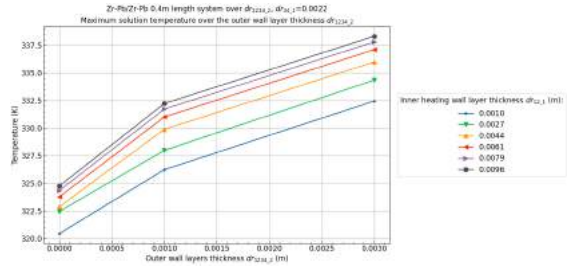
(c) Velocity over the outer wall layer thickness $dr_{1234,2}$ and inner heating wall thickness $dr_{12,1}$ at a cooling wall thickness $dr_{34,1} = 0.0057m$



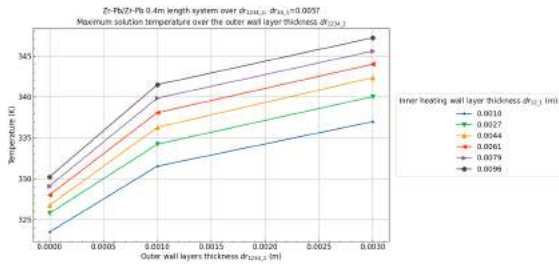
(d) Velocity over the outer wall layer thickness $dr_{1234,2}$ and inner heating wall thickness $dr_{12,1}$ at a cooling wall thickness $dr_{34,1} = 0.0092m$



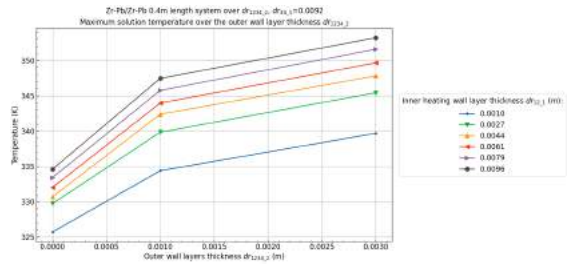
(e) Maximum target solution temperature over the outer wall layer thickness $dr_{1234,2}$ and inner heating wall thickness $dr_{12,1}$ at a cooling wall thickness $dr_{34,1} = 0.0005m$



(f) Maximum target solution temperature over the outer wall layer thickness $dr_{1234,2}$ and inner heating wall thickness $dr_{12,1}$ at a cooling wall thickness $dr_{34,1} = 0.0022m$

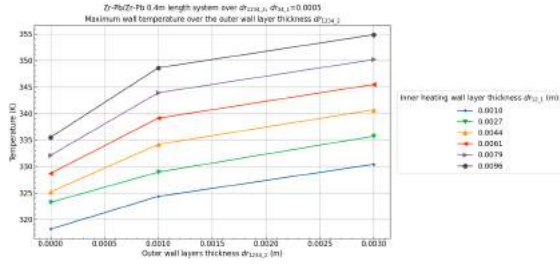


(g) Maximum target solution temperature over the outer wall layer thickness $dr_{1234,2}$ and inner heating wall thickness $dr_{12,1}$ at a cooling wall thickness $dr_{34,1} = 0.0057m$

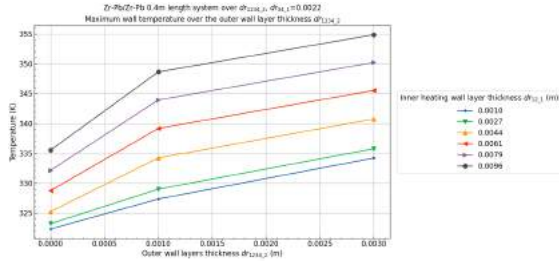


(h) Maximum target solution temperature over the outer wall layer thickness $dr_{1234,2}$ and inner heating wall thickness $dr_{12,1}$ at a cooling wall thickness $dr_{34,1} = 0.0092m$

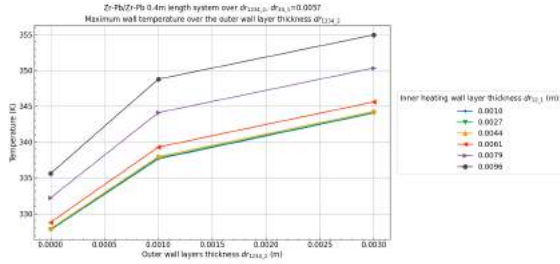
Figure B.34: Zr-Pb/Zr-Pb (Inner Heat_Outer Heat/Inner Cool_Outer Cool) system results over the wall thicknesses of the inner heating, inner cooling and outer wall ($dr_{12,1}$, $dr_{34,1}$, and $dr_{1234,2}$ respectively) with a system length (L) of $0.4m$, an inner radius (Ri) of $0.007m$ and a pipe angle (θ) of 5° .



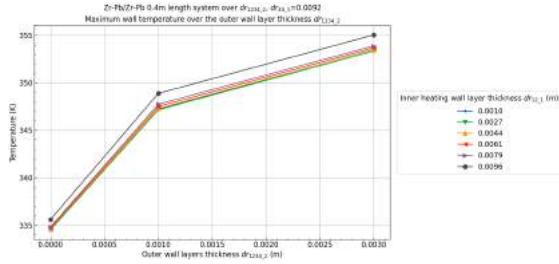
(a) Maximum wall temperature over the outer wall layer thickness dr_{1234_2} and inner heating wall thickness dr_{12_1} at a cooling wall thickness $dr_{34_1} = 0.0005m$



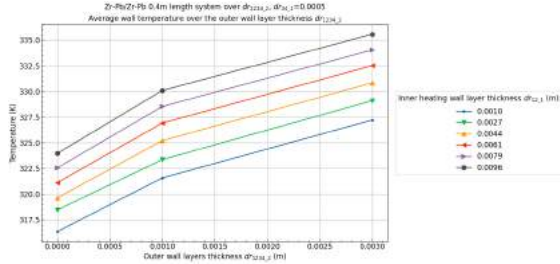
(b) Maximum wall temperature over the outer wall layer thickness dr_{1234_2} and inner heating wall thickness dr_{12_1} at a cooling wall thickness $dr_{34_1} = 0.0022m$



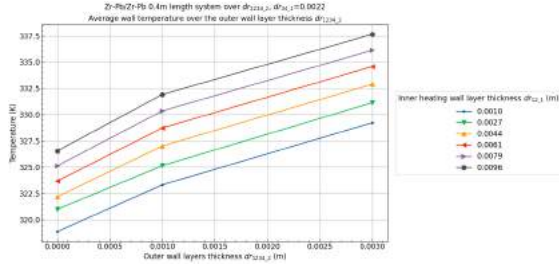
(c) Maximum wall temperature over the outer wall layer thickness dr_{1234_2} and inner heating wall thickness dr_{12_1} at a cooling wall thickness $dr_{34_1} = 0.0057m$



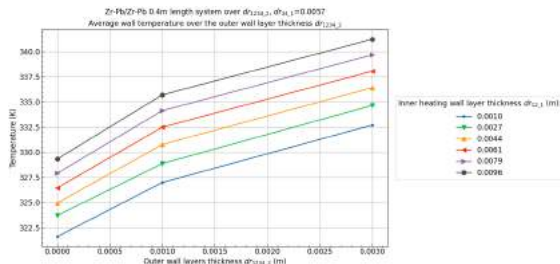
(d) Maximum wall temperature over the outer wall layer thickness dr_{1234_2} and inner heating wall thickness dr_{12_1} at a cooling wall thickness $dr_{34_1} = 0.0092m$



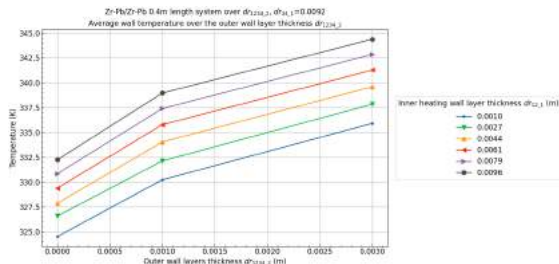
(e) Average wall temperature over the outer wall layer thickness dr_{1234_2} and inner heating wall thickness dr_{12_1} at a cooling wall thickness $dr_{34_1} = 0.0005m$



(f) Average wall temperature over the outer wall layer thickness dr_{1234_2} and inner heating wall thickness dr_{12_1} at a cooling wall thickness $dr_{34_1} = 0.0022m$

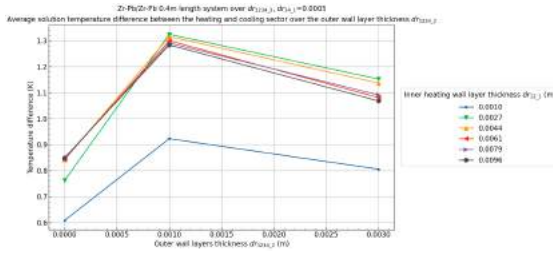


(g) Average wall temperature over the outer wall layer thickness dr_{1234_2} and inner heating wall thickness dr_{12_1} at a cooling wall thickness $dr_{34_1} = 0.0057m$

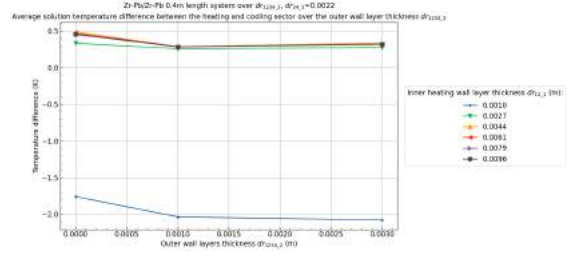


(h) Average wall temperature over the outer wall layer thickness dr_{1234_2} and inner heating wall thickness dr_{12_1} at a cooling wall thickness $dr_{34_1} = 0.0092m$

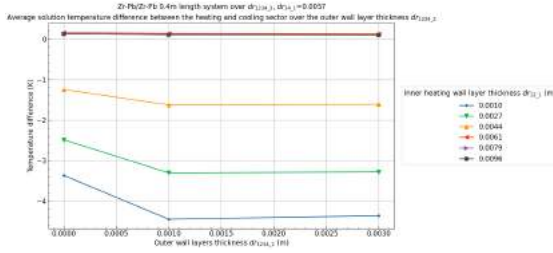
Figure B.35: Zr-Pb/Zr-Pb (Inner Heat_Outer Heat/Inner Cool_Outer Cool) continued system results over the wall thicknesses of the inner heating, inner cooling and outer wall (dr_{12_1} , dr_{34_1} , and dr_{1234_2} respectively) with a system length (L) of $0.4m$, an inner radius (Ri) of $0.007m$ and a pipe angle (θ) of 5° .



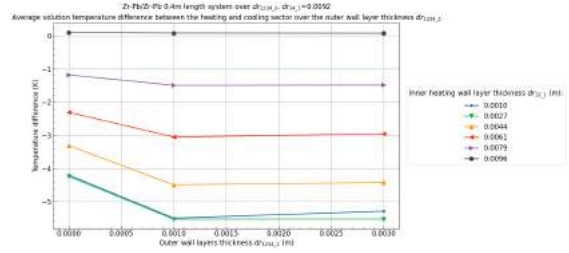
(a) Average target solution temperature difference between the heating and cooling sectors over the outer wall layer thickness dr_{1234_2} and inner heating wall thickness dr_{12_1} at a cooling wall thickness $dr_{34_1} = 0.005m$



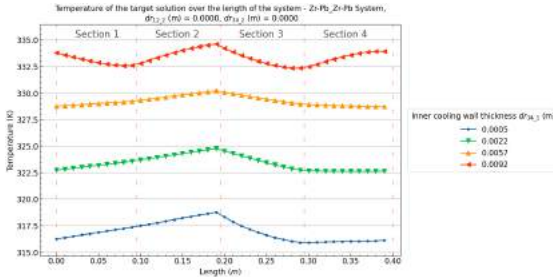
(b) Average target solution temperature difference between the heating and cooling sectors over the outer wall layer thickness dr_{1234_2} and inner heating wall thickness dr_{12_1} at a cooling wall thickness $dr_{34_1} = 0.022m$



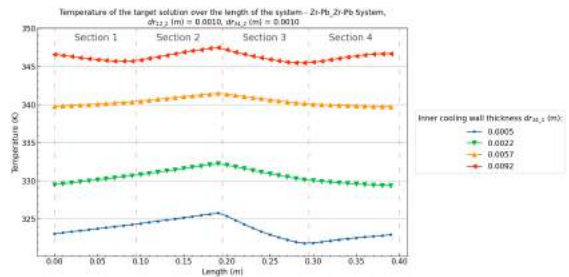
(c) Average target solution temperature difference between the heating and cooling sectors over the outer wall layer thickness dr_{1234_2} and inner heating wall thickness dr_{12_1} at a cooling wall thickness $dr_{34_1} = 0.057m$



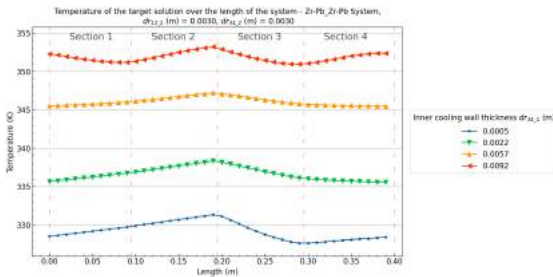
(d) Average target solution temperature difference between the heating and cooling sectors over the outer wall layer thickness dr_{1234_2} and inner heating wall thickness dr_{12_1} at a cooling wall thickness $dr_{34_1} = 0.092m$



(e) Target solution temperature profile over the length of the Zr-Pb/Zr-Pb system with an inner heating wall thickness of $dr_{12_1} = 0.0096$ and an outer wall thickness of $dr_{1234_2} = 0.000m$



(f) Target solution temperature profile over the length of the Zr-Pb/Zr-Pb system with an inner heating wall thickness of $dr_{12_1} = 0.0096$ and an outer wall thickness of $dr_{1234_2} = 0.010m$



(g) Target solution temperature profile over the length of the Zr-Pb/Zr-Pb system with an inner heating wall thickness of $dr_{12_1} = 0.0096$ and an outer wall thickness of $dr_{1234_2} = 0.030m$

Figure B.36: Zr-Pb/Zr-Pb (Inner Heat_Outer Heat/Inner Cool_Outer Cool) continued system results over the wall thicknesses of the inner heating, inner cooling and outer wall (dr_{12_1} , dr_{34_1} , and dr_{1234_2} respectively) with a system length (L) of $0.4m$, an inner radius (R_i) of $0.007m$ and a pipe angle (θ) of 5° .

B.2. Inner Radius (R_i), Wall material & Wall thickness

The general trends for the single layer wall materials and wall thicknesses in these systems are:

- The general profile of the velocity over the inner radius shows a fast increase in the velocity at low inner radii values followed by a maximum velocity that is reached. After the maximum velocity is reached the velocity drops almost linearly with the inner radius.
- Systems that have a lower energy deposition, such as smaller overall wall thicknesses and the Al/Al systems have their maximum velocities at larger inner radii.
- Increasing the cooling wall thickness increases the velocity in systems with a positive velocity and decreases the velocity in systems with negative velocities.
- The highest velocities are seen in Pb/Al systems, the drop after the maximum velocity that is reached is also significantly larger than systems with the same materials.
- When the cooling wall thickness is smaller than the heating wall thicknesses (in the Al/Al, Pb/Pb and Zr/Zr systems), the average and maximum temperatures of the target solution initially increase with the inner radius. After the velocity starts to flatten to its maximum value, the maximum solution temperature drops significantly over the radius.
- When the cooling wall thickness is larger than the heating wall thickness (in the Al/Al, Pb/Pb and Zr/Zr systems), the average and maximum temperatures of the target solution initially slightly decrease with the inner radius. Increasing the inner radius further will increase these temperatures.
- When the cooling and heating wall thicknesses are similar (in the Al/Al, Pb/Pb and Zr/Zr systems), the average and maximum temperatures of the target solution increase with the inner radius.
- In the Pb/Al system, the maximum target solution temperature generally slightly increases initially until the maximum velocity is reached. Afterwards a significant decrease in maximum temperatures is seen. The average temperatures follow the same trend as other systems.
- Increasing the inner radius drops the absolute temperature difference between the heating and cooling sector significantly.
- Systems with positive velocities have a significantly smaller temperature range in the target solution temperature profiles over the length compared to systems with negative velocities.
- Systems with small inner radii show the largest temperature differences in the temperature profiles over the length of the system as well as the average temperature differences between the heating and cooling sectors.
- Increasing the heating wall thickness moves maximum velocities that are seen to smaller inner radii.

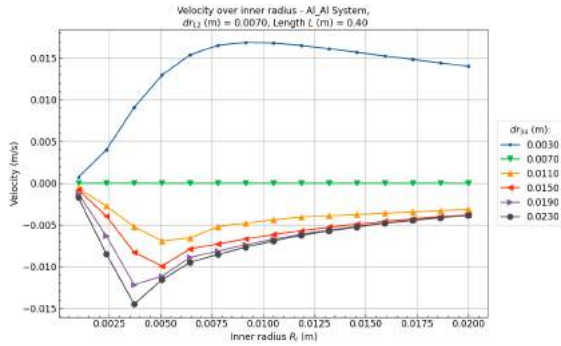
Table B.4: System specifications for the inner radius variable results

System Variable	Values	Reference
Multi layer wall materials	Al/Al	B.37 - B.44 (Page 131 - 138)
	Pb/Pb	B.45 - B.52 (Page 139 - 146)
	Zr/Zr	B.53 - B.60 (Page 147 - 154)
	Pb/Al	B.61 - B.64 (Page 155 - 162)
Heating wall thickness (dr_{12_1})	0.0070m	Al/Al - B.37 - B.38 (Page 131 - 132)
		Pb/Pb - B.45 - B.46 (Page 139 - 140)
		Zr/Zr - B.53 - B.54 (Page 147 - 148)
		Pb/Al - B.61 - B.62 (Page 155 - 156)
	0.0110m	Al/Al - B.39 - B.40 (Page 133 - 134)
		Pb/Pb - B.47 - B.48 (Page 141 - 142)
		Zr/Zr - B.55 - B.56 (Page 149 - 150)
		Pb/Al - B.63 - B.64 (Page 157 - 158)
	0.0150m	Al/Al - B.41 - B.42 (Page 135 - 136)
		Pb/Pb - B.49 - B.50 (Page 143 - 144)
		Zr/Zr - B.57 - B.58 (Page 151 - 152)
		Pb/Al - B.65 - B.66 (Page 159 - 160)
0.0230m	Al/Al - B.43 - B.44 (Page 137 - 138)	
	Pb/Pb - B.51 - B.52 (Page 145 - 146)	
	Zr/Zr - B.59 - B.60 (Page 153 - 154)	
	Pb/Al - B.67 - B.68 (Page 161 - 162)	
Cooling wall thickness (dr_{34_1})	0.003 – 0.0230m	
Inner radius (R_i)	0.001 – 0.0200m	
Length (L)	0.4m	
Pipe angle (θ)	5°	
Section 2 length fraction ($Frac$)	1.0	

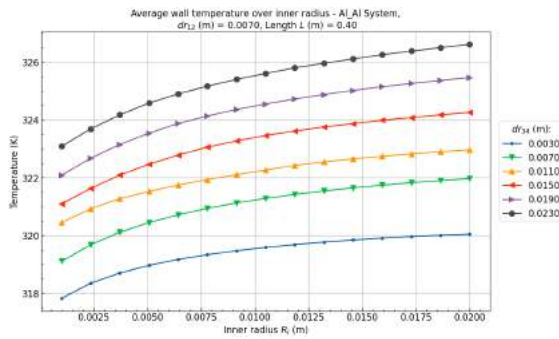
B.2.1. Al/Al - Inner Radius (R_i) & Wall thickness

Al/Al - $dr_{12} = 0.0070m$

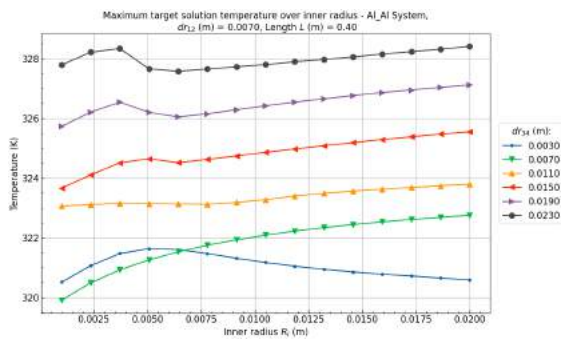
[Back to overview - B.2](#)



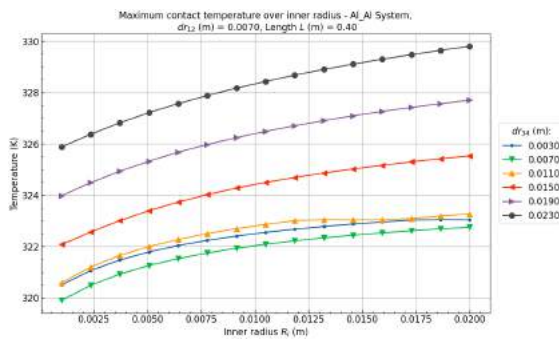
(a) Velocity over the inner radius R_i at $dr_{12} = 0.0070m$.



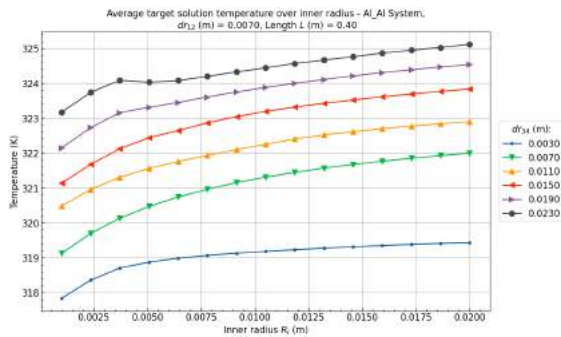
(b) Average wall temperature over the inner radius R_i at $dr_{12} = 0.0070m$.



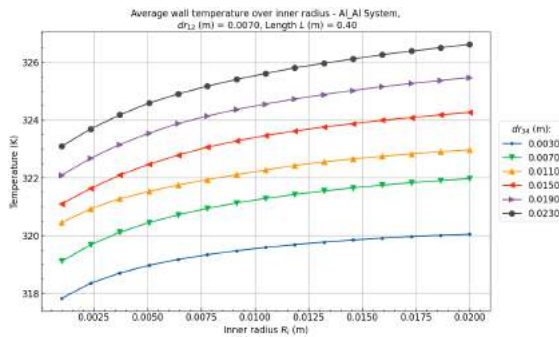
(c) Maximum target solution temperature over the inner radius R_i at $dr_{12} = 0.0070m$.



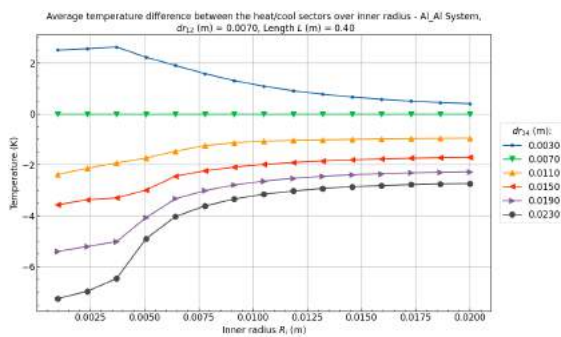
(d) Maximum contact temperature between the wall and the target solution over the inner radius R_i at $dr_{12} = 0.0070m$.



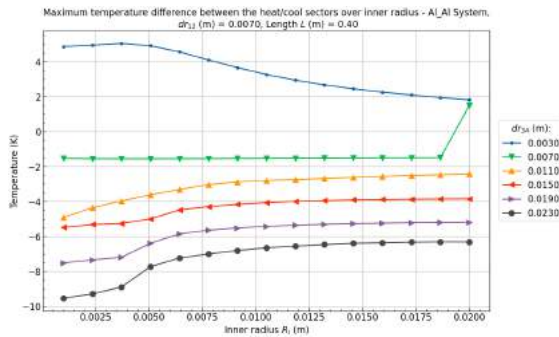
(e) Average target solution temperature over the inner radius R_i at $dr_{12} = 0.0070m$.



(f) Average wall temperature over the inner radius R_i at $dr_{12} = 0.0070m$.

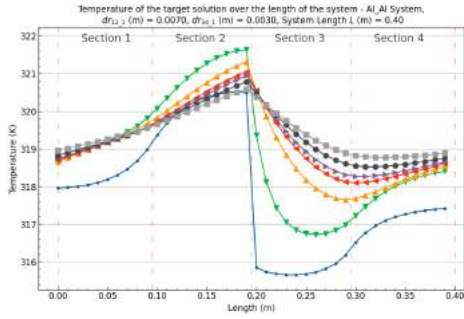


(g) Average target solution temperature difference between heating and cooling sectors over the inner radius R_i at $dr_{12} = 0.0070m$.

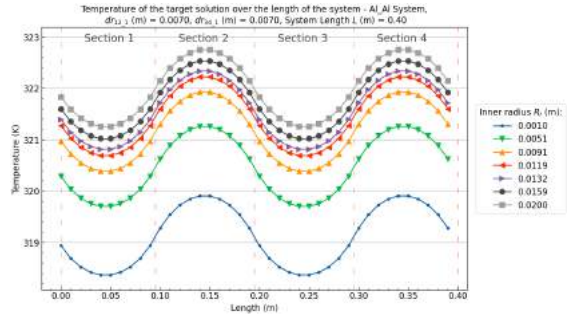


(h) Maximum target solution temperature difference between heating and cooling sectors over the inner radius R_i at $dr_{12} = 0.0070m$.

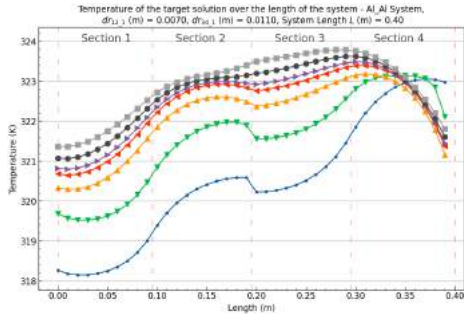
Figure B.37: Al/Al (Heat/Cool) System results over the inner radius R_i and cooling wall thickness dr_{34} at a heating wall thickness of $dr_{12} = 0.0070m$, a system length (L) of $0.4m$, and a pipe angle (θ) of 5° .



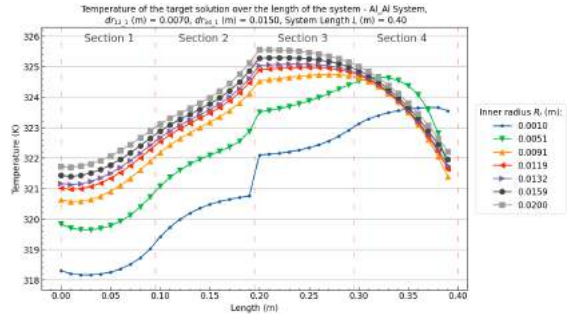
(a) Target solution temperature profiles over the length in systems over the inner radius R_i with $dr_{12_1}(m) = 0.0070$ and $dr_{34_1}(m) = 0.0030$



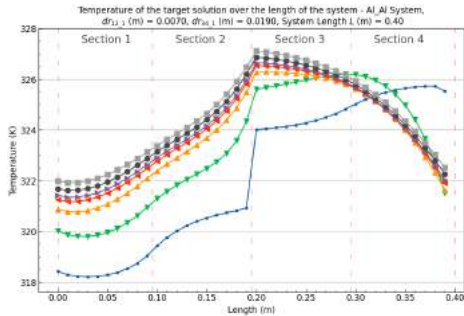
(b) Target solution temperature profiles over the length in systems over the inner radius R_i with $dr_{12_1}(m) = 0.0070$ and $dr_{34_1}(m) = 0.0070$



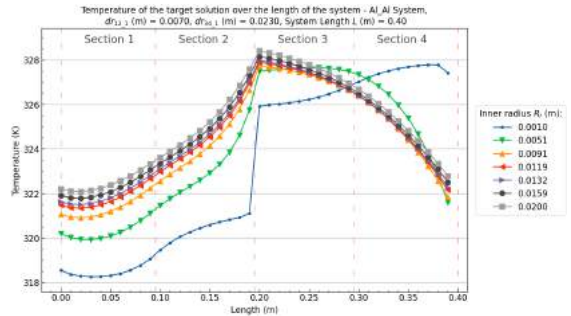
(c) Target solution temperature profiles over the length in systems over the inner radius R_i with $dr_{12_1}(m) = 0.0070$ and $dr_{34_1}(m) = 0.0110$



(d) Target solution temperature profiles over the length in systems over the inner radius R_i with $dr_{12_1}(m) = 0.0070$ and $dr_{34_1}(m) = 0.0150$



(e) Target solution temperature profiles over the length in systems over the inner radius R_i with $dr_{12_1}(m) = 0.0070$ and $dr_{34_1}(m) = 0.0190$

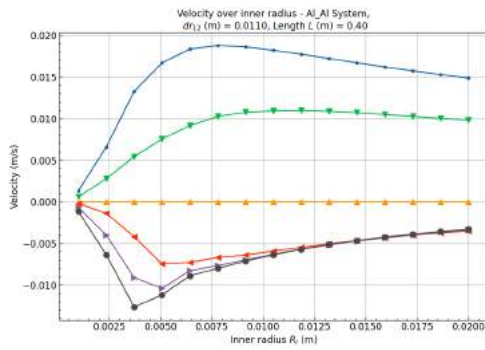


(f) Target solution temperature profiles over the length in systems over the inner radius R_i with $dr_{12_1}(m) = 0.0070$ and $dr_{34_1}(m) = 0.0230$

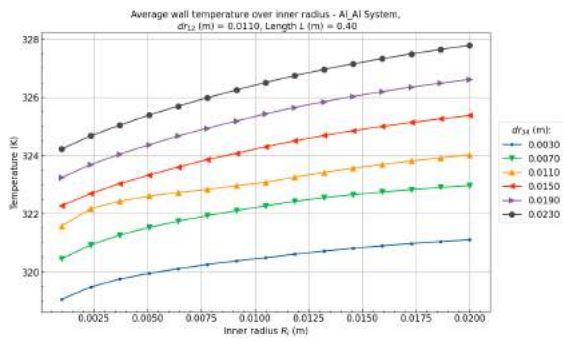
Figure B.38: Al/Al (Heat/Cool) System target solution temperature profiles over the inner radius R_i and cooling wall thickness dr_{34} at a heating wall thickness of $dr_{12} = 0.0070m$, a system length (L) of $0.4m$, and a pipe angle (θ) of 5° .

Al/Al - $dr_{12} = 0.0110m$

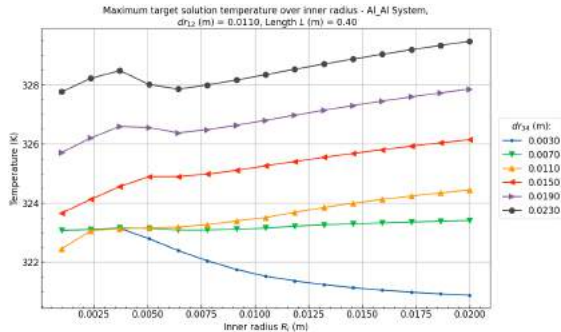
[Back to overview - B.2](#)



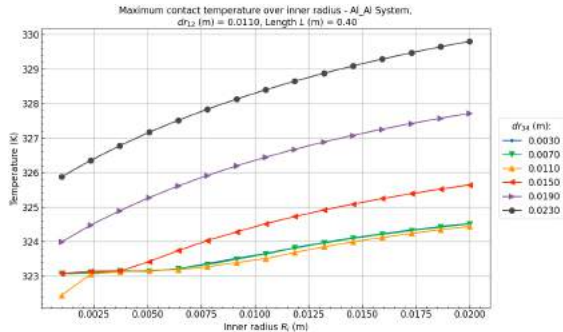
(a) Velocity over the inner radius R_i at $dr_{12} = 0.0110m$.



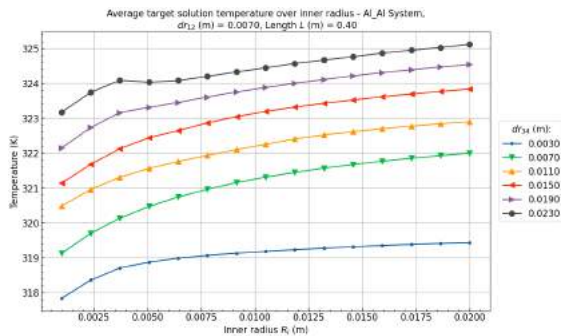
(b) Average wall temperature over the inner radius R_i at $dr_{12} = 0.0110m$.



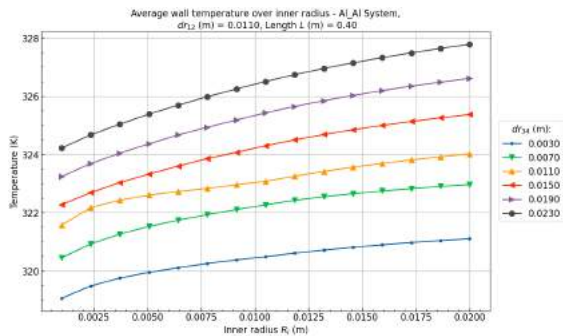
(c) Maximum target solution temperature over the inner radius R_i at $dr_{12} = 0.0110m$.



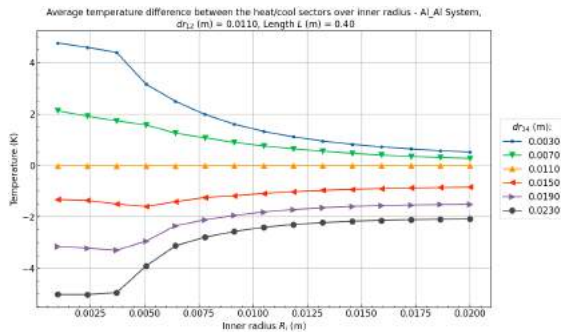
(d) Maximum contact temperature between the wall and the target solution over the inner radius R_i at $dr_{12} = 0.0110m$.



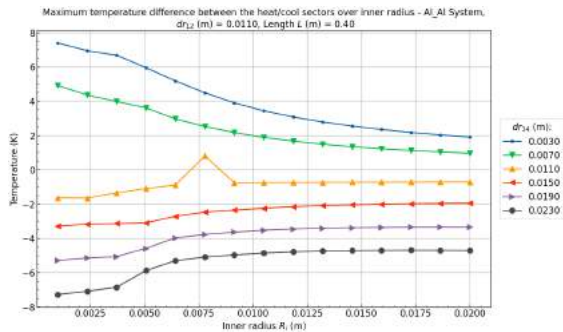
(e) Average target solution temperature over the inner radius R_i at $dr_{12} = 0.0110m$.



(f) Average wall temperature over the inner radius R_i at $dr_{12} = 0.0110m$.

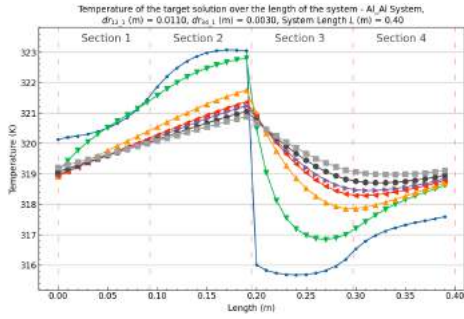


(g) Average target solution temperature difference between heating and cooling sectors over the inner radius R_i at $dr_{12} = 0.0110m$.

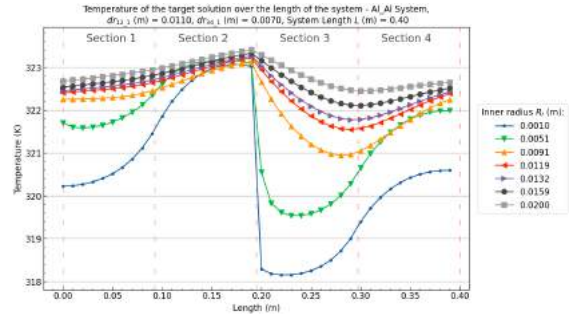


(h) Maximum target solution temperature difference between heating and cooling sectors over the inner radius R_i at $dr_{12} = 0.0110m$.

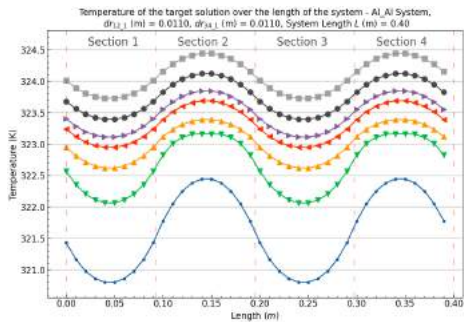
Figure B.39: Al/Al (Heat/Cool) System results over the inner radius R_i and cooling wall thickness dr_{34} at a heating wall thickness of $dr_{12} = 0.0110m$, a system length (L) of $0.4m$, and a pipe angle (θ) of 5° .



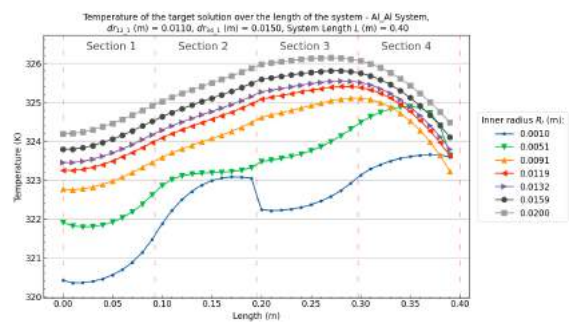
(a) Target solution temperature profiles over the length in systems over the inner radius R_i with $dr_{12_1}(m) = 0.0110$ and $dr_{34_1}(m) = 0.0030$



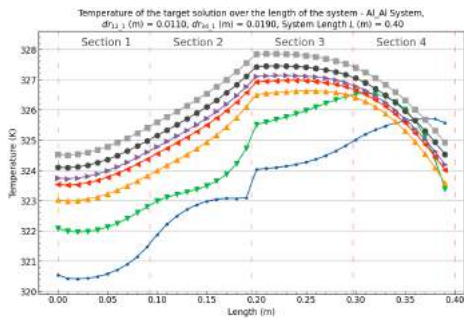
(b) Target solution temperature profiles over the length in systems over the inner radius R_i with $dr_{12_1}(m) = 0.0110$ and $dr_{34_1}(m) = 0.0070$



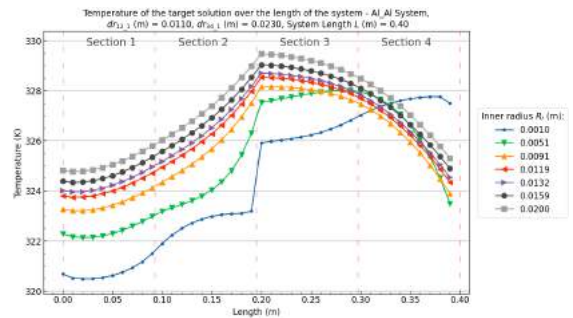
(c) Target solution temperature profiles over the length in systems over the inner radius R_i with $dr_{12_1}(m) = 0.0110$ and $dr_{34_1}(m) = 0.0110$



(d) Target solution temperature profiles over the length in systems over the inner radius R_i with $dr_{12_1}(m) = 0.0110$ and $dr_{34_1}(m) = 0.0150$



(e) Target solution temperature profiles over the length in systems over the inner radius R_i with $dr_{12_1}(m) = 0.0110$ and $dr_{34_1}(m) = 0.0190$

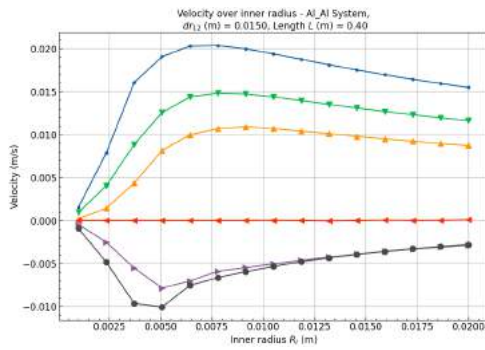


(f) Target solution temperature profiles over the length in systems over the inner radius R_i with $dr_{12_1}(m) = 0.0110$ and $dr_{34_1}(m) = 0.0230$

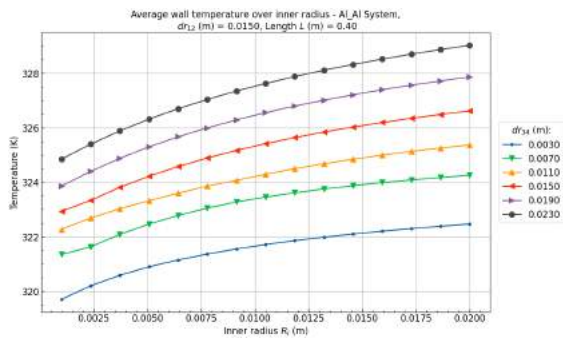
Figure B.40: Al/Al (Heat/Cool) System target solution temperature profiles over the inner radius R_i and cooling wall thickness dr_{34} at a heating wall thickness of $dr_{12} = 0.0110m$, a system length (L) of $0.4m$, and a pipe angle (θ) of 5° .

Al/Al - $dr_{12} = 0.0150m$

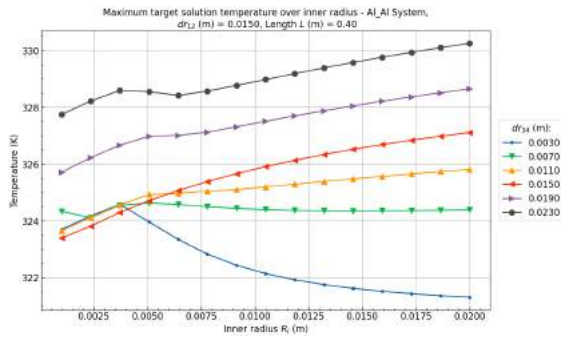
Back to overview - B.2



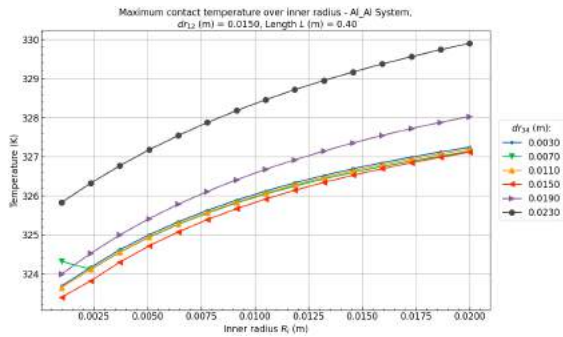
(a) Velocity over the inner radius R_i at $dr_{12} = 0.0150m$.



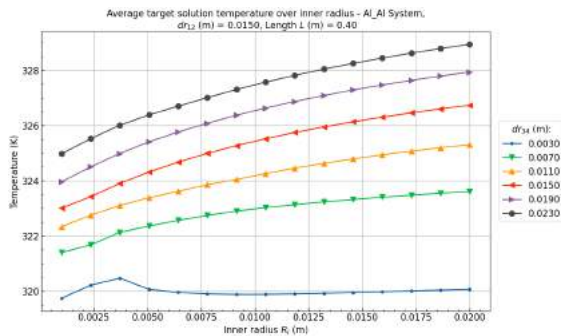
(b) Average wall temperature over the inner radius R_i at $dr_{12} = 0.0150m$.



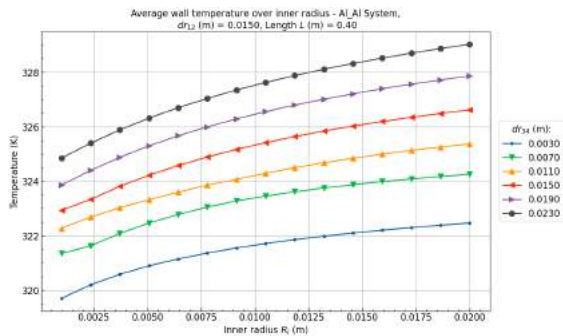
(c) Maximum target solution temperature over the inner radius R_i at $dr_{12} = 0.0150m$.



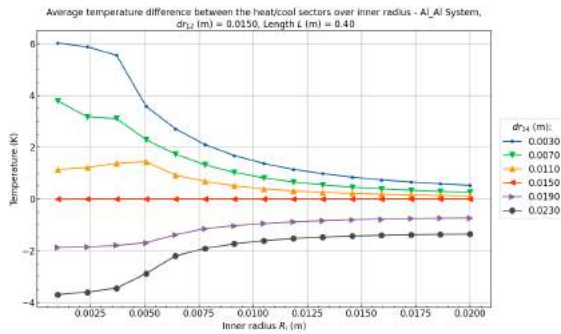
(d) Maximum contact temperature between the wall and the target solution over the inner radius R_i at $dr_{12} = 0.0150m$.



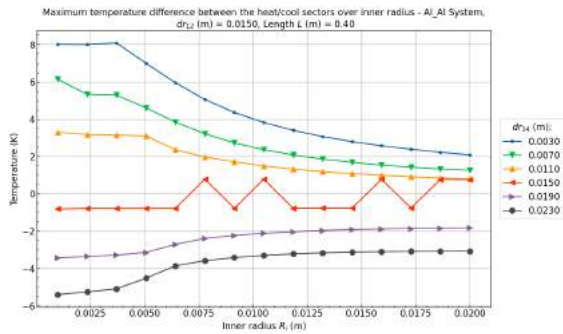
(e) Average target solution temperature over the inner radius R_i at $dr_{12} = 0.0150m$.



(f) Average wall temperature over the inner radius R_i at $dr_{12} = 0.0150m$.

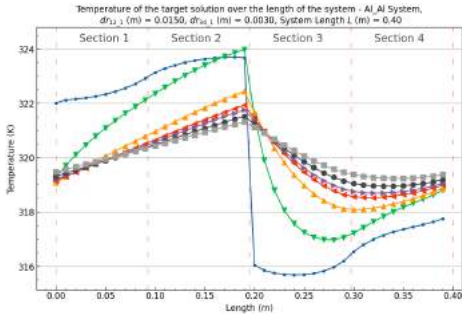


(g) Average target solution temperature difference between heating and cooling sectors over the inner radius R_i at $dr_{12} = 0.0150m$.

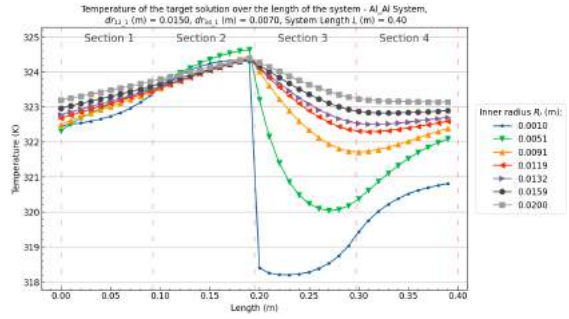


(h) Maximum target solution temperature difference between heating and cooling sectors over the inner radius R_i at $dr_{12} = 0.0150m$.

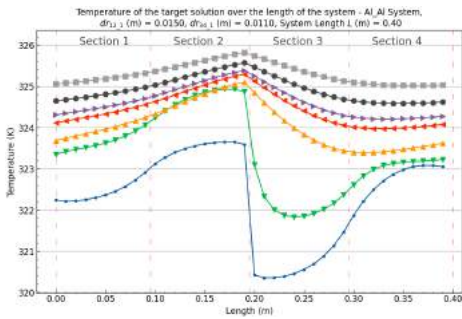
Figure B.41: Al/Al (Heat/Cool) System results over the inner radius R_i and cooling wall thickness dr_{34} at a heating wall thickness of $dr_{12} = 0.0150m$, a system length (L) of $0.4m$, and a pipe angle (θ) of 5° .



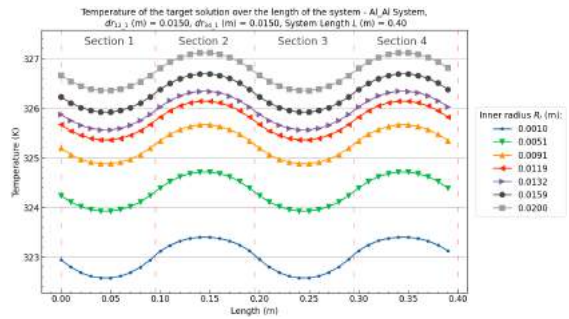
(a) Target solution temperature profiles over the length in systems over the inner radius R_i with $dr_{12_1}(m) = 0.0110$ and $dr_{34_1}(m) = 0.0030$



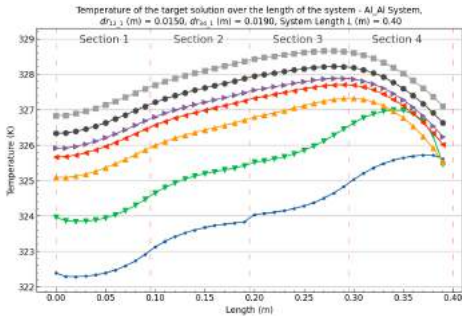
(b) Target solution temperature profiles over the length in systems over the inner radius R_i with $dr_{12_1}(m) = 0.0110$ and $dr_{34_1}(m) = 0.0070$



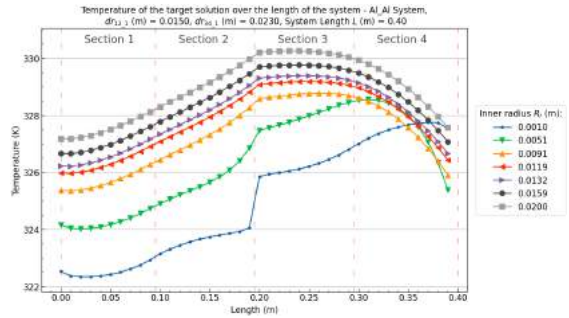
(c) Target solution temperature profiles over the length in systems over the inner radius R_i with $dr_{12_1}(m) = 0.0110$ and $dr_{34_1}(m) = 0.0110$



(d) Target solution temperature profiles over the length in systems over the inner radius R_i with $dr_{12_1}(m) = 0.0110$ and $dr_{34_1}(m) = 0.0150$



(e) Target solution temperature profiles over the length in systems over the inner radius R_i with $dr_{12_1}(m) = 0.0110$ and $dr_{34_1}(m) = 0.0190$

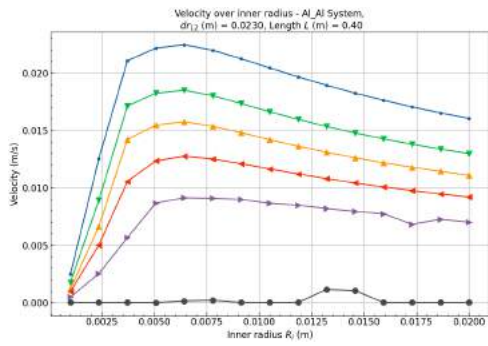


(f) Target solution temperature profiles over the length in systems over the inner radius R_i with $dr_{12_1}(m) = 0.0110$ and $dr_{34_1}(m) = 0.0230$

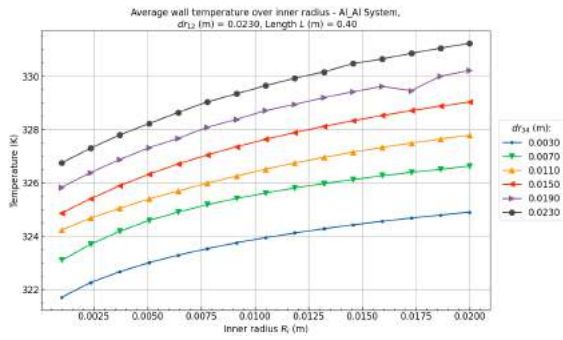
Figure B.42: Al/Al (Heat/Cool) System target solution temperature profiles over the inner radius R_i and cooling wall thickness dr_{34} at a heating wall thickness of $dr_{12} = 0.0150m$, a system length (L) of $0.4m$, and a pipe angle (θ) of 5° .

Al/Al - $dr_{12} = 0.0230m$

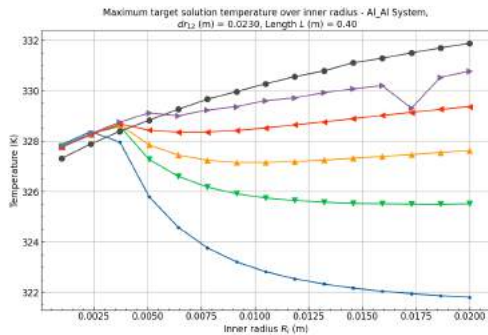
[Back to overview - B.2](#)



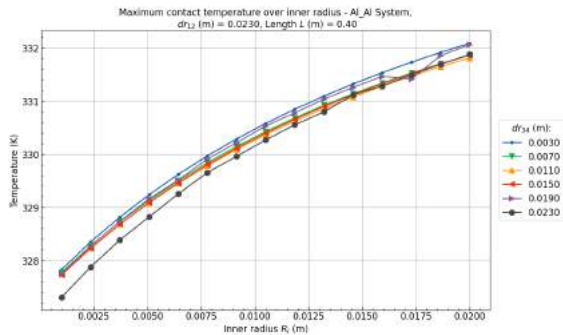
(a) Velocity over the inner radius R_i at $dr_{12} = 0.0230m$.



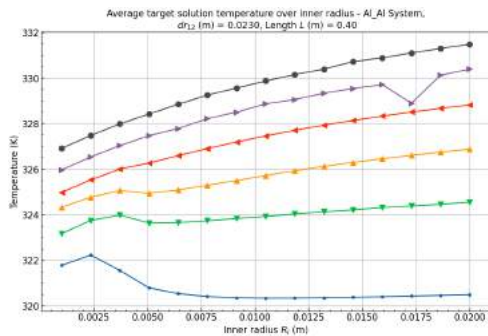
(b) Average wall temperature over the inner radius R_i at $dr_{12} = 0.0230m$.



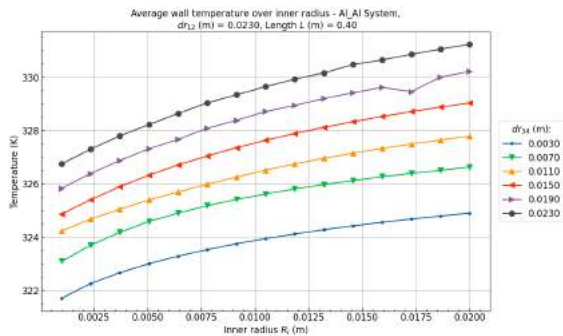
(c) Maximum target solution temperature over the inner radius R_i at $dr_{12} = 0.0230m$.



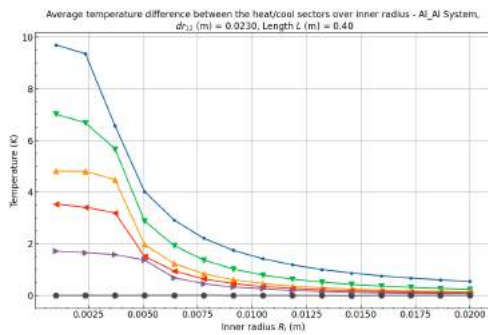
(d) Maximum contact temperature temperature between the wall and the target solution over the inner radius R_i at $dr_{12} = 0.0230m$.



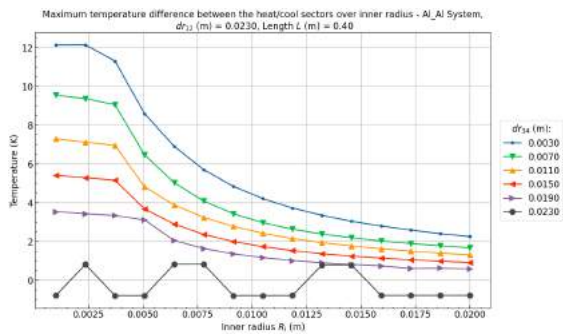
(e) Average target solution temperature over the inner radius R_i at $dr_{12} = 0.0230m$.



(f) Average wall temperature over the inner radius R_i at $dr_{12} = 0.0230m$.

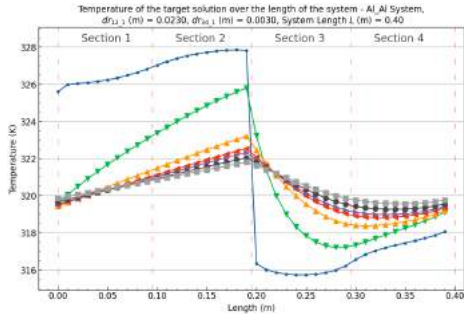


(g) Average target solution temperature difference between heating and cooling sectors over the inner radius R_i at $dr_{12} = 0.0230m$.

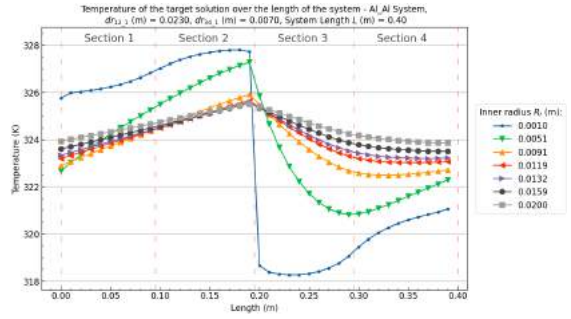


(h) Maximum target solution temperature difference between heating and cooling sectors over the inner radius R_i at $dr_{12} = 0.0230m$.

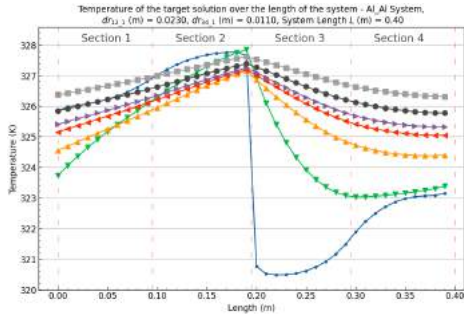
Figure B.43: Al/Al (Heat/Cool) System results over the inner radius R_i and cooling wall thickness dr_{34} at a heating wall thickness of $dr_{12} = 0.0230m$, a system length (L) of $0.4m$, and a pipe angle (θ) of 5° .



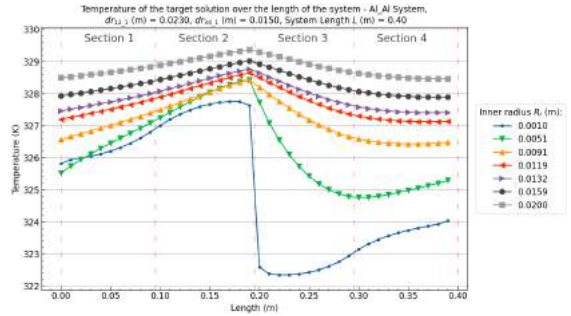
(a) Target solution temperature profiles over the length in systems over the inner radius R_i with $dr_{121}(m) = 0.0230$ and $dr_{341}(m) = 0.0030$



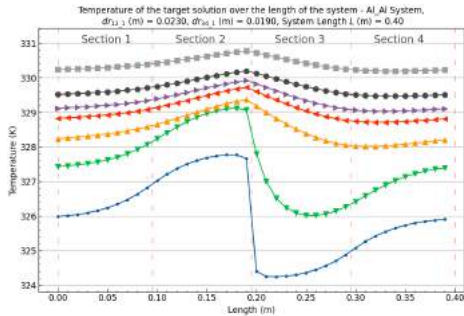
(b) Target solution temperature profiles over the length in systems over the inner radius R_i with $dr_{121}(m) = 0.0110$ and $dr_{341}(m) = 0.0070$



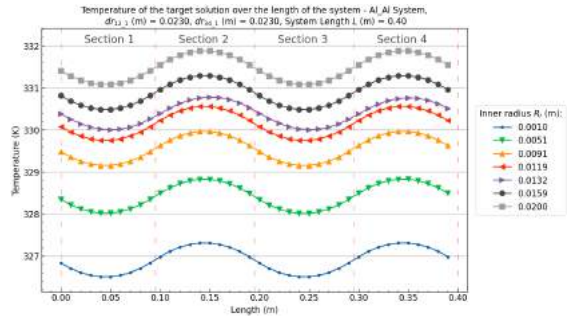
(c) Target solution temperature profiles over the length in systems over the inner radius R_i with $dr_{121}(m) = 0.0110$ and $dr_{341}(m) = 0.0110$



(d) Target solution temperature profiles over the length in systems over the inner radius R_i with $dr_{121}(m) = 0.0110$ and $dr_{341}(m) = 0.0150$



(e) Target solution temperature profiles over the length in systems over the inner radius R_i with $dr_{121}(m) = 0.0110$ and $dr_{341}(m) = 0.0190$

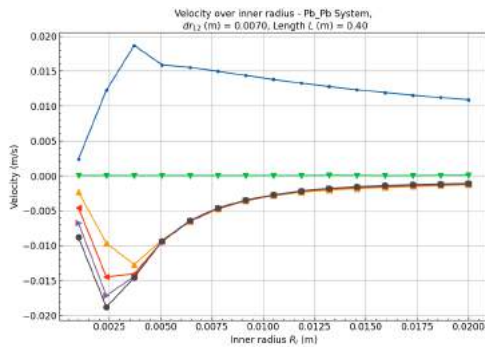


(f) Target solution temperature profiles over the length in systems over the inner radius R_i with $dr_{121}(m) = 0.0110$ and $dr_{341}(m) = 0.0230$

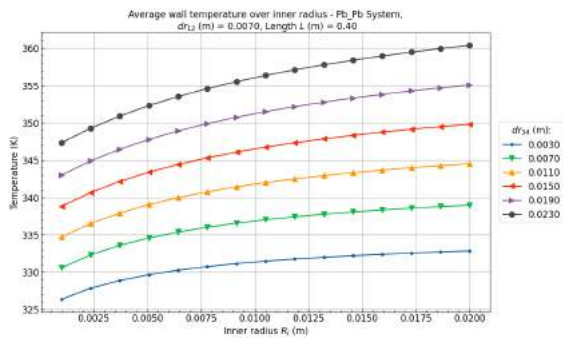
Figure B.44: Al/Al (Heat/Cool) System target solution temperature profiles over the inner radius R_i and cooling wall thickness dr_{34} at a heating wall thickness of $dr_{12} = 0.0230m$, a system length (L) of $0.4m$, and a pipe angle (θ) of 5° .

Pb/Pb - $dr_{12} = 0.0070m$

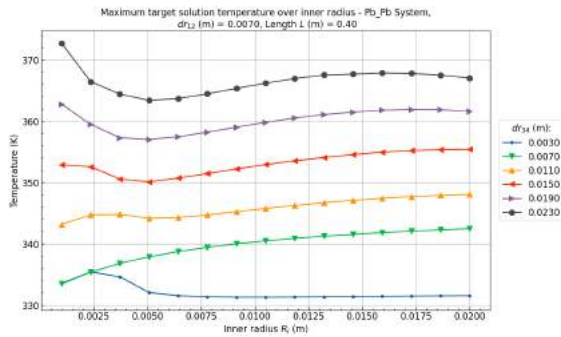
Back to overview - B.2



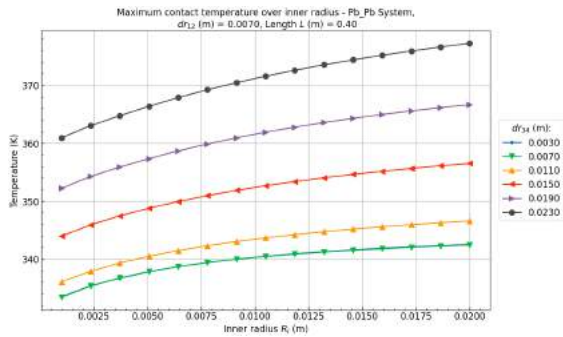
(a) Velocity over the inner radius R_i at $dr_{12} = 0.0070m$.



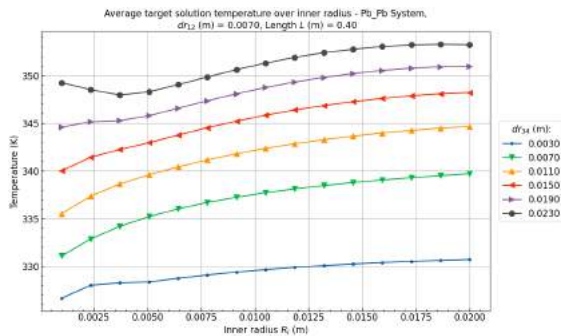
(b) Average wall temperature over the inner radius R_i at $dr_{12} = 0.0070m$.



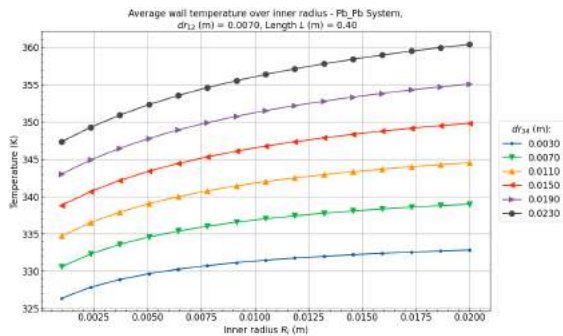
(c) Maximum target solution temperature over the inner radius R_i at $dr_{12} = 0.0070m$.



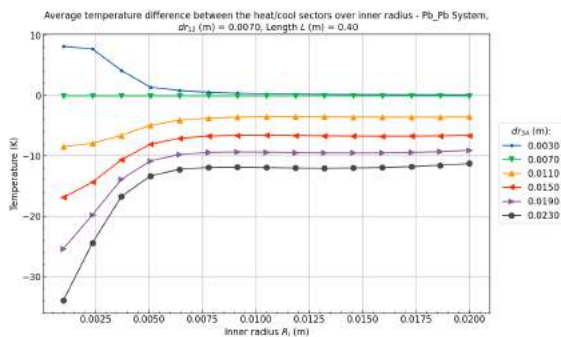
(d) Maximum contact temperature between the wall and the target solution over the inner radius R_i at $dr_{12} = 0.0070m$.



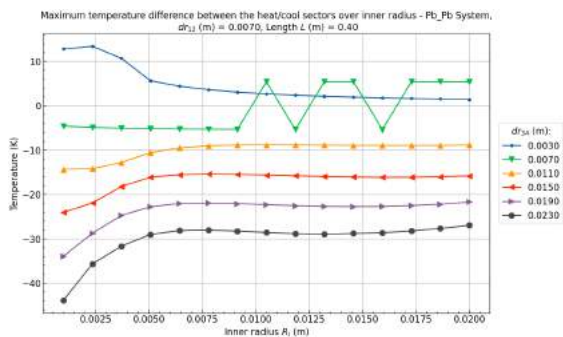
(e) Average target solution temperature over the inner radius R_i at $dr_{12} = 0.0070m$.



(f) Average wall temperature over the inner radius R_i at $dr_{12} = 0.0070m$.

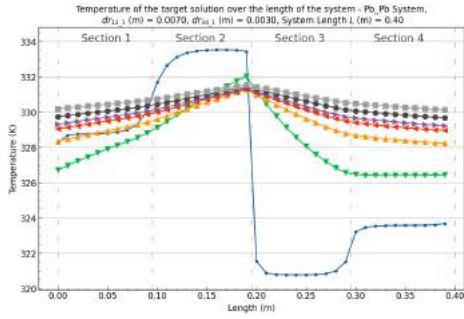


(g) Average target solution temperature difference between heating and cooling sectors over the inner radius R_i at $dr_{12} = 0.0070m$.

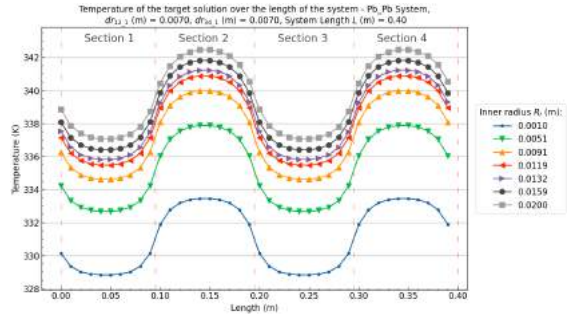


(h) Maximum target solution temperature difference between heating and cooling sectors over the inner radius R_i at $dr_{12} = 0.0070m$.

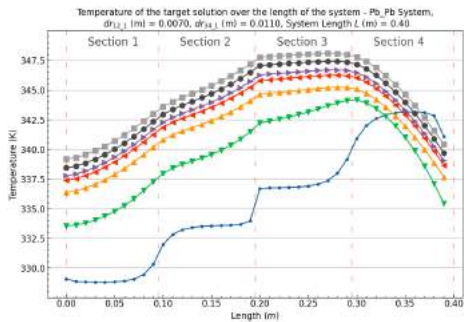
Figure B.45: Pb/Pb (Heat/Cool) System results over the inner radius R_i and cooling wall thickness dr_{34} at a heating wall thickness of $dr_{12} = 0.0070m$, a system length (L) of $0.4m$, and a pipe angle (θ) of 5° .



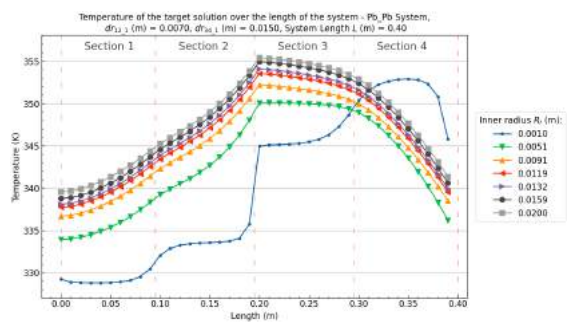
(a) Target solution temperature profiles over the length in systems over the inner radius R_i with $dr_{12_1}(m) = 0.0070$ and $dr_{34_1}(m) = 0.0030$



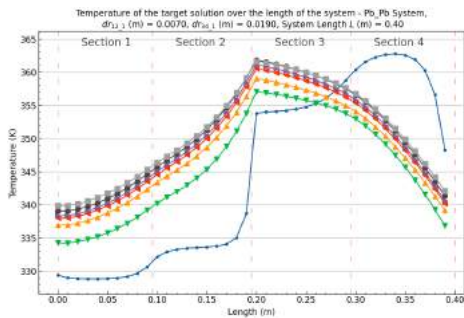
(b) Target solution temperature profiles over the length in systems over the inner radius R_i with $dr_{12_1}(m) = 0.0070$ and $dr_{34_1}(m) = 0.0070$



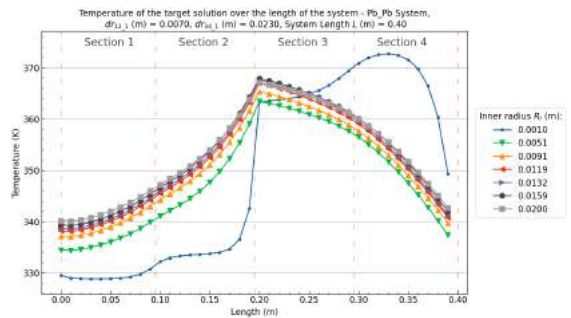
(c) Target solution temperature profiles over the length in systems over the inner radius R_i with $dr_{12_1}(m) = 0.0070$ and $dr_{34_1}(m) = 0.0110$



(d) Target solution temperature profiles over the length in systems over the inner radius R_i with $dr_{12_1}(m) = 0.0070$ and $dr_{34_1}(m) = 0.0150$



(e) Target solution temperature profiles over the length in systems over the inner radius R_i with $dr_{12_1}(m) = 0.0070$ and $dr_{34_1}(m) = 0.0190$

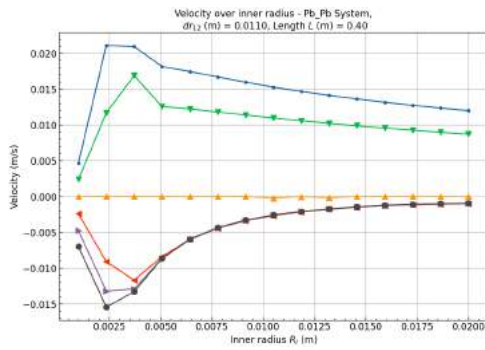


(f) Target solution temperature profiles over the length in systems over the inner radius R_i with $dr_{12_1}(m) = 0.0070$ and $dr_{34_1}(m) = 0.0230$

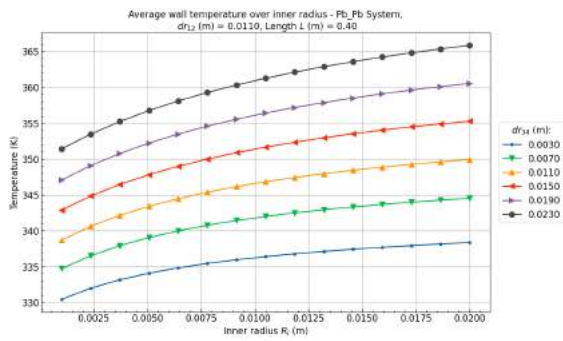
Figure B.46: Pb/Pb (Heat/Cool) System target solution temperature profiles over the inner radius R_i and cooling wall thickness dr_{34} at a heating wall thickness of $dr_{12} = 0.0070m$, a system length (L) of $0.4m$, and a pipe angle (θ) of 5° .

Pb/Pb - $dr_{12} = 0.0110m$

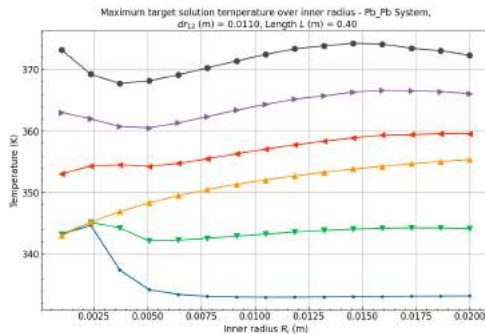
Back to overview - B.2



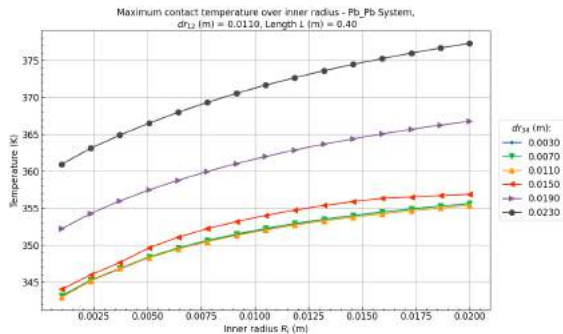
(a) Velocity over the inner radius R_i at $dr_{12} = 0.0110m$.



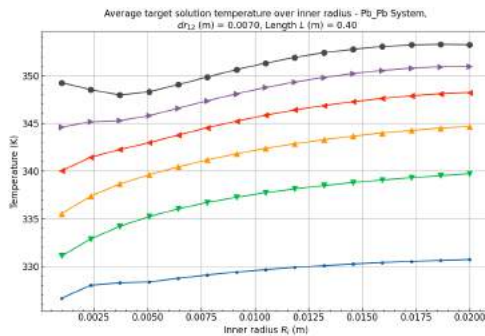
(b) Average wall temperature over the inner radius R_i at $dr_{12} = 0.0110m$.



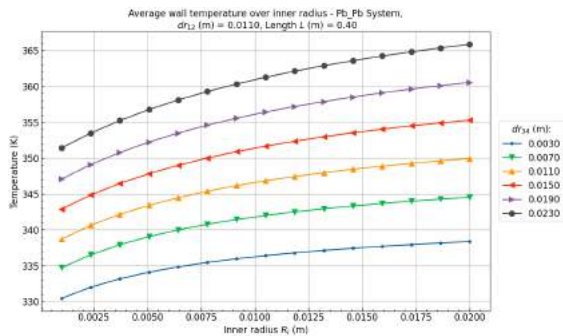
(c) Maximum target solution temperature over the inner radius R_i at $dr_{12} = 0.0110m$.



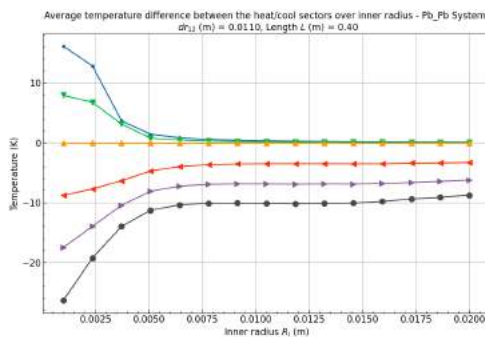
(d) Maximum contact temperature between the wall and the target solution over the inner radius R_i at $dr_{12} = 0.0110m$.



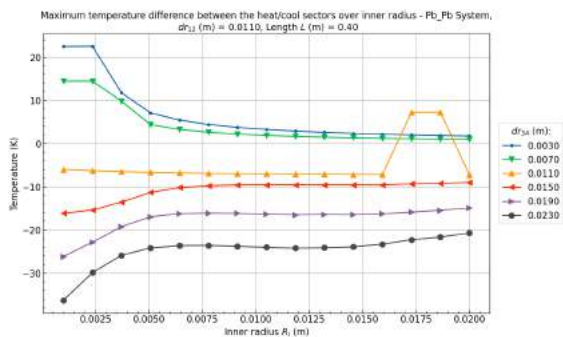
(e) Average target solution temperature over the inner radius R_i at $dr_{12} = 0.0110m$.



(f) Average wall temperature over the inner radius R_i at $dr_{12} = 0.0110m$.

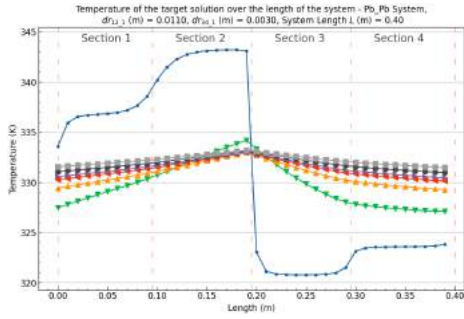


(g) Average target solution temperature difference between heating and cooling sectors over the inner radius R_i at $dr_{12} = 0.0110m$.

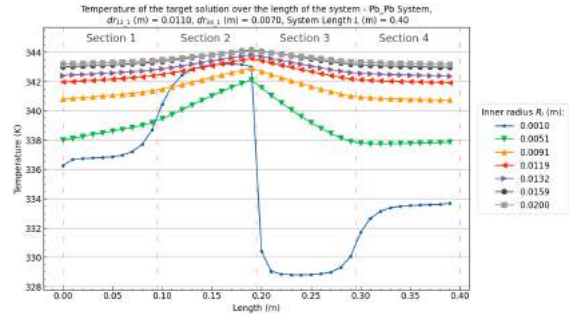


(h) Maximum target solution temperature difference between heating and cooling sectors over the inner radius R_i at $dr_{12} = 0.0110m$.

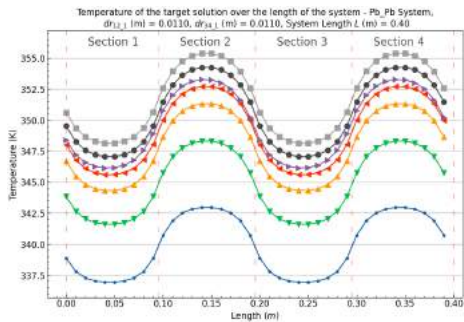
Figure B.47: Pb/Pb (Heat/Cool) System results over the inner radius R_i and cooling wall thickness dr_{34} at a heating wall thickness of $dr_{12} = 0.0110m$, a system length (L) of $0.4m$, and a pipe angle (θ) of 5° .



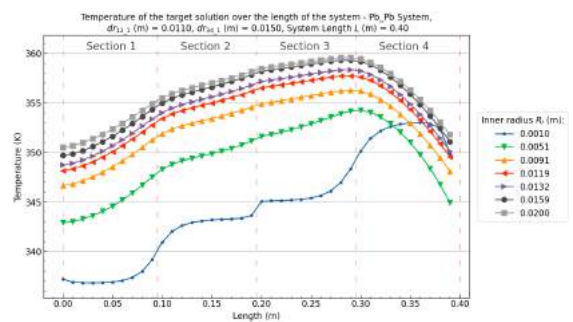
(a) Target solution temperature profiles over the length in systems over the inner radius R_i with $dr_{12_1}(m) = 0.0110$ and $dr_{34_1}(m) = 0.0030$



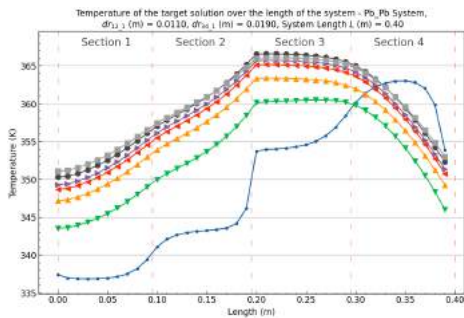
(b) Target solution temperature profiles over the length in systems over the inner radius R_i with $dr_{12_1}(m) = 0.0110$ and $dr_{34_1}(m) = 0.0070$



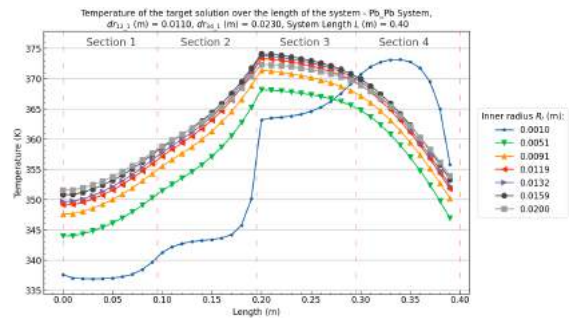
(c) Target solution temperature profiles over the length in systems over the inner radius R_i with $dr_{12_1}(m) = 0.0110$ and $dr_{34_1}(m) = 0.0110$



(d) Target solution temperature profiles over the length in systems over the inner radius R_i with $dr_{12_1}(m) = 0.0110$ and $dr_{34_1}(m) = 0.0150$



(e) Target solution temperature profiles over the length in systems over the inner radius R_i with $dr_{12_1}(m) = 0.0110$ and $dr_{34_1}(m) = 0.0190$

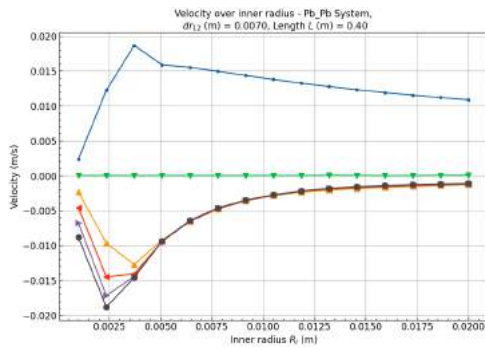


(f) Target solution temperature profiles over the length in systems over the inner radius R_i with $dr_{12_1}(m) = 0.0110$ and $dr_{34_1}(m) = 0.0230$

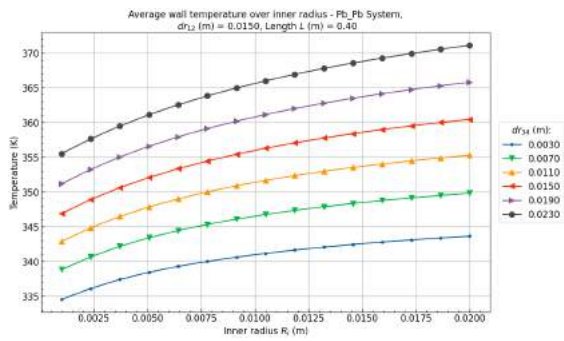
Figure B.48: Pb/Pb (Heat/Cool) System target solution temperature profiles over the inner radius R_i and cooling wall thickness dr_{34} at a heating wall thickness of $dr_{12} = 0.0110m$, a system length (L) of $0.4m$, and a pipe angle (θ) of 5° .

Pb/Pb - $dr_{12} = 0.0150m$

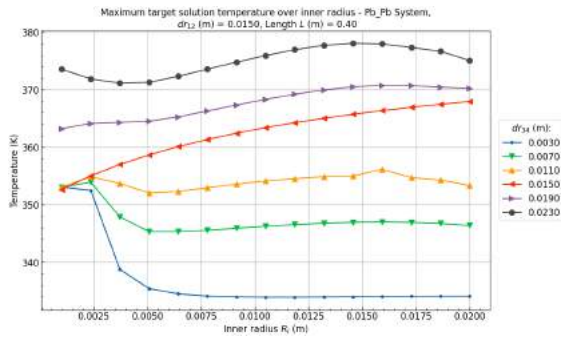
Back to overview - B.2



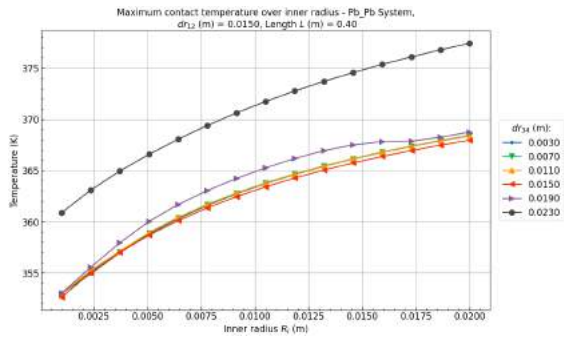
(a) Velocity over the inner radius R_i at $dr_{12} = 0.0150m$.



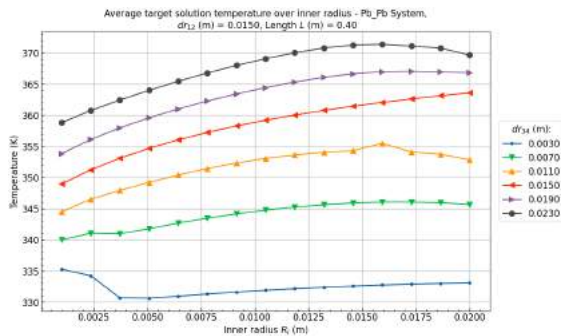
(b) Average wall temperature over the inner radius R_i at $dr_{12} = 0.0150m$.



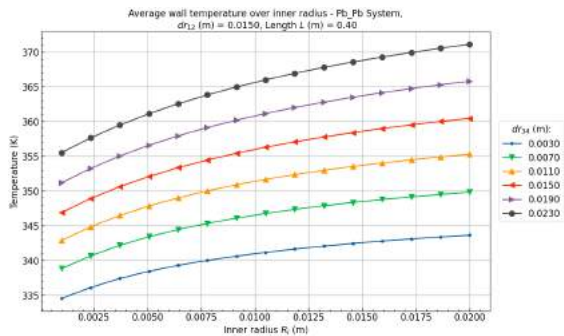
(c) Maximum target solution temperature over the inner radius R_i at $dr_{12} = 0.0150m$.



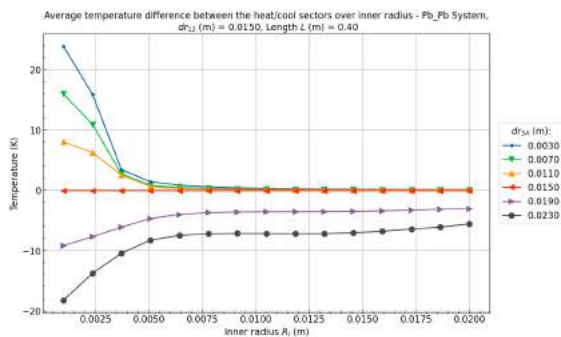
(d) Maximum contact temperature between the wall and the target solution over the inner radius R_i at $dr_{12} = 0.0150m$.



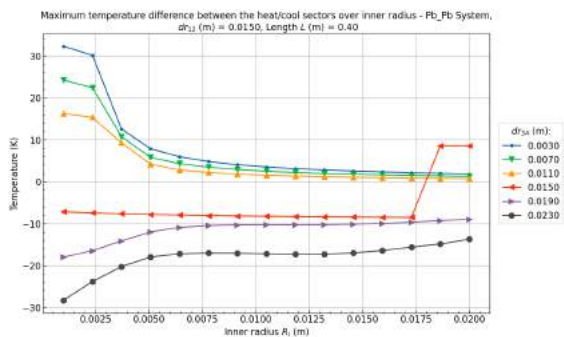
(e) Average target solution temperature over the inner radius R_i at $dr_{12} = 0.0150m$.



(f) Average wall temperature over the inner radius R_i at $dr_{12} = 0.0150m$.

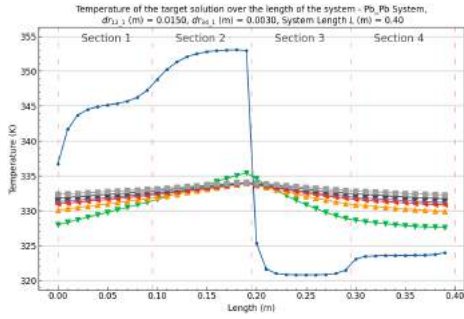


(g) Average target solution temperature difference between heating and cooling sectors over the inner radius R_i at $dr_{12} = 0.0150m$.

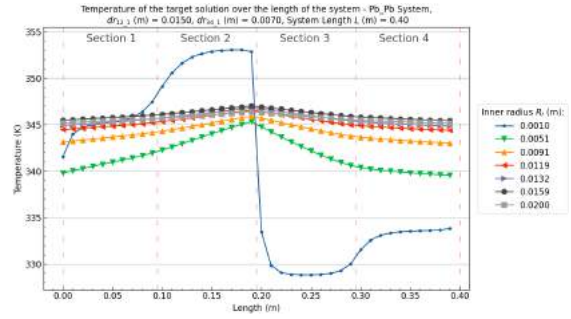


(h) Maximum target solution temperature difference between heating and cooling sectors over the inner radius R_i at $dr_{12} = 0.0150m$.

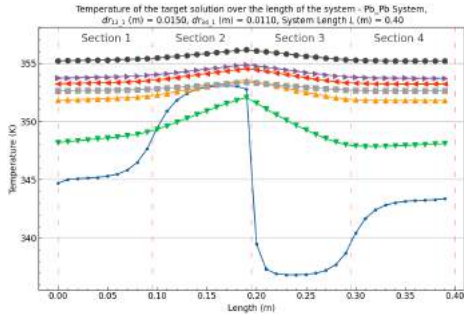
Figure B.49: Pb/Pb (Heat/Cool) System results over the inner radius R_i and cooling wall thickness dr_{34} at a heating wall thickness of $dr_{12} = 0.0150m$, a system length (L) of $0.4m$, and a pipe angle (θ) of 5° .



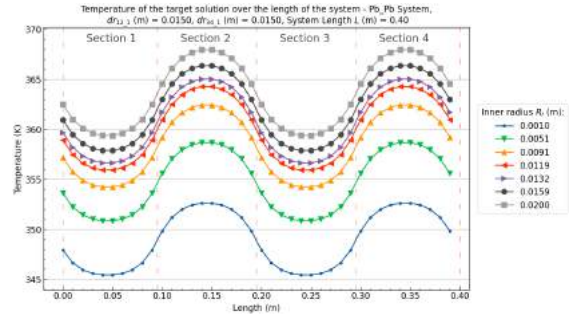
(a) Target solution temperature profiles over the length in systems over the inner radius R_i with $dr_{12_1}(m) = 0.0110$ and $dr_{34_1}(m) = 0.0030$



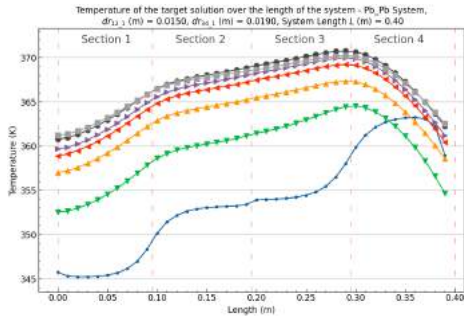
(b) Target solution temperature profiles over the length in systems over the inner radius R_i with $dr_{12_1}(m) = 0.0110$ and $dr_{34_1}(m) = 0.0070$



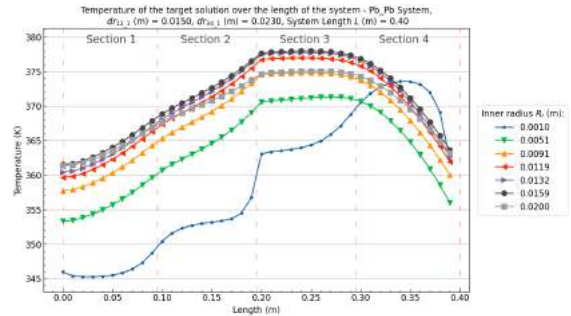
(c) Target solution temperature profiles over the length in systems over the inner radius R_i with $dr_{12_1}(m) = 0.0110$ and $dr_{34_1}(m) = 0.0110$



(d) Target solution temperature profiles over the length in systems over the inner radius R_i with $dr_{12_1}(m) = 0.0110$ and $dr_{34_1}(m) = 0.0150$



(e) Target solution temperature profiles over the length in systems over the inner radius R_i with $dr_{12_1}(m) = 0.0110$ and $dr_{34_1}(m) = 0.0190$

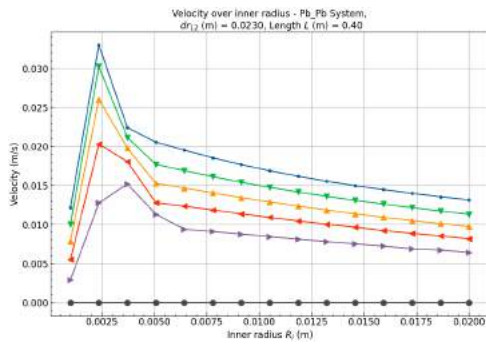


(f) Target solution temperature profiles over the length in systems over the inner radius R_i with $dr_{12_1}(m) = 0.0110$ and $dr_{34_1}(m) = 0.0230$

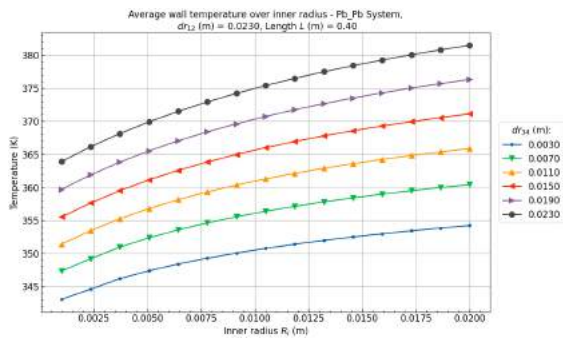
Figure B.50: Pb/Pb (Heat/Cool) System target solution temperature profiles over the inner radius R_i and cooling wall thickness dr_{34} at a heating wall thickness of $dr_{12} = 0.0150m$, a system length (L) of $0.4m$, and a pipe angle (θ) of 5° .

Pb/Pb - $dr_{12} = 0.0230m$

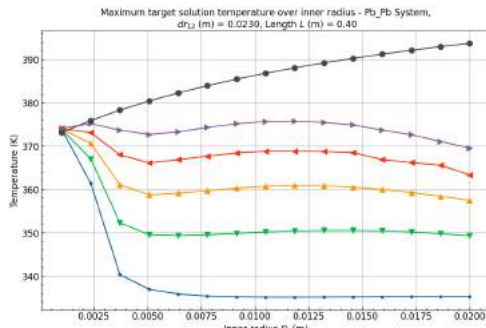
Back to overview - B.2



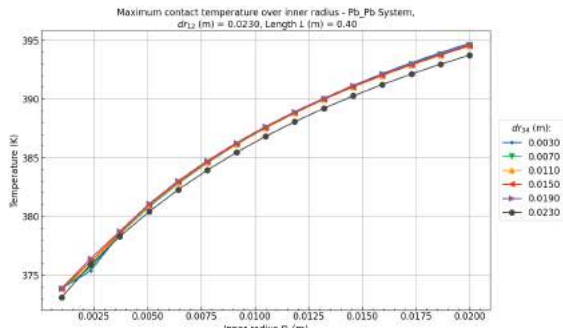
(a) Velocity over the inner radius R_i at $dr_{12} = 0.0230m$.



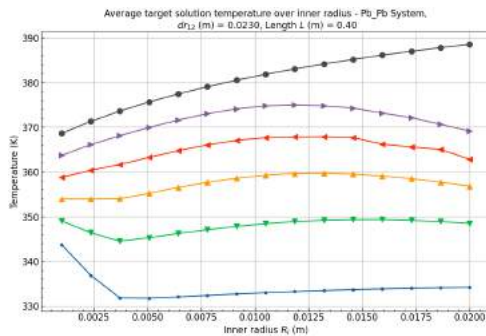
(b) Average wall temperature over the inner radius R_i at $dr_{12} = 0.0230m$.



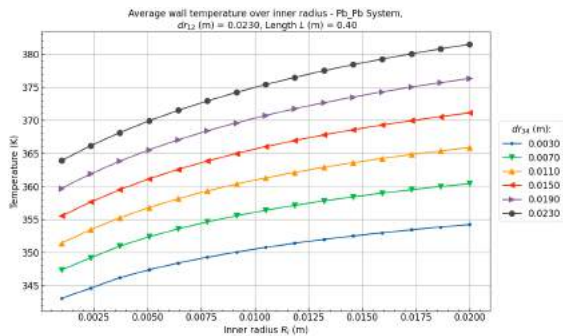
(c) Maximum target solution temperature over the inner radius R_i at $dr_{12} = 0.0230m$.



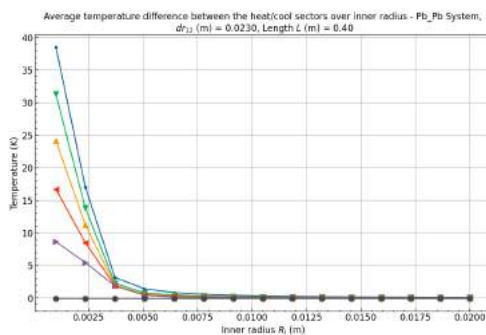
(d) Maximum contact temperature temperature between the wall and the target solution over the inner radius R_i at $dr_{12} = 0.0230m$.



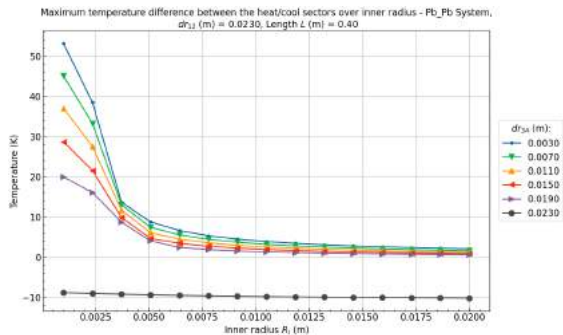
(e) Average target solution temperature over the inner radius R_i at $dr_{12} = 0.0230m$.



(f) Average wall temperature over the inner radius R_i at $dr_{12} = 0.0230m$.

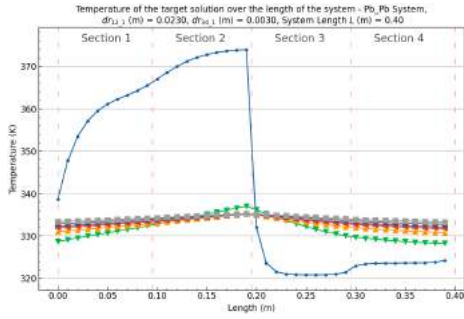


(g) Average target solution temperature difference between heating and cooling sectors over the inner radius R_i at $dr_{12} = 0.0230m$.

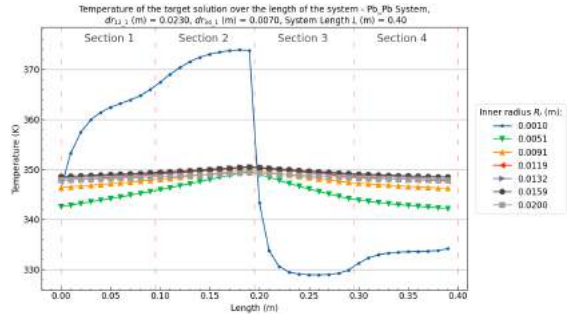


(h) Maximum target solution temperature difference between heating and cooling sectors over the inner radius R_i at $dr_{12} = 0.0230m$.

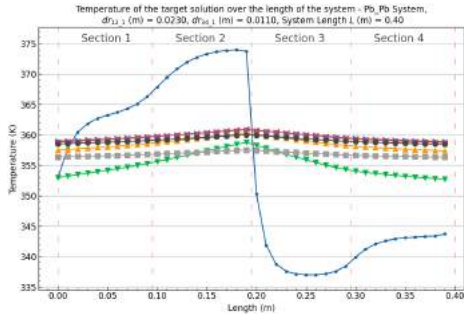
Figure B.51: Pb/Pb (Heat/Cool) System results over the inner radius R_i and cooling wall thickness dr_{34} at a heating wall thickness of $dr_{12} = 0.0230m$, a system length (L) of $0.4m$, and a pipe angle (θ) of 5° .



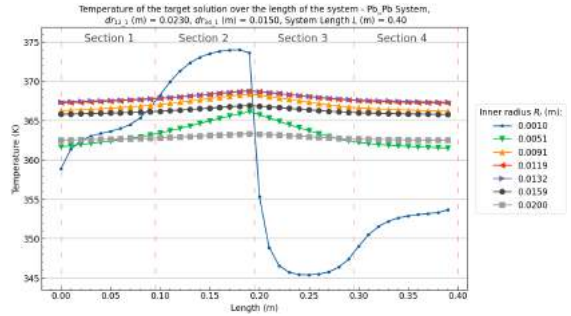
(a) Target solution temperature profiles over the length in systems over the inner radius R_i with $dr_{12_1}(m) = 0.0230$ and $dr_{34_1}(m) = 0.0030$



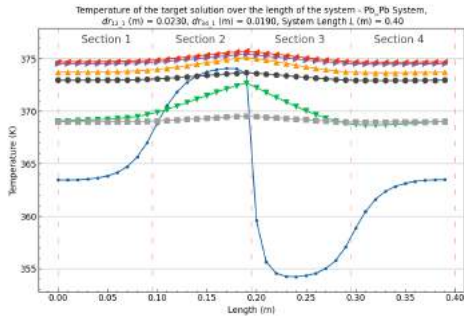
(b) Target solution temperature profiles over the length in systems over the inner radius R_i with $dr_{12_1}(m) = 0.0110$ and $dr_{34_1}(m) = 0.0070$



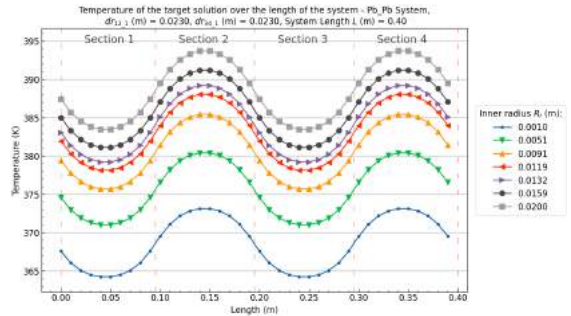
(c) Target solution temperature profiles over the length in systems over the inner radius R_i with $dr_{12_1}(m) = 0.0110$ and $dr_{34_1}(m) = 0.0110$



(d) Target solution temperature profiles over the length in systems over the inner radius R_i with $dr_{12_1}(m) = 0.0110$ and $dr_{34_1}(m) = 0.0150$



(e) Target solution temperature profiles over the length in systems over the inner radius R_i with $dr_{12_1}(m) = 0.0110$ and $dr_{34_1}(m) = 0.0190$

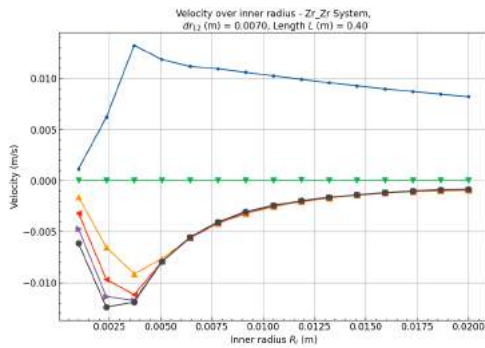


(f) Target solution temperature profiles over the length in systems over the inner radius R_i with $dr_{12_1}(m) = 0.0110$ and $dr_{34_1}(m) = 0.0230$

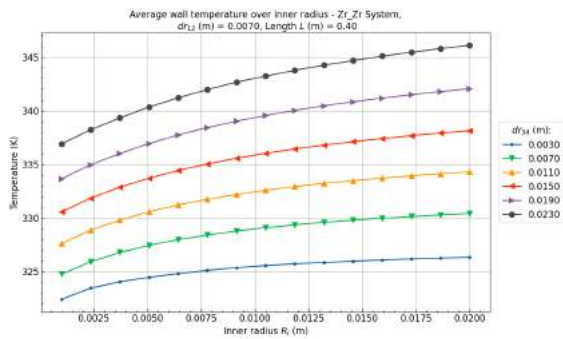
Figure B.52: Pb/Pb (Heat/Cool) System target solution temperature profiles over the inner radius R_i and cooling wall thickness dr_{34} at a heating wall thickness of $dr_{12} = 0.0230m$, a system length (L) of $0.4m$, and a pipe angle (θ) of 5° .

$Zr/Zr - dr_{12} = 0.0070m$

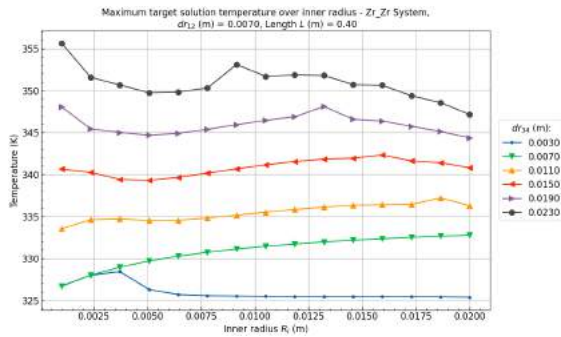
[Back to overview - B.2](#)



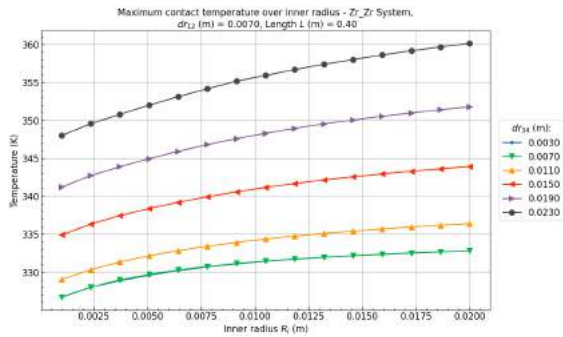
(a) Velocity over the inner radius R_i at $dr_{12} = 0.0070m$.



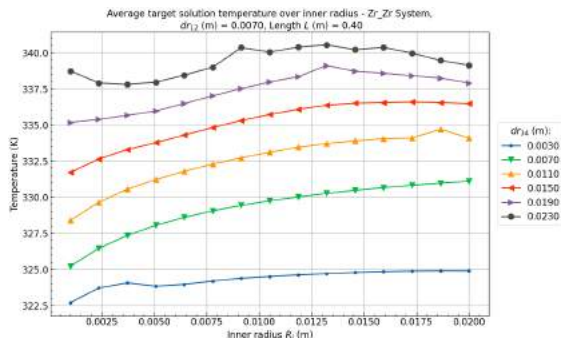
(b) Average wall temperature over the inner radius R_i at $dr_{12} = 0.0070m$.



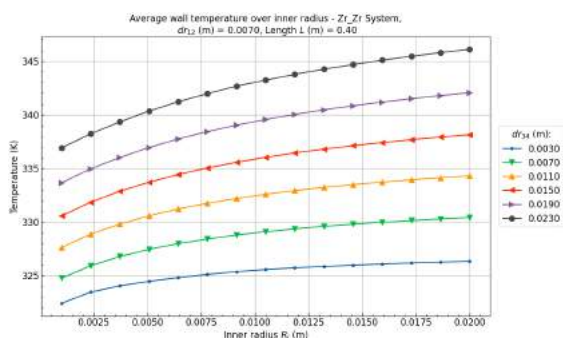
(c) Maximum target solution temperature over the inner radius R_i at $dr_{12} = 0.0070m$.



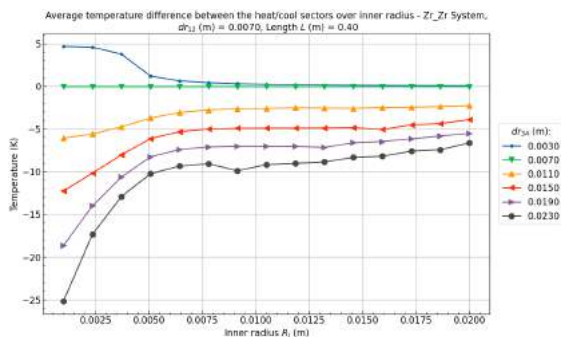
(d) Maximum contact temperature between the wall and the target solution over the inner radius R_i at $dr_{12} = 0.0070m$.



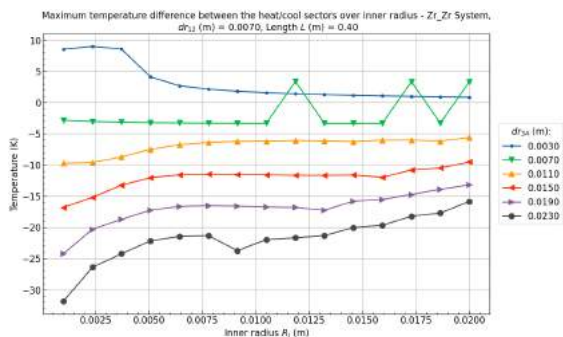
(e) Average target solution temperature over the inner radius R_i at $dr_{12} = 0.0070m$.



(f) Average wall temperature over the inner radius R_i at $dr_{12} = 0.0070m$.

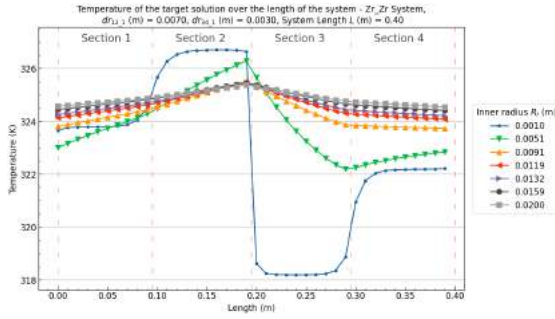


(g) Average target solution temperature difference between heating and cooling sectors over the inner radius R_i at $dr_{12} = 0.0070m$.

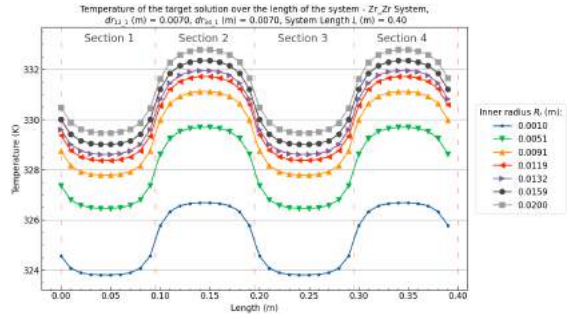


(h) Maximum target solution temperature difference between heating and cooling sectors over the inner radius R_i at $dr_{12} = 0.0070m$.

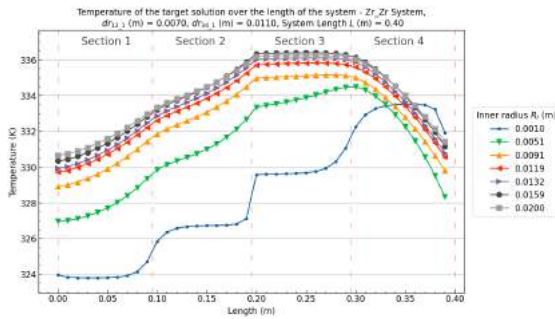
Figure B.53: Zr/Zr (Heat/Cool) System results over the inner radius R_i and cooling wall thickness dr_{34} at a heating wall thickness of $dr_{12} = 0.0070m$, a system length (L) of $0.4m$, and a pipe angle (θ) of 5° .



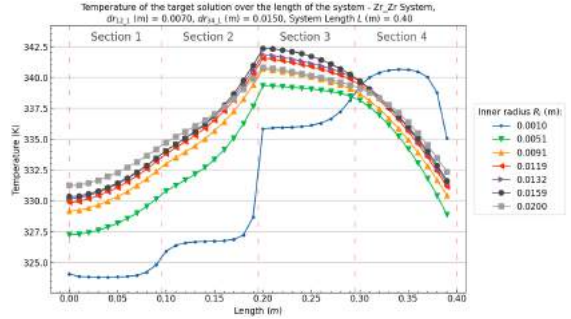
(a) Target solution temperature profiles over the length in systems over the inner radius R_i with $dr_{12_1}(m) = 0.0070$ and $dr_{34_1}(m) = 0.0030$



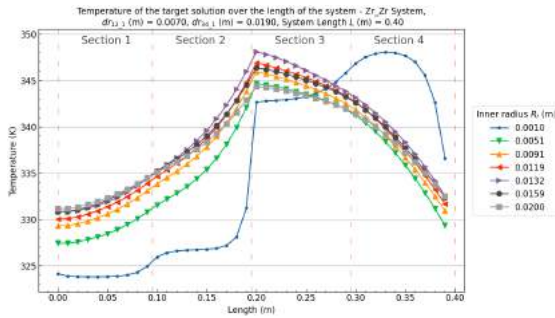
(b) Target solution temperature profiles over the length in systems over the inner radius R_i with $dr_{12_1}(m) = 0.0070$ and $dr_{34_1}(m) = 0.0070$



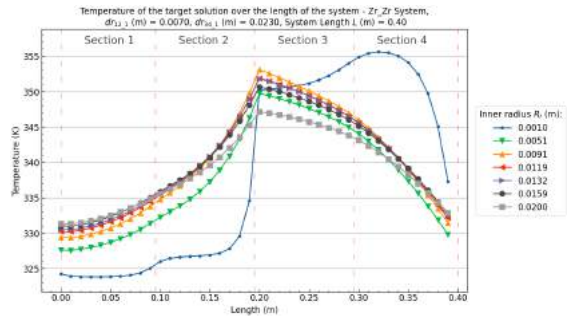
(c) Target solution temperature profiles over the length in systems over the inner radius R_i with $dr_{12_1}(m) = 0.0070$ and $dr_{34_1}(m) = 0.0110$



(d) Target solution temperature profiles over the length in systems over the inner radius R_i with $dr_{12_1}(m) = 0.0070$ and $dr_{34_1}(m) = 0.0150$



(e) Target solution temperature profiles over the length in systems over the inner radius R_i with $dr_{12_1}(m) = 0.0070$ and $dr_{34_1}(m) = 0.0190$

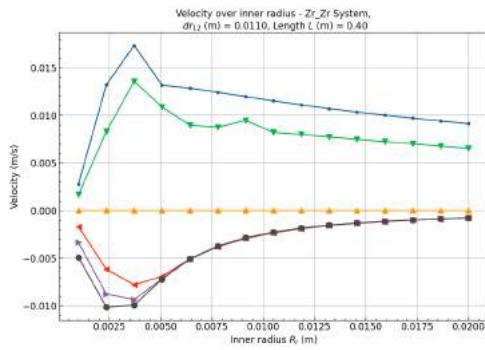


(f) Target solution temperature profiles over the length in systems over the inner radius R_i with $dr_{12_1}(m) = 0.0070$ and $dr_{34_1}(m) = 0.0230$

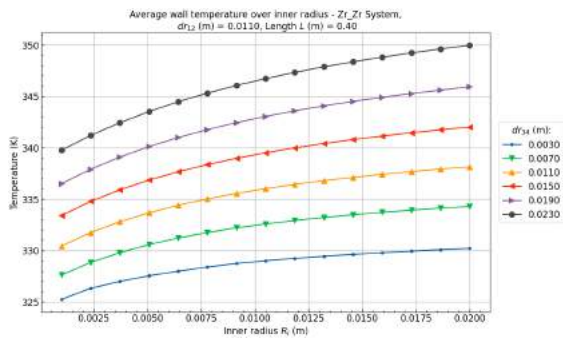
Figure B.54: Zr/Zr (Heat/Cool) System target solution temperature profiles over the inner radius R_i and cooling wall thickness dr_{34} at a heating wall thickness of $dr_{12} = 0.0070m$, a system length (L) of $0.4m$, and a pipe angle (θ) of 5° .

$Zr/Zr - dr_{12} = 0.0110m$

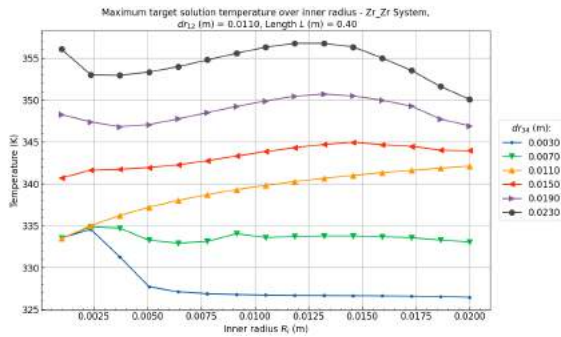
[Back to overview - B.2](#)



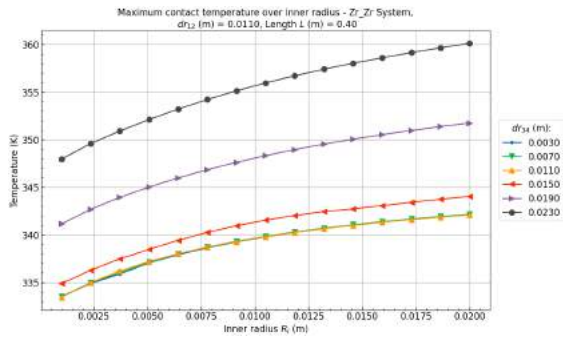
(a) Velocity over the inner radius R_i at $dr_{12} = 0.0110m$.



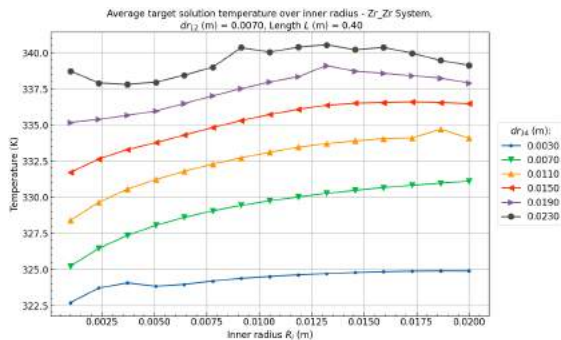
(b) Average wall temperature over the inner radius R_i at $dr_{12} = 0.0110m$.



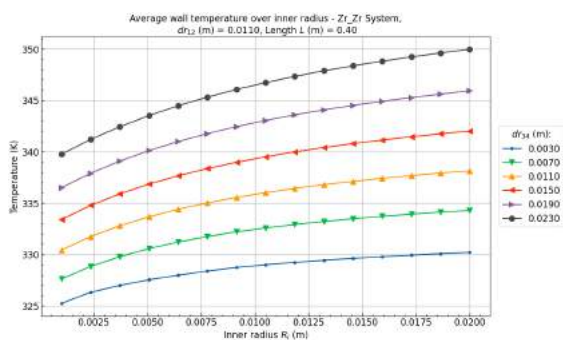
(c) Maximum target solution temperature over the inner radius R_i at $dr_{12} = 0.0110m$.



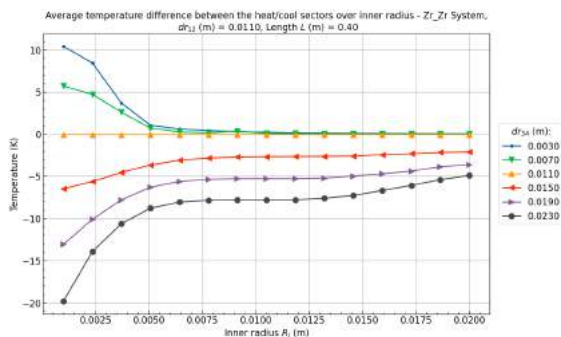
(d) Maximum contact temperature between the wall and the target solution over the inner radius R_i at $dr_{12} = 0.0110m$.



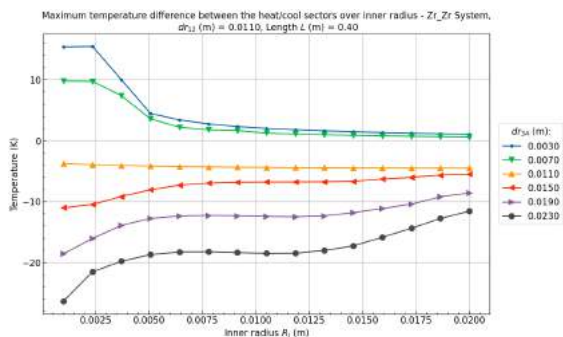
(e) Average target solution temperature over the inner radius R_i at $dr_{12} = 0.0110m$.



(f) Average wall temperature over the inner radius R_i at $dr_{12} = 0.0110m$.

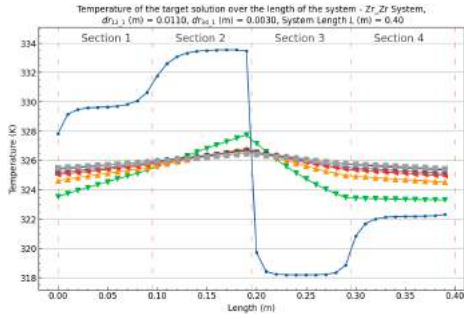


(g) Average target solution temperature difference between heating and cooling sectors over the inner radius R_i at $dr_{12} = 0.0110m$.

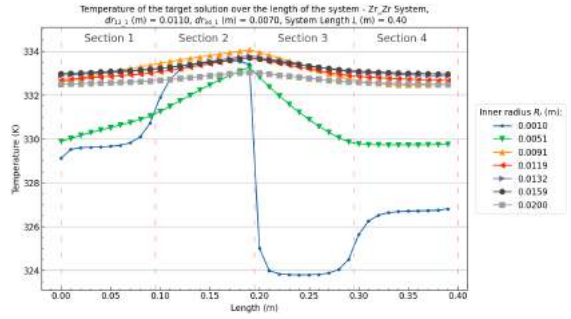


(h) Maximum target solution temperature difference between heating and cooling sectors over the inner radius R_i at $dr_{12} = 0.0110m$.

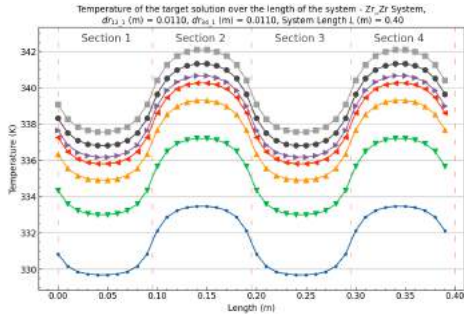
Figure B.55: Zr/Zr (Heat/Cool) System results over the inner radius R_i and cooling wall thickness dr_{34} at a heating wall thickness of $dr_{12} = 0.0110m$, a system length (L) of $0.4m$, and a pipe angle (θ) of 5° .



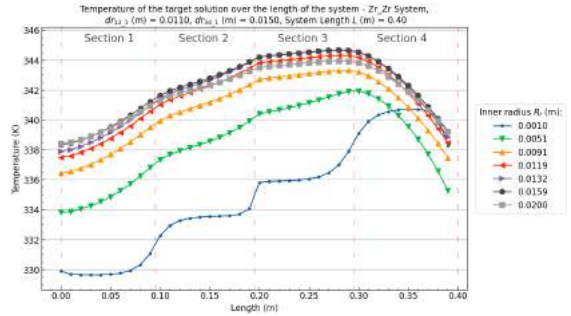
(a) Target solution temperature profiles over the length in systems over the inner radius R_i with $dr_{12_1}(m) = 0.0110$ and $dr_{34_1}(m) = 0.0030$



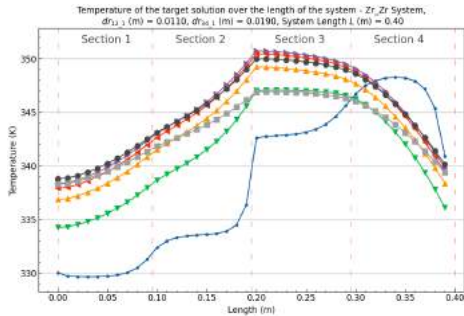
(b) Target solution temperature profiles over the length in systems over the inner radius R_i with $dr_{12_1}(m) = 0.0110$ and $dr_{34_1}(m) = 0.0070$



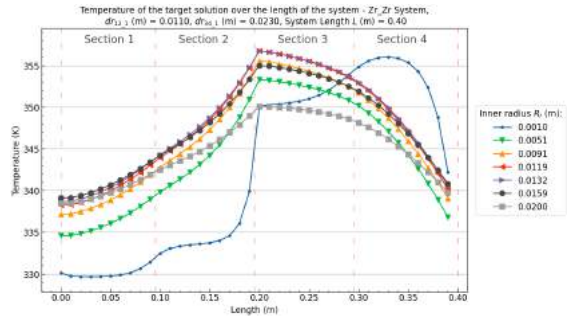
(c) Target solution temperature profiles over the length in systems over the inner radius R_i with $dr_{12_1}(m) = 0.0110$ and $dr_{34_1}(m) = 0.0110$



(d) Target solution temperature profiles over the length in systems over the inner radius R_i with $dr_{12_1}(m) = 0.0110$ and $dr_{34_1}(m) = 0.0150$



(e) Target solution temperature profiles over the length in systems over the inner radius R_i with $dr_{12_1}(m) = 0.0110$ and $dr_{34_1}(m) = 0.0190$

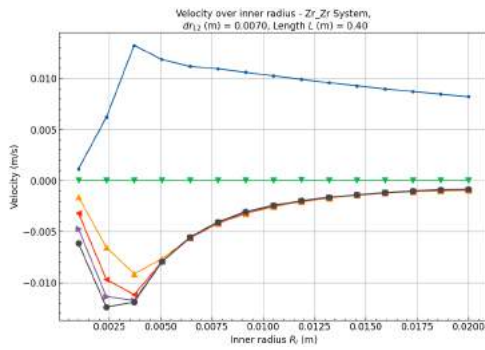


(f) Target solution temperature profiles over the length in systems over the inner radius R_i with $dr_{12_1}(m) = 0.0110$ and $dr_{34_1}(m) = 0.0230$

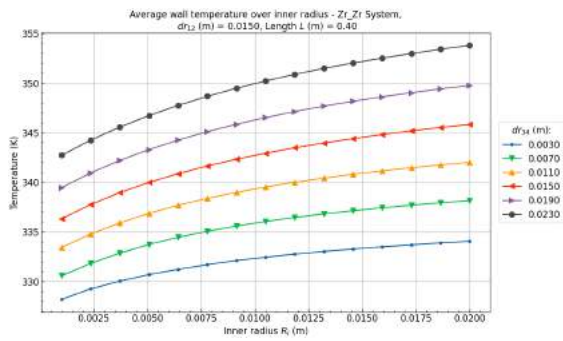
Figure B.56: Zr/Zr (Heat/Cool) System target solution temperature profiles over the inner radius R_i and cooling wall thickness dr_{34} at a heating wall thickness of $dr_{12} = 0.0110m$, a system length (L) of $0.4m$, and a pipe angle (θ) of 5° .

$Zr/Zr - dr_{12} = 0.0150m$

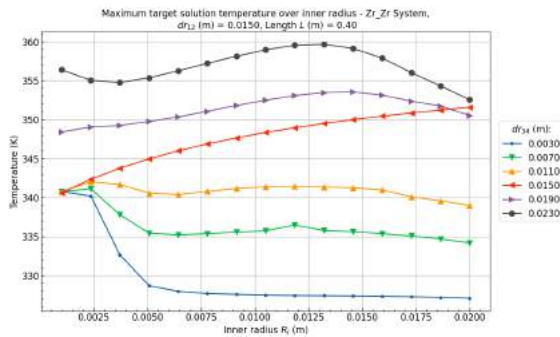
[Back to overview - B.2](#)



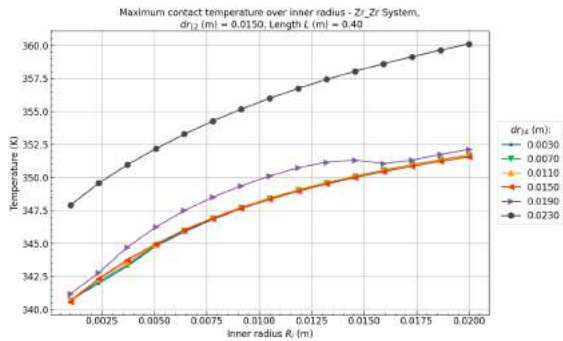
(a) Velocity over the inner radius R_i at $dr_{12} = 0.0150m$.



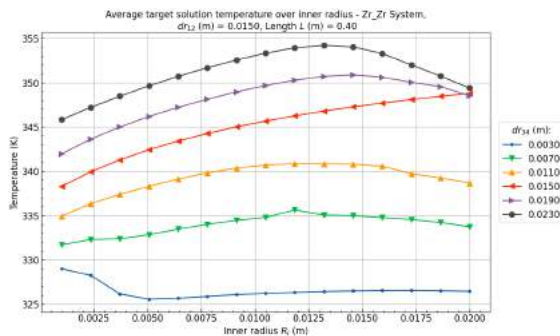
(b) Average wall temperature over the inner radius R_i at $dr_{12} = 0.0150m$.



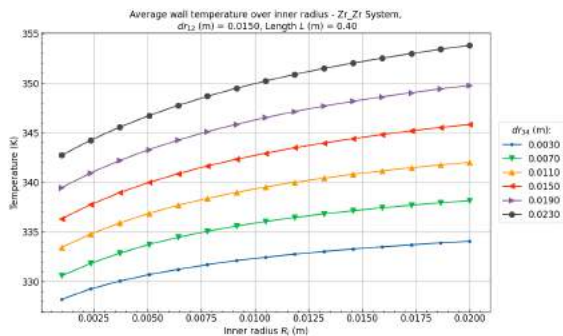
(c) Maximum target solution temperature over the inner radius R_i at $dr_{12} = 0.0150m$.



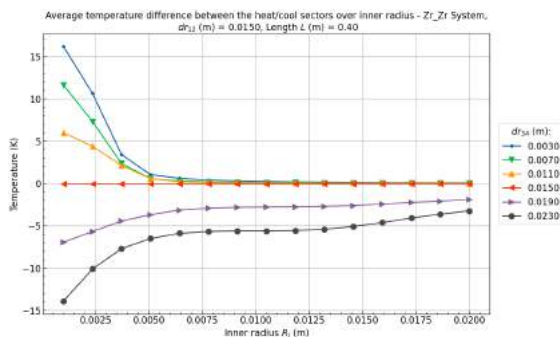
(d) Maximum contact temperature between the wall and the target solution over the inner radius R_i at $dr_{12} = 0.0150m$.



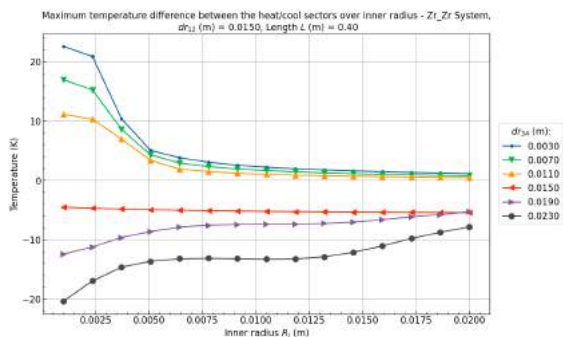
(e) Average target solution temperature over the inner radius R_i at $dr_{12} = 0.0150m$.



(f) Average wall temperature over the inner radius R_i at $dr_{12} = 0.0150m$.

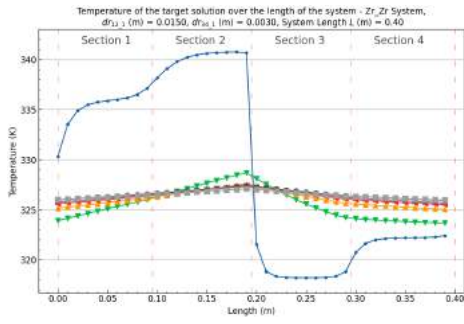


(g) Average target solution temperature difference between heating and cooling sectors over the inner radius R_i at $dr_{12} = 0.0150m$.

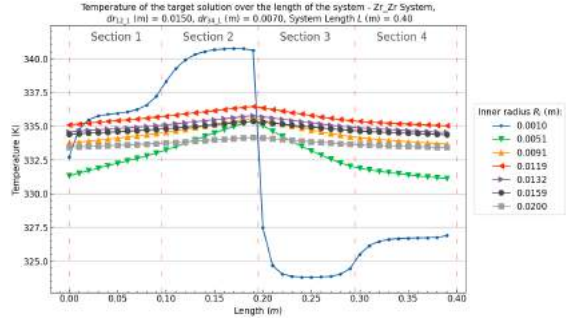


(h) Maximum target solution temperature difference between heating and cooling sectors over the inner radius R_i at $dr_{12} = 0.0150m$.

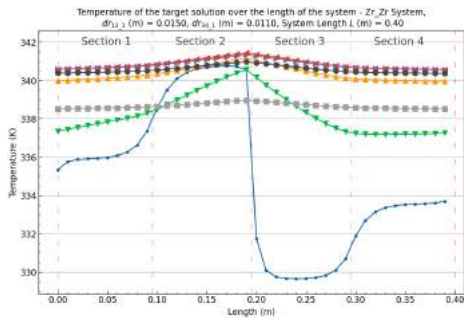
Figure B.57: Zr/Zr (Heat/Cool) System results over the inner radius R_i and cooling wall thickness dr_{34} at a heating wall thickness of $dr_{12} = 0.0150m$, a system length (L) of $0.4m$, and a pipe angle (θ) of 5° .



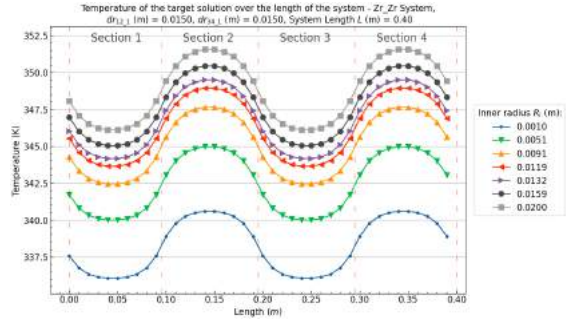
(a) Target solution temperature profiles over the length in systems over the inner radius R_i with $dr_{12_1}(m) = 0.0110$ and $dr_{34_1}(m) = 0.0030$



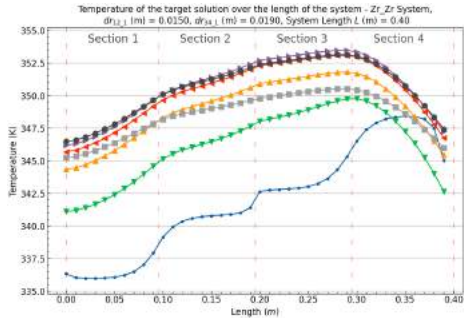
(b) Target solution temperature profiles over the length in systems over the inner radius R_i with $dr_{12_1}(m) = 0.0110$ and $dr_{34_1}(m) = 0.0070$



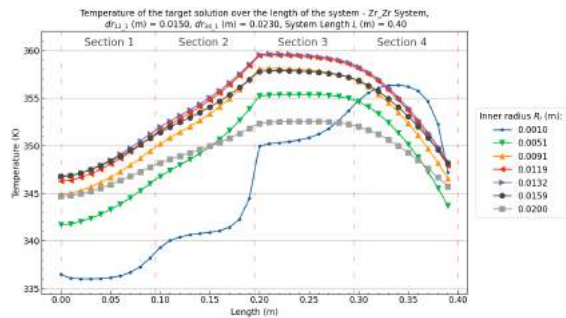
(c) Target solution temperature profiles over the length in systems over the inner radius R_i with $dr_{12_1}(m) = 0.0110$ and $dr_{34_1}(m) = 0.0110$



(d) Target solution temperature profiles over the length in systems over the inner radius R_i with $dr_{12_1}(m) = 0.0110$ and $dr_{34_1}(m) = 0.0150$



(e) Target solution temperature profiles over the length in systems over the inner radius R_i with $dr_{12_1}(m) = 0.0110$ and $dr_{34_1}(m) = 0.0190$

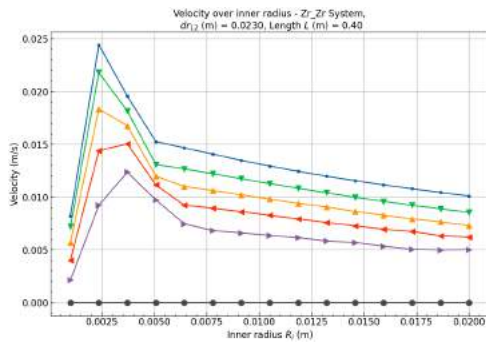


(f) Target solution temperature profiles over the length in systems over the inner radius R_i with $dr_{12_1}(m) = 0.0110$ and $dr_{34_1}(m) = 0.0230$

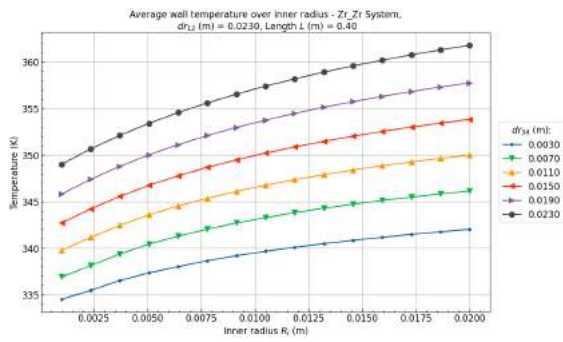
Figure B.58: Zr/Zr (Heat/Cool) System target solution temperature profiles over the inner radius R_i and cooling wall thickness dr_{34} at a heating wall thickness of $dr_{12} = 0.0150m$, a system length (L) of $0.4m$, and a pipe angle (θ) of 5° .

$Zr/Zr - dr_{12} = 0.0230m$

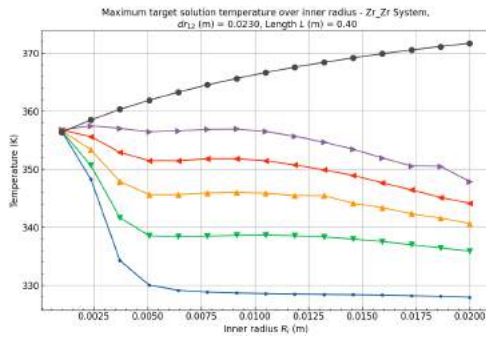
[Back to overview - B.2](#)



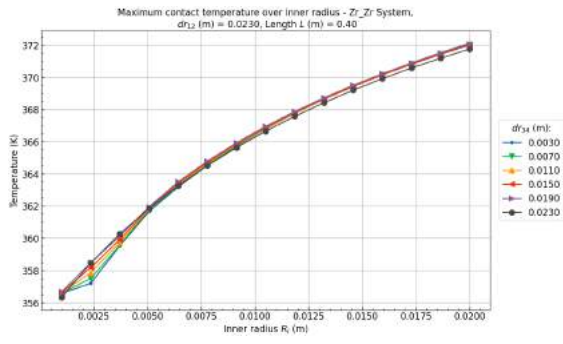
(a) Velocity over the inner radius R_i at $dr_{12} = 0.0230m$.



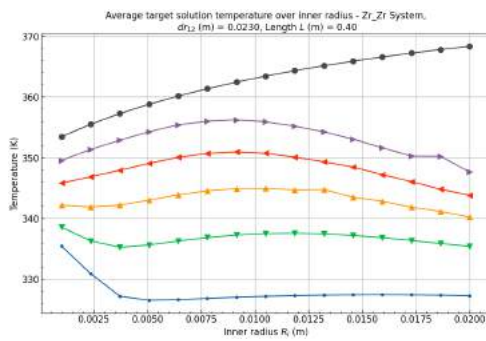
(b) Average wall temperature over the inner radius R_i at $dr_{12} = 0.0230m$.



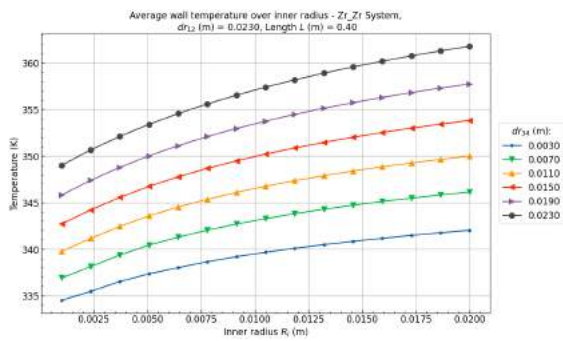
(c) Maximum target solution temperature over the inner radius R_i at $dr_{12} = 0.0230m$.



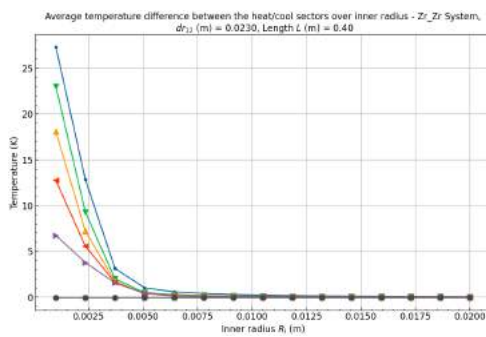
(d) Maximum contact temperature temperature between the wall and the target solution over the inner radius R_i at $dr_{12} = 0.0230m$.



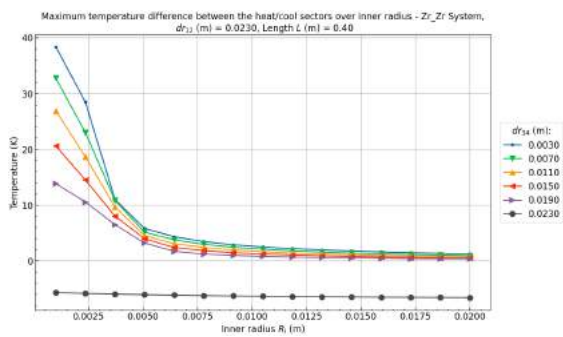
(e) Average target solution temperature over the inner radius R_i at $dr_{12} = 0.0230m$.



(f) Average wall temperature over the inner radius R_i at $dr_{12} = 0.0230m$.

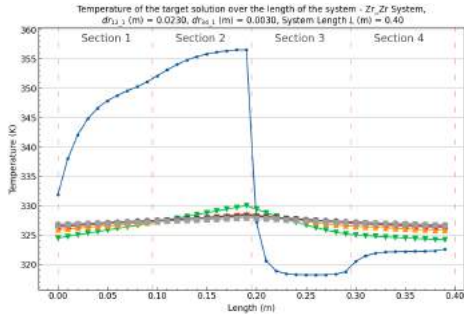


(g) Average target solution temperature difference between heating and cooling sectors over the inner radius R_i at $dr_{12} = 0.0230m$.

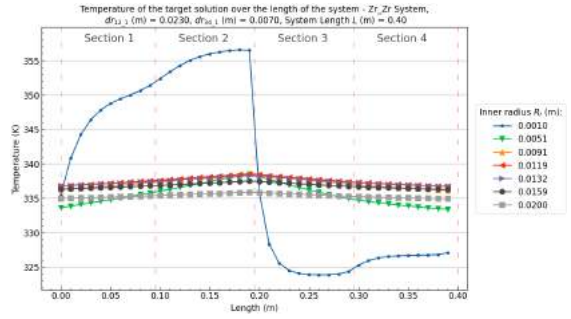


(h) Maximum target solution temperature difference between heating and cooling sectors over the inner radius R_i at $dr_{12} = 0.0230m$.

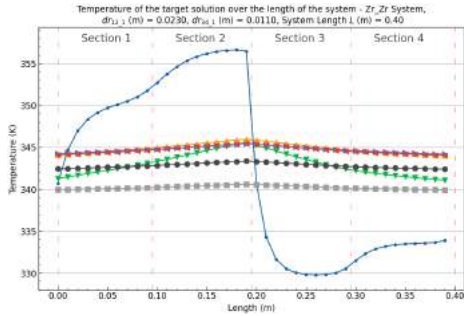
Figure B.59: Zr/Zr (Heat/Cool) System results over the inner radius R_i and cooling wall thickness dr_{34} at a heating wall thickness of $dr_{12} = 0.0230m$, a system length (L) of $0.4m$, and a pipe angle (θ) of 5° .



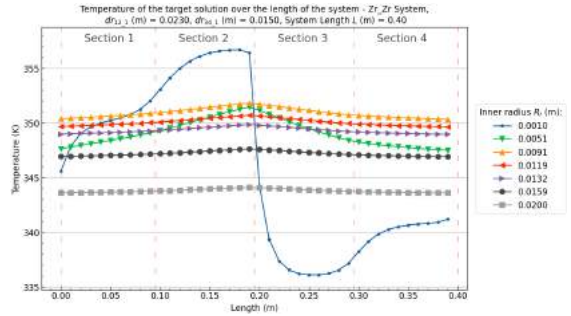
(a) Target solution temperature profiles over the length in systems over the inner radius R_i with $dr_{12_1}(m) = 0.0230$ and $dr_{34_1}(m) = 0.0030$



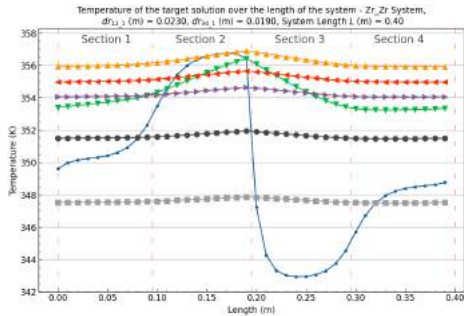
(b) Target solution temperature profiles over the length in systems over the inner radius R_i with $dr_{12_1}(m) = 0.0110$ and $dr_{34_1}(m) = 0.0070$



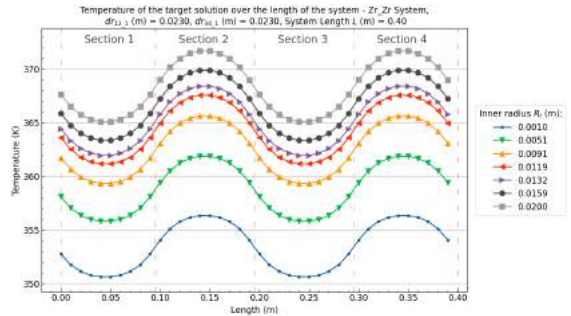
(c) Target solution temperature profiles over the length in systems over the inner radius R_i with $dr_{12_1}(m) = 0.0110$ and $dr_{34_1}(m) = 0.0110$



(d) Target solution temperature profiles over the length in systems over the inner radius R_i with $dr_{12_1}(m) = 0.0110$ and $dr_{34_1}(m) = 0.0150$



(e) Target solution temperature profiles over the length in systems over the inner radius R_i with $dr_{12_1}(m) = 0.0110$ and $dr_{34_1}(m) = 0.0190$

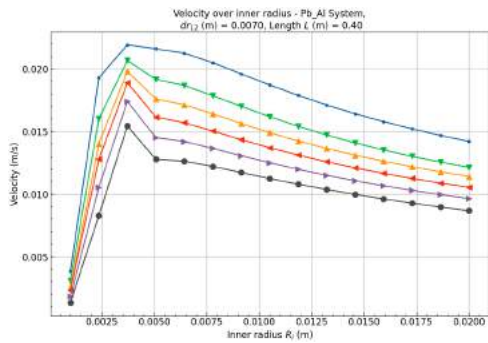


(f) Target solution temperature profiles over the length in systems over the inner radius R_i with $dr_{12_1}(m) = 0.0110$ and $dr_{34_1}(m) = 0.0230$

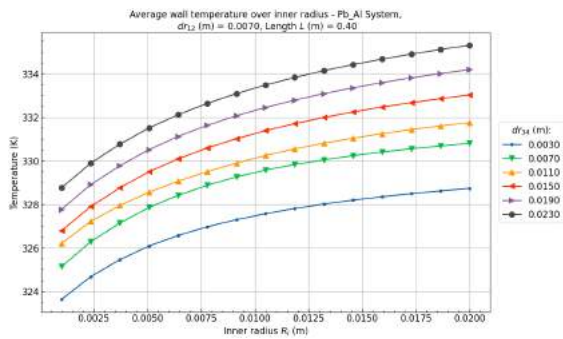
Figure B.60: Zr/Zr (Heat/Cool) System target solution temperature profiles over the inner radius R_i and cooling wall thickness dr_{34} at a heating wall thickness of $dr_{12} = 0.0230m$, a system length (L) of $0.4m$, and a pipe angle (θ) of 5° .

Pb/Al - $dr_{12} = 0.0070m$

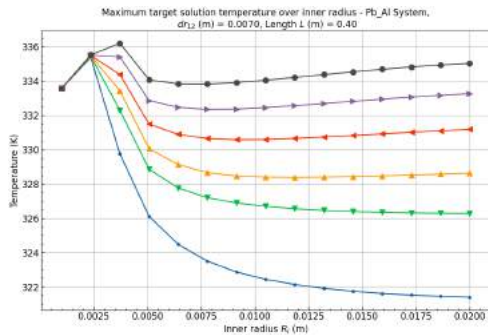
[Back to overview - B.2](#)



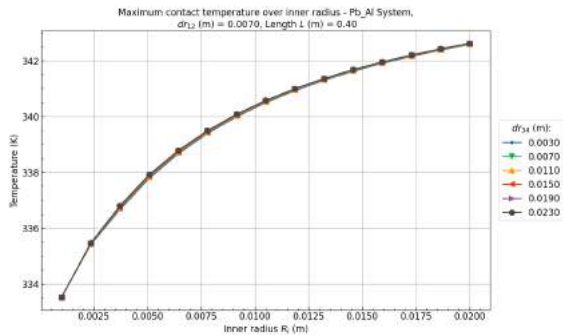
(a) Velocity over the inner radius R_i at $dr_{12} = 0.0070m$.



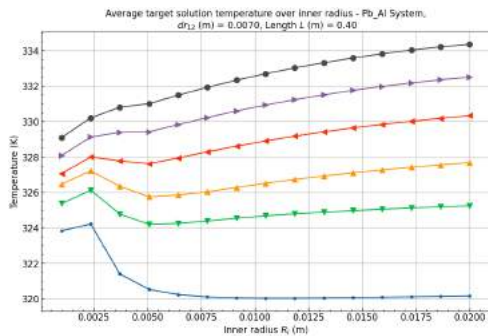
(b) Average wall temperature over the inner radius R_i at $dr_{12} = 0.0070m$.



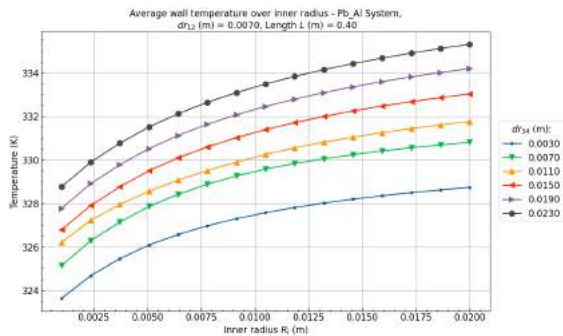
(c) Maximum target solution temperature over the inner radius R_i at $dr_{12} = 0.0070m$.



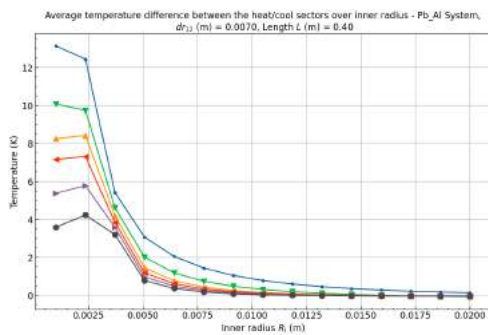
(d) Maximum contact temperature between the wall and the target solution over the inner radius R_i at $dr_{12} = 0.0070m$.



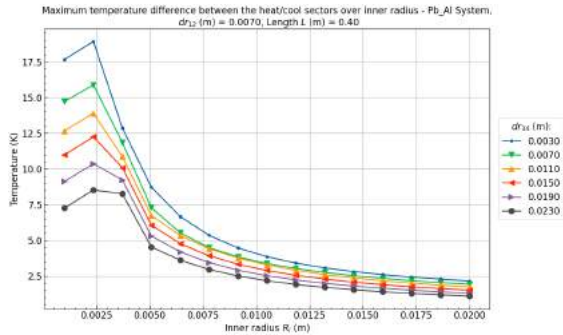
(e) Average target solution temperature over the inner radius R_i at $dr_{12} = 0.0070m$.



(f) Average wall temperature over the inner radius R_i at $dr_{12} = 0.0070m$.

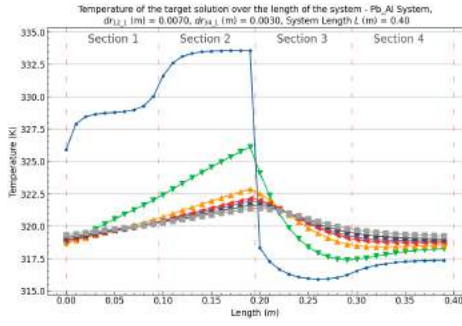


(g) Average target solution temperature difference between heating and cooling sectors over the inner radius R_i at $dr_{12} = 0.0070m$.

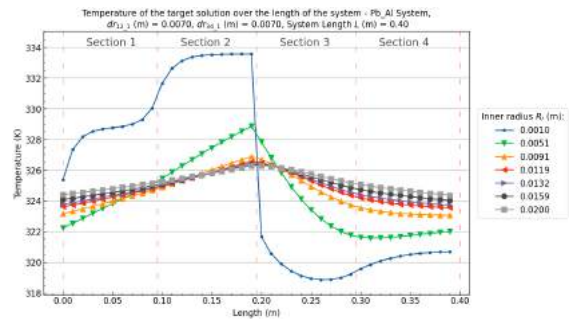


(h) Maximum target solution temperature difference between heating and cooling sectors over the inner radius R_i at $dr_{12} = 0.0070m$.

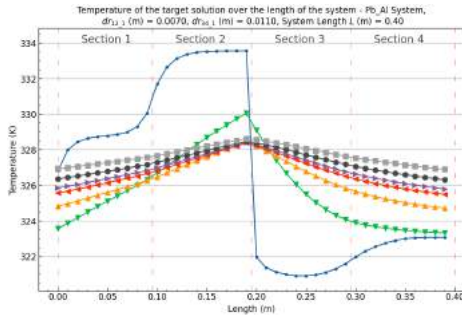
Figure B.61: Pb/Al (Heat/Cool) System results over the inner radius R_i and cooling wall thickness dr_{34} at a heating wall thickness of $dr_{12} = 0.0070m$, a system length (L) of $0.4m$, and a pipe angle (θ) of 5° .



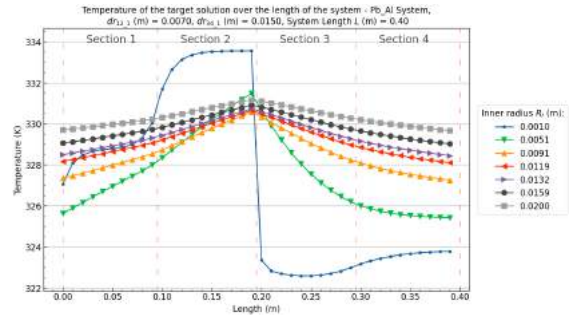
(a) Target solution temperature profiles over the length in systems over the inner radius R_i with $dr_{12_1}(m) = 0.0070$ and $dr_{34_1}(m) = 0.0030$



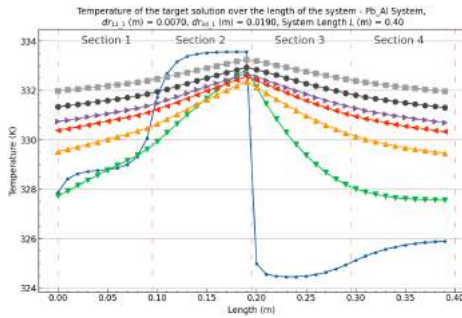
(b) Target solution temperature profiles over the length in systems over the inner radius R_i with $dr_{12_1}(m) = 0.0070$ and $dr_{34_1}(m) = 0.0070$



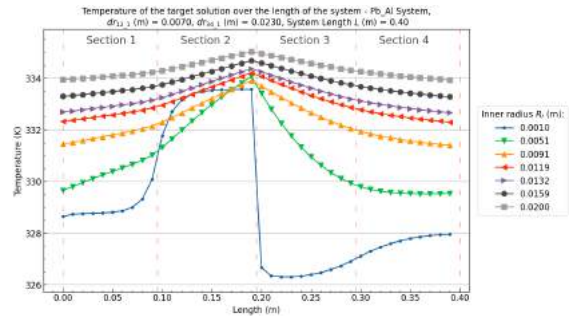
(c) Target solution temperature profiles over the length in systems over the inner radius R_i with $dr_{12_1}(m) = 0.0070$ and $dr_{34_1}(m) = 0.0110$



(d) Target solution temperature profiles over the length in systems over the inner radius R_i with $dr_{12_1}(m) = 0.0070$ and $dr_{34_1}(m) = 0.0150$



(e) Target solution temperature profiles over the length in systems over the inner radius R_i with $dr_{12_1}(m) = 0.0070$ and $dr_{34_1}(m) = 0.0190$

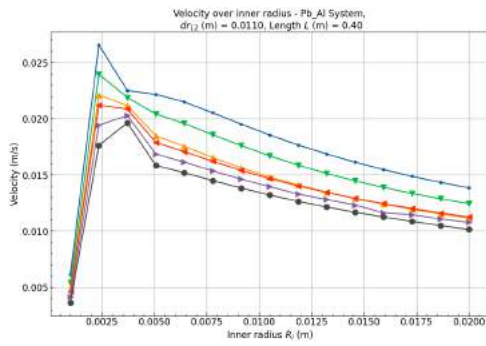


(f) Target solution temperature profiles over the length in systems over the inner radius R_i with $dr_{12_1}(m) = 0.0070$ and $dr_{34_1}(m) = 0.0230$

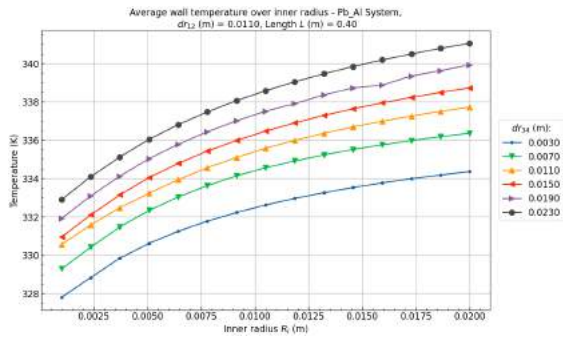
Figure B.62: Pb/Al (Heat/Cool) System target solution temperature profiles over the inner radius R_i and cooling wall thickness dr_{34} at a heating wall thickness of $dr_{12} = 0.0070m$, a system length (L) of $0.4m$, and a pipe angle (θ) of 5° .

Pb/Al - $dr_{12} = 0.0110m$

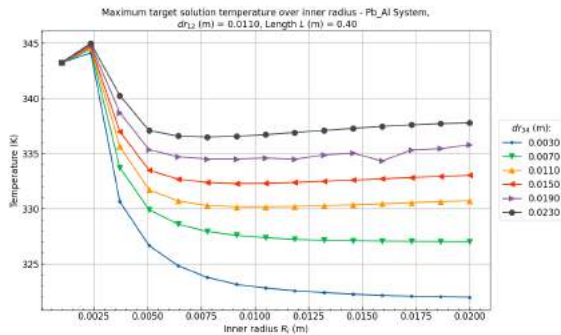
Back to overview - B.2



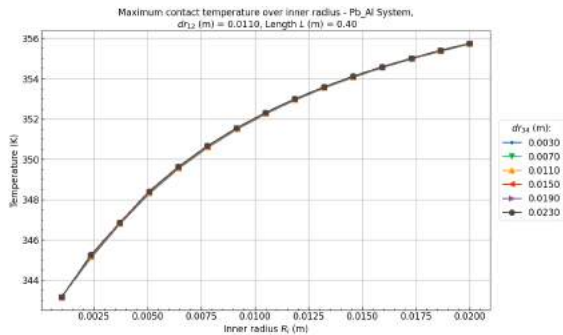
(a) Velocity over the inner radius R_i at $dr_{12} = 0.0110m$.



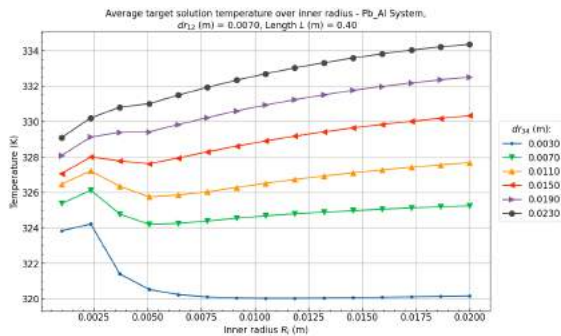
(b) Average wall temperature over the inner radius R_i at $dr_{12} = 0.0110m$.



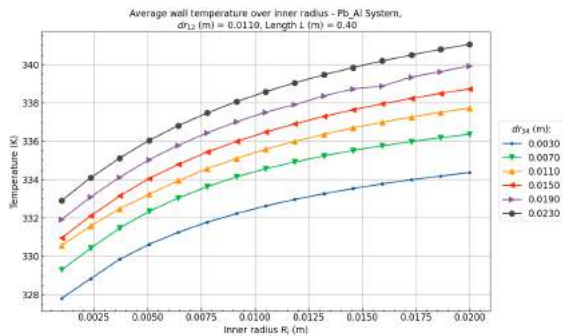
(c) Maximum target solution temperature over the inner radius R_i at $dr_{12} = 0.0110m$.



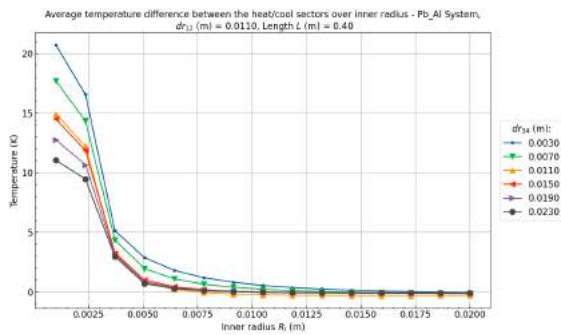
(d) Maximum contact temperature between the wall and the target solution over the inner radius R_i at $dr_{12} = 0.0110m$.



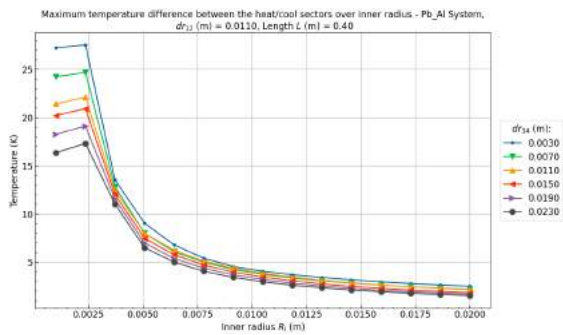
(e) Average target solution temperature over the inner radius R_i at $dr_{12} = 0.0110m$.



(f) Average wall temperature over the inner radius R_i at $dr_{12} = 0.0110m$.

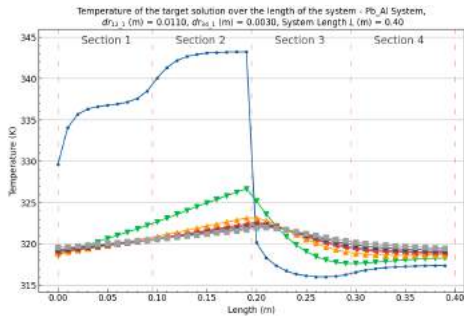


(g) Average target solution temperature difference between heating and cooling sectors over the inner radius R_i at $dr_{12} = 0.0110m$.

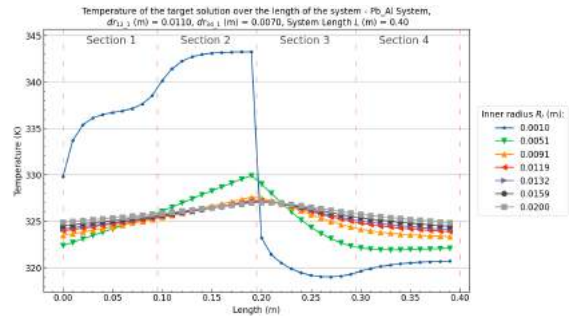


(h) Maximum target solution temperature difference between heating and cooling sectors over the inner radius R_i at $dr_{12} = 0.0110m$.

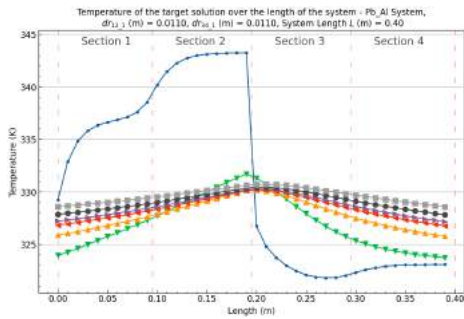
Figure B.63: Pb/Al (Heat/Cool) System results over the inner radius R_i and cooling wall thickness dr_{34} at a heating wall thickness of $dr_{12} = 0.0110m$, a system length (L) of $0.4m$, and a pipe angle (θ) of 5° .



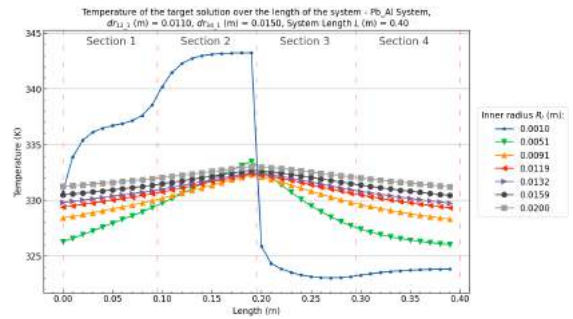
(a) Target solution temperature profiles over the length in systems over the inner radius R_i with $dr_{12_1}(m) = 0.0110$ and $dr_{34_1}(m) = 0.0030$



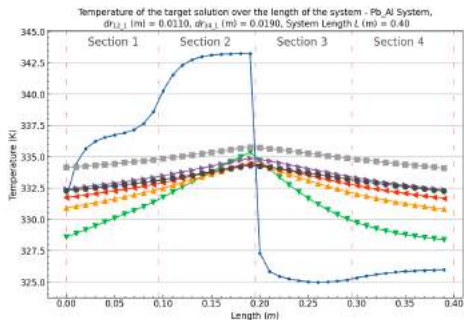
(b) Target solution temperature profiles over the length in systems over the inner radius R_i with $dr_{12_1}(m) = 0.0110$ and $dr_{34_1}(m) = 0.0070$



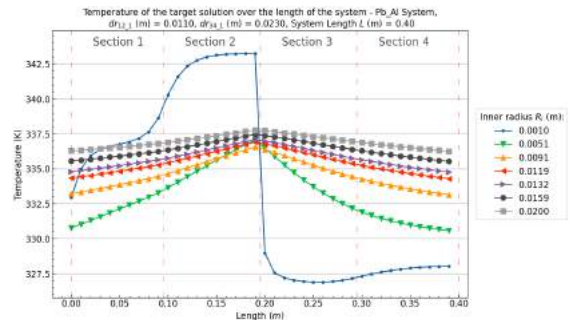
(c) Target solution temperature profiles over the length in systems over the inner radius R_i with $dr_{12_1}(m) = 0.0110$ and $dr_{34_1}(m) = 0.0110$



(d) Target solution temperature profiles over the length in systems over the inner radius R_i with $dr_{12_1}(m) = 0.0110$ and $dr_{34_1}(m) = 0.0150$



(e) Target solution temperature profiles over the length in systems over the inner radius R_i with $dr_{12_1}(m) = 0.0110$ and $dr_{34_1}(m) = 0.0190$

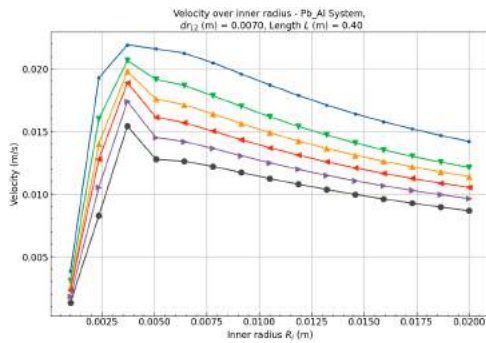


(f) Target solution temperature profiles over the length in systems over the inner radius R_i with $dr_{12_1}(m) = 0.0110$ and $dr_{34_1}(m) = 0.0230$

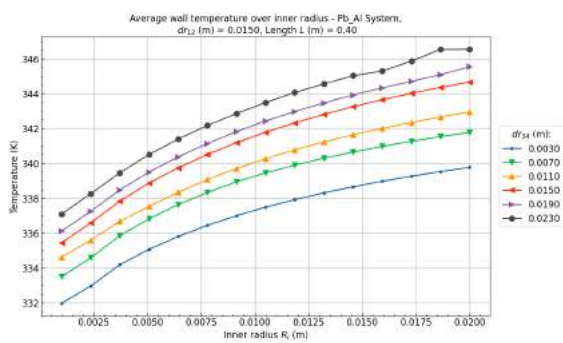
Figure B.64: Pb/Al (Heat/Cool) System target solution temperature profiles over the inner radius R_i and cooling wall thickness dr_{34} at a heating wall thickness of $dr_{12} = 0.0110m$, a system length (L) of $0.4m$, and a pipe angle (θ) of 5° .

Pb/Al - $dr_{12} = 0.0150m$

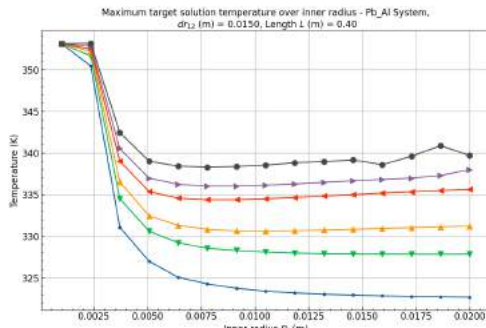
[Back to overview - B.2](#)



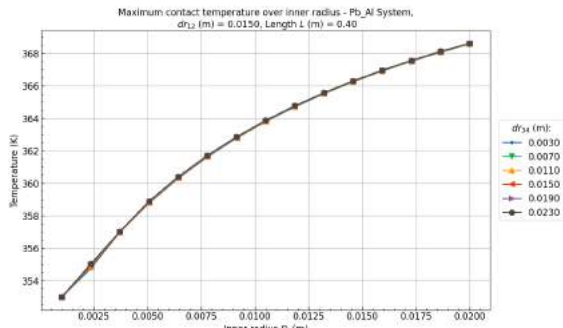
(a) Velocity over the inner radius R_i at $dr_{12} = 0.0150m$.



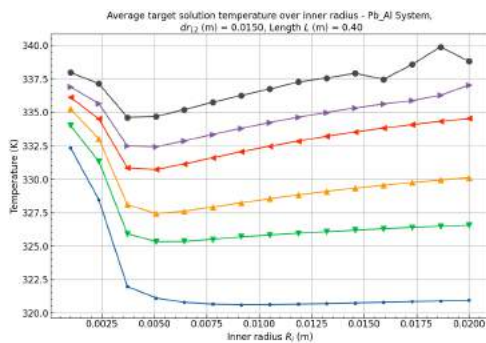
(b) Average wall temperature over the inner radius R_i at $dr_{12} = 0.0150m$.



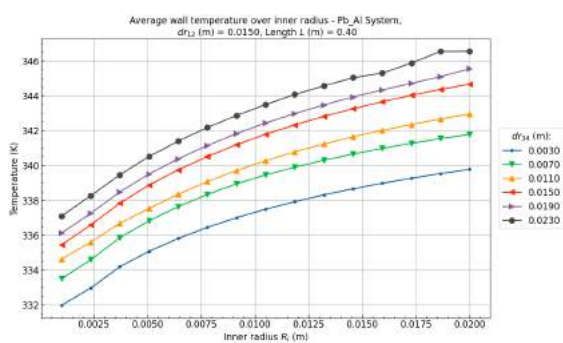
(c) Maximum target solution temperature over the inner radius R_i at $dr_{12} = 0.0150m$.



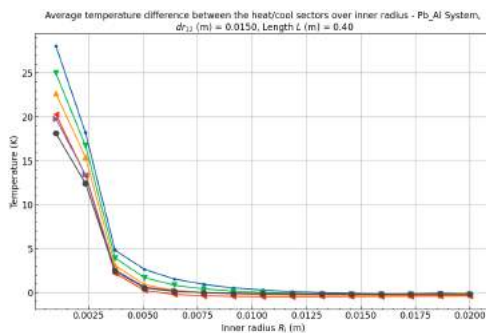
(d) Maximum contact temperature between the wall and the target solution over the inner radius R_i at $dr_{12} = 0.0150m$.



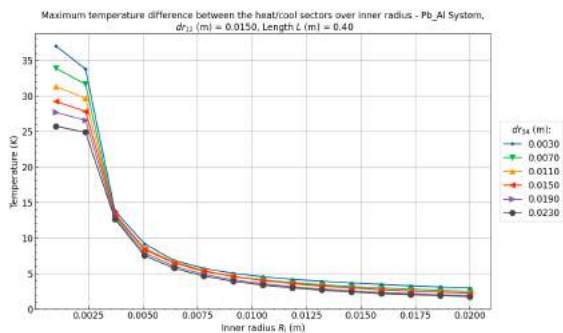
(e) Average target solution temperature over the inner radius R_i at $dr_{12} = 0.0150m$.



(f) Average wall temperature over the inner radius R_i at $dr_{12} = 0.0150m$.

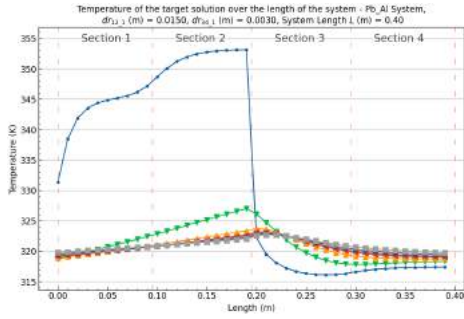


(g) Average target solution temperature difference between heating and cooling sectors over the inner radius R_i at $dr_{12} = 0.0150m$.

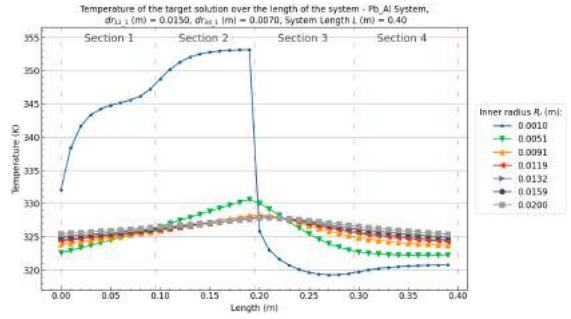


(h) Maximum target solution temperature difference between heating and cooling sectors over the inner radius R_i at $dr_{12} = 0.0150m$.

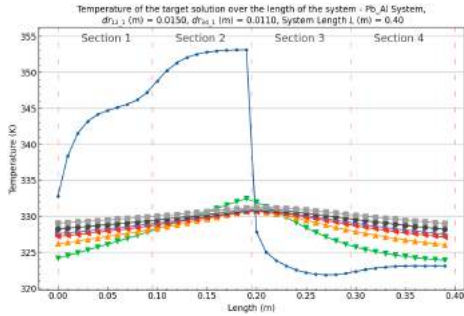
Figure B.65: Pb/Al (Heat/Cool) System results over the inner radius R_i and cooling wall thickness dr_{34} at a heating wall thickness of $dr_{12} = 0.0150m$, a system length (L) of $0.4m$, and a pipe angle (θ) of 5° .



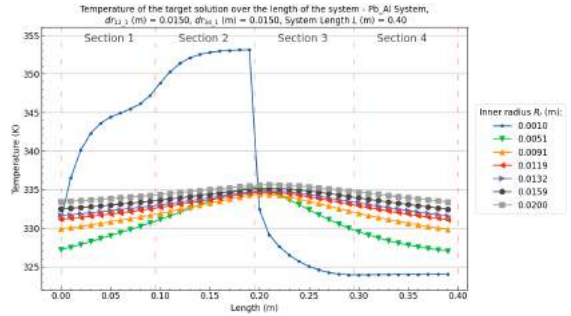
(a) Target solution temperature profiles over the length in systems over the inner radius R_i with $dr_{12_1}(m) = 0.0110$ and $dr_{34_1}(m) = 0.0030$



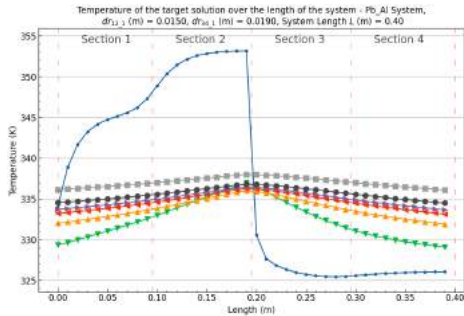
(b) Target solution temperature profiles over the length in systems over the inner radius R_i with $dr_{12_1}(m) = 0.0110$ and $dr_{34_1}(m) = 0.0070$



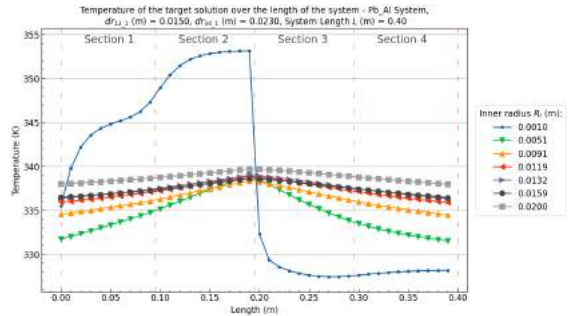
(c) Target solution temperature profiles over the length in systems over the inner radius R_i with $dr_{12_1}(m) = 0.0110$ and $dr_{34_1}(m) = 0.0110$



(d) Target solution temperature profiles over the length in systems over the inner radius R_i with $dr_{12_1}(m) = 0.0110$ and $dr_{34_1}(m) = 0.0150$



(e) Target solution temperature profiles over the length in systems over the inner radius R_i with $dr_{12_1}(m) = 0.0110$ and $dr_{34_1}(m) = 0.0190$

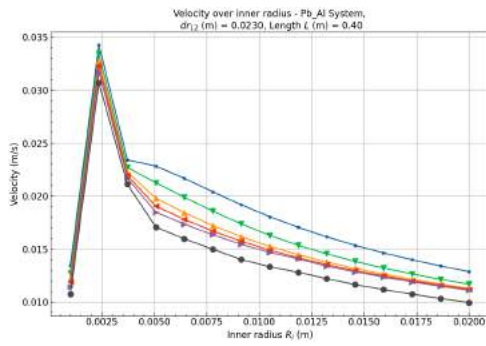


(f) Target solution temperature profiles over the length in systems over the inner radius R_i with $dr_{12_1}(m) = 0.0110$ and $dr_{34_1}(m) = 0.0230$

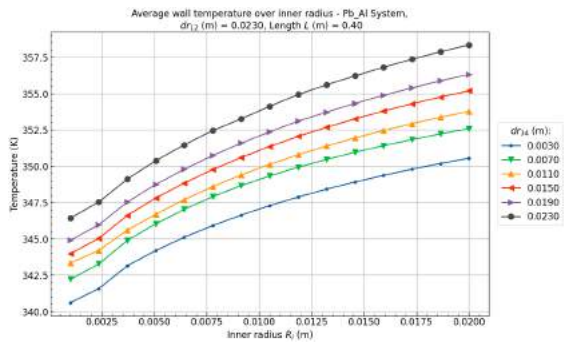
Figure B.66: Pb/Al (Heat/Cool) System target solution temperature profiles over the inner radius R_i and cooling wall thickness dr_{34} at a heating wall thickness of $dr_{12} = 0.0150m$, a system length (L) of $0.4m$, and a pipe angle (θ) of 5° .

Pb/Al - $dr_{12} = 0.0230\text{m}$

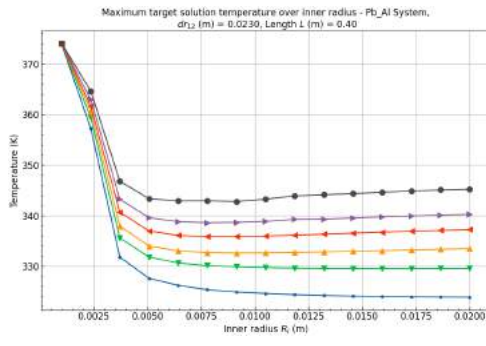
[Back to overview - B.2](#)



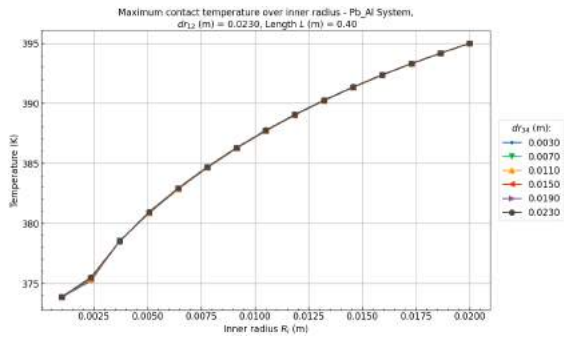
(a) Velocity over the inner radius R_i at $dr_{12} = 0.0230\text{m}$.



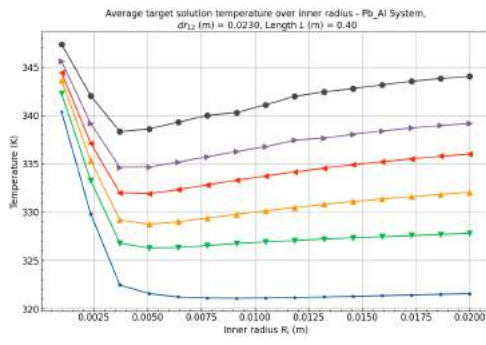
(b) Average wall temperature over the inner radius R_i at $dr_{12} = 0.0230\text{m}$.



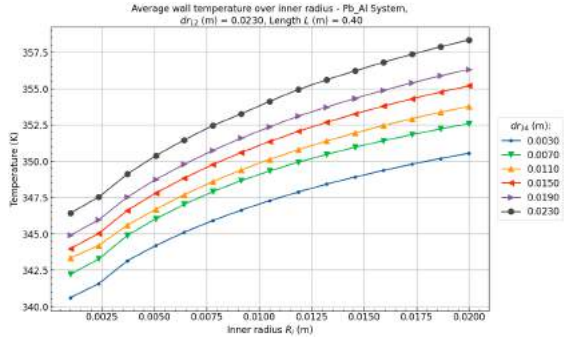
(c) Maximum target solution temperature over the inner radius R_i at $dr_{12} = 0.0230\text{m}$.



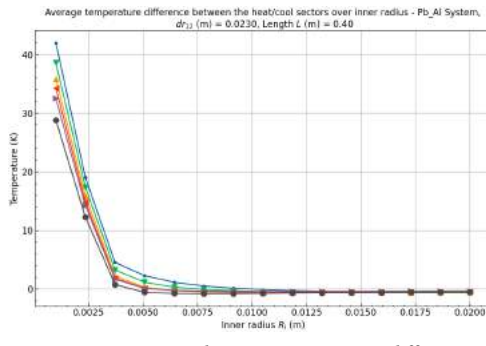
(d) Maximum contact temperature between the wall and the target solution over the inner radius R_i at $dr_{12} = 0.0230\text{m}$.



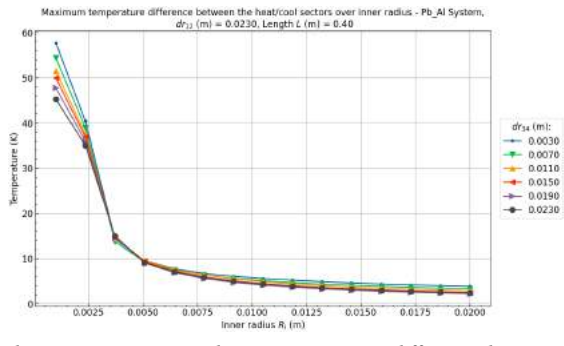
(e) Average target solution temperature over the inner radius R_i at $dr_{12} = 0.0230\text{m}$.



(f) Average wall temperature over the inner radius R_i at $dr_{12} = 0.0230\text{m}$.

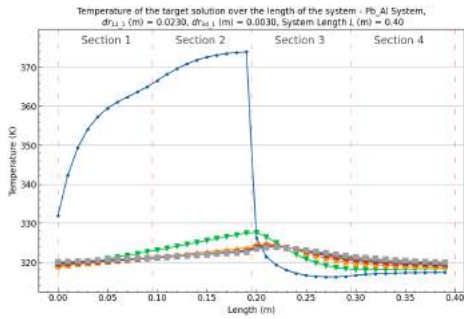


(g) Average target solution temperature difference between heating and cooling sectors over the inner radius R_i at $dr_{12} = 0.0230\text{m}$.

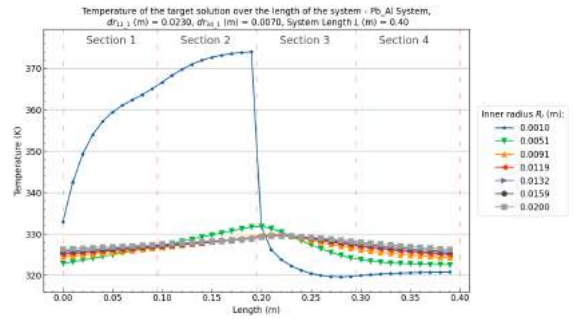


(h) Maximum target solution temperature difference between heating and cooling sectors over the inner radius R_i at $dr_{12} = 0.0230\text{m}$.

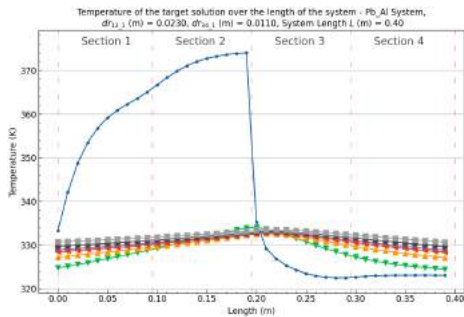
Figure B.67: Pb/Al (Heat/Cool) System results over the inner radius R_i and cooling wall thickness dr_{34} at a heating wall thickness of $dr_{12} = 0.0230\text{m}$, a system length (L) of 0.4m , and a pipe angle (θ) of 5° .



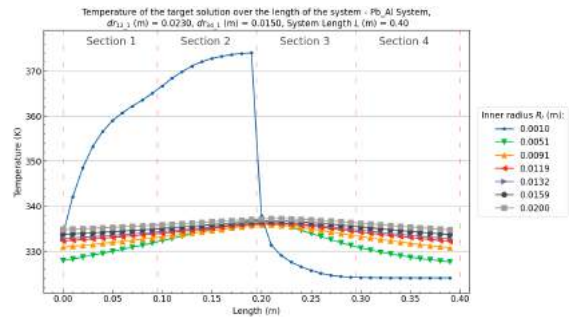
(a) Target solution temperature profiles over the length in systems over the inner radius R_i with $dr_{12_1}(m) = 0.0230$ and $dr_{34_1}(m) = 0.0030$



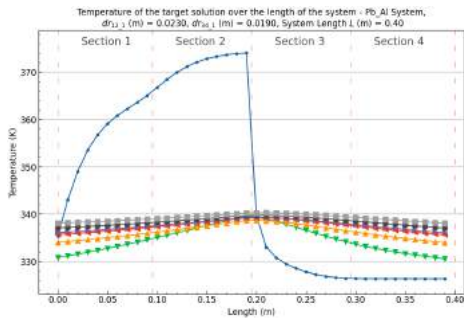
(b) Target solution temperature profiles over the length in systems over the inner radius R_i with $dr_{12_1}(m) = 0.0110$ and $dr_{34_1}(m) = 0.0070$



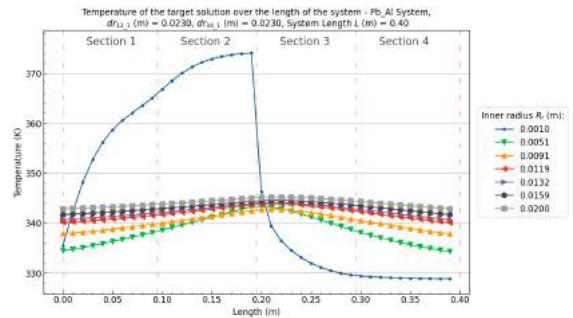
(c) Target solution temperature profiles over the length in systems over the inner radius R_i with $dr_{12_1}(m) = 0.0110$ and $dr_{34_1}(m) = 0.0110$



(d) Target solution temperature profiles over the length in systems over the inner radius R_i with $dr_{12_1}(m) = 0.0110$ and $dr_{34_1}(m) = 0.0150$



(e) Target solution temperature profiles over the length in systems over the inner radius R_i with $dr_{12_1}(m) = 0.0110$ and $dr_{34_1}(m) = 0.0190$



(f) Target solution temperature profiles over the length in systems over the inner radius R_i with $dr_{12_1}(m) = 0.0110$ and $dr_{34_1}(m) = 0.0230$

Figure B.68: Pb/Al (Heat/Cool) System target solution temperature profiles over the inner radius R_i and cooling wall thickness dr_{34} at a heating wall thickness of $dr_{12} = 0.0230m$, a system length (L) of $0.4m$, and a pipe angle (θ) of 5° .

B.3. Pipe angle (θ), System length (L) & Inner radius (L)

The general trends for the single layer wall materials and wall thicknesses in these systems are:

- The angle has the most influence on the velocity in systems with a small length
- At smaller inner radii ($R_i = 0.0010 - 0.0052m$) an increase in the pipe angle increases velocity slightly, except for some systems with a large system length. This increase in velocity is the largest in systems with an inner radius of $R_i = 0.0010m$.
- The increase in velocity over the pipe angle in smaller inner radii is the largest in Al/Al systems.
- At larger inner radii ($R_i > 0.0052$) the velocity either remains stable over an increase in the pipe angle or decreases slightly.
- Extreme pipe angle values below -20° or more are prone to add instabilities to the systems.
- There is almost no difference between the temperature profiles of the systems over the pipe angle.
- Larger system lengths result in a higher velocity in the systems. The reason for this is that by changing the system length variable the system height is changed as well increasing the total buoyancy force in the momentum equation. Changing the system length also increases the density difference between the vertical sectors.

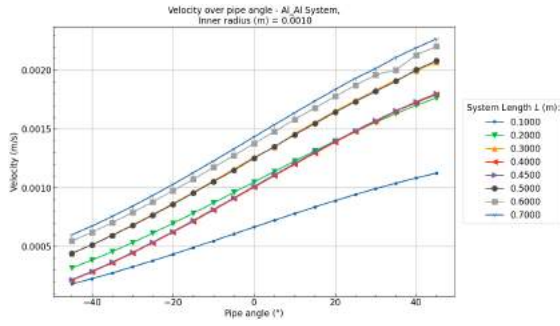
Table B.5: System specifications for the inner radius and length variable results

System Variable	Values	Reference
Multi layer wall materials	Al/Al	B.69-B.80 (Page 165 - 176)
	Pb/Pb	B.81-B.92 (Page 178 - 189)
	Zr/Zr	B.93-B.104 (Page 191 - 176)
Heating wall thickness (dr_{12_1})	0.015m	
Cooling wall thickness (dr_{34_1})	0.005m	
Inner radius (R_i)	0.0010m	Al/Al - B.69 - B.70 (Page 165 - 166)
		Pb/Pb - B.81 - B.82 (Page 178 - 179)
		Zr/Zr - B.93 - B.94 (Page 191 - 192)
	0.0024m	Al/Al - B.71 - B.72 (Page 167 - 168)
		Pb/Pb - B.83 - B.84 (Page 180 - 181)
		Zr/Zr - B.95 - B.96 (Page 193 - 194)
	0.0051m	Al/Al - B.73 - B.74 (Page 169 - 170)
Pb/Pb - B.85 - B.86 (Page 182 - 183)		
Zr/Zr - B.97 - B.98 (Page 195 - 196)		
0.0105m	Al/Al - B.75 - B.76 (Page 171 - 172)	
	Pb/Pb - B.87 - B.88 (Page 184 - 185)	
	Zr/Zr - B.99 - B.100 (Page 197 - 198)	
0.0159m	Al/Al - B.77 - B.78 (Page 173 - 174)	
	Pb/Pb - B.89 - B.90 (Page 186 - 187)	
	Zr/Zr - B.101 - B.102 (Page 199 - 200)	
0.0200m	Al/Al - B.79 - B.80 (Page 175 - 176)	
	Pb/Pb - B.91 - B.92 (Page 188 - 189)	
	Zr/Zr - B.103 - B.104 (Page 201 - 202)	
Pipe angle (θ)	$-45^\circ - 45^\circ$	
Length (L)	0.1 - 0.7m	
Section 2 length fraction ($Frac$)	1.0	

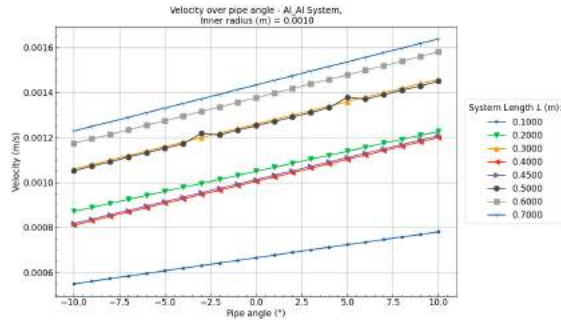
B.3.1. Al/Al - Pipe angle, System length & Inner radius

Al/Al - $R_i = 0.0010m$

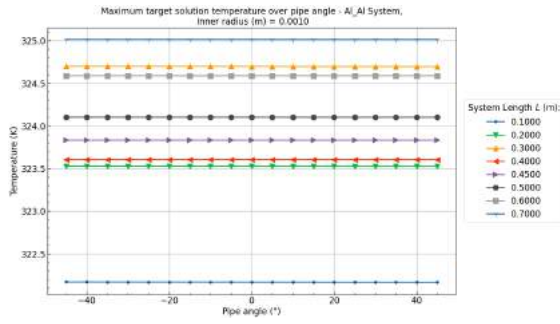
[Back to overview - B.3](#)



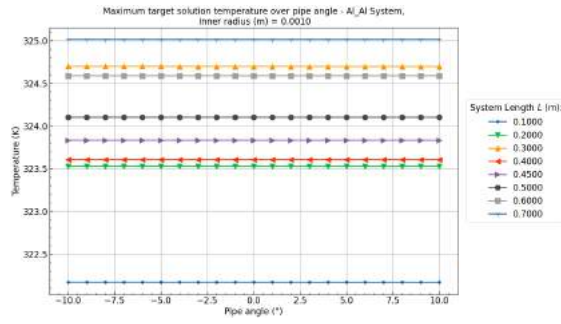
(a) Velocity over pipe angle between -45° and 45° at an inner radius $R_i = 0.0010m$.



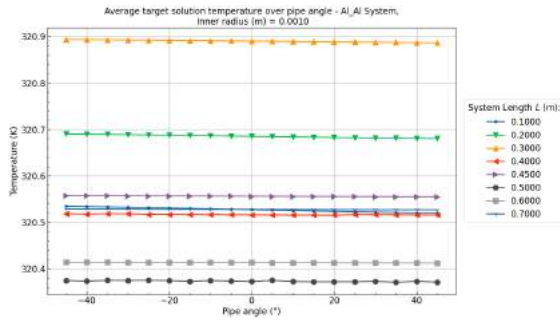
(b) Velocity over pipe angle between -10° and 10° at an inner radius $R_i = 0.0010m$.



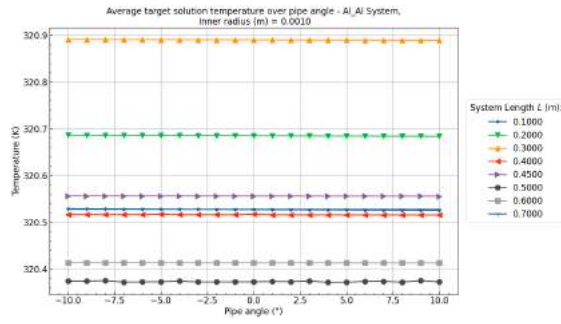
(c) Maximum target solution temperature over the pipe angle between -45° and 45° at an inner radius $R_i = 0.0010m$.



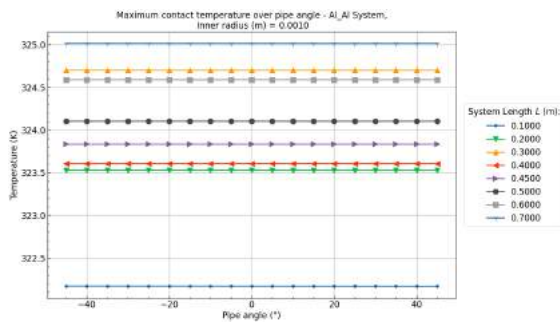
(d) Maximum target solution temperature over the pipe angle between -10° and 10° at an inner radius $R_i = 0.0010m$.



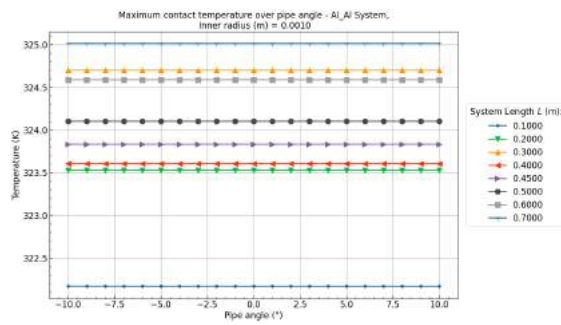
(e) Average target solution temperature over the pipe angle between -45° and 45° at an inner radius $R_i = 0.0010m$.



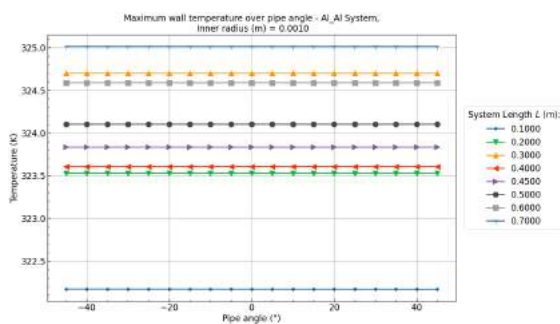
(f) Average target solution temperature over the pipe angle between -10° and 10° at an inner radius $R_i = 0.0010m$.



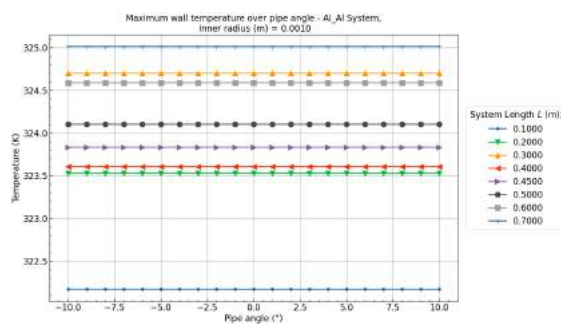
(g) Maximum contact temperature over the pipe angle between -45° and 45° at an inner radius $R_i = 0.0010m$.



(h) Maximum contact temperature over the pipe angle between -10° and 10° at an inner radius $R_i = 0.0010m$.

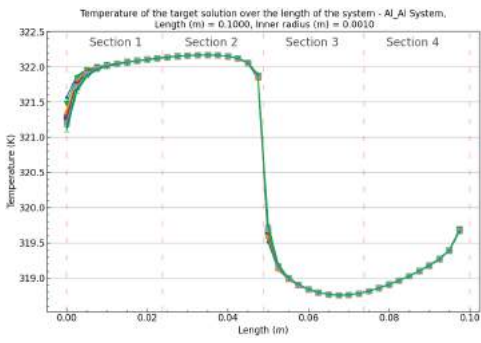


(i) Maximum wall temperature over the pipe angle between -45° and 45° at an inner radius $R_i = 0.0010m$.

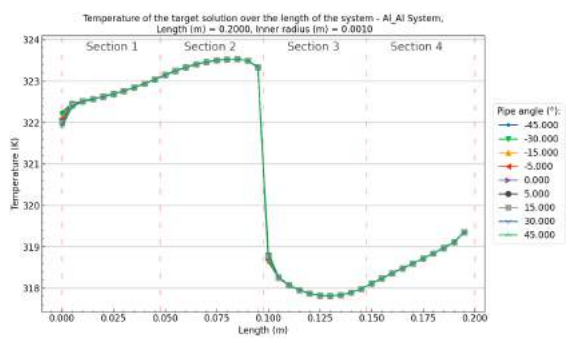


(j) Maximum wall temperature over the pipe angle between -10° and 10° at an inner radius $R_i = 0.0010m$.

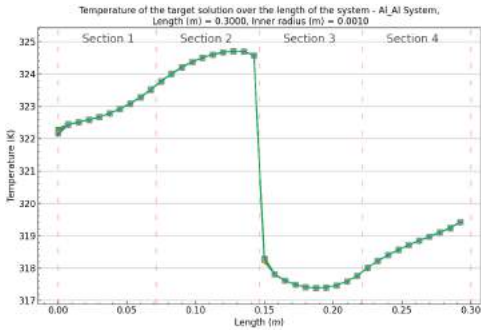
Figure B.69: Al/Al (Heat/Cool) System results over the pipe angle θ and system length L at an inner radius of $R_i = 0.0010m$, heating wall thickness of $dr_{12} = 0.015m$ and cooling wall thickness $dr_{34} (m) = 0.005m$



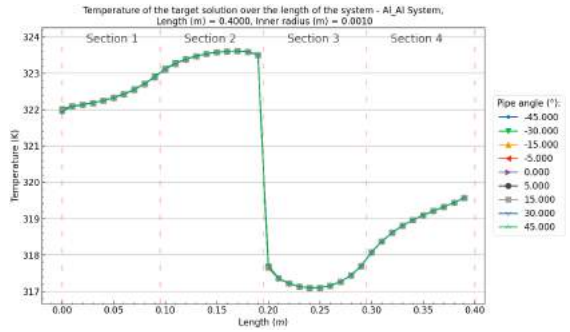
(a) Target solution temperature profile over the length of the system and pipe angles at a total system length of $L = 0.10m$ and inner radius $R_i = 0.0010m$.



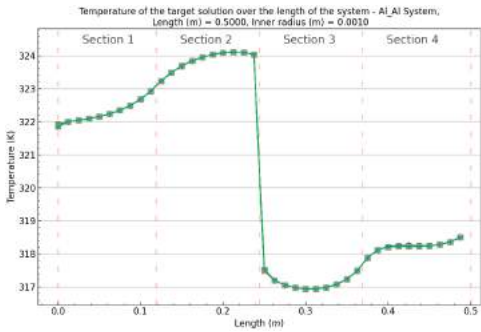
(b) Target solution temperature profile over the length of the system and pipe angles at a total system length of $L = 0.20m$ and inner radius $R_i = 0.0010m$.



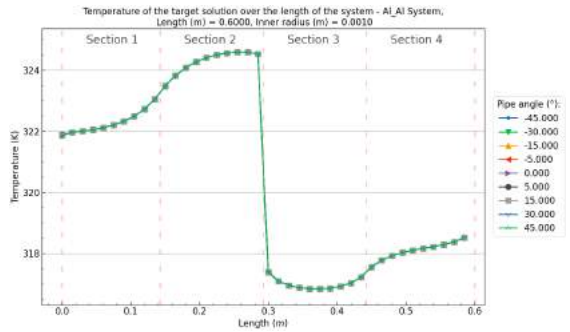
(c) Target solution temperature profile over the length of the system and pipe angles at a total system length of $L = 0.30m$ and inner radius $R_i = 0.0010m$.



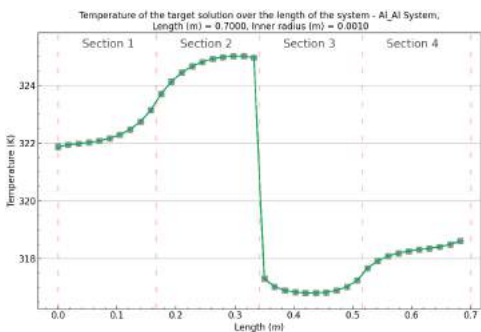
(d) Target solution temperature profile over the length of the system and pipe angles at a total system length of $L = 0.40m$ and inner radius $R_i = 0.0010m$.



(e) Target solution temperature profile over the length of the system and pipe angles at a total system length of $L = 0.50m$ and inner radius $R_i = 0.0010m$.



(f) Target solution temperature profile over the length of the system and pipe angles at a total system length of $L = 0.60m$ and inner radius $R_i = 0.0010m$.

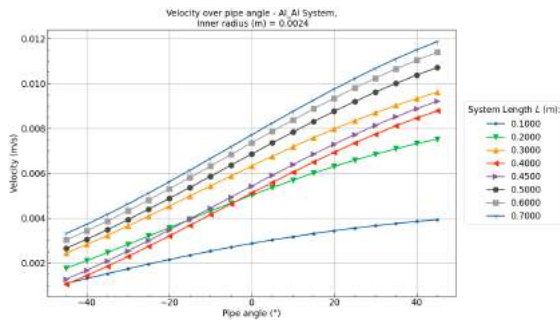


(g) Target solution temperature profile over the length of the system and pipe angles at a total system length of $L = 0.70m$ and inner radius $R_i = 0.0010m$.

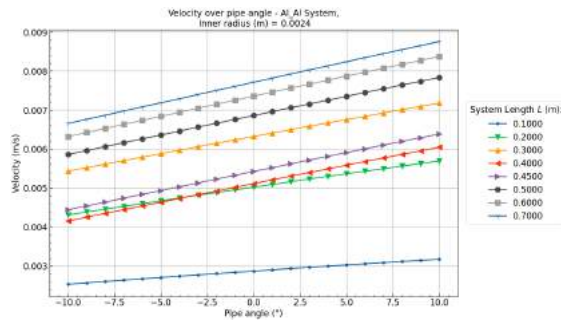
Figure B.70: Al/Al (Heat/Cool) System target solution temperature profiles over the pipe angle θ and system length L at an inner radius of $R_i = 0.0010m$, a heating wall thickness of $dr_{12} = 0.015m$ and cooling wall thickness $dr_{34}(m) = 0.005m$

Al/Al - $R_i = 0.0024m$

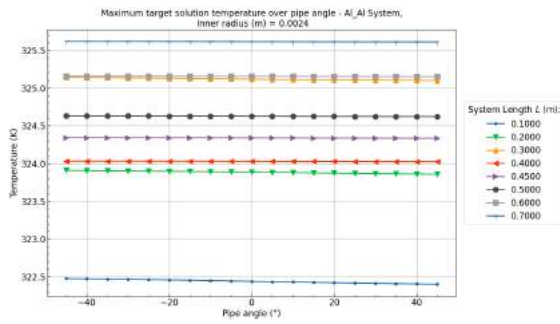
[Back to overview - B.3](#)



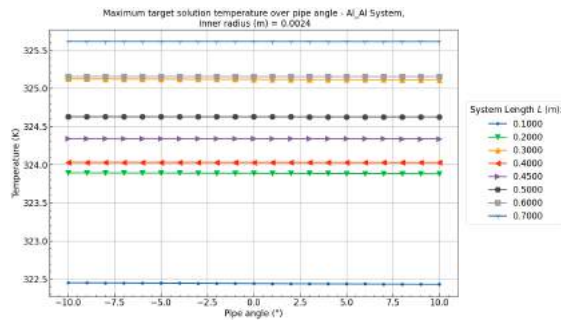
(a) Velocity over pipe angle between -45° and 45° at an inner radius $R_i = 0.0024m$.



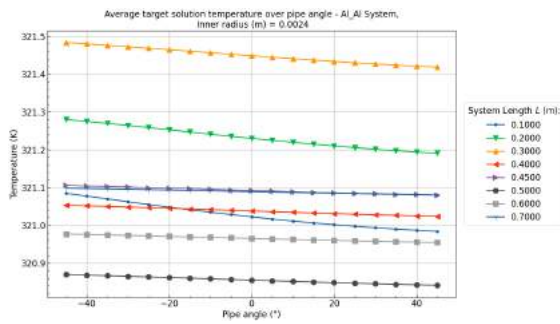
(b) Velocity over pipe angle between -10° and 10° at an inner radius $R_i = 0.0024m$.



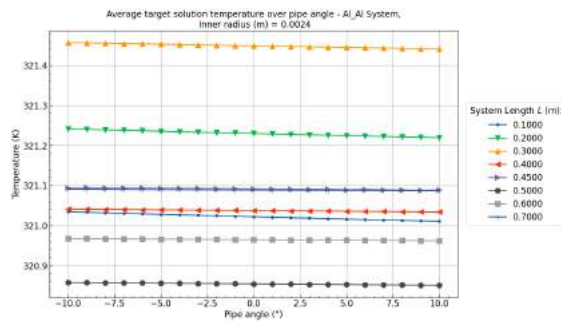
(c) Maximum target solution temperature over the pipe angle between -45° and 45° at an inner radius $R_i = 0.0024m$.



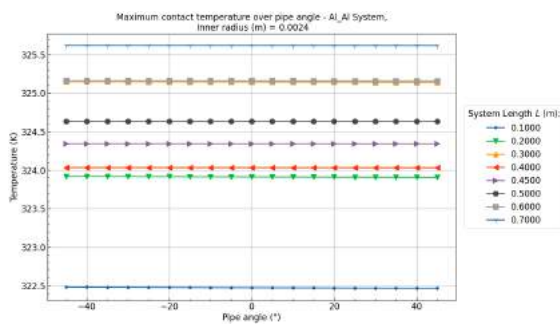
(d) Maximum target solution temperature over the pipe angle between -10° and 10° at an inner radius $R_i = 0.0024m$.



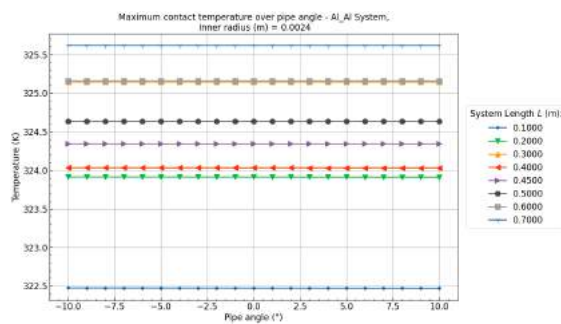
(e) Average target solution temperature over the pipe angle between -45° and 45° at an inner radius $R_i = 0.0024m$.



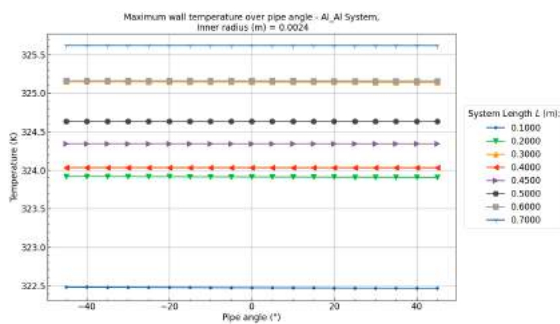
(f) Average target solution temperature over the pipe angle between -10° and 10° at an inner radius $R_i = 0.0024m$.



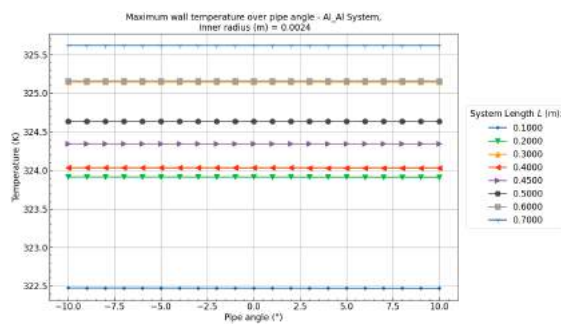
(g) Maximum contact temperature over the pipe angle between -45° and 45° at an inner radius $R_i = 0.0024m$.



(h) Maximum contact temperature over the pipe angle between -10° and 10° at an inner radius $R_i = 0.0024m$.

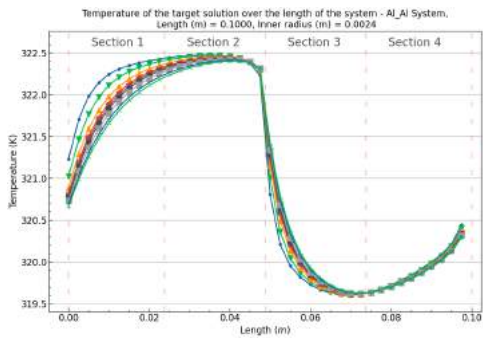


(i) Maximum wall temperature over the pipe angle between -45° and 45° at an inner radius $R_i = 0.0024m$.

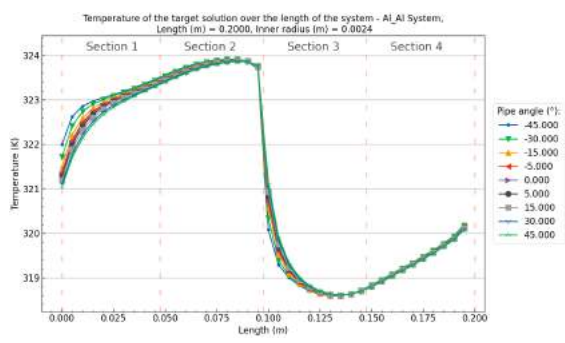


(j) Maximum wall temperature over the pipe angle between -10° and 10° at an inner radius $R_i = 0.0024m$.

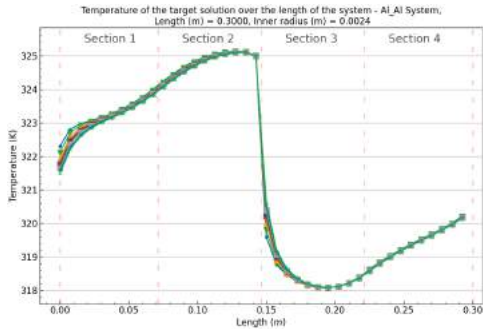
Figure B.71: Al/Al (Heat/Cool) System results over the pipe angle θ and system length L at an inner radius of $R_i = 0.0024m$, heating wall thickness of $dr_{12} = 0.015m$ and cooling wall thickness $dr_{34} (m) = 0.005m$



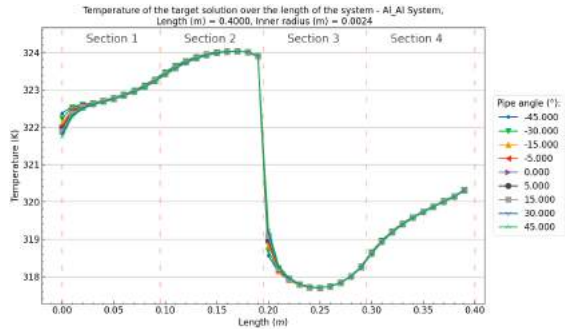
(a) Target solution temperature profile over the length of the system and pipe angles at a total system length of $L = 0.10m$ and inner radius $R_i = 0.0024m$.



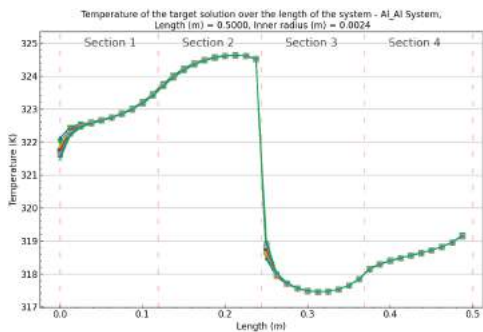
(b) Target solution temperature profile over the length of the system and pipe angles at a total system length of $L = 0.20m$ and inner radius $R_i = 0.0024m$.



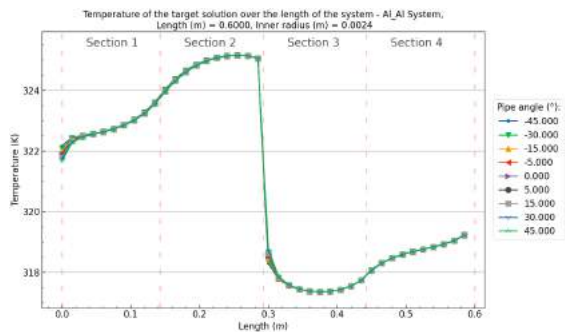
(c) Target solution temperature profile over the length of the system and pipe angles at a total system length of $L = 0.30m$ and inner radius $R_i = 0.0024m$.



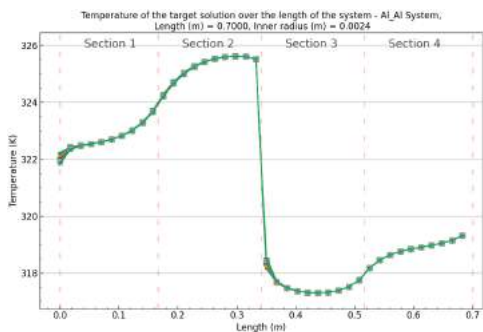
(d) Target solution temperature profile over the length of the system and pipe angles at a total system length of $L = 0.40m$ and inner radius $R_i = 0.0024m$.



(e) Target solution temperature profile over the length of the system and pipe angles at a total system length of $L = 0.50m$ and inner radius $R_i = 0.0024m$.



(f) Target solution temperature profile over the length of the system and pipe angles at a total system length of $L = 0.60m$ and inner radius $R_i = 0.0024m$.

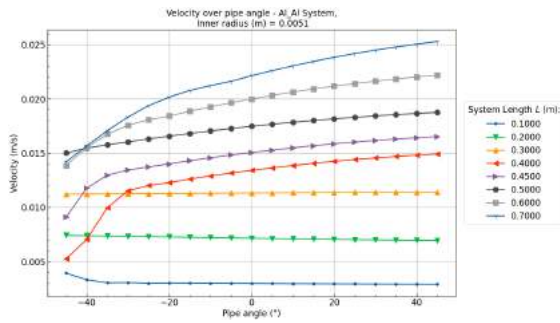


(g) Target solution temperature profile over the length of the system and pipe angles at a total system length of $L = 0.70m$ and inner radius $R_i = 0.0024m$.

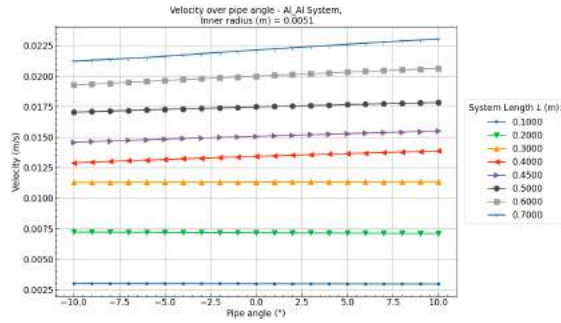
Figure B.72: Al/Al (Heat/Cool) System target solution temperature profiles over the pipe angle θ and system length L at an inner radius of $R_i = 0.0024m$, a heating wall thickness of $dr_{12} = 0.015m$ and cooling wall thickness $dr_{34}(m) = 0.005m$

Al/Al - $R_i = 0.0051\text{ m}$

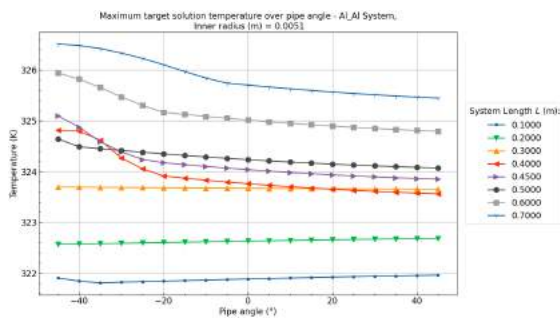
[Back to overview - B.3](#)



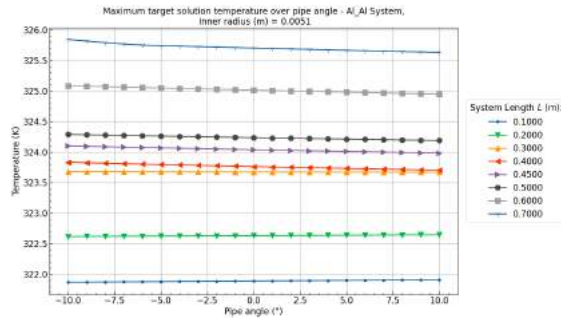
(a) Velocity over pipe angle between -45° and 45° at an inner radius $R_i = 0.0051\text{ m}$.



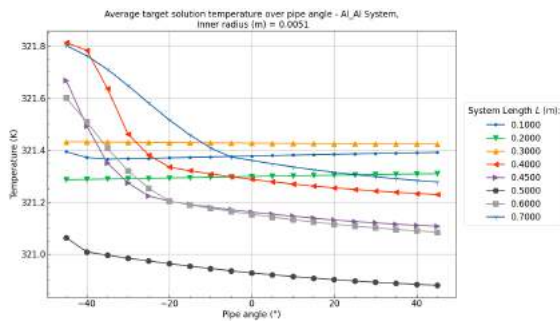
(b) Velocity over pipe angle between -10° and 10° at an inner radius $R_i = 0.0051\text{ m}$.



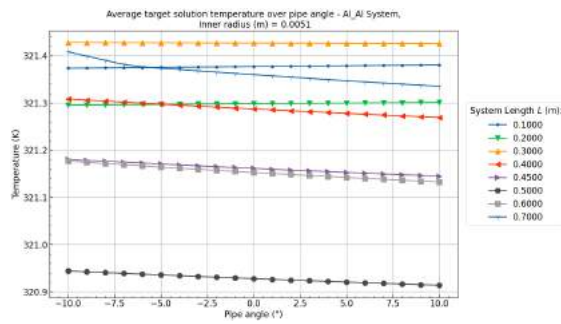
(c) Maximum target solution temperature over the pipe angle between -45° and 45° at an inner radius $R_i = 0.0051\text{ m}$.



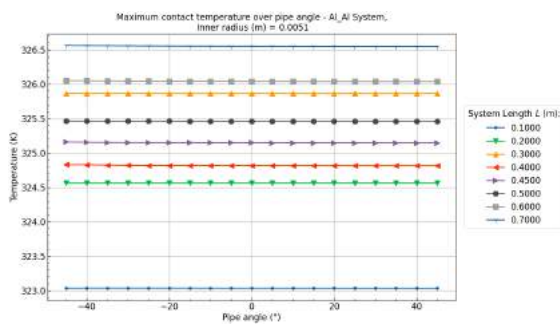
(d) Maximum target solution temperature over the pipe angle between -10° and 10° at an inner radius $R_i = 0.0051\text{ m}$.



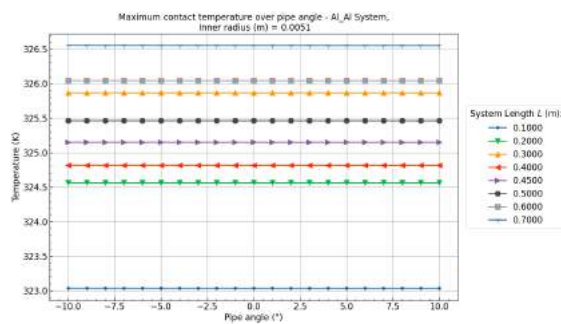
(e) Average target solution temperature over the pipe angle between -45° and 45° at an inner radius $R_i = 0.0051\text{ m}$.



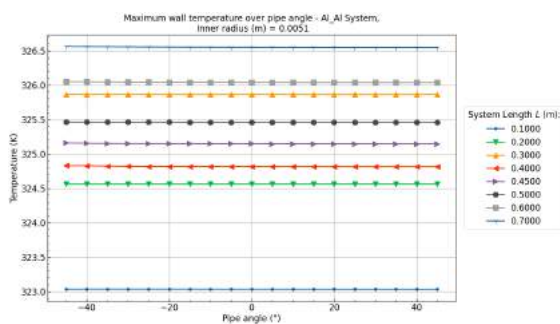
(f) Average target solution temperature over the pipe angle between -10° and 10° at an inner radius $R_i = 0.0051\text{ m}$.



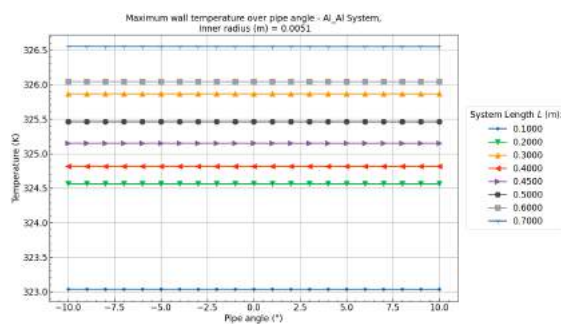
(g) Maximum contact temperature over the pipe angle between -45° and 45° at an inner radius $R_i = 0.0051\text{ m}$.



(h) Maximum contact temperature over the pipe angle between -10° and 10° at an inner radius $R_i = 0.0051\text{ m}$.

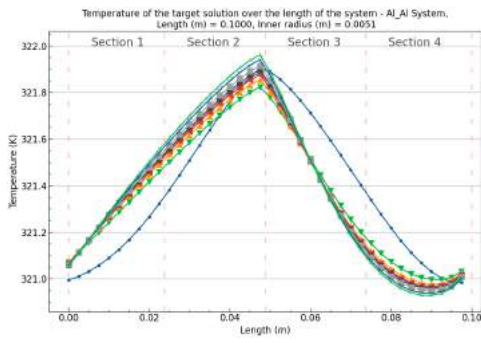


(i) Maximum wall temperature over the pipe angle between -45° and 45° at an inner radius $R_i = 0.0051\text{ m}$.

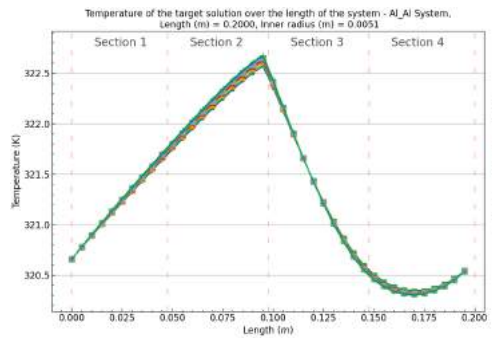


(j) Maximum wall temperature over the pipe angle between -10° and 10° at an inner radius $R_i = 0.0051\text{ m}$.

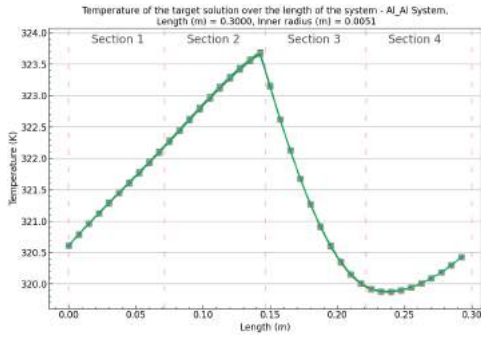
Figure B.73: Al/Al (Heat/Cool) System results over the pipe angle θ and system length L at an inner radius of $R_i = 0.0051\text{ m}$, heating wall thickness of $dr_{12} = 0.015\text{ m}$ and cooling wall thickness $dr_{34} (m) = 0.005\text{ m}$



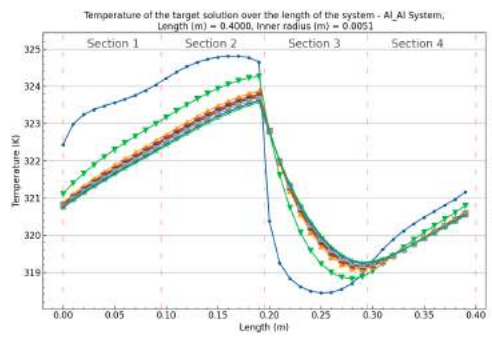
(a) Target solution temperature profile over the length of the system and pipe angles at a total system length of $L = 0.10m$ and inner radius $R_i = 0.0051m$.



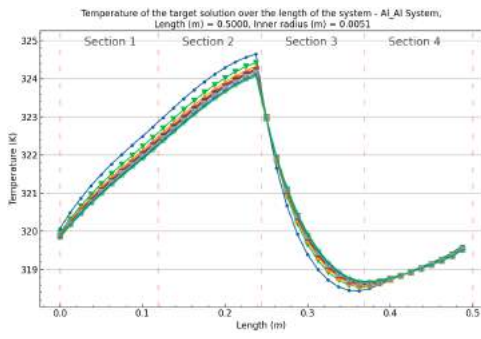
(b) Target solution temperature profile over the length of the system and pipe angles at a total system length of $L = 0.20m$ and inner radius $R_i = 0.0051m$.



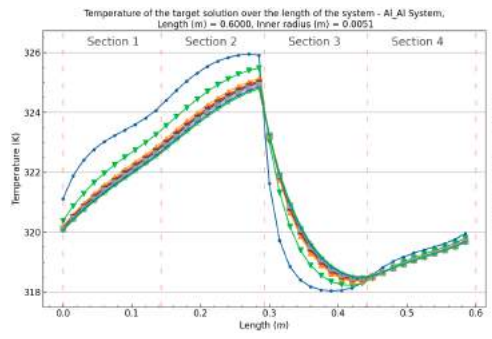
(c) Target solution temperature profile over the length of the system and pipe angles at a total system length of $L = 0.30m$ and inner radius $R_i = 0.0051m$.



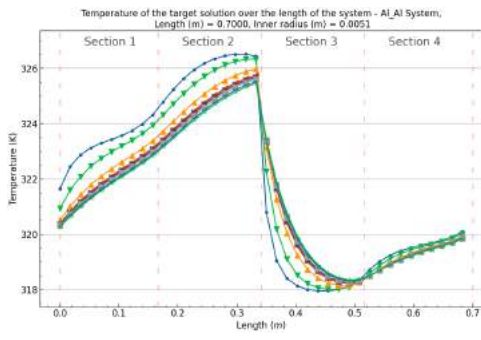
(d) Target solution temperature profile over the length of the system and pipe angles at a total system length of $L = 0.40m$ and inner radius $R_i = 0.0051m$.



(e) Target solution temperature profile over the length of the system and pipe angles at a total system length of $L = 0.50m$ and inner radius $R_i = 0.0051m$.



(f) Target solution temperature profile over the length of the system and pipe angles at a total system length of $L = 0.60m$ and inner radius $R_i = 0.0051m$.

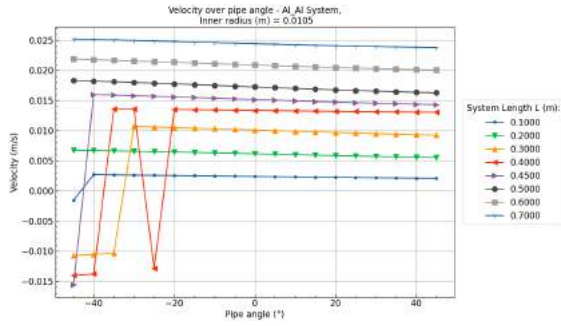


(g) Target solution temperature profile over the length of the system and pipe angles at a total system length of $L = 0.70m$ and inner radius $R_i = 0.0051m$.

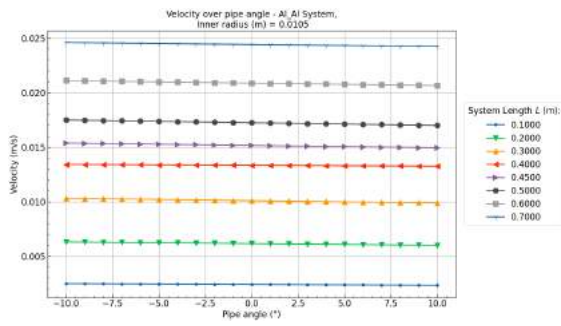
Figure B.74: Al/Al (Heat/Cool) System target solution temperature profiles over the pipe angle θ and system length L at an inner radius of $R_i = 0.0051m$, a heating wall thickness of $dr_{12} = 0.015m$ and cooling wall thickness $dr_{34}(m) = 0.005m$

Al/Al - $R_i = 0.0105m$

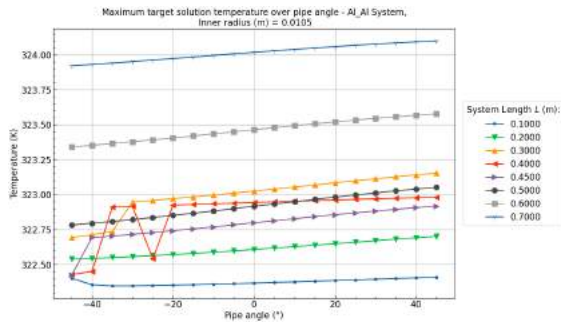
[Back to overview - B.3](#)



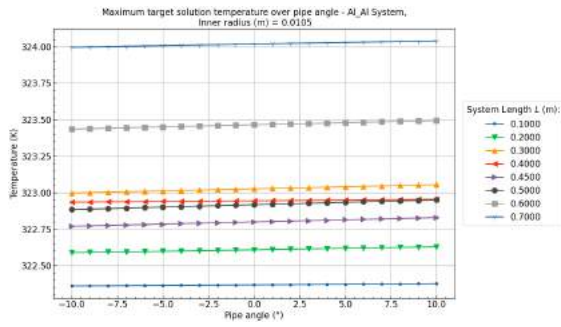
(a) Velocity over pipe angle between -45° and 45° at an inner radius $R_i = 0.0105m$.



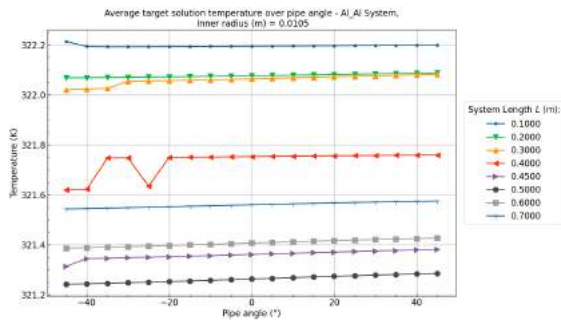
(b) Velocity over pipe angle between -10° and 10° at an inner radius $R_i = 0.0105m$.



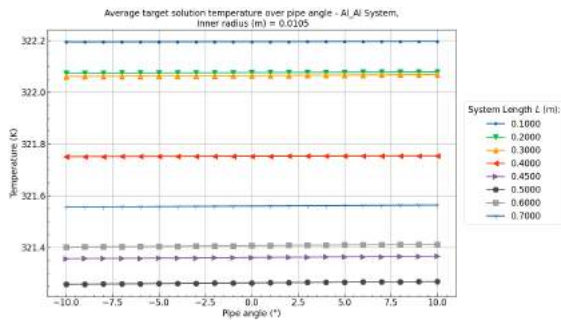
(c) Maximum target solution temperature over the pipe angle between -45° and 45° at an inner radius $R_i = 0.0105m$.



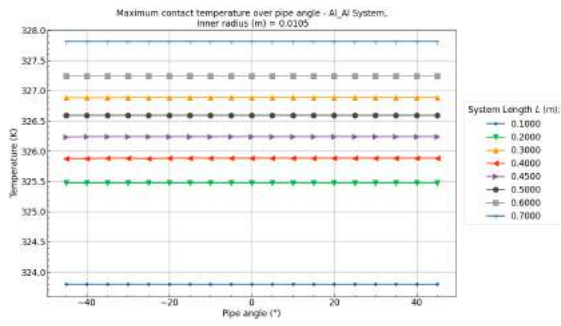
(d) Maximum target solution temperature over the pipe angle between -10° and 10° at an inner radius $R_i = 0.0105m$.



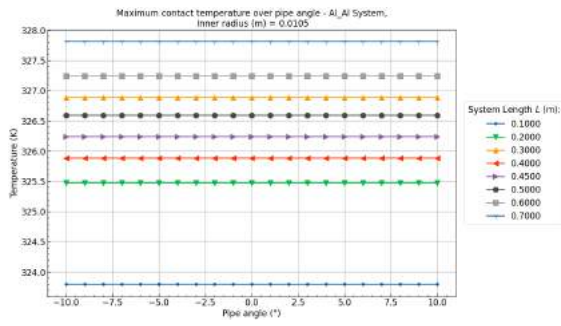
(e) Average target solution temperature over the pipe angle between -45° and 45° at an inner radius $R_i = 0.0105m$.



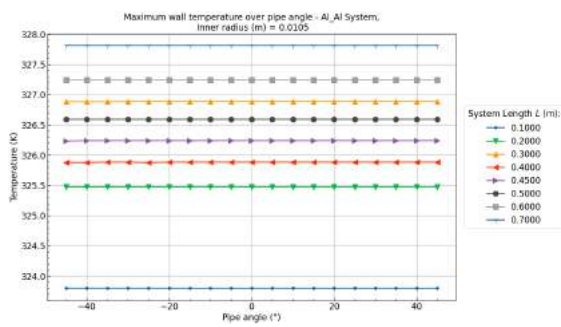
(f) Average target solution temperature over the pipe angle between -10° and 10° at an inner radius $R_i = 0.0105m$.



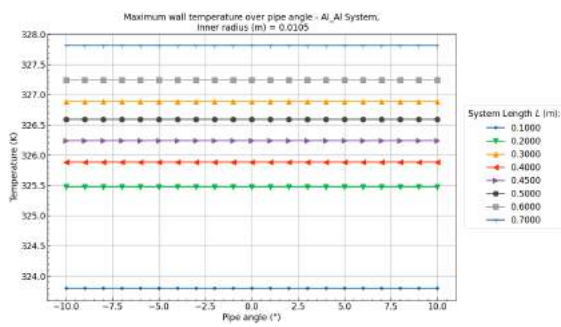
(g) Maximum contact temperature over the pipe angle between -45° and 45° at an inner radius $R_i = 0.0105m$.



(h) Maximum contact temperature over the pipe angle between -10° and 10° at an inner radius $R_i = 0.0105m$.

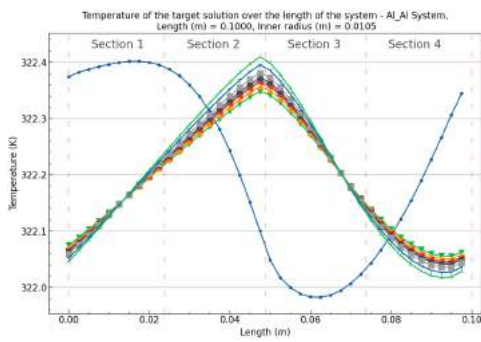


(i) Maximum wall temperature over the pipe angle between -45° and 45° at an inner radius $R_i = 0.0105m$.

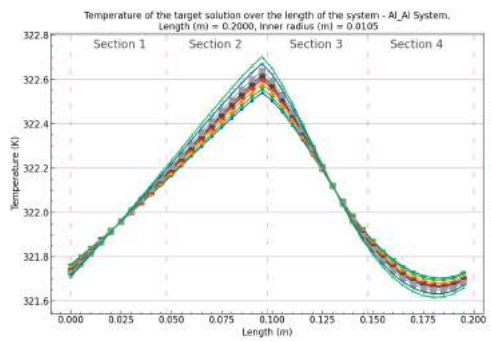


(j) Maximum wall temperature over the pipe angle between -10° and 10° at an inner radius $R_i = 0.0105m$.

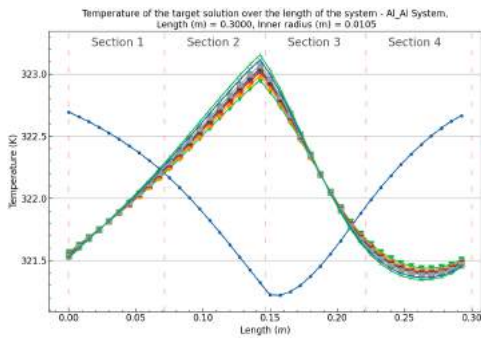
Figure B.75: Al/Al (Heat/Cool) System results over the pipe angle θ and system length L at an inner radius of $R_i = 0.0105m$, heating wall thickness of $dr_{12} = 0.015m$ and cooling wall thickness $dr_{34} (m) = 0.005m$



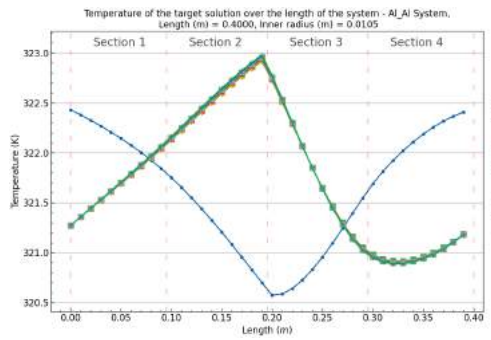
(a) Target solution temperature profile over the length of the system and pipe angles at a total system length of $L = 0.10m$ and inner radius $R_i = 0.0105m$.



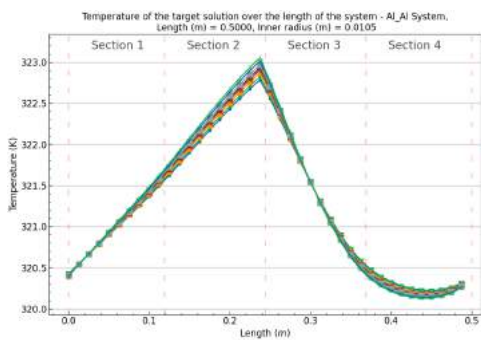
(b) Target solution temperature profile over the length of the system and pipe angles at a total system length of $L = 0.20m$ and inner radius $R_i = 0.0105m$.



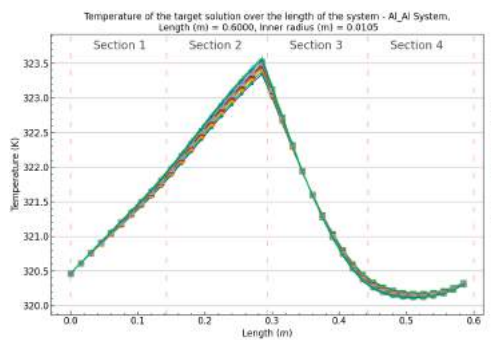
(c) Target solution temperature profile over the length of the system and pipe angles at a total system length of $L = 0.30m$ and inner radius $R_i = 0.0105m$.



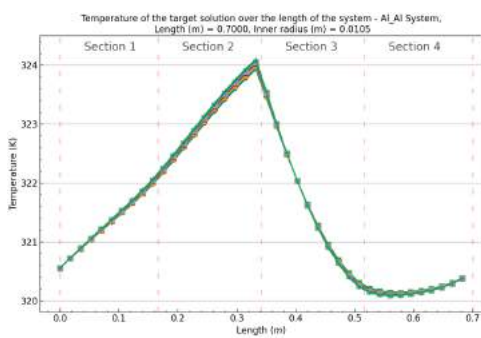
(d) Target solution temperature profile over the length of the system and pipe angles at a total system length of $L = 0.40m$ and inner radius $R_i = 0.0105m$.



(e) Target solution temperature profile over the length of the system and pipe angles at a total system length of $L = 0.50m$ and inner radius $R_i = 0.0105m$.



(f) Target solution temperature profile over the length of the system and pipe angles at a total system length of $L = 0.60m$ and inner radius $R_i = 0.0105m$.

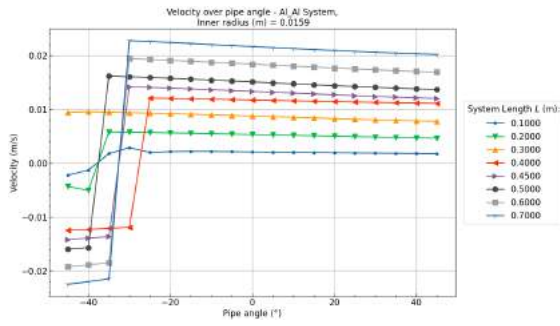


(g) Target solution temperature profile over the length of the system and pipe angles at a total system length of $L = 0.70m$ and inner radius $R_i = 0.0105m$.

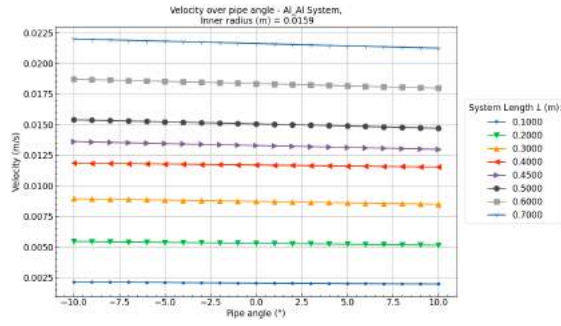
Figure B.76: Al/Al (Heat/Cool) System target solution temperature profiles over the pipe angle θ and system length L at an inner radius of $R_i = 0.0105m$, a heating wall thickness of $dr_{12} = 0.015m$ and cooling wall thickness $dr_{34}(m) = 0.005m$

Al/Al - $R_i = 0.0159m$

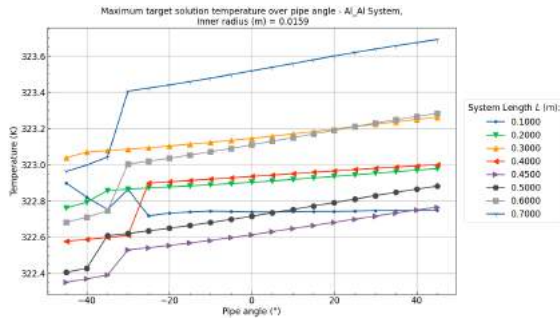
[Back to overview - B.3](#)



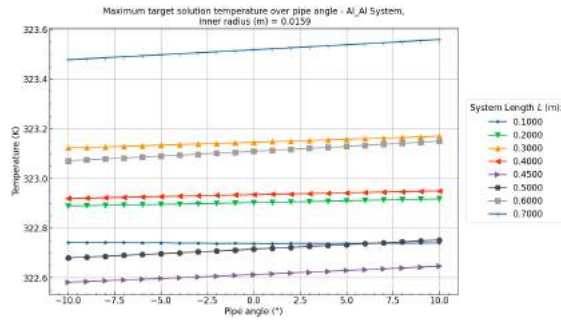
(a) Velocity over pipe angle between -45° and 45° at an inner radius $R_i = 0.0159m$.



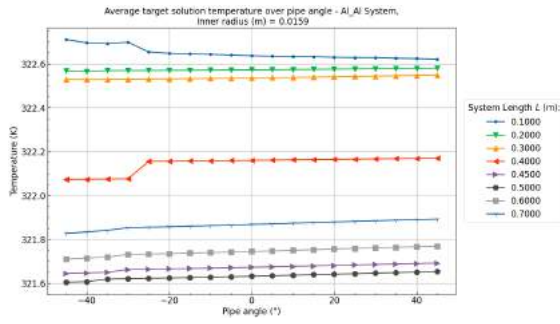
(b) Velocity over pipe angle between -10° and 10° at an inner radius $R_i = 0.0159m$.



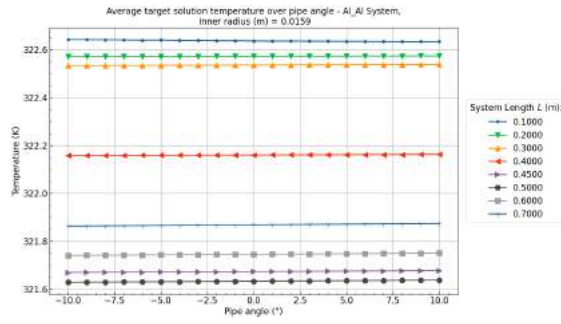
(c) Maximum target solution temperature over the pipe angle between -45° and 45° at an inner radius $R_i = 0.0159m$.



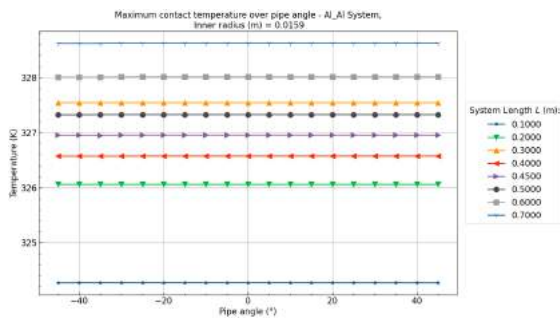
(d) Maximum target solution temperature over the pipe angle between -10° and 10° at an inner radius $R_i = 0.0159m$.



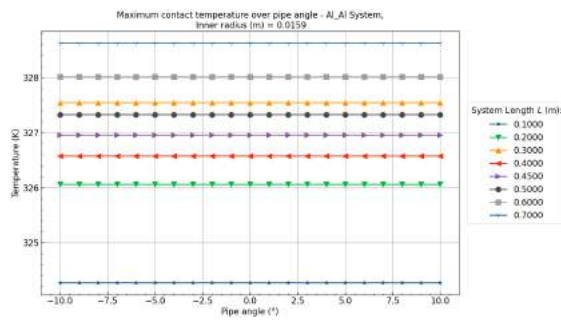
(e) Average target solution temperature over the pipe angle between -45° and 45° at an inner radius $R_i = 0.0159m$.



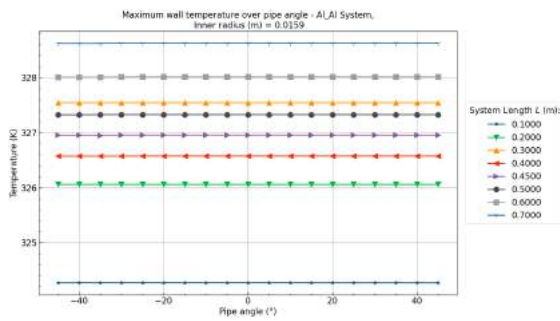
(f) Average target solution temperature over the pipe angle between -10° and 10° at an inner radius $R_i = 0.0159m$.



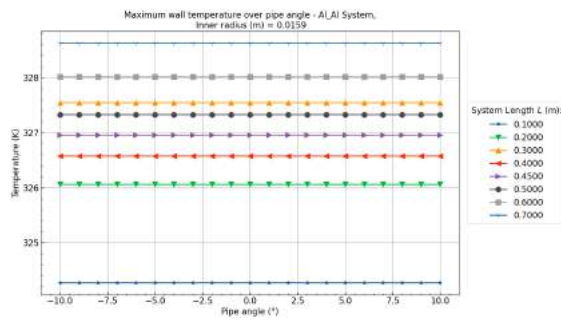
(g) Maximum contact temperature over the pipe angle between -45° and 45° at an inner radius $R_i = 0.0159m$.



(h) Maximum contact temperature over the pipe angle between -10° and 10° at an inner radius $R_i = 0.0159m$.

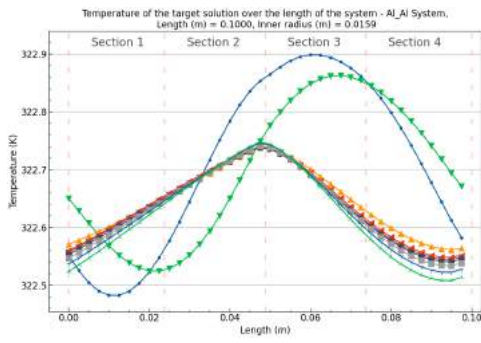


(i) Maximum wall temperature over the pipe angle between -45° and 45° at an inner radius $R_i = 0.0159m$.

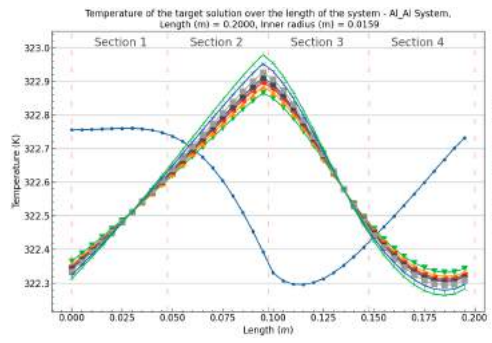


(j) Maximum wall temperature over the pipe angle between -10° and 10° at an inner radius $R_i = 0.0159m$.

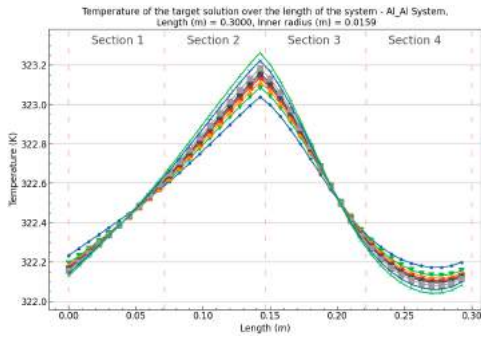
Figure B.77: Al/Al (Heat/Cool) System results over the pipe angle θ and system length L at an inner radius of $R_i = 0.0159m$, heating wall thickness of $dr_{12} = 0.015m$ and cooling wall thickness $dr_{34} (m) = 0.005m$



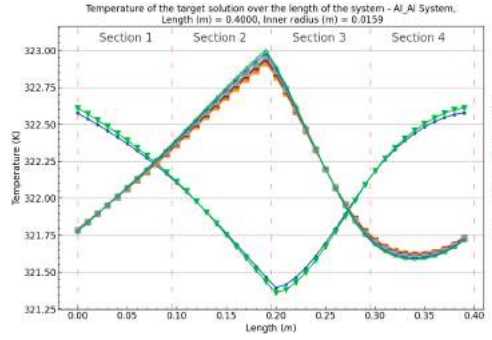
(a) Target solution temperature profile over the length of the system and pipe angles at a total system length of $L = 0.10m$ and inner radius $R_i = 0.0159m$.



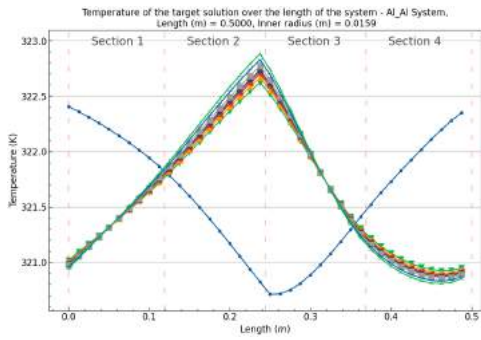
(b) Target solution temperature profile over the length of the system and pipe angles at a total system length of $L = 0.20m$ and inner radius $R_i = 0.0159m$.



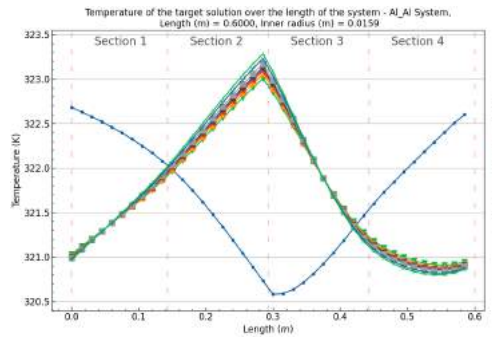
(c) Target solution temperature profile over the length of the system and pipe angles at a total system length of $L = 0.30m$ and inner radius $R_i = 0.0159m$.



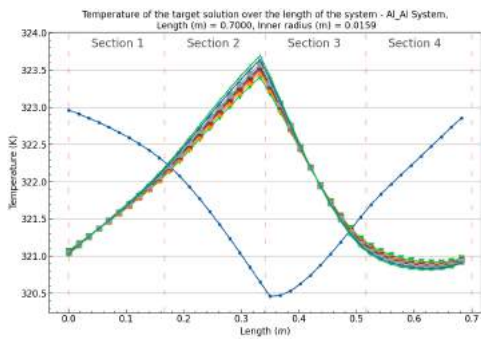
(d) Target solution temperature profile over the length of the system and pipe angles at a total system length of $L = 0.40m$ and inner radius $R_i = 0.0159m$.



(e) Target solution temperature profile over the length of the system and pipe angles at a total system length of $L = 0.50m$ and inner radius $R_i = 0.0159m$.



(f) Target solution temperature profile over the length of the system and pipe angles at a total system length of $L = 0.60m$ and inner radius $R_i = 0.0159m$.

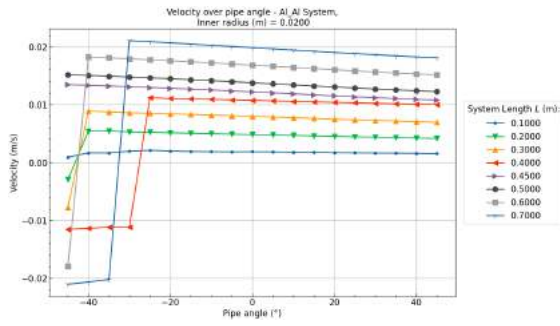


(g) Target solution temperature profile over the length of the system and pipe angles at a total system length of $L = 0.70m$ and inner radius $R_i = 0.0159m$.

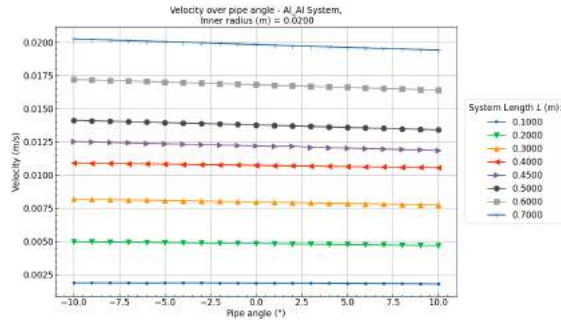
Figure B.78: Al/Al (Heat/Cool) System target solution temperature profiles over the pipe angle θ and system length L at an inner radius of $R_i = 0.0159m$, a heating wall thickness of $dr_{12} = 0.015m$ and cooling wall thickness $dr_{34}(m) = 0.005m$

Al/Al - $R_i = 0.0200m$

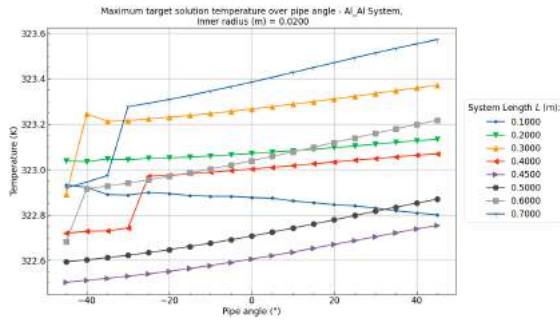
[Back to overview - B.3](#)



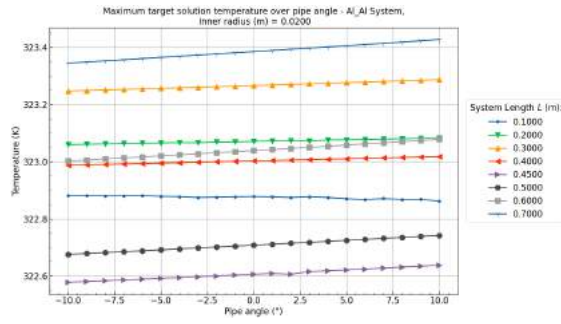
(a) Velocity over pipe angle between -45° and 45° at an inner radius $R_i = 0.0200m$.



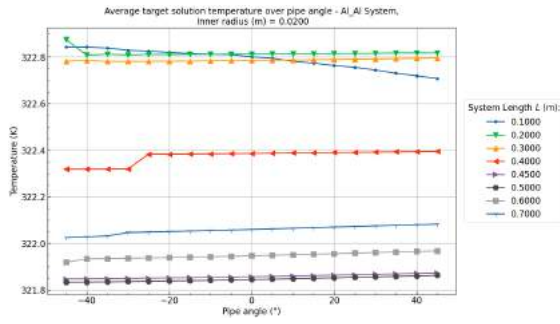
(b) Velocity over pipe angle between -10° and 10° at an inner radius $R_i = 0.0200m$.



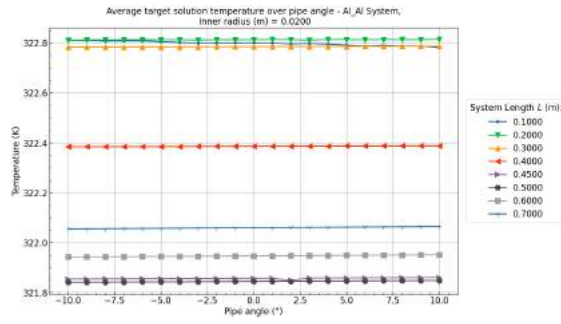
(c) Maximum target solution temperature over the pipe angle between -45° and 45° at an inner radius $R_i = 0.0200m$.



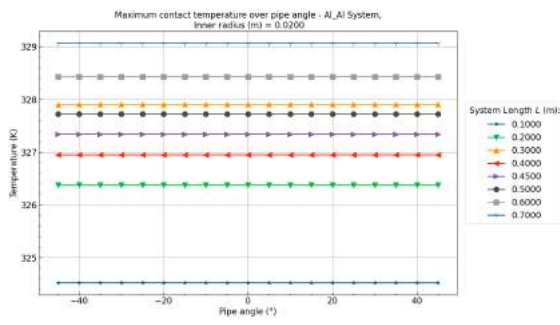
(d) Maximum target solution temperature over the pipe angle between -10° and 10° at an inner radius $R_i = 0.0200m$.



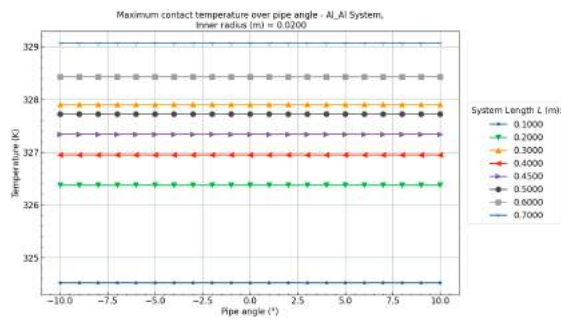
(e) Average target solution temperature over the pipe angle between -45° and 45° at an inner radius $R_i = 0.0200m$.



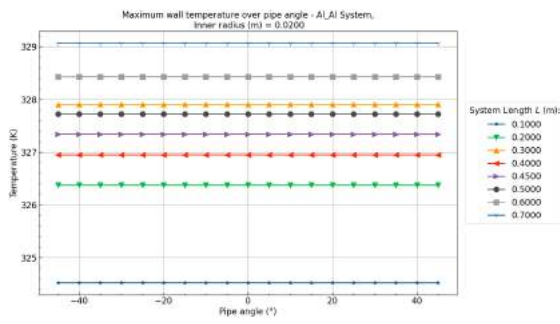
(f) Average target solution temperature over the pipe angle between -10° and 10° at an inner radius $R_i = 0.0200m$.



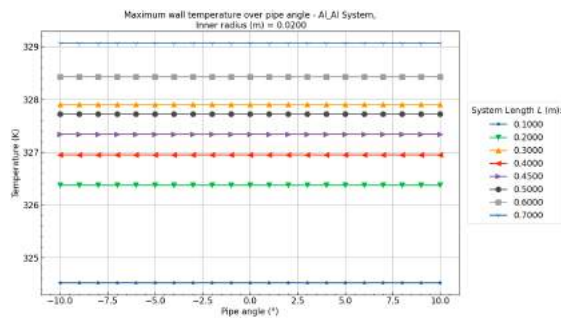
(g) Maximum contact temperature over the pipe angle between -45° and 45° at an inner radius $R_i = 0.0200m$.



(h) Maximum contact temperature over the pipe angle between -10° and 10° at an inner radius $R_i = 0.0200m$.

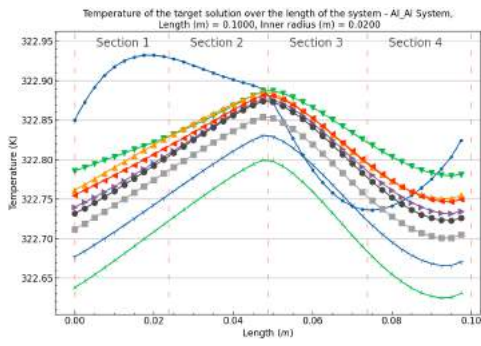


(i) Maximum wall temperature over the pipe angle between -45° and 45° at an inner radius $R_i = 0.0200m$.

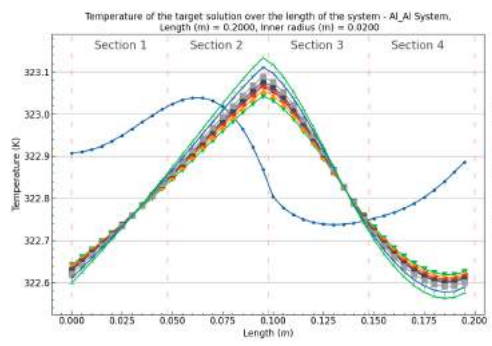


(j) Maximum wall temperature over the pipe angle between -10° and 10° at an inner radius $R_i = 0.0200m$.

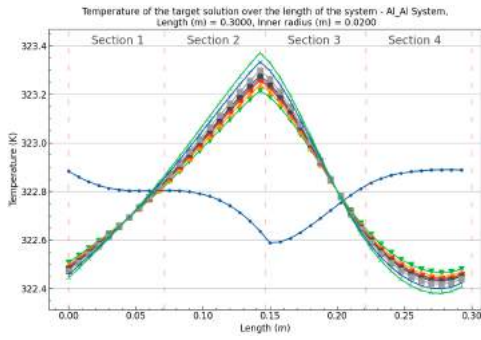
Figure B.79: Al/Al (Heat/Cool) System results over the pipe angle θ and system length L at an inner radius of $R_i = 0.0200m$, heating wall thickness of $dr_{12} = 0.015m$ and cooling wall thickness $dr_{34} (m) = 0.005m$



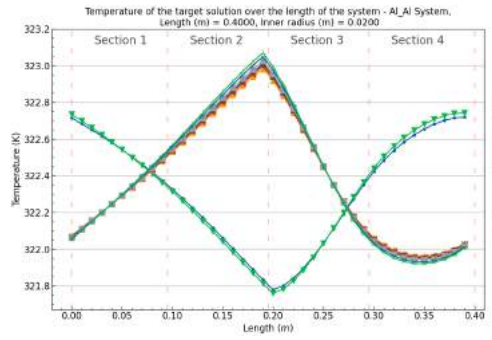
(a) Target solution temperature profile over the length of the system and pipe angles at a total system length of $L = 0.10m$ and inner radius $R_i = 0.0200m$.



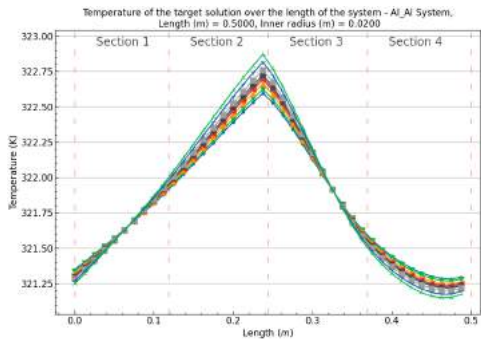
(b) Target solution temperature profile over the length of the system and pipe angles at a total system length of $L = 0.20m$ and inner radius $R_i = 0.0200m$.



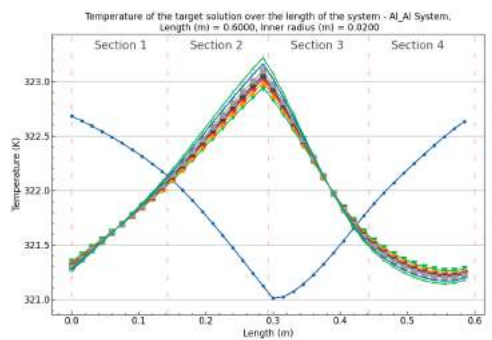
(c) Target solution temperature profile over the length of the system and pipe angles at a total system length of $L = 0.30m$ and inner radius $R_i = 0.0200m$.



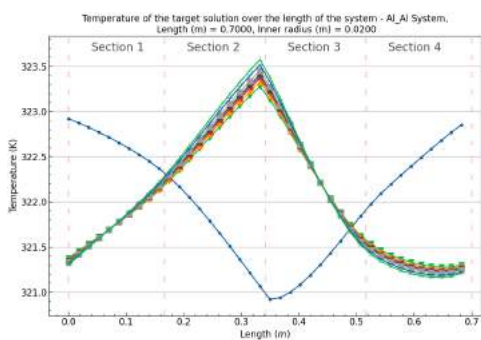
(d) Target solution temperature profile over the length of the system and pipe angles at a total system length of $L = 0.40m$ and inner radius $R_i = 0.0200m$.



(e) Target solution temperature profile over the length of the system and pipe angles at a total system length of $L = 0.50m$ and inner radius $R_i = 0.0200m$.



(f) Target solution temperature profile over the length of the system and pipe angles at a total system length of $L = 0.60m$ and inner radius $R_i = 0.0200m$.



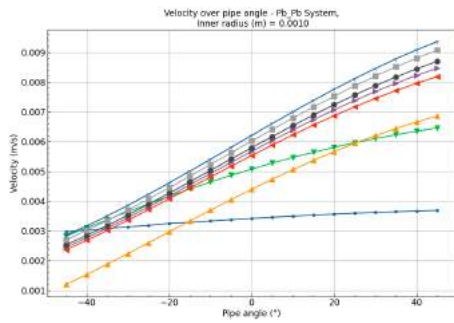
(g) Target solution temperature profile over the length of the system and pipe angles at a total system length of $L = 0.70m$ and inner radius $R_i = 0.0200m$.

Figure B.80: Al/Al (Heat/Cool) System target solution temperature profiles over the pipe angle θ and system length L at an inner radius of $R_i = 0.0200m$, a heating wall thickness of $dr_{12} = 0.015m$ and cooling wall thickness $dr_{34}(m) = 0.005m$

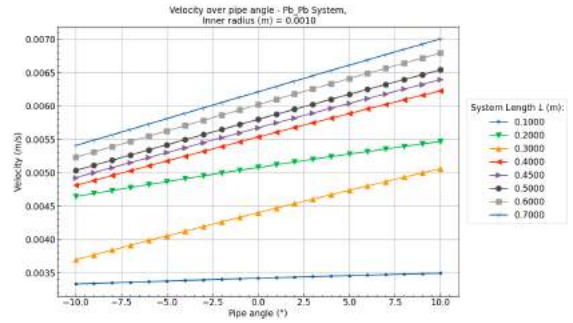
B.3.2. Pb/Pb - Pipe angle, System length & Inner radius

Pb/Pb - $R_i = 0.0010m$

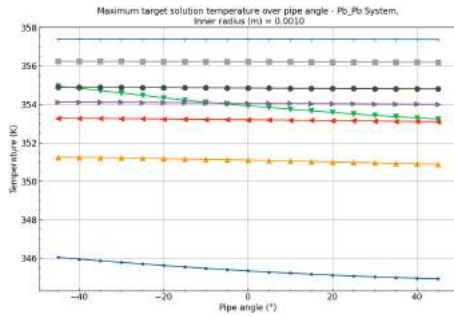
Back to overview - B.3



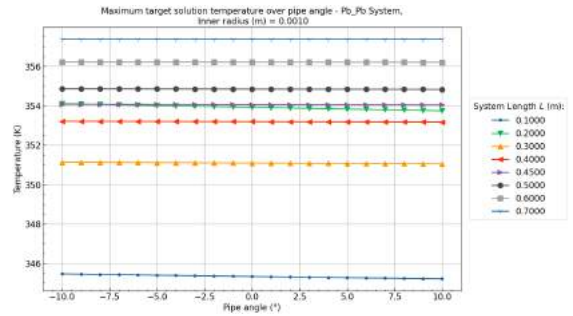
(a) Velocity over pipe angle between -45° and 45° at an inner radius $R_i = 0.0010m$.



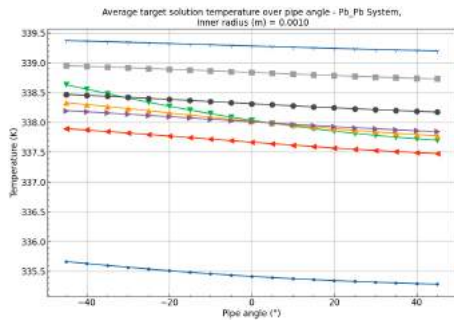
(b) Velocity over pipe angle between -10° and 10° at an inner radius $R_i = 0.0010m$.



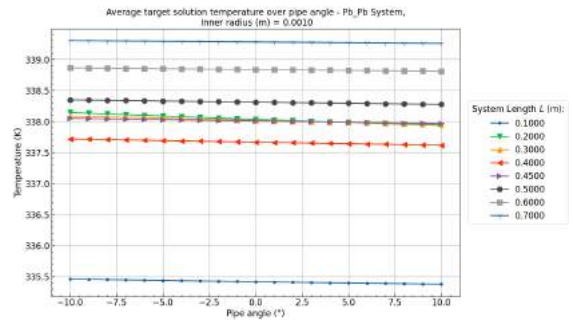
(c) Maximum target solution temperature over the pipe angle between -45° and 45° at an inner radius $R_i = 0.0010m$.



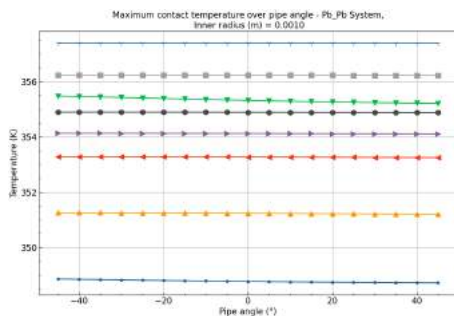
(d) Maximum target solution temperature over the pipe angle between -10° and 10° at an inner radius $R_i = 0.0010m$.



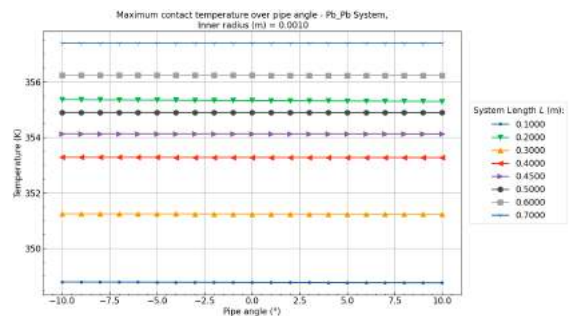
(e) Average target solution temperature over the pipe angle between -45° and 45° at an inner radius $R_i = 0.0010m$.



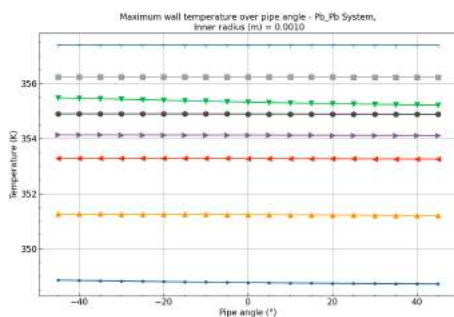
(f) Average target solution temperature over the pipe angle between -10° and 10° at an inner radius $R_i = 0.0010m$.



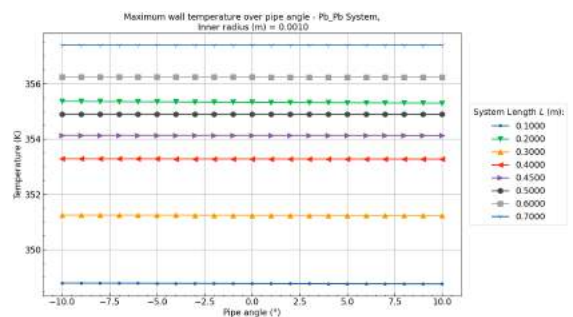
(g) Maximum contact temperature over the pipe angle between -45° and 45° at an inner radius $R_i = 0.0010m$.



(h) Maximum contact temperature over the pipe angle between -10° and 10° at an inner radius $R_i = 0.0010m$.

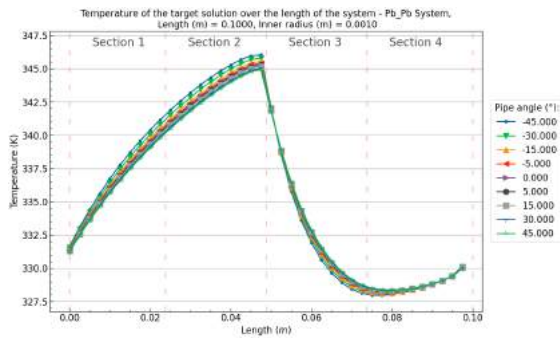


(i) Maximum wall temperature over the pipe angle between -45° and 45° at an inner radius $R_i = 0.0010m$.

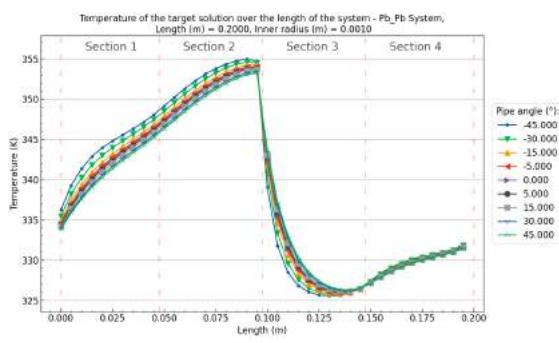


(j) Maximum wall temperature over the pipe angle between -10° and 10° at an inner radius $R_i = 0.0010m$.

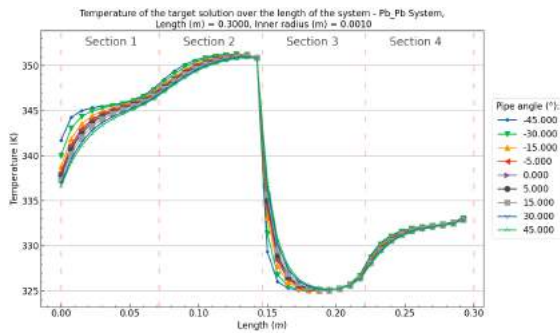
Figure B.81: Pb/Pb (Heat/Cool) System results over the pipe angle θ and system length L at an inner radius of $R_i = 0.0010m$, heating wall thickness of $dr_{12} = 0.015m$ and cooling wall thickness $dr_{34}(m) = 0.005m$



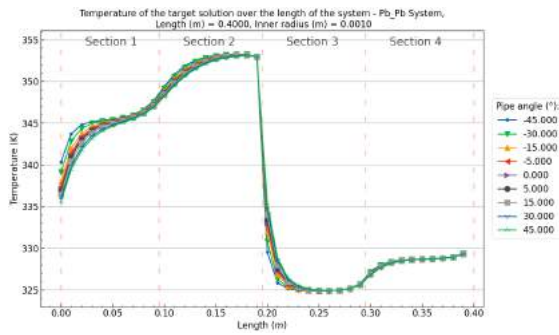
(a) Target solution temperature profile over the length of the system and pipe angles at a total system length of $L = 0.10m$ and inner radius $R_i = 0.0010m$.



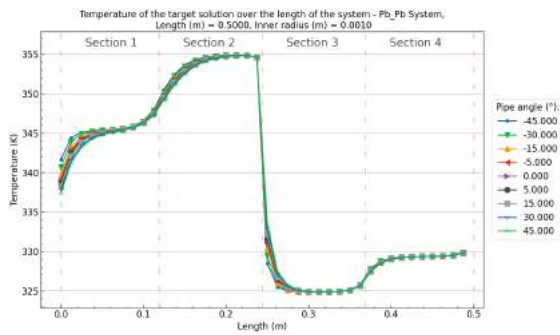
(b) Target solution temperature profile over the length of the system and pipe angles at a total system length of $L = 0.20m$ and inner radius $R_i = 0.0010m$.



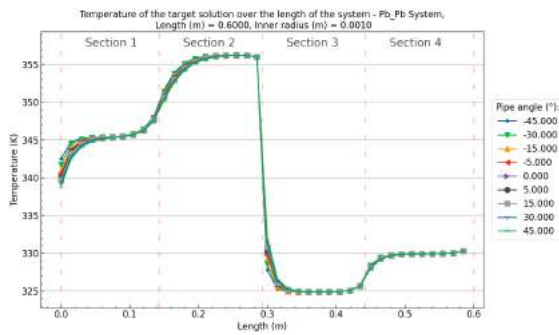
(c) Target solution temperature profile over the length of the system and pipe angles at a total system length of $L = 0.30m$ and inner radius $R_i = 0.0010m$.



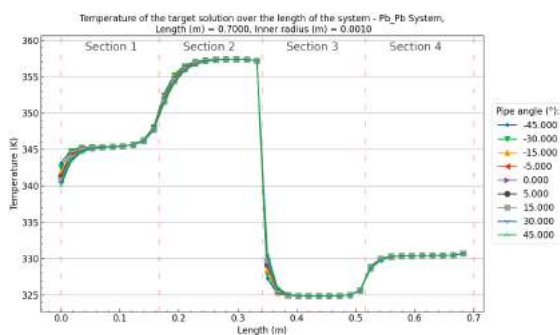
(d) Target solution temperature profile over the length of the system and pipe angles at a total system length of $L = 0.40m$ and inner radius $R_i = 0.0010m$.



(e) Target solution temperature profile over the length of the system and pipe angles at a total system length of $L = 0.50m$ and inner radius $R_i = 0.0010m$.



(f) Target solution temperature profile over the length of the system and pipe angles at a total system length of $L = 0.60m$ and inner radius $R_i = 0.0010m$.

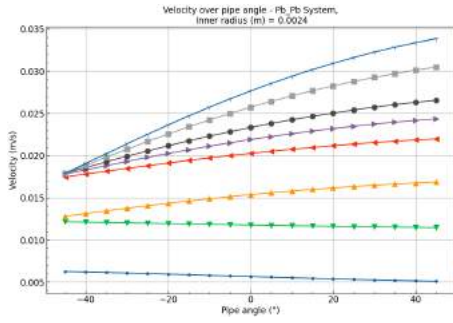


(g) Target solution temperature profile over the length of the system and pipe angles at a total system length of $L = 0.70m$ and inner radius $R_i = 0.0010m$.

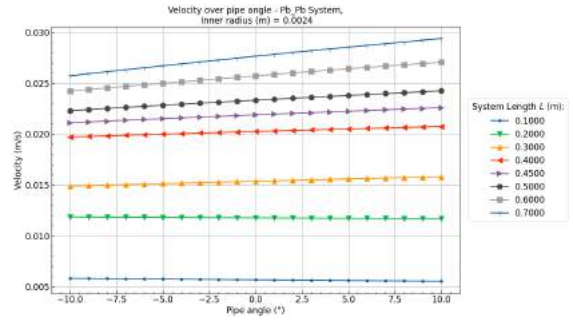
Figure B.82: Pb/Pb (Heat/Cool) System target solution temperature profiles over the pipe angle θ and system length L at an inner radius of $R_i = 0.0010m$, a heating wall thickness of $dr_{12} = 0.015m$ and cooling wall thickness $dr_{34}(m) = 0.005m$

Pb/Pb - $R_i = 0.0024m$

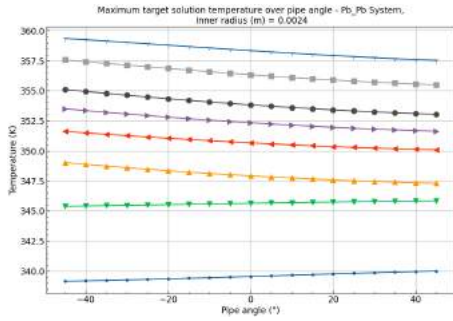
Back to overview - B.3



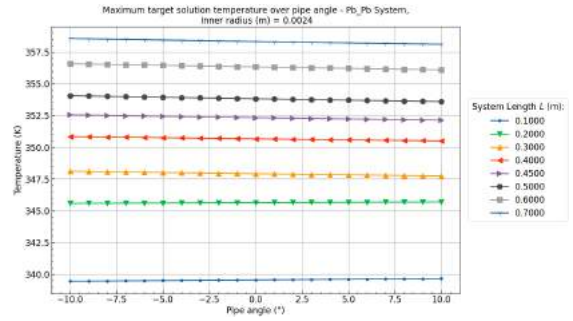
(a) Velocity over pipe angle between -45° and 45° at an inner radius $R_i = 0.0024m$.



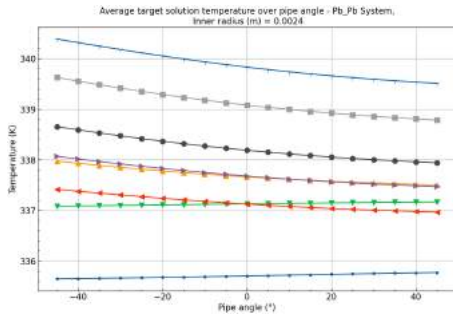
(b) Velocity over pipe angle between -10° and 10° at an inner radius $R_i = 0.0024m$.



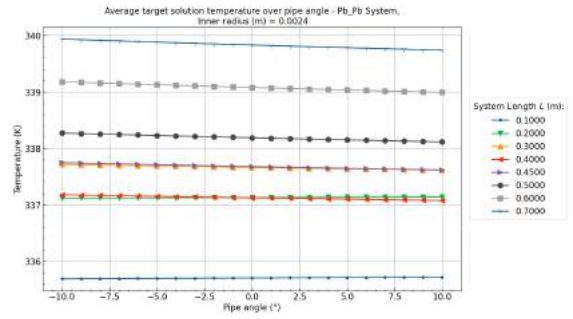
(c) Maximum target solution temperature over the pipe angle between -45° and 45° at an inner radius $R_i = 0.0024m$.



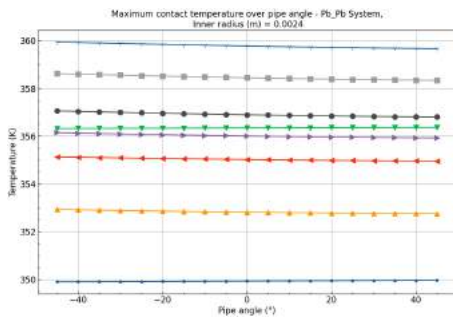
(d) Maximum target solution temperature over the pipe angle between -10° and 10° at an inner radius $R_i = 0.0024m$.



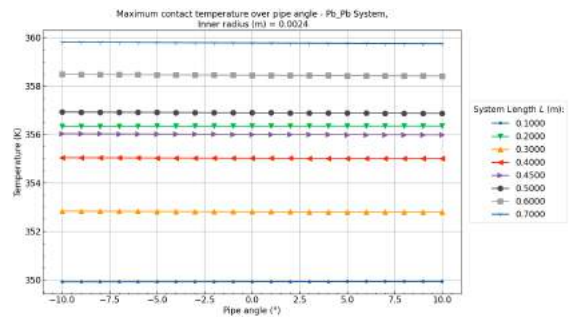
(e) Average target solution temperature over the pipe angle between -45° and 45° at an inner radius $R_i = 0.0024m$.



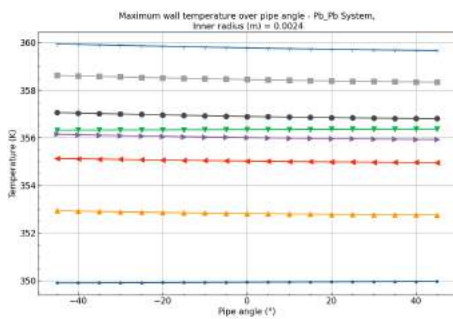
(f) Average target solution temperature over the pipe angle between -10° and 10° at an inner radius $R_i = 0.0024m$.



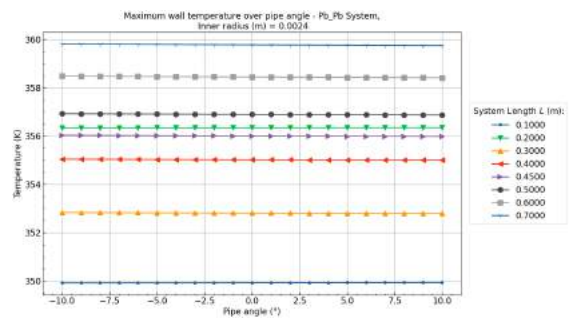
(g) Maximum contact temperature over the pipe angle between -45° and 45° at an inner radius $R_i = 0.0024m$.



(h) Maximum contact temperature over the pipe angle between -10° and 10° at an inner radius $R_i = 0.0024m$.

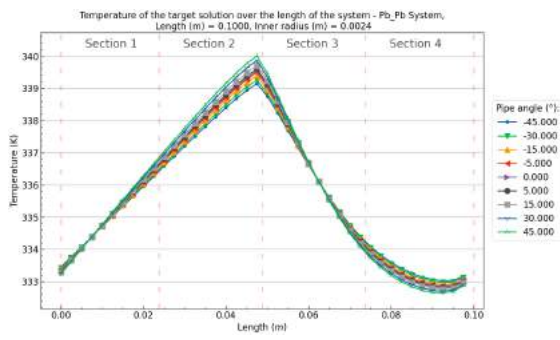


(i) Maximum wall temperature over the pipe angle between -45° and 45° at an inner radius $R_i = 0.0024m$.

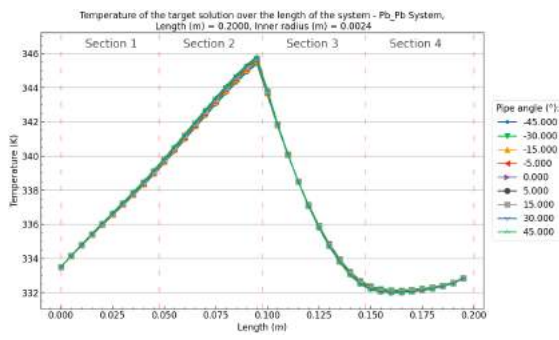


(j) Maximum wall temperature over the pipe angle between -10° and 10° at an inner radius $R_i = 0.0024m$.

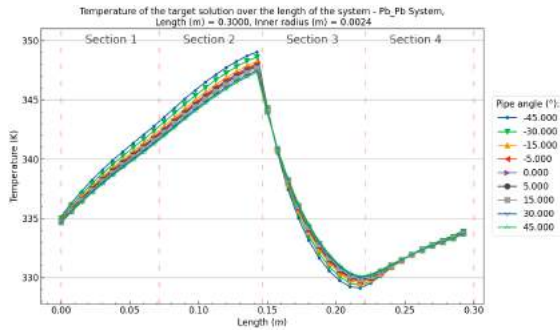
Figure B.83: Pb/Pb (Heat/Cool) System results over the pipe angle θ and system length L at an inner radius of $R_i = 0.0024m$, heating wall thickness of $dr_{12} = 0.015m$ and cooling wall thickness $dr_{34} (m) = 0.005m$



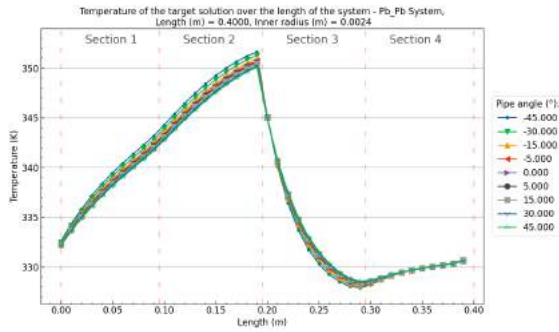
(a) Target solution temperature profile over the length of the system and pipe angles at a total system length of $L = 0.10m$ and inner radius $R_i = 0.0024m$.



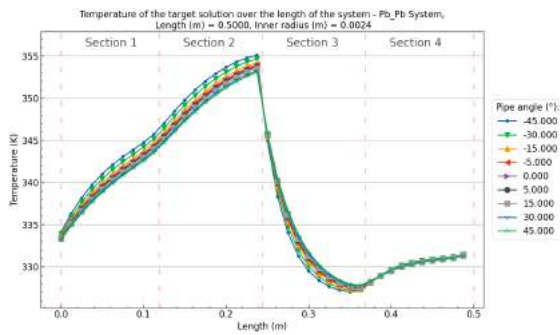
(b) Target solution temperature profile over the length of the system and pipe angles at a total system length of $L = 0.20m$ and inner radius $R_i = 0.0024m$.



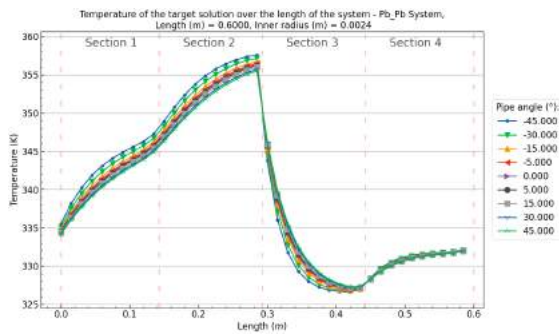
(c) Target solution temperature profile over the length of the system and pipe angles at a total system length of $L = 0.30m$ and inner radius $R_i = 0.0024m$.



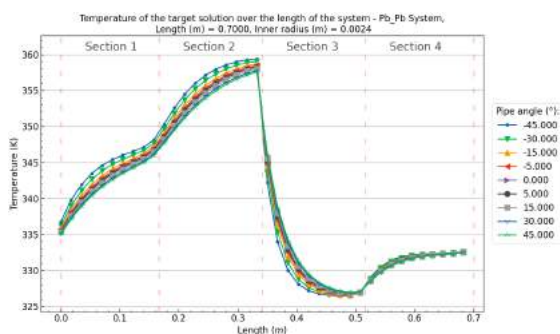
(d) Target solution temperature profile over the length of the system and pipe angles at a total system length of $L = 0.40m$ and inner radius $R_i = 0.0024m$.



(e) Target solution temperature profile over the length of the system and pipe angles at a total system length of $L = 0.50m$ and inner radius $R_i = 0.0024m$.



(f) Target solution temperature profile over the length of the system and pipe angles at a total system length of $L = 0.60m$ and inner radius $R_i = 0.0024m$.

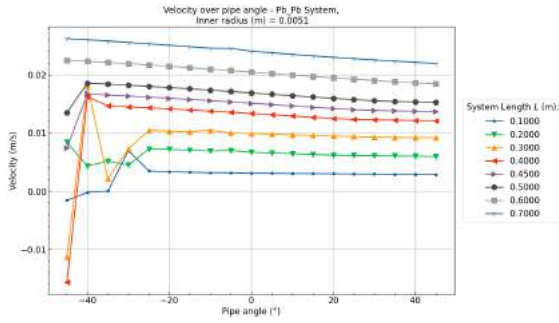


(g) Target solution temperature profile over the length of the system and pipe angles at a total system length of $L = 0.70m$ and inner radius $R_i = 0.0024m$.

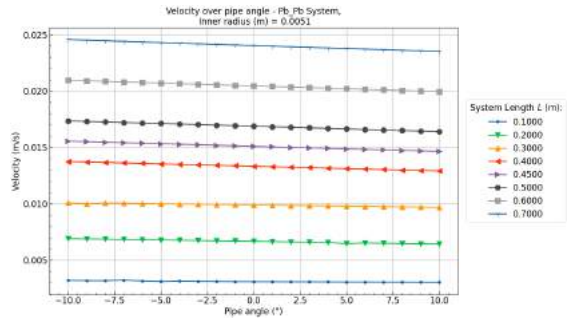
Figure B.84: Pb/Pb (Heat/Cool) System target solution temperature profiles over the pipe angle θ and system length L at an inner radius of $R_i = 0.0024m$, a heating wall thickness of $dr_{12} = 0.015m$ and cooling wall thickness $dr_{34}(m) = 0.005m$

Pb/Pb - $R_i = 0.0051 m$

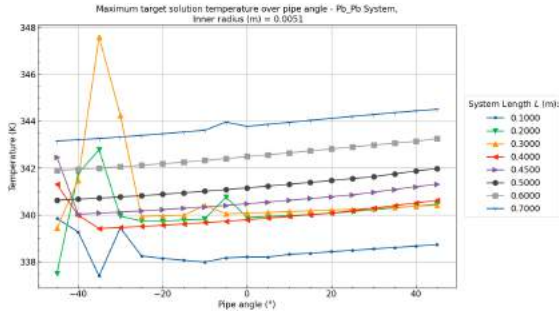
Back to overview - B.3



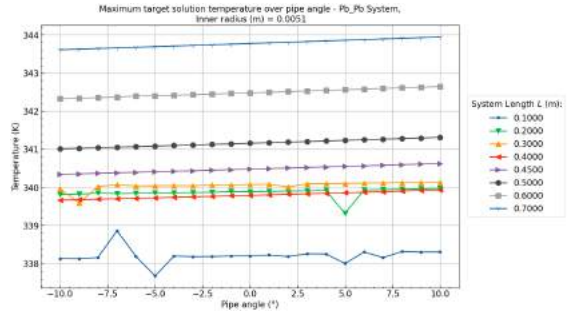
(a) Velocity over pipe angle between -45° and 45° at an inner radius $R_i = 0.0051 m$.



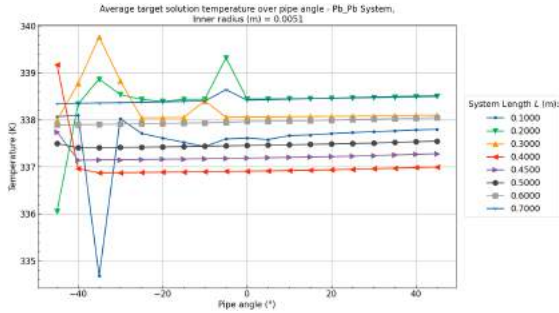
(b) Velocity over pipe angle between -10° and 10° at an inner radius $R_i = 0.0051 m$.



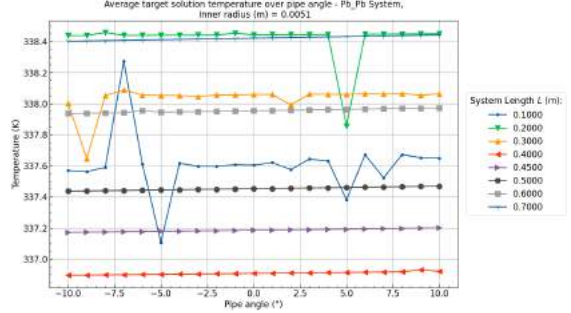
(c) Maximum target solution temperature over the pipe angle between -45° and 45° at an inner radius $R_i = 0.0051 m$.



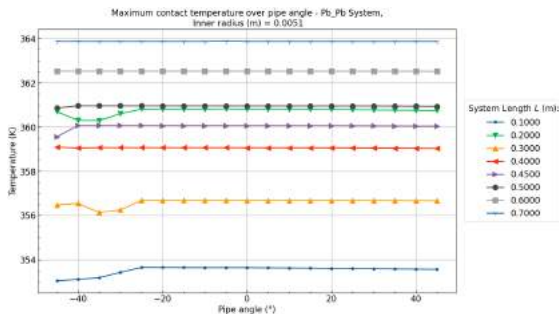
(d) Maximum target solution temperature over the pipe angle between -10° and 10° at an inner radius $R_i = 0.0051 m$.



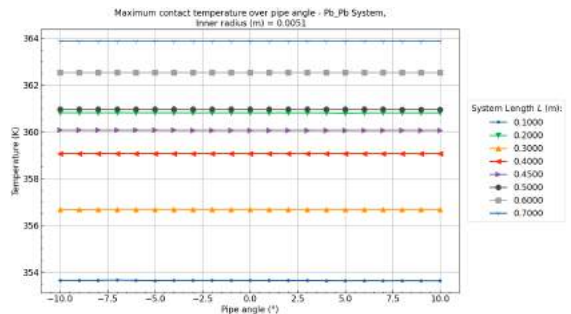
(e) Average target solution temperature over the pipe angle between -45° and 45° at an inner radius $R_i = 0.0051 m$.



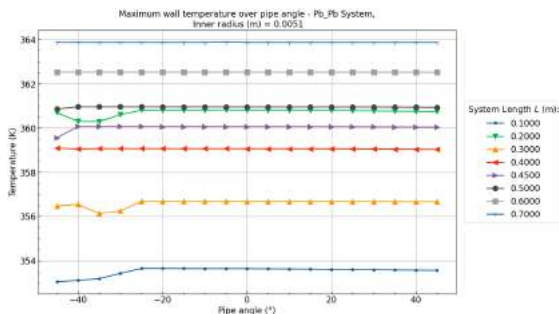
(f) Average target solution temperature over the pipe angle between -10° and 10° at an inner radius $R_i = 0.0051 m$.



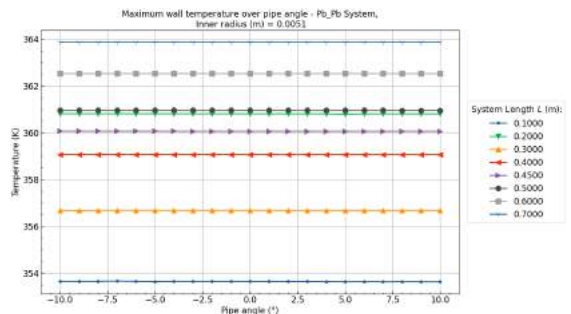
(g) Maximum contact temperature over the pipe angle between -45° and 45° at an inner radius $R_i = 0.0051 m$.



(h) Maximum contact temperature over the pipe angle between -10° and 10° at an inner radius $R_i = 0.0051 m$.

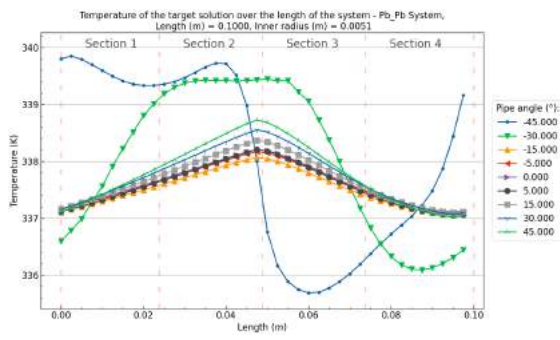


(i) Maximum wall temperature over the pipe angle between -45° and 45° at an inner radius $R_i = 0.0051 m$.

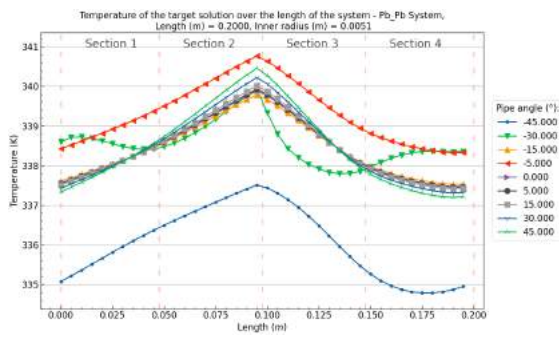


(j) Maximum wall temperature over the pipe angle between -10° and 10° at an inner radius $R_i = 0.0051 m$.

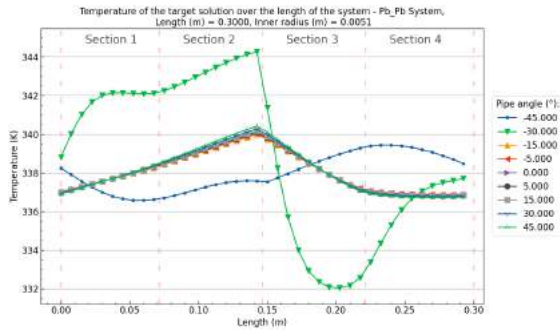
Figure B.85: Pb/Pb (Heat/Cool) System results over the pipe angle θ and system length L at an inner radius of $R_i = 0.0051 m$, heating wall thickness of $dr_{12} = 0.015 m$ and cooling wall thickness $dr_{34} (m) = 0.005 m$



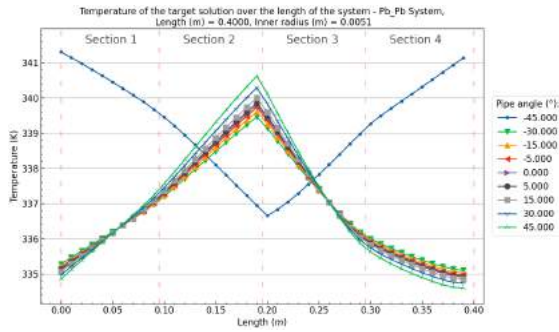
(a) Target solution temperature profile over the length of the system and pipe angles at a total system length of $L = 0.10m$ and inner radius $R_i = 0.0051m$.



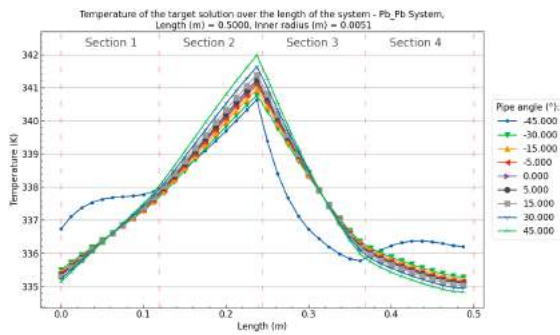
(b) Target solution temperature profile over the length of the system and pipe angles at a total system length of $L = 0.20m$ and inner radius $R_i = 0.0051m$.



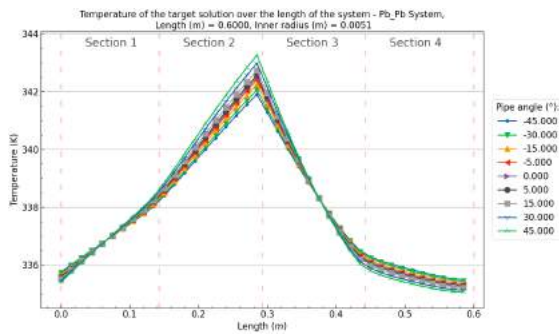
(c) Target solution temperature profile over the length of the system and pipe angles at a total system length of $L = 0.30m$ and inner radius $R_i = 0.0051m$.



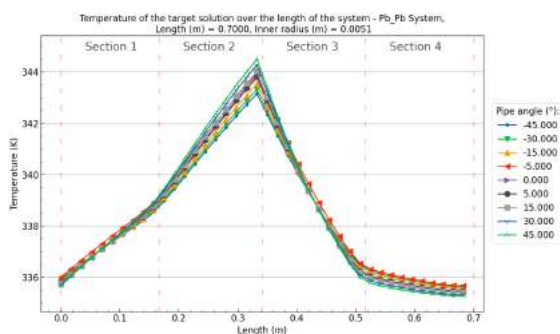
(d) Target solution temperature profile over the length of the system and pipe angles at a total system length of $L = 0.40m$ and inner radius $R_i = 0.0051m$.



(e) Target solution temperature profile over the length of the system and pipe angles at a total system length of $L = 0.50m$ and inner radius $R_i = 0.0051m$.



(f) Target solution temperature profile over the length of the system and pipe angles at a total system length of $L = 0.60m$ and inner radius $R_i = 0.0051m$.

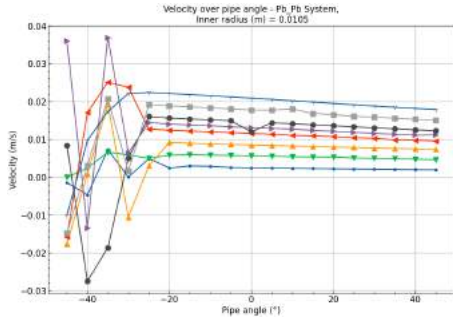


(g) Target solution temperature profile over the length of the system and pipe angles at a total system length of $L = 0.70m$ and inner radius $R_i = 0.0051m$.

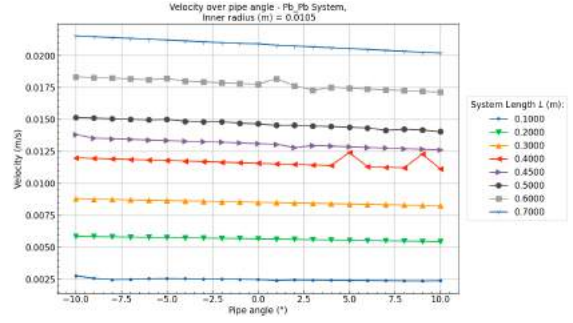
Figure B.86: Pb/Pb (Heat/Cool) System target solution temperature profiles over the pipe angle θ and system length L at an inner radius of $R_i = 0.0051m$, a heating wall thickness of $dr_{12} = 0.015m$ and cooling wall thickness $dr_{34}(m) = 0.005m$

Pb/Pb - $R_i = 0.0105m$

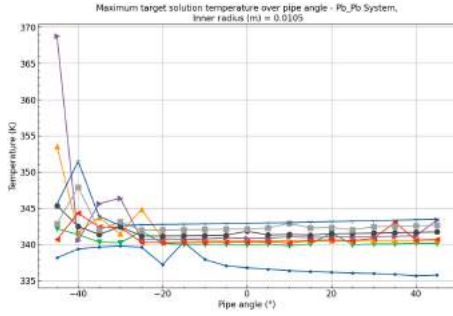
Back to overview - B.3



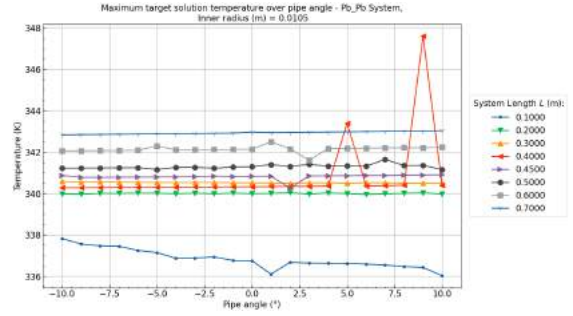
(a) Velocity over pipe angle between -45° and 45° at an inner radius $R_i = 0.0105m$.



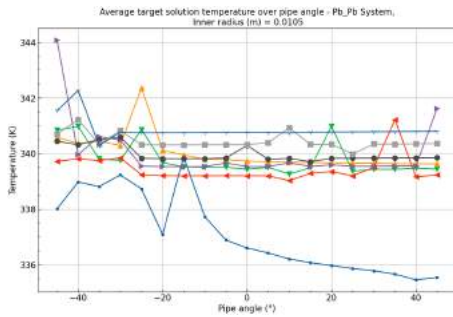
(b) Velocity over pipe angle between -10° and 10° at an inner radius $R_i = 0.0105m$.



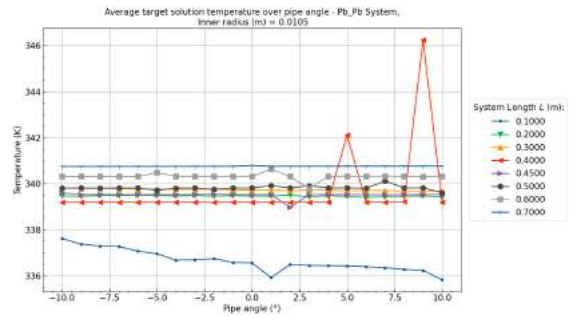
(c) Maximum target solution temperature over the pipe angle between -45° and 45° at an inner radius $R_i = 0.0105m$.



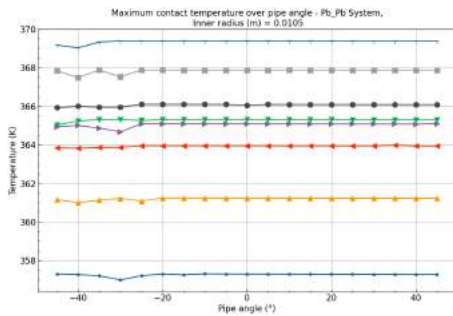
(d) Maximum target solution temperature over the pipe angle between -10° and 10° at an inner radius $R_i = 0.0105m$.



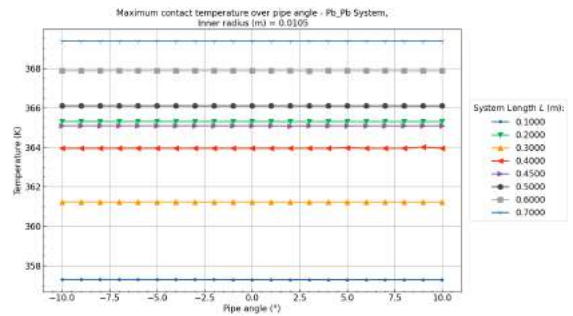
(e) Average target solution temperature over the pipe angle between -45° and 45° at an inner radius $R_i = 0.0105m$.



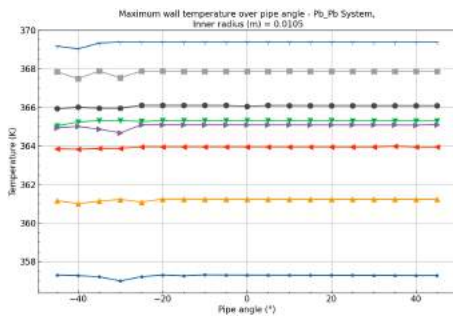
(f) Average target solution temperature over the pipe angle between -10° and 10° at an inner radius $R_i = 0.0105m$.



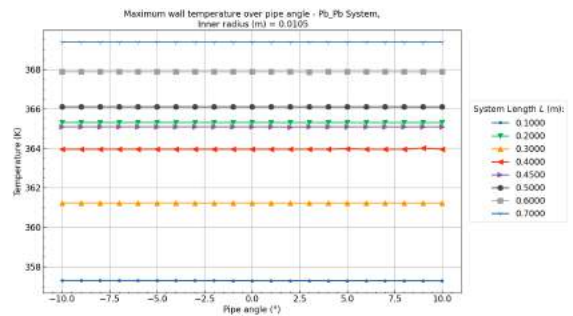
(g) Maximum contact temperature over the pipe angle between -45° and 45° at an inner radius $R_i = 0.0105m$.



(h) Maximum contact temperature over the pipe angle between -10° and 10° at an inner radius $R_i = 0.0105m$.

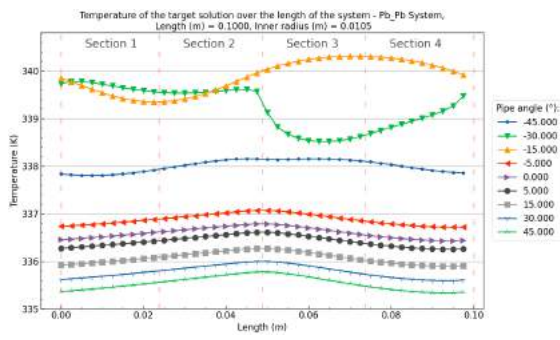


(i) Maximum wall temperature over the pipe angle between -45° and 45° at an inner radius $R_i = 0.0105m$.

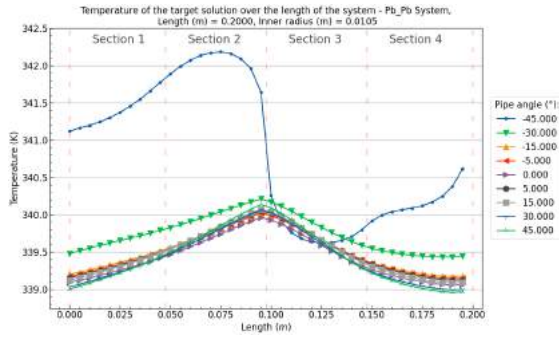


(j) Maximum wall temperature over the pipe angle between -10° and 10° at an inner radius $R_i = 0.0105m$.

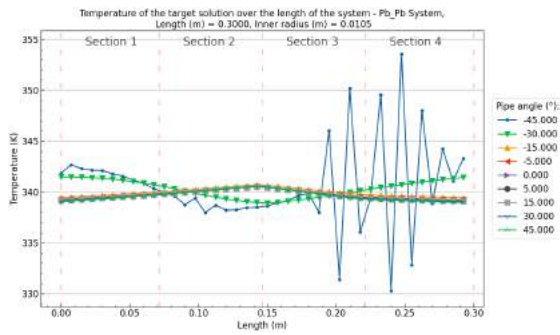
Figure B.87: Pb/Pb (Heat/Cool) System results over the pipe angle θ and system length L at an inner radius of $R_i = 0.0105m$, heating wall thickness of $dr_{12} = 0.015m$ and cooling wall thickness $dr_{34} (m) = 0.005m$



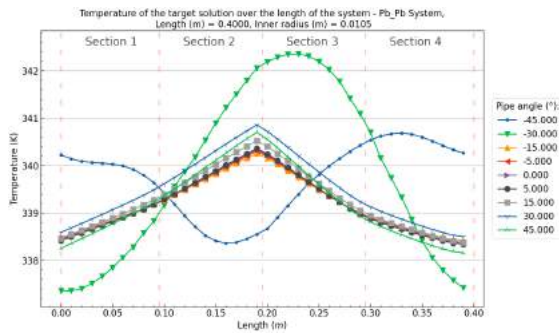
(a) Target solution temperature profile over the length of the system and pipe angles at a total system length of $L = 0.10m$ and inner radius $R_i = 0.0105m$.



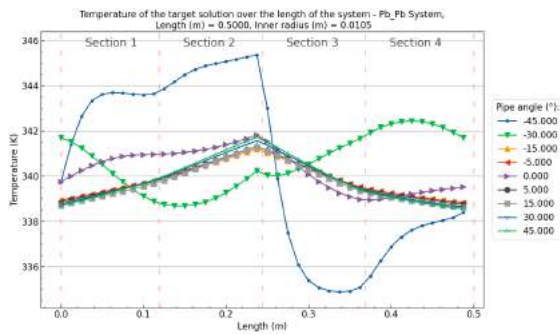
(b) Target solution temperature profile over the length of the system and pipe angles at a total system length of $L = 0.20m$ and inner radius $R_i = 0.0105m$.



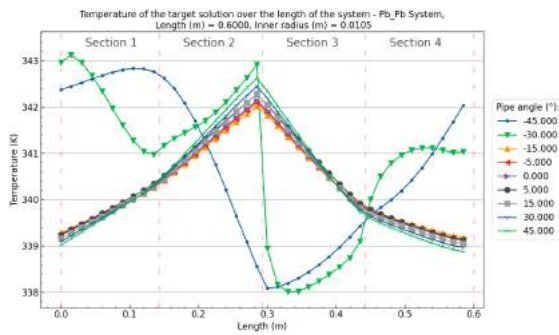
(c) Target solution temperature profile over the length of the system and pipe angles at a total system length of $L = 0.30m$ and inner radius $R_i = 0.0105m$.



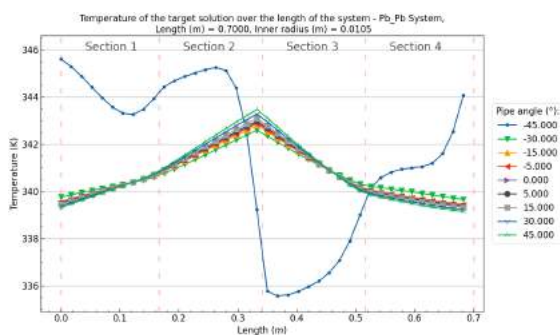
(d) Target solution temperature profile over the length of the system and pipe angles at a total system length of $L = 0.40m$ and inner radius $R_i = 0.0105m$.



(e) Target solution temperature profile over the length of the system and pipe angles at a total system length of $L = 0.50m$ and inner radius $R_i = 0.0105m$.



(f) Target solution temperature profile over the length of the system and pipe angles at a total system length of $L = 0.60m$ and inner radius $R_i = 0.0105m$.

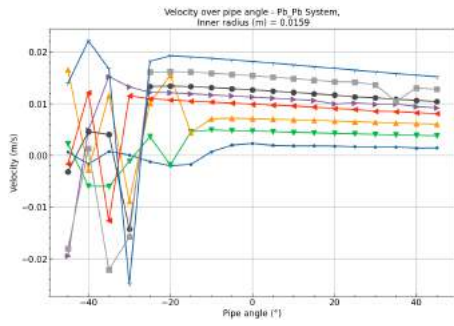


(g) Target solution temperature profile over the length of the system and pipe angles at a total system length of $L = 0.70m$ and inner radius $R_i = 0.0105m$.

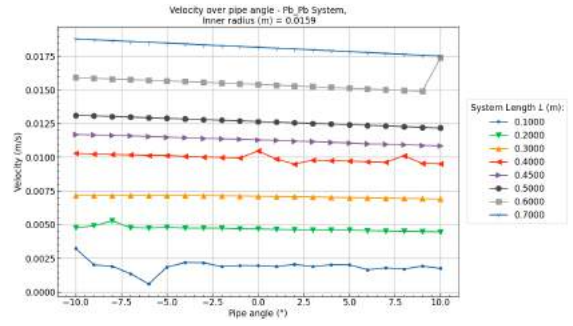
Figure B.88: Pb/Pb (Heat/Cool) System target solution temperature profiles over the pipe angle θ and system length L at an inner radius of $R_i = 0.0105m$, a heating wall thickness of $dr_{12} = 0.015m$ and cooling wall thickness $dr_{34}(m) = 0.005m$

Pb/Pb - $R_i = 0.0159m$

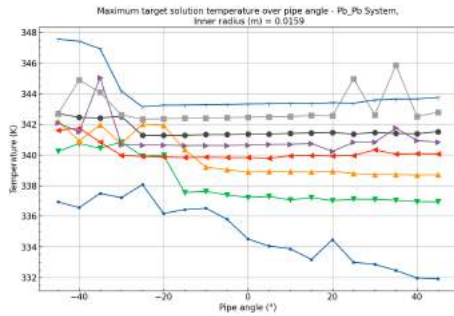
Back to overview - B.3



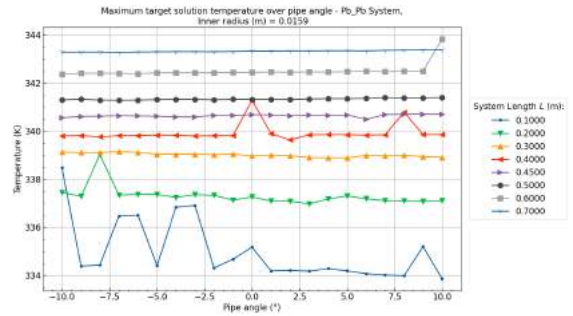
(a) Velocity over pipe angle between -45° and 45° at an inner radius $R_i = 0.0159m$.



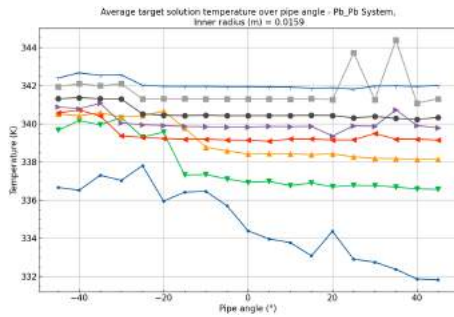
(b) Velocity over pipe angle between -10° and 10° at an inner radius $R_i = 0.0159m$.



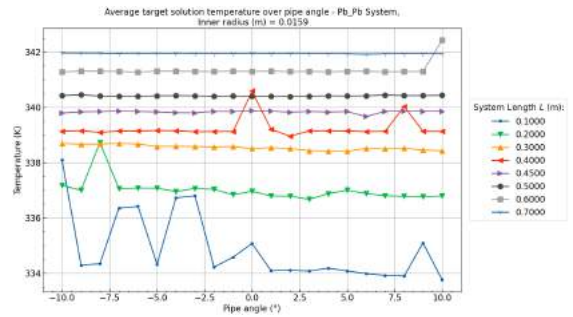
(c) Maximum target solution temperature over the pipe angle between -45° and 45° at an inner radius $R_i = 0.0159m$.



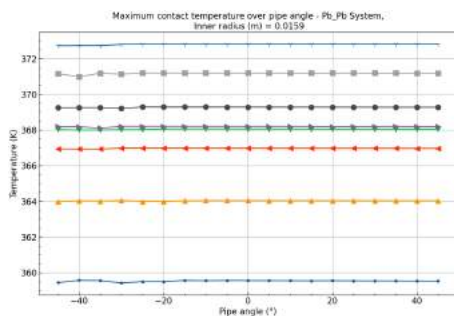
(d) Maximum target solution temperature over the pipe angle between -10° and 10° at an inner radius $R_i = 0.0159m$.



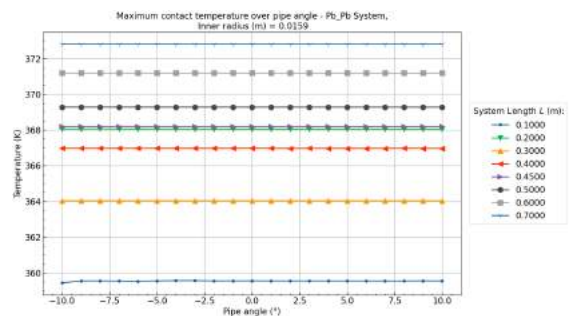
(e) Average target solution temperature over the pipe angle between -45° and 45° at an inner radius $R_i = 0.0159m$.



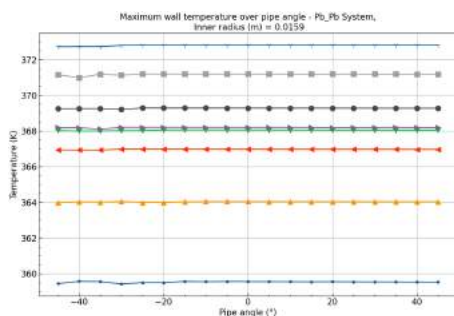
(f) Average target solution temperature over the pipe angle between -10° and 10° at an inner radius $R_i = 0.0159m$.



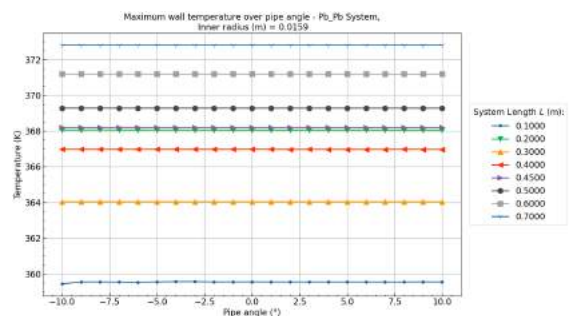
(g) Maximum contact temperature over the pipe angle between -45° and 45° at an inner radius $R_i = 0.0159m$.



(h) Maximum contact temperature over the pipe angle between -10° and 10° at an inner radius $R_i = 0.0159m$.

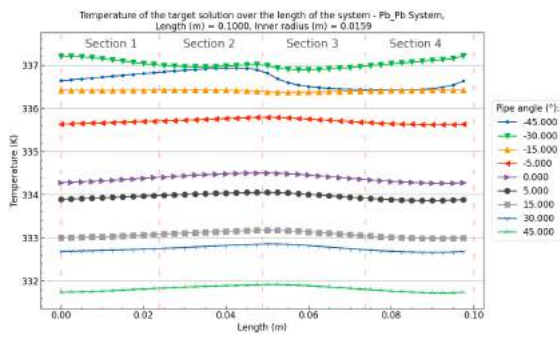


(i) Maximum wall temperature over the pipe angle between -45° and 45° at an inner radius $R_i = 0.0159m$.

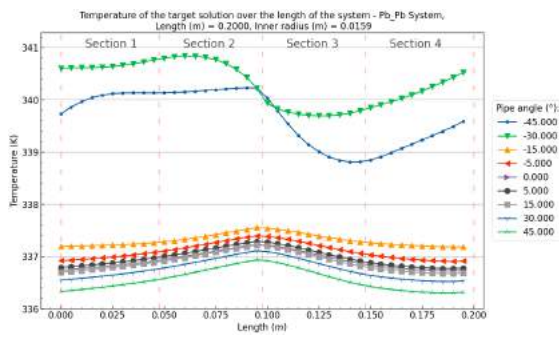


(j) Maximum wall temperature over the pipe angle between -10° and 10° at an inner radius $R_i = 0.0159m$.

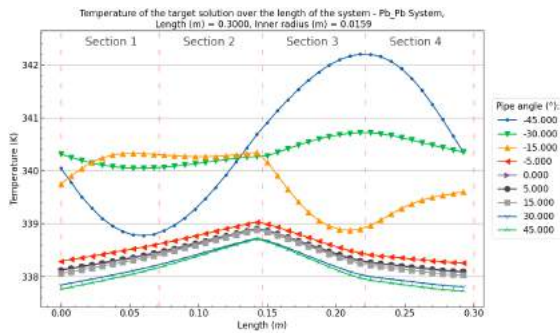
Figure B.89: Pb/Pb (Heat/Cool) System results over the pipe angle θ and system length L at an inner radius of $R_i = 0.0159m$, heating wall thickness of $dr_{12} = 0.015m$ and cooling wall thickness $dr_{34} (m) = 0.005m$



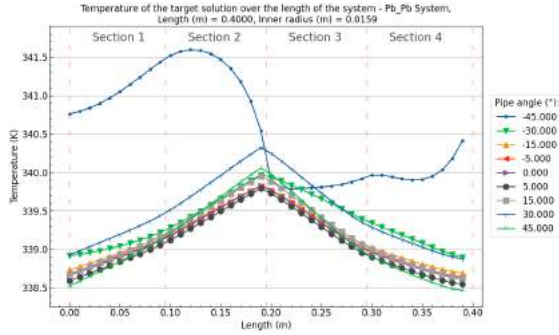
(a) Target solution temperature profile over the length of the system and pipe angles at a total system length of $L = 0.10m$ and inner radius $R_i = 0.0159m$.



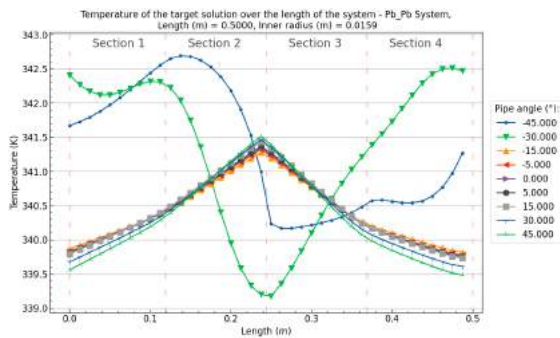
(b) Target solution temperature profile over the length of the system and pipe angles at a total system length of $L = 0.20m$ and inner radius $R_i = 0.0159m$.



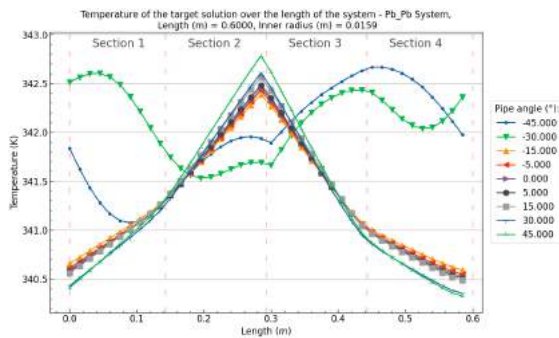
(c) Target solution temperature profile over the length of the system and pipe angles at a total system length of $L = 0.30m$ and inner radius $R_i = 0.0159m$.



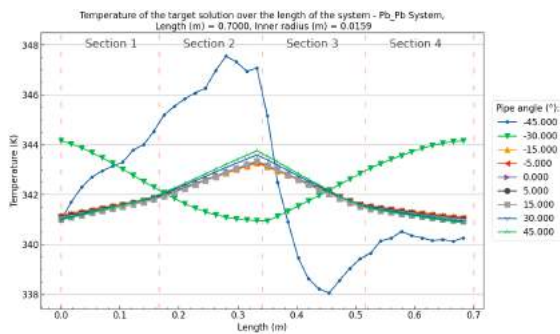
(d) Target solution temperature profile over the length of the system and pipe angles at a total system length of $L = 0.40m$ and inner radius $R_i = 0.0159m$.



(e) Target solution temperature profile over the length of the system and pipe angles at a total system length of $L = 0.50m$ and inner radius $R_i = 0.0159m$.



(f) Target solution temperature profile over the length of the system and pipe angles at a total system length of $L = 0.60m$ and inner radius $R_i = 0.0159m$.

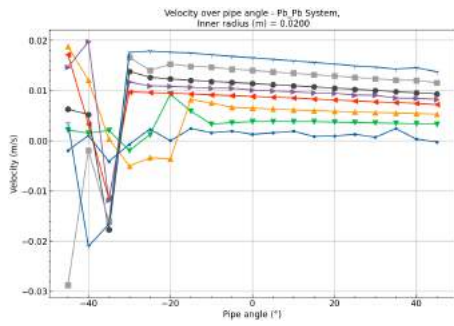


(g) Target solution temperature profile over the length of the system and pipe angles at a total system length of $L = 0.70m$ and inner radius $R_i = 0.0159m$.

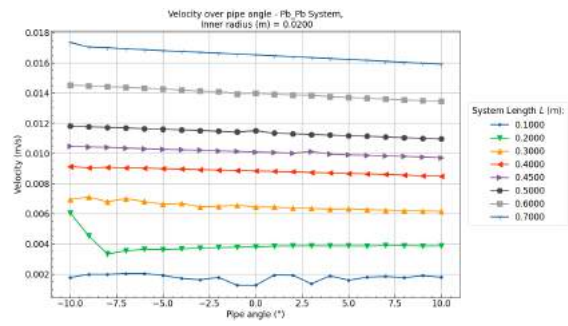
Figure B.90: Pb/Pb (Heat/Cool) System target solution temperature profiles over the pipe angle θ and system length L at an inner radius of $R_i = 0.0159m$, a heating wall thickness of $dr_{12} = 0.015m$ and cooling wall thickness $dr_{34}(m) = 0.005m$

Pb/Pb - $R_i = 0.0200m$

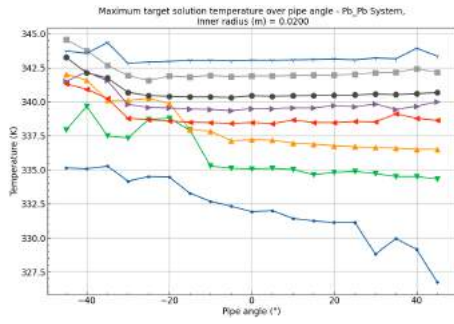
Back to overview - B.3



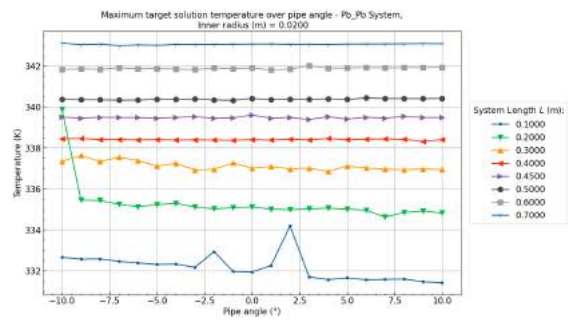
(a) Velocity over pipe angle between -45° and 45° at an inner radius $R_i = 0.0200m$.



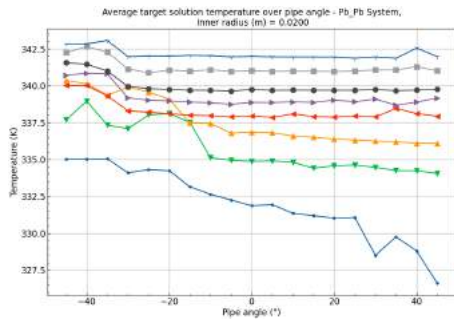
(b) Velocity over pipe angle between -10° and 10° at an inner radius $R_i = 0.0200m$.



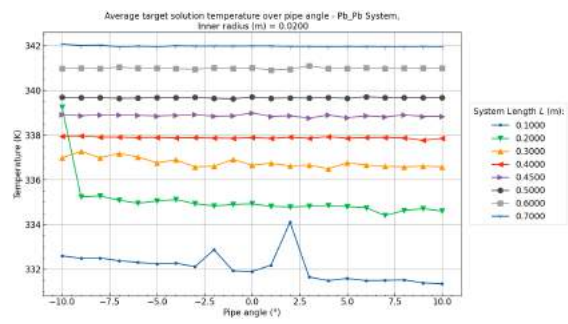
(c) Maximum target solution temperature over the pipe angle between -45° and 45° at an inner radius $R_i = 0.0200m$.



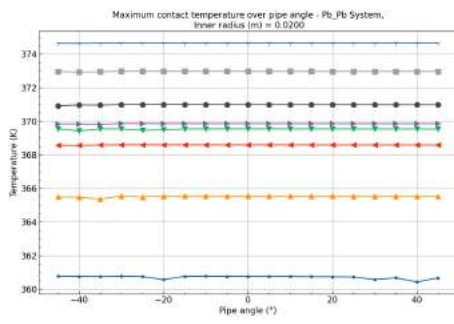
(d) Maximum target solution temperature over the pipe angle between -10° and 10° at an inner radius $R_i = 0.0200m$.



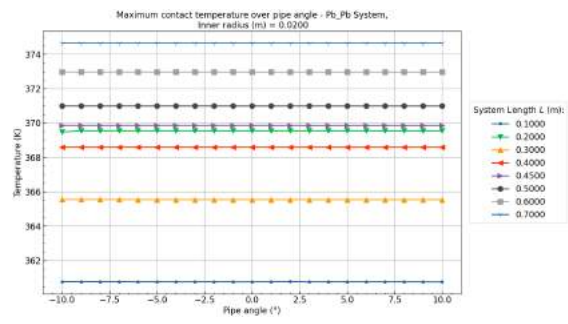
(e) Average target solution temperature over the pipe angle between -45° and 45° at an inner radius $R_i = 0.0200m$.



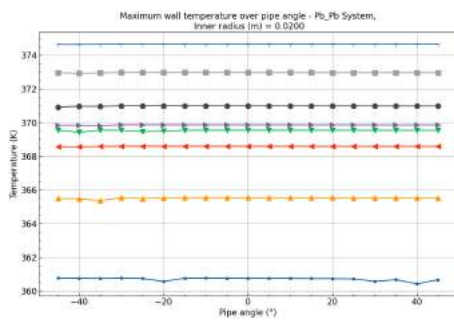
(f) Average target solution temperature over the pipe angle between -10° and 10° at an inner radius $R_i = 0.0200m$.



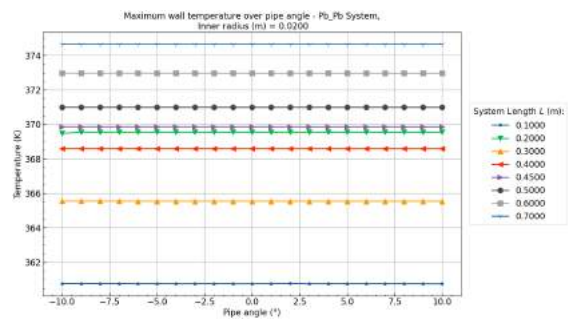
(g) Maximum contact temperature over the pipe angle between -45° and 45° at an inner radius $R_i = 0.0200m$.



(h) Maximum contact temperature over the pipe angle between -10° and 10° at an inner radius $R_i = 0.0200m$.

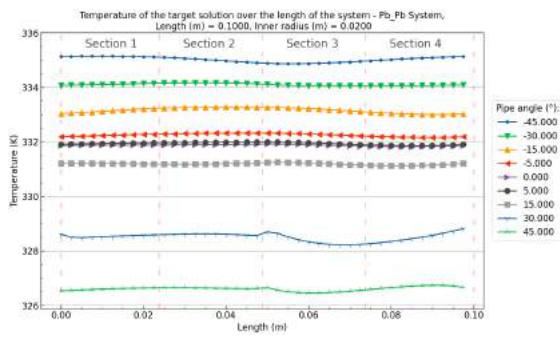


(i) Maximum wall temperature over the pipe angle between -45° and 45° at an inner radius $R_i = 0.0200m$.

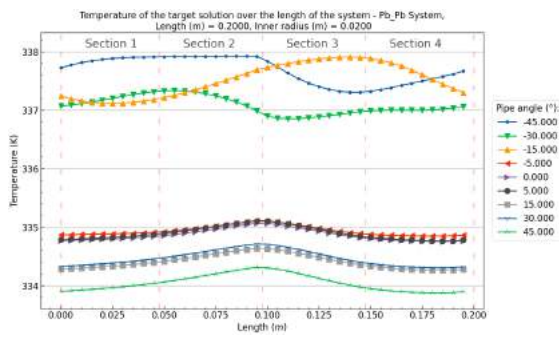


(j) Maximum wall temperature over the pipe angle between -10° and 10° at an inner radius $R_i = 0.0200m$.

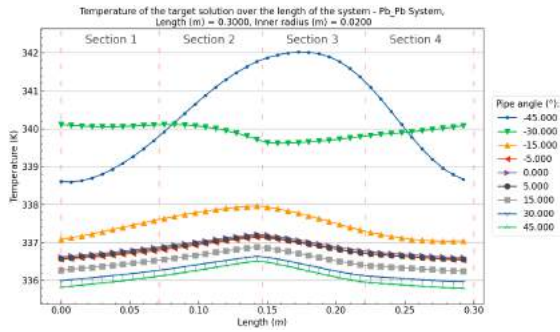
Figure B.91: Pb/Pb (Heat/Cool) System results over the pipe angle θ and system length L at an inner radius of $R_i = 0.0200m$, heating wall thickness of $dr_{12} = 0.015m$ and cooling wall thickness $dr_{34}(m) = 0.005m$



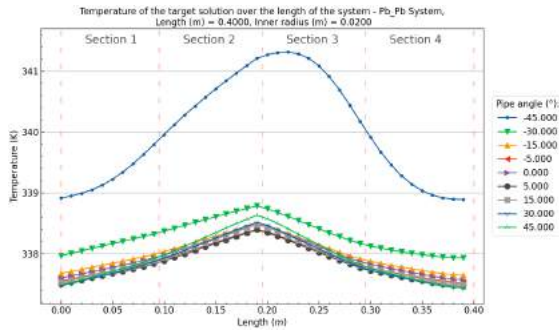
(a) Target solution temperature profile over the length of the system and pipe angles at a total system length of $L = 0.10m$ and inner radius $R_i = 0.0200m$.



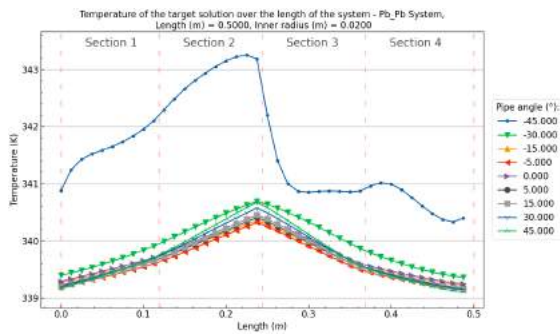
(b) Target solution temperature profile over the length of the system and pipe angles at a total system length of $L = 0.20m$ and inner radius $R_i = 0.0200m$.



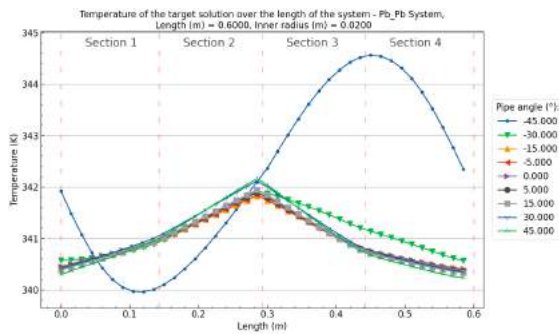
(c) Target solution temperature profile over the length of the system and pipe angles at a total system length of $L = 0.30m$ and inner radius $R_i = 0.0200m$.



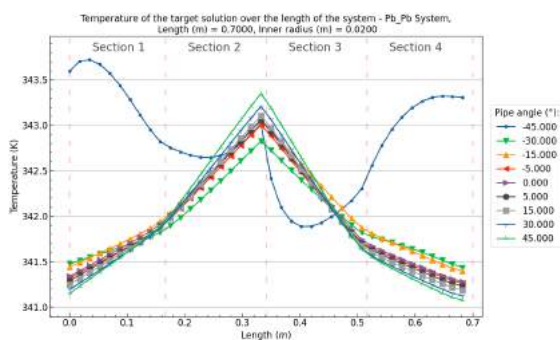
(d) Target solution temperature profile over the length of the system and pipe angles at a total system length of $L = 0.40m$ and inner radius $R_i = 0.0200m$.



(e) Target solution temperature profile over the length of the system and pipe angles at a total system length of $L = 0.50m$ and inner radius $R_i = 0.0200m$.



(f) Target solution temperature profile over the length of the system and pipe angles at a total system length of $L = 0.60m$ and inner radius $R_i = 0.0200m$.



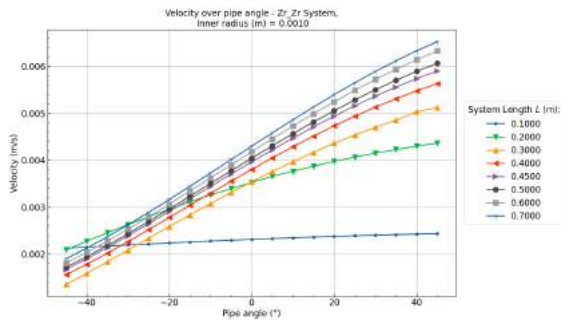
(g) Target solution temperature profile over the length of the system and pipe angles at a total system length of $L = 0.70m$ and inner radius $R_i = 0.0200m$.

Figure B.92: Pb/Pb (Heat/Cool) System target solution temperature profiles over the pipe angle θ and system length L at an inner radius of $R_i = 0.0200m$, a heating wall thickness of $dr_{12} = 0.015m$ and cooling wall thickness $dr_{34}(m) = 0.005m$

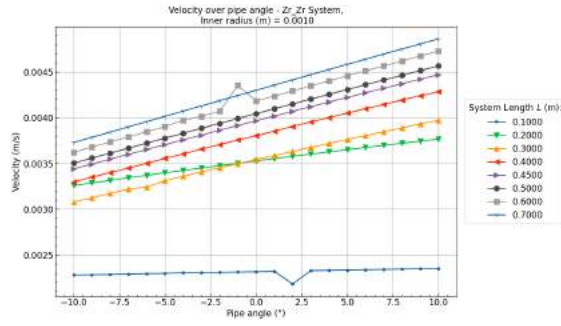
B.3.3. Zr/Zr - Pipe angle, System length & Inner radius

$Z_r/Z_r - R_i = 0.0010m$

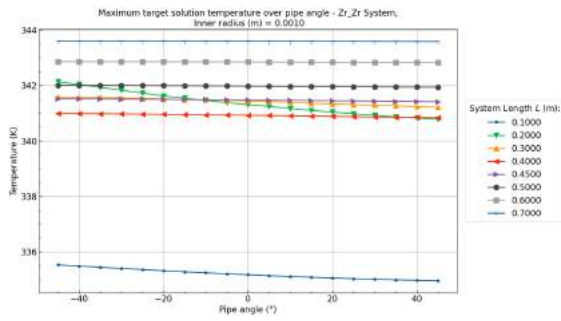
[Back to overview - B.3](#)



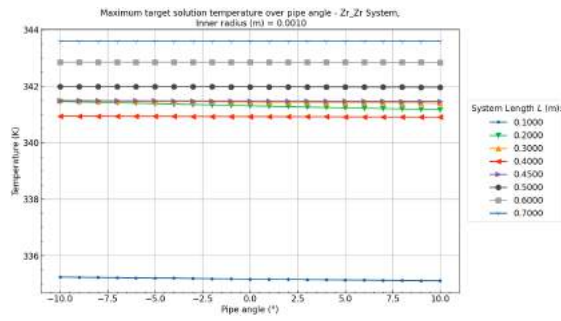
(a) Velocity over pipe angle between -45° and 45° at an inner radius $R_i = 0.0010m$.



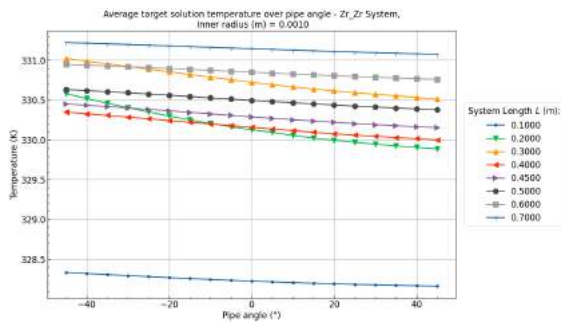
(b) Velocity over pipe angle between -10° and 10° at an inner radius $R_i = 0.0010m$.



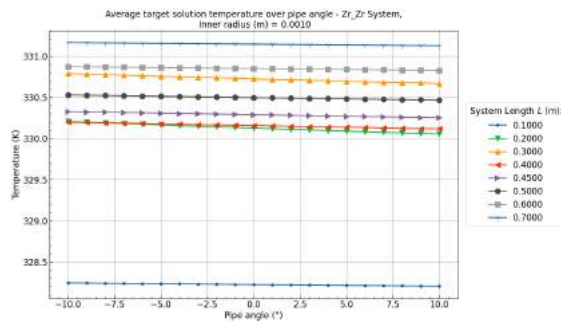
(c) Maximum target solution temperature over the pipe angle between -45° and 45° at an inner radius $R_i = 0.0010m$.



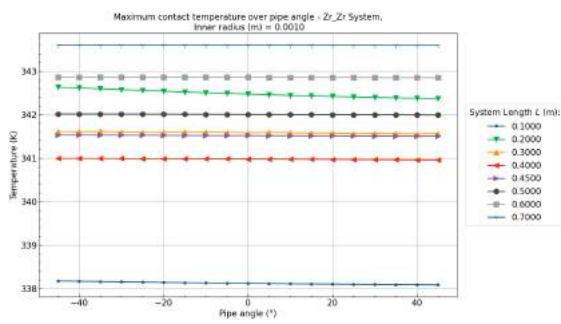
(d) Maximum target solution temperature over the pipe angle between -10° and 10° at an inner radius $R_i = 0.0010m$.



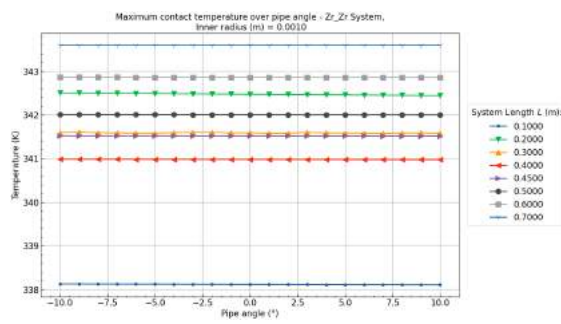
(e) Average target solution temperature over the pipe angle between -45° and 45° at an inner radius $R_i = 0.0010m$.



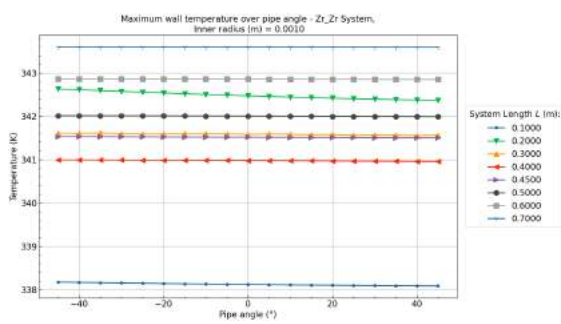
(f) Average target solution temperature over the pipe angle between -10° and 10° at an inner radius $R_i = 0.0010m$.



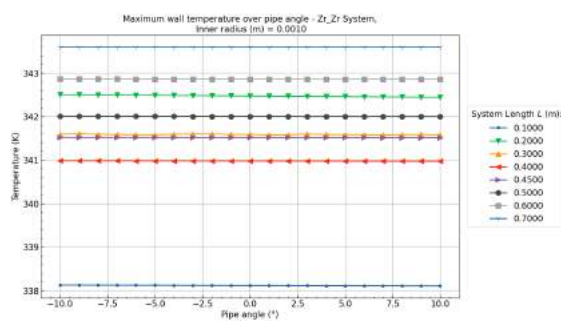
(g) Maximum contact temperature over the pipe angle between -45° and 45° at an inner radius $R_i = 0.0010m$.



(h) Maximum contact temperature over the pipe angle between -10° and 10° at an inner radius $R_i = 0.0010m$.

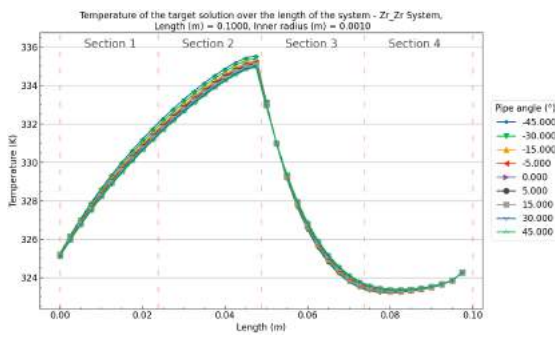


(i) Maximum wall temperature over the pipe angle between -45° and 45° at an inner radius $R_i = 0.0010m$.

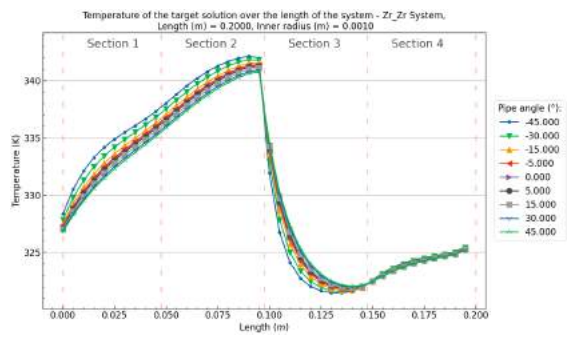


(j) Maximum wall temperature over the pipe angle between -10° and 10° at an inner radius $R_i = 0.0010m$.

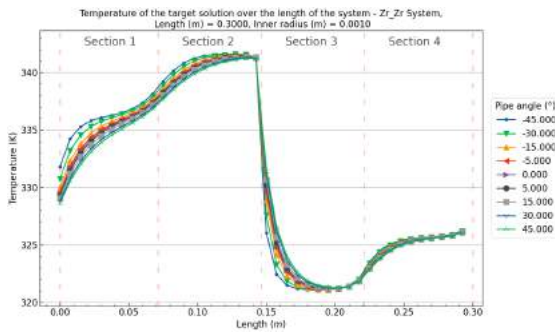
Figure B.93: Z_r/Z_r (Heat/Cool) System results over the pipe angle θ and system length L at an inner radius of $R_i = 0.0010m$, heating wall thickness of $dr_{12} = 0.015m$ and cooling wall thickness $dr_{34} (m) = 0.005m$



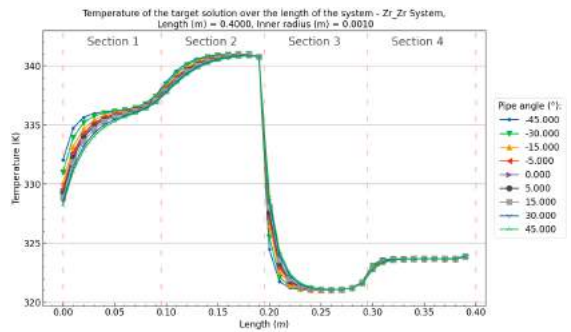
(a) Target solution temperature profile over the length of the system and pipe angles at a total system length of $L = 0.10m$ and inner radius $R_i = 0.0010m$.



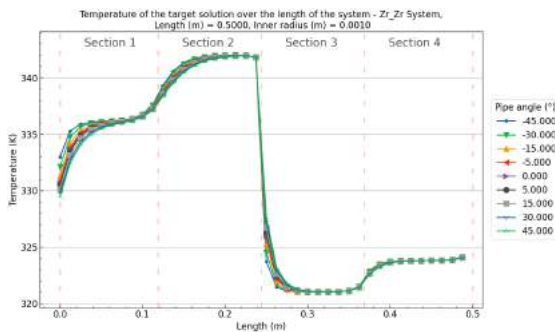
(b) Target solution temperature profile over the length of the system and pipe angles at a total system length of $L = 0.20m$ and inner radius $R_i = 0.0010m$.



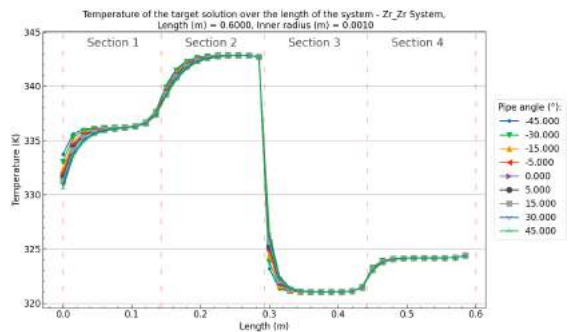
(c) Target solution temperature profile over the length of the system and pipe angles at a total system length of $L = 0.30m$ and inner radius $R_i = 0.0010m$.



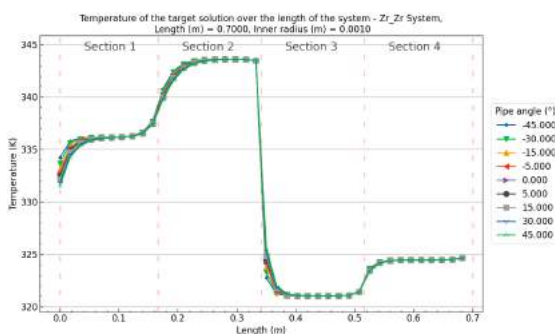
(d) Target solution temperature profile over the length of the system and pipe angles at a total system length of $L = 0.40m$ and inner radius $R_i = 0.0010m$.



(e) Target solution temperature profile over the length of the system and pipe angles at a total system length of $L = 0.50m$ and inner radius $R_i = 0.0010m$.



(f) Target solution temperature profile over the length of the system and pipe angles at a total system length of $L = 0.60m$ and inner radius $R_i = 0.0010m$.

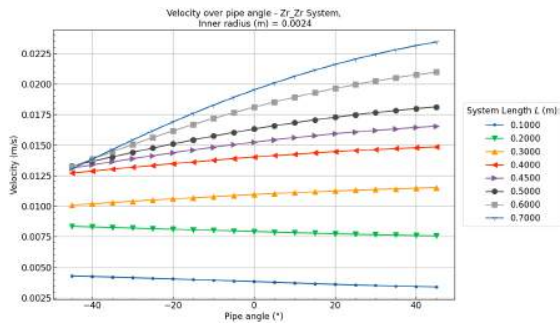


(g) Target solution temperature profile over the length of the system and pipe angles at a total system length of $L = 0.70m$ and inner radius $R_i = 0.0010m$.

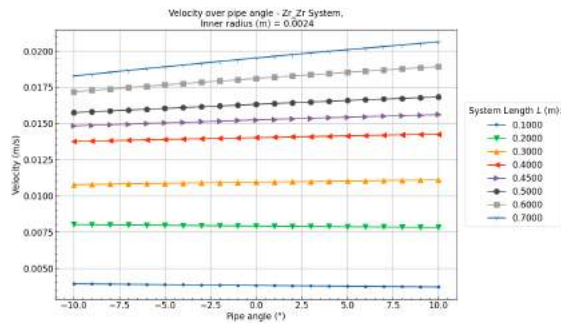
Figure B.94: Zr/Zr (Heat/Cool) System target solution temperature profiles over the pipe angle θ and system length L at an inner radius of $R_i = 0.0010m$, a heating wall thickness of $dr_{12} = 0.015m$ and cooling wall thickness $dr_{34}(m) = 0.005m$

$Z_r/Z_r - R_i = 0.0024m$

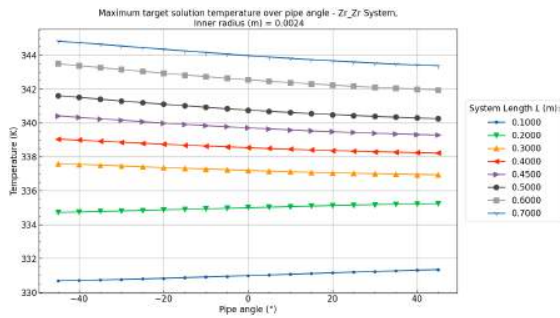
[Back to overview - B.3](#)



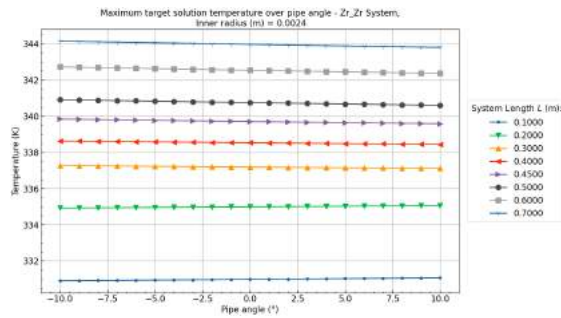
(a) Velocity over pipe angle between -45° and 45° at an inner radius $R_i = 0.0024m$.



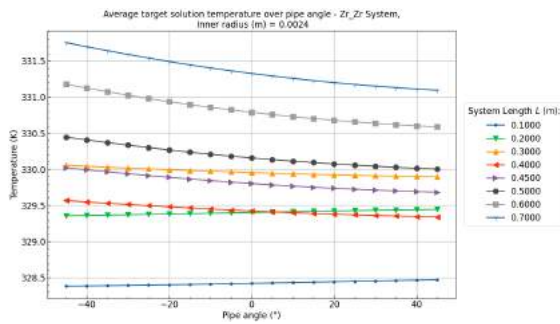
(b) Velocity over pipe angle between -10° and 10° at an inner radius $R_i = 0.0024m$.



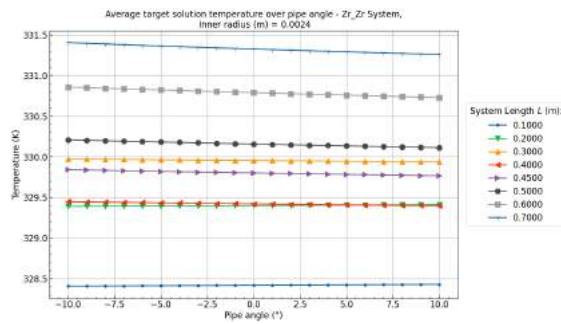
(c) Maximum target solution temperature over the pipe angle between -45° and 45° at an inner radius $R_i = 0.0024m$.



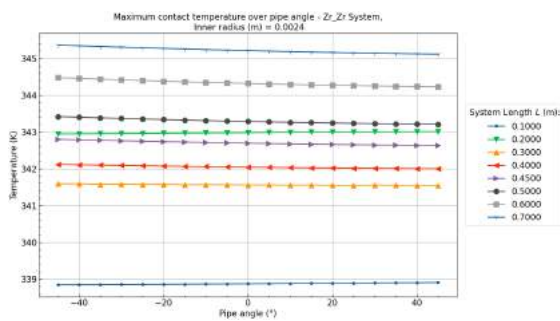
(d) Maximum target solution temperature over the pipe angle between -10° and 10° at an inner radius $R_i = 0.0024m$.



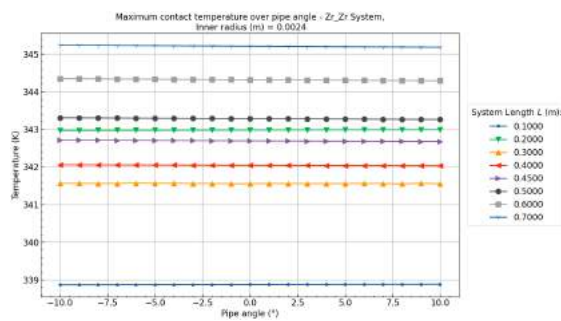
(e) Average target solution temperature over the pipe angle between -45° and 45° at an inner radius $R_i = 0.0024m$.



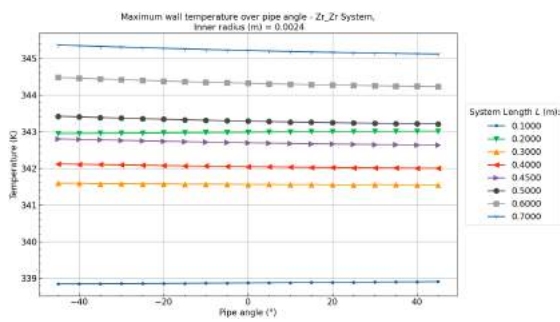
(f) Average target solution temperature over the pipe angle between -10° and 10° at an inner radius $R_i = 0.0024m$.



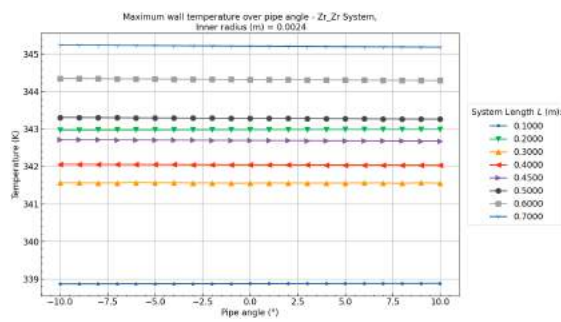
(g) Maximum contact temperature over the pipe angle between -45° and 45° at an inner radius $R_i = 0.0024m$.



(h) Maximum contact temperature over the pipe angle between -10° and 10° at an inner radius $R_i = 0.0024m$.

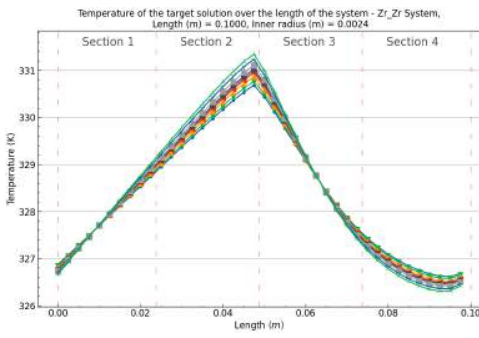


(i) Maximum wall temperature over the pipe angle between -45° and 45° at an inner radius $R_i = 0.0024m$.

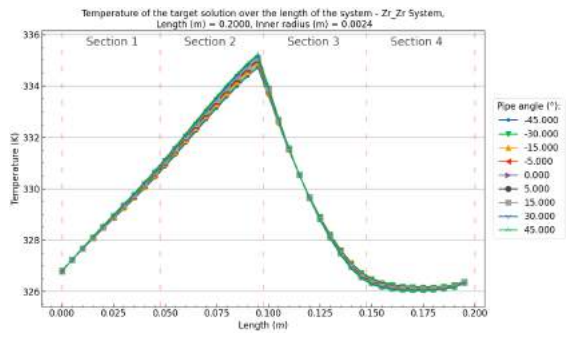


(j) Maximum wall temperature over the pipe angle between -10° and 10° at an inner radius $R_i = 0.0024m$.

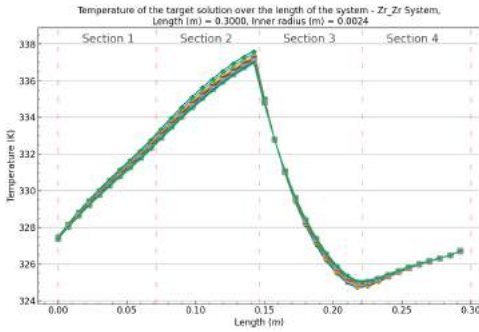
Figure B.95: Z_r/Z_r (Heat/Cool) System results over the pipe angle θ and system length L at an inner radius of $R_i = 0.0024m$, heating wall thickness of $dr_{12} = 0.015m$ and cooling wall thickness $dr_{34} (m) = 0.005m$



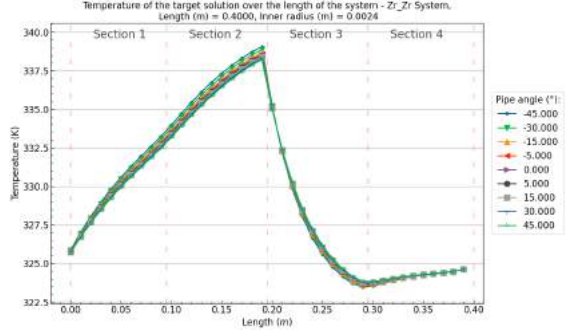
(a) Target solution temperature profile over the length of the system and pipe angles at a total system length of $L = 0.10m$ and inner radius $R_i = 0.0024m$.



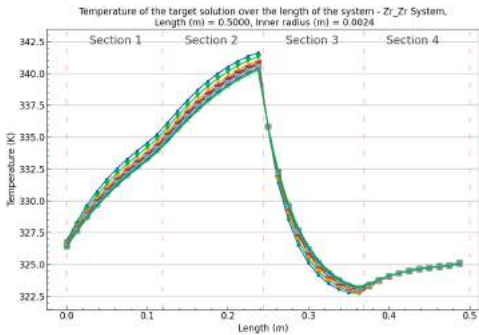
(b) Target solution temperature profile over the length of the system and pipe angles at a total system length of $L = 0.20m$ and inner radius $R_i = 0.0024m$.



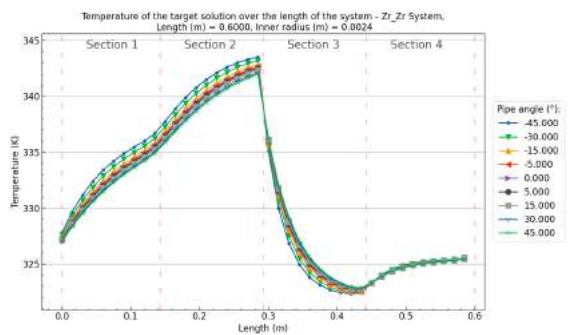
(c) Target solution temperature profile over the length of the system and pipe angles at a total system length of $L = 0.30m$ and inner radius $R_i = 0.0024m$.



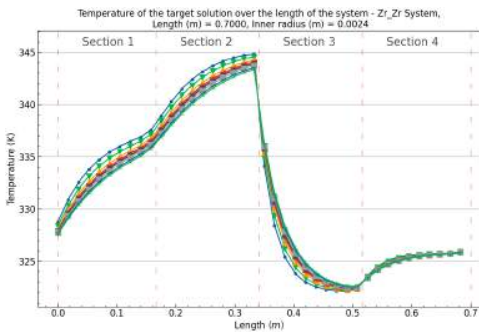
(d) Target solution temperature profile over the length of the system and pipe angles at a total system length of $L = 0.40m$ and inner radius $R_i = 0.0024m$.



(e) Target solution temperature profile over the length of the system and pipe angles at a total system length of $L = 0.50m$ and inner radius $R_i = 0.0024m$.



(f) Target solution temperature profile over the length of the system and pipe angles at a total system length of $L = 0.60m$ and inner radius $R_i = 0.0024m$.

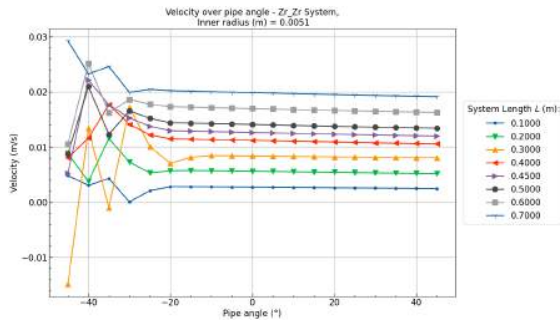


(g) Target solution temperature profile over the length of the system and pipe angles at a total system length of $L = 0.70m$ and inner radius $R_i = 0.0024m$.

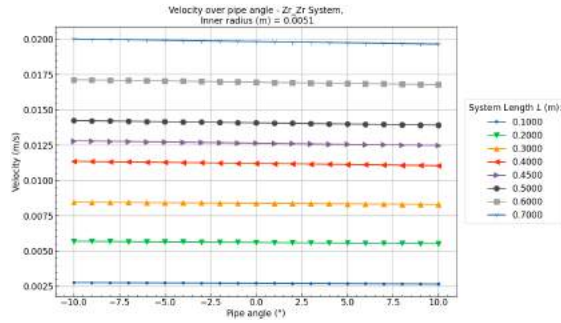
Figure B.96: Zr/Zr (Heat/Cool) System target solution temperature profiles over the pipe angle θ and system length L at an inner radius of $R_i = 0.0024m$, a heating wall thickness of $dr_{12} = 0.015m$ and cooling wall thickness $dr_{34}(m) = 0.005m$

$Zr/Zr - R_i = 0.0051 m$

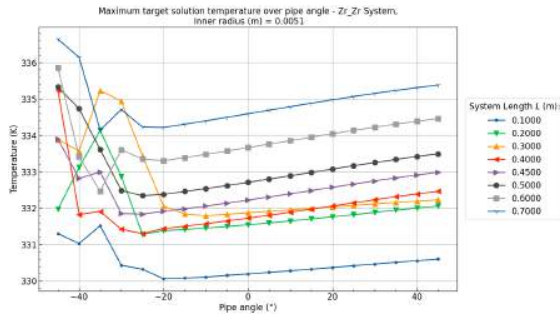
[Back to overview - B.3](#)



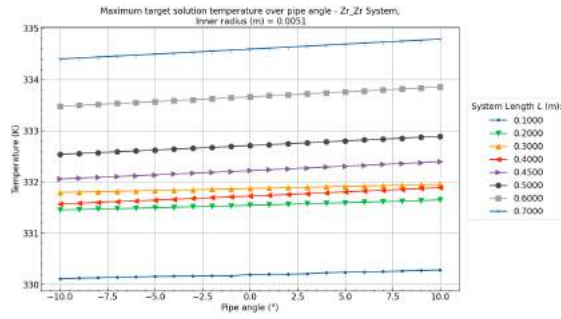
(a) Velocity over pipe angle between -45° and 45° at an inner radius $R_i = 0.0051 m$.



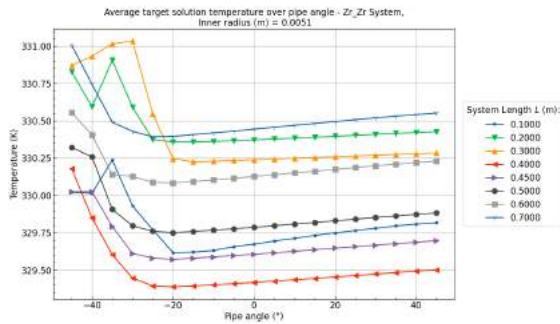
(b) Velocity over pipe angle between -10° and 10° at an inner radius $R_i = 0.0051 m$.



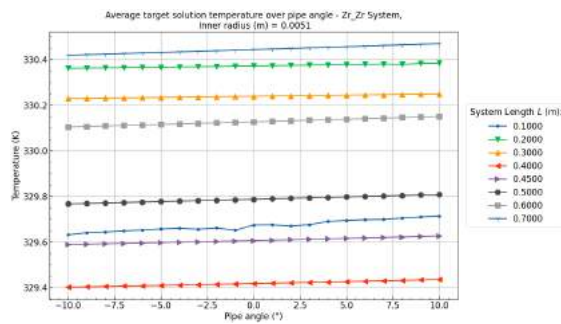
(c) Maximum target solution temperature over the pipe angle between -45° and 45° at an inner radius $R_i = 0.0051 m$.



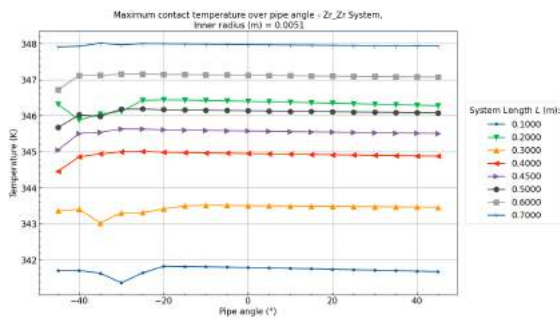
(d) Maximum target solution temperature over the pipe angle between -10° and 10° at an inner radius $R_i = 0.0051 m$.



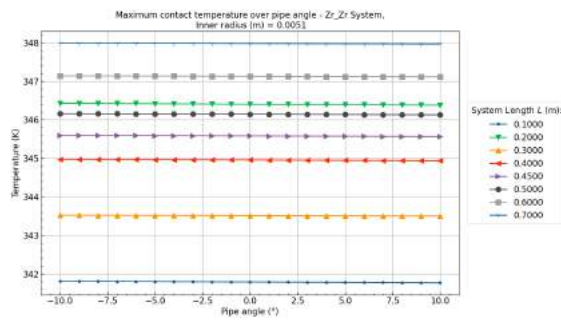
(e) Average target solution temperature over the pipe angle between -45° and 45° at an inner radius $R_i = 0.0051 m$.



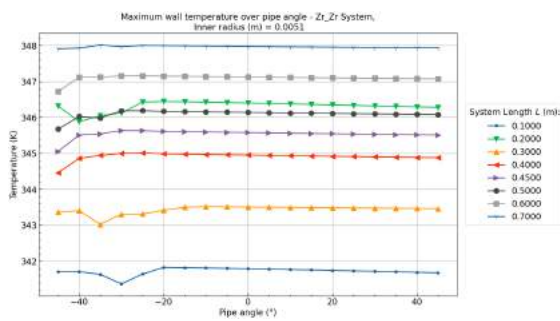
(f) Average target solution temperature over the pipe angle between -10° and 10° at an inner radius $R_i = 0.0051 m$.



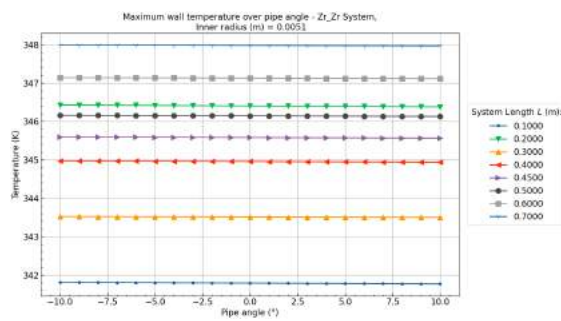
(g) Maximum contact temperature over the pipe angle between -45° and 45° at an inner radius $R_i = 0.0051 m$.



(h) Maximum contact temperature over the pipe angle between -10° and 10° at an inner radius $R_i = 0.0051 m$.

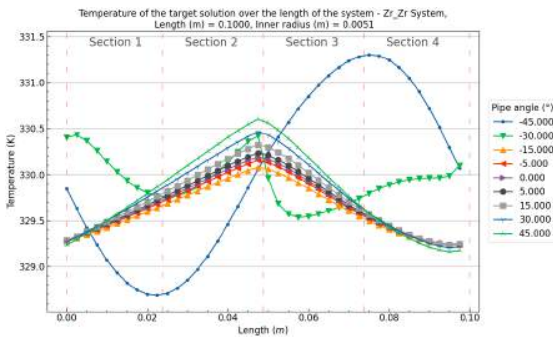


(i) Maximum wall temperature over the pipe angle between -45° and 45° at an inner radius $R_i = 0.0051 m$.

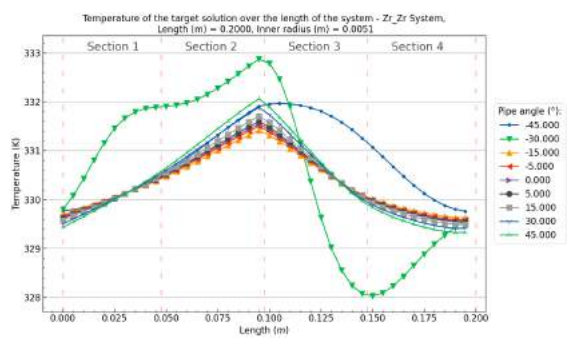


(j) Maximum wall temperature over the pipe angle between -10° and 10° at an inner radius $R_i = 0.0051 m$.

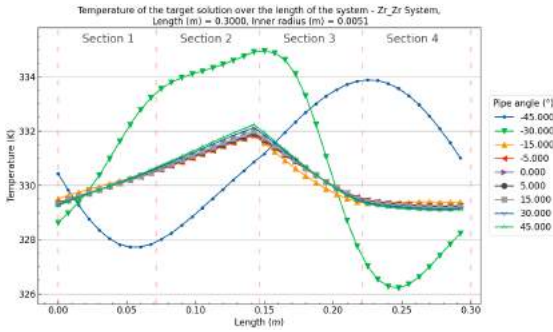
Figure B.97: Zr/Zr (Heat/Cool) System results over the pipe angle θ and system length L at an inner radius of $R_i = 0.0051 m$, heating wall thickness of $dr_{12} = 0.015 m$ and cooling wall thickness $dr_{34} (m) = 0.005 m$



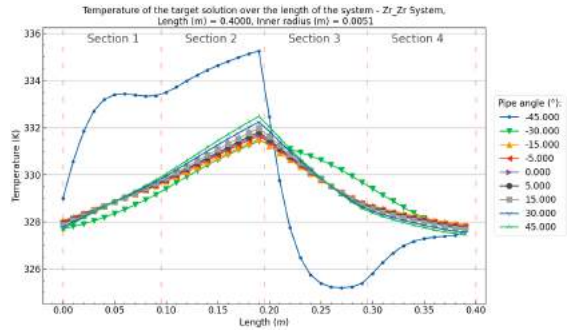
(a) Target solution temperature profile over the length of the system and pipe angles at a total system length of $L = 0.10m$ and inner radius $R_i = 0.0051m$.



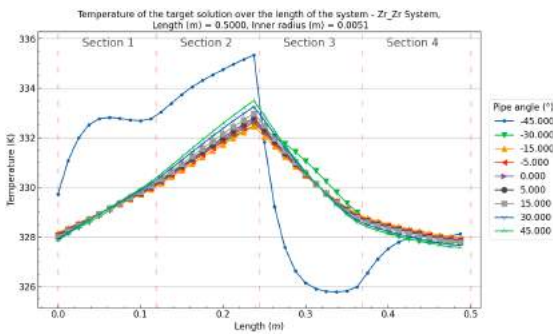
(b) Target solution temperature profile over the length of the system and pipe angles at a total system length of $L = 0.20m$ and inner radius $R_i = 0.0051m$.



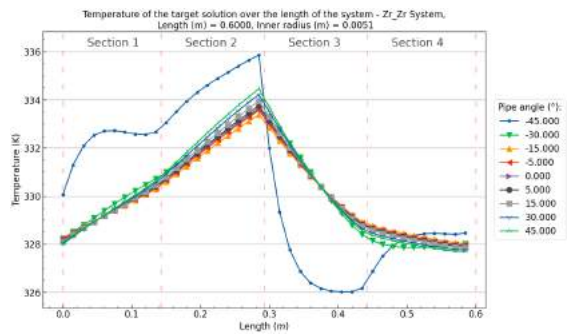
(c) Target solution temperature profile over the length of the system and pipe angles at a total system length of $L = 0.30m$ and inner radius $R_i = 0.0051m$.



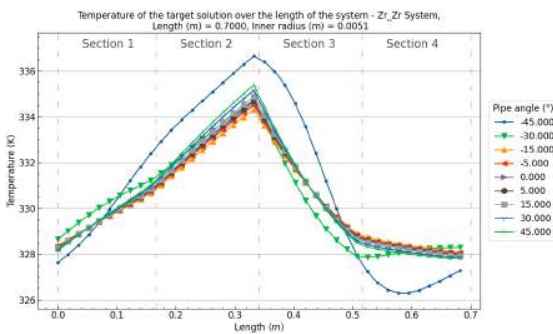
(d) Target solution temperature profile over the length of the system and pipe angles at a total system length of $L = 0.40m$ and inner radius $R_i = 0.0051m$.



(e) Target solution temperature profile over the length of the system and pipe angles at a total system length of $L = 0.50m$ and inner radius $R_i = 0.0051m$.



(f) Target solution temperature profile over the length of the system and pipe angles at a total system length of $L = 0.60m$ and inner radius $R_i = 0.0051m$.

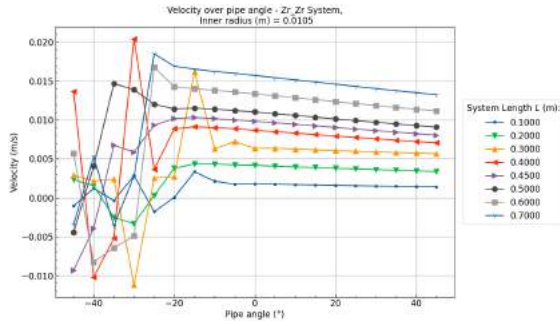


(g) Target solution temperature profile over the length of the system and pipe angles at a total system length of $L = 0.70m$ and inner radius $R_i = 0.0051m$.

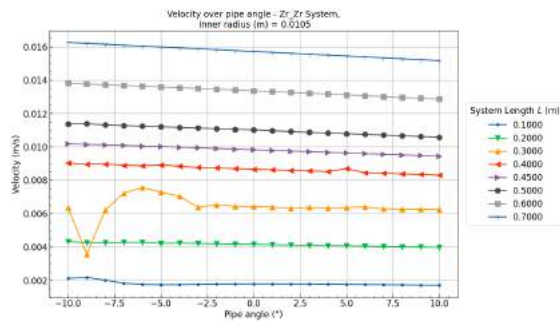
Figure B.98: Zr/Zr (Heat/Cool) System target solution temperature profiles over the pipe angle θ and system length L at an inner radius of $R_i = 0.0051m$, a heating wall thickness of $dr_{12} = 0.015m$ and cooling wall thickness $dr_{34}(m) = 0.005m$

$Zr/Zr - R_i = 0.0105m$

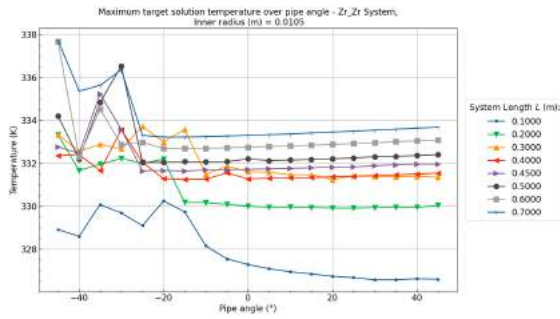
[Back to overview - B.3](#)



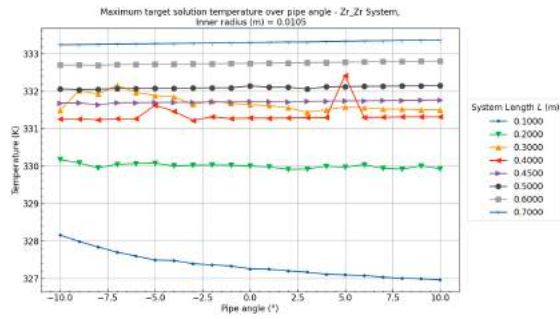
(a) Velocity over pipe angle between -45° and 45° at an inner radius $R_i = 0.0105m$.



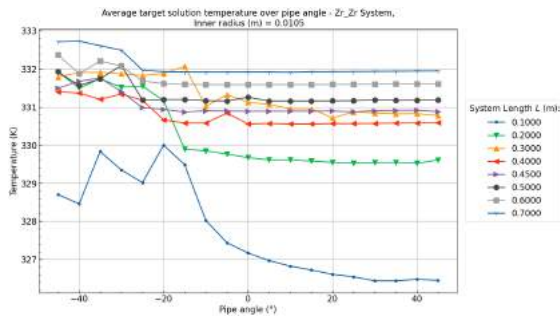
(b) Velocity over pipe angle between -10° and 10° at an inner radius $R_i = 0.0105m$.



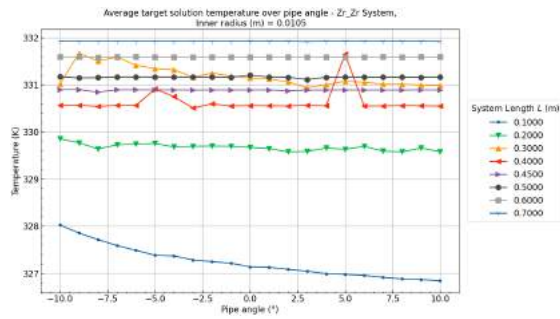
(c) Maximum target solution temperature over the pipe angle between -45° and 45° at an inner radius $R_i = 0.0105m$.



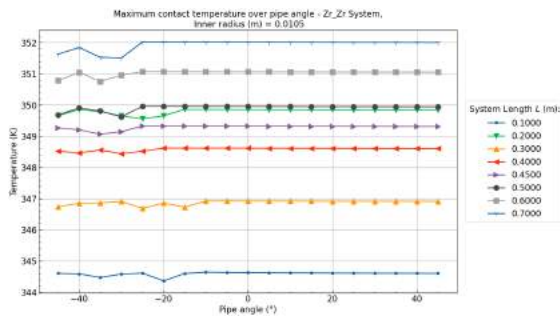
(d) Maximum target solution temperature over the pipe angle between -10° and 10° at an inner radius $R_i = 0.0105m$.



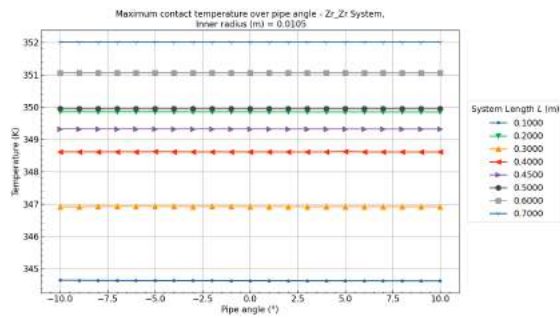
(e) Average target solution temperature over the pipe angle between -45° and 45° at an inner radius $R_i = 0.0105m$.



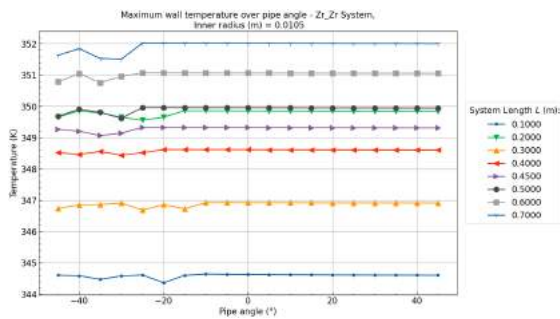
(f) Average target solution temperature over the pipe angle between -10° and 10° at an inner radius $R_i = 0.0105m$.



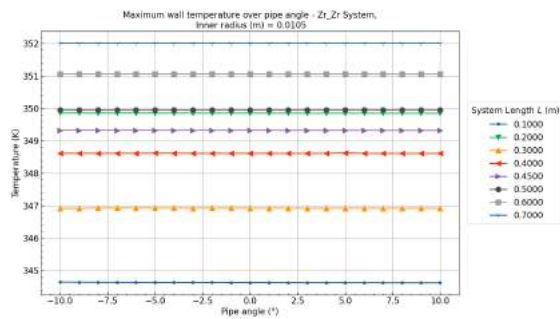
(g) Maximum contact temperature over the pipe angle between -45° and 45° at an inner radius $R_i = 0.0105m$.



(h) Maximum contact temperature over the pipe angle between -10° and 10° at an inner radius $R_i = 0.0105m$.

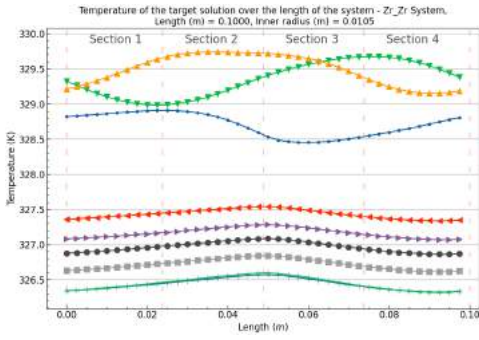


(i) Maximum wall temperature over the pipe angle between -45° and 45° at an inner radius $R_i = 0.0105m$.

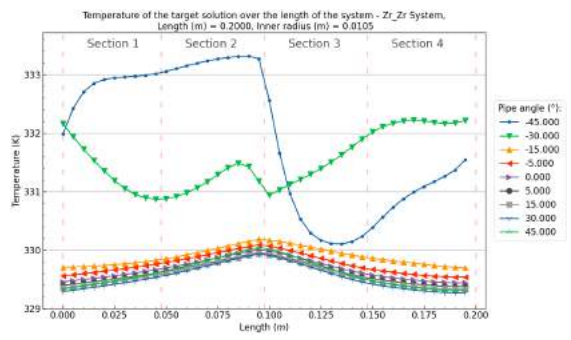


(j) Maximum wall temperature over the pipe angle between -10° and 10° at an inner radius $R_i = 0.0105m$.

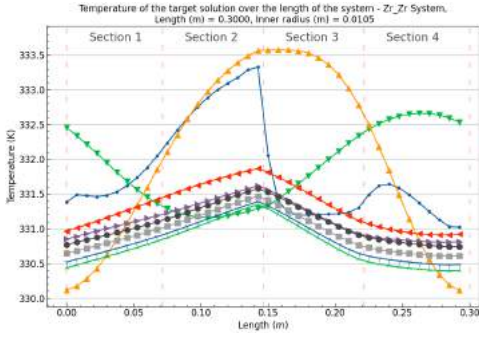
Figure B.99: Zr/Zr (Heat/Cool) System results over the pipe angle θ and system length L at an inner radius of $R_i = 0.0105m$, heating wall thickness of $dr_{12} = 0.015m$ and cooling wall thickness $dr_{34} (m) = 0.005m$



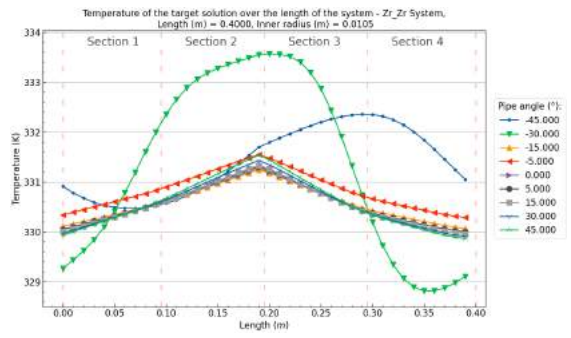
(a) Target solution temperature profile over the length of the system and pipe angles at a total system length of $L = 0.10m$ and inner radius $R_i = 0.0105m$.



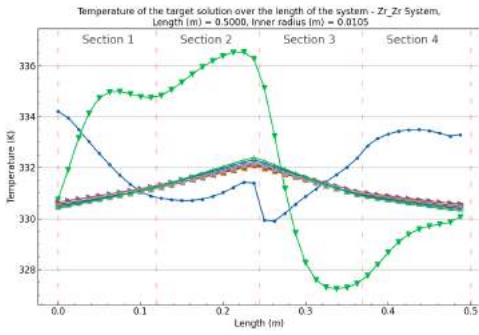
(b) Target solution temperature profile over the length of the system and pipe angles at a total system length of $L = 0.20m$ and inner radius $R_i = 0.0105m$.



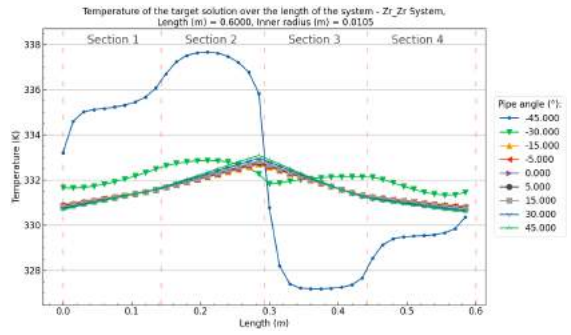
(c) Target solution temperature profile over the length of the system and pipe angles at a total system length of $L = 0.30m$ and inner radius $R_i = 0.0105m$.



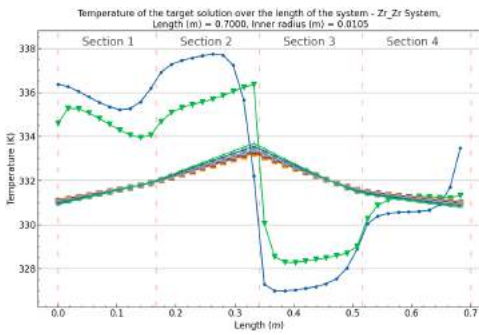
(d) Target solution temperature profile over the length of the system and pipe angles at a total system length of $L = 0.40m$ and inner radius $R_i = 0.0105m$.



(e) Target solution temperature profile over the length of the system and pipe angles at a total system length of $L = 0.50m$ and inner radius $R_i = 0.0105m$.



(f) Target solution temperature profile over the length of the system and pipe angles at a total system length of $L = 0.60m$ and inner radius $R_i = 0.0105m$.

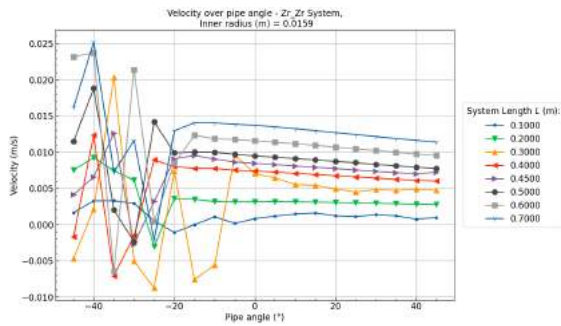


(g) Target solution temperature profile over the length of the system and pipe angles at a total system length of $L = 0.70m$ and inner radius $R_i = 0.0105m$.

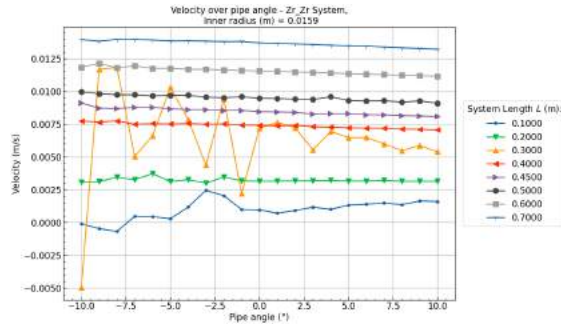
Figure B.100: Zr/Zr (Heat/Cool) System target solution temperature profiles over the pipe angle θ and system length L at an inner radius of $R_i = 0.0105m$, a heating wall thickness of $dr_{12} = 0.015m$ and cooling wall thickness $dr_{34}(m) = 0.005m$

$Zr/Zr - R_i = 0.0159m$

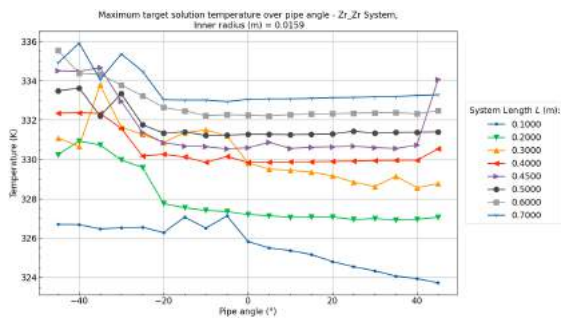
[Back to overview - B.3](#)



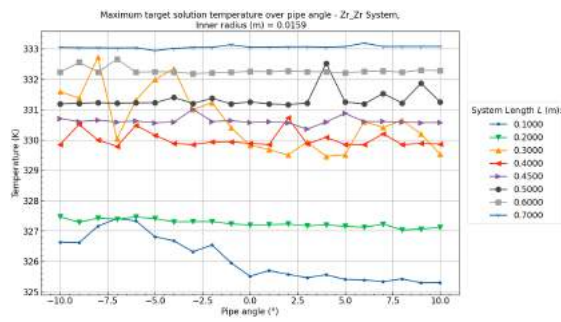
(a) Velocity over pipe angle between -45° and 45° at an inner radius $R_i = 0.0159m$.



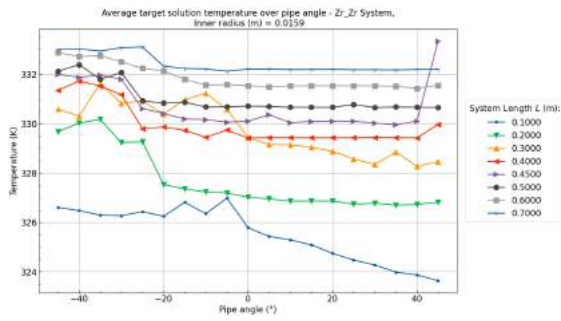
(b) Velocity over pipe angle between -10° and 10° at an inner radius $R_i = 0.0159m$.



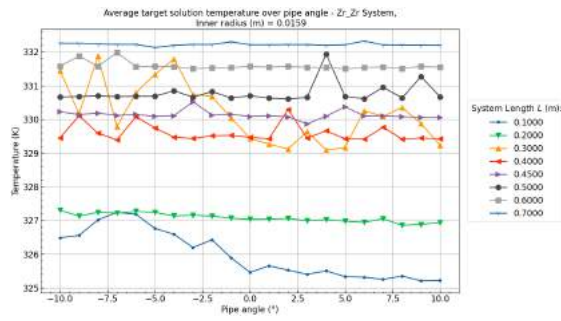
(c) Maximum target solution temperature over the pipe angle between -45° and 45° at an inner radius $R_i = 0.0159m$.



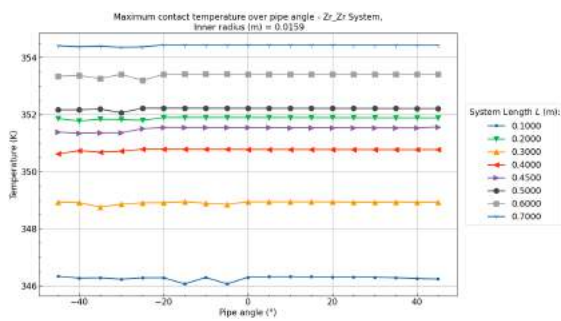
(d) Maximum target solution temperature over the pipe angle between -10° and 10° at an inner radius $R_i = 0.0159m$.



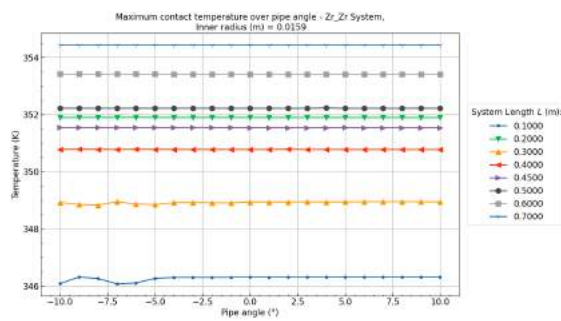
(e) Average target solution temperature over the pipe angle between -45° and 45° at an inner radius $R_i = 0.0159m$.



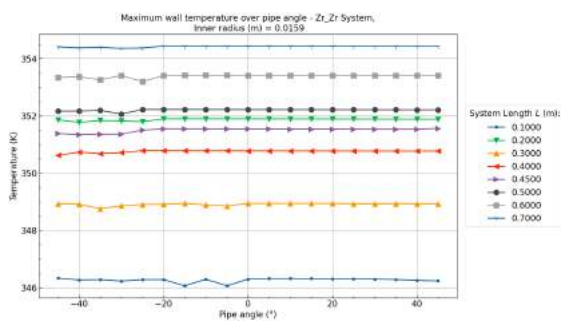
(f) Average target solution temperature over the pipe angle between -10° and 10° at an inner radius $R_i = 0.0159m$.



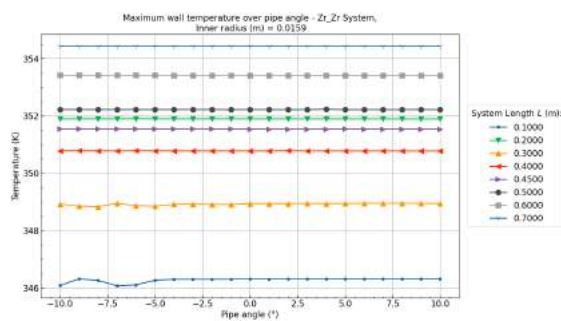
(g) Maximum contact temperature over the pipe angle between -45° and 45° at an inner radius $R_i = 0.0159m$.



(h) Maximum contact temperature over the pipe angle between -10° and 10° at an inner radius $R_i = 0.0159m$.

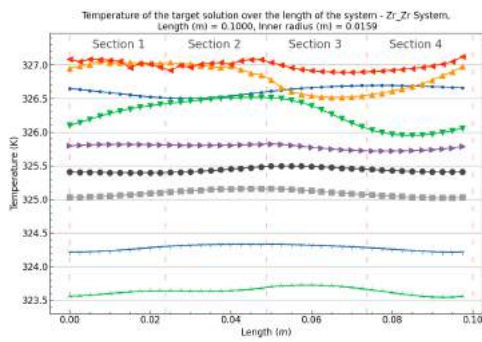


(i) Maximum wall temperature over the pipe angle between -45° and 45° at an inner radius $R_i = 0.0159m$.

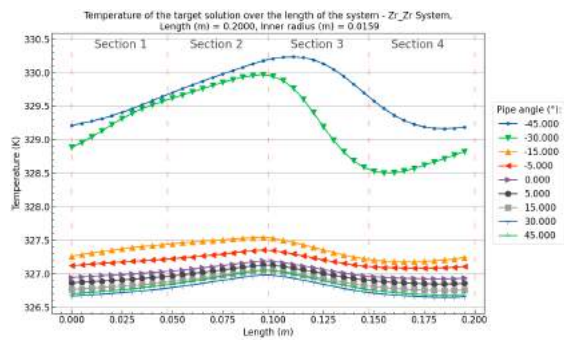


(j) Maximum wall temperature over the pipe angle between -10° and 10° at an inner radius $R_i = 0.0159m$.

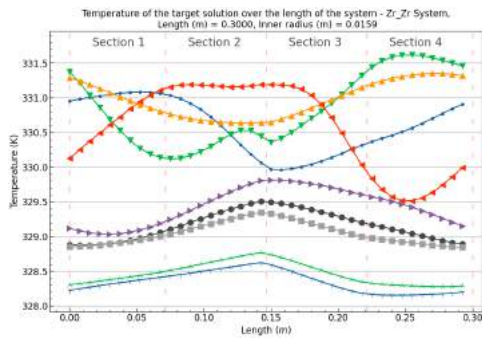
Figure B.101: Zr/Zr (Heat/Cool) System results over the pipe angle θ and system length L at an inner radius of $R_i = 0.0159m$, heating wall thickness of $dr_{12} = 0.015m$ and cooling wall thickness $dr_{34} (m) = 0.005m$



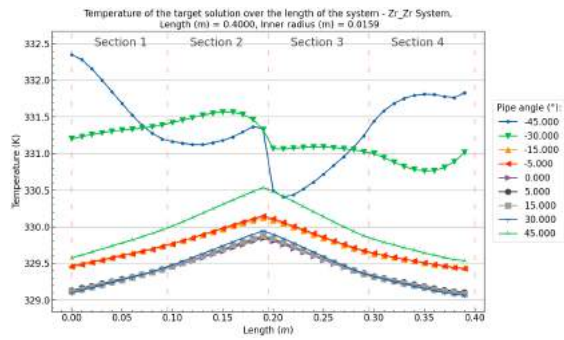
(a) Target solution temperature profile over the length of the system and pipe angles at a total system length of $L = 0.10m$ and inner radius $R_i = 0.0159m$.



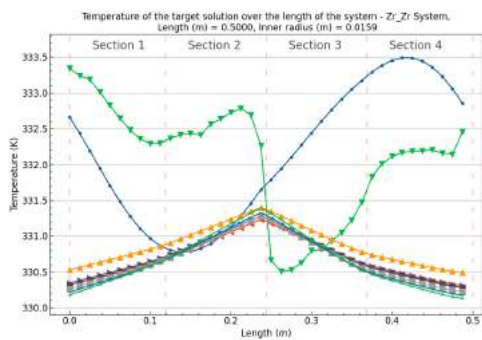
(b) Target solution temperature profile over the length of the system and pipe angles at a total system length of $L = 0.20m$ and inner radius $R_i = 0.0159m$.



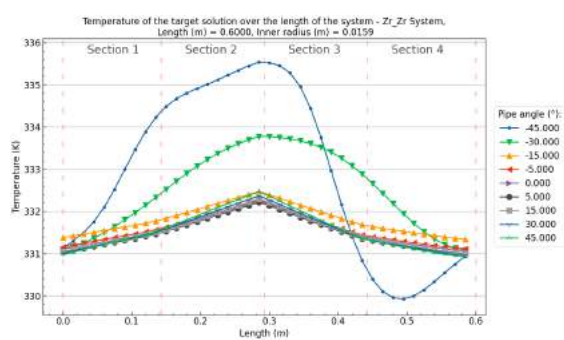
(c) Target solution temperature profile over the length of the system and pipe angles at a total system length of $L = 0.30m$ and inner radius $R_i = 0.0159m$.



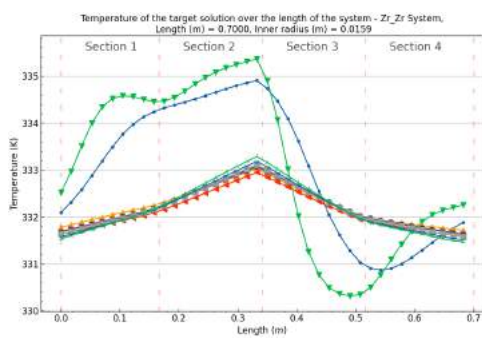
(d) Target solution temperature profile over the length of the system and pipe angles at a total system length of $L = 0.40m$ and inner radius $R_i = 0.0159m$.



(e) Target solution temperature profile over the length of the system and pipe angles at a total system length of $L = 0.50m$ and inner radius $R_i = 0.0159m$.



(f) Target solution temperature profile over the length of the system and pipe angles at a total system length of $L = 0.60m$ and inner radius $R_i = 0.0159m$.

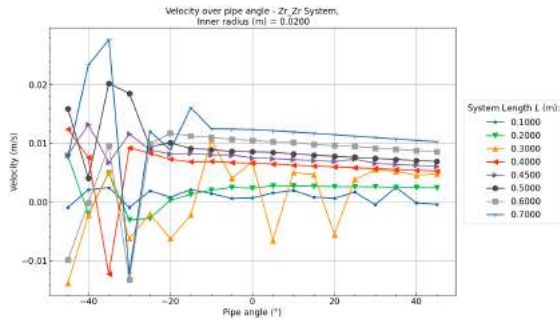


(g) Target solution temperature profile over the length of the system and pipe angles at a total system length of $L = 0.70m$ and inner radius $R_i = 0.0159m$.

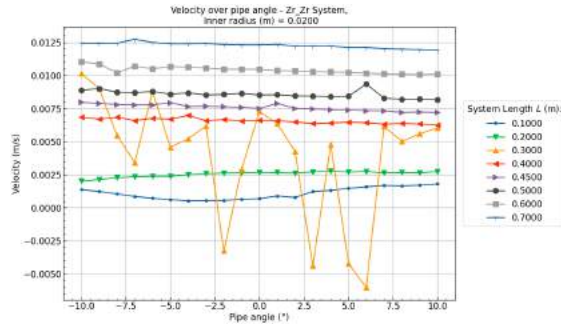
Figure B.102: Zr/Zr (Heat/Cool) System target solution temperature profiles over the pipe angle θ and system length L at an inner radius of $R_i = 0.0159m$, a heating wall thickness of $dr_{12} = 0.015m$ and cooling wall thickness $dr_{34}(m) = 0.005m$

$Zr/Zr - R_i = 0.0200m$

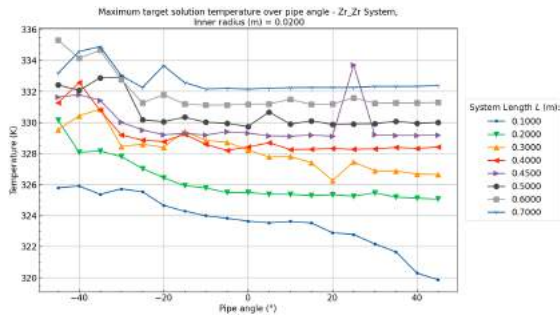
[Back to overview - B.3](#)



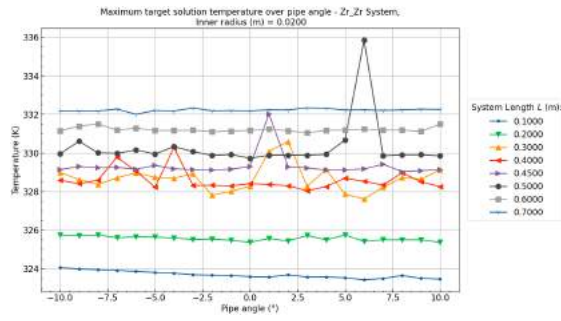
(a) Velocity over pipe angle between -45° and 45° at an inner radius $R_i = 0.0200m$.



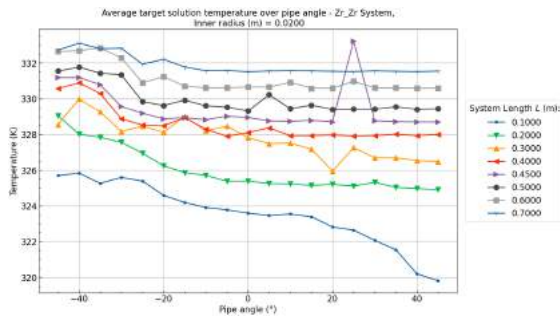
(b) Velocity over pipe angle between -10° and 10° at an inner radius $R_i = 0.0200m$.



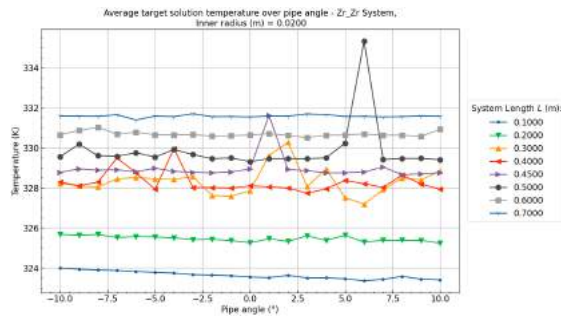
(c) Maximum target solution temperature over the pipe angle between -45° and 45° at an inner radius $R_i = 0.0200m$.



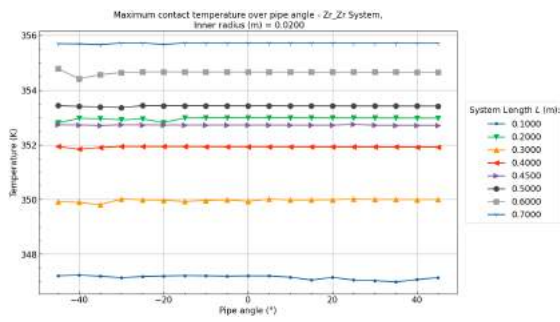
(d) Maximum target solution temperature over the pipe angle between -10° and 10° at an inner radius $R_i = 0.0200m$.



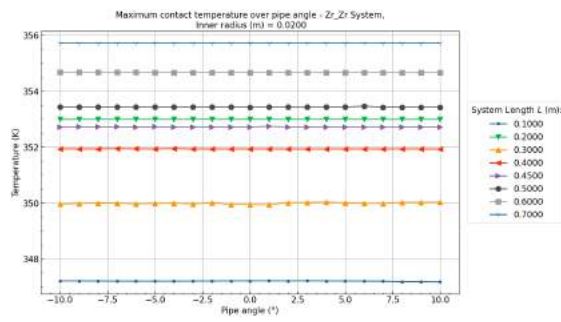
(e) Average target solution temperature over the pipe angle between -45° and 45° at an inner radius $R_i = 0.0200m$.



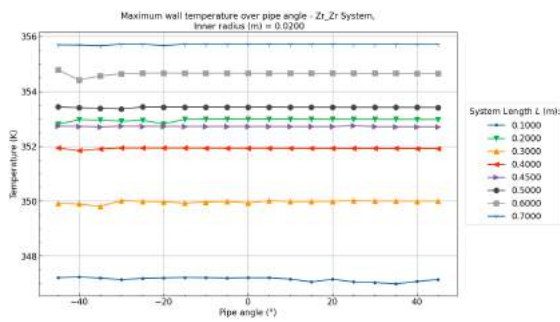
(f) Average target solution temperature over the pipe angle between -10° and 10° at an inner radius $R_i = 0.0200m$.



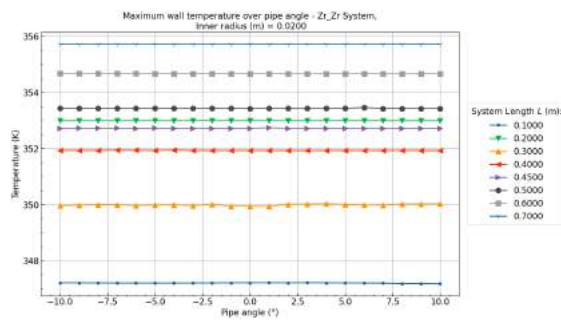
(g) Maximum contact temperature over the pipe angle between -45° and 45° at an inner radius $R_i = 0.0200m$.



(h) Maximum contact temperature over the pipe angle between -10° and 10° at an inner radius $R_i = 0.0200m$.

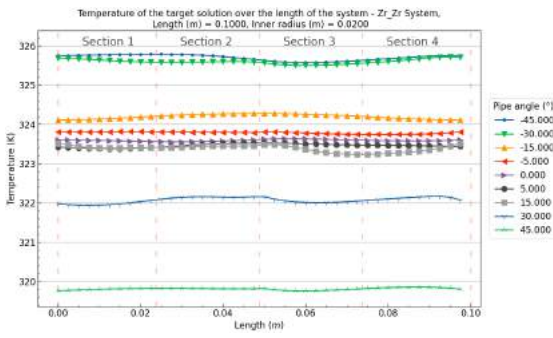


(i) Maximum wall temperature over the pipe angle between -45° and 45° at an inner radius $R_i = 0.0200m$.

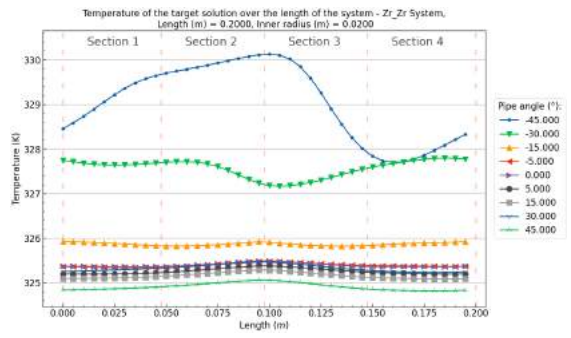


(j) Maximum wall temperature over the pipe angle between -10° and 10° at an inner radius $R_i = 0.0200m$.

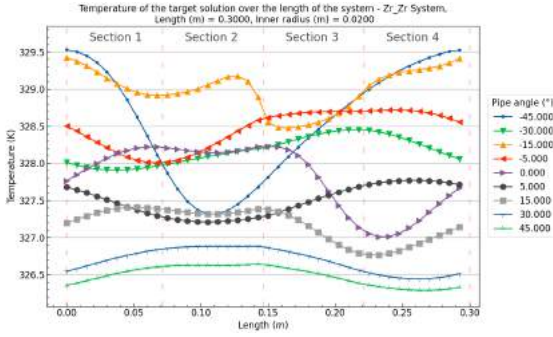
Figure B.103: Zr/Zr (Heat/Cool) System results over the pipe angle θ and system length L at an inner radius of $R_i = 0.0200m$, heating wall thickness of $dr_{12} = 0.015m$ and cooling wall thickness $dr_{34} (m) = 0.005m$



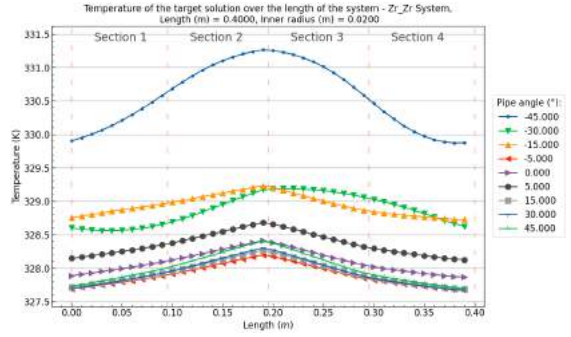
(a) Target solution temperature profile over the length of the system and pipe angles at a total system length of $L = 0.10m$ and inner radius $R_i = 0.0200m$.



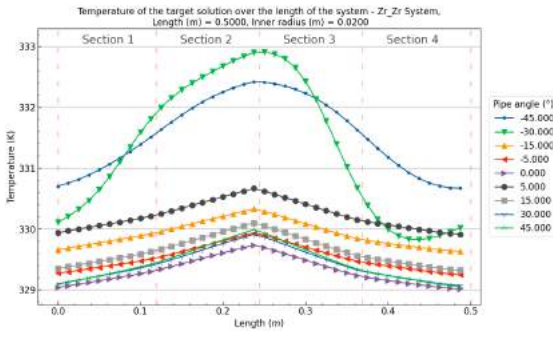
(b) Target solution temperature profile over the length of the system and pipe angles at a total system length of $L = 0.20m$ and inner radius $R_i = 0.0200m$.



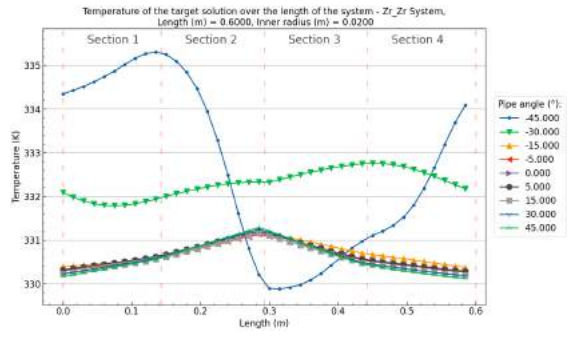
(c) Target solution temperature profile over the length of the system and pipe angles at a total system length of $L = 0.30m$ and inner radius $R_i = 0.0200m$.



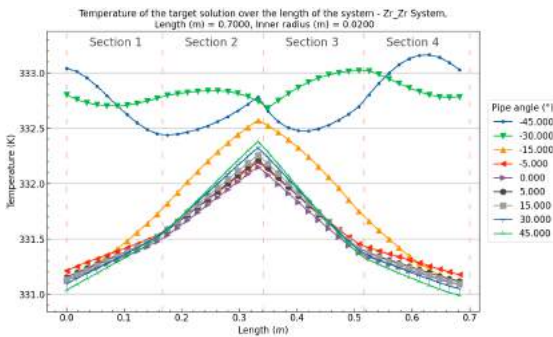
(d) Target solution temperature profile over the length of the system and pipe angles at a total system length of $L = 0.40m$ and inner radius $R_i = 0.0200m$.



(e) Target solution temperature profile over the length of the system and pipe angles at a total system length of $L = 0.50m$ and inner radius $R_i = 0.0200m$.



(f) Target solution temperature profile over the length of the system and pipe angles at a total system length of $L = 0.60m$ and inner radius $R_i = 0.0200m$.



(g) Target solution temperature profile over the length of the system and pipe angles at a total system length of $L = 0.70m$ and inner radius $R_i = 0.0200m$.

Figure B.104: Zr/Zr (Heat/Cool) System target solution temperature profiles over the pipe angle θ and system length L at an inner radius of $R_i = 0.0200m$, a heating wall thickness of $dr_{12} = 0.015m$ and cooling wall thickness $dr_{34}(m) = 0.005m$

B.4. Section 2 length fraction ($Frac$) & Wall thickness

The general trends for the single layer wall materials and wall thicknesses in these systems are:

- Increasing the section 2 fraction ($Frac$) from 0.1 always results in an absolute velocity increase. The maximum velocity is found at a section 2 fraction ($Frac$) of 1.0
- If the heating wall thickness (dr_{12_1}) is larger than the cooling wall thickness (dr_{34_1}) the maximum and average target solution temperatures increase over the section 2 fraction ($Frac$).
- For Pb/Pb and Zr/Zr systems, if the cooling wall thickness (dr_{34_1}) is larger than the heating wall thickness (dr_{12_1}) the maximum and average target solution temperature decrease over the section 2 fraction ($Frac$).
- For Al/Al systems, if the cooling wall thickness (dr_{34_1}) is larger than the heating wall thickness (dr_{12_1}) only the average target solution temperature decreases over the section 2 fraction ($Frac$). The maximum target solution either climbs slightly or remains equal over the
- The section 2 fraction significantly alters the temperature profile over the length in both section 2 and 4.

Table B.6: System specifications for the inner radius variable results

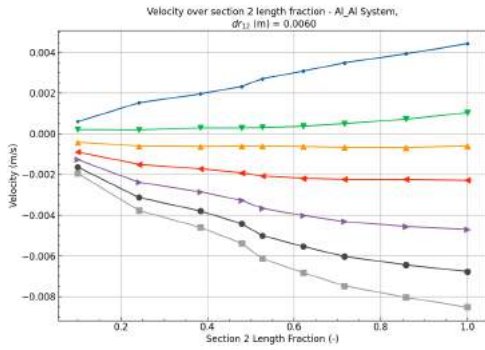
System Variable	Values	Reference
Multi layer wall materials	Al/Al	B.105 - B.112 (Page 204 - 211)
	Pb/Pb	B.113 - B.120 (Page 212 - 219)
	Zr/Zr	B.121 - B.128 (Page 220 - 227)
Heating wall thickness (dr_{12_1})	0.0060m	Al/Al - B.105 - B.106 (Page 204 - 205) Pb/Pb - B.113 - B.114 (Page 212 - 213) Zr/Zr - B.121 - B.122 (Page 220 - 221)
	0.0100m	Al/Al - B.107 - B.108 (Page 206 - 207) Pb/Pb - B.115 - B.116 (Page 214 - 215) Zr/Zr - B.123 - B.124 (Page 222 - 223)
	0.0140m	Al/Al - B.109 - B.110 (Page 208 - 209) Pb/Pb - B.117 - B.118 (Page 216 - 217) Zr/Zr - B.125 - B.126 (Page 224 - 225)
	0.0180m	Al/Al - B.111 - B.112 (Page 210 - 211) Pb/Pb - B.119 - B.120 (Page 218 - 219) Zr/Zr - B.127 - B.128 (Page 226 - 227)
	Cooling wall thickness (dr_{34_1})	0.0050 – 0.0175m
	Inner radius (R_i)	0.007m
	Length (L)	0.4m
	Pipe angle (θ)	5°
	Section 2 length fraction ($Frac$)	0.1 – 1.0

B.4.1. Al/Al - Section 2 length fraction & Wall thickness

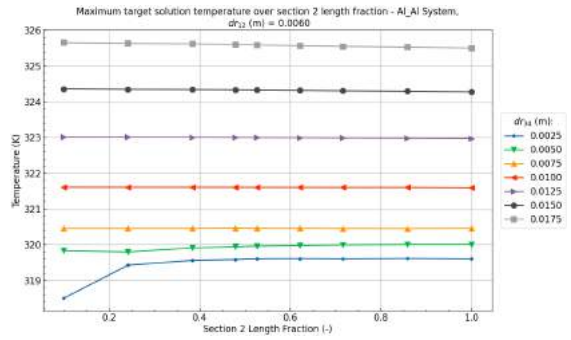
Al/Al - Section 2 length fraction at $dr_{12_1} = 0.0060m$

[Back to overview - B.4](#)

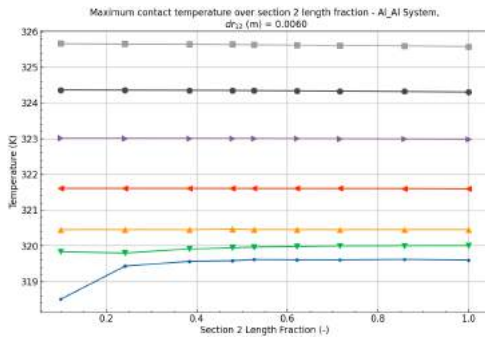
B.4



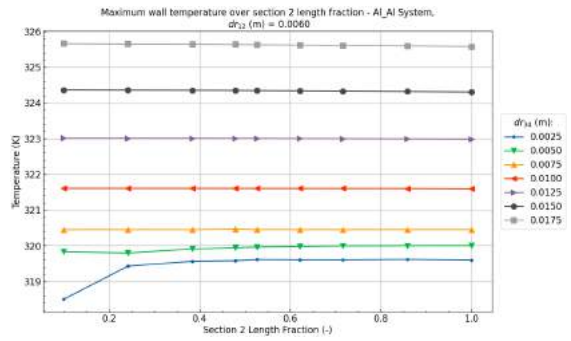
(a) Velocity over the section 2 fraction at $dr_{12_1} = 0.0060m$



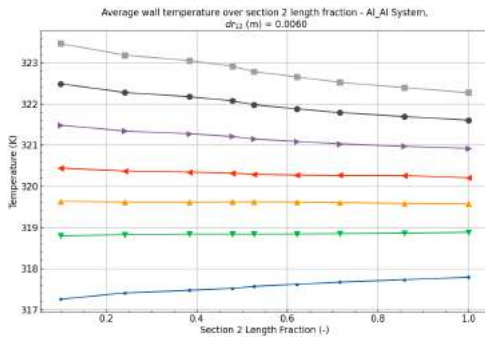
(b) Maximum target solution temperature over the section 2 fraction at $dr_{12_1} = 0.0060m$



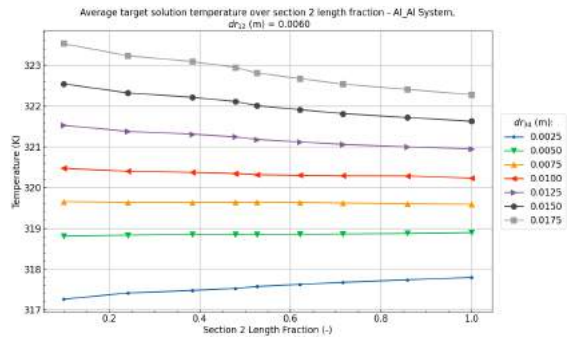
(c) Maximum contact temperature between the wall and the target solution over the section 2 fraction at $dr_{12_1} = 0.0060m$



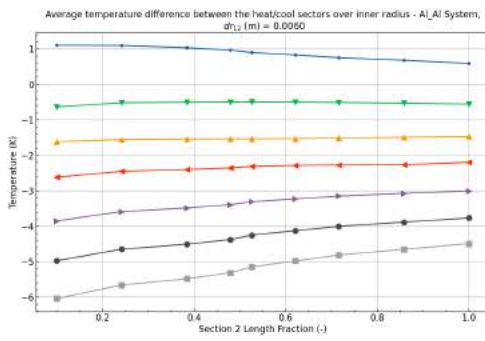
(d) Maximum wall temperature over the section 2 fraction at $dr_{12_1} = 0.0060m$



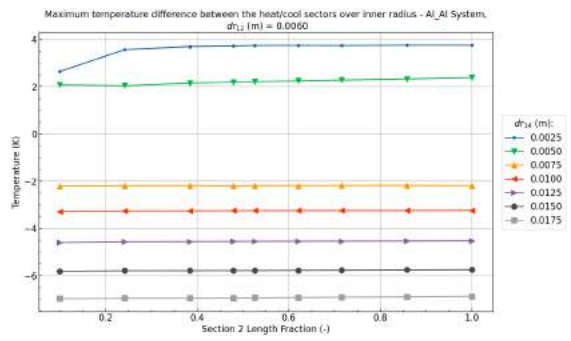
(e) Average target solution temperature over the section 2 fraction at $dr_{12_1} = 0.0060m$



(f) Average wall temperature over the section 2 fraction at $dr_{12_1} = 0.0060m$

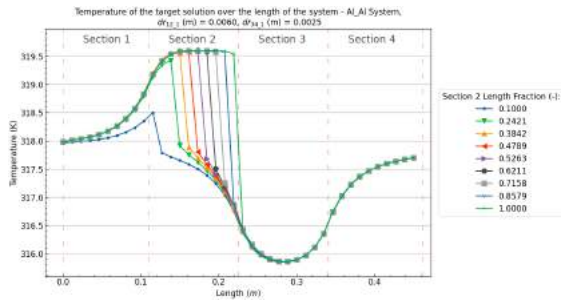


(g) Average target solution temperature difference between heating and cooling sectors over the section 2 fraction at $dr_{12_1} = 0.0060m$

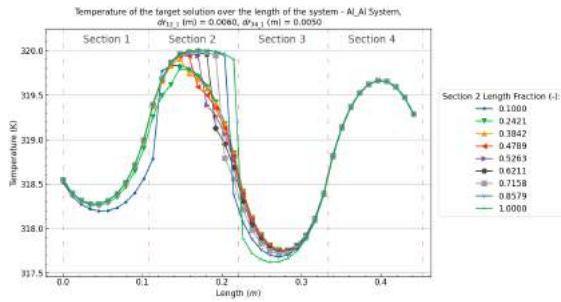


(h) Maximum target solution temperature difference between heating and cooling sectors over the section 2 fraction at $dr_{12_1} = 0.0060m$

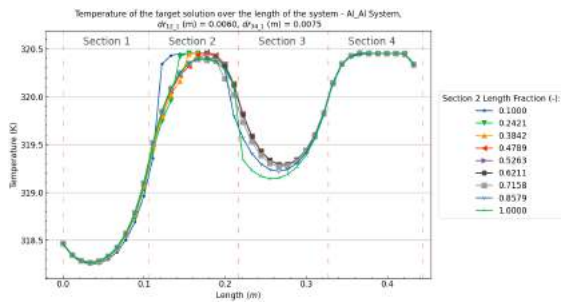
Figure B.105: Al/Al (Heat/Cool) System results over the section 2 fraction and cooling wall thickness dr_{34} at a heating wall thickness of $dr_{12} = 0.0060m$, a system length (L) of $0.4m$, and a pipe angle (θ) of 5° .



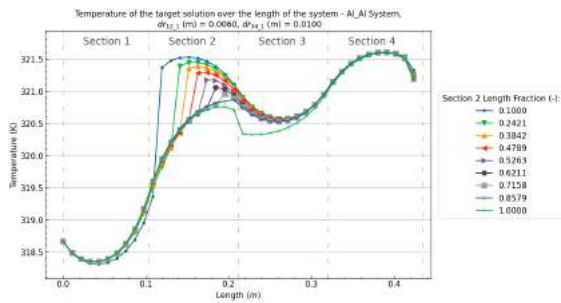
(a) Target solution temperature profiles over the the length of the system at different section 2 fractions at with $dr_{12_1}(m) = 0.0060m$ and $dr_{34_1}(m) = 0.0025$



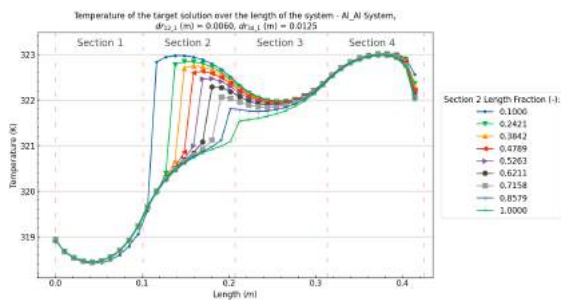
(b) Target solution temperature profiles over the the length of the system at different section 2 fractions at with $dr_{12_1}(m) = 0.0060m$ and $dr_{34_1}(m) = 0.0050$



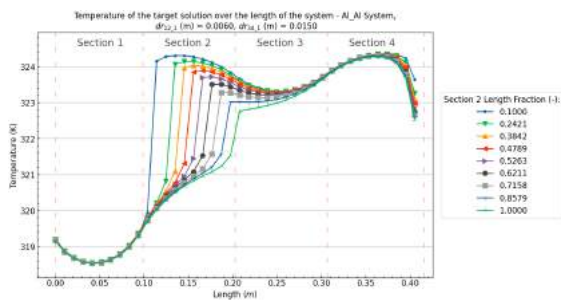
(c) Target solution temperature profiles over the the length of the system at different section 2 fractions at with $dr_{12_1}(m) = 0.0060m$ and $dr_{34_1}(m) = 0.0075$



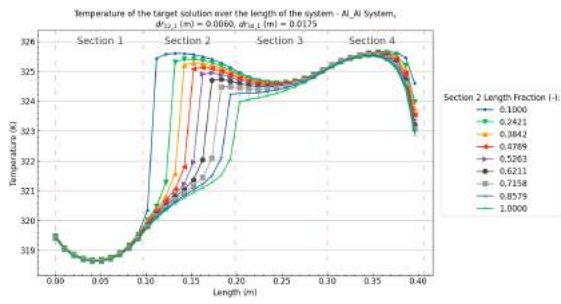
(d) Target solution temperature profiles over the the length of the system at different section 2 fractions at with $dr_{12_1}(m) = 0.0060m$ and $dr_{34_1}(m) = 0.0100$



(e) Target solution temperature profiles over the the length of the system at different section 2 fractions at with $dr_{12_1}(m) = 0.0060m$ and $dr_{34_1}(m) = 0.0125$



(f) Target solution temperature profiles over the the length of the system at different section 2 fractions at with $dr_{12_1}(m) = 0.0060m$ and $dr_{34_1}(m) = 0.0150$

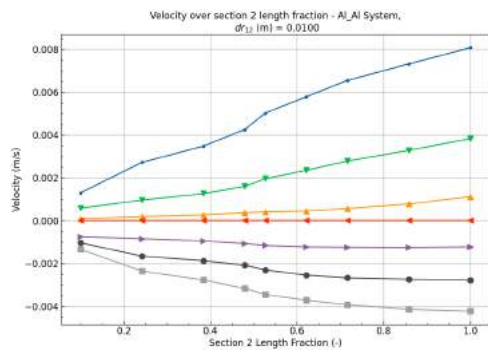


(g) Target solution temperature profiles over the the length of the system at different section 2 fractions at with $dr_{12_1}(m) = 0.0060m$ and $dr_{34_1}(m) = 0.0175$

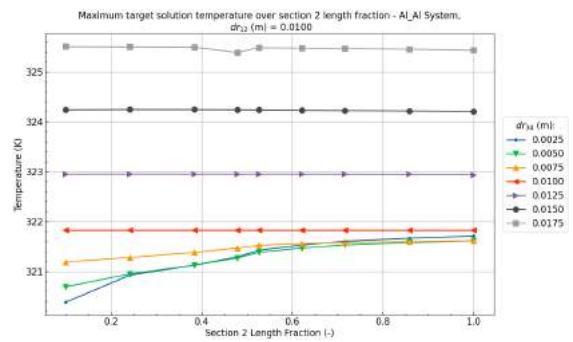
Figure B.106: Al/Al (Heat/Cool) System target solution temperature profiles over the section 2 fraction and cooling wall thickness dr_{34} at a heating wall thickness of $dr_{12} = 0.0060m$, a system length (L) of $0.4m$, and a pipe angle (θ) of 5° .

Al/Al - Section 2 length fraction at $dr_{12_1} = 0.0100m$ B.4

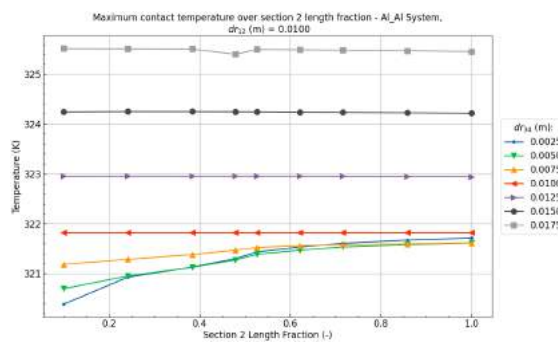
[Back to overview -](#)



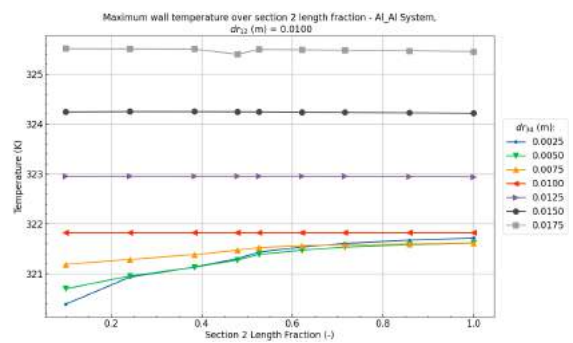
(a) Velocity over the section 2 fraction at $dr_{12_1} = 0.0100m$



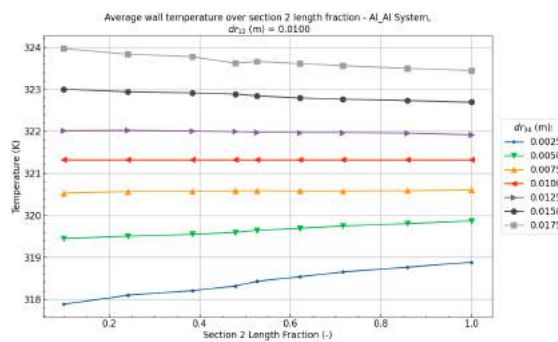
(b) Maximum target solution temperature over the section 2 fraction at $dr_{12_1} = 0.0100m$



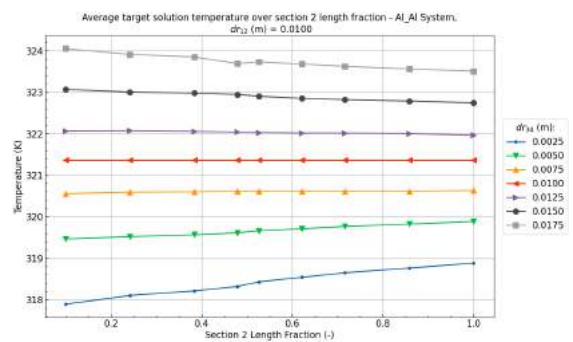
(c) Maximum contact temperature between the wall and the target solution over the section 2 fraction at $dr_{12_1} = 0.0100m$



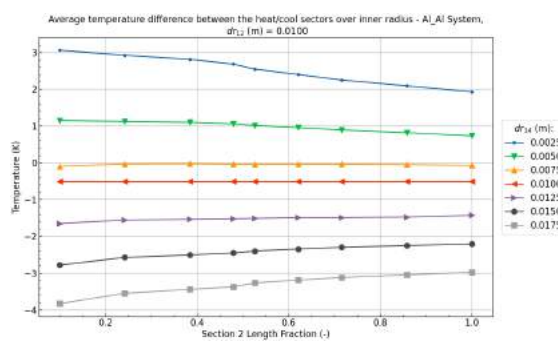
(d) Maximum wall temperature over the section 2 fraction at $dr_{12_1} = 0.0100m$



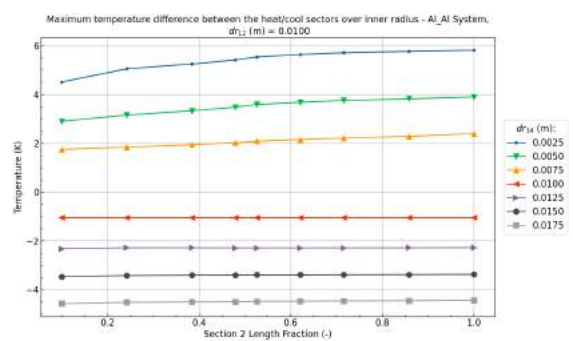
(e) Average target solution temperature over the section 2 fraction at $dr_{12_1} = 0.0100m$



(f) Average wall temperature over the section 2 fraction at $dr_{12_1} = 0.0100m$

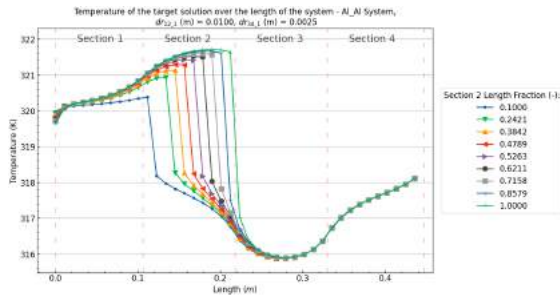


(g) Average target solution temperature difference between heating and cooling sectors over the section 2 fraction at $dr_{12_1} = 0.0100m$

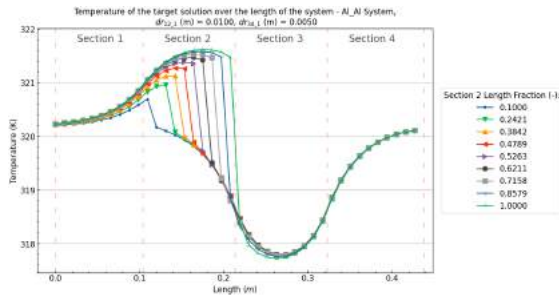


(h) Maximum target solution temperature difference between heating and cooling sectors over the section 2 fraction at $dr_{12_1} = 0.0100m$

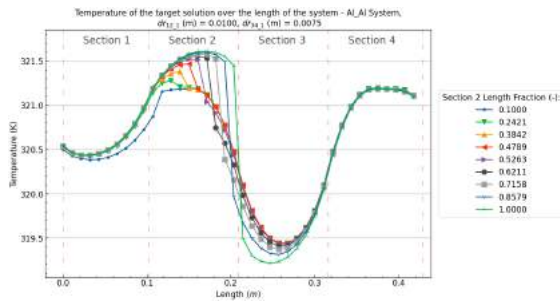
Figure B.107: Al/Al (Heat/Cool) System results over the section 2 fraction and cooling wall thickness dr_{34} at a heating wall thickness of $dr_{12} = 0.0100m$, a system length (L) of $0.4m$, and a pipe angle (θ) of 5° .



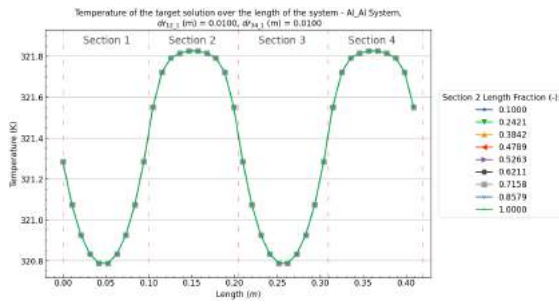
(a) Target solution temperature profiles over the the length of the system at different section 2 fractions at with $dr_{12_1}(m) = 0.0100m$ and $dr_{34_1}(m) = 0.0025$



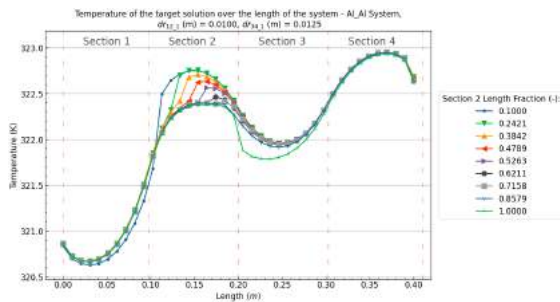
(b) Target solution temperature profiles over the the length of the system at different section 2 fractions at with $dr_{12_1}(m) = 0.0100m$ and $dr_{34_1}(m) = 0.0050$



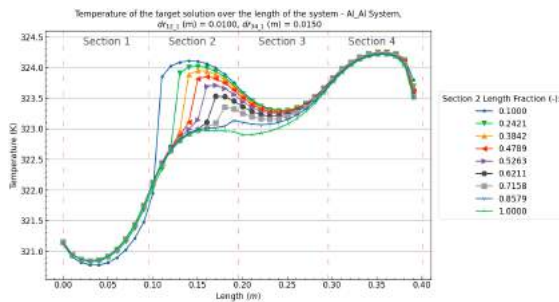
(c) Target solution temperature profiles over the the length of the system at different section 2 fractions at with $dr_{12_1}(m) = 0.0100m$ and $dr_{34_1}(m) = 0.0075$



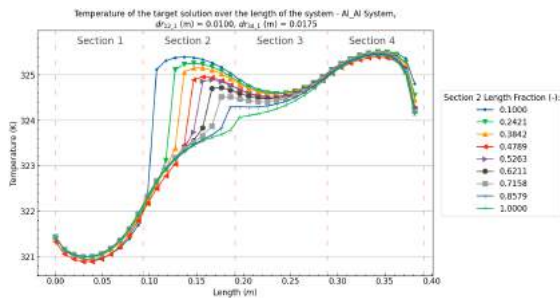
(d) Target solution temperature profiles over the the length of the system at different section 2 fractions at with $dr_{12_1}(m) = 0.0100m$ and $dr_{34_1}(m) = 0.0100$



(e) Target solution temperature profiles over the the length of the system at different section 2 fractions at with $dr_{12_1}(m) = 0.0100m$ and $dr_{34_1}(m) = 0.0125$



(f) Target solution temperature profiles over the the length of the system at different section 2 fractions at with $dr_{12_1}(m) = 0.0100m$ and $dr_{34_1}(m) = 0.0150$

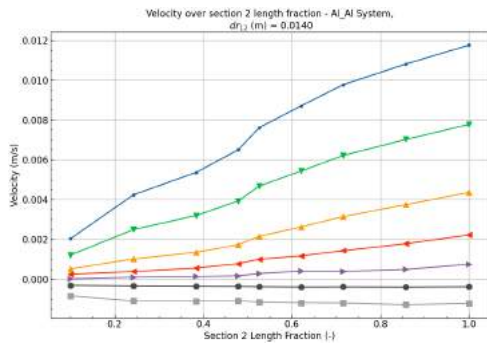


(g) Target solution temperature profiles over the the length of the system at different section 2 fractions at with $dr_{12_1}(m) = 0.0100m$ and $dr_{34_1}(m) = 0.0175$

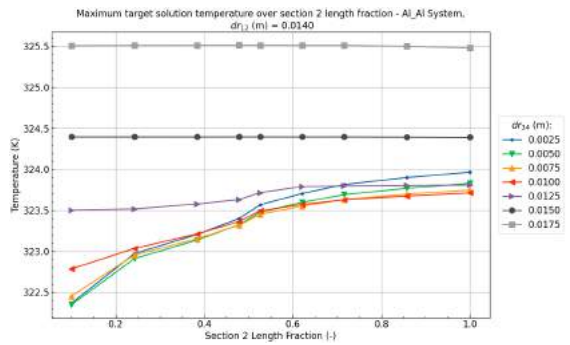
Figure B.108: Al/Al (Heat/Cool) System target solution temperature profiles over the section 2 fraction and cooling wall thickness dr_{34} at a heating wall thickness of $dr_{12} = 0.0100m$, a system length (L) of $0.4m$, and a pipe angle (θ) of 5° .

Al/Al - Section 2 length fraction at $dr_{12_1} = 0.0140m$
B.4

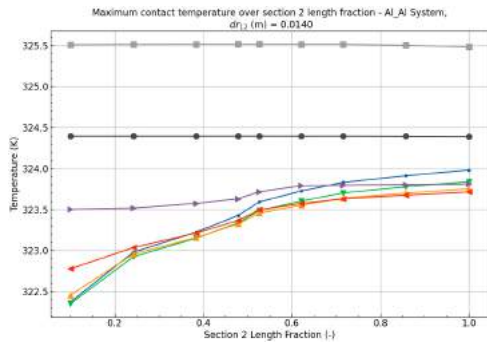
[Back to overview -](#)



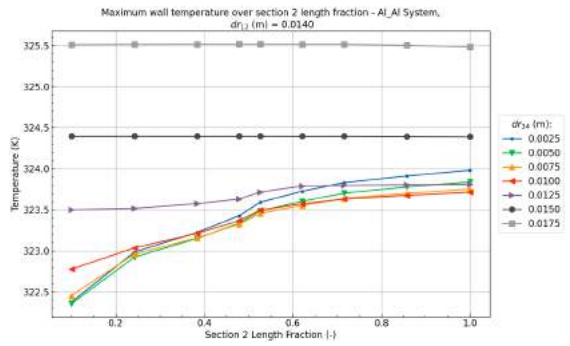
(a) Velocity over the section 2 fraction at $dr_{12_1} = 0.0140m$



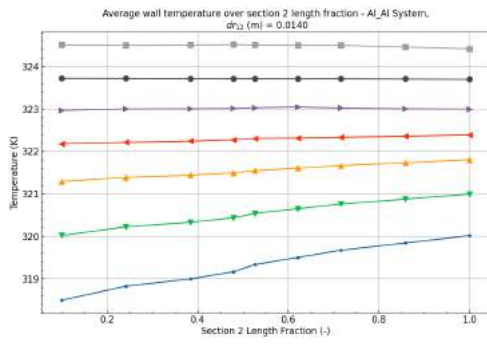
(b) Maximum target solution temperature over the section 2 fraction at $dr_{12_1} = 0.0140m$



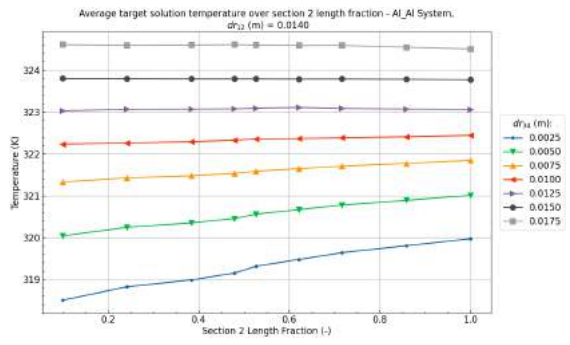
(c) Maximum contact temperature between the wall and the target solution over the section 2 fraction at $dr_{12_1} = 0.0140m$



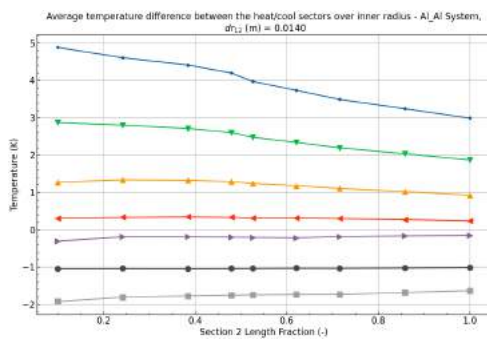
(d) Maximum wall temperature over the section 2 fraction at $dr_{12_1} = 0.0140m$



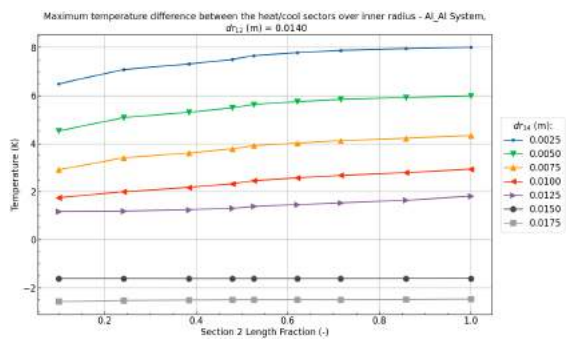
(e) Average target solution temperature over the section 2 fraction at $dr_{12_1} = 0.0140m$



(f) Average wall temperature over the section 2 fraction at $dr_{12_1} = 0.0140m$

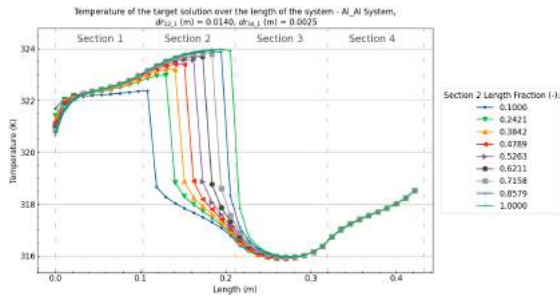


(g) Average target solution temperature difference between heating and cooling sectors over the section 2 fraction at $dr_{12_1} = 0.0140m$

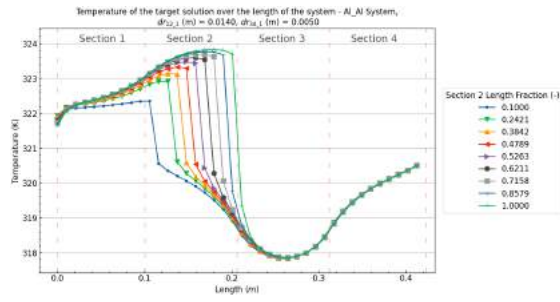


(h) Maximum target solution temperature difference between heating and cooling sectors over the section 2 fraction at $dr_{12_1} = 0.0140m$

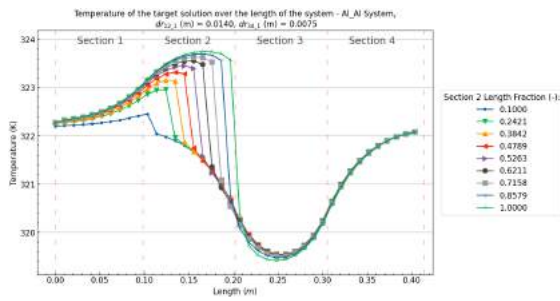
Figure B.109: Al/Al (Heat/Cool) System results over the section 2 fraction and cooling wall thickness dr_{34} at a heating wall thickness of $dr_{12} = 0.0140m$, a system length (L) of $0.4m$, and a pipe angle (θ) of 5° .



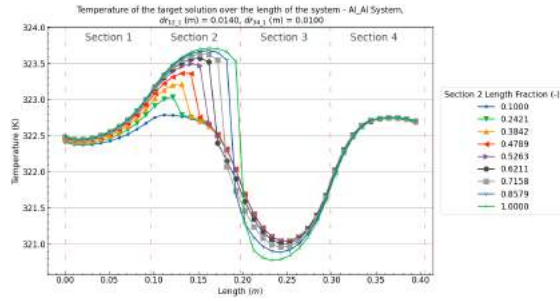
(a) Target solution temperature profiles over the the length of the system at different section 2 fractions at with $dr_{12_1}(m) = 0.0140m$ and $dr_{34_1}(m) = 0.0025$



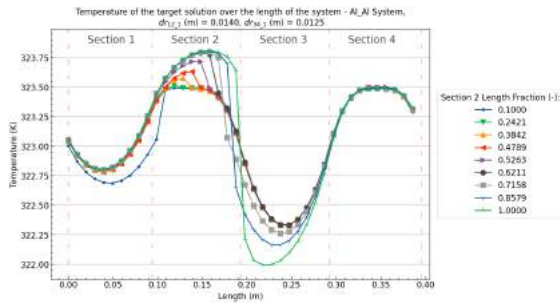
(b) Target solution temperature profiles over the the length of the system at different section 2 fractions at with $dr_{12_1}(m) = 0.0140m$ and $dr_{34_1}(m) = 0.0050$



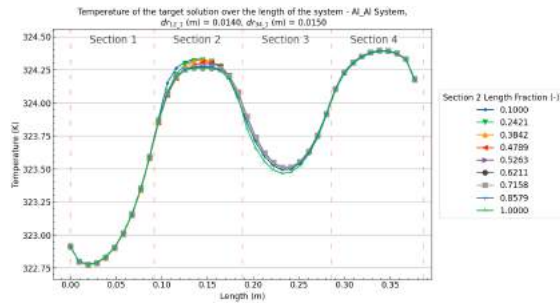
(c) Target solution temperature profiles over the the length of the system at different section 2 fractions at with $dr_{12_1}(m) = 0.0140m$ and $dr_{34_1}(m) = 0.0075$



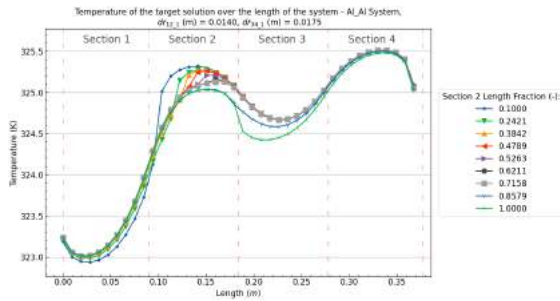
(d) Target solution temperature profiles over the the length of the system at different section 2 fractions at with $dr_{12_1}(m) = 0.0140m$ and $dr_{34_1}(m) = 0.0100$



(e) Target solution temperature profiles over the the length of the system at different section 2 fractions at with $dr_{12_1}(m) = 0.0140m$ and $dr_{34_1}(m) = 0.0125$



(f) Target solution temperature profiles over the the length of the system at different section 2 fractions at with $dr_{12_1}(m) = 0.0140m$ and $dr_{34_1}(m) = 0.0150$

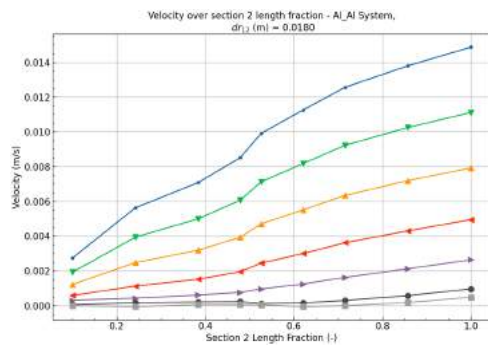


(g) Target solution temperature profiles over the the length of the system at different section 2 fractions at with $dr_{12_1}(m) = 0.0140m$ and $dr_{34_1}(m) = 0.0175$

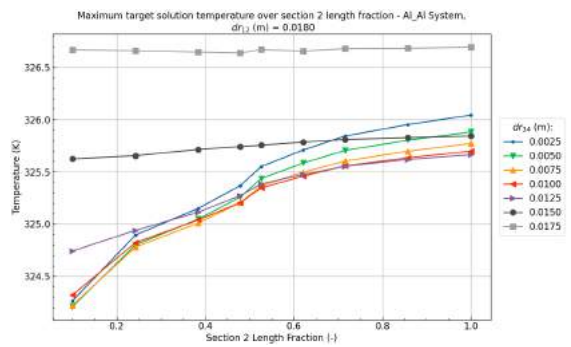
Figure B.110: Al/Al (Heat/Cool) System target solution temperature profiles over the section 2 fraction and cooling wall thickness dr_{34} at a heating wall thickness of $dr_{12} = 0.0140m$, a system length (L) of $0.4m$, and a pipe angle (θ) of 5° .

Al/Al - Section 2 length fraction at $dr_{12_1} = 0.0180m$ B.4

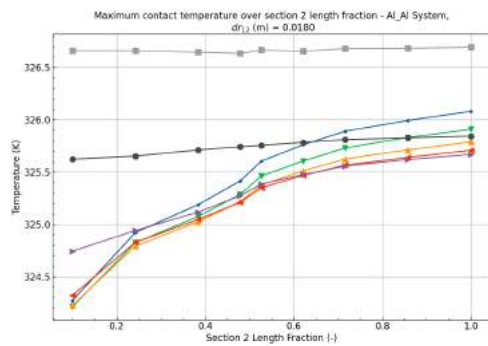
[Back to overview -](#)



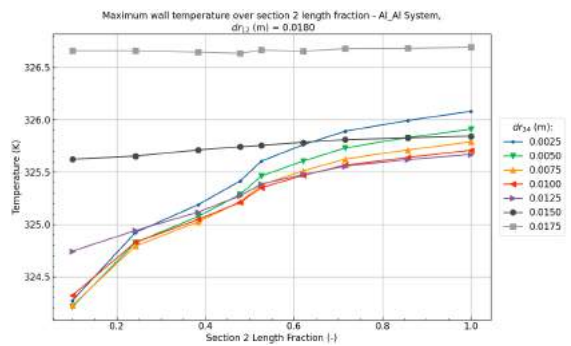
(a) Velocity over the section 2 fraction at $dr_{12_1} = 0.0180m$



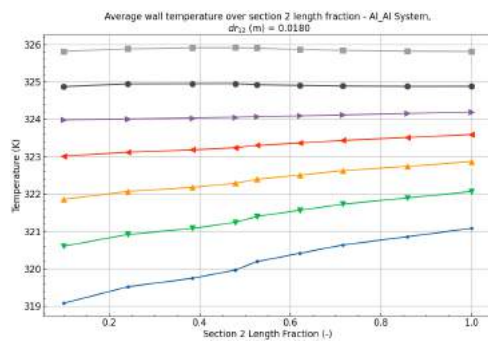
(b) Maximum target solution temperature over the section 2 fraction at $dr_{12_1} = 0.0180m$



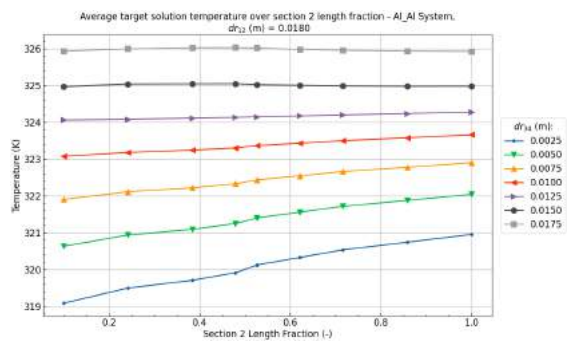
(c) Maximum contact temperature between the wall and the target solution over the section 2 fraction at $dr_{12_1} = 0.0180m$



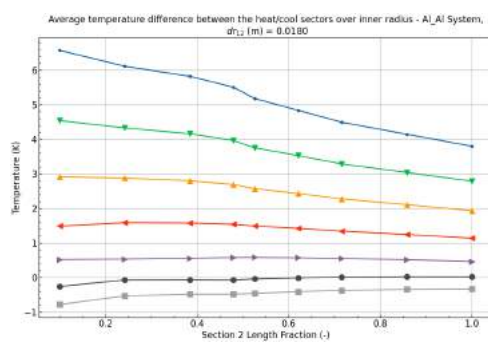
(d) Maximum wall temperature over the section 2 fraction at $dr_{12_1} = 0.0180m$



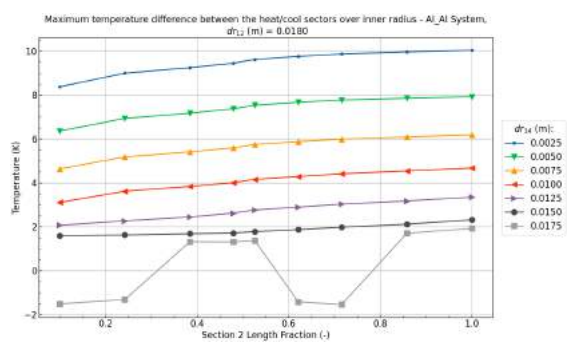
(e) Average target solution temperature over the section 2 fraction at $dr_{12_1} = 0.0180m$



(f) Average wall temperature over the section 2 fraction at $dr_{12_1} = 0.0180m$

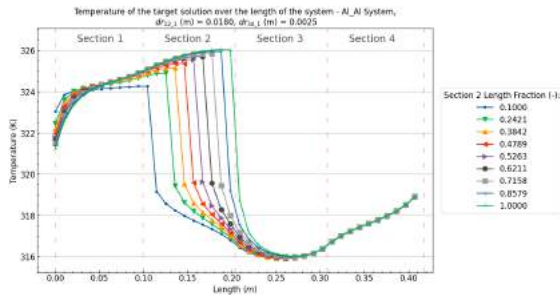


(g) Average target solution temperature difference between heating and cooling sectors over the section 2 fraction at $dr_{12_1} = 0.0180m$

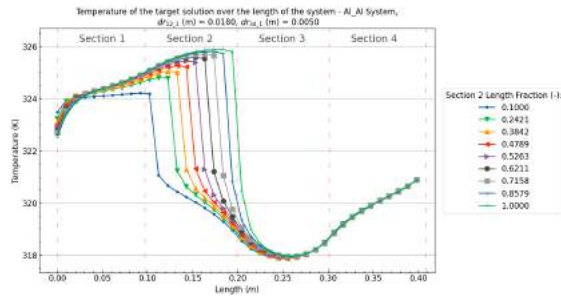


(h) Maximum target solution temperature difference between heating and cooling sectors over the section 2 fraction at $dr_{12_1} = 0.0180m$

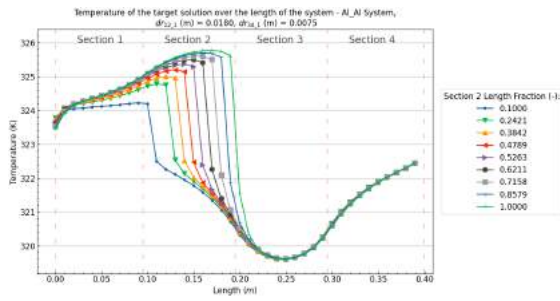
Figure B.111: Al/Al (Heat/Cool) System results over the section 2 fraction and cooling wall thickness dr_{34} at a heating wall thickness of $dr_{12} = 0.0180m$, a system length (L) of $0.4m$, and a pipe angle (θ) of 5° .



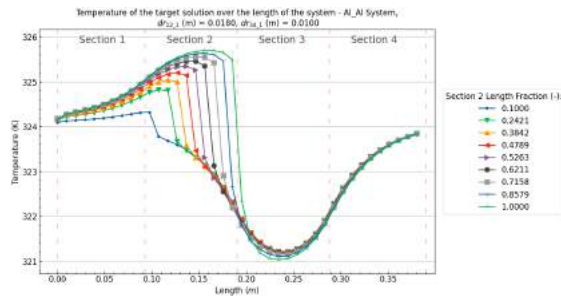
(a) Target solution temperature profiles over the the length of the system at different section 2 fractions at with $dr_{12_1}(m) = 0.0180m$ and $dr_{34_1}(m) = 0.0025$



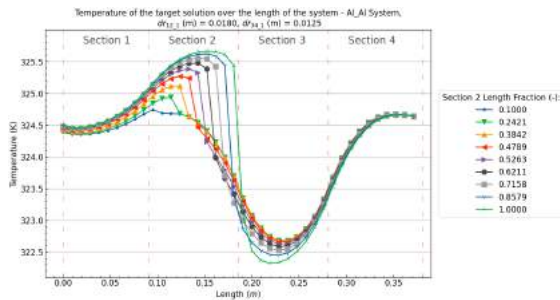
(b) Target solution temperature profiles over the the length of the system at different section 2 fractions at with $dr_{12_1}(m) = 0.0180m$ and $dr_{34_1}(m) = 0.0050$



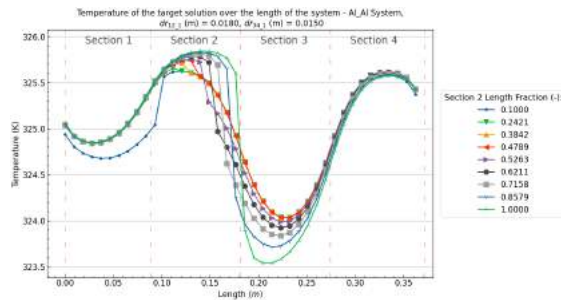
(c) Target solution temperature profiles over the the length of the system at different section 2 fractions at with $dr_{12_1}(m) = 0.0180m$ and $dr_{34_1}(m) = 0.0075$



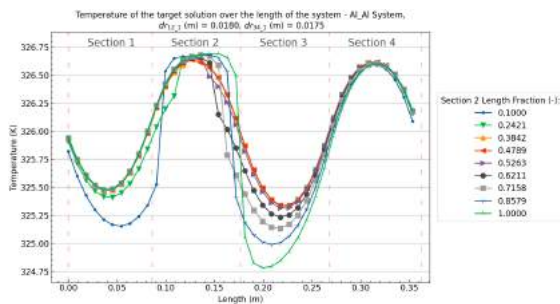
(d) Target solution temperature profiles over the the length of the system at different section 2 fractions at with $dr_{12_1}(m) = 0.0180m$ and $dr_{34_1}(m) = 0.0100$



(e) Target solution temperature profiles over the the length of the system at different section 2 fractions at with $dr_{12_1}(m) = 0.0180m$ and $dr_{34_1}(m) = 0.0125$



(f) Target solution temperature profiles over the the length of the system at different section 2 fractions at with $dr_{12_1}(m) = 0.0180m$ and $dr_{34_1}(m) = 0.0150$



(g) Target solution temperature profiles over the the length of the system at different section 2 fractions at with $dr_{12_1}(m) = 0.0180m$ and $dr_{34_1}(m) = 0.0175$

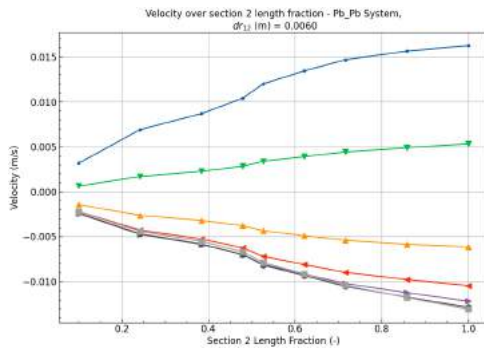
Figure B.112: Al/Al (Heat/Cool) System target solution temperature profiles over the section 2 fraction and cooling wall thickness dr_{34} at a heating wall thickness of $dr_{12} = 0.0180m$, a system length (L) of $0.4m$, and a pipe angle (θ) of 5° .

B.4.2. Pb/Pb - Section 2 length fraction & Wall thickness

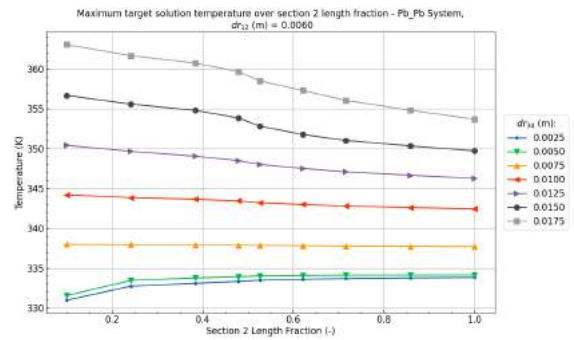
Pb/Pb - Section 2 length fraction at $dr_{12_1} = 0.0060m$

[Back to overview -](#)

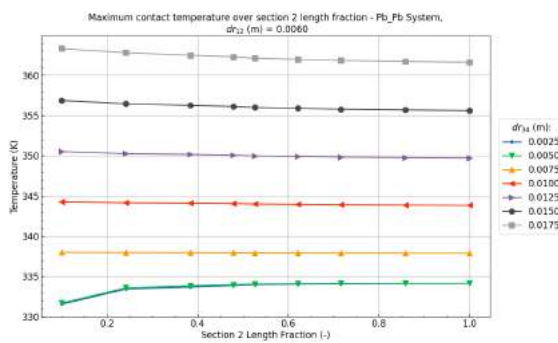
B.4



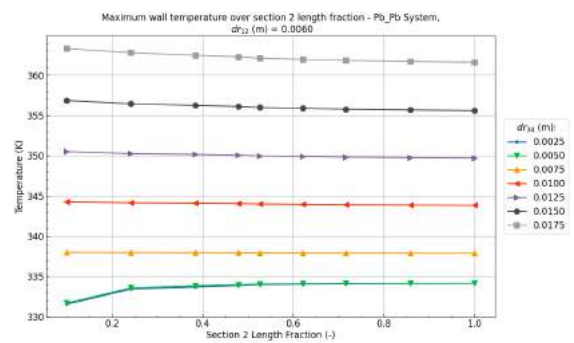
(a) Velocity over the section 2 fraction at $dr_{12_1} = 0.0060m$



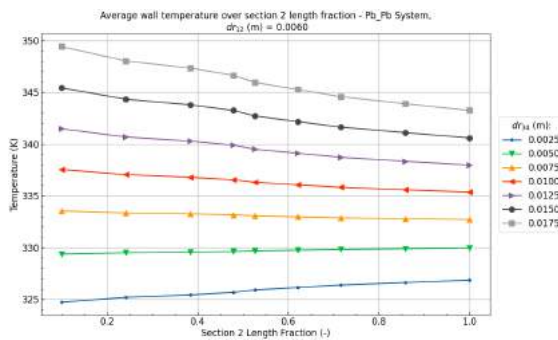
(b) Maximum target solution temperature over the section 2 fraction at $dr_{12_1} = 0.0060m$



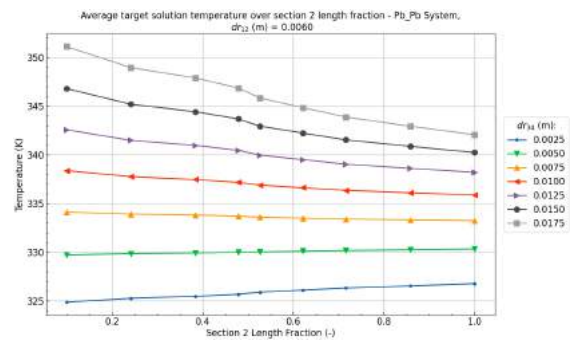
(c) Maximum contact temperature between the wall and the target solution over the section 2 fraction at $dr_{12_1} = 0.0060m$



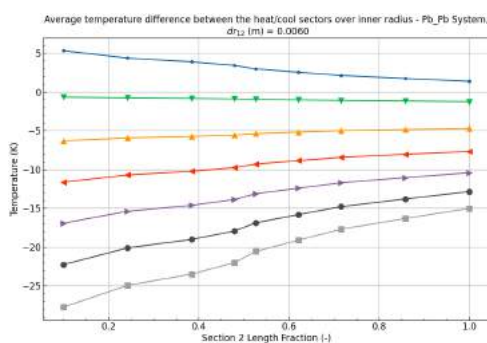
(d) Maximum wall temperature over the section 2 fraction at $dr_{12_1} = 0.0060m$



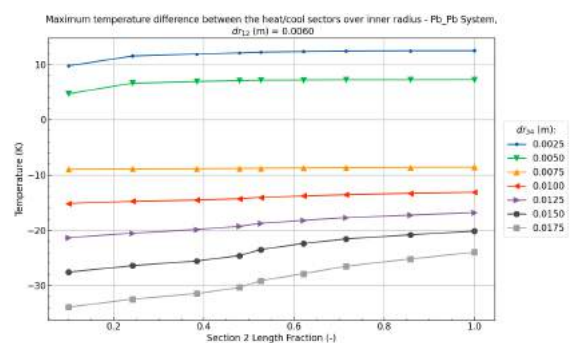
(e) Average target solution temperature over the section 2 fraction at $dr_{12_1} = 0.0060m$



(f) Average wall temperature over the section 2 fraction at $dr_{12_1} = 0.0060m$

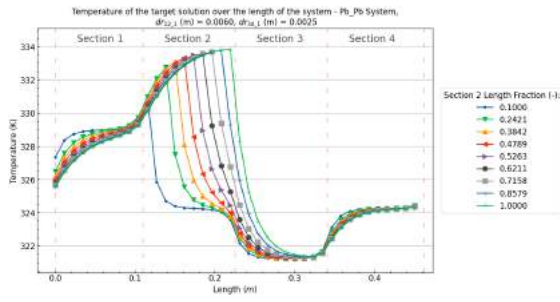


(g) Average target solution temperature difference between heating and cooling sectors over the section 2 fraction at $dr_{12_1} = 0.0060m$

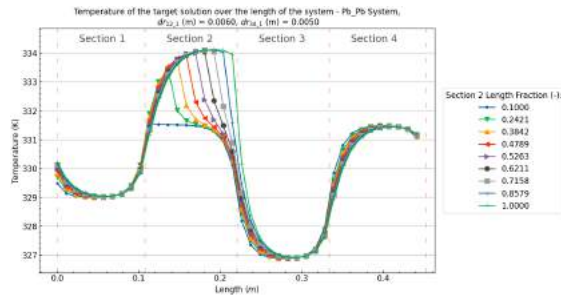


(h) Maximum target solution temperature difference between heating and cooling sectors over the section 2 fraction at $dr_{12_1} = 0.0060m$

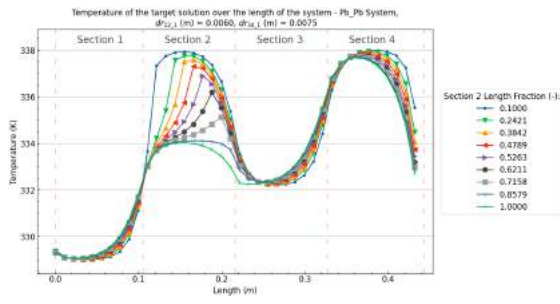
Figure B.113: Pb/Pb (Heat/Cool) System results over the section 2 fraction and cooling wall thickness dr_{34} at a heating wall thickness of $dr_{12} = 0.0060m$, a system length (L) of $0.4m$, and a pipe angle (θ) of 5° .



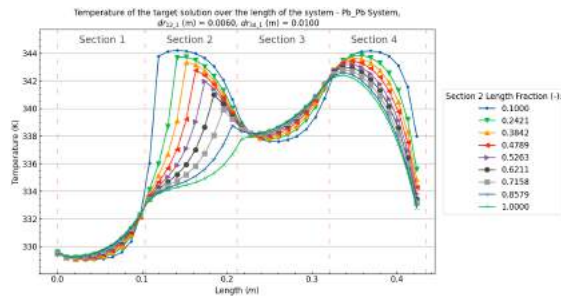
(a) Target solution temperature profiles over the the length of the system at different section 2 fractions at with $dr_{12,1}(m) = 0.0060m$ and $dr_{34,1}(m) = 0.0025$



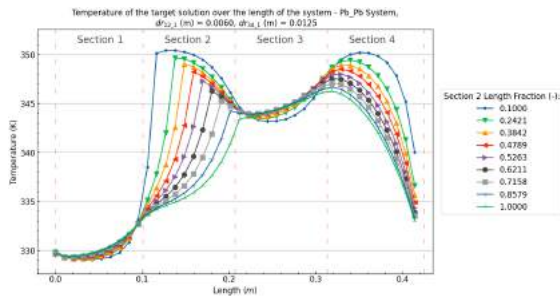
(b) Target solution temperature profiles over the the length of the system at different section 2 fractions at with $dr_{12,1}(m) = 0.0060m$ and $dr_{34,1}(m) = 0.0050$



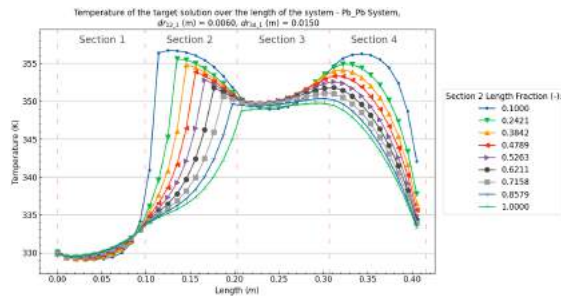
(c) Target solution temperature profiles over the the length of the system at different section 2 fractions at with $dr_{12,1}(m) = 0.0060m$ and $dr_{34,1}(m) = 0.0075$



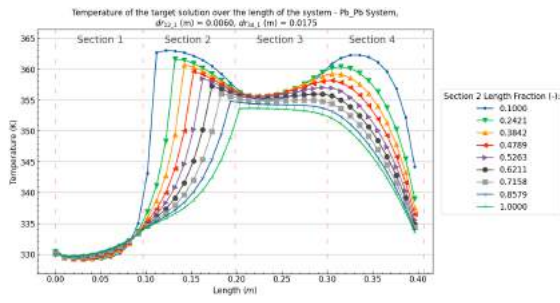
(d) Target solution temperature profiles over the the length of the system at different section 2 fractions at with $dr_{12,1}(m) = 0.0060m$ and $dr_{34,1}(m) = 0.0100$



(e) Target solution temperature profiles over the the length of the system at different section 2 fractions at with $dr_{12,1}(m) = 0.0060m$ and $dr_{34,1}(m) = 0.0125$



(f) Target solution temperature profiles over the the length of the system at different section 2 fractions at with $dr_{12,1}(m) = 0.0060m$ and $dr_{34,1}(m) = 0.0150$

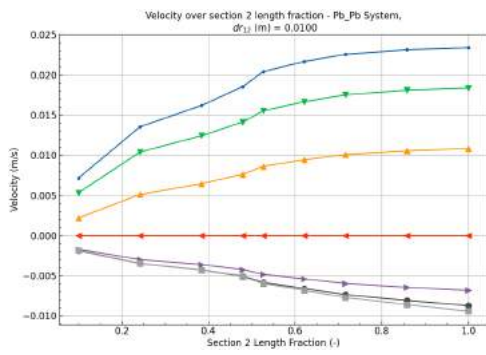


(g) Target solution temperature profiles over the the length of the system at different section 2 fractions at with $dr_{12,1}(m) = 0.0060m$ and $dr_{34,1}(m) = 0.0175$

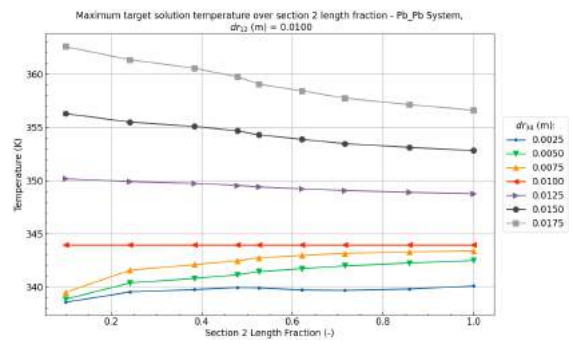
Figure B.114: Pb/Pb (Heat/Cool) System target solution temperature profiles over the section 2 fraction and cooling wall thickness dr_{34} at a heating wall thickness of $dr_{12} = 0.0060m$, a system length (L) of $0.4m$, and a pipe angle (θ) of 5° .

Pb/Pb - Section 2 length fraction at $dr_{12_1} = 0.0100m$ B.4

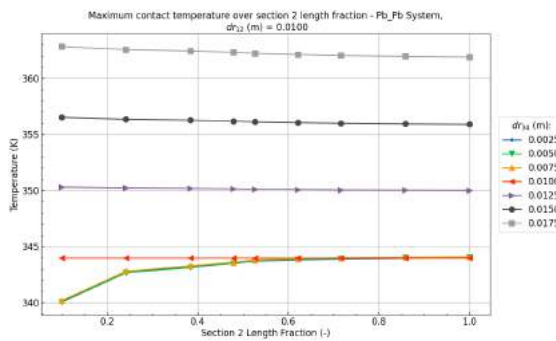
[Back to overview -](#)



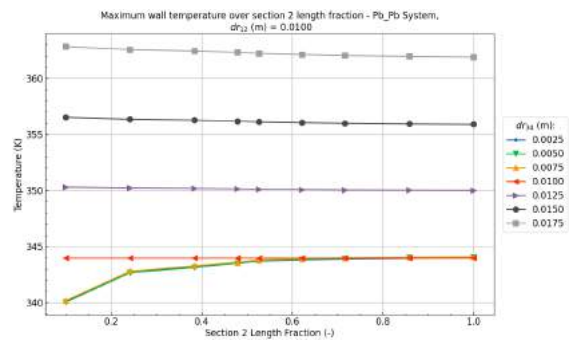
(a) Velocity over the section 2 fraction at $dr_{12_1} = 0.0100m$



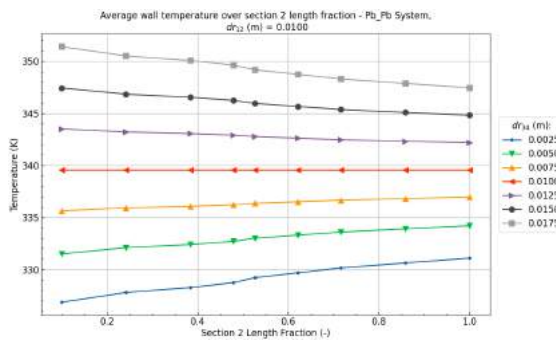
(b) Maximum target solution temperature over the section 2 fraction at $dr_{12_1} = 0.0100m$



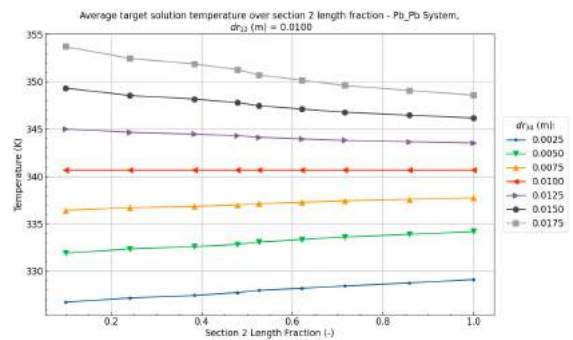
(c) Maximum contact temperature between the wall and the target solution over the section 2 fraction at $dr_{12_1} = 0.0100m$



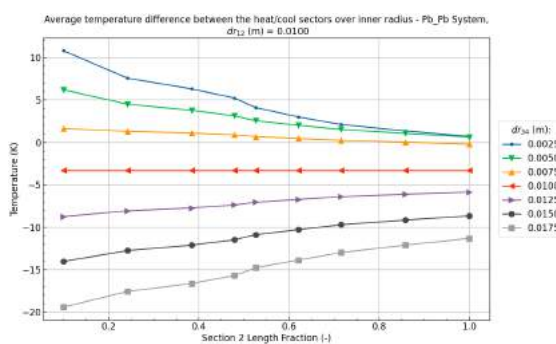
(d) Maximum wall temperature over the section 2 fraction at $dr_{12_1} = 0.0100m$



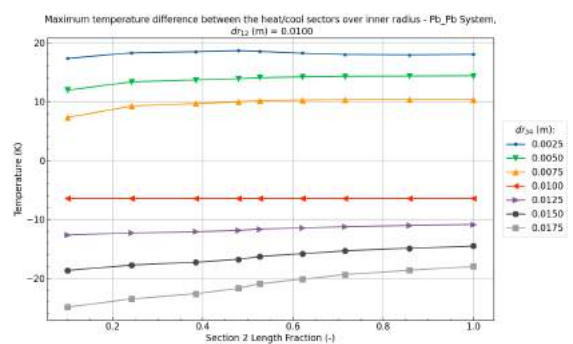
(e) Average target solution temperature over the section 2 fraction at $dr_{12_1} = 0.0100m$



(f) Average wall temperature over the section 2 fraction at $dr_{12_1} = 0.0100m$

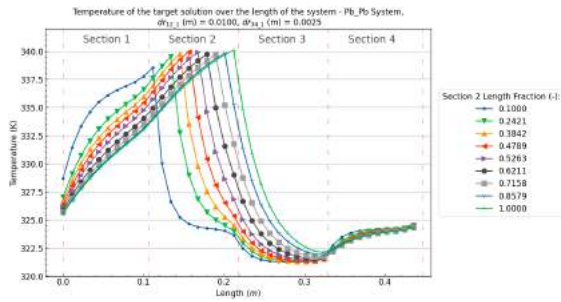


(g) Average target solution temperature difference between heating and cooling sectors over the section 2 fraction at $dr_{12_1} = 0.0100m$

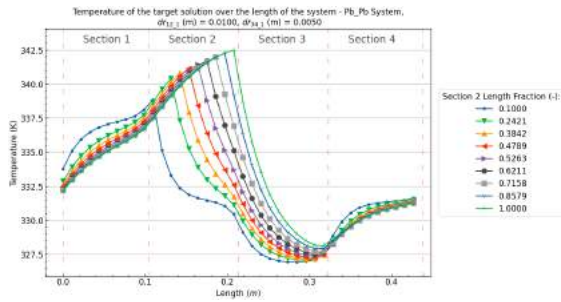


(h) Maximum target solution temperature difference between heating and cooling sectors over the section 2 fraction at $dr_{12_1} = 0.0100m$

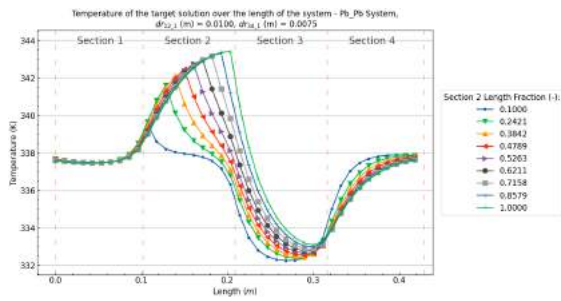
Figure B.115: Pb/Pb (Heat/Cool) System results over the section 2 fraction and cooling wall thickness dr_{34} at a heating wall thickness of $dr_{12} = 0.0100m$, a system length (L) of $0.4m$, and a pipe angle (θ) of 5° .



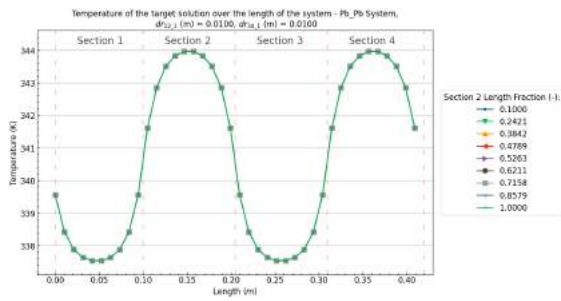
(a) Target solution temperature profiles over the the length of the system at different section 2 fractions at with $dr_{12_1}(m) = 0.0100m$ and $dr_{34_1}(m) = 0.0025$



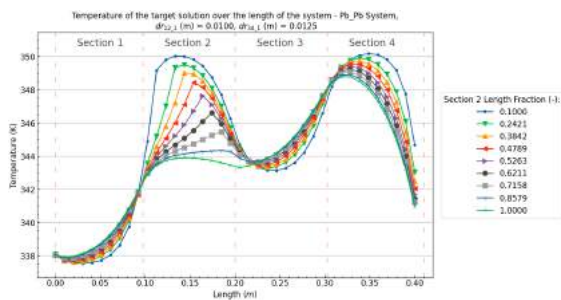
(b) Target solution temperature profiles over the the length of the system at different section 2 fractions at with $dr_{12_1}(m) = 0.0100m$ and $dr_{34_1}(m) = 0.0050$



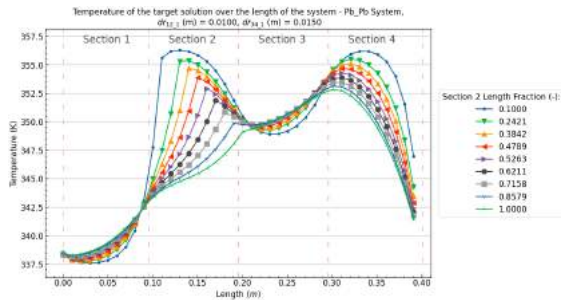
(c) Target solution temperature profiles over the the length of the system at different section 2 fractions at with $dr_{12_1}(m) = 0.0100m$ and $dr_{34_1}(m) = 0.0075$



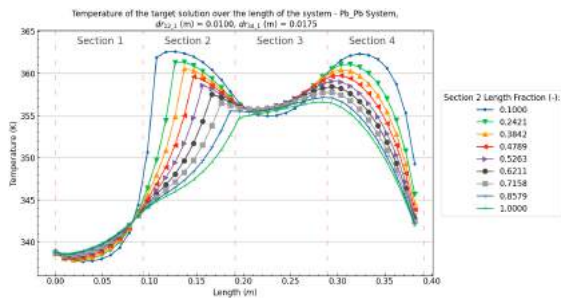
(d) Target solution temperature profiles over the the length of the system at different section 2 fractions at with $dr_{12_1}(m) = 0.0100m$ and $dr_{34_1}(m) = 0.0100$



(e) Target solution temperature profiles over the the length of the system at different section 2 fractions at with $dr_{12_1}(m) = 0.0100m$ and $dr_{34_1}(m) = 0.0125$



(f) Target solution temperature profiles over the the length of the system at different section 2 fractions at with $dr_{12_1}(m) = 0.0100m$ and $dr_{34_1}(m) = 0.0150$

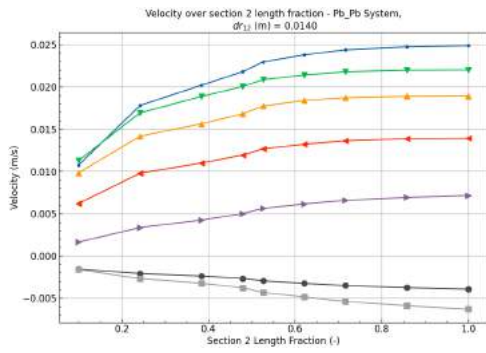


(g) Target solution temperature profiles over the the length of the system at different section 2 fractions at with $dr_{12_1}(m) = 0.0100m$ and $dr_{34_1}(m) = 0.0175$

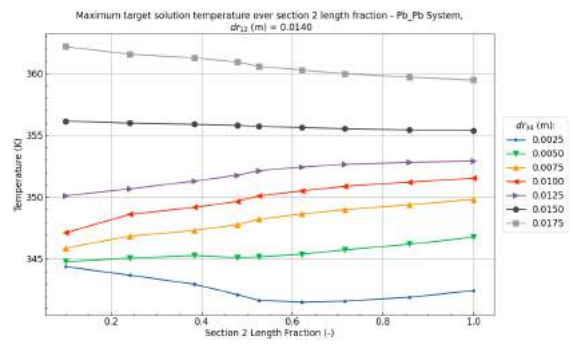
Figure B.116: Pb/Pb (Heat/Cool) System target solution temperature profiles over the section 2 fraction and cooling wall thickness dr_{34} at a heating wall thickness of $dr_{12} = 0.0100m$, a system length (L) of $0.4m$, and a pipe angle (θ) of 5° .

Pb/Pb - Section 2 length fraction at $dr_{12_1} = 0.0140m$ B.4

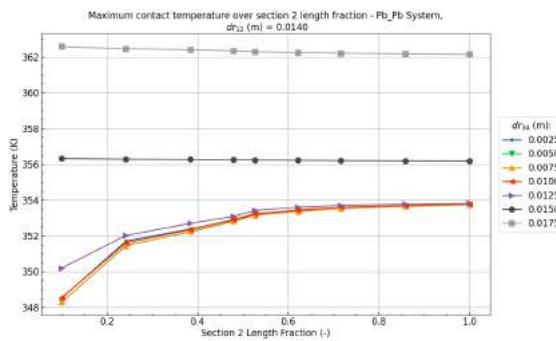
[Back to overview -](#)



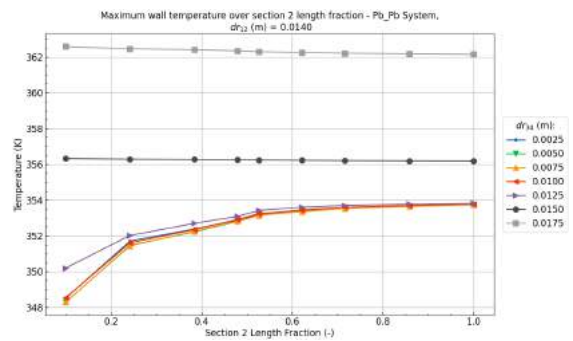
(a) Velocity over the section 2 fraction at $dr_{12_1} = 0.0140m$



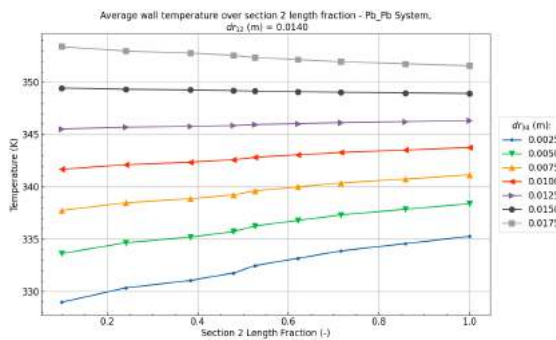
(b) Maximum target solution temperature over the section 2 fraction at $dr_{12_1} = 0.0140m$



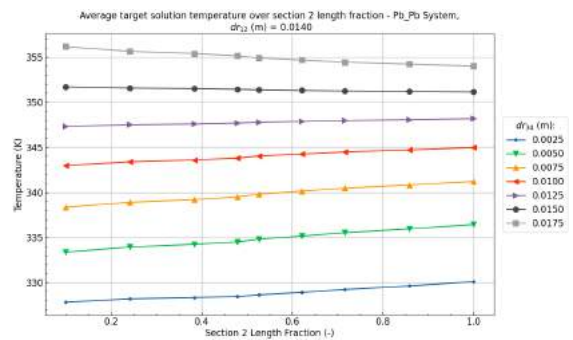
(c) Maximum contact temperature between the wall and the target solution over the section 2 fraction at $dr_{12_1} = 0.0140m$



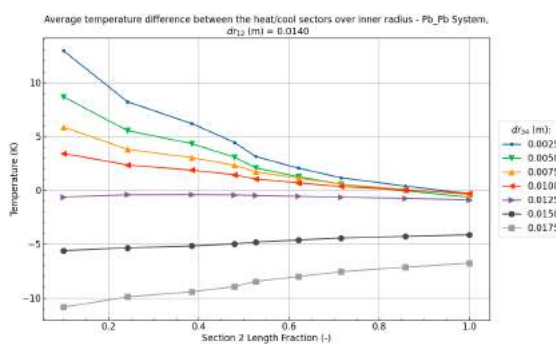
(d) Maximum wall temperature over the section 2 fraction at $dr_{12_1} = 0.0140m$



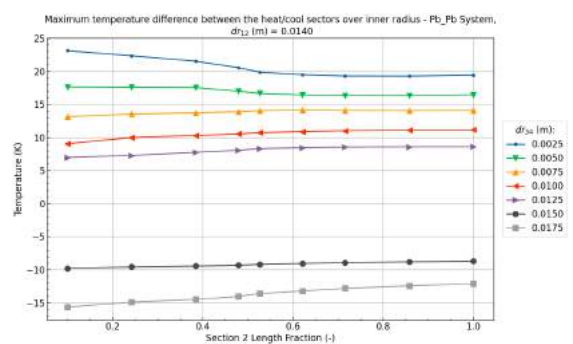
(e) Average target solution temperature over the section 2 fraction at $dr_{12_1} = 0.0140m$



(f) Average wall temperature over the section 2 fraction at $dr_{12_1} = 0.0140m$

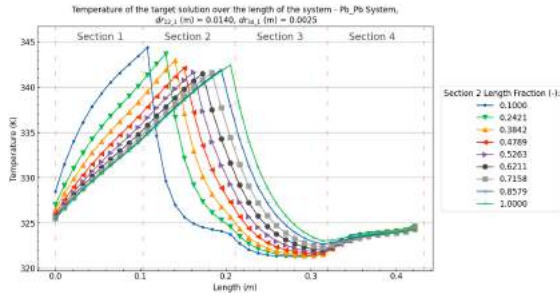


(g) Average target solution temperature difference between heating and cooling sectors over the section 2 fraction at $dr_{12_1} = 0.0140m$

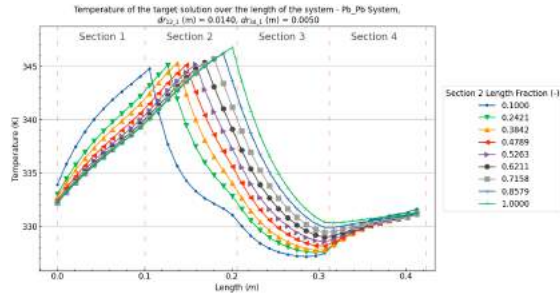


(h) Maximum target solution temperature difference between heating and cooling sectors over the section 2 fraction at $dr_{12_1} = 0.0140m$

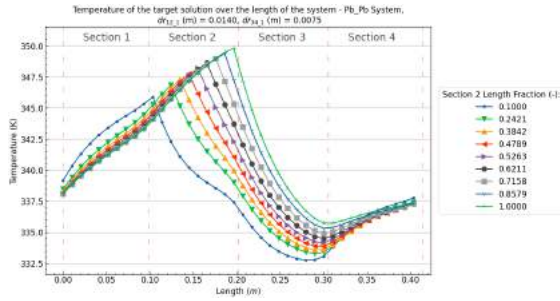
Figure B.117: Pb/Pb (Heat/Cool) System results over the section 2 fraction and cooling wall thickness dr_{34} at a heating wall thickness of $dr_{12} = 0.0140m$, a system length (L) of $0.4m$, and a pipe angle (θ) of 5° .



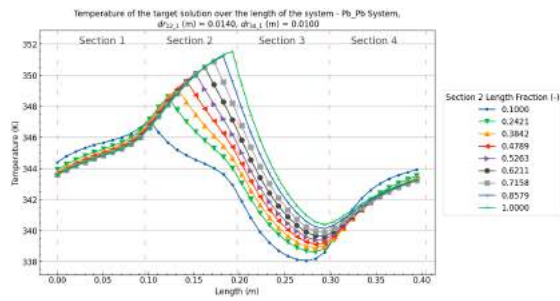
(a) Target solution temperature profiles over the the length of the system at different section 2 fractions at with $dr_{12_1}(m) = 0.0140m$ and $dr_{34_1}(m) = 0.0025$



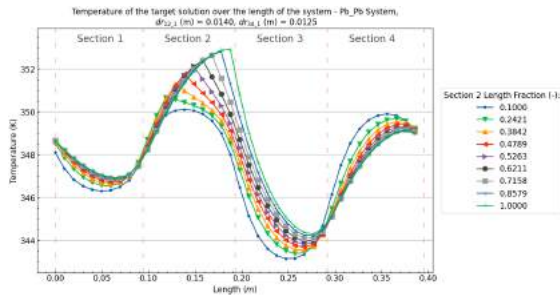
(b) Target solution temperature profiles over the the length of the system at different section 2 fractions at with $dr_{12_1}(m) = 0.0140m$ and $dr_{34_1}(m) = 0.0050$



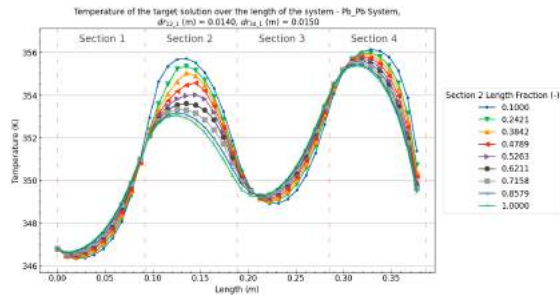
(c) Target solution temperature profiles over the the length of the system at different section 2 fractions at with $dr_{12_1}(m) = 0.0140m$ and $dr_{34_1}(m) = 0.0075$



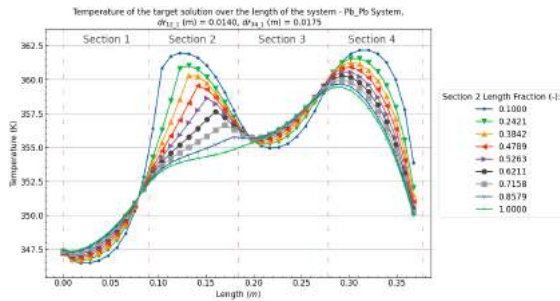
(d) Target solution temperature profiles over the the length of the system at different section 2 fractions at with $dr_{12_1}(m) = 0.0140m$ and $dr_{34_1}(m) = 0.0100$



(e) Target solution temperature profiles over the the length of the system at different section 2 fractions at with $dr_{12_1}(m) = 0.0140m$ and $dr_{34_1}(m) = 0.0125$



(f) Target solution temperature profiles over the the length of the system at different section 2 fractions at with $dr_{12_1}(m) = 0.0140m$ and $dr_{34_1}(m) = 0.0150$

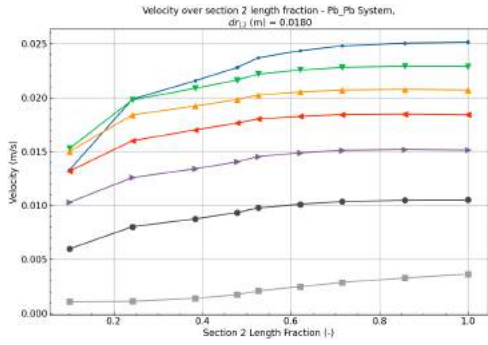


(g) Target solution temperature profiles over the the length of the system at different section 2 fractions at with $dr_{12_1}(m) = 0.0140m$ and $dr_{34_1}(m) = 0.0175$

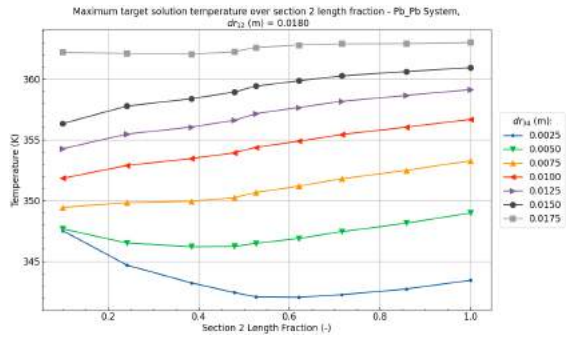
Figure B.118: Pb/Pb (Heat/Cool) System target solution temperature profiles over the section 2 fraction and cooling wall thickness dr_{34} at a heating wall thickness of $dr_{12} = 0.0140m$, a system length (L) of $0.4m$, and a pipe angle (θ) of 5° .

Pb/Pb - Section 2 length fraction at $dr_{12_1} = 0.0180m$
B.4

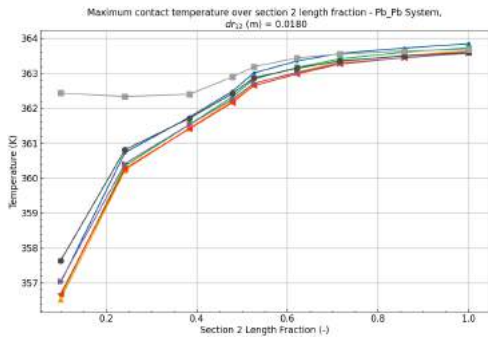
[Back to overview -](#)



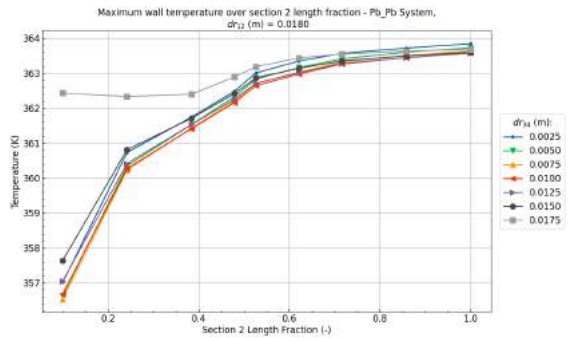
(a) Velocity over the section 2 fraction at $dr_{12_1} = 0.0180m$



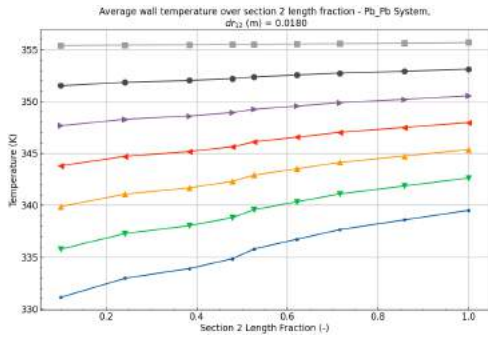
(b) Maximum target solution temperature over the section 2 fraction at $dr_{12_1} = 0.0180m$



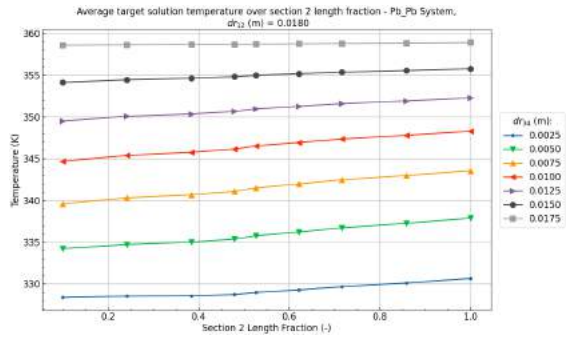
(c) Maximum contact temperature between the wall and the target solution over the section 2 fraction at $dr_{12_1} = 0.0180m$



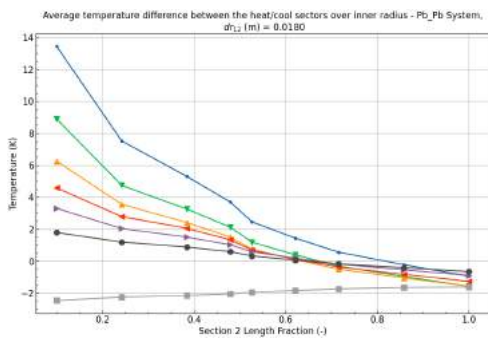
(d) Maximum wall temperature over the section 2 fraction at $dr_{12_1} = 0.0180m$



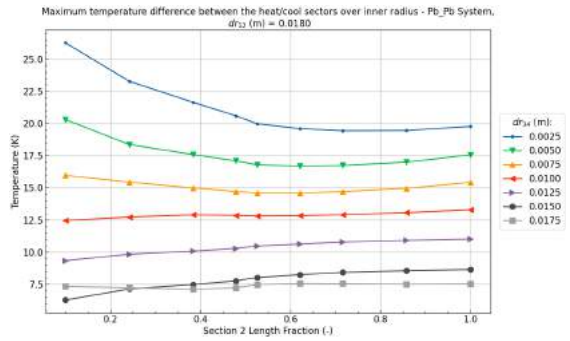
(e) Average target solution temperature over the section 2 fraction at $dr_{12_1} = 0.0180m$



(f) Average wall temperature over the section 2 fraction at $dr_{12_1} = 0.0180m$

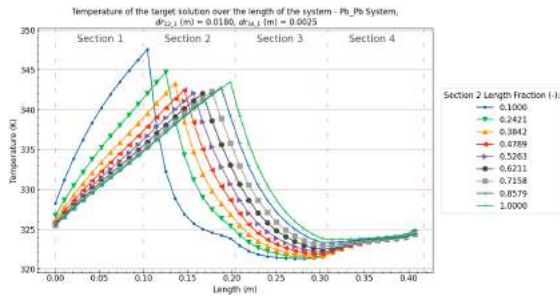


(g) Average target solution temperature difference between heating and cooling sectors over the section 2 fraction at $dr_{12_1} = 0.0180m$

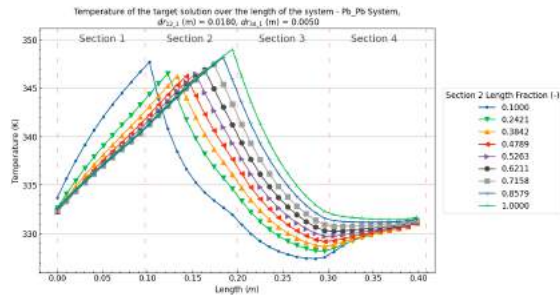


(h) Maximum target solution temperature difference between heating and cooling sectors over the section 2 fraction at $dr_{12_1} = 0.0180m$

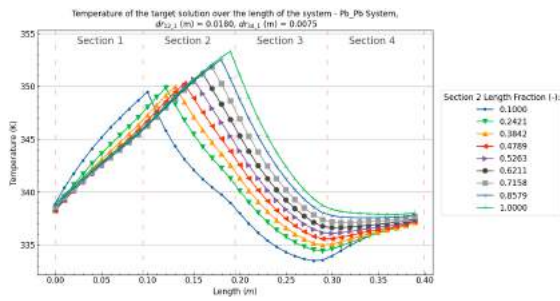
Figure B.119: Pb/Pb (Heat/Cool) System results over the section 2 fraction and cooling wall thickness dr_{34} at a heating wall thickness of $dr_{12} = 0.0180m$, a system length (L) of $0.4m$, and a pipe angle (θ) of 5° .



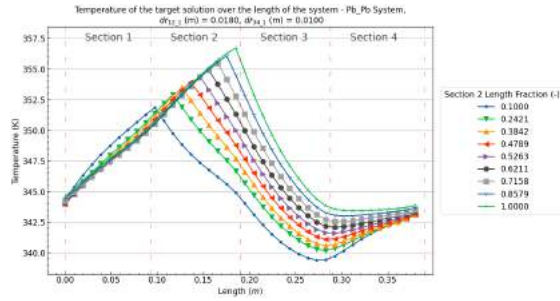
(a) Target solution temperature profiles over the the length of the system at different section 2 fractions at with $dr_{12_1}(m) = 0.0180m$ and $dr_{34_1}(m) = 0.0025$



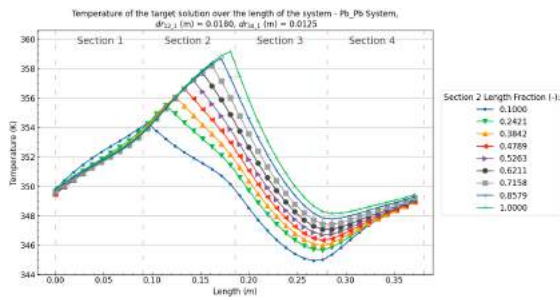
(b) Target solution temperature profiles over the the length of the system at different section 2 fractions at with $dr_{12_1}(m) = 0.0180m$ and $dr_{34_1}(m) = 0.0050$



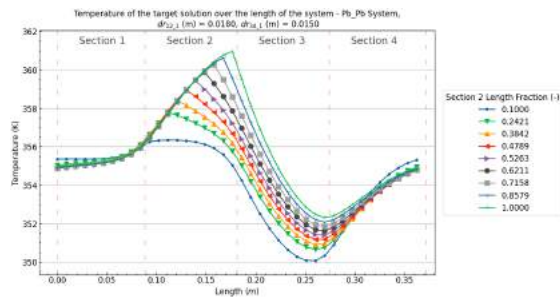
(c) Target solution temperature profiles over the the length of the system at different section 2 fractions at with $dr_{12_1}(m) = 0.0180m$ and $dr_{34_1}(m) = 0.0075$



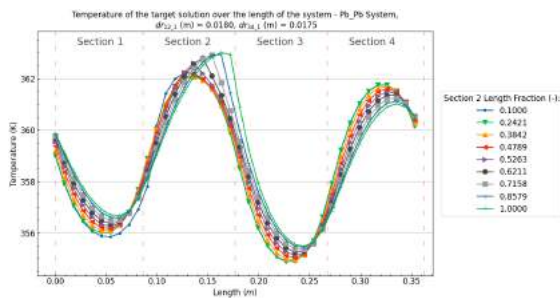
(d) Target solution temperature profiles over the the length of the system at different section 2 fractions at with $dr_{12_1}(m) = 0.0180m$ and $dr_{34_1}(m) = 0.0100$



(e) Target solution temperature profiles over the the length of the system at different section 2 fractions at with $dr_{12_1}(m) = 0.0180m$ and $dr_{34_1}(m) = 0.0125$



(f) Target solution temperature profiles over the the length of the system at different section 2 fractions at with $dr_{12_1}(m) = 0.0180m$ and $dr_{34_1}(m) = 0.0150$



(g) Target solution temperature profiles over the the length of the system at different section 2 fractions at with $dr_{12_1}(m) = 0.0180m$ and $dr_{34_1}(m) = 0.0175$

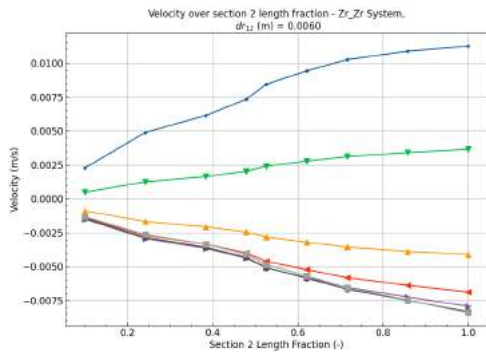
Figure B.120: Pb/Pb (Heat/Cool) System target solution temperature profiles over the section 2 fraction and cooling wall thickness dr_{34} at a heating wall thickness of $dr_{12} = 0.0180m$, a system length (L) of $0.4m$, and a pipe angle (θ) of 5° .

B.4.3. Zr/Zr - Section 2 length fraction & Wall thickness

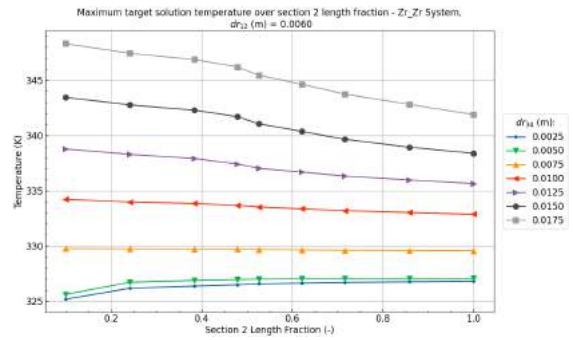
Zr/Zr - Section 2 length fraction at $dr_{12_1} = 0.0060m$

[Back to overview -](#)

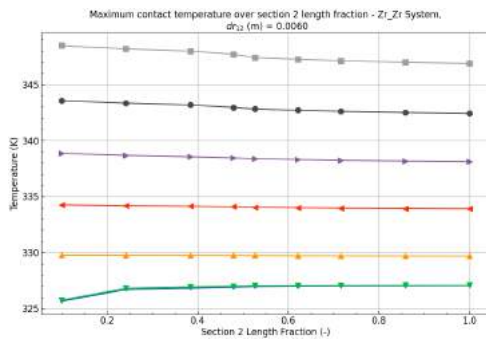
B.4



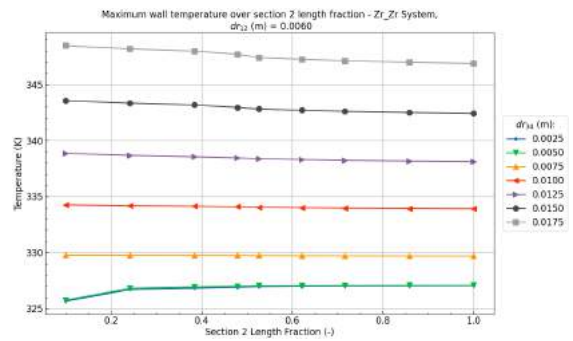
(a) Velocity over the section 2 fraction at $dr_{12_1} = 0.0060m$



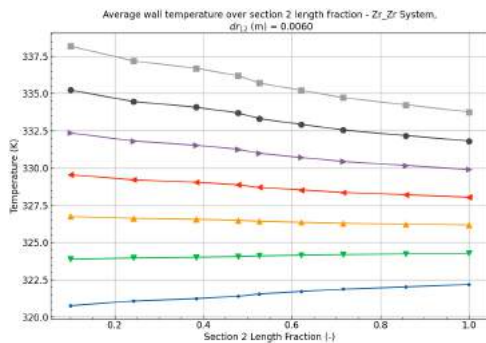
(b) Maximum target solution temperature over the section 2 fraction at $dr_{12_1} = 0.0060m$



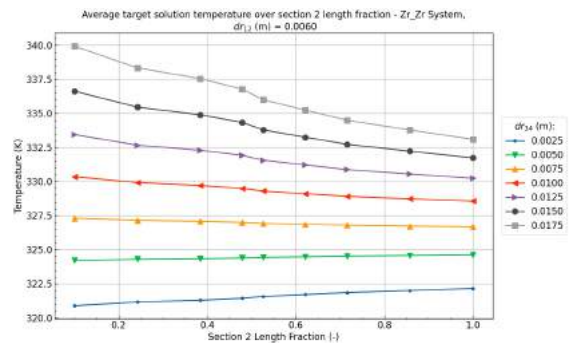
(c) Maximum contact temperature between the wall and the target solution over the section 2 fraction at $dr_{12_1} = 0.0060m$



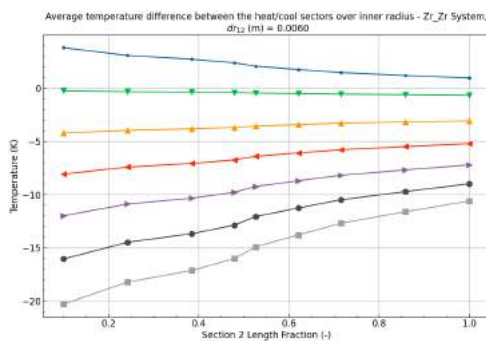
(d) Maximum wall temperature over the section 2 fraction at $dr_{12_1} = 0.0060m$



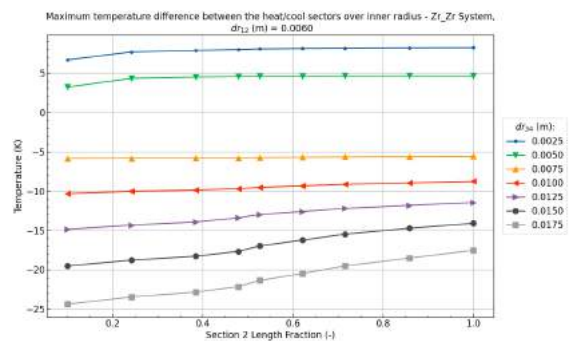
(e) Average target solution temperature over the section 2 fraction at $dr_{12_1} = 0.0060m$



(f) Average wall temperature over the section 2 fraction at $dr_{12_1} = 0.0060m$

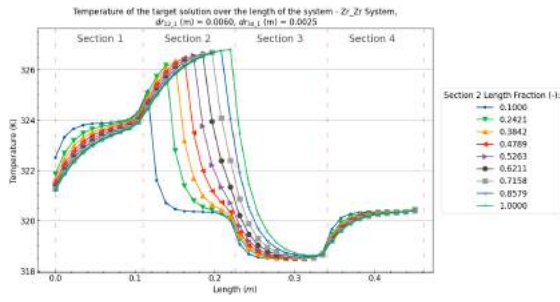


(g) Average target solution temperature difference between heating and cooling sectors over the section 2 fraction at $dr_{12_1} = 0.0060m$

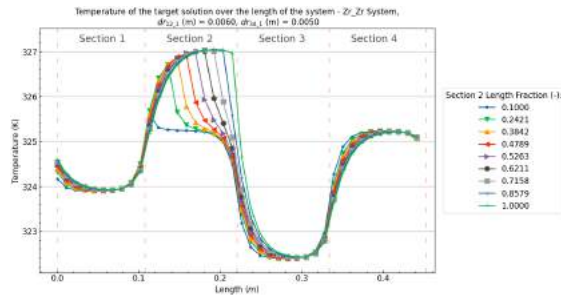


(h) Maximum target solution temperature difference between heating and cooling sectors over the section 2 fraction at $dr_{12_1} = 0.0060m$

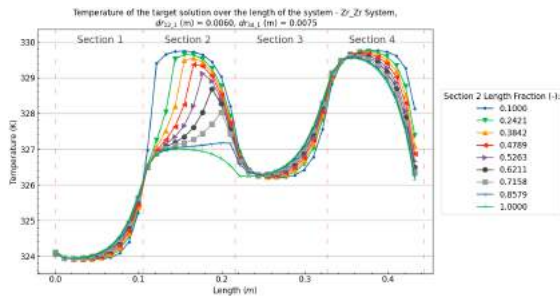
Figure B.121: Zr/Zr (Heat/Cool) System results over the section 2 fraction and cooling wall thickness dr_{34} at a heating wall thickness of $dr_{12} = 0.0060m$, a system length (L) of $0.4m$, and a pipe angle (θ) of 5° .



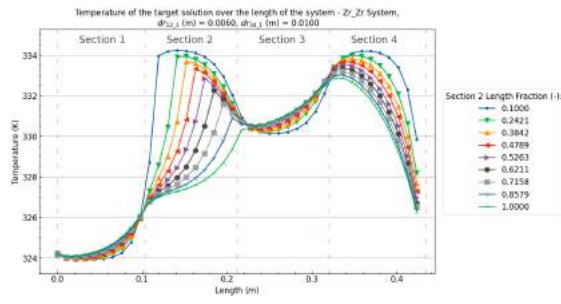
(a) Target solution temperature profiles over the the length of the system at different section 2 fractions at with $dr_{12,1}(m) = 0.0060m$ and $dr_{34,1}(m) = 0.0025$



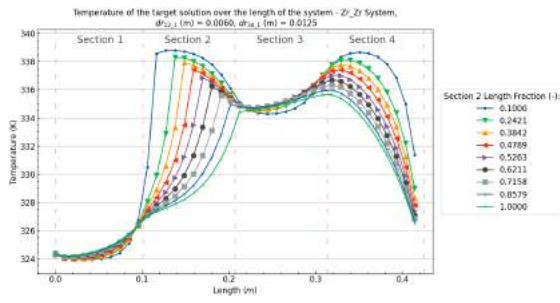
(b) Target solution temperature profiles over the the length of the system at different section 2 fractions at with $dr_{12,1}(m) = 0.0060m$ and $dr_{34,1}(m) = 0.0050$



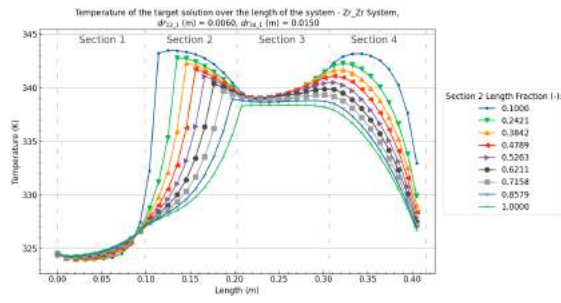
(c) Target solution temperature profiles over the the length of the system at different section 2 fractions at with $dr_{12,1}(m) = 0.0060m$ and $dr_{34,1}(m) = 0.0075$



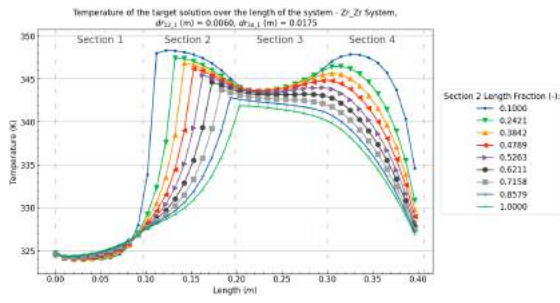
(d) Target solution temperature profiles over the the length of the system at different section 2 fractions at with $dr_{12,1}(m) = 0.0060m$ and $dr_{34,1}(m) = 0.0100$



(e) Target solution temperature profiles over the the length of the system at different section 2 fractions at with $dr_{12,1}(m) = 0.0060m$ and $dr_{34,1}(m) = 0.0125$



(f) Target solution temperature profiles over the the length of the system at different section 2 fractions at with $dr_{12,1}(m) = 0.0060m$ and $dr_{34,1}(m) = 0.0150$

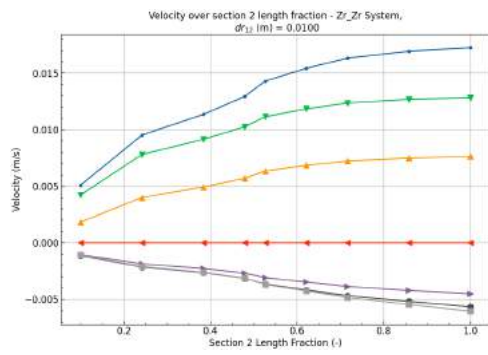


(g) Target solution temperature profiles over the the length of the system at different section 2 fractions at with $dr_{12,1}(m) = 0.0060m$ and $dr_{34,1}(m) = 0.0175$

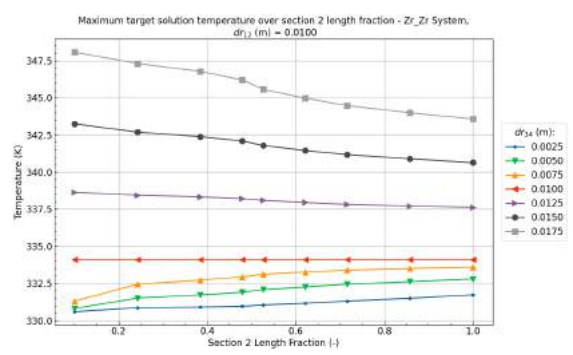
Figure B.122: Zr/Zr (Heat/Cool) System target solution temperature profiles over the section 2 fraction and cooling wall thickness dr_{34} at a heating wall thickness of $dr_{12} = 0.0060m$, a system length (L) of $0.4m$, and a pipe angle (θ) of 5° .

Zr/Zr - Section 2 length fraction at $dr_{12_1} = 0.0100m$ B.4

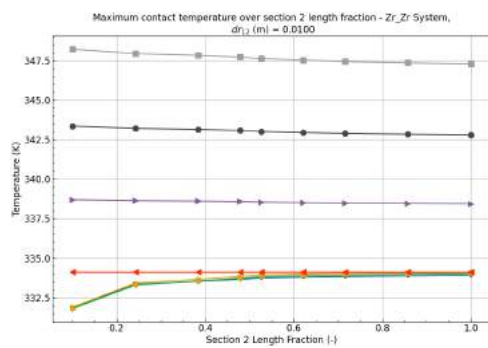
[Back to overview -](#)



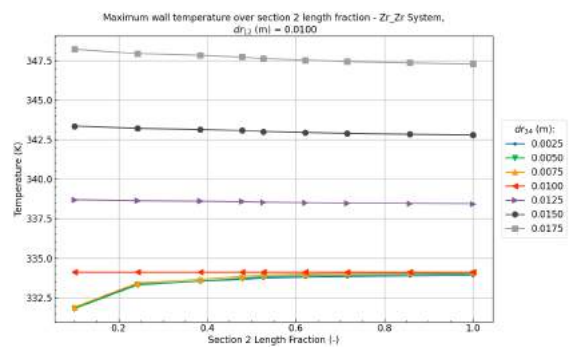
(a) Velocity over the section 2 fraction at $dr_{12_1} = 0.0100m$



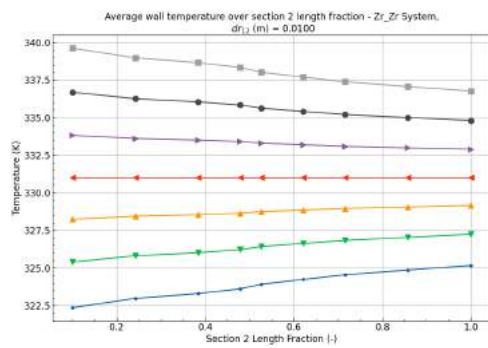
(b) Maximum target solution temperature over the section 2 fraction at $dr_{12_1} = 0.0100m$



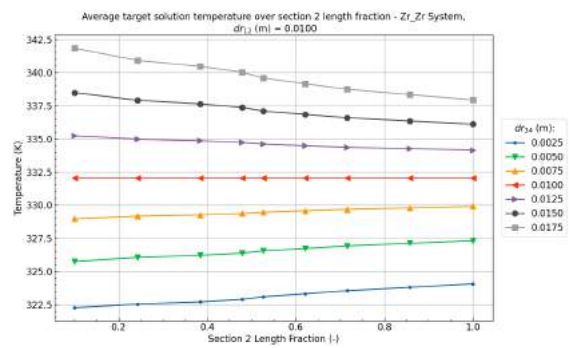
(c) Maximum contact temperature between the wall and the target solution over the section 2 fraction at $dr_{12_1} = 0.0100m$



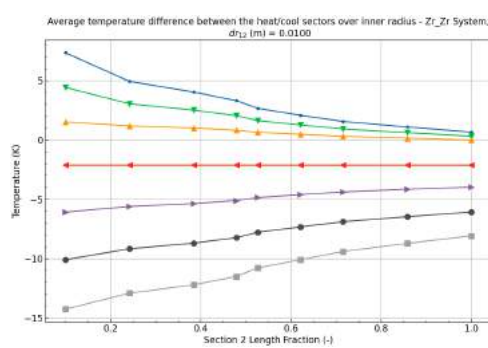
(d) Maximum wall temperature over the section 2 fraction at $dr_{12_1} = 0.0100m$



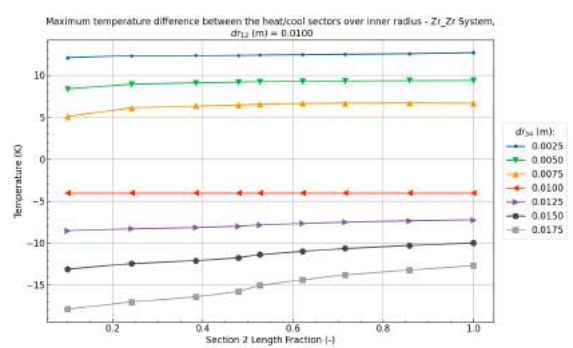
(e) Average target solution temperature over the section 2 fraction at $dr_{12_1} = 0.0100m$



(f) Average wall temperature over the section 2 fraction at $dr_{12_1} = 0.0100m$

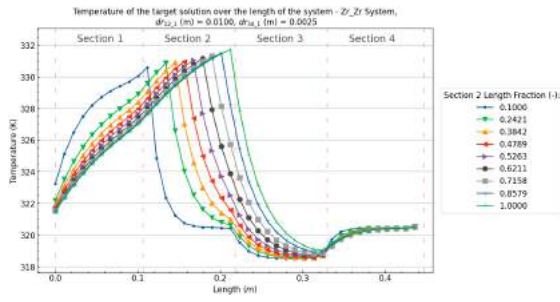


(g) Average target solution temperature difference between heating and cooling sectors over the section 2 fraction at $dr_{12_1} = 0.0100m$

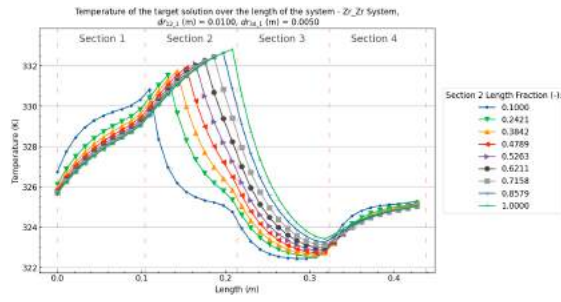


(h) Maximum target solution temperature difference between heating and cooling sectors over the section 2 fraction at $dr_{12_1} = 0.0100m$

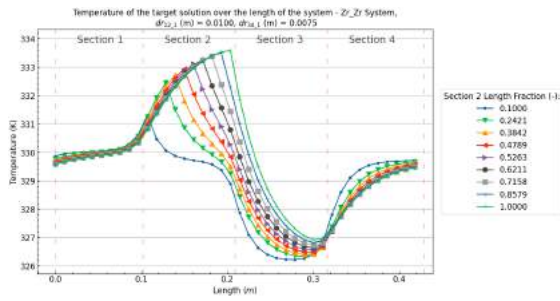
Figure B.123: Zr/Zr (Heat/Cool) System results over the section 2 fraction and cooling wall thickness dr_{34} at a heating wall thickness of $dr_{12} = 0.0100m$, a system length (L) of $0.4m$, and a pipe angle (θ) of 5° .



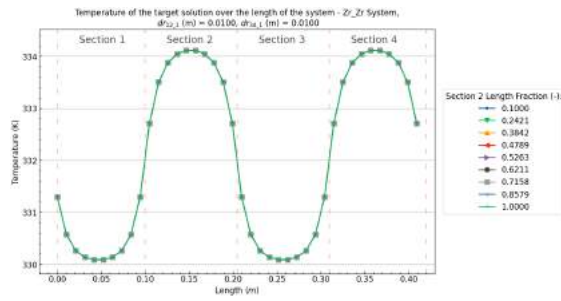
(a) Target solution temperature profiles over the the length of the system at different section 2 fractions at with $dr_{12,1}(m) = 0.0100m$ and $dr_{34,1}(m) = 0.0025$



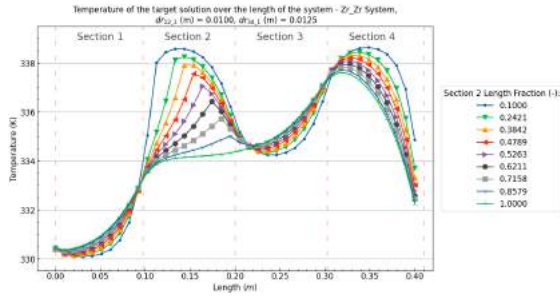
(b) Target solution temperature profiles over the the length of the system at different section 2 fractions at with $dr_{12,1}(m) = 0.0100m$ and $dr_{34,1}(m) = 0.0050$



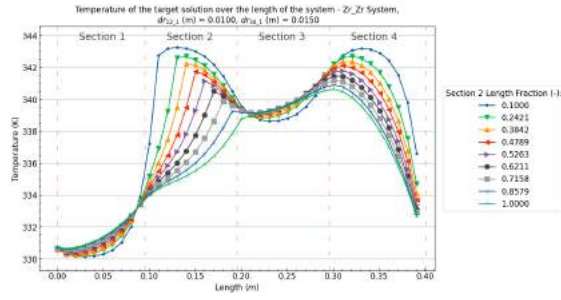
(c) Target solution temperature profiles over the the length of the system at different section 2 fractions at with $dr_{12,1}(m) = 0.0100m$ and $dr_{34,1}(m) = 0.0075$



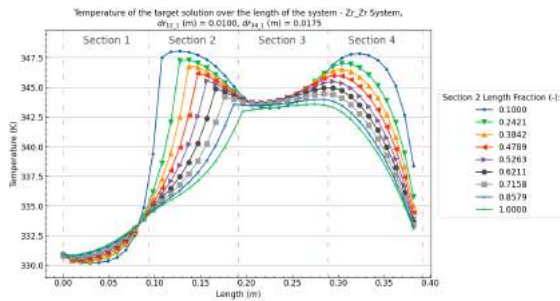
(d) Target solution temperature profiles over the the length of the system at different section 2 fractions at with $dr_{12,1}(m) = 0.0100m$ and $dr_{34,1}(m) = 0.0100$



(e) Target solution temperature profiles over the the length of the system at different section 2 fractions at with $dr_{12,1}(m) = 0.0100m$ and $dr_{34,1}(m) = 0.0125$



(f) Target solution temperature profiles over the the length of the system at different section 2 fractions at with $dr_{12,1}(m) = 0.0100m$ and $dr_{34,1}(m) = 0.0150$

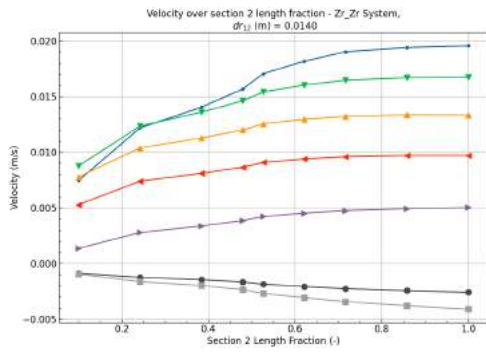


(g) Target solution temperature profiles over the the length of the system at different section 2 fractions at with $dr_{12,1}(m) = 0.0100m$ and $dr_{34,1}(m) = 0.0175$

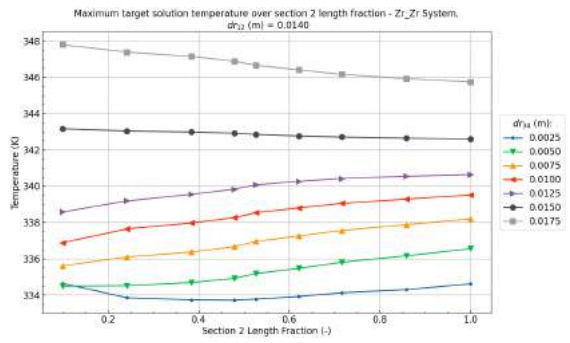
Figure B.124: Zr/Zr (Heat/Cool) System target solution temperature profiles over the section 2 fraction and cooling wall thickness dr_{34} at a heating wall thickness of $dr_{12} = 0.0100m$, a system length (L) of $0.4m$, and a pipe angle (θ) of 5° .

Zr/Zr - Section 2 length fraction at $dr_{12_1} = 0.0140m$
B.4

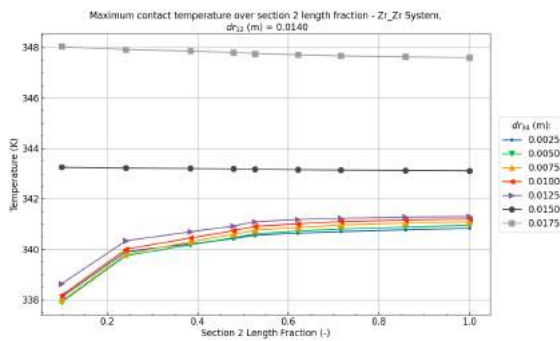
[Back to overview -](#)



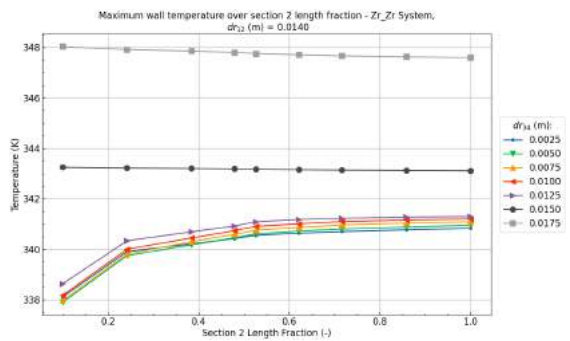
(a) Velocity over the section 2 fraction at $dr_{12_1} = 0.0140m$



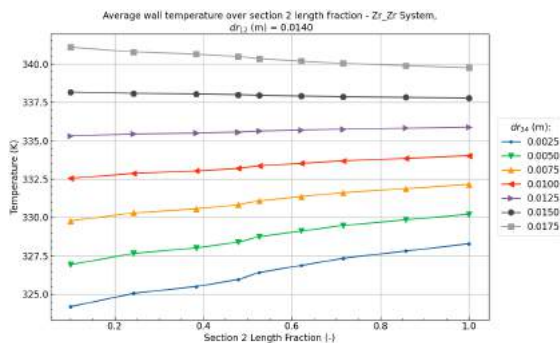
(b) Maximum target solution temperature over the section 2 fraction at $dr_{12_1} = 0.0140m$



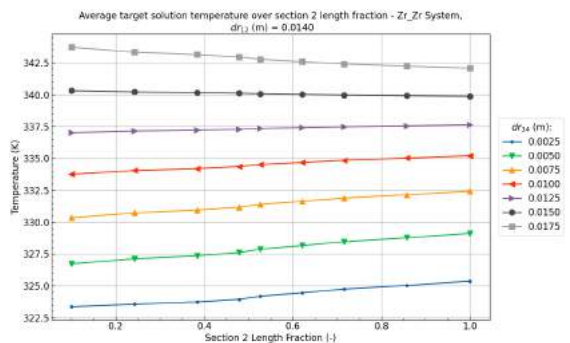
(c) Maximum contact temperature between the wall and the target solution over the section 2 fraction at $dr_{12_1} = 0.0140m$



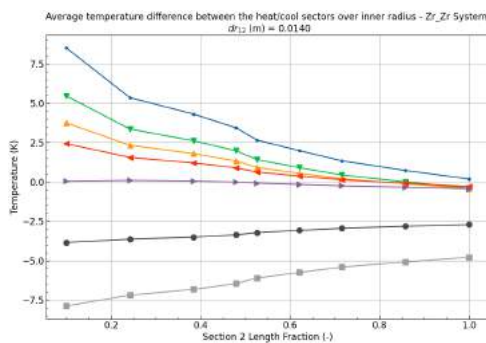
(d) Maximum wall temperature over the section 2 fraction at $dr_{12_1} = 0.0140m$



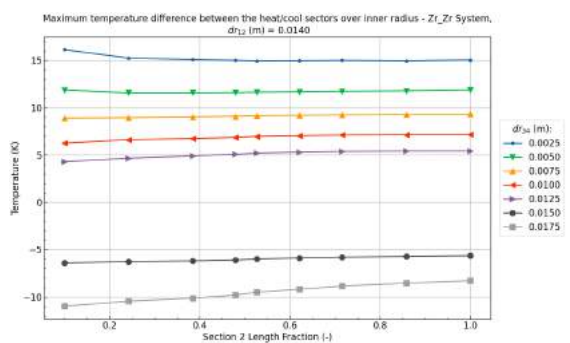
(e) Average target solution temperature over the section 2 fraction at $dr_{12_1} = 0.0140m$



(f) Average wall temperature over the section 2 fraction at $dr_{12_1} = 0.0140m$

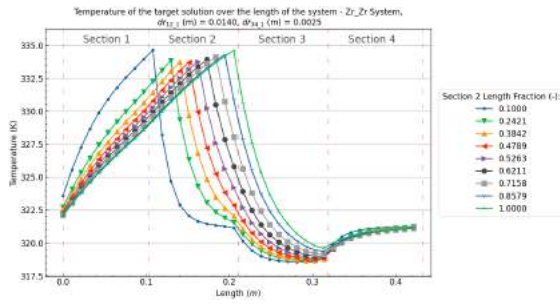


(g) Average target solution temperature difference between heating and cooling sectors over the section 2 fraction at $dr_{12_1} = 0.0140m$

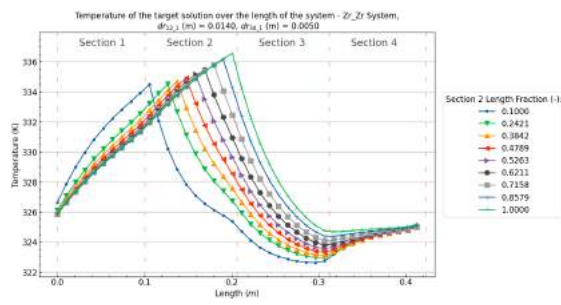


(h) Maximum target solution temperature difference between heating and cooling sectors over the section 2 fraction at $dr_{12_1} = 0.0140m$

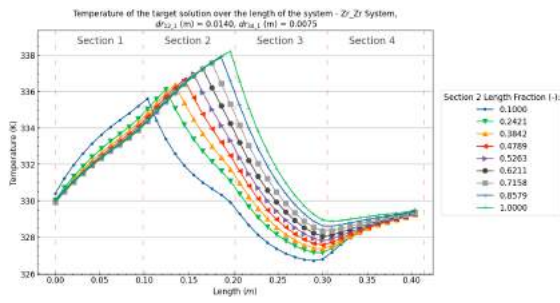
Figure B.125: Zr/Zr (Heat/Cool) System results over the section 2 fraction and cooling wall thickness dr_{34} at a heating wall thickness of $dr_{12} = 0.0140m$, a system length (L) of $0.4m$, and a pipe angle (θ) of 5° .



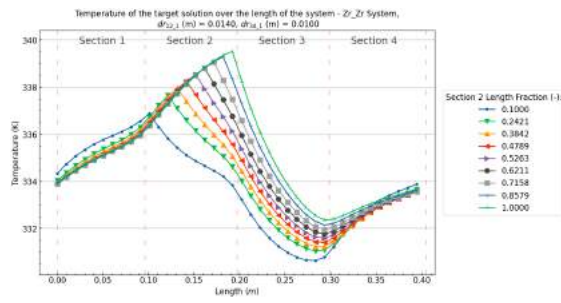
(a) Target solution temperature profiles over the the length of the system at different section 2 fractions at with $dr_{12_1}(m) = 0.0140m$ and $dr_{34_1}(m) = 0.0025$



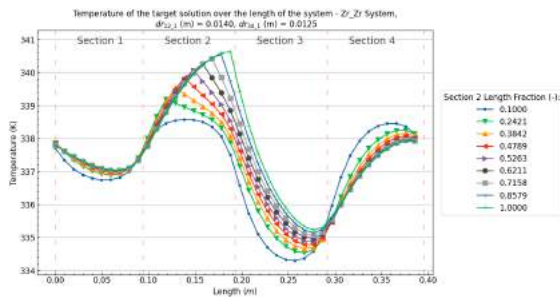
(b) Target solution temperature profiles over the the length of the system at different section 2 fractions at with $dr_{12_1}(m) = 0.0140m$ and $dr_{34_1}(m) = 0.0050$



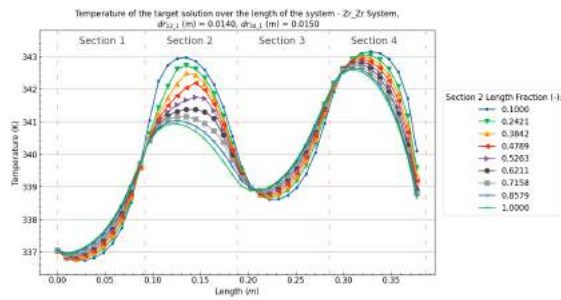
(c) Target solution temperature profiles over the the length of the system at different section 2 fractions at with $dr_{12_1}(m) = 0.0140m$ and $dr_{34_1}(m) = 0.0075$



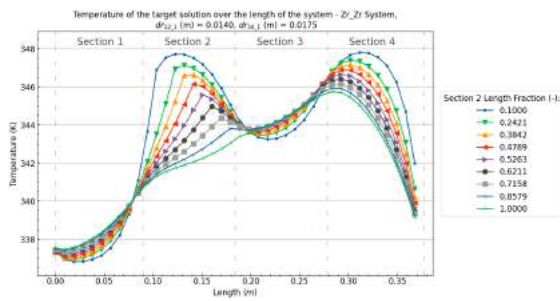
(d) Target solution temperature profiles over the the length of the system at different section 2 fractions at with $dr_{12_1}(m) = 0.0140m$ and $dr_{34_1}(m) = 0.0100$



(e) Target solution temperature profiles over the the length of the system at different section 2 fractions at with $dr_{12_1}(m) = 0.0140m$ and $dr_{34_1}(m) = 0.0125$



(f) Target solution temperature profiles over the the length of the system at different section 2 fractions at with $dr_{12_1}(m) = 0.0140m$ and $dr_{34_1}(m) = 0.0150$

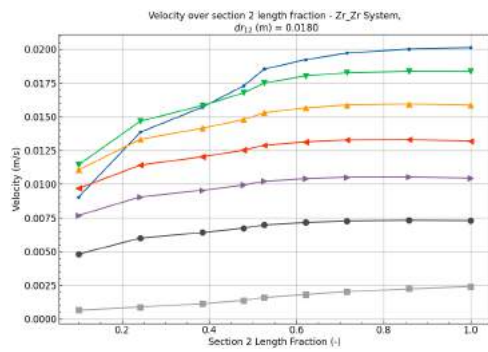


(g) Target solution temperature profiles over the the length of the system at different section 2 fractions at with $dr_{12_1}(m) = 0.0140m$ and $dr_{34_1}(m) = 0.0175$

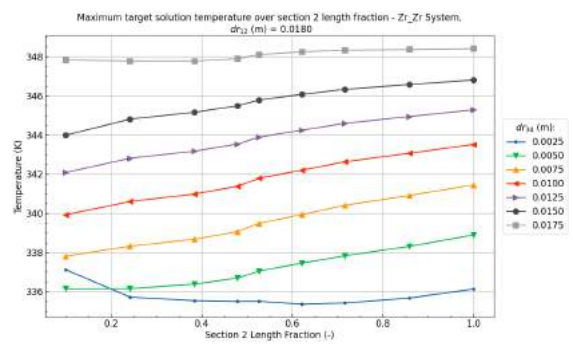
Figure B.126: Zr/Zr (Heat/Cool) System target solution temperature profiles over the section 2 fraction and cooling wall thickness dr_{34} at a heating wall thickness of $dr_{12} = 0.0140m$, a system length (L) of $0.4m$, and a pipe angle (θ) of 5° .

Zr/Zr - Section 2 length fraction at $dr_{12_1} = 0.0180m$ B.4

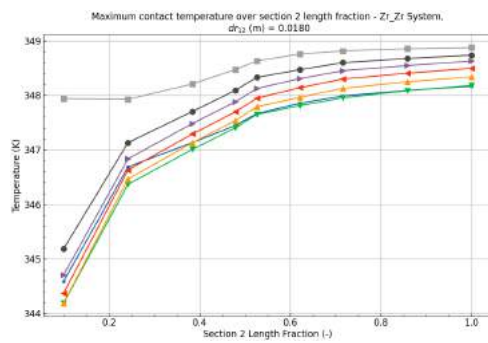
[Back to overview -](#)



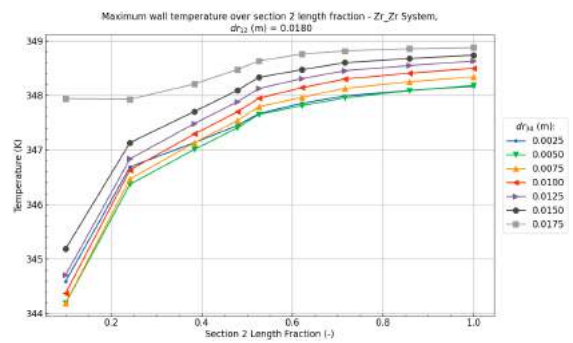
(a) Velocity over the section 2 fraction at $dr_{12_1} = 0.0180m$



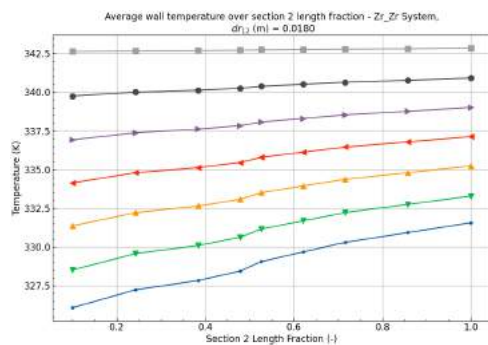
(b) Maximum target solution temperature over the section 2 fraction at $dr_{12_1} = 0.0180m$



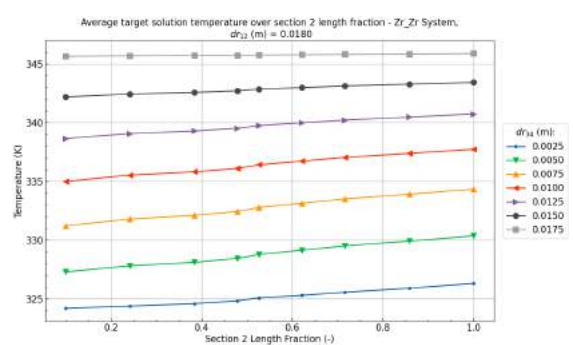
(c) Maximum contact temperature between the wall and the target solution over the section 2 fraction at $dr_{12_1} = 0.0180m$



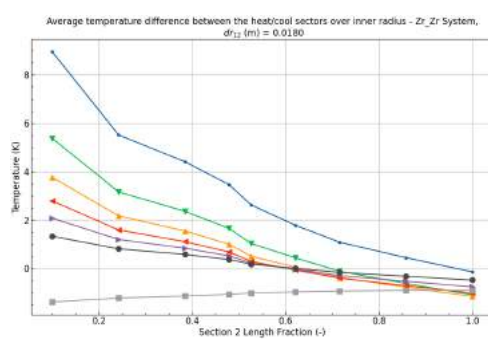
(d) Maximum wall temperature over the section 2 fraction at $dr_{12_1} = 0.0180m$



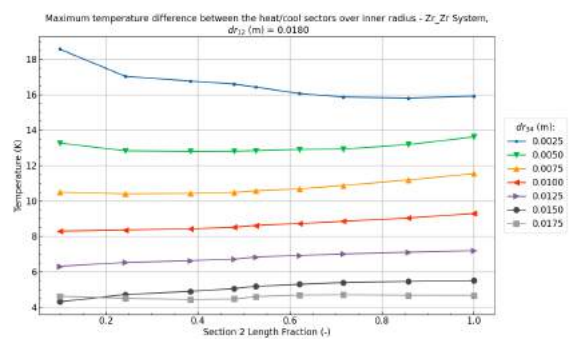
(e) Average target solution temperature over the section 2 fraction at $dr_{12_1} = 0.0180m$



(f) Average wall temperature over the section 2 fraction at $dr_{12_1} = 0.0180m$

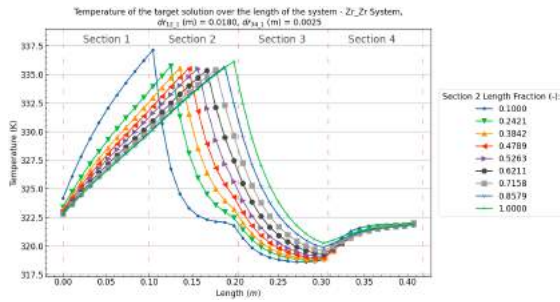


(g) Average target solution temperature difference between heating and cooling sectors over the section 2 fraction at $dr_{12_1} = 0.0180m$

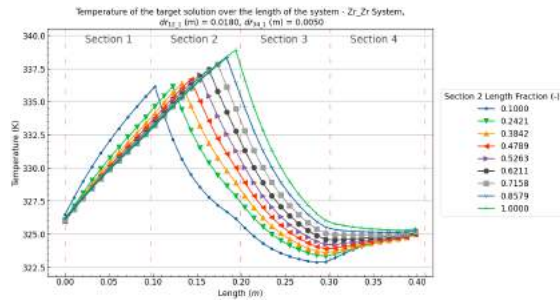


(h) Maximum target solution temperature difference between heating and cooling sectors over the section 2 fraction at $dr_{12_1} = 0.0180m$

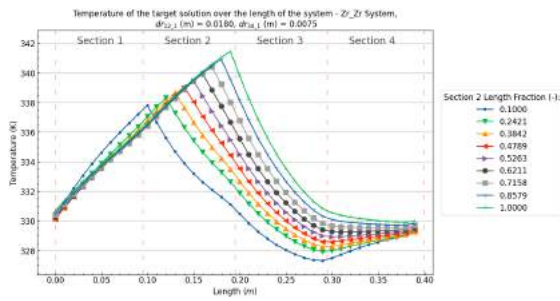
Figure B.127: Zr/Zr (Heat/Cool) System results over the section 2 fraction and cooling wall thickness dr_{34} at a heating wall thickness of $dr_{12} = 0.0180m$, a system length (L) of $0.4m$, and a pipe angle (θ) of 5° .



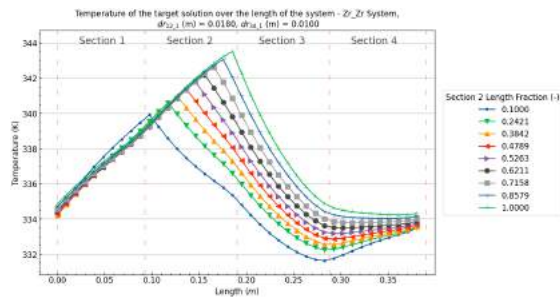
(a) Target solution temperature profiles over the the length of the system at different section 2 fractions at with $dr_{12_1}(m) = 0.0180m$ and $dr_{34_1}(m) = 0.0025$



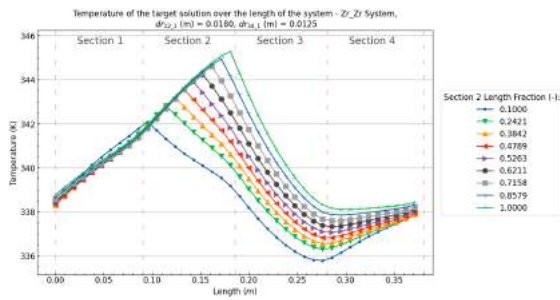
(b) Target solution temperature profiles over the the length of the system at different section 2 fractions at with $dr_{12_1}(m) = 0.0180m$ and $dr_{34_1}(m) = 0.0050$



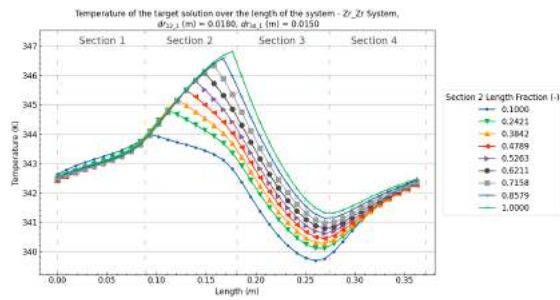
(c) Target solution temperature profiles over the the length of the system at different section 2 fractions at with $dr_{12_1}(m) = 0.0180m$ and $dr_{34_1}(m) = 0.0075$



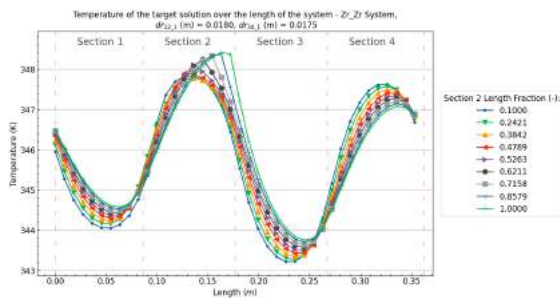
(d) Target solution temperature profiles over the the length of the system at different section 2 fractions at with $dr_{12_1}(m) = 0.0180m$ and $dr_{34_1}(m) = 0.0100$



(e) Target solution temperature profiles over the the length of the system at different section 2 fractions at with $dr_{12_1}(m) = 0.0180m$ and $dr_{34_1}(m) = 0.0125$



(f) Target solution temperature profiles over the the length of the system at different section 2 fractions at with $dr_{12_1}(m) = 0.0180m$ and $dr_{34_1}(m) = 0.0150$



(g) Target solution temperature profiles over the the length of the system at different section 2 fractions at with $dr_{12_1}(m) = 0.0180m$ and $dr_{34_1}(m) = 0.0175$

Figure B.128: Zr/Zr (Heat/Cool) System target solution temperature profiles over the section 2 fraction and cooling wall thickness dr_{34} at a heating wall thickness of $dr_{12} = 0.0180m$, a system length (L) of $0.4m$, and a pipe angle (θ) of 5° .

C

Appendix - Gamma and neutron source normalization

C.0.1. Gamma source profile and normalisation

The fractional gamma flux profile of the planar gamma source within the Serpent simulations was compared to the fractional flux profile of the ACRR on which it is based on. This comparison can be found in figure C.1.

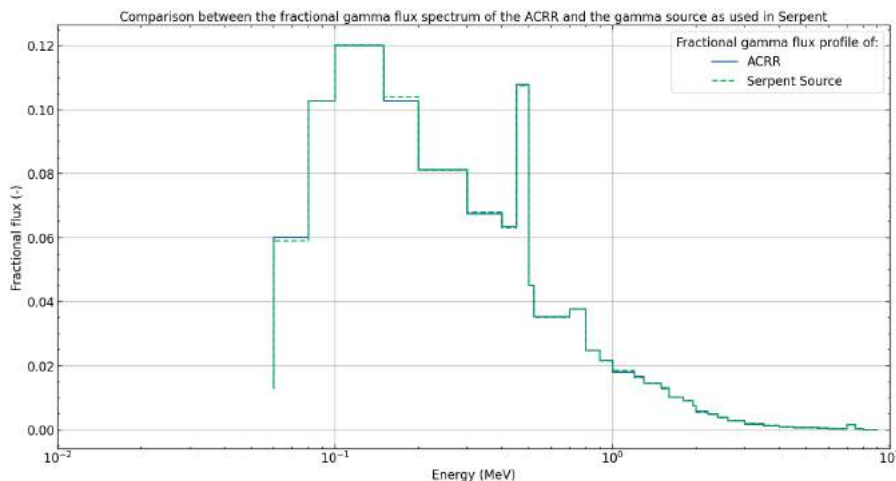


Figure C.1: Comparison between the fractional gamma flux profile from the data from the free field of the ACRR [48] and from the planar source as coded within Serpent.

Gamma Source Normalization

The source rate of the source plane within Serpent was normalized at a value of 1.232013×10^{22} . This source rate corresponds to a heat deposition rate of $299.691 \pm 0.018 W/kg$ to Zr with the flux profile as seen in C.1.

This normalization of the gamma flux was used in the further heat deposition and gamma dose rate results.

C.0.2. Neutron Source Normalization

By simulating the neutron output of the HOR at a power of $2 MWh$ onto the DLDR tube within Serpent, a sourcefile for the neutrons passing through the wall of the DLDR tube was created. From this simulation the value for the source rate for the neutron source within the DLDR tube wall material in Serpent was found at a value of 5.534101×10^{18} .

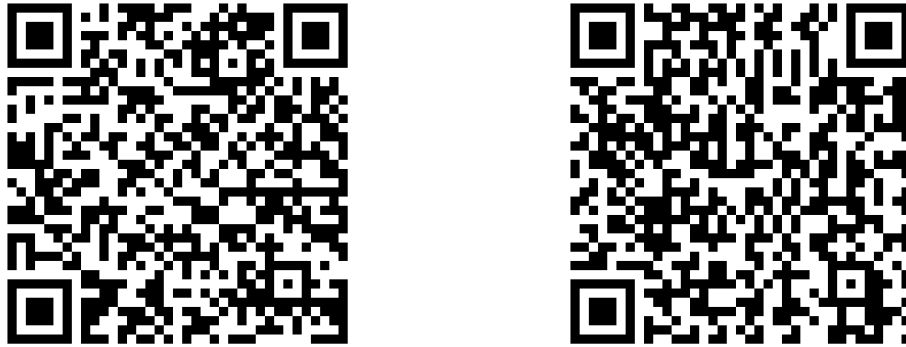


Figure C.2: QR code to a GitLab repository containing the code that generates the geometry and material files used in a Serpent simulation (left) and an example of files used inside Serpent simulations (right).

C.0.3. Code Example

The code for the Serpent simulations of a HEAL geometry are generated via python code. The files that this python code generates for a specific HEAL geometry and material consists consists of 6 different files:

1. materials.inp, consists of the definition of the the materials in the HEAL
2. geometry.inp, consists of the geometries that define the HEAL
3. det_n.inp, contains the different detectors for neutrons in certain parts of the geometry
4. det_p.inp, contains the different detectors for photons in certain parts of the geometry
5. system_n.inp, combines the other files to run the neutron simulation also contains the definition of the DLDR tube
6. system_p.inp, combines the other files to run the photon simulation also contains the definition of the DLDR tube

QR codes to a GitLab repository containing the code that generates these files and an example of files that have been generated by this code on an Aluminium-Lead walled system with an inner radius of 3mm , an aluminium wall thickness of 5mm and a lead wall thickness of 7mm can be found in figures C.2.

Listing C.1: materials.inp

```
set title "materials"

%-----Materials-----
%Inner_fluid
mat Inner_fluid -0.9982300000000001 moder lwtr 1001 %0.9982300000000001 g/cm^3
1001.80c 0.66667
8016.80c 0.33333

%Outer_fluid
mat Outer_fluid -0.98323 moder lwtr 1001 %0.98323 g/cm^3
1001.80c 0.66667
8016.80c 0.33333

%LuDOTA
mat LuDOTA -0.9982300000000001 %0.9982300000000001 g/cm^3
1001.80c 0.45283
6000.80c 0.301887
7014.80c 0.075197
7015.80c 0.0002747
8016.80c 0.1509434
```

```
71175.80c 0.0183792
71176.80c 0.000488678

%Lead
mat Lead -11.34 %11.34 g/cm^3
82204.80c 0.014
82206.80c 0.241
82207.80c 0.221
82208.80c 0.524

%Aluminium
mat Aluminium -2.7 %2.7 g/cm^3
13027.80c 1.0

%Zirconium
mat Zirconium -6.55 %6.55 g/cm^3
40090.80c 0.5145
40091.80c 0.1122
40092.80c 0.1715
40094.80c 0.1738
40096.80c 0.028

%Mix for target_solution
mix target_solution
Outer_fluid 0.9999942259432004
LuDOTA 5.774056799622566e-06

%Mix for target
mat target 1.0
71176.80c 1.0

%-----DLDR Tube definition-----
mat AlMg3 -2.66 % AlMg3
13027.80c 0.95000
12024.80c 0.03950
12025.80c 0.00500
12026.80c 0.00550
```


D

Appendix - LuDOTA Kinetics

D.1. Chemical reaction fitting

In figure D.1 a fit of a second order chemical reaction to the labeling efficiency of lutetium ions to DOTA molecules using the second order rate constant k_1 from 4.17.

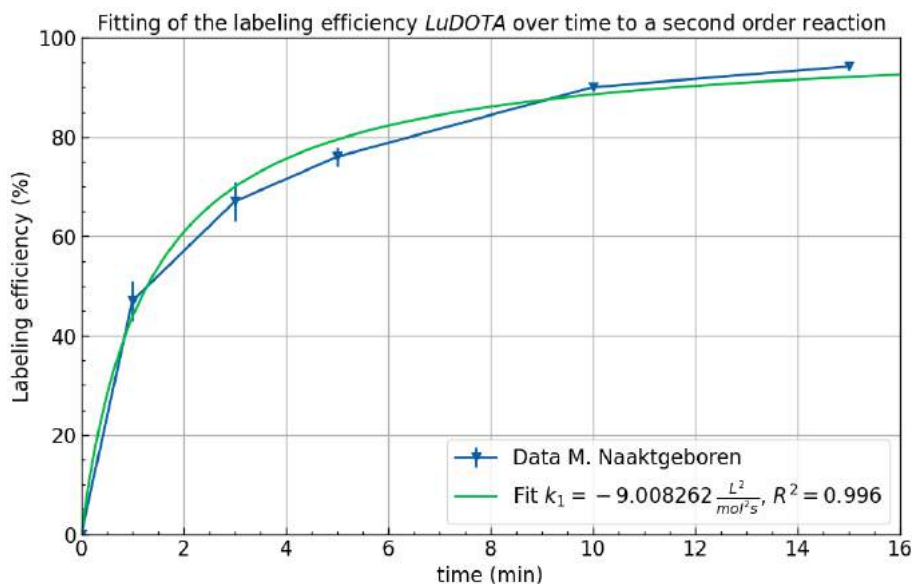


Figure D.1: Fit of a second order chemical reaction to the labeling efficiency over time from data from Naaktgeboren for the labeling of Lutetium ions and DOTA molecules at 40°C in a 1M sodium acetate acetic acid pH 4.3 buffer.

D.2. Gamma damage cross section

The cross section of gamma damage σ_{γ_dam1} and σ_{γ_dam2} in table 4.8 were calculated using the total mass attenuation coefficient data from the XCOM database [8] at a photon energy of 0.015MeV. This by summing the cross sections of the individual atoms that are present inside the LuDOTA complex for σ_{γ_dam1} and DOTA chelator for σ_{γ_dam2} . Plots of the mass attenuation coefficients of both LuDOTA and DOTA over the photon energy can be found in figure D.2. The individual cross sections from this data were calculated using equation D.1.

$$\sigma = \left(\frac{\mu}{\rho}\right) \frac{MW}{N_A} \quad (D.1)$$

With $(\frac{\mu}{\rho})$ the mass attenuation coefficient in $\frac{cm^2}{g}$, MW the molar weight of the molecule in $\frac{g}{mol}$, and N_A Avogadro's constant in $\frac{\#}{mol}$.

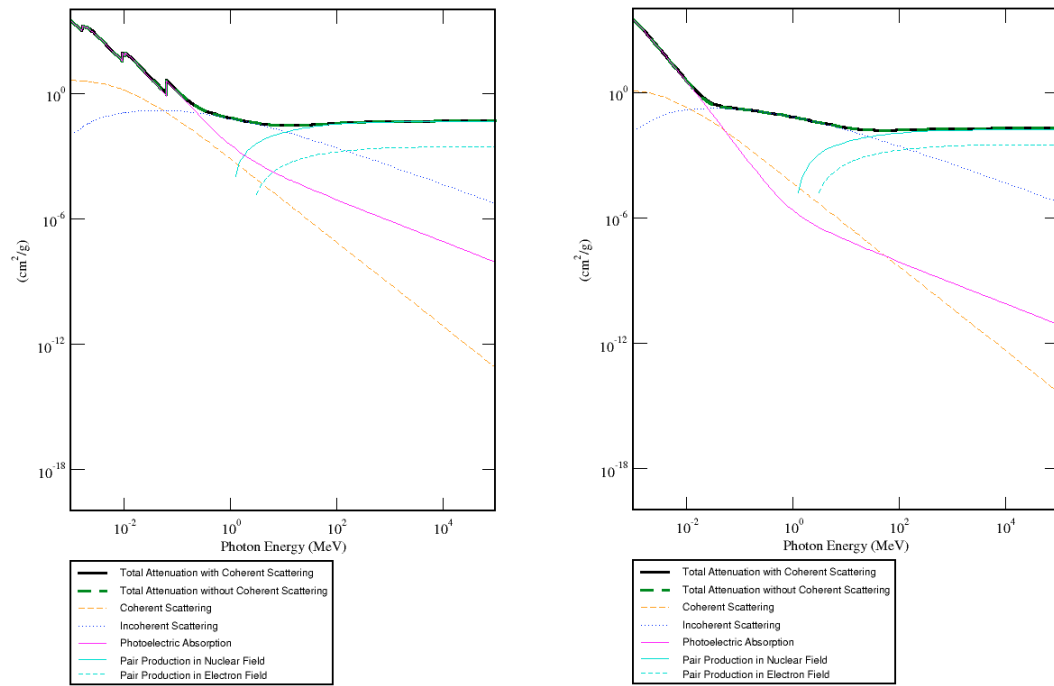


Figure D.2: Mass attenuation data over the photon energy spectrum with LuDOTA on the left and DOTA on the right.

E

Appendix - OpenFOAM code and settings

This appendix also includes an example of the used OpenFOAM boundary conditions and transportProperties for the systems solved with the buoyantBoussinesqPimpleFoam solver as well as the temperature boundary conditions from the scalarTransportFoam simulations.

The code consists of 6 different files:

1. U - buoyantBoussinesqPimpleFoam
2. T - buoyantBoussinesqPimpleFoam
3. p - buoyantBoussinesqPimpleFoam
4. p_rgh - buoyantBoussinesqPimpleFoam
5. transportProperties - buoyantBoussinesqPimpleFoam
6. T - scalarTransportFoam
7. U - scalarTransportFoam

A QR code containing a link to GitLab that includes examples of these files is given in E.1.



Figure E.1: QR codes linking to examples for the buoyantBoussinesqPimpleFoam code (left) and scalarTransportFoam pulse input (right)

Table E.1: The velocity values used in the x-coordinate of the uniformFixedValue of the inlet boundary condition for the different OpenFOAM simulations, from low to high

System Geometry	Inlet x-coordinate velocity value (m/s)							
	Velocity 1	Velocity 2	Velocity 3	Velocity 4	Velocity 5	Velocity 6	Velocity 7	Velocity 8
1	0.000163	0.000818	0.001644	0.003321	0.004172	0.008564	0.013193	0.018079
2	0.000069	0.000348	0.000699	0.001412	0.001774	0.003641	0.005609	0.007686
3	-0.000160	-0.000802	-0.001612	-0.003257	-0.004092	-0.008399	-0.012939	-0.017731
4	-0.000073	-0.000367	-0.000738	-0.001491	-0.001873	-0.003845	-0.005923	-0.008117
5	0.000325	0.001631	0.003278	0.006622	0.008320	0.017078	0.026310	0.036054
6	0.000053	0.000267	0.000537	0.001085	0.001363	0.002797	0.004309	0.005905
7	0.000375	0.001883	0.003784	0.007645	0.009606	0.019717	0.030374	0.041624
8	0.000031	0.000156	0.000313	0.000632	0.000794	0.001630	0.002511	0.003441
9	-0.000380	-0.001908	-0.003835	-0.007748	-0.009734	-0.019981	-0.030781	-0.042182
10	-0.000032	-0.000163	-0.000328	-0.000662	-0.000832	-0.001708	-0.002632	-0.003606
11	0.000376	0.001888	0.003794	0.007666	0.009631	0.019769	0.030456	0.041736
12	0.000014	0.000071	0.000143	0.000289	0.000363	0.000746	0.001149	0.001574
13	0.000409	0.002053	0.004128	0.008339	0.010478	0.021507	0.033132	0.045403
14	0.000016	0.000078	0.000157	0.000317	0.000399	0.000819	0.001261	0.001728
15	-0.000409	-0.002053	-0.004126	-0.008337	-0.010475	-0.021501	-0.033123	-0.045390
16	-0.000011	-0.000054	-0.000108	-0.000218	-0.000274	-0.000563	-0.000868	-0.001189
17	0.000439	0.002205	0.004432	0.008954	0.011250	0.023092	0.035575	0.048750
18	0.000009	0.000047	0.000094	0.000189	0.000237	0.000487	0.000751	0.001029

F

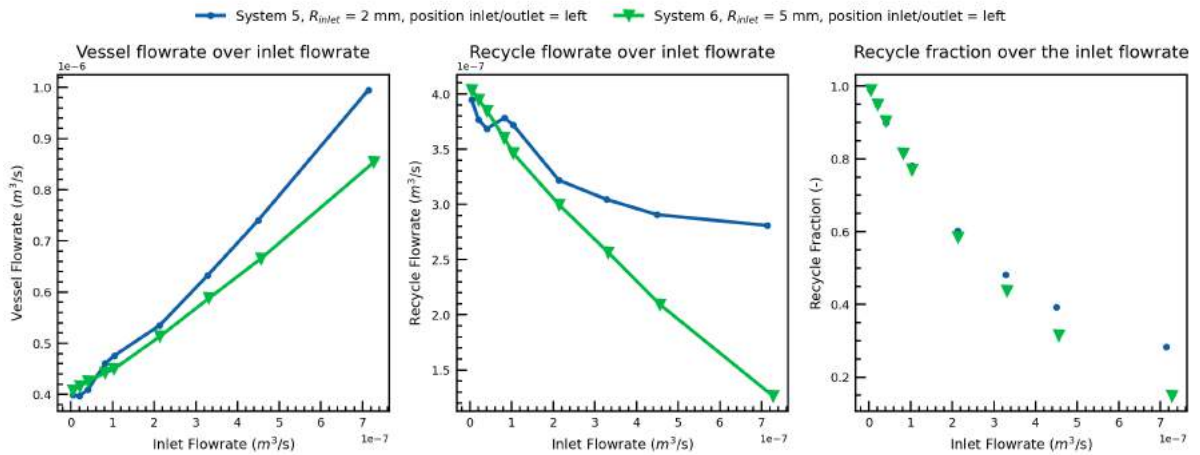
Appendix - Extra CFD and Tanks-In-Series results.

This appendix includes extra results from the CFD simulation and Tanks-In-Series compartment modelling. E-curves and TIS model parameters of the vessel segment can be found from appendix F2.1, for the recycle segment results and TIS model parameters F2.2 can be referred to.

F.1. Extended flowrate results

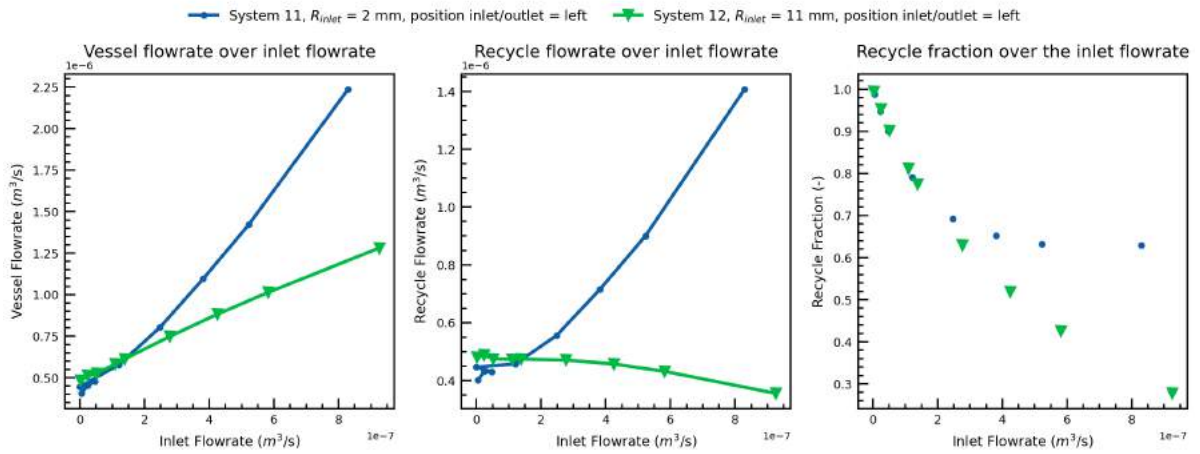
In figure F.1 flowrate results in vessels with 5, 11 and 15mm inner radius can be found. These contain similar results as in the results & discussion section. In table F.1 an overview of all the flowrates in all systems can be found as well as the dimensionless variance of the RTD response curve.

CFD flowrate results on systems with an inner radius of 5 mm



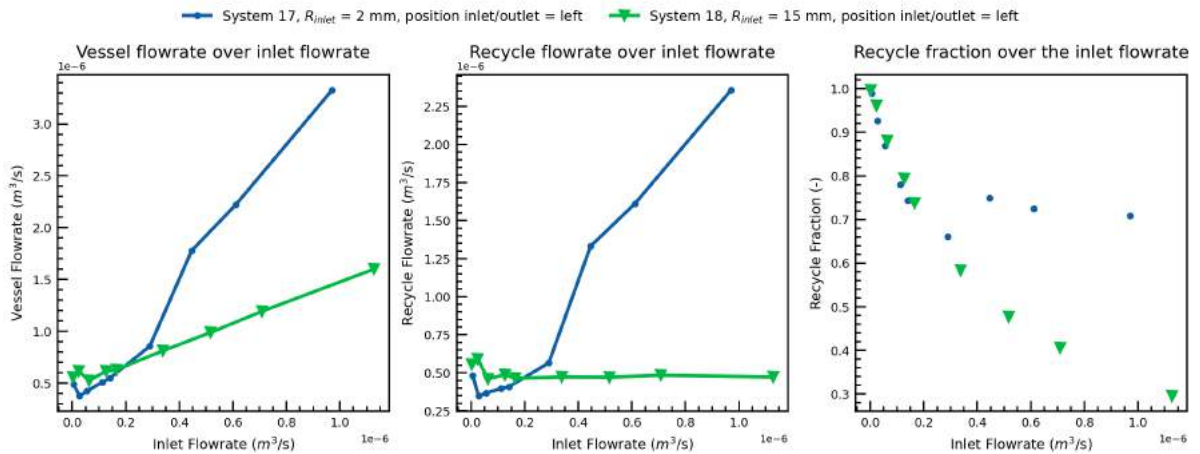
(a) 5 mm inner radius

CFD flowrate results on systems with an inner radius of 11 mm



(b) 11 mm inner radius

CFD flowrate results on systems with an inner radius of 15 mm



(c) 15 mm inner radius

Figure F1: CFD flowrate anresults on HEAL systems with an inner radius of 5, 11 and 15 mm (a, b, and c respectively) from the vessel and recycle segments with different inlet/outlet radii. Showing the increase in flowrate in the vessel segment at higher inlet flowrates and the divergence between the small and large inlet/outlet radii in the recycle flowrate over the inlet flowrate from the increase in resistance in the 2mm outlet. This limits the recycle fraction range in the small inlet/outlet radius systems within the same inlet flowrate range.

Table F1: Extended results showing all of the CFD simulation flowrate, mean residence time (\bar{t}) and dimensionless variance (σ_{θ}^2) results of both the vessel segment and recycle segments

System Number	Inlet Flow ($\frac{cm^3}{s}$)	Vessel Segment			Recycle Segment			Recycle Ratio	Recycle Fraction
		Vessel Flowrate ($\frac{cm^3}{s}$)	\bar{t} (s)	σ_{θ}^2 (-)	Recycle Flowrate ($\frac{cm^3}{s}$)	\bar{t} (s)	σ_{θ}^2 (-)		
1	0.00204	0.196	45.676	0.0654	0.196	14.196	0.3495	95.951	0.990
1	0.01023	0.207	43.835	0.0653	0.197	14.121	0.3417	19.239	0.951
1	0.02057	0.215	42.192	0.0631	0.195	14.286	0.3258	9.466	0.904
1	0.04156	0.223	40.800	0.0630	0.181	15.362	0.2934	4.357	0.813
1	0.05220	0.222	40.933	0.0639	0.170	16.391	0.2638	3.251	0.765
1	0.10707	0.244	37.221	0.0642	0.137	20.318	0.1801	1.279	0.561
1	0.16490	0.270	33.630	0.0708	0.105	26.443	0.1087	0.638	0.389
1	0.22598	0.308	29.496	0.0790	0.082	33.930	0.0641	0.363	0.268
1	0.33894	0.409	22.200	0.0988	0.050	53.370	0.0199	0.140	0.123
2	0.00197	0.202	46.373	0.0000	0.200	13.877	0.3380	101.683	0.990
2	0.01020	0.205	43.694	0.0853	0.195	14.246	0.3278	19.126	0.950
2	0.02015	0.213	43.973	0.0813	0.193	14.391	0.3259	9.581	0.905
2	0.04019	0.221	42.500	0.0938	0.180	15.399	0.2955	4.490	0.818
2	0.05590	0.225	41.680	0.0993	0.175	15.908	0.2804	3.473	0.776
2	0.10236	0.245	38.350	0.0973	0.142	19.547	0.2004	1.389	0.581
2	0.15738	0.271	34.631	0.0864	0.113	24.505	0.1310	0.721	0.419
2	0.21560	0.309	30.333	0.0944	0.094	29.706	0.0852	0.434	0.303
2	0.34247	0.401	23.392	0.1066	0.058	47.568	0.0794	0.171	0.146
3	0.00203	0.204	44.554	0.0945	0.202	13.775	0.2098	99.715	0.990
3	0.01003	0.211	43.007	0.0723	0.201	13.827	0.2047	20.056	0.953
3	0.02015	0.205	44.294	0.0694	0.185	15.042	0.1785	9.179	0.902
3	0.04071	0.213	42.566	0.0649	0.173	16.108	0.1536	4.242	0.809
3	0.05115	0.217	41.815	0.0642	0.166	16.749	0.1401	3.247	0.765
3	0.10602	0.246	37.162	0.0858	0.139	19.363	0.0864	1.328	0.570
3	0.16181	0.281	32.291	0.0713	0.120	23.278	0.0756	0.739	0.425
3	0.22175	0.319	28.548	0.0781	0.097	28.548	0.0806	0.439	0.305
3	0.35223	0.418	21.719	0.0964	0.066	42.151	0.1187	0.158	0.158
4	0.00207	0.203	46.214	0.1878	0.201	13.837	-	96.994	0.990
4	0.01032	0.211	43.368	0.1120	0.201	13.831	-	19.462	0.951
4	0.02079	0.216	43.320	0.1003	0.196	14.202	-	9.414	0.904
4	0.04198	0.224	41.803	0.1609	0.182	15.241	-	4.344	0.816
4	0.05275	0.220	42.576	0.1149	0.167	16.592	-	3.175	0.760
4	0.10824	0.257	36.416	0.1176	0.149	18.619	-	1.379	0.580
4	0.16683	0.285	33.192	0.0965	0.116	23.964	-	0.698	0.410
4	0.22832	0.325	28.881	0.0971	0.096	28.841	-	0.422	0.297
4	0.36284	0.430	21.814	0.1984	0.067	41.337	0.2019	0.185	0.156
5	0.00417	0.399	60.226	0.0598	0.395	18.034	0.2115	94.675	0.990
5	0.02032	0.397	60.511	0.0539	0.377	18.897	0.1893	18.542	0.949
5	0.04063	0.409	58.864	0.0523	0.369	19.315	0.1766	9.028	0.900
5	0.08253	0.461	52.132	0.0556	0.378	18.817	0.1726	4.584	0.821
5	0.10371	0.476	50.506	0.0569	0.372	19.138	0.1626	3.587	0.782
5	0.21292	0.535	44.912	0.0664	0.322	22.108	0.1277	1.512	0.602
5	0.32804	0.632	37.986	0.0954	0.304	23.384	0.1173	0.928	0.481
5	0.44951	0.740	32.458	0.1548	0.291	24.491	0.2409	0.647	0.393
5	0.71391	0.995	24.149	0.0619	0.281	25.340	0.2373	0.393	0.282
6	0.00445	0.408	62.230	0.1660	0.404	17.598	0.2037	90.706	0.989
6	0.02100	0.416	61.078	0.1153	0.395	17.993	0.2027	18.797	0.949
6	0.04103	0.426	59.637	0.0825	0.385	18.460	0.1901	9.377	0.904
6	0.08218	0.442	57.383	0.0865	0.360	19.172	0.1723	4.384	0.814
6	0.10345	0.450	56.438	0.0850	0.346	20.501	0.1586	3.348	0.770
6	0.21376	0.514	49.442	0.0743	0.300	23.692	0.1433	1.402	0.584
6	0.33114	0.588	43.171	0.0758	0.257	27.689	0.2208	0.774	0.436
6	0.45616	0.685	38.132	0.0883	0.269	33.928	0.3094	0.459	0.315
6	0.72751	0.854	29.729	0.1522	0.127	56.136	0.3476	0.174	0.148
7	0.00474	0.449	100.346	0.0761	0.444	28.783	0.1827	93.613	0.989
7	0.02361	0.465	97.379	0.0698	0.442	28.940	0.1834	18.713	0.949
7	0.04745	0.483	93.828	0.0650	0.436	29.334	0.2127	9.178	0.902
7	0.09588	0.527	86.015	0.0584	0.431	29.665	0.2586	4.495	0.818
7	0.12046	0.552	82.119	0.0584	0.431	29.637	0.2627	3.581	0.780
7	0.24729	0.700	64.700	0.0865	0.453	28.215	0.1469	1.832	0.647
7	0.36998	0.896	50.549	0.1543	0.518	24.798	0.1681	1.353	0.575
7	0.52210	1.085	41.766	0.2554	0.363	22.712	0.1922	1.078	0.519
7	0.82918	1.534	29.548	0.3015	0.704	18.148	0.3194	0.850	0.459
8	0.00379	0.458	105.970	0.1807	0.455	28.019	0.6922	119.809	0.992
8	0.02316	0.486	100.005	0.2599	0.463	27.536	0.1741	19.975	0.952
8	0.04772	0.481	101.023	0.1223	0.433	28.409	0.1983	9.016	0.901
8	0.09579	0.519	93.655	0.1158	0.423	30.122	0.1910	4.411	0.815
8	0.11936	0.537	90.413	0.1128	0.418	30.479	0.1937	3.501	0.778
8	0.24166	0.631	76.962	0.0873	0.389	32.702	0.2602	1.612	0.617
8	0.37328	0.732	66.385	0.0819	0.338	35.536	0.3002	0.960	0.490
8	0.51552	0.813	59.767	0.0910	0.297	42.854	0.3310	0.577	0.366
8	0.82225	1.044	46.527	0.1203	0.222	57.440	0.3904	0.270	0.212
9	0.00474	0.450	100.698	0.1065	0.445	28.711	0.4871	93.843	0.989
9	0.02380	0.462	98.050	0.0794	0.438	29.163	0.5436	18.417	0.948
9	0.04785	0.479	94.655	0.0606	0.431	29.662	0.5856	9.007	0.900
9	0.09667	0.523	88.617	0.0349	0.426	29.975	0.5928	4.412	0.815
9	0.12145	0.542	83.689	0.0286	0.420	30.427	0.5854	3.459	0.756
9	0.24918	0.665	68.162	0.0226	0.416	30.757	0.4840	1.668	0.625
9	0.38363	0.831	54.530	0.0286	0.447	28.575	0.7981	1.166	0.538
9	0.52555	1.041	43.534	0.0338	0.515	24.806	0.5022	0.981	0.495
9	0.83457	1.472	30.783	0.0636	0.638	20.052	0.1520	0.764	0.433

System Number	Inlet Flow ($\frac{cm^3}{s}$)	Vessel Segment			Recycle Segment			Recycle Ratio	Recycle Fraction
		Vessel Flowrate ($\frac{cm^3}{s}$)	\bar{t} (s)	σ_{θ}^2 (-)	Recycle Flowrate ($\frac{cm^3}{s}$)	\bar{t} (s)	σ_{θ}^2 (-)		
10	0.00502	0.467	104.061	0.2778	0.462	27.592	0.6272	91.867	0.989
10	0.02532	0.476	102.024	0.1226	0.451	28.264	0.5567	17.795	0.947
10	0.05039	0.484	100.289	0.1359	0.434	29.361	0.5485	8.609	0.896
10	0.10094	0.528	91.956	0.1786	0.427	29.819	0.4978	4.232	0.809
10	0.12667	0.550	88.352	0.1926	0.423	30.114	0.5088	3.359	0.770
10	0.02366	0.454	228.503	0.1069	0.431	59.893	0.2440	18.197	0.948
10	0.04017	0.753	64.497	0.0887	0.353	36.110	0.5258	0.881	0.468
10	0.05055	0.869	55.869	0.0924	0.319	39.974	0.5288	0.579	0.367
10	0.07565	1.121	43.318	0.1195	0.245	51.910	0.3132	0.280	0.219
11	0.00477	0.406	255.874	0.1011	0.401	64.330	0.2046	84.029	0.988
11	0.02366	0.454	228.503	0.1069	0.431	59.893	0.2440	18.197	0.948
11	0.04757	0.478	217.325	0.1091	0.430	59.969	0.2826	9.040	0.900
11	0.09000	0.447	232.416	-	0.447	57.745	0.1969	-	1.000
11	0.12070	0.578	179.545	0.1078	0.457	56.381	0.1818	3.790	0.791
11	0.24782	0.803	129.246	0.1337	0.555	46.427	0.1703	2.243	0.692
11	0.38133	1.096	94.714	0.2015	0.715	36.091	0.2275	1.874	0.652
11	0.52238	1.422	72.985	0.3210	0.900	28.662	0.2947	1.722	0.633
11	0.82937	2.237	46.395	0.3705	1.408	18.318	0.5575	1.697	0.629
12	0.00241	0.482	236.619	0.1068	0.479	53.332	0.4014	199.185	0.995
12	0.02404	0.512	222.597	0.1251	0.488	52.376	0.4003	29.299	0.953
12	0.05171	0.526	216.647	0.1378	0.474	54.086	0.3419	9.171	0.902
12	0.10998	0.583	195.442	0.1096	0.473	54.223	0.3774	4.302	0.811
12	0.13837	0.612	186.131	0.1062	0.474	54.134	0.3094	3.424	0.774
12	0.27727	0.748	132.389	0.1215	0.471	54.518	0.2590	1.697	0.629
12	0.42502	0.882	129.159	0.1299	0.457	56.988	0.3623	1.076	0.518
12	0.58168	1.013	112.464	0.1294	0.432	59.437	0.3859	0.742	0.426
12	0.92574	1.281	88.945	0.1531	0.355	72.165	0.3619	0.384	0.277
13	0.00521	0.412	338.724	0.1044	0.406	78.670	0.2527	78.024	0.987

F.2. Tank-In-Series Compartment Model

The Tanks-In-Series compartment model parameters for the systems ran in OpenFOAM can be found in table F.2 for systems 1 to 9 and F.3 for systems 10-18. The resultant RTD curves from the model parameters and the RTD curves of the systems from the OpenFOAM simulations can be found for each system and segment in figures F.2 to F.17 for the vessel segment and figures F.18 to F.33 for the recycle segments.

Table F.2: Overview of the Tanks-In-Series compartment model parameters for the CFD results of the systems 1 to 9 in the vessel (ves) and recycle (rec) segments as defined in table 4.9.

System Nr. (4,9)	Inlet Flowrate (cm ³ /s)	Vessel Flowrate (cm ³ /s)	Segment Flowrate (cm ³ /s)	N1 [ves/rec]	N2 [ves/rec]	N3 [ves/rec]	N4 [ves/rec]	N5 [ves/rec]	V1 (m ³) [ves/rec]	V2 [ves/rec]	V3 (m ³) [ves/rec]	V4 (m ³) [ves/rec]	V5 (m ³) [ves/rec]	frac1 (-) [ves/rec]	frac2 (-) [ves/rec]	frac3 (-) [ves/rec]	frac4 (-) [ves/rec]	frac5 (-) [ves/rec]	R ² [ves/rec]	Residual F ₀ [ves/rec]
1	0.0020	0.1940	0.1940	115/130	27/11	33/1	13/0	2/0	6.44E-06/1.60E-06	4.62E-07/1.15E-08	2.34E-07/1.17E-06	7.75E-07/0.00E+00	1.17E-06/0.00E+00	0.088/0.325	0.934/0.675	0.296/0.000	0.211/0.000	0.915/0.977	0.915/0.977	3.74/1.423
2	0.0020	0.1940	0.1940	115/130	27/11	33/1	13/0	2/0	6.44E-06/1.60E-06	4.62E-07/1.15E-08	2.34E-07/1.17E-06	7.75E-07/0.00E+00	1.17E-06/0.00E+00	0.088/0.325	0.934/0.675	0.296/0.000	0.211/0.000	0.915/0.977	0.915/0.977	3.74/1.423
3	0.0020	0.1940	0.1940	115/130	27/11	33/1	13/0	2/0	6.44E-06/1.60E-06	4.62E-07/1.15E-08	2.34E-07/1.17E-06	7.75E-07/0.00E+00	1.17E-06/0.00E+00	0.088/0.325	0.934/0.675	0.296/0.000	0.211/0.000	0.915/0.977	0.915/0.977	3.74/1.423
4	0.0020	0.1940	0.1940	115/130	27/11	33/1	13/0	2/0	6.44E-06/1.60E-06	4.62E-07/1.15E-08	2.34E-07/1.17E-06	7.75E-07/0.00E+00	1.17E-06/0.00E+00	0.088/0.325	0.934/0.675	0.296/0.000	0.211/0.000	0.915/0.977	0.915/0.977	3.74/1.423
5	0.0020	0.1940	0.1940	115/130	27/11	33/1	13/0	2/0	6.44E-06/1.60E-06	4.62E-07/1.15E-08	2.34E-07/1.17E-06	7.75E-07/0.00E+00	1.17E-06/0.00E+00	0.088/0.325	0.934/0.675	0.296/0.000	0.211/0.000	0.915/0.977	0.915/0.977	3.74/1.423
6	0.0020	0.1940	0.1940	115/130	27/11	33/1	13/0	2/0	6.44E-06/1.60E-06	4.62E-07/1.15E-08	2.34E-07/1.17E-06	7.75E-07/0.00E+00	1.17E-06/0.00E+00	0.088/0.325	0.934/0.675	0.296/0.000	0.211/0.000	0.915/0.977	0.915/0.977	3.74/1.423
7	0.0020	0.1940	0.1940	115/130	27/11	33/1	13/0	2/0	6.44E-06/1.60E-06	4.62E-07/1.15E-08	2.34E-07/1.17E-06	7.75E-07/0.00E+00	1.17E-06/0.00E+00	0.088/0.325	0.934/0.675	0.296/0.000	0.211/0.000	0.915/0.977	0.915/0.977	3.74/1.423
8	0.0020	0.1940	0.1940	115/130	27/11	33/1	13/0	2/0	6.44E-06/1.60E-06	4.62E-07/1.15E-08	2.34E-07/1.17E-06	7.75E-07/0.00E+00	1.17E-06/0.00E+00	0.088/0.325	0.934/0.675	0.296/0.000	0.211/0.000	0.915/0.977	0.915/0.977	3.74/1.423
9	0.0020	0.1940	0.1940	115/130	27/11	33/1	13/0	2/0	6.44E-06/1.60E-06	4.62E-07/1.15E-08	2.34E-07/1.17E-06	7.75E-07/0.00E+00	1.17E-06/0.00E+00	0.088/0.325	0.934/0.675	0.296/0.000	0.211/0.000	0.915/0.977	0.915/0.977	3.74/1.423

Table F3: Overview of the Tanks-In-Series compartment model parameters for the CFD results of the systems 10 to 18 in the vessel (ves) and recycle (rec) segments as defined in table 4.9.

System No. (4,9)	Inlet Flowrate (cm^3/s)	Vessel Flowrate (cm^3/s)	Segment Flowrate (cm^3/s)	N1 [ves/rec]	N2 [ves/rec]	N3 [ves/rec]	N4 [ves/rec]	N5 [ves/rec]	V1 (m^3) [ves/rec]	V2 (m^3) [ves/rec]	V3 (m^3) [ves/rec]	V4 (m^3) [ves/rec]	V5 (m^3) [ves/rec]	frac1 (-) [ves/rec]	frac2 (-) [ves/rec]	frac3 (-) [ves/rec]	frac4 (-) [ves/rec]	frac5 (-) [ves/rec]	Residual F_{C0} [ves/rec]
10	0.0050	0.667	0.4616	107/9	1/20	10/24	5/22	3/1	3.36E-05/4.05E-06	2.7E-06/6.91E-07	1.8E-06/5.56E-07	3.28E-06/3.33E-06	6.82E-06/4.91E-06	0.197/0.074	0.477/0.150	0.254/0.033	0.192/0.383	0.98E/0.996	0.728/0.188
10	0.0253	0.7680	0.4506	107/9	14/39	15/38	8/22	3/1	3.90E-05/4.21E-06	3.2E-06/6.01E-07	1.07E-06/5.79E-07	3.34E-06/7.40E-06	6.08E-06/4.95E-06	0.78E/0.053	0.442/0.332	0.182/0.392	0.190/0.402	0.98E/0.998	0.651/0.334
10	0.0564	0.4682	0.4338	103/93	18/34	18/42	11/20	2/1	3.57E-05/4.30E-06	2.2E-06/6.81E-07	1.07E-06/5.91E-07	3.12E-06/7.39E-06	6.43E-06/4.8E-06	0.08E/0.053	0.475/0.153	0.251/0.394	0.188/0.400	0.99E/0.997	0.653/0.134
10	0.1069	0.5281	0.4271	105/93	23/33	12/42	9/18	2/1	3.40E-05/4.71E-06	2.38E-06/6.51E-07	1.37E-06/5.41E-07	3.61E-06/7.29E-06	7.27E-06/4.63E-06	0.002/0.053	0.459/0.153	0.266/0.397	0.192/0.386	0.99E/0.996	0.447/0.174
10	0.1936	0.4936	0.4420	104/96	22/29	14/45	8/18	2/1	3.94E-05/4.78E-06	2.49E-06/6.57E-07	1.37E-06/5.63E-07	3.61E-06/7.29E-06	7.43E-06/4.94E-06	0.002/0.053	0.470/0.158	0.270/0.389	0.194/0.386	0.99E/0.986	0.470/0.160
10	0.3002	0.7529	0.4357	115/107	9/18	35/42	2/17	3/2	3.02E-06/1.92E-06	3.20E-06/1.92E-06	1.80E-06/1.29E-06	1.50E-06/2.00E-06	6.77E-06/4.00E-06	0.129/0.049	0.490/0.153	0.196/0.388	0.186/0.410	0.97E/0.978	1.04/1.227
10	0.4665	0.8692	0.3186	115/107	9/18	36/1	2/8	3/2	3.55E-05/5.30E-06	2.50E-06/1.15E-06	1.40E-06/1.13E-06	1.80E-06/2.92E-06	6.93E-06/2.92E-06	0.170/0.127	0.470/0.159	0.207/0.359	0.170/0.127	0.97E/0.959	1.861/2.239
10	0.8757	1.2010	0.2454	125/106	26/1	41/3	3/2	3.26E-06/7.51E-06	5.97E-06/1.49E-06	1.39E-06/2.62E-06	7.93E-06/2.62E-06	7.93E-06/2.62E-06	6.79E-06/4.00E-06	0.070/0.119	0.458/0.424	0.275/0.279	0.196/0.177	0.993/0.974	0.961/0.329
10	0.0048	0.4056	0.4009	55/68	15/3	3/14	6/10	3/1	7.28E-05/4.24E-06	5.47E-06/1.49E-06	3.94E-06/1.97E-05	9.34E-06/2.98E-07	1.23E-05/2.19E-07	0.247/0.240	0.437/0.740	0.247/0.240	0.147/0.200	0.96E/0.995	0.38E/0.251
10	0.0237	0.4572	0.4306	55/68	18/2	2/13	6/31	3/26	5.24E-06/1.96E-05	8.32E-06/2.40E-07	6.35E-06/1.96E-05	8.52E-06/2.40E-07	1.37E-05/2.18E-07	0.080/0.216	0.432/0.743	0.271/0.202	0.220/0.200	0.96E/0.996	1.151/0.242
11	0.0076	0.4776	0.4300	55/127	14/3	2/11	7/11	2/1	7.08E-05/5.08E-06	5.50E-06/1.31E-06	8.47E-06/1.83E-05	8.47E-06/1.83E-05	1.42E-05/2.27E-07	0.077/0.219	0.432/0.757	0.271/0.202	0.220/0.200	0.959/0.993	0.359/0.386
11	0.0000	0.4466	0.4466	55/105	16/2	1/12	5/31	2/26	7.03E-05/6.62E-06	4.93E-06/1.39E-06	9.31E-06/2.00E-07	9.31E-06/2.00E-07	1.39E-05/2.01E-07	0.074/0.206	0.428/0.751	0.276/0.203	0.222/0.201	0.967/0.997	1.032/0.149
11	0.1207	0.5781	0.4574	55/105	17/2	1/12	4/31	2/26	7.14E-05/5.94E-06	5.38E-06/1.38E-06	4.68E-06/1.80E-05	8.88E-06/1.68E-07	1.36E-05/2.01E-07	0.075/0.209	0.426/0.748	0.270/0.202	0.220/0.201	0.966/0.995	1.086/0.243
11	0.2476	0.6031	0.5555	67/130	13/2	2/12	6/1	3/21	7.32E-05/4.32E-06	5.87E-06/1.61E-06	6.48E-06/1.84E-05	6.37E-06/1.23E-06	1.54E-05/2.27E-07	0.090/0.226	0.446/0.769	0.262/0.200	0.195/0.005	0.987/0.999	0.312/0.105
11	0.3313	0.8959	0.7145	67/130	9/4	4/5	6/2	2/11	6.81E-05/4.21E-06	6.80E-06/1.43E-06	3.90E-06/1.50E-05	7.34E-06/2.94E-06	1.82E-05/1.92E-07	0.097/0.177	0.450/0.722	0.264/0.069	0.192/0.032	0.974/0.993	0.511/0.424
11	0.5224	1.4221	0.8988	70/125	2/36	3/2	3/11	4/41	4.51E-06/9.94E-06	6.99E-06/1.68E-06	7.91E-06/5.14E-06	7.91E-06/5.14E-06	2.50E-05/1.91E-07	0.089/0.143	0.440/0.916	0.265/0.000	0.195/0.041	0.968/0.974	0.688/0.184
11	0.8294	2.2372	1.4078	95/115	1/32	3/1	5/2	5/31	4.96E-05/1.15E-05	7.09E-06/2.45E-07	6.01E-06/1.88E-06	1.41E-05/4.43E-06	2.70E-05/7.98E-08	0.087/0.190	0.435/0.691	0.276/0.066	0.202/0.053	0.927/0.984	1.973/0.388
12	0.0024	0.4816	0.4792	59/129	22/3	1/12	6/1	3/21	7.81E-05/3.92E-06	6.19E-06/1.95E-06	5.99E-06/1.83E-05	8.00E-06/1.52E-06	1.57E-05/2.18E-07	0.087/0.225	0.422/0.753	0.277/0.000	0.210/0.280	0.951/0.971	1.460/0.890
12	0.0047	0.5119	0.4879	59/129	37/2	1/10	4/1	2/21	7.47E-05/4.79E-06	2.13E-06/1.49E-06	6.11E-06/1.75E-05	1.18E-05/6.14E-06	1.91E-05/2.17E-07	0.087/0.228	0.421/0.768	0.268/0.000	0.226/0.004	0.975/0.982	0.813/0.531
12	0.0817	0.5298	0.4743	59/129	8/3	1/14	4/1	2/21	7.57E-05/4.12E-06	6.80E-06/1.98E-06	5.30E-06/1.84E-05	1.06E-05/6.14E-06	1.59E-05/2.17E-07	0.076/0.225	0.437/0.753	0.268/0.000	0.226/0.004	0.949/0.982	1.631/0.517
12	0.1180	0.8831	0.4731	59/127	2/1	1/14	5/1	2/21	8.01E-05/5.33E-06	5.73E-06/1.48E-06	4.73E-06/1.70E-05	8.39E-06/1.60E-06	1.50E-05/2.28E-07	0.080/0.238	0.431/0.762	0.271/0.000	0.210/0.000	0.96E/0.989	1.657/0.310
12	0.1304	0.6122	0.4739	55/127	13/1	1/15	6/1	3/1	8.26E-05/5.35E-06	5.29E-06/1.45E-06	3.62E-06/1.74E-05	7.50E-06/1.23E-06	1.50E-05/2.28E-07	0.080/0.238	0.440/0.772	0.268/0.000	0.210/0.000	0.96E/0.989	1.546/0.380
12	0.2773	0.7478	0.4705	77/126	13/1	6/12	4/2	3/1	8.33E-05/5.37E-06	6.20E-06/2.89E-06	2.87E-06/1.62E-05	5.83E-06/1.09E-06	1.52E-05/1.92E-07	0.106/0.219	0.452/0.748	0.248/0.000	0.194/0.042	0.93E/0.987	1.728/0.590
12	0.4250	0.8823	0.4573	113/125	9/1	3/28	3/1	8.33E-05/5.37E-06	6.7E-06/6.85E-06	2.89E-06/1.45E-05	5.46E-06/5.70E-07	1.56E-05/1.92E-07	0.106/0.219	0.452/0.748	0.248/0.000	0.194/0.042	0.93E/0.987	1.728/0.590	
12	0.5817	1.0133	0.4316	115/124	7/2	3/4	3/1	8.17E-05/5.15E-06	6.07E-06/7.20E-06	3.37E-06/1.40E-05	4.59E-06/1.46E-07	1.72E-05/1.46E-07	0.131/0.200	0.478/0.734	0.205/0.063	0.186/0.003	0.867/0.983	3.655/1.542	
12	0.9257	1.2812	0.3555	120/75	20/18	4/16	7/36	3/35	7.76E-05/7.58E-06	6.00E-06/7.09E-06	3.42E-06/1.00E-05	8.08E-06/6.82E-07	1.89E-05/2.28E-07	0.086/0.226	0.445/0.752	0.276/0.012	0.193/0.010	0.817/0.984	5.772/0.609
13	0.0052	0.4115	0.4063	62/105	17/2	1/14	6/19	4/21	9.48E-05/4.57E-06	7.78E-06/1.58E-06	5.68E-06/2.51E-05	1.27E-05/3.86E-07	0.074/0.223	0.074/0.223	0.249/0.724	0.284/0.031	0.213/0.023	0.968/0.995	0.912/0.197
13	0.0256	1.1307	1.0051	95/115	28/6	1/5	8/25	4/17	8.47E-05/7.02E-06	5.76E-06/1.42E-06	6.38E-06/2.16E-05	1.43E-05/2.50E-07	2.82E-05/1.69E-06	0.124/0.173	0.420/0.761	0.249/0.047	0.227/0.019	0.924/0.994	1.661/0.147
13	0.0515	1.1473	1.0657	84/115	27/6	1/3	9/23	4/31	8.57E-05/6.90E-06	6.23E-06/2.17E-05	1.41E-05/2.67E-07	1.41E-05/2.67E-07	2.70E-05/2.98E-07	0.125/0.174	0.438/0.750	0.246/0.050	0.228/0.019	0.941/0.984	1.661/0.136
13	0.1041	1.1688	1.0647	84/115	35/2	1/3	9/23	4/31	8.61E-05/6.97E-06	5.27E-06/6.72E-07	6.90E-06/2.15E-05	1.40E-05/2.83E-07	2.70E-05/2.98E-07	0.129/0.175	0.400/0.805	0.246/0.010	0.230/0.010	0.937/0.997	1.351/0.081
13	0.1368	1.1920	1.0512	69/115	10/4	1/3	17/31	4/31	8.66E-05/6.33E-06	6.55E-06/1.02E-06	6.69E-06/2.20E-05	1.23E-05/7.68E-07	2.52E-05/2.92E-07	0.085/0.178	0.422/0.801	0.279/0.010	0.215/0.010	0.954/0.984	0.98E/0.135
13	0.2484	1.3906	1.1224	58/125	4/4	1/5	6/2	3/3	8.75E-05/6.35E-06	8.81E-06/1.11E-06	1.24E-05/6.39E-07	1.24E-05/6.39E-07	2.53E-05/2.93E-07	0.091/0.269	0.417/0.789	0.262/0.000	0.210/0.002	0.96E/0.986	1.500/0.253
13	0.4134	1.6354	1.2220	58/125	2/3	1/16	6/1	2/21	8.51E-05/7.11E-06	7.20E-06/1.18E-06	6.20E-06/1.70E-05	9.86E-06/6.34E-06	2.38E-05/2.11E-07	0.060/0.258	0.424/0.742	0.262/0.000	0.210/0.000	0.96E/0.984	1.690/0.126
13	0.5865	1.8802	1.3237	59/125	8/5	1/8	6/1	2/21	9.25E-05/1.18E-05	7.90E-06/1.39E-06	6.53E-06/1.81E-06	9.86E-06/6.34E-06	2.28E-05/2.11E-07	0.084/0.232	0.434/0.761	0.267/0.000	0.210/0.000	0.97E/0.996	0.370/0.077
13	0.8966	2.5331	1.6333	59/115	9/27	1/1	3/11	2/32	8.14E-05/1.91E-05	6.17E-06/8.35E-07	6.53E-06/1.81E-06	1.27E-05/6.97E-08	2.28E-05/2.11E-07	0.084/0.232	0.434/0.761	0.267/0.000	0.210/0.000	0.981/0.995	0.370/0.077
14	0.0057	0.5181	0.5182	59/126	16/2	1/17	6/1	3/1	1.07E-04/4.78E-06	8.62E-06/6.59E-06	6.11E-06/2.39E-05	1.37E-05/9.50E-07	2.04E-05/2.40E-07	0.076/0.412	0.428/0.557	0.275/0.000	0.210/0.000	0.957/0.987	1.011/0.490
14	0.0373	0.5635	0.5284	59/125	23/3	1/19	5/31	2/1	1.04E-04/4.44E-06	7.83E-06/2.83E-06	6.11E-06/2.39E-05	1.39E-05/9.50E-07	2.08E-05/2.70E-07	0.076/0.259	0.428/0.688	0.271/0.021	0.226/0.031	0.949/0.989	1.217/0.424
14	0.0829	0.5232	0.4403	55/124	18/2	2/15	5/31	3/1	1.03E-04/4.34E-06	6.03E-06/2.43E-05	1.50E-05/2.82E-07	1.50E-05/2.82E-07	2.08E-05/2.70E-07	0.076/0.277	0.440/0.700	0.269/0.022	0.214/0.000	0.959/0.984	1.211/0.625
14	0.1678	0.6536	0.4858	55/123	18/1	1/17	6/1	3/1	1.03E-04/4.34E-06	5.91E-06/2.10E-05	1.17E-05/1.13E-06	1.17E-05/1.13E-06	2.08E-05/2.68E-07	0.083/0.302	0.437/0.690	0.269/0.022	0.213/0.009	0.957/0.981	1.885/0.537
14	0.2108	0.6990	0.4882	55/122	4/1	1/27	7/1	1/27	1.12E-04/4.86E-06	4.90E-06/1.95E-05	3.20E-06/9.86E-07	1.33E-05/2.27E-07	1.33E-05/2.27E-07	0.086/0.267	0.443/0.666	0.276/0.000	0.211/0.057	0.968/0.998	1.570/0.105
14																			

F2.1. Vessel segment RTD curves

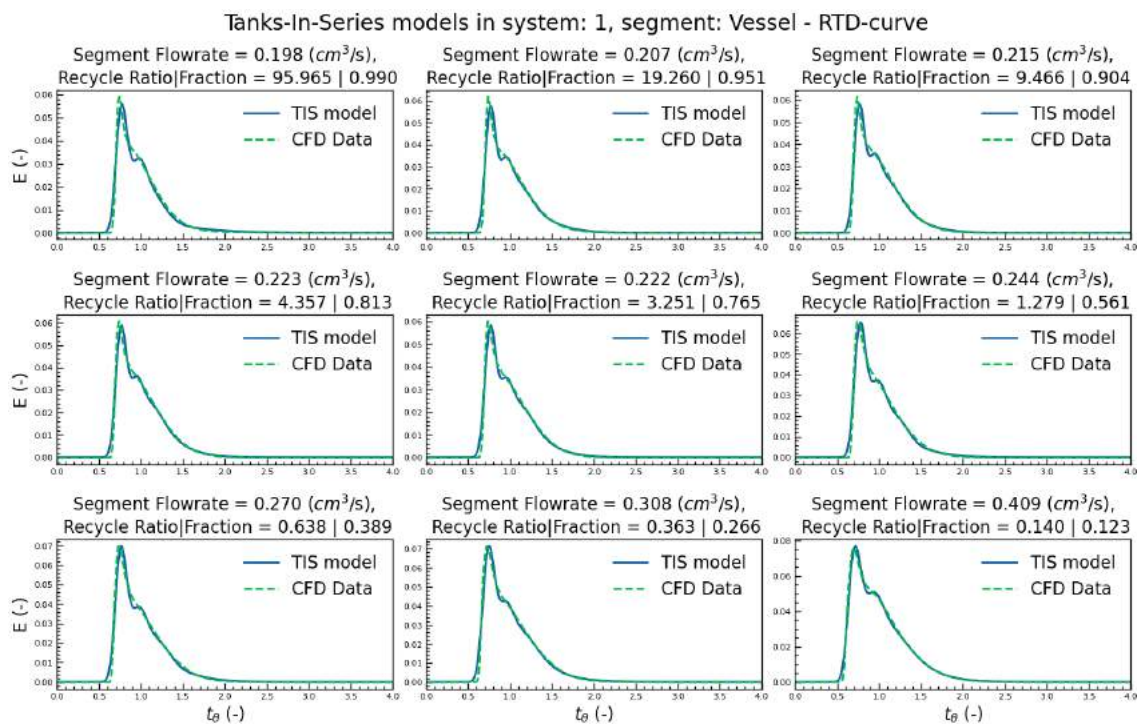


Figure E2: Vessel segment RTD curves from flowrates in system 1 and their respective determined Tanks-In-Series compartment model

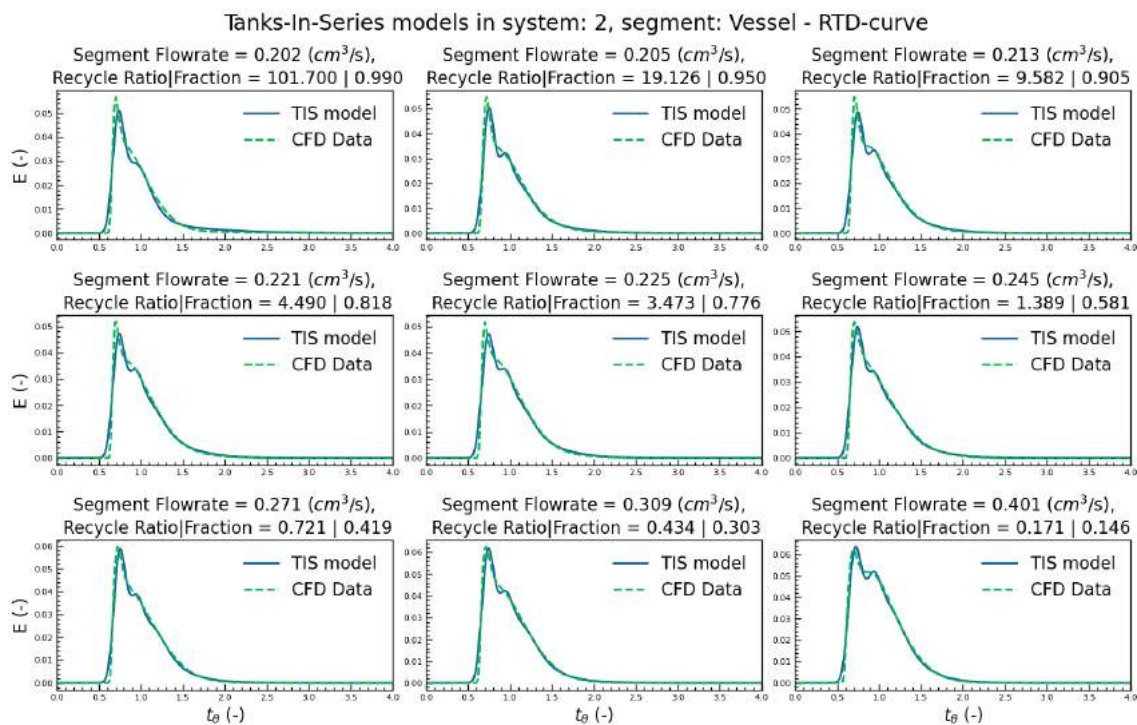


Figure E3: Vessel segment RTD curves from flowrates in system 2 and their respective determined Tanks-In-Series compartment model

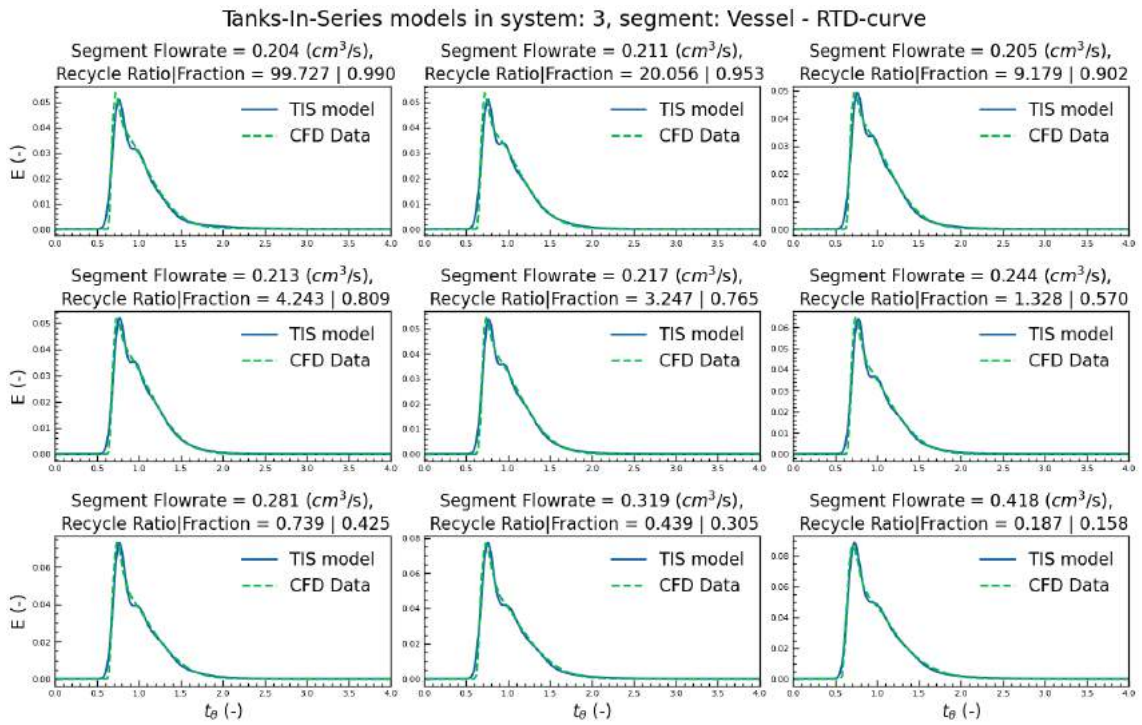


Figure E4: Vessel segment RTD curves from flowrates in system 3 and their respective determined Tanks-In-Series compartment model

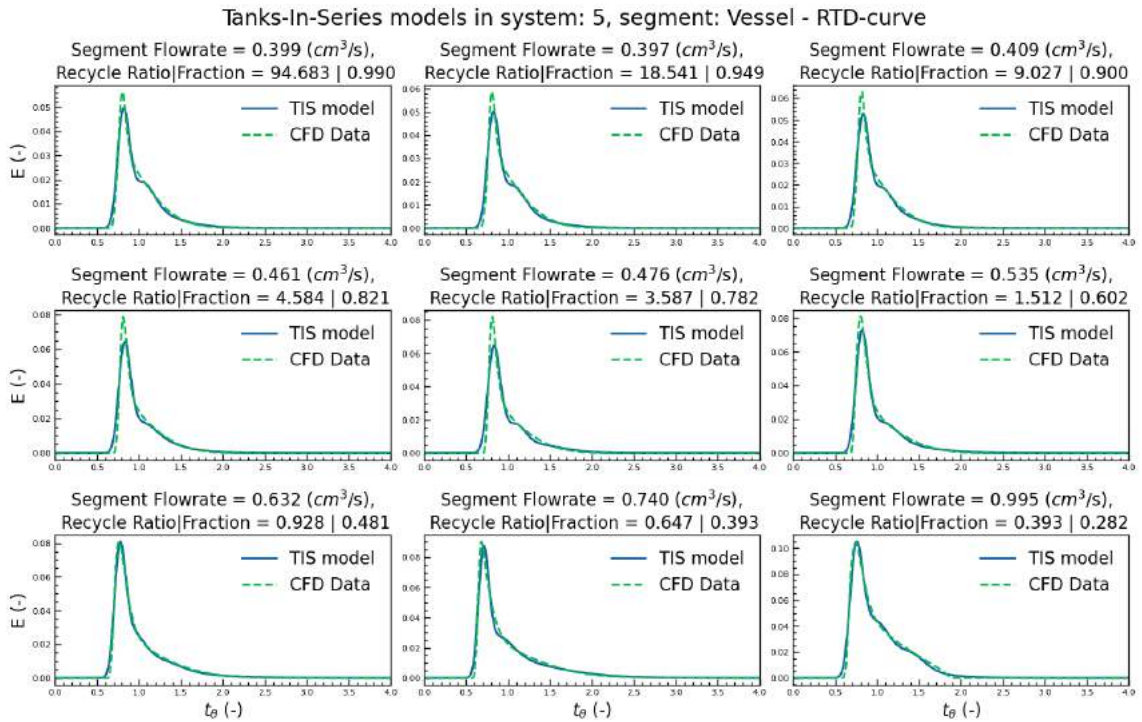


Figure E5: Recycle segment RTD curves from flowrates in system 5 and their respective determined Tanks-In-Series compartment model

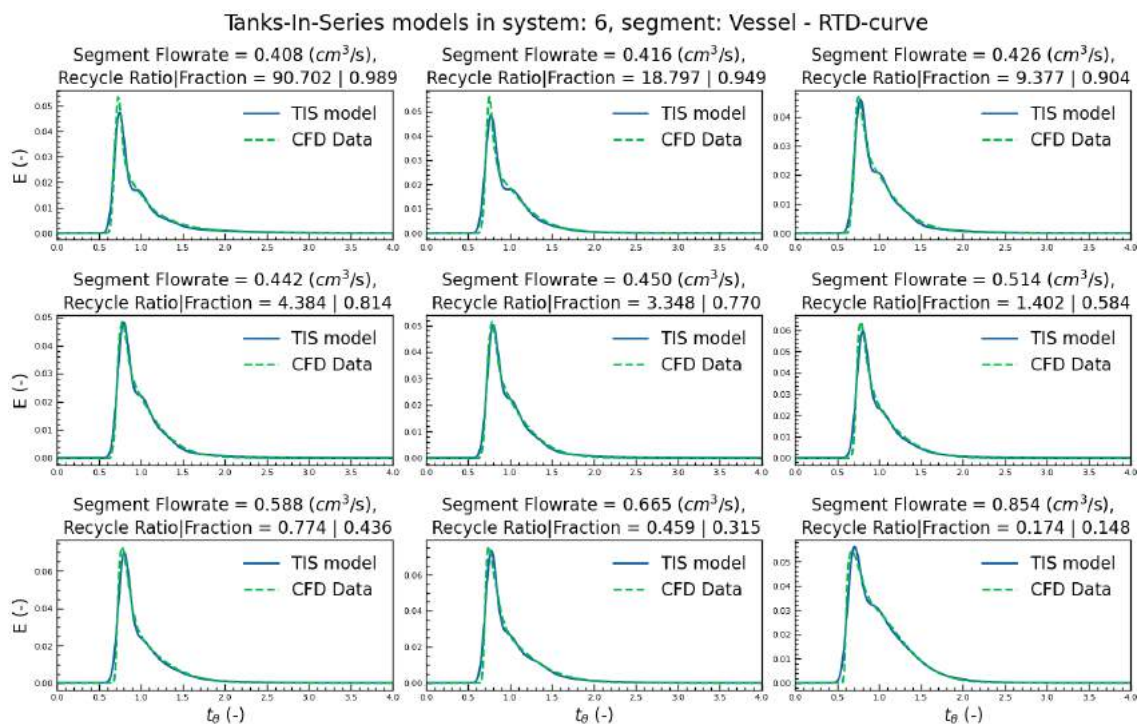


Figure E6: Vessel segment RTD curves from flowrates in system 6 and their respective determined Tanks-In-Series compartment model

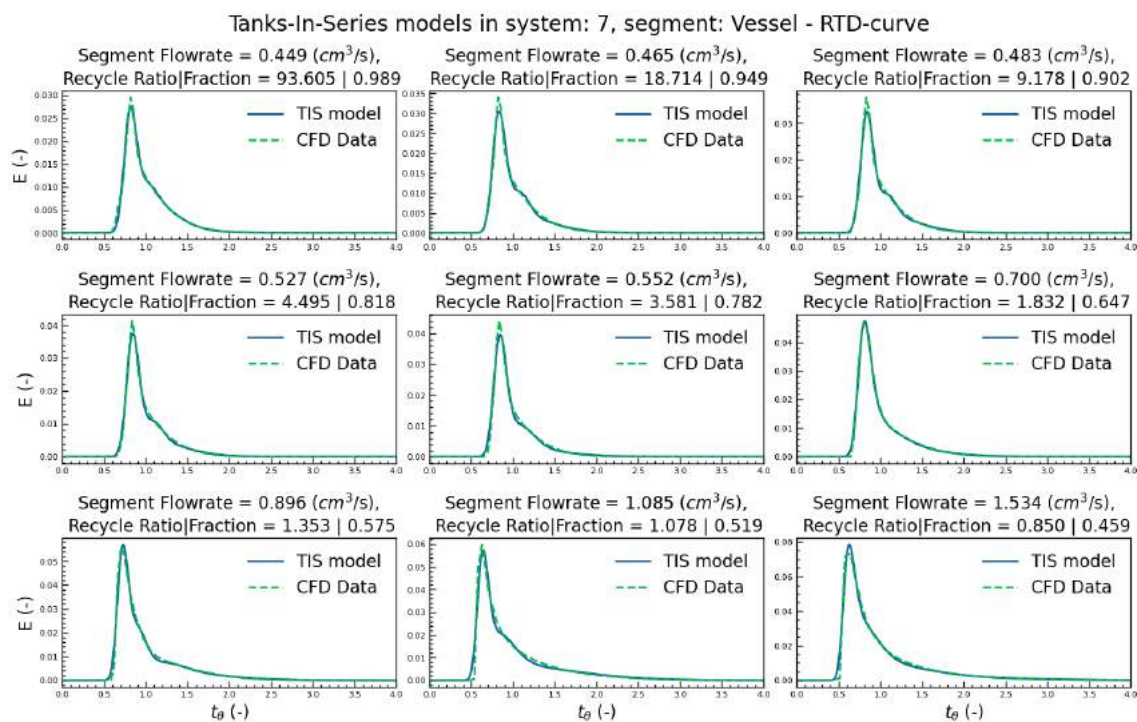


Figure E7: Vessel segment RTD curves from flowrates in system 7 and their respective determined Tanks-In-Series compartment model

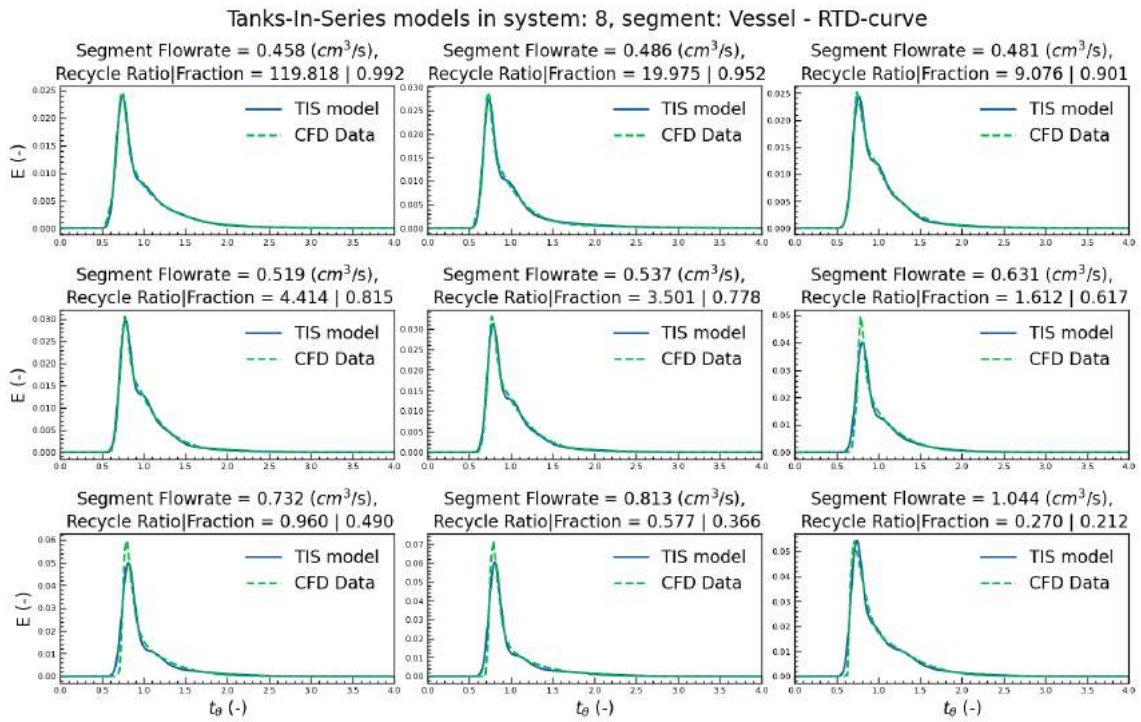


Figure E8: Vessel segment RTD curves from flowrates in system 8 and their respective determined Tanks-In-Series compartment model

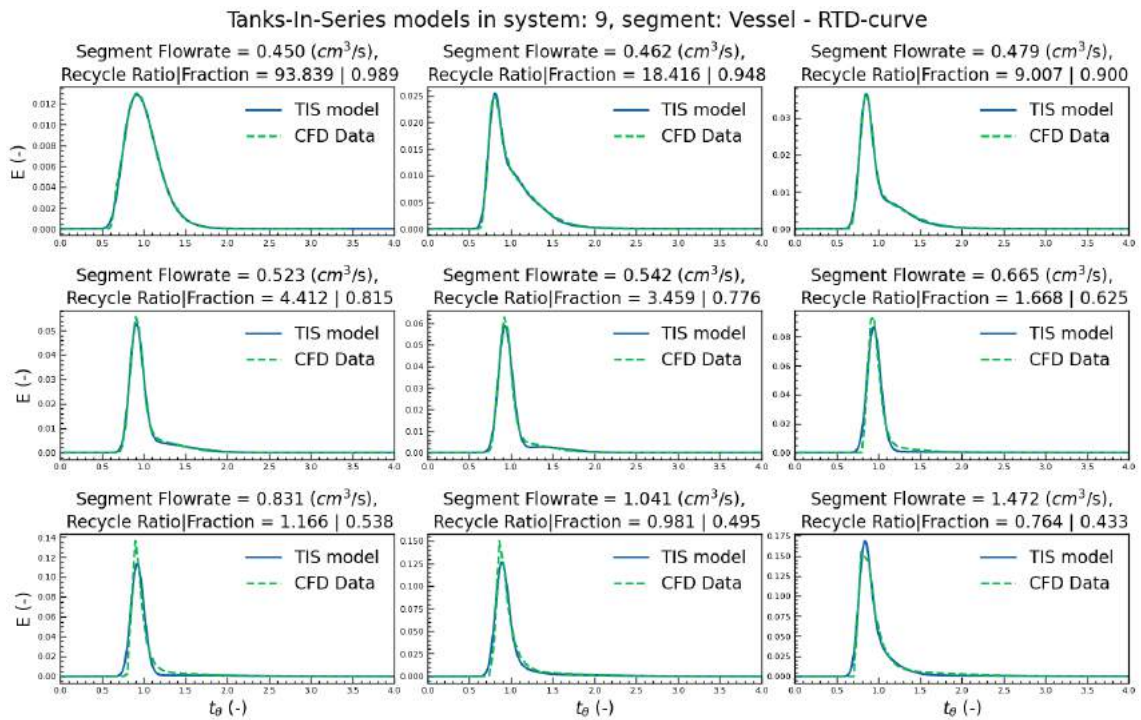


Figure E9: Vessel segment RTD curves from flowrates in system 9 and their respective determined Tanks-In-Series compartment model

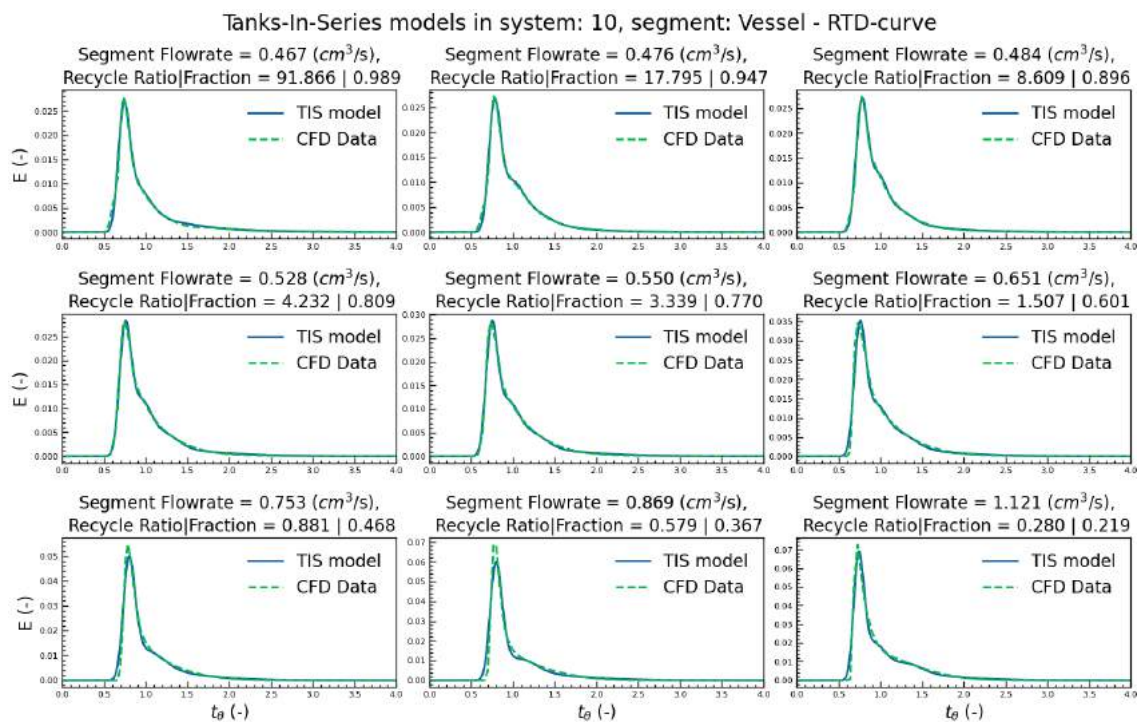


Figure F.10: Vessel segment RTD curves from flowrates in system 10 and their respective determined Tanks-In-Series compartment model

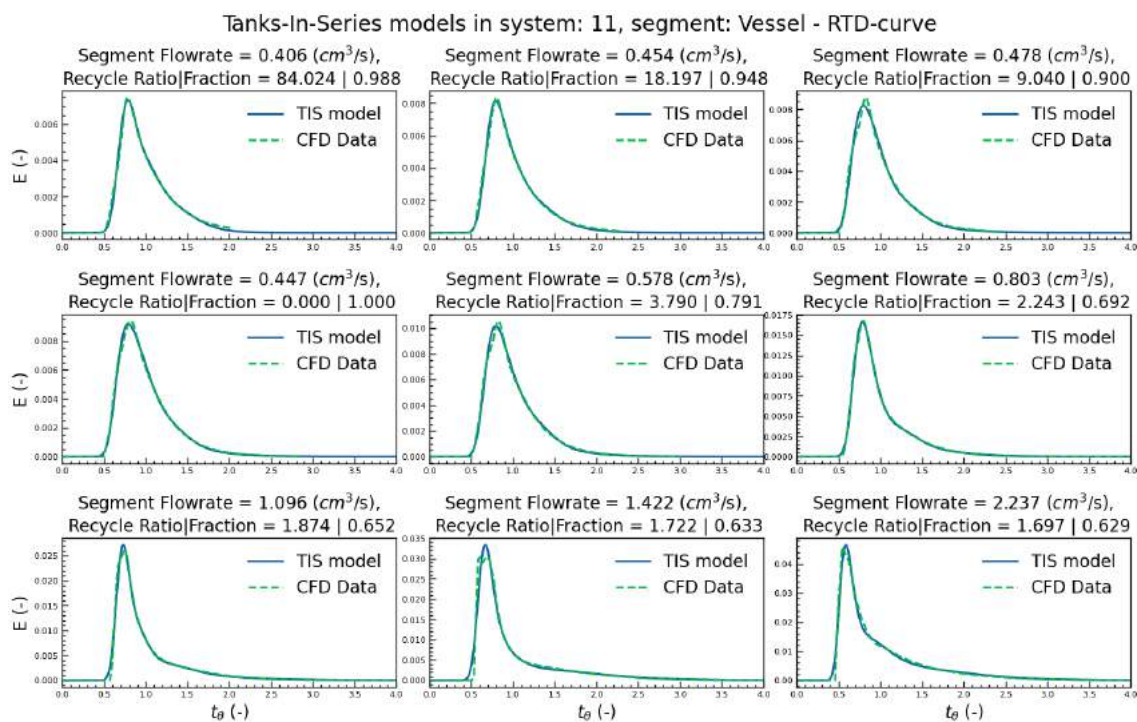


Figure F.11: Vessel segment RTD curves from flowrates in system 11 and their respective determined Tanks-In-Series compartment model

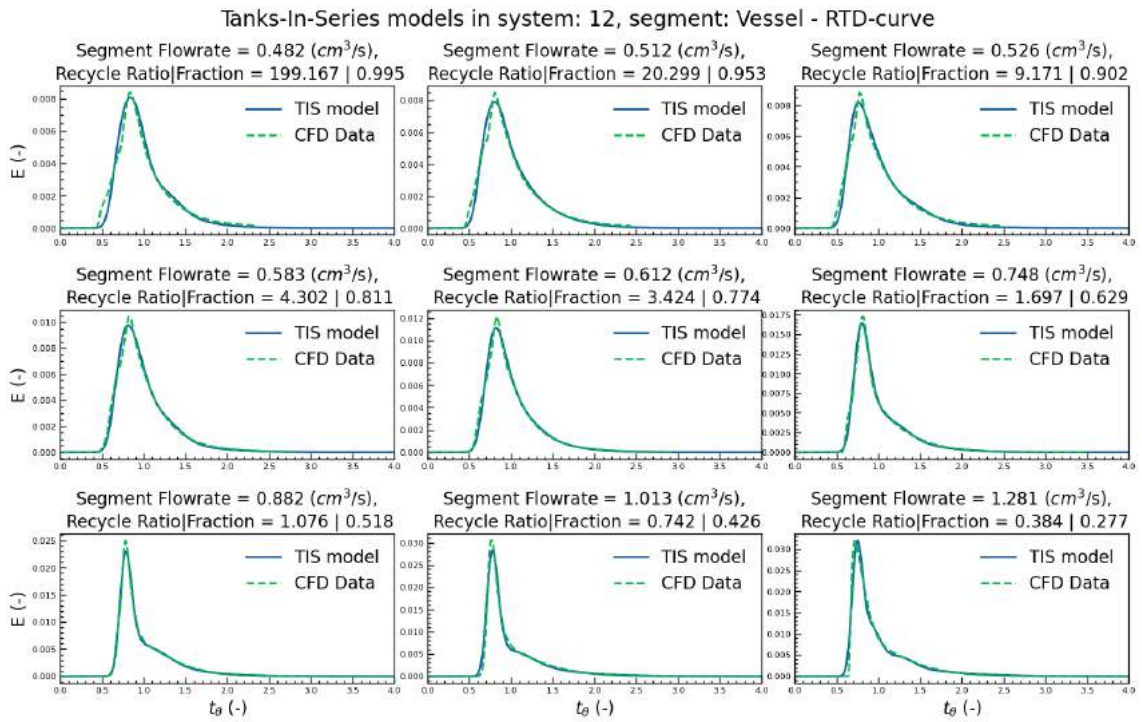


Figure F.12: Vessel segment RTD curves from flowrates in system 12 and their respective determined Tanks-In-Series compartment model

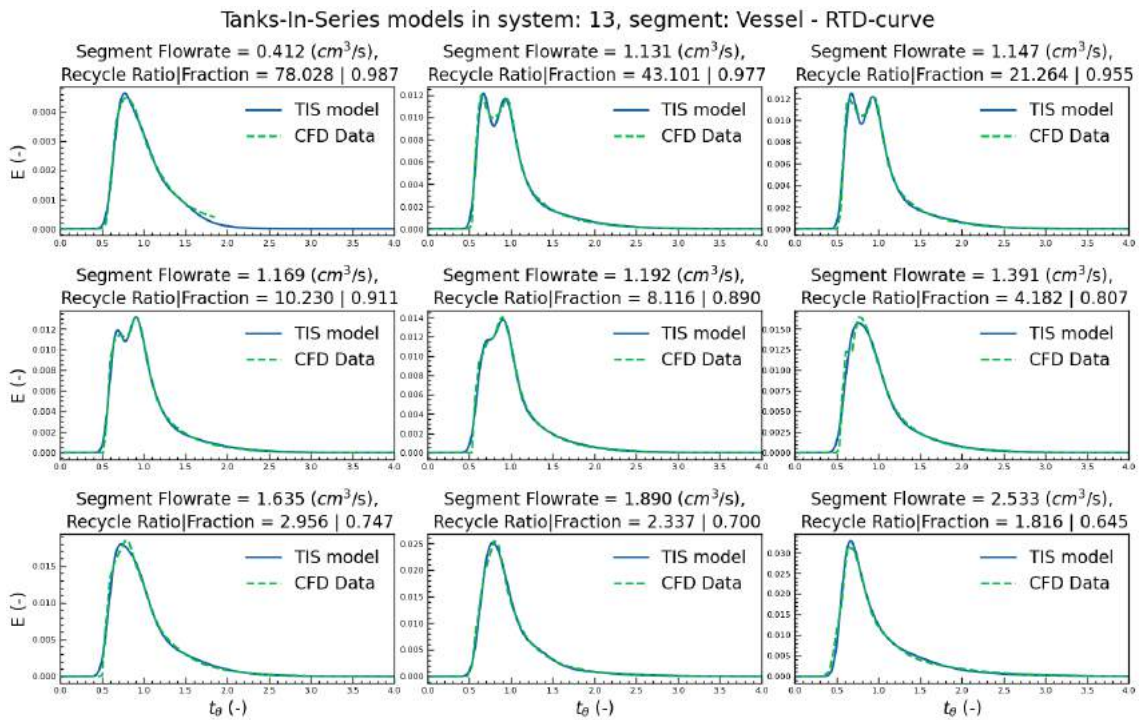


Figure F.13: Vessel segment RTD curves from flowrates in system 13 and their respective determined Tanks-In-Series compartment model

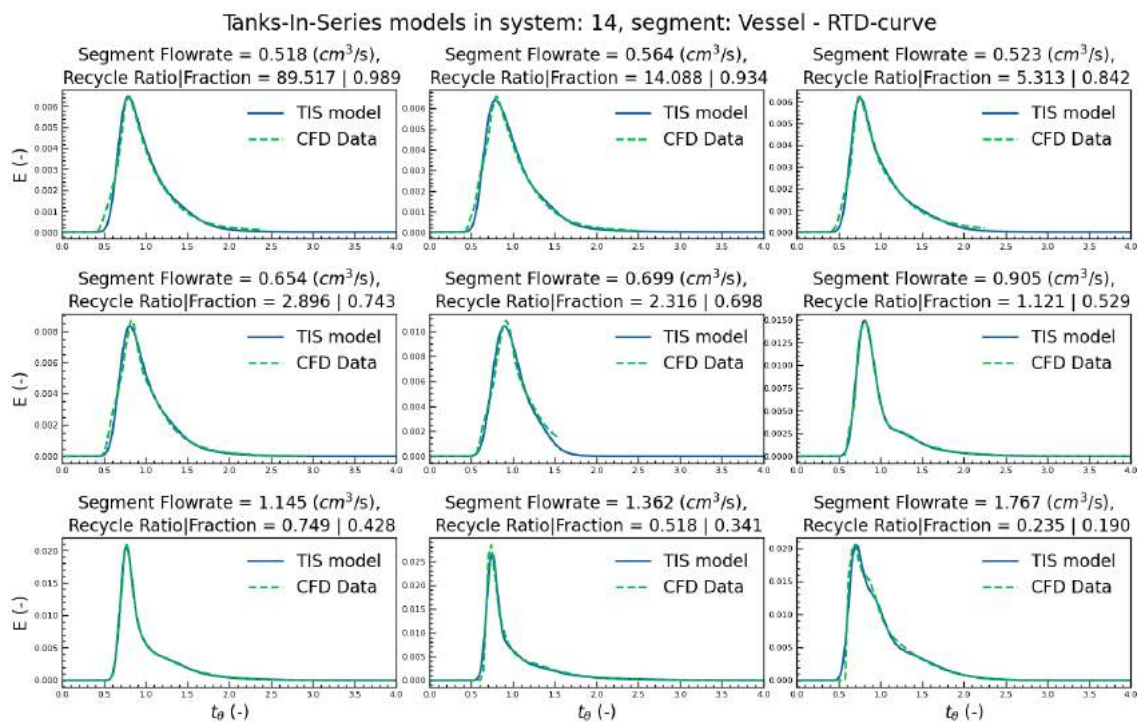


Figure F.14: Vessel segment RTD curves from flowrates in system 14 and their respective determined Tanks-In-Series compartment model

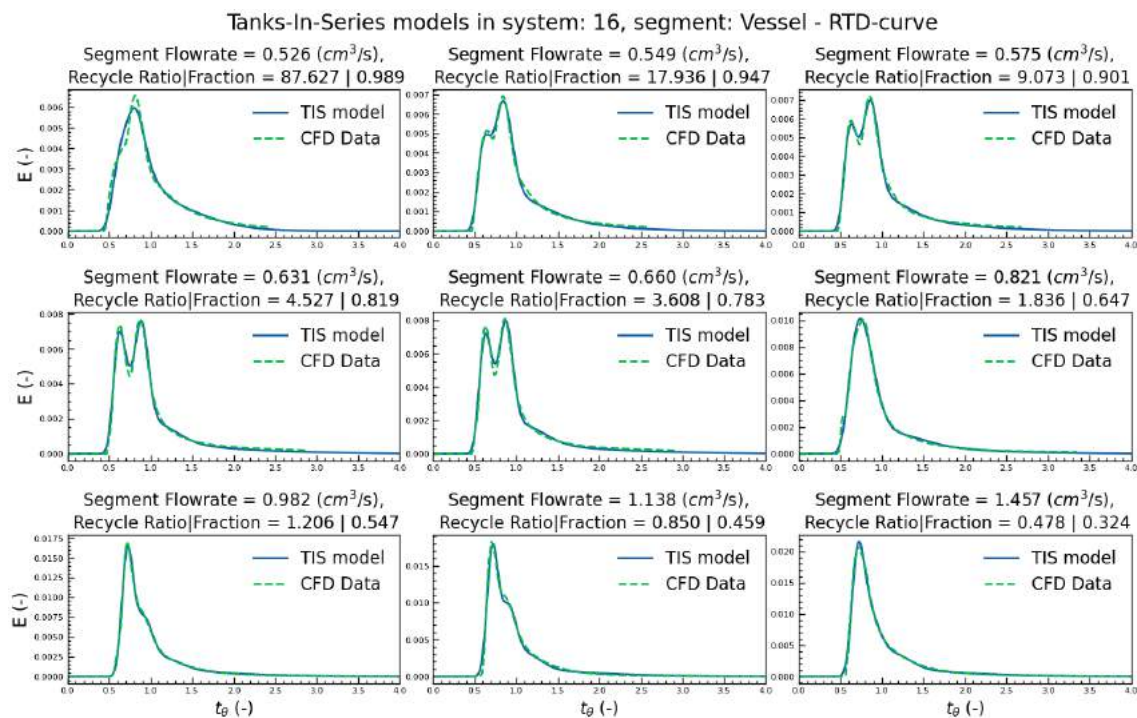


Figure F.15: Vessel segment RTD curves from flowrates in system 16 and their respective determined Tanks-In-Series compartment model

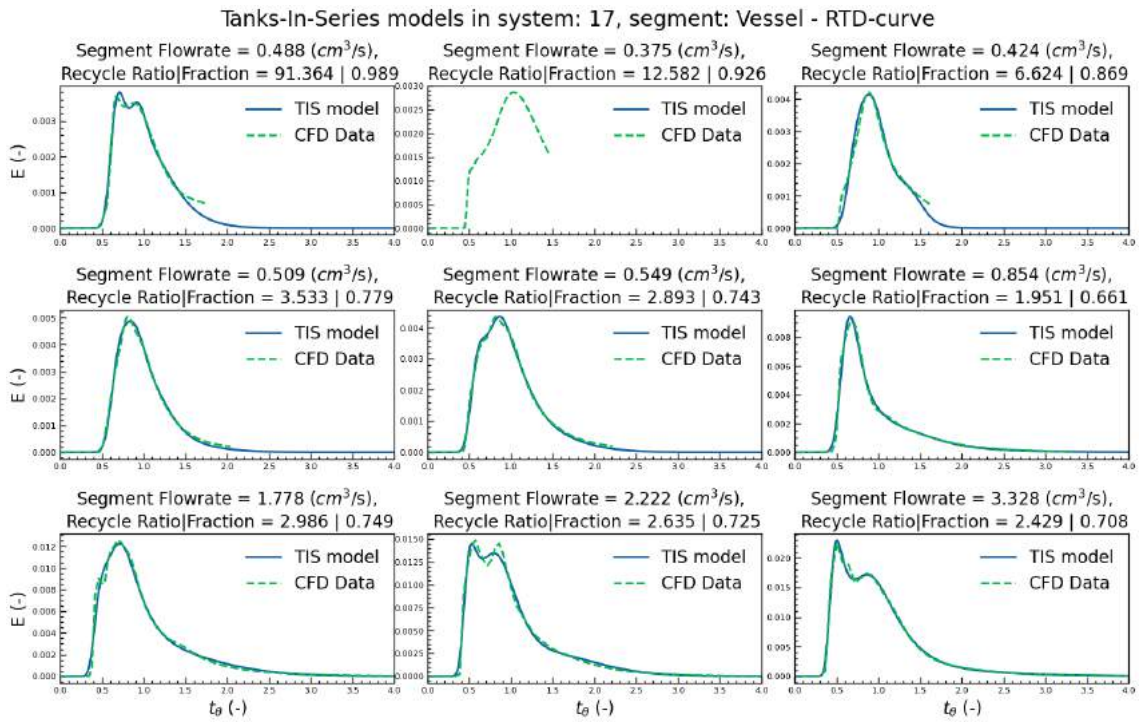


Figure F.16: Vessel segment RTD curves from flowrates in system 17 and their respective determined Tanks-In-Series compartment model

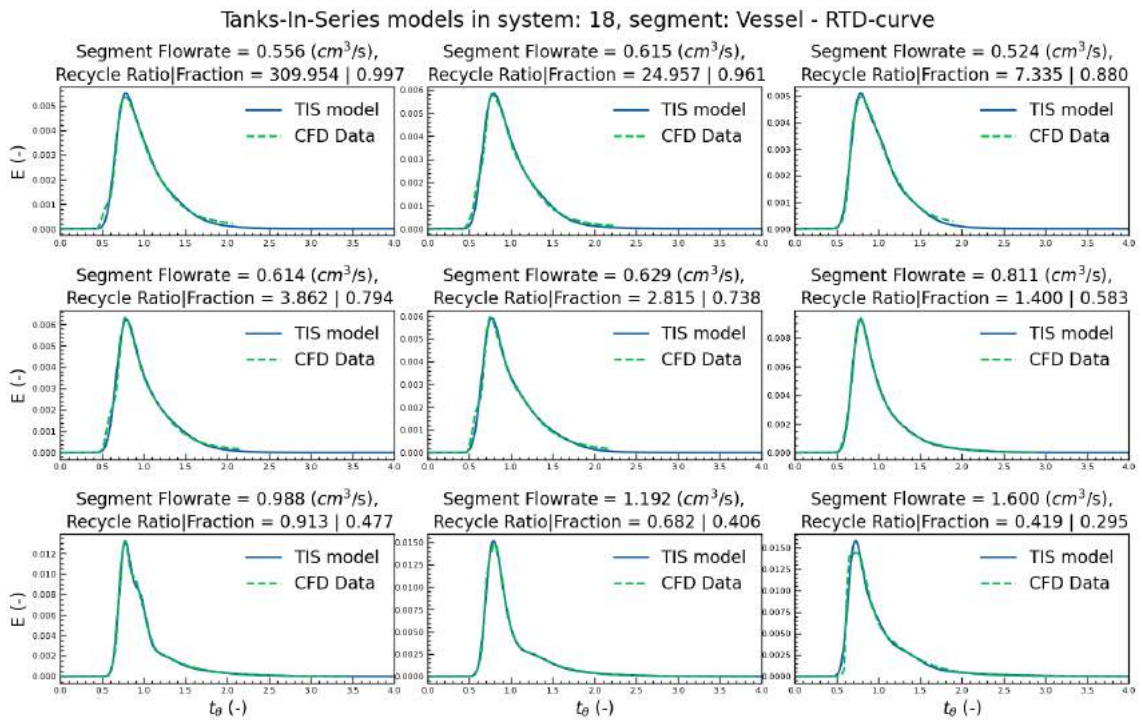


Figure F.17: Vessel segment RTD curves from flowrates in system 18 and their respective determined Tanks-In-Series compartment model

F.2.2. Recycle segment RTD curves

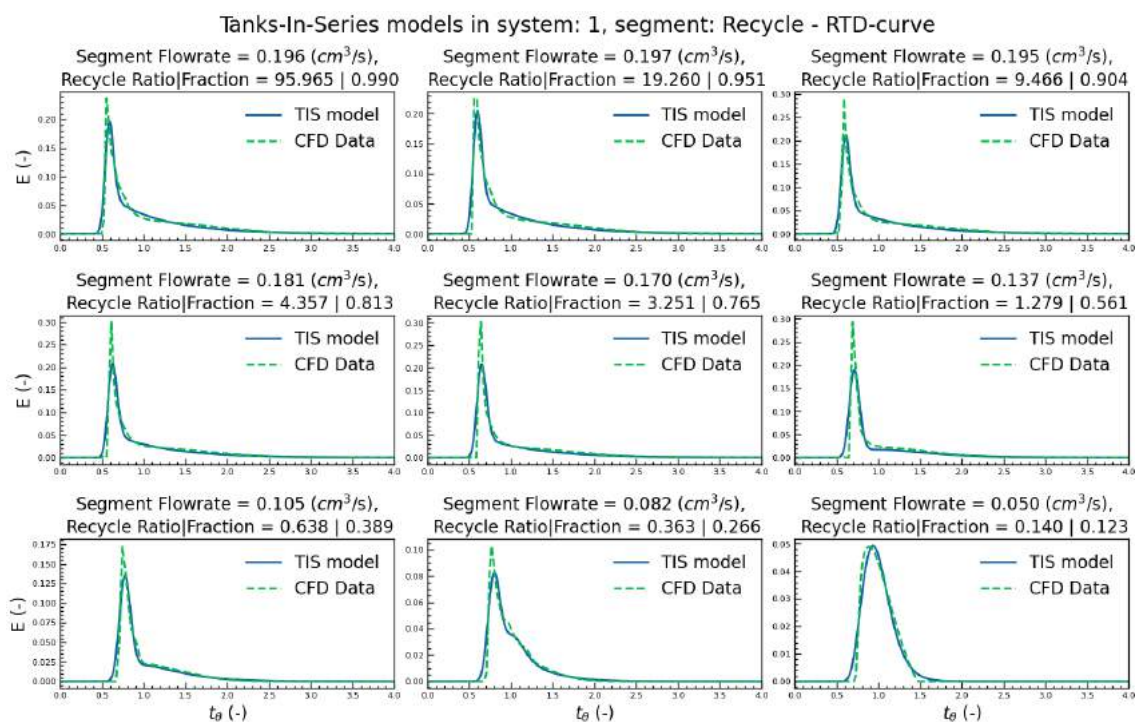


Figure F.18: Recycle segment RTD curves from flowrates in system 1 and their respective determined Tanks-In-Series compartment model

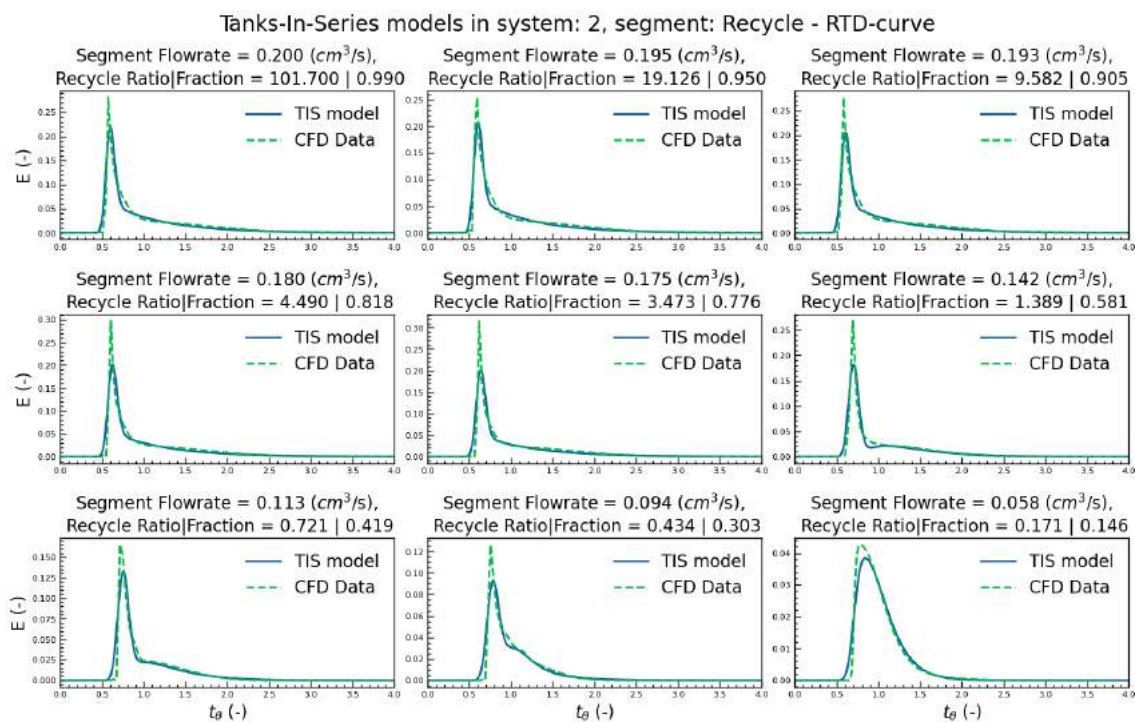


Figure F.19: Recycle segment RTD curves from flowrates in system 2 and their respective determined Tanks-In-Series compartment model

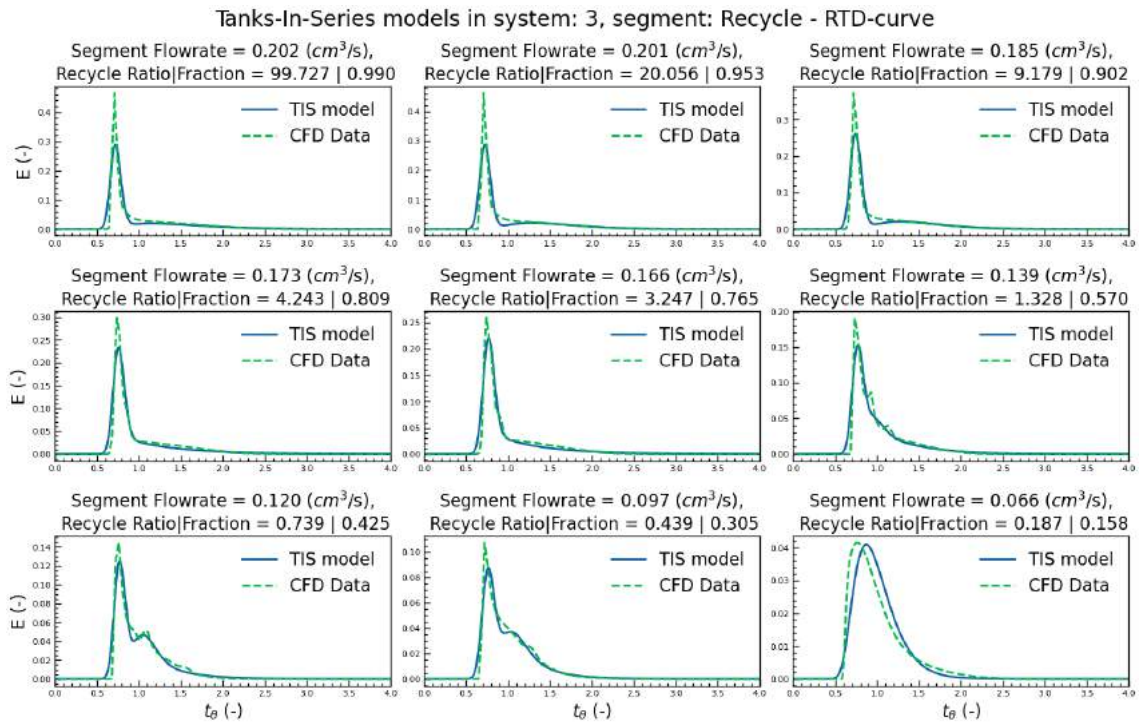


Figure E20: Recycle segment RTD curves from flowrates in system 3 and their respective determined Tanks-In-Series compartment model

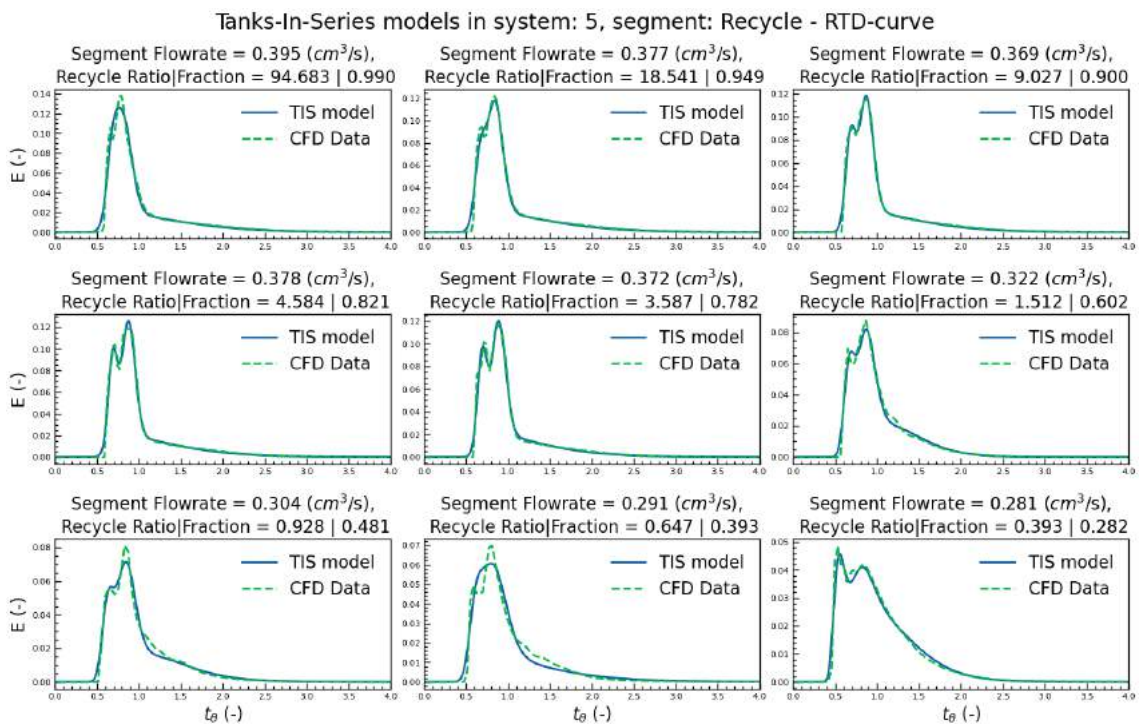


Figure E21: Recycle segment RTD curves from flowrates in system 5 and their respective determined Tanks-In-Series compartment model

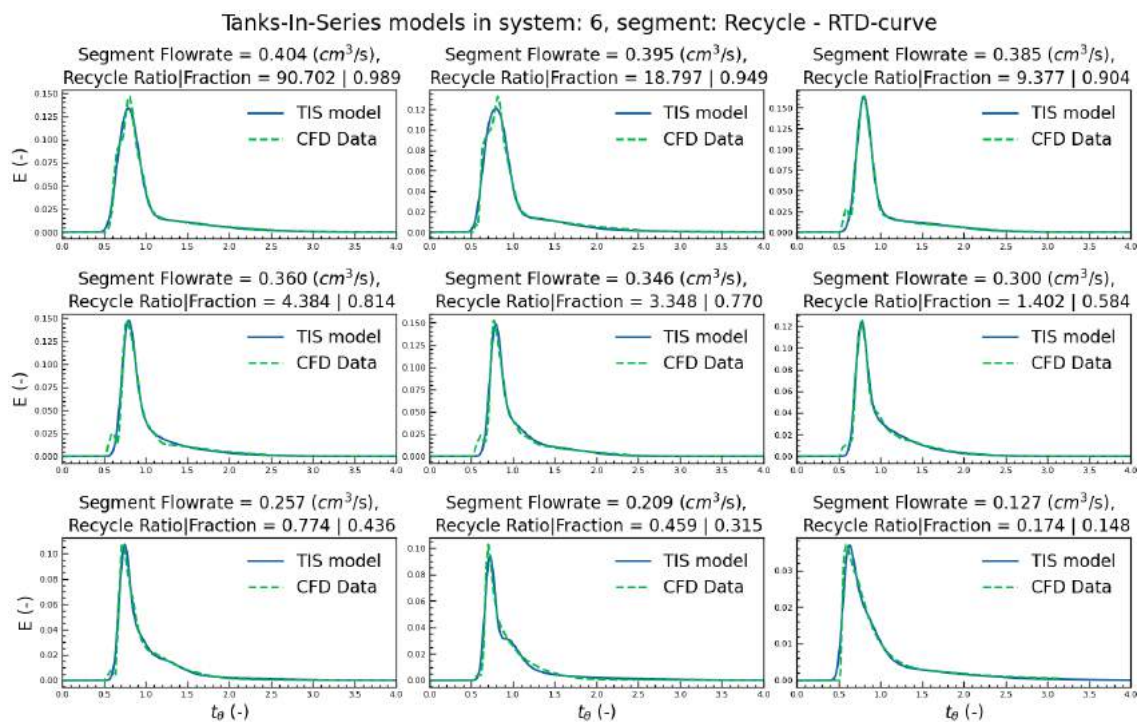


Figure E22: Recycle segment RTD curves from flowrates in system 6 and their respective determined Tanks-In-Series compartment model

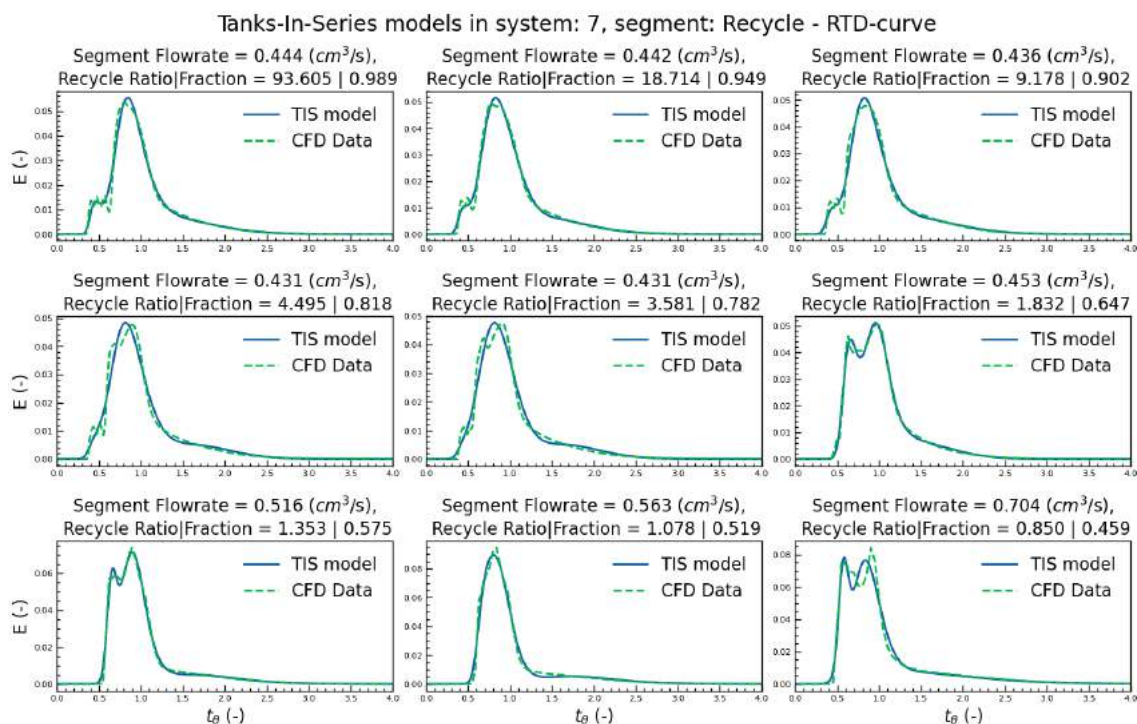


Figure E23: Recycle segment RTD curves from flowrates in system 7 and their respective determined Tanks-In-Series compartment model

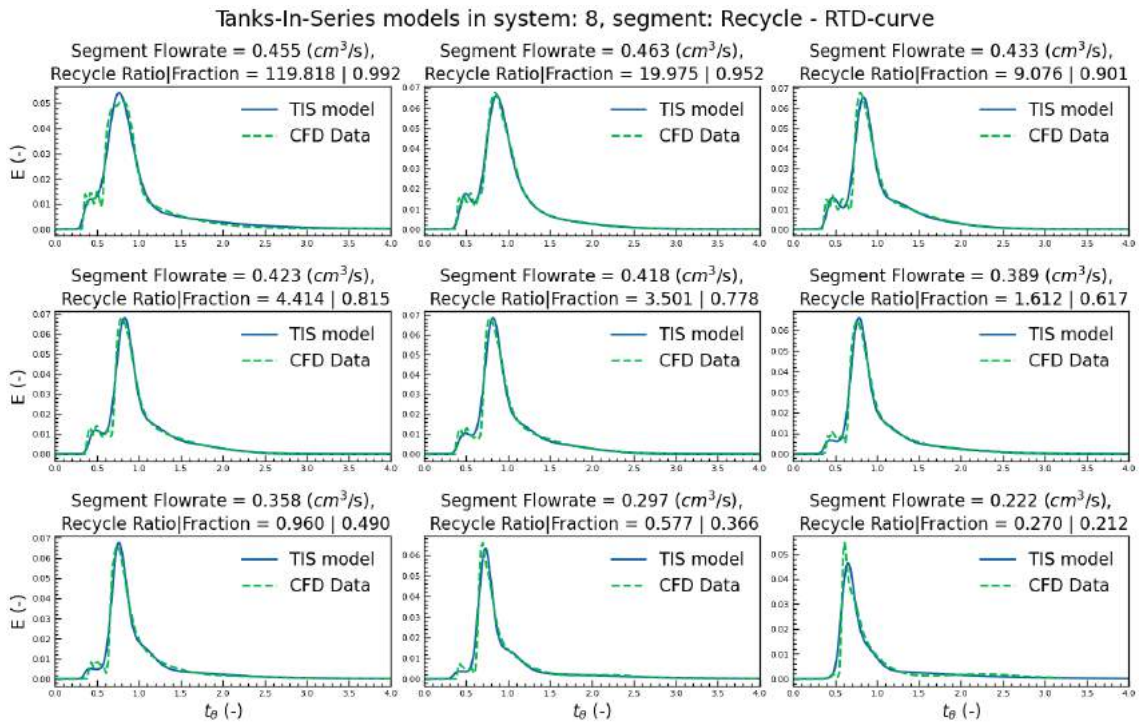


Figure E24: Recycle segment RTD curves from flowrates in system 8 and their respective determined Tanks-In-Series compartment model

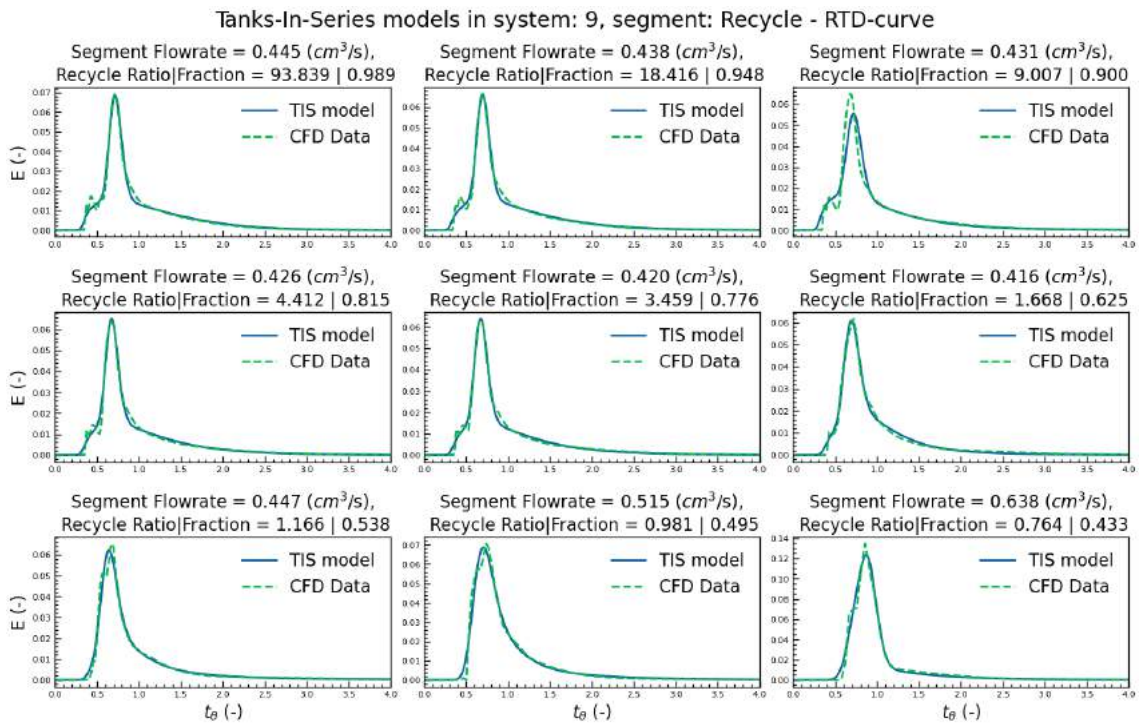


Figure E25: Recycle segment RTD curves from flowrates in system 9 and their respective determined Tanks-In-Series compartment model

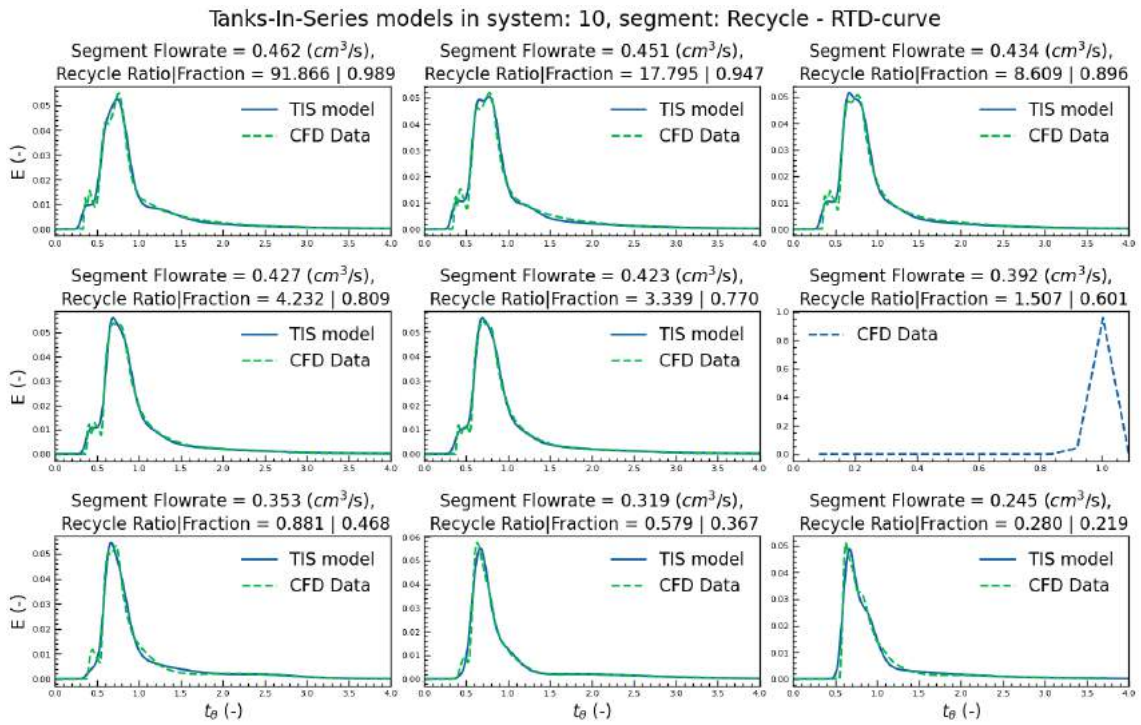


Figure E.26: Recycle segment RTD curves from flowrates in system 10 and their respective determined Tanks-In-Series compartment model

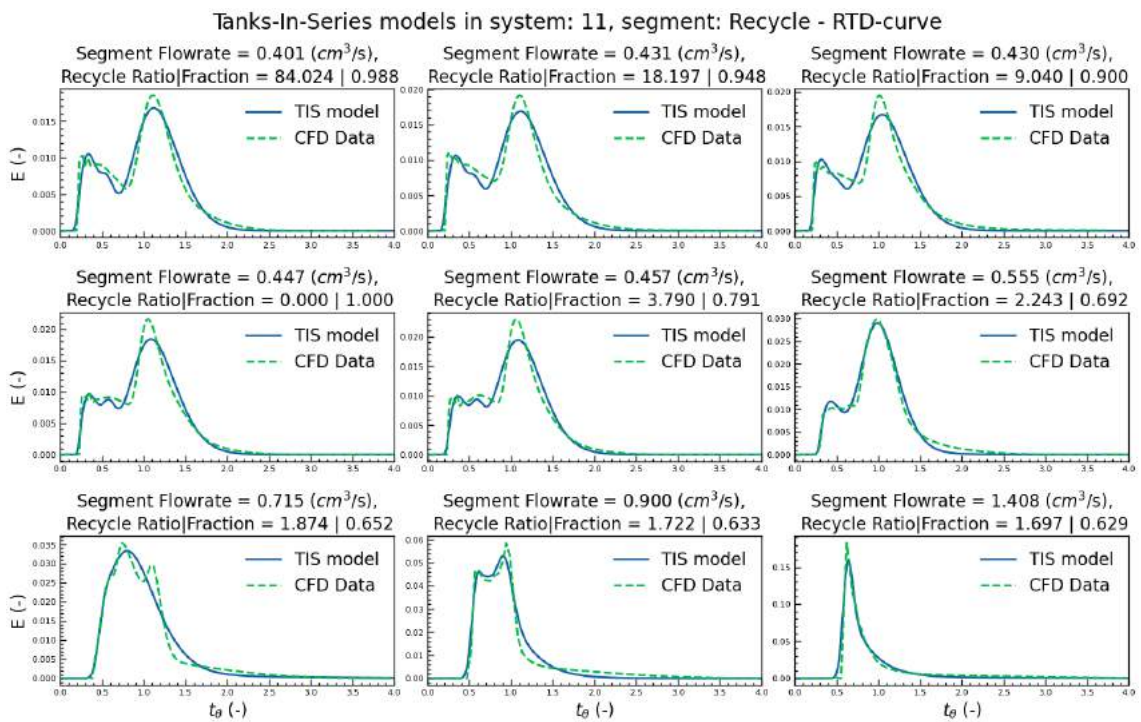


Figure E.27: Recycle segment RTD curves from flowrates in system 11 and their respective determined Tanks-In-Series compartment model

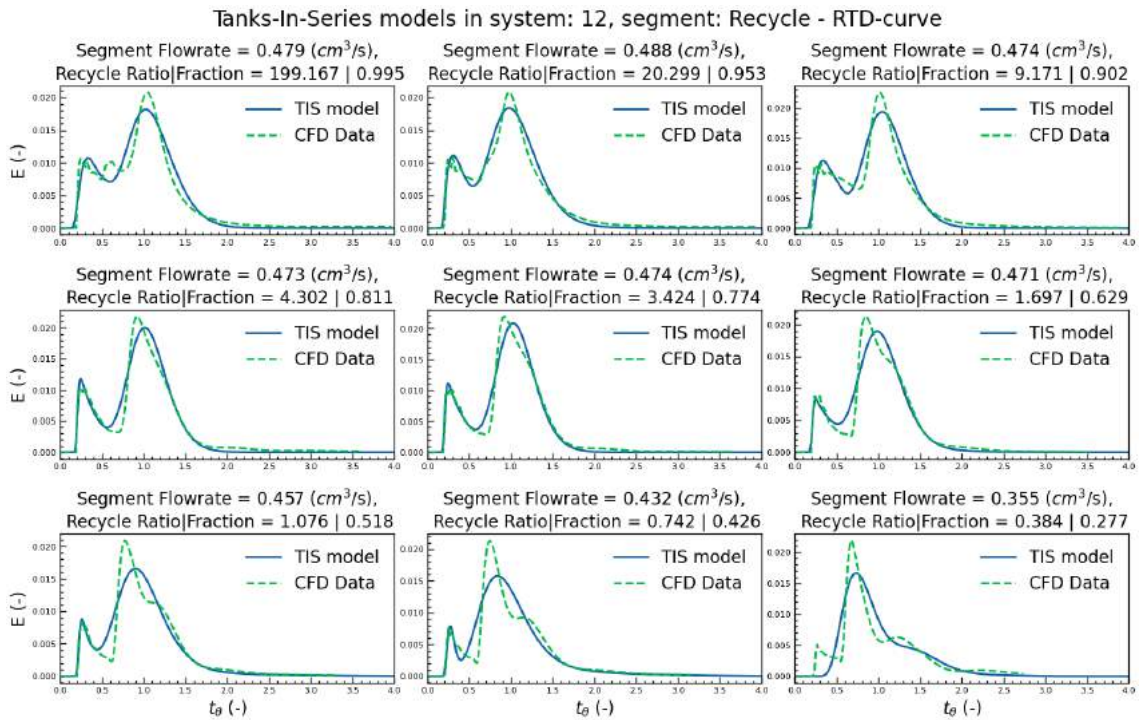


Figure E28: Recycle segment RTD curves from flowrates in system 12 and their respective determined Tanks-In-Series compartment model

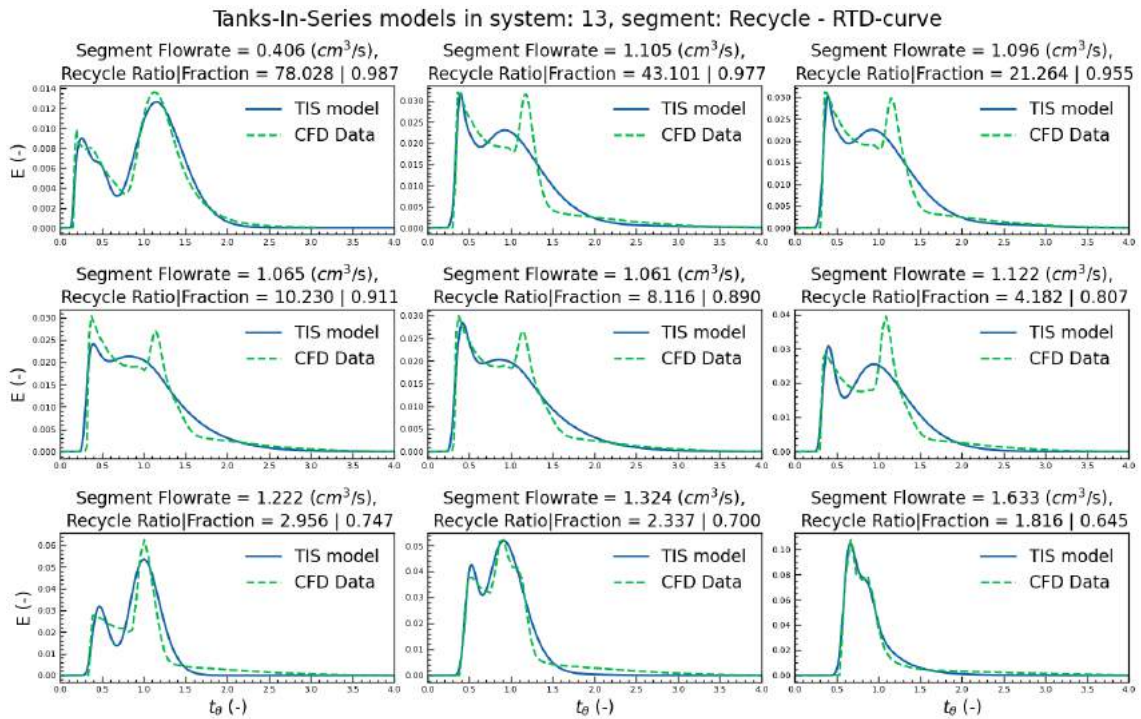


Figure E29: Recycle segment RTD curves from flowrates in system 13 and their respective determined Tanks-In-Series compartment model

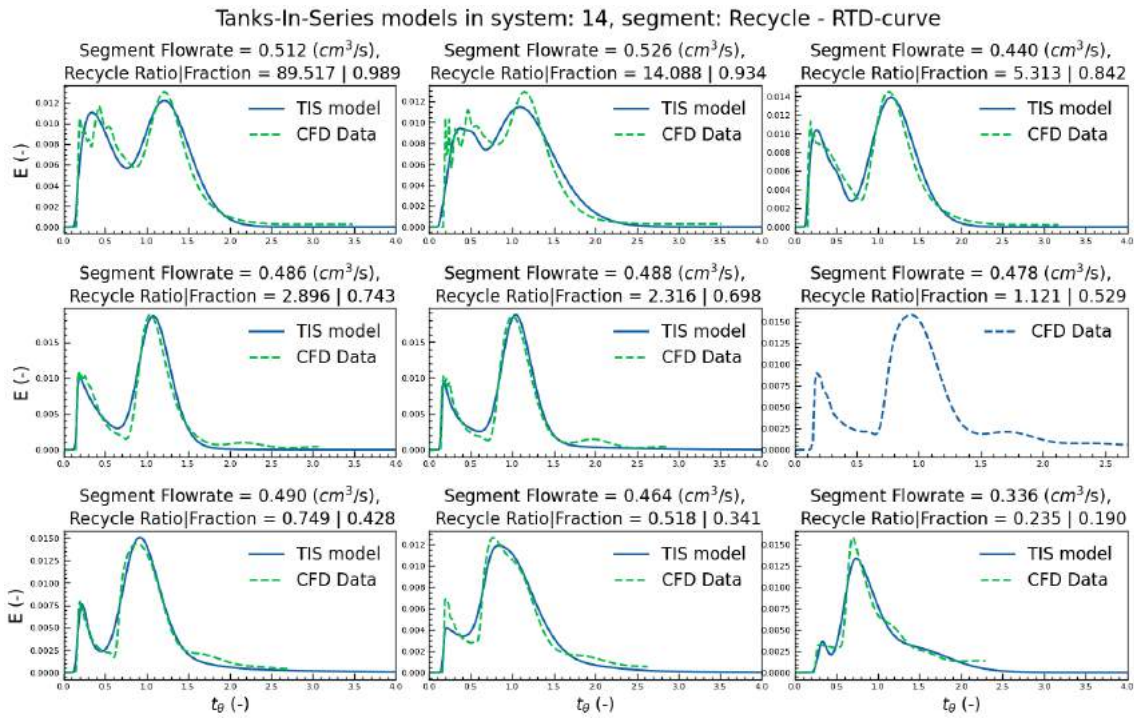


Figure E30: Recycle segment RTD curves from flowrates in system 14 and their respective determined Tanks-In-Series compartment model

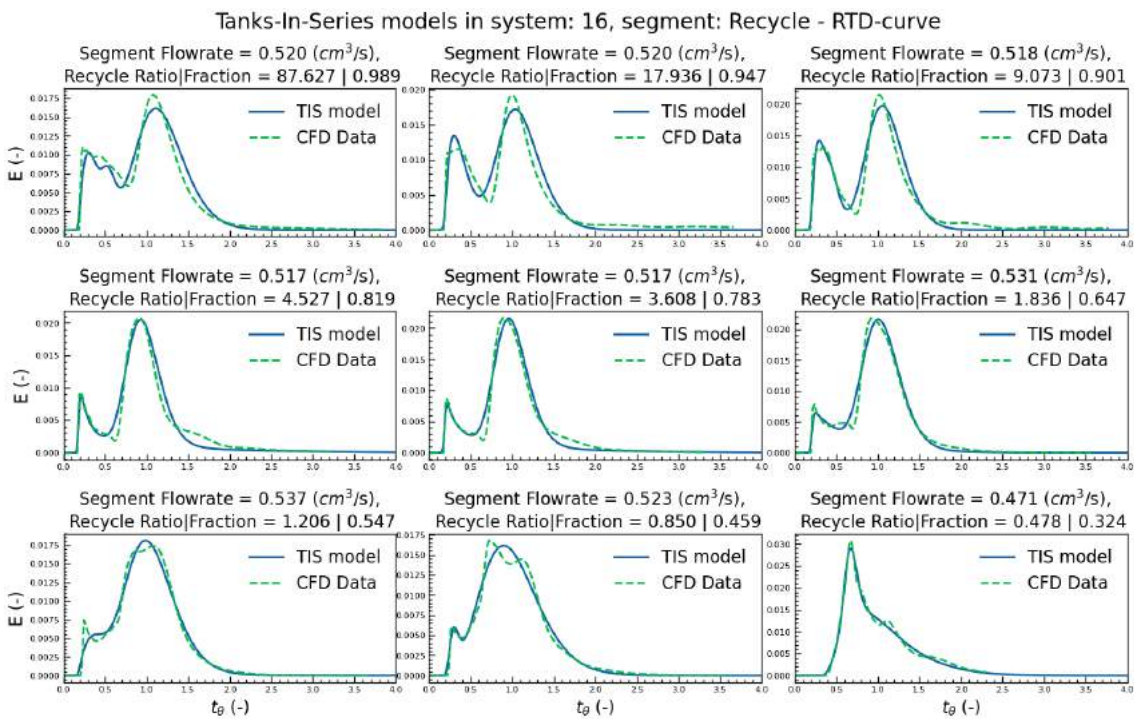


Figure E31: Recycle segment RTD curves from flowrates in system 16 and their respective determined Tanks-In-Series compartment model

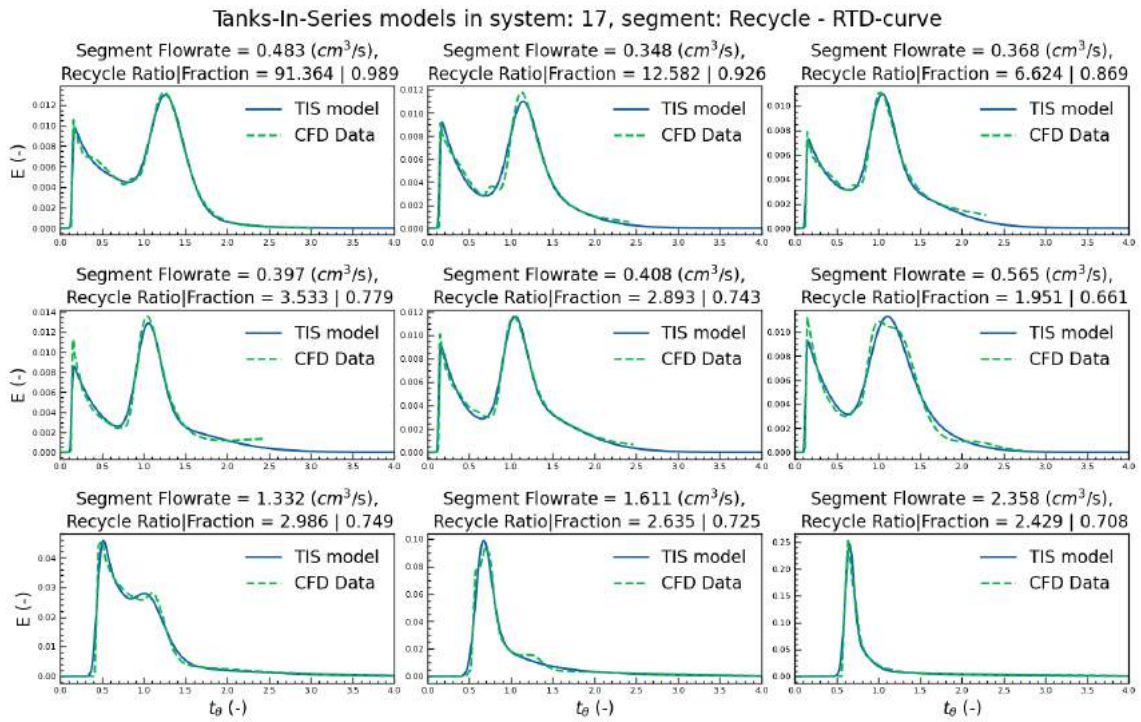


Figure E32: Recycle segment RTD curves from flowrates in system 17 and their respective determined Tanks-In-Series compartment model

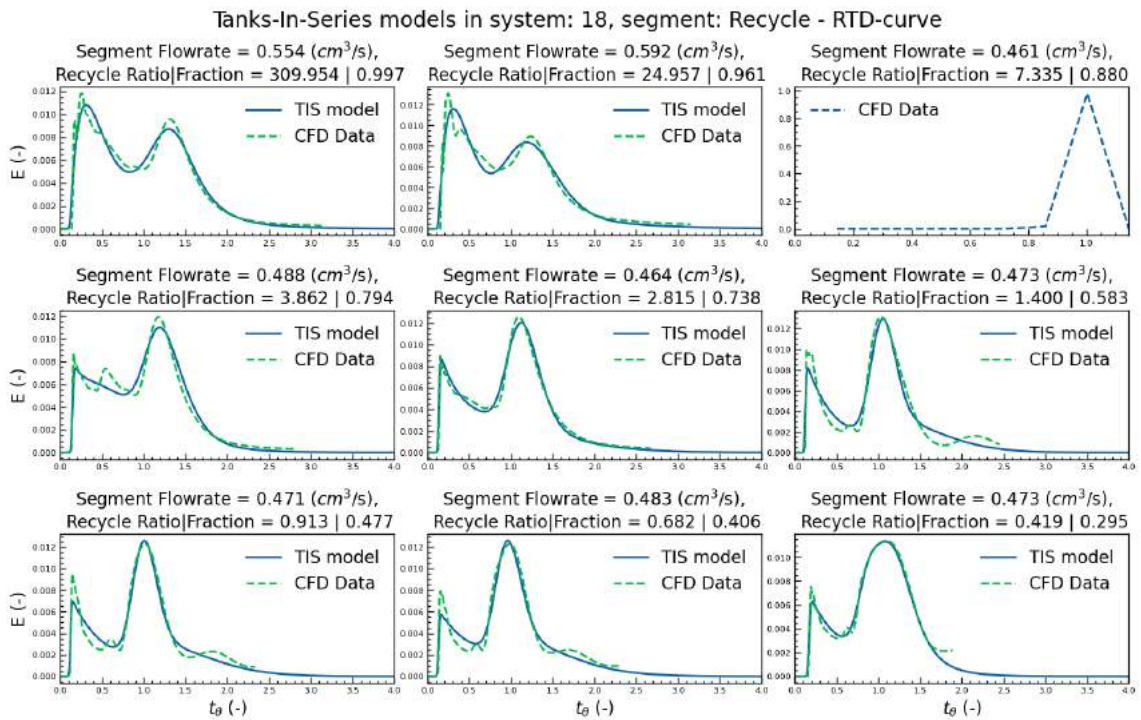


Figure E33: Vessel segment RTD curves from flowrates in system 18 and their respective determined Tanks-In-Series compartment model